



Universitat Autònoma de Barcelona

**ADVERTIMENT.** L'accés als continguts d'aquesta tesi queda condicionat a l'acceptació de les condicions d'ús establertes per la següent llicència Creative Commons:  [http://cat.creativecommons.org/?page\\_id=184](http://cat.creativecommons.org/?page_id=184)

**ADVERTENCIA.** El acceso a los contenidos de esta tesis queda condicionado a la aceptación de las condiciones de uso establecidas por la siguiente licencia Creative Commons:  <http://es.creativecommons.org/blog/licencias/>

**WARNING.** The access to the contents of this doctoral thesis it is limited to the acceptance of the use conditions set by the following Creative Commons license:  <https://creativecommons.org/licenses/?lang=en>



Universitat Autònoma  
de Barcelona

# **Confining Reactions in a Droplet: Synthesis of MOFs, COFs and Composites using Spray-Drying**

**Luis Carlos Garzón Tovar**

Doctoral Thesis  
PhD in Chemistry

Supervisors  
Prof. Dr. Daniel Maspoch and Dr. Inhar Imaz

Tutor  
Dr. Félix Busqué

Catalan Institute of Nanoscience and Nanotechnology  
Department of Chemistry-Faculty of Science

2018



Memòria presentada per aspirar al Grau de Doctor per Luis Carlos Garzón Tovar

Luis Carlos Garzón Tovar

Vist i plau

Prof. Dr. Daniel Maspoch

ICREA Research Professor & Group Leader

Supramolecular NanoChemistry & Materials Group

Catalan Institute of Nanoscience and Nanotechnology

Dr. Inhar Imaz

Senior Researcher & Division Coordinator

Supramolecular NanoChemistry & Materials Group

Catalan Institute of Nanoscience and Nanotechnology

Dr. Félix Busqué Sánchez

Professor Agregat

Departament de Química

Universitat Autònoma de Barcelona

Bellaterra, 14 de Junio de 2018



## Table of Contents

<i>Table of contents</i> .....	<i>i</i>
<i>Abstract</i> .....	<i>v</i>
<i>Resumen</i> .....	<i>vii</i>
<i>Acknowledgments</i> .....	<i>ix</i>
<b>Chapter 1: Introduction to Metal-Organic Frameworks and Covalent-Organic Frameworks: From Design Principles to Synthetic Methodologies</b> .....	<b>1</b>
1.1 Introduction.....	3
1.2 Metal-Organic Frameworks.....	4
1.2.1 Historical Overview: From Robson to MOF-5.....	5
1.2.2 Secondary Building Units (SBUs) and Reticular Chemistry.....	11
1.3 Covalent Organic Frameworks.....	14
1.3.1 Structural diversity.....	15
1.4 Applications of MOFs and COFs.....	18
1.4.1 Gas storage.....	18
1.4.1.1 CO <sub>2</sub> sequestration.....	19
1.4.1.2 CH <sub>4</sub> adsorption.....	22
1.4.1.3 H <sub>2</sub> adsorption.....	24
1.4.2 Catalysis.....	26
1.4.3 Water adsorption applications.....	29
1.4.3.1 Water harvesting applications.....	30
1.4.3.2 Humidity control.....	33
1.4.3.3 Adsorption Heat Transformation Applications.....	34
1.5 Synthesis of MOFs and COFs towards their industrial exploitation.....	37
1.5.1 Electrochemical synthesis.....	38
1.5.2 Mechanochemical synthesis.....	41
1.5.2.1 Solvent-Free Grinding Approach.....	41
1.5.2.2 Liquid-Assisted Grinding (LAG) Approach.....	43
1.5.2.3 Ion-and Liquid Assisted Grinding (ILAG).....	44
1.5.3 Flow Synthesis.....	45
1.5.4 Spray-Drying Technique.....	47
1.5.4.1 Synthesis of MOFs by Spray-Drying.....	49

1.6 References .....	53
<b>Chapter 2: Objectives .....</b>	<b>59</b>
<b>Chapter 3: Synthesis of Microspherical High-Nuclearity MOFs by Spray-Drying Continuous-Flow Method .....</b>	<b>63</b>
3.1 Introduction.....	65
3.2 Results and Discussion .....	67
3.2.1 Synthesis of UiO-66.....	67
3.2.2 Isoreticular synthesis of UiO-66 series.....	76
3.2.3 Synthesis of Fe-BTC/MIL-100 and $[\text{Ni}_8(\text{OH})_4(\text{H}_2\text{O})_2(\text{L})_6]_n$ .....	78
3.2.4 Synthesis of MTV-MOFs.....	80
3.3 Conclusions.....	83
3.4 Experimental Section.....	83
3.5 References.....	87
<b>Chapter 4: Continuous One-Step Synthesis of Porous M-XF<sub>6</sub>-based Metal- Organic and Hydrogen-Bonded Frameworks .....</b>	<b>89</b>
4.1 Introduction.....	91
4.2 Results and Discussion .....	93
4.2.1 Synthesis and characterization of SIFSIX-3-M materials.....	93
4.2.1.1 Stability of SIFSIX-3-M materials in different media.....	95
4.2.2 Reticular chemistry: organic ligand and anionic pillar tuning.....	98
4.2.2.1 Synthesis and characterization of SIFSIX-1-Zn.....	98
4.2.2.2 Synthesis and characterization of TIFSIX-1-Cu.....	100
4.2.3 Synthesis and characterization of supramolecular open material.....	101
4.3 Conclusions.....	103
4.4 Experimental Section.....	104
4.5 References.....	108
<b>Chapter 5: Composite Salt in Porous Metal-Organic Frameworks for Adsorption Heat Transformation.....</b>	<b>111</b>
5.1 Introduction.....	113
5.2 Results and Discussion .....	115

5.2.1 Continuous-flow spray-drying synthesis .....	115
5.2.2 Water sorption properties .....	118
5.2.3 Tuning the composition of CaCl <sub>2</sub> .....	120
5.2.4 Synthesis of LiCl@UiO-66 and CaCl <sub>2</sub> @UiO-66-NH <sub>2</sub> composites .....	123
5.2.5 Thermal batteries application .....	125
5.2.6 Adsorption chillers application.....	127
5.3 Conclusions .....	132
5.4 Experimental Section .....	133
5.5 References .....	136
<b>Chapter 6: Spray-Drying for making Covalent Chemistry: Post-Synthetic Modification of Metal-Organic Frameworks .....</b>	<b>139</b>
6.1 Introduction .....	141
6.2 Results and Discussion .....	143
6.2.1 Organic Schiff-base condensation reactions conducted via spray-drying .	143
6.2.2 PSM of UiO-66-NH <sub>2</sub> .....	146
6.2.3 PSM of ZIF-90 .....	151
6.2.4 PSM of ZIF-90 with a diamine molecule .....	158
6.3 Conclusions .....	161
6.4 Experimental Section .....	162
6.5 References .....	170
<b>Chapter 7: Spray Drying for Making Covalent Chemistry II: Synthesis of Covalent–Organic Framework Superstructures and related Composites ....</b>	<b>173</b>
7.1 Introduction .....	175
7.2 Results and Discussion .....	176
7.2.1 Synthesis of COF-TAPB-BTCA .....	176
7.2.2 Synthesis of COF-LZU1 and COF-TAPB-PDA.....	180
7.2.3 Synthesis of COF-based Composites .....	183
7.2.3.1 Synthesis of Rose-bengal@COF-TAPB-BTCA.....	183
7.2.3.2 Synthesis of Fe <sub>3</sub> O <sub>4</sub> @COF-TAPB-BTCA.....	185
7.3 Conclusions .....	187
7.4 Experimental Section .....	187

7.5 References.....	193
<b>Conclusions .....</b>	<b>195</b>
<b>Glossary .....</b>	<b>201</b>
Acronyms.....	203
<b>Annex 1.....</b>	<b>211</b>
List of Publications.....	213
List of Patents.....	297
<b>Annex 2.....</b>	<b>299</b>

## Abstract

The present PhD Thesis has been dedicated to the study and implementation of the spray-drying technique as a versatile and general method for the synthesis of metal-organic frameworks (MOFs), covalent-organic frameworks (COFs) and composite materials.

In the first Chapter, we review the state of the art in the field of these porous materials, including the antecedents that gave rise to the origin of these materials. A brief introduction to the most relevant concepts for the design of these materials and the main applications is given. Additionally, we pay special attention to the current methodologies that are used for synthesizing these materials, with the aim of placing the reader in the context of this thesis.

In Chapter 2, the general and specific objectives of this Thesis are introduced.

Chapter 3 describes a new methodology based on coupling two processes — spray-drying and continuous flow— for continuous synthesis of MOFs assembled from high-nuclearity secondary building units (SBUs). The impact of the main experimental parameters on the synthesis of the material known as UiO-66 is studied. Finally, the versatility and generality of this method have been proven by synthesizing different high-nuclearity MOFs.

In Chapter 4, the use of the spray-drying technique has been extended to the synthesis of other families of MOFs. We show that this methodology can be used to synthesize materials based on another type of coordination beyond the metal-carboxylate coordination. In this sense, we present the synthesis of the family known as SIFSIX-3-M, which are obtained from the coordination of metals with nitrogen-donor ligands and anionic pillars. Additionally, for the first time, the synthesis of porous materials based on hydrogen bonds is presented.

Chapter 5 demonstrates that the spray-drying-continuous flow method can be used not only to synthesize MOF superstructures but also to incorporate functional species, thereby providing a new route for the synthesis of MOF-based composites. Following this approach, we show how UiO-66 superstructures can encapsulate  $\text{CaCl}_2$  and  $\text{LiCl}$  to form functional composite materials. Here, we demonstrate that the unique properties arising from this assembly can be exploited for applications such as thermal batteries and cooling systems.

In Chapter 6, we extend the use of spray-drying technique to covalent chemistry. To this end, we show that different imines can be synthesized from Schiff-base condensation reactions between discrete aldehydes and amines using the spray-drying. We also show that this chemistry can be extended to post-synthetically modify MOFs. For example, we show the post-synthetic modification of two MOFs, the amine-terminated UiO-66- $\text{NH}_2$  and the aldehyde-terminated ZIF-90. Moreover, we demonstrate that the spray-drying can be used to post-synthetically cross-link the aldehyde groups of ZIF-90 using a diamine molecule.

Chapter 7 shows that the Schiff-base condensation reactions can be extended to the synthesis of COFs. Thus, we prove that spherical superstructures made from the assembly of imine-based COF nanocrystals can be obtained by combining the spray-drying technique with a dynamic covalent chemistry process. In addition, we show that this methodology enables the integration of other functional materials such as dyes and magnetic nanoparticles into these superstructures forming COF-based composites.

## Resumen

La presente Tesis Doctoral se ha dedicado al estudio e implementación de la técnica de secado por pulverización como un método versátil y general para la síntesis de redes metal-orgánicas (MOFs, por sus siglas en inglés), redes orgánicas covalentes (COFs, por sus siglas en inglés) y materiales compuestos.

En el Capítulo 1, se presenta una revisión bibliográfica del estado del arte en el campo de estos materiales porosos. Se describen los antecedentes que dieron lugar al origen de estos materiales, una breve introducción a los conceptos más relevantes para el diseño de estos materiales y las principales aplicaciones. Adicionalmente, se hace especial énfasis en las diferentes metodologías de síntesis de estos materiales con el objetivo de situar al lector en el contexto de la presente Tesis.

En el Capítulo 2, se introduce el objetivo general y específicos de la Tesis.

En el Capítulo 3, se presenta un nuevo método para la síntesis de MOFs basados en unidades de construcción secundarias complejas empleando el secado por atomización acoplado a un sistema de flujo-continuo. Además, se estudian los principales parámetros experimentales que influyen en la síntesis del material conocido como UiO-66. Finalmente, se presenta la síntesis de diferentes MOFs con el objetivo de validar la generalidad de esta nueva metodología.

En el Capítulo 4 se extiende el uso de la técnica de secado por pulverización en la síntesis de nuevas familias de MOFs. En particular, se muestra que esta metodología puede ser usada para sintetizar materiales basados en otro tipo de coordinación (más allá de metal-carboxilato). De esta manera, se presenta la síntesis de la familia conocida como SIFSIX-3-M, la cual se obtienen a partir de la coordinación de metales con ligandos nitrogenados y pilares aniónicos. Adicionalmente, se presenta por primera vez la síntesis de materiales porosos basados en puentes de hidrógeno.

En el Capítulo 5 se demuestra que el método de secado por atomización acoplado a un sistema de flujo-continuo puede ser usado no solo para sintetizar MOFs, sino también para incorporar especies funcionales. De este modo, se introduce una nueva ruta para la síntesis de materiales compuestos. En particular, se demuestra que las superestructuras de UiO-66 pueden encapsular  $\text{CaCl}_2$  y  $\text{LiCl}$  para así obtener materiales composites funcionales. Finalmente, se demuestra que las nuevas propiedades derivadas de este ensamblaje pueden ser explotadas para aplicaciones, tales como baterías térmicas y sistemas de refrigeración.

En el Capítulo 6, se extiende el uso de la técnica de secado por pulverización a la química covalente. De esta manera, se muestra que diferentes iminas pueden ser sintetizadas a partir de reacciones de condensación entre aldehídos y aminas. Además, también demostramos que los MOFs pueden ser fácilmente modificados. De esta manera, usando la técnica de secado por pulverización, mostramos la modificación post-sintética de dos MOFs, el amino-terminal UiO-66-NH<sub>2</sub> y el aldehído-terminal ZIF-90. Además, también se demuestra que esta metodología puede ser usada para modificar de manera cruzada los grupos aldehídos del ZIF-90 usando una diamina.

El capítulo 7 muestra que las reacciones de condensación pueden extenderse para la síntesis de COFs. Así, demostramos que superestructuras esféricas creadas a partir del ensamblaje de nanocristales de COF pueden ser obtenidas en un proceso de dos pasos, que incluye el secado por pulverización seguido de una transformación amorfo-cristalino del material. Además, se demuestra como las superestructuras resultantes pueden ser utilizadas para encapsular diferentes materiales, tales como moléculas fluorescentes y nanopartículas magnéticas.

## Acknowledgments

En primer lugar quiero agradecer a mis dos excelentes directores, Prof. Dr. Daniel MasPOCH y Dr. Inhar Imaz, quienes me brindaron la valiosa oportunidad de realizar esta Tesis bajo su dirección y de los cuales he aprendido tanto. En especial, quiero agradecerles por su apoyo constante, exigencia, rigurosidad, capacidad de trabajo, dedicación y paciencia durante estos años. Sin lugar a dudas, sin su guía el desarrollo de esta Tesis no hubiera sido el mismo.

Quiero agradecer a todos los investigadores que han participado y colaborado a lo largo de esta Tesis. A los doctores Arnau Carné, Carlos Carbonell, Vincent GuillerM, Sabina Rodriguez, Javier Pérez y Mary Cano. En particular, quiero agradecer al Dr. Arnau Carné quien me introdujo en el mundo del Spray-Drying y quien me guio en las etapas iniciales de este doctorado. A la Dra. Sabina Rodriguez por toda su colaboración, apoyo y amistad en estos años, como también por todos los consejos científicos y no tan científicos. Al Dr. Javier Pérez por toda su colaboración desde el primer momento en que llego a NanoUp, por las infinitas discusiones de nuestros proyectos y las interminables horas que pasamos esperando el step o que aumentara el water uptake en el DVS, además de su amistad. También quiero agradecer a todos los técnicos por los diferentes análisis. En particular, al servicio de NMR en estado sólido de la UAB y a Marcos y al servicio de microscopia del ICN2.

Como no agradecer a todos mis compañeros y excompañeros de NanoUp con quienes compartí durante todo este proceso e hicieron que fuera mucho más agradable y de quienes me llevo un recuerdo muy especial: Claudia, Civan, Heng, Nereida, Sonia, Marta, Javier T, Thais, Ram y Kyriakos. A mis compañeros de oficina con quienes siempre hubo espacio para las discusiones y no solo de trabajo: Amiralí, Ceren, Jorge, Gerard, Blanca, Anna, Yang y Cristina. También quiero agradecer la valiosa amistad fuera de las fronteras del ICN2 de amigos como Jordi, Abraham, Lau, Ivan y Xavi.

Por supuesto quiero agradecer a mis amigos, en especial al Colombian Team, Oscar, Cristina, Jackeline quien me enseñó todo de Barcelona desde que llegue al ICN2 y a Javi por estar en momentos difíciles y estar dispuesto siempre a escucharme, por las caminatas a Cerdanyola que tanto extrañare y sobre todo por su valiosa amistad.

A Allison, quien ha sido parte fundamental de mi vida. Gracias por tu apoyo desde el primer momento en que decidí emprender el viaje hacia Barcelona. Como no agradecerte que hayas decidido dejarlo todo y venir a estar conmigo en esta etapa final del doctorado. Gracias por tu aliento, comprensión, paciencia, motivación y sobre todo porque has hecho que esta etapa fuera mucho más fácil. Y sobre todo por seguir apoyándome en el nuevo ciclo que empieza y que compartiremos juntos.

Finalmente, quiero agradecer a mi madre por su apoyo y entrega incondicional en todos los instantes de mi vida, por ser esa referencia en el camino y fuente de motivación diaria. Siempre con las palabras adecuadas en los momentos más difíciles de este doctorado. Gracias por tus enseñanzas y por hacerme creer que era posible y darme el empujón que necesitaba para venir. Simplemente, gracias por todo.

# Chapter 1

---

**Introduction to Metal-Organic  
Frameworks and Covalent-Organic  
Frameworks: From Design Principles to  
Synthetic Methodologies**



## 1.1 Introduction

In Chemistry, it is widely recognized that the properties of the materials are determined by their structures; meaning that “function follows form”. Understanding this “form” can then lead to accurately predict experimental and physical outcomes. As suggested in his famous citation “...I can hardly doubt that when we have some control of the arrangement of things on a small scale we will get an enormously greater range of possible properties that substances can have, and of different things that we can do”, Feynman understood that knowing and controlling structural outcomes would lead to a variety of new properties and to an array of methods by which scientists could manipulate forms to create highly specific functions.

In this sense, crystalline porous materials clearly represent a perfect example of the axiom “function follows form” (Figure 1.1). The distribution of sizes, shapes and volumes of the channels/cavities in these porous materials directly relates to their performance in a particular application. For example, zeolites with uniform micropores can separate molecules based on their size by selectively adsorbing a small molecule from a mixture containing molecules of different sizes. In addition, the nature of the building blocks of the frameworks can be important. For instance, hydrophobic molecular sieves built up from pure silica can absorb organic components from water, whereas hydrophilic porous materials can adsorb water from organic solvents. Thus, it is not surprising that the traditional applications of crystalline porous materials, such as ion exchange, adsorption, separation and catalysis, strongly depend on the nature and “form” of the frameworks.<sup>1</sup>

Among crystalline porous materials, Metal-Organic Frameworks (MOFs) and Covalent-Organic Frameworks (COFs) exemplify the manner in which chemistry is practiced to “dial in” almost any function in a porous material by molecular-level control over structure. Thus, the function can be predicted by understanding the relationship between structure and property. In these sense, the

structural/compositional flexibility and the uniformity in pore size and shape confer MOFs/COFs with myriad physical and chemical properties, making them good candidates for multiple applications, including gas storage and separation, catalysis, sensing, and drug delivery, among many others.

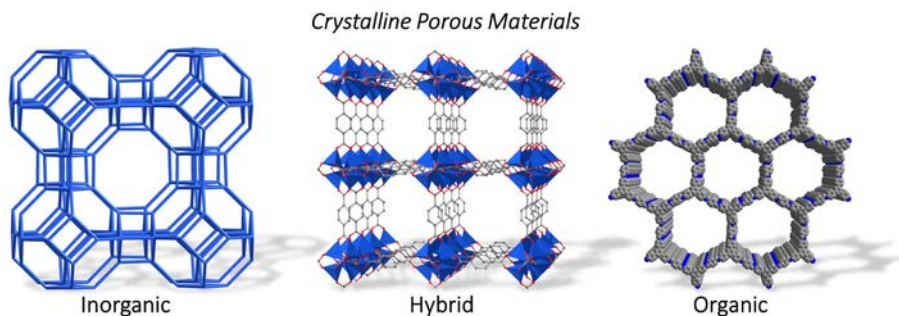


**Figure 1.1.** Classes of crystalline porous materials according to the nature of the building blocks forming the frameworks

## 1.2 Metal-Organic Frameworks

Metal-Organic Frameworks (MOFs) (also known as Porous Coordination Polymers (PCPs)) are a class of porous crystalline materials, where one-(1D), two-(2D) or three-dimensional (3D) frameworks are formed from metal ions or clusters and organic molecules linked through coordination bonds. According with the International Union of Pure and Applied Chemistry (IUPAC), a MOF can be defined as: “*a coordination network with organic ligands containing potential voids*”.<sup>2</sup> In fact, the presence of “*voids*” confer them high porosity, making MOFs as one of the most attractive porous materials today for multiple applications. The high interest of the scientific community in this field can be illustrated with the *ca.* 54000 crystal structures of MOFs deposited in the Cambridge Structural Database (CSD) over the last 20 years.<sup>3</sup>

### 1.2.1 Historical Overview: From Robson to MOF-5

The history of MOFs can be traced back to the work of Robson and Hoskins in 1989. They described the first 3D framework based on tetrahedral Cu(I) centers connected through the tetrahedral ligand 4,4',4'',4'''-tetracyanotetraphenylmethane (tctpm). The infinite framework adopts a diamond-like lattice with large tetragonally adamantane-like cavities (Figure 1.2).<sup>4</sup>

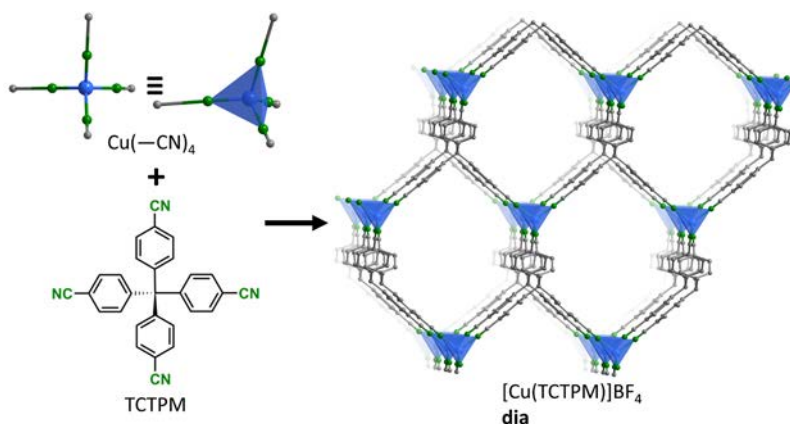


**Figure 1.2.** Diamond-like framework consisting of tetrahedral Cu(I) units linked together by tetrahedral organic linkers. Colour code: Cu (blue), C (grey) and N (green).

One year later, Robson and co-workers provided an important basis for the design and synthesis of these compounds by introducing the concept of building unit. They proposed that frameworks constructed from tetrahedral building metal units connected by cyano-based organic ligands might adopt diamond-like structures.<sup>5</sup> Based on this geometric design principle many diamond-like structures could indeed be synthesized. Later, they expanded this concept by proposing that different 3D networks could be constructed by selecting the appropriate geometry of the building units. For example, nets structurally related to platinum (II) sulphide (PtS) should be obtained from a mixture of square-planar and tetrahedral (1:1) building units. They also proposed that  $\alpha$ -polonium ( $\alpha$ -Po)-nets should be constructed from octahedral centers. Following this strategy, in 1994, a PtS-type framework was synthesized from a

tetracyano-porphyrin as the square-planar building and Cu(I) as the tetrahedral center.<sup>6</sup> In addition, they suggested that these 3D networks can offer remarkable features such as: (i) ion-exchange properties due to the diffusion of ionic or molecular species throughout the cavities; (ii) introduction of catalytic centers by the functionalization of the ligands; and (iii) low density materials with large cavities and thermal and chemical stability by devise of ligands with sufficient rigidity.<sup>5</sup>

The contribution of Robson opened a new field in coordination chemistry, not only in the design and synthesis of open-framework materials —given the endless possibilities of combinations between metal ions and organic ligands— but also in the exploration of the intriguing properties that they could exhibit (*vide supra*). In this sense, Fujita and co-workers explored, for the first time, the heterogeneous catalysis of a two-dimensional square network material assembled by the coordination of 4,4'-bipyridine (4,4'-bpy) and  $\text{Cd}(\text{NO}_3)_2$  (Figure 1.3). This 2D-network was catalytically active for the cyanosilylation of aldehydes, being also effective for the separation of *o*-dichlorobenzene from the isomeric mixtures by clathration.<sup>7</sup>

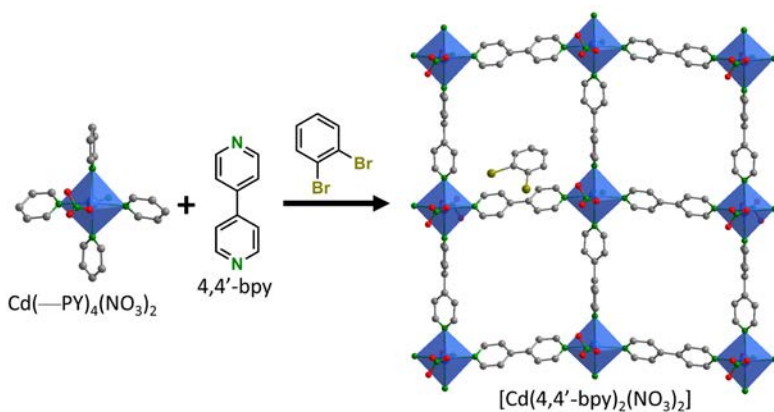


**Figure 1.3.** Structure of  $[\text{Cd}(4,4'\text{-bpy})_2(\text{NO}_3)_2]$ , displaying the clathration of *o*-dibromobenzene in the channels. Colour code: Cd (blue), C (grey) and N (green).

The potential of the ditopic, rigid and linear 4,4'-bpy as a building block for the assembly of MOFs was then demonstrated by Prof. Yaghi and co-workers in 1995. They

synthesized a diamond-like structure with formula  $\text{Cu}(4,4'\text{-bpy})_{1.5}(\text{NO}_3)$  by the coordination of trigonal planar  $\text{Cu}(\text{I})$  centers and 4,4'-bpy. This six-interpenetrated framework contained two rectangular channels with dimensions of  $8 \times 6 \text{ \AA}$  and  $4 \times 5 \text{ \AA}$ , which are filled by charge-balancing nitrate anions (Figure 1.4). In this contribution, Prof. Yaghi further demonstrated that hydrothermal synthesis was a viable methodology for the synthesis of such frameworks, naming them as Metal-Organic Frameworks for the first time.<sup>8</sup>

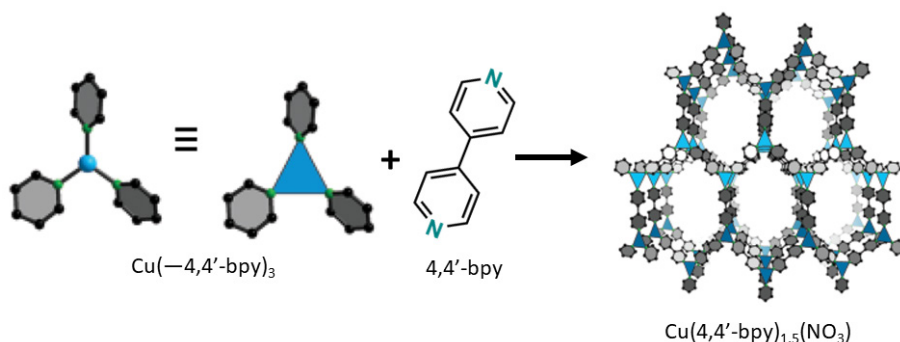


**Figure 1.4.** Representation of the framework  $\text{Cu}(4,4'\text{-bpy})_{1.5}(\text{NO}_3)$  built up from 4,4'-bpy and  $\text{Cu}(\text{I})$  building units. Colour code: Cu (blue), C (black) and N (green).

At the same time, Zaworotko *et al.* synthesized the first example of a neutral and non-interpenetrated 3D framework. In this solid, octahedral  $\text{Zn}(\text{II})$  ions were coordinated with four 4,4'-bpy ligands to form a square grid nets that are axially connected by the anionic  $\text{SiF}_6^{2-}$  units. This connectivity resulted in a structure with large square channels with pore size of  $8 \times 8 \text{ \AA}$  and high potential porosity (50 % of the total unit cell volume; Figure 1.5). However, this porosity could not be exploited because the structure collapsed after guest removal from its cavities.<sup>9</sup>

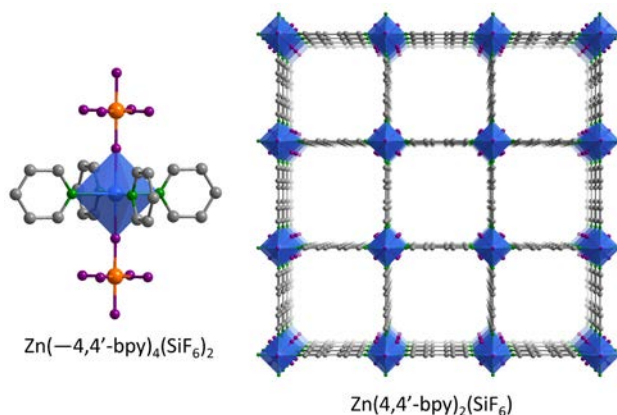


**Figure 1.5.** Representation of the MOF  $\text{Zn}(4,4'\text{-bpy})_2(\text{SiF}_6)$  (right) and their Zn(II) building unit (left). Colour code: Zn (blue), C (grey), N (green), Si (orange) and F (purple).

In general, this first generation of MOFs was characterized for their lack of permanent porosity (stability in the fully evacuated state), related to the flexible and fragile nature of the coordination bonds between monodentate N-donor ligands and single metal cations. In these initial examples, MOFs showed flexible structures that irreversibly collapse upon removal of guest molecules. In fact, it was not until 1997 when Prof. Kitagawa and co-workers showed the first evidence that MOFs could exhibit permanent porosity. They studied the gas adsorption properties of a T-shaped structure with formula  $\text{Co}_2(4,4'\text{-bpy})_3(\text{NO}_3)_4$ , showing that this solid could adsorb  $\text{CH}_4$ ,  $\text{N}_2$  and  $\text{O}_2$  at 298 K and high pressures (up to 36 atm).<sup>10</sup>

In 1998, a revolutionary strategy was introduced by Prof. Yaghi and co-workers. They proposed the use of carboxylic acids to make robust extended structures, in which their strength arises from the strong electrostatic interactions between metal ions and carboxylate functions. Moreover, the different modes of coordination of the carboxylate ligands permit bridging and/or chelation of metal cations to produce rigid and geometrically defined metal-carboxyl clusters. In addition, neutral frameworks could be obtained due to the presence of carboxylate groups, precluding the need for extra counterions that usually occupy the channels.<sup>11</sup> Following this strategy, Yaghi and co-workers reported the first permanently microporous framework, named MOF-2,

with formula  $\text{Zn}(\text{BDC})(\text{DMF})(\text{H}_2\text{O})$  (BDC = 1,4-benzenedicarboxylate). In this structure, two square pyramidal  $\text{Zn}^{2+}$  ions are coordinated by the carboxylate groups (in a bismonodentate fashion) of four BDC ligands and by two water molecules in the axial position, forming a dinuclear Zn-carboxylate cluster (also known, as square paddlewheel). The resulting 2D grid networks are held together along the  $a$ -axis by hydrogen bonds between the axial water ligands of one layer and the oxygen atoms of the carboxylate of the adjacent layer (Figure 1.6).  $\text{N}_2$  adsorption studies at 77 K demonstrated that the evacuated Zn-(BDC) framework is microporous with a Langmuir apparent surface area of  $270 \text{ m}^2 \text{ g}^{-1}$  and a micropore volume of  $0.094 \text{ cm}^3 \text{ g}^{-1}$ .<sup>12</sup>

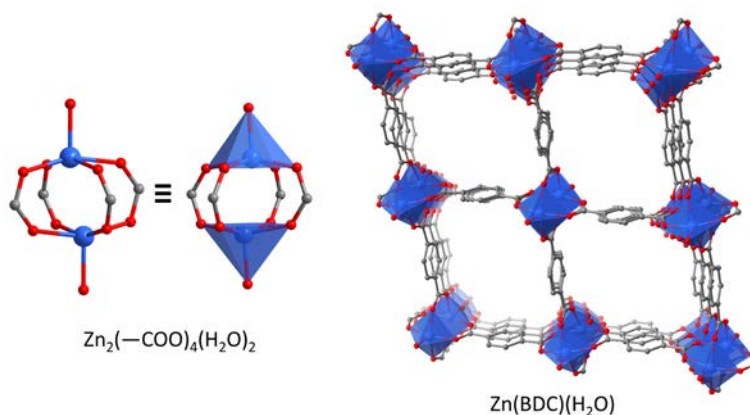


**Figure 1.6.** Structure of MOF-2 (right) and their Zn-building unit (left). Colour code: Zn (blue), C (grey) and O (red).

The publication of this MOF was very important for the MOF field as it showed that the generation of rigid clusters with fixed geometry, rather than individual ions, was ideal building blocks for the formation of robust frameworks. This led to the design of a second generation of MOFs based on this paddlewheel unit and other carboxylate-based clusters; most of them showing permanent porosity and stability even after guest removal from its pores.<sup>13</sup>

Soon thereafter, in 1999, two key microporous MOFs were synthesized following this latter strategy. The first of these MOFs known as HKUST-1 (HKUST =

Hong Kong University of Science and Technology) was obtained from the assembly of Cu(II)-paddle wheel clusters ( $\text{Cu}_2(-\text{COO})_4(\text{H}_2\text{O})_2$ , similar to the one of MOF-2) and benzene-1,3,5-tricarboxylic acid (BTC) (Figure 1.7). The neutral 3D framework with formula  $[\text{Cu}_3(\text{BTC})_2(\text{H}_2\text{O})_2]_n$  revealed the presence of around 1nm-size channels and a Brunauer-Emmett-Teller (BET) surface area of  $692 \text{ m}^2 \text{ g}^{-1}$  (recent  $\text{N}_2$  adsorption measurements have yielded BET surface areas of  $1800 \text{ m}^2 \text{ g}^{-1}$  for this MOF)<sup>14</sup>, comparable with most zeolites.<sup>15</sup>

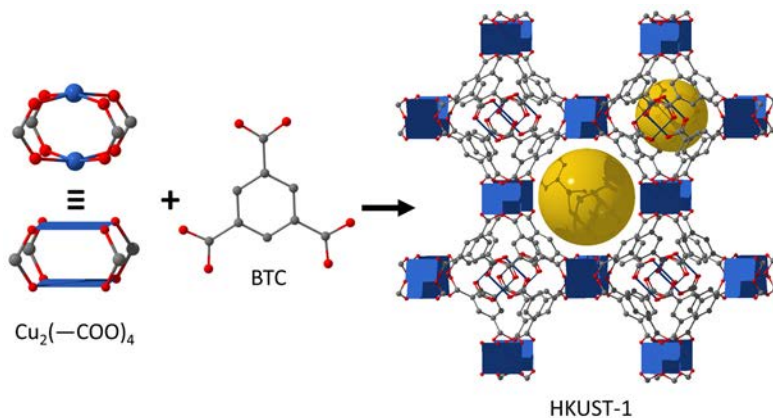


**Figure 1.7.** Representation of HKUST-1 obtained from the assembly of Cu(II)-paddle wheel clusters ( $\text{Cu}_2(-\text{COO})_4$ ) and BTC linkers. Colour code: Cu (blue), C (grey) and O (red).

The second MOF, termed MOF-5, was synthesized using 1,4-benzene dicarboxylic (BDC) and zinc nitrate under solvothermal conditions. Under these conditions, octahedral zinc acetate clusters ( $\text{Zn}_4\text{O}(-\text{COO})_6$ ) were *in situ* formed. These clusters are composed of a tetrahedral central oxide surrounded by four tetrahedrally coordinated  $\text{Zn}^{2+}$  ions ( $\text{Zn}_4\text{O}$ ) that are in turn bound by six bridging carboxylate groups. The extended 3D framework was formed by linking the  $\text{Zn}_4\text{O}(-\text{COO})_6$  units through BDC ligands (Figure 1.8).  $\text{N}_2$  sorption studies at 77 K of the activated framework (after DMF exchange with chloroform) revealed a highly porous material with a very high surface area of  $2900 \text{ m}^2 \text{ g}^{-1}$  and a pore volume of  $0.61 \text{ cm}^3 \text{ cm}^{-3}$ , which were higher than that of most zeolites.<sup>16</sup>

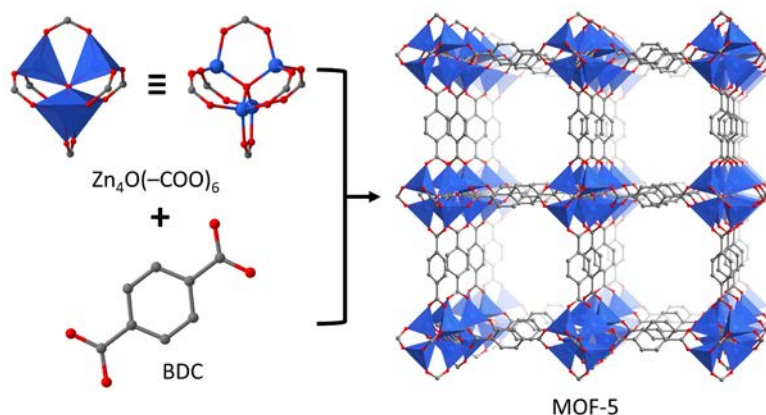


**Figure 1.8.** Representation of MOF-5 obtained from the assembly of  $Zn_4O(-COO)_6$  clusters and BDC ligands.  
Colour code: Zn (blue), C (grey) and O (red).

All these seminal contributions, and especially the discovery of the high and permanent porosity of HKUST-1 and MOF-5, represented a turning-point in the field. Since then, there has been an enormous scientific interest in MOFs due to: (i) the possibility to design robust materials with very high porosities (much larger than the traditional porous materials); and (ii) the structural diversity that MOFs can show based on the endless combinations of metal clusters and organic ligands. In fact, the use of multi-nuclear metal clusters allowed a rapid and explosive expansion in MOFs chemistry that continues until the present.

### 1.2.2 Secondary Building Units (SBUs) and Reticular Chemistry

Because of the exponential growth in this area, there was a need to rationalize the structure of MOFs. To this end, Yaghi and co-workers introduced the concept of Secondary Building Unit (SBU) as a critical design element for understanding and predicting the topology of MOFs. The SBUs are defined as rigid and directional clusters of metal ions linked together by chelating multidentate organic ligands. Thus, these SBUs serve as large rigid vertices that can be connected by rigid organic linkers leading to a vast variety MOFs with structural stability (Figure 1.9).<sup>17-19</sup>

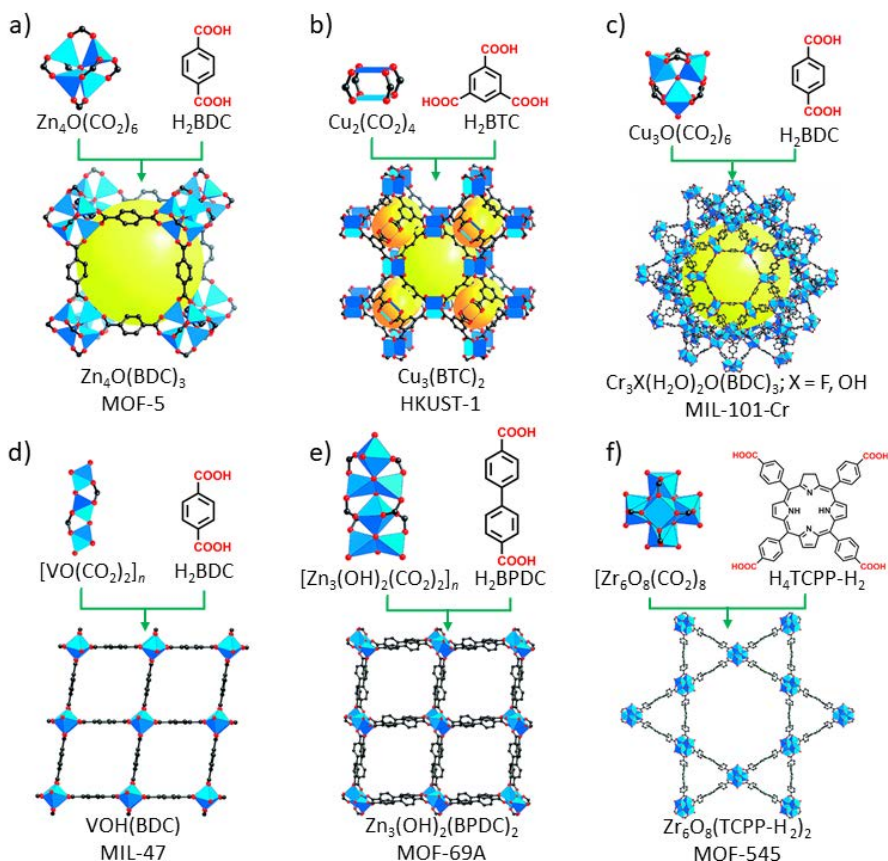
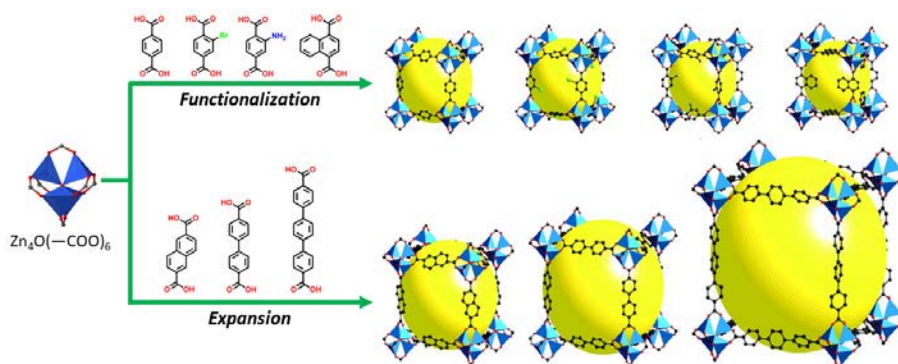


Figure 1.9. Synthesis of MOFs by linking SBUs with organic ligands.<sup>20</sup>

In addition, the SBU approach led to introduce the concept of reticular chemistry, which is nowadays defined as “the chemistry of linking molecular building blocks by strong bonds into crystalline extended structures”.<sup>21</sup> Reticular synthesis is based on the formation of periodic networks in which pore size and functionality could be varied systematically. In practice, for a given structure, increasing the distance between the SBUs (nodes) can be achieved by substitution of the linkers with other linkers of different size (“expansion”), while keeping the same SBU and structural topology. Thus, after identification of the synthetic conditions necessary for the generation of the SBU (*in situ*), tuning the functionalities and dimensions of the network become feasible.<sup>11</sup> The first example of reticular synthesis was reported by

Yaghi and co-workers in which sixteen isorecticular MOFs (IRMOFs) based on MOF-5 were synthesized. In these family of isorecticular MOFs, the expansion of the network was achieved by replacing the BDC linker by longer aromatic dicarboxylates ligands (e.g. naphthalene-2,6-dicarboxylate), increasing the pore size from 3.8 to 28.8 Å (Figure 1.10) without changing the original primitive cubic topology. In addition, the pore functionality was also tuned by replacing the BDC linker by its functionalized version (e.g. Br-BDC, NH<sub>2</sub>-BDC, etc).<sup>22</sup>



**Figure 1.10.** Schematic representation of the IRMOF series obtained through reticular synthesis.

This example clearly illustrates the potential of the SBUs approach and reticular chemistry, which use has permitted to enlarge and enrich the discovery of thousands of MOFs (Figure 1.11).

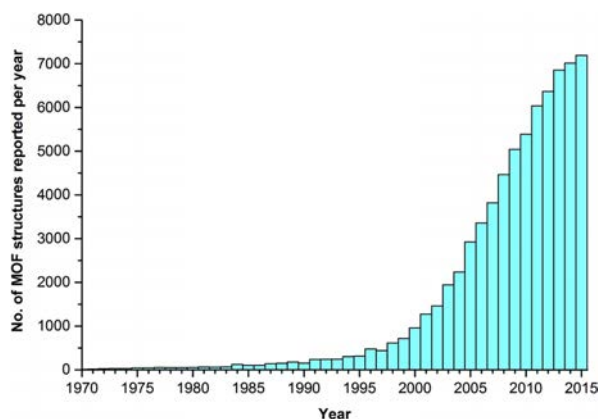


**Figure 1.11.** MOF structures reported in the CSD from 1970 to 2015.<sup>20</sup>

### 1.3 Covalent Organic Frameworks

The principles of reticular chemistry proposed by Yaghi and co-workers were further extrapolated to covalent chemistry, replacing the SBUs to purely organic molecular units. Thus, 2D or 3D crystalline porous organic frameworks (also known as Covalent-Organic Frameworks (COFs)) can be formed from organic building blocks linked by dynamic covalent bonds. As their MOFs counterparts, COFs are characterized by their high porosity, high thermal stability and low mass density.<sup>21,23</sup>

The first COFs were synthesized by Côté *et al.* in 2005. COF-1 was obtained by self-condensation reaction of benzene-1,4-diboronic acid (BDDBA), resulting in a 2D structure consisting of extended layers stacked in staggered form to give hexagonal pores with 15 Å in diameter and a BET surface area of 711 m<sup>2</sup> g<sup>-1</sup> (Figure 1.12).<sup>24</sup> In contrast, COF-5 was obtained by condensation of BDDBA acid and 2,3,6,7,10,11-Hexahydroxytriphenylene (HHTP), in which a 2D structure was formed by the stacking of the layers in an eclipsed fashion, giving a hexagonal array of 1D mesopores of a size of 27 Å in diameter and a BET surface area of 1590 m<sup>2</sup> g<sup>-1</sup>.<sup>24</sup>

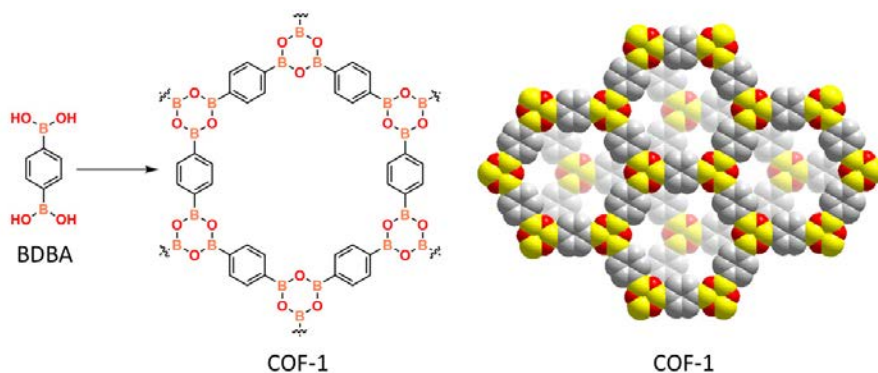


**Figure 1.12.** Schematic representation of the formation of COF-1 (left) and space filling diagram of COF-1 (right).<sup>25</sup>

This seminal contribution paved the way for the design of new COFs based on condensation reactions, including the formation of B–O (boronate, boroxine, and

borosilicate), B–N (borazine) and C–N (triazine, imide, imine and hydrazine) bond linkages.<sup>26</sup> However, it is important to mention that the formation of crystalline extended structures is not always straightforward because of the strong bond energy between the organic building blocks. In fact, amorphous materials (kinetic product) can be readily obtained by the linkage of organic building units due to the irreversibility of the covalent bonds. In order to afford an extended crystalline solid, the formation of linkages should be reversible.<sup>27</sup> In this sense, dynamic covalent chemistry (DCC) leads to carried out reversible chemical reactions under thermodynamic control. Thus, two important aspects should be considered for the synthesis of stable COFs: (i) the use of rigid building blocks containing reactive groups that trigger dynamic covalent bond formation; and (ii) the reaction must occur under conditions in which reversible bond formation is possible (thermodynamic control).<sup>28</sup>

### 1.3.1 Structural diversity

As mentioned above, reversible reactions that are used in the formation of COFs can be classified in terms of the linkages they form. To date, over six linkage types are known, including: (i) B–O (boroxine, boronate ester, borosilicate, and spiroborate); (ii) C=N (imine, hydrazone, squaraine, and azine); (iii) C=N<sub>Ar</sub> (triazine, phenazine and oxazole); (iv) C–N ( $\beta$ -ketoenamine, imide, and amide); (v) C=C (alkene); and (vi) B=N (borazine). These reactions are summarized in Figure 1.13. The most relevant examples are provided below:

*B-O linkages:* Boronate ester-based COFs are formed by the reaction of boronic acids with catechols. For example, the 3D COF-108 was obtained by a condensation reaction between a tetrahedral *tetra*(4-dihydroxyborylphenyl)methane (TBPM) and a triangular HHTP building blocks. This COF exhibited an extremely low density of 0.17 g cm<sup>-1</sup>. Alternatively, boroxine-based COF are obtained by the self-condensation of boronic acids. In this way, COF-103 was prepared by the self-condensation of *tetra*(4-dihydroxyborylphenyl) silane (TBPS). The resulting 3D COF exhibited a high BET surface

area of  $4210 \text{ m}^2 \text{ g}^{-1}$ . However, despite the high porosity and thermal stability of most of these B-O-based COFs, they are unstable due to the decomposition of their boronate or boroxine bonds in the presence of water and protic solvents.<sup>29</sup>

*C=N linkages:* Imine-based COFs (C=N bond) are obtained by the condensation of aldehydes and amines. The chemical stability of the resulting COFs is higher compared with that of boronate ester-based COFs. The first imine-based COF (termed COF-300) was obtained by the reaction between *tetra*(4-aminophenyl)methane (TAM) and terephthalaldehyde (PDA), resulting in a 5-fold interpenetrated framework with a BET surface area of  $1360 \text{ m}^2 \text{ g}^{-1}$ .<sup>30</sup> In another example, Jiang *et al.* reported the synthesis of a 2D COF named TPB-DMTP-COF. This material was obtained by the condensation of 1,3,5-tris-(4-aminophenyl)benzene (TAPB) with dimethoxyterephthalaldehyde (DMTP). This COF was thermally stable up to  $400 \text{ }^\circ\text{C}$  and highly porous, showing a BET surface area of  $2105 \text{ m}^2 \text{ g}^{-1}$ .<sup>31</sup> Similarly, hydrazone based-COFs are formed by the reaction between aldehydes and hydrazide building units. For instance, TFPT-COF was formed from the reaction of 1,3,5-tris-(4-formylphenyl)triazine (TFPT) and 2,5-diethoxy-terephthalohydrazide (DETH). This TFPT-COF shows a layered structure with honeycomb pores (3.8 nm in diameter) and a BET surface area of  $1603 \text{ m}^2 \text{ g}^{-1}$ .<sup>32</sup>

*C-N linkages:* Triazine-based COFs (also known as covalent triazine frameworks) are obtained by condensation of aromatic nitriles at high temperatures and in molten salts. For example, CTF-1 was obtained from the trimerization of 1,4-dicyanobenzene in a  $\text{ZnCl}_2$  melt at  $400 \text{ }^\circ\text{C}$ . The 2D structure, which is isoelectronic with COF-1, showed a surface area of  $791 \text{ m}^2 \text{ g}^{-1}$ .<sup>33</sup>

*C-C linkages:* C-C-based COFs are prepared through the condensation of aldehydes with nitriles. Recently, a 2D COF (termed  $\text{sp}^2\text{c}$ -COF) was made by the reaction between 1,3,6,8-tetrakis(4-formylphenyl)pyrene (TFPPy) and 1,4-phenylenediacetonitrile (PDAN). The 2D structure was formed from stacked layers (3.58 Å separation) and consisted of  $\text{sp}^2$  carbon chains extended along the x and y

directions. The  $sp^2c$ -COF exhibited a BET surface area of  $692 \text{ m}^2 \text{ g}^{-1}$  and a pore size of  $1.88 \text{ nm}$ .<sup>34</sup>

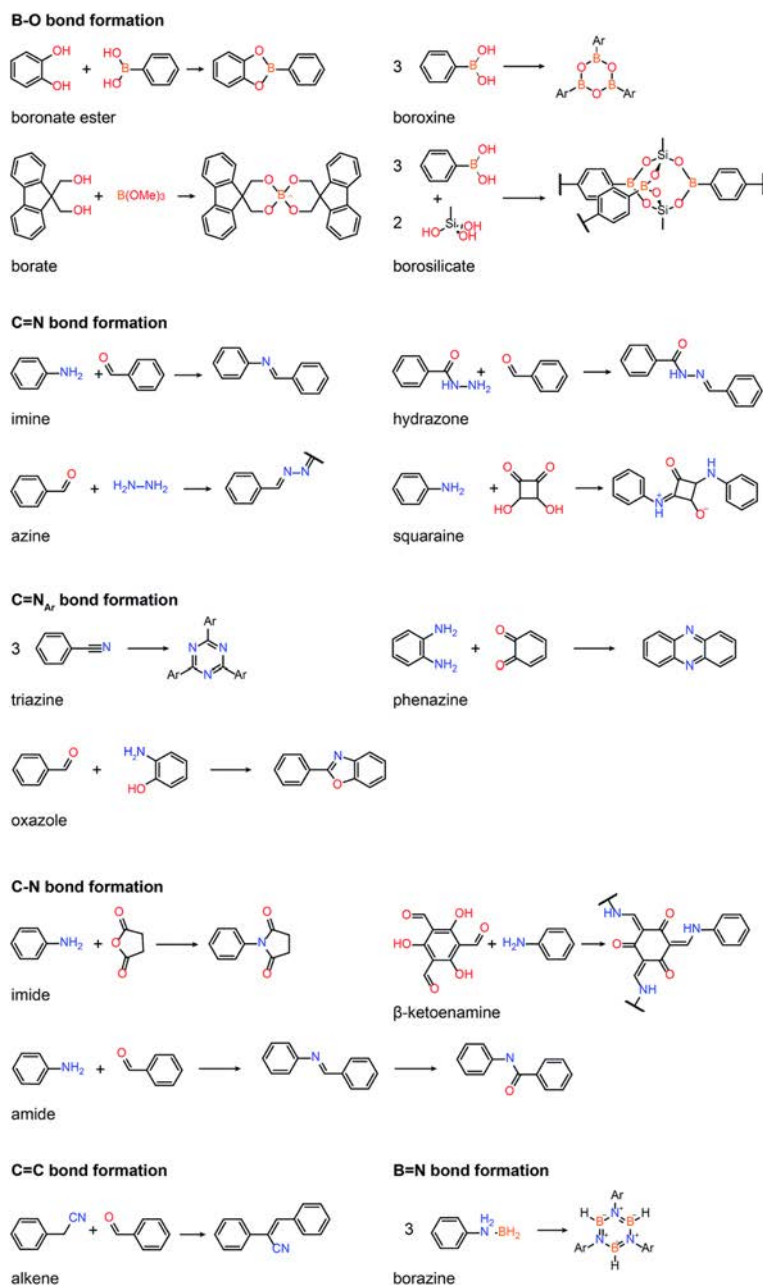


**Figure 1.13.** Scheme showing the main linkages used for the formation of COFs.<sup>23</sup>

## 1.4 Applications of MOFs and COFs

The exceptional properties of MOFs and COFs, such as their high porosity, high structural/compositional flexibility and low densities (for COFs), but also their electronic, magnetism, and optical properties, make them good candidates for multiple applications, including gas storage and separation, catalysis, sensing, and drug delivery, among many others (Figure 1.14). In this section, a general and brief overview of some of these applications is provided.

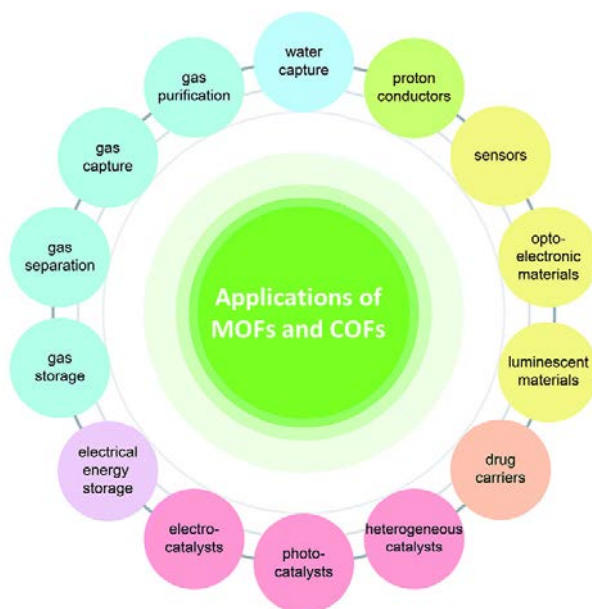


*Figure 1.14. Applications of reticular materials ranging from energy storage, gas separation, water capture, and catalysis to biomedical applications.<sup>20</sup>*

### 1.4.1 Gas storage

The environmental impact associated with energy demand is a major problem worldwide. To address the current and future energy needs while mitigating the environmental impact, one of the strategies has been the development of efficient capture, storage and separation porous materials for achieving cleaner combustible

supplies. In this sense, MOFs and COFs are very attractive adsorbents for many gases (*e.g.* CO<sub>2</sub>, H<sub>2</sub> and CH<sub>4</sub>) due to their high adsorption and storage capacities and their high degree of tunability of the frameworks. The potential of these materials as adsorbents for some of these gases are addressed in the following sections.

#### 1.4.1.1 CO<sub>2</sub> sequestration

MOFs and COFs have demonstrated to be efficient materials for CO<sub>2</sub> capture at high and low pressures. At high pressures, both types of materials with ultrahigh surface areas exhibit the largest CO<sub>2</sub> adsorption capacities. For example, Yaghi and co-workers reported that the highly porous MOF-177 (BET surface area = 4500 m<sup>2</sup> g<sup>-1</sup>) exhibited CO<sub>2</sub> adsorption capacity of 33.5 mmol g<sup>-1</sup> (320 cm<sup>3</sup> (STP) cm<sup>-3</sup>) at 35 bar; meaning that a gas cylinder filled with MOF-177 can capture and store nine times the amount of CO<sub>2</sub> than a cylinder without the MOF.<sup>35</sup> A record CO<sub>2</sub> adsorption capacity of 65.2 mmol g<sup>-1</sup> at 50 bar has been achieved by the ultrahighly porous MOF-210 (BET surface area = 6240 m<sup>2</sup> g<sup>-1</sup>). This value is the highest CO<sub>2</sub> capacity at high pressure reported so far.<sup>36</sup> On the other hand, El-Kaderi and co-workers reported a mesoporous imine-COF (IL-COF-1), which was synthesized by the condensation reaction between TFPPy and *p*-phenylenediamine (PPD). This COF exhibited a BET surface area of 2723 m<sup>2</sup> g<sup>-1</sup> and a CO<sub>2</sub> uptake of 29.3 mmol g<sup>-1</sup> at 40 bar and 298 K.<sup>37</sup>

At low-pressures (<1.2 bar), the chemical features of the pore surface in MOFs/COFs also play an important role in the CO<sub>2</sub> adsorption due to the interactions between CO<sub>2</sub> and the framework. The structural and chemical features of MOFs and COFs that give rise to their potential as CO<sub>2</sub> adsorbents are: (i) the presence of unsaturated metal centers (only for MOFs); (ii) the introduction of basic Lewis groups; and (iii) the presence of non-metallic groups in the SBU or in the framework.<sup>38</sup> The unsaturated metal ions can act as Lewis acid centers that induce the polarization of the adsorbed CO<sub>2</sub> due to their large quadrupole moment and therefore, the selectivity for CO<sub>2</sub> increases due to the stronger electrostatic interactions with the exposed metal

sites. Among unsaturated-based MOFs, the microporous  $M_2(\text{dhtp})$  series [termed M-MOF-74/CPO-27-M, where dhtp = 2,5-dihydroxyterephthalic acid and M = Mg(II), Co(II), Ni(II) and Zn(II)] have been intensively studied due to the strong interactions between the unsaturated metal sites and the  $\text{CO}_2$  molecules. In fact, crystallographic studies showed that  $\text{CO}_2$  molecules coordinate to the metal ions (five-coordinated) in an end-on-fashion through one of its oxygen atoms. Particularly, among the different MOFs in this series, Mg-MOF-74 has the highest uptake capacity (27.5 wt%) ever reported at ambient temperature and 1 bar. This effect was not only due to the lighter weight of the metal but also due to their higher heat of adsorption of  $47 \text{ kJ mol}^{-1}$  (Figure 1.15a).<sup>39,40</sup>

The introduction of basic Lewis groups (*e.g.* amines, imines, amides, etc) into the frameworks is also reported as a promising approach to improve the  $\text{CO}_2$  adsorption. The advantage of introducing amines is that the  $\text{CO}_2$  is adsorbed in a chemisorptive process due to the interaction of the quadrupole moment of  $\text{CO}_2$  with the lone-pair of the nitrogen atoms, thus increasing the  $\text{CO}_2$  adsorption.<sup>41</sup> A clear example of the efficacy of this approach was the functionalization of the unsaturated Mg(II) ions of the  $\text{Mg}_2(\text{dobpdc})$  (dobpdc = 4,4'-dioxido-3,3'-biphenyldicarboxylic acid) compound with N,N-dimethylethylenediamine (mmen). It was found that the mmen-functionalized MOF exhibited a  $\text{CO}_2$  adsorption of  $2.0 \text{ mmol g}^{-1}$  (8.1 wt %) at 298 K and 0.39 mbar, which is 15 times the capacity of the non-functionalized MOF (Figure 1.15b).<sup>42</sup> In a subsequent report, the IRMOF-74-III [ $\text{Mg}_2(\text{DH}_3\text{PhDC})$ , where  $\text{H}_4\text{DH}_3\text{PhDC}$  = 2',5'-dimethyl-3,3''-dihydroxy-[1,1':4',1''-terphenyl]-4,4''-dicarboxylic acid] was covalently functionalized with a primary amine and used for the selective capture of  $\text{CO}_2$  at 65 % of relative humidity, achieving an uptake of  $3.2 \text{ mmol g}^{-1}$  (12.7 wt %) at 298 K and 1.1 bar. Notably, the non-functionalized MOF showed a loss of 80 % in capacity under this wet conditions.<sup>43</sup>

Huang *et al.* reported the synthesis of an imine-linked COF with accessible and reactive ethynyl groups located on the 1D pore walls. They systematically tuned the

pore surface by click reactions between the ethynyl groups and azide compounds. The resulting functionalized-COFs exhibited an enhanced affinity for CO<sub>2</sub> compared with the non-functionalized COF. For example, the ethylamine-functionalized COF ([EtNH<sub>2</sub>]<sub>50</sub>-H<sub>2</sub>P-COF) showed a CO<sub>2</sub> adsorption of 82 mg g<sup>-1</sup> (17.7 wt %) at 298 K and 1 bar, which was almost 3-fold greater than the non-functionalized COF (Figure 1.15d).<sup>44</sup>

Finally, the CO<sub>2</sub> adsorption capacity can be enhanced by the strong interactions between the CO<sub>2</sub> molecules and non-metallic groups that are part of framework (e.g. inorganic anions) since the inorganic moieties can be comparable to the unsaturated metal centers in terms of their affinity for CO<sub>2</sub>. For instance, MOFs constructed from the assembly of pre-made fluorinated M-XF<sub>6</sub> pillars (M = Co, Ni, Cu and Zn; X = Si, Ti and Sn) with N-donor type ligands (e.g. pyrazine (pyz), pyridyl-based ligands, etc.) (*vide supra*) show exceptional uptake and selectivity towards CO<sub>2</sub> due to the combined effect of the small pore size of the 1D channels and the presence of a periodic array of fluorine atoms.<sup>45,46</sup> In fact, the MOF termed SIFSIX-2-Cu-i showed a CO<sub>2</sub> uptake of 5.41 mmol g<sup>-1</sup> (19.2 wt %) at 298 K and 1 bar; the highest uptake reported for a MOF without unsaturated metal sites (Figure 1.15c).<sup>47</sup> Recently, a highly water stable fluorinated MOF (termed NbOFFIVE-1-Ni) with formula NiNbOF<sub>5</sub>(pyz)<sub>2</sub>·2H<sub>2</sub>O was reported. This MOF displayed the highest CO<sub>2</sub> adsorption capacity (1.3 mmol g<sup>-1</sup> and 51.4 cm<sup>3</sup> (STP) cm<sup>-3</sup>) at 400 ppm of CO<sub>2</sub> (CO<sub>2</sub> concentration in air) and 298 K. These values are 300 % higher than the reference physical adsorbent (SAPO-34(Sr<sup>2+</sup>)).<sup>48,49</sup>

Very recently, Jiang *et al.* synthesized an ionic crystalline porous imine-COF (termed PyTTA-BFBIm-iCOF) by the reaction between 4,4',4'',4'''-(pyrene-1,3,6,8-tetrayl) tetraaniline (PyTTA) and 5,6-bis(4-formylbenzyl)-1,3-dimethyl-benzimidazolium bromide (BFBIm). The CO<sub>2</sub> uptake of PyTTA-BFBIm-iCOF was enhanced by three fold (93 mg g<sup>-1</sup> at 298 K and 1 bar) compared to the neutral analog (36 mg g<sup>-1</sup> at 298 K and 1 bar) due to the dipole–quadrupole interactions between the ionic surface of the COF (benzimidazolium cationic sites) and CO<sub>2</sub> (Figure 1.15e).<sup>50</sup>

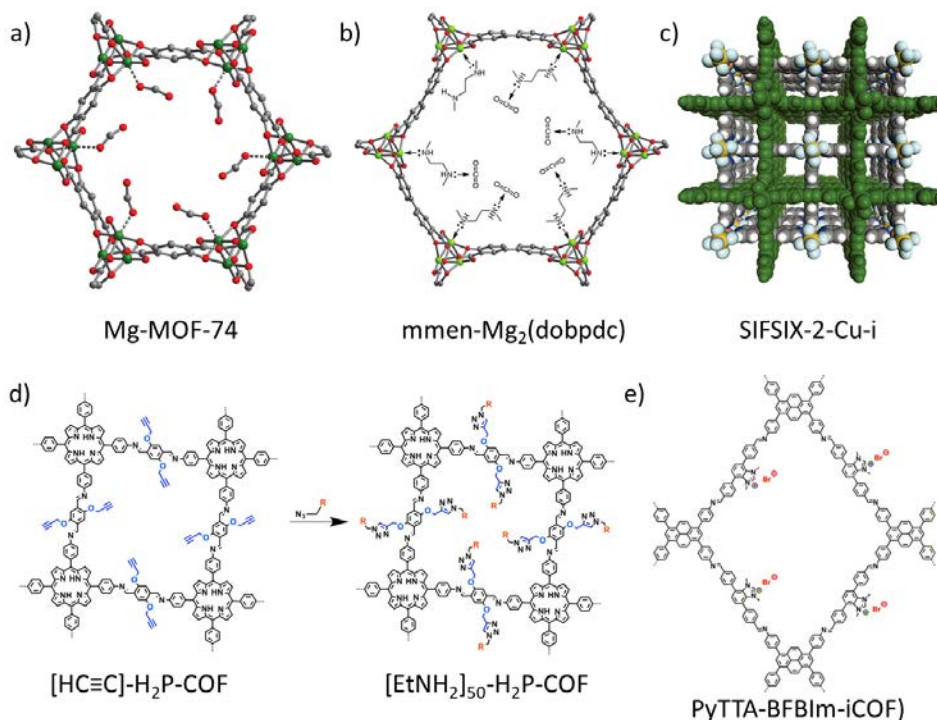


**Figure 1.15.** (a) Crystallographic structure of Mg-MOF-74 in which the interaction of CO<sub>2</sub> with the unsaturated Mg(II) ions is shown by a dotted line.<sup>39</sup> (b) Illustration of the functionalization of Mg<sub>2</sub>(dobpdc) through binding N,N-dimethylethylenediamine (mmen) to the unsaturated metal sites.<sup>42</sup> (c) Representation of SIFSIX-2-Cu-i obtained from the assembly of Cu-SiF<sub>6</sub> pillars and 4,4'-bpy.<sup>47</sup> (d) Schematic pore surface modification of the imine-linked COF with the corresponding azide.<sup>44</sup> (e) Structure of the ionic PyTTA-BFBIm-iCOF.<sup>50</sup>

### 1.4.1.2 CH<sub>4</sub> adsorption

Natural gas (NG), which mainly consists of methane, is considered an environmentally friendly candidate to replace petroleum (gasoline) due to the reduction of the CO<sub>2</sub> emissions during the combustion related with its higher research octane number (RON = 107). However, the low energy density of methane under ambient conditions (0.04 MJ L<sup>-1</sup>, compare to 32.4 MJ L<sup>-1</sup> for gasoline) limits its use for transportation applications. In this sense, several strategies have been proposed to overcome this limitation. For example, energy density of approximately 10 MJ L<sup>-1</sup> can

be reached when methane is stored as a supercritical fluid at room temperature and high pressures (200-300 bar) (compressed natural gas (CNG)). However, safety concerns have been raised due to the presence of heavy and highly pressurized steel cylinders in the cars. Recently, adsorbed natural gas (ANG) have become a promising strategy because methane can be stored in a porous solid at lower pressures (below 100 bar) and at room temperature.<sup>51</sup>

In this sense, MOFs have shown excellent capabilities to store high amounts of methane at low pressures compared to an empty tank. The benchmark material, HKUST-1 (*vide supra*), has been one of the most widely studied MOFs due to its exceptional high volumetric methane adsorption capacity exceeding any material reported so far.<sup>51</sup> In fact, HKUST-1 is the only material capable of achieving the volumetric storage target set by the US Department of Energy (DOE) ( $263 \text{ cm}^3 \text{ (STP) cm}^{-3}$ )<sup>52</sup> if the packing efficiency loss is ignored, reaching a maximum uptake of  $270 \text{ cm}^3 \text{ (STP) cm}^{-3}$  at 65 bar and 298 K. However, the volumetric adsorption capacity was reduced down to  $180 \text{ cm}^3 \text{ (STP) cm}^{-3}$  when HKUST-1 was densified due to the partial collapse of the framework.<sup>53</sup> Recently, Fairen-Jimenez and co-workers reported the synthesis of a porous monolithic HKUST-1, which after successful packing and densification reaches  $259 \text{ cm}^3 \text{ (STP) cm}^{-3}$  methane capacity at 65 bar, being the first example to achieve the DOE target after densification and shaping due to the high bulk density of the monolithic structure (Figure 1.16a).<sup>54</sup> From a mechanistic point of view, the high uptake of methane in HKUST-1 can be attributed to the combination of the strong interaction of the  $\text{CH}_4$  molecules with the unsaturated metal sites at low pressures and the interactions with the oxygen atoms of the small octahedral cages of the frameworks at high pressure (Figure 1.16b).<sup>55</sup> Besides HKUST-1, other MOFs have been outstanding materials having high volumetric storage capacities, as for example: MOF-905 ( $203 \text{ cm}^3 \text{ cm}^{-3}$  at 80 bar), Ni-MOF-74 ( $260 \text{ cm}^3 \text{ cm}^{-3}$  at 65 bar), PCN-14 ( $239 \text{ cm}^3 \text{ cm}^{-3}$  at 65 bar), NOTT-100 ( $230 \text{ cm}^3 \text{ cm}^{-3}$  at 65 bar) and UTSA-20 ( $230 \text{ cm}^3 \text{ cm}^{-3}$  at 65 bar).<sup>56</sup>

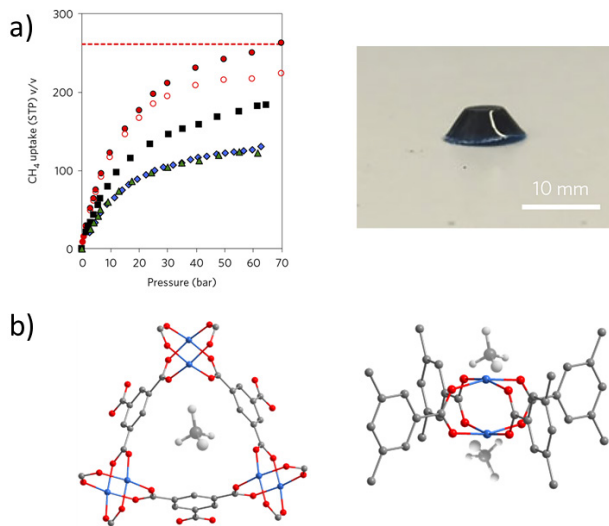


**Figure 1.16.** (a) Absolute volumetric (red filled circles) and excess volumetric (red open circles) methane adsorption isotherms at 298 K on monolithic HKUST-1 (left) and photograph of the monolithic HKUST-1 (right).<sup>54</sup> (b) Representation of the interaction of the CH<sub>4</sub> molecules with the unsaturated metal sites (right) and the octahedral cage of the HKUST-1 (left).<sup>55</sup>

COFs have also proven to be good candidates for methane storage at room temperature due to their large surface areas and pore volumes. For instance, Yaghi *et al.* reported the synthesis of a highly porous (BET surface area = 3472 m<sup>2</sup> g<sup>-1</sup>) 3D COF (termed COF-102) by self-condensation of TBPM linker. This COF exhibited a methane storage capacity of 203 cm<sup>3</sup> (STP) cm<sup>-3</sup> (25 wt%) at 298 K and 80 bar.<sup>57</sup>

### 1.4.1.3 H<sub>2</sub> adsorption

Hydrogen is one of the most promising energy vectors due to its abundance, high energy density and its non-polluting emissions after combustion. Despite these, one of the challenges precluding its applicability is its storage and transport. Even though the gravimetric energy density of hydrogen (120 MJ kg<sup>-1</sup> or 33.3 kWh kg<sup>-1</sup>) is almost three times higher than that of gasoline (44.4 MJ kg<sup>-1</sup> or 12.4 kWh kg<sup>-1</sup>), its energy density on a volumetric basis (8 MJ L<sup>-1</sup>) is very low compared to gasoline (32 MJ L<sup>-1</sup>), which means that 1 kg of H<sub>2</sub> occupies 11250 L at room temperature. This implies

the use of pressurized tanks at high pressures of 700 bar to store large amount of liquid on board, which is neither safe nor practical.<sup>58</sup> In these sense, MOFs appear to be competitive materials for adsorptive hydrogen storage because of their large surface areas and their structural properties. As mentioned in the previous sections, the presence of unsaturated metal sites in the framework also improves the H<sub>2</sub> storage capacity due to the charge-induced dipole interactions between the metal centers and the H<sub>2</sub> molecules. For instance, the ultra-highly porous Cu-paddel-wheel-based MOF termed NU-100 (NU = Northwestern University; BET surface area = 6143 m<sup>2</sup> g<sup>-1</sup>) with formula Cu<sub>3</sub>(L)(H<sub>2</sub>O)<sub>3</sub> (L = 1,3,5-tris[(1,3-carboxylic acid-5-(4-(ethynyl)phenyl)ethynyl]-benzene) exhibited the highest H<sub>2</sub> storage capacity reported so far (99.5 mg g<sup>-1</sup> at 77 K and 56 bar) (Figure 1.17).<sup>59</sup> Another structural feature that affects the H<sub>2</sub> sorption capacity is the catenation. In fact, the positive effect of catenation in H<sub>2</sub> adsorption was demonstrated by Zhou and co-workers. They compared the H<sub>2</sub> adsorption capacities of two isostructural MOFs, PCN-6 (catenated) and PCN-6' (non-catenated) (both have the formula Cu<sub>3</sub>(TATB)<sub>2</sub>, where TATB = 4,4',4''-s-triazine-2,4,6-triyltribenzoate). The catenated structure showed an excess H<sub>2</sub> uptake of 72 mg g<sup>-1</sup> at 77 K and 50 bar, while the non-catenated structure exhibited an excess H<sub>2</sub> uptake of 42 mg g<sup>-1</sup> under the same conditions. This fact is due to the stronger interactions between the H<sub>2</sub> molecules and the organic linkers in the catenated framework than in non-catenated framework.<sup>60</sup> Despite these possibilities, the application of MOFs for H<sub>2</sub> storage is still limited due to that they do not meet the DOE storage targets for an on-board hydrogen systems.

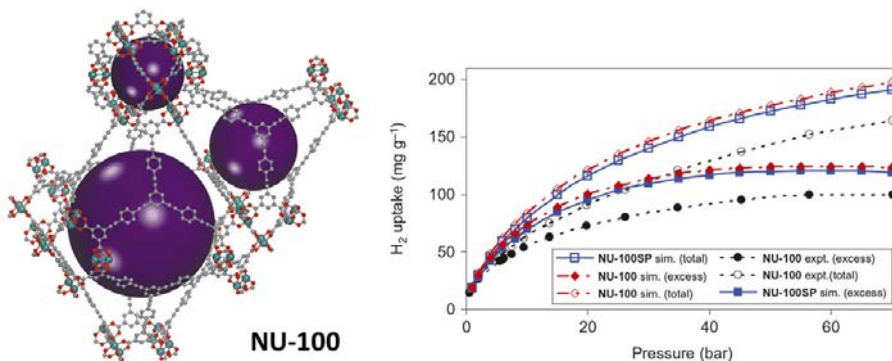


**Figure 1.17.** Representation of the X-ray structure of NU-100 (left) and its experimental H<sub>2</sub> adsorption isotherms (black circles) at high-pressure and 77 K (right).<sup>59</sup>

### 1.4.2 Catalysis

Catalysis is one of the most attractive applications of MOFs and COFs due to their potential to merge the benefits of homogeneous and heterogeneous catalysts into a single material. In these sense, three different strategies have been used to design and synthesize catalytically active MOFs and COFs.

The first approach consists on introducing active sites by removing coordinated solvent molecules from the metal clusters of MOFs. The resulting unsaturated metal sites can be used as Lewis acid catalysts. For example, it has been demonstrated that the mesoporous  $M_3X(H_2O)_2O(BDC)_3$  (known as MIL-101-(M), where  $M = Cr^{3+}$  and  $Fe^{3+}$ ;  $X = F$  and  $OH$ ) is catalytically active for several reactions, such as cyanosilylation, oxidation and cycloaddition, due to the presence of large pores (cages of 25 and 29 Å) and active unsaturated metal sites generated after removal of the coordinated water molecules.<sup>61</sup> Alternatively, Long *et al.* used a Mn-based MOF  $[Mn_3[(Mn_4Cl)_3(BTT)_8(CH_3OH)_{10}]_2]$ ; where  $H_3BTT = 1,3,5$ -tris(2H-tetrazol-5-yl)benzene] as a catalyst for cyanosilylation and Mukaiyama-aldol reactions. They found that the high concentration of active unsaturated Mn (II) ions (Lewis acid) on the internal surfaces of the MOF lead to high yield of conversions (up to 98 %) in a short reaction time.<sup>62</sup>

The second approach is based on the incorporation of catalytic sites into the framework. For instance, organocatalysts or transition metal catalysts can be directly incorporated as organic building blocks (*e.g.* porphyrin ligands) or through post-synthetic modification procedures, either by covalent modification of the organic linkers or by grafting molecules in the unsaturated metal sites. For example, Hupp and co-workers reported the post-synthetic modification of the mesoporous NU-1000  $[(Zr_6(\mu_3-OH)_8(OH)_8-TBAPy)_2]$ , where  $H_4TBAPy = 1,3,6,8$ -tetra(4'-carboxyphenyl)pyrene] by atomic layer deposition. The exposed  $-OH$  groups on the mesoporous hexagonal channels (31 Å diameter) of the kagome-based-framework were post-synthetically metalated by deposition of Zn and Al. The modified NU-1000 showed higher activity as a catalyst for Knoevenagel condensation reactions due to the presence of Lewis acidic Al(III) and Zn(II) sites in the framework (Figure 1.18a-b).<sup>63</sup> In another example, Nguyen and co-workers used a porphyrin-based ligand to synthesize a zinc-based, pillared paddlewheel ZnPO-MOF with formula  $[Zn_2(tcpb)(Zn-PO)]$  (where,  $tcpb = 1,2,4,5$ -tetrakis(4-carboxyphenyl)benzene and  $PO = 5,15$ -dipyridyl-10,20-bis(pentafluorophenyl) porphyrin). The catalytic performance of ZnPO-MOF was demonstrated for acyl transfer reactions, where a 2420-fold rate enhancement were observed compared with the control experiment. This enhance in activity was mainly due to the presence of Lewis acid sites in the Zn-based porphyrin.<sup>64</sup> Similarly, Lin and co-workers also used a porphyrin-based ligand [5,10,15,20-tetrakis(4-aminophenyl)-21*H*,23*H*-porphine cobalt(II) [Co(TAP)]] to prepare an imine-based COF (termed COF-366-Co) by condensation with 1,4-benzenedicarboxaldehyde (BDA). This material exhibited high catalytic performance for aqueous electrochemical reduction of  $CO_2$  to CO. In fact, COF-366-Co produced 36 mL  $mg^{-1}$  of CO over the course of 24 h with overpotential of  $-0.55$  volts and Faradaic efficiency of 90 % (Figure 1.18c).<sup>65</sup>

COFs can also be functionalized to contain active sites to be used as heterogeneous catalysis. For example, Bavykina and co-workers functionalized a covalent triazine framework (CTF) with a molecular catalyst based on  $Ir^{III}Cp^*$  ( $Cp^* =$ pentamethylcyclopentadienyl). The resulting material catalyzed the production

of  $\text{H}_2$  from formic acid with initial turnover frequencies (TOFs) up to  $27\,000\text{ h}^{-1}$  and turnover numbers (TONs) of more than one million in a continuous mode operation.<sup>66</sup>

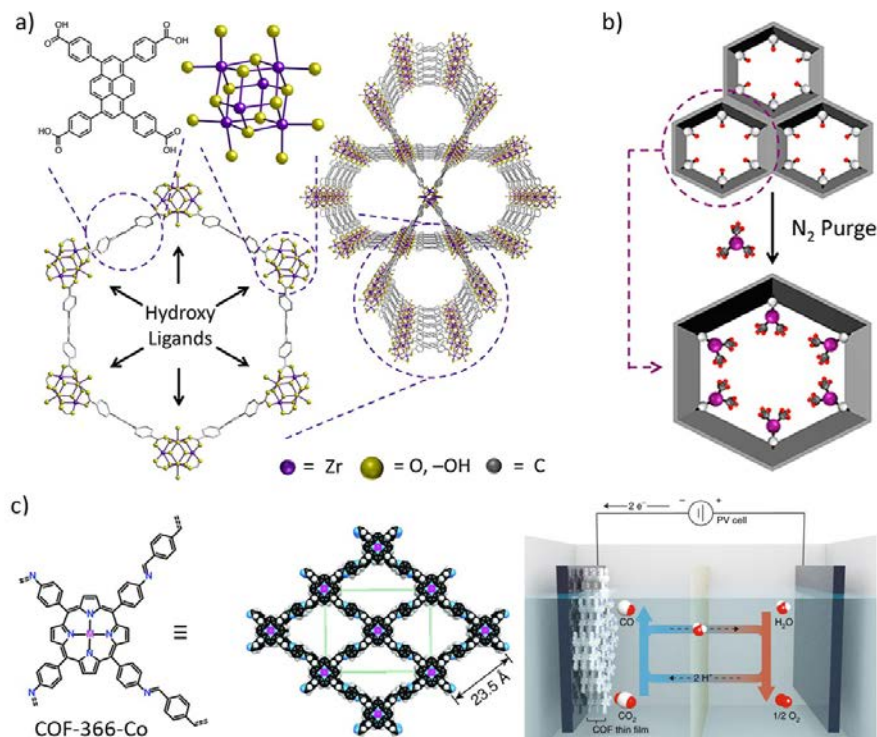


**Figure 1.18.** (a) Structural representation of NU-1000. (b) Illustration of the metalation by atomic layer deposition of NU-1000.<sup>63</sup> (c) Structural representation of COF-366-Co and schematic of the electrocatalytic reduction of  $\text{CO}_2$  to CO by COF-366(Co) in an electrochemical cell.<sup>65,67</sup>

The third approach consists in the introduction of active guest species into the pores of the MOFs. These species can be inorganic nanoparticles (iNPs), polyoxometalates, metalloporphyrins, or metal complexes. For example, iNPs are highly attractive materials for catalysis. However, they are thermodynamically unstable and tend to aggregate due to their high surface energy, resulting in a loss of their activity.<sup>68,69</sup> In this context, MOFs can be used as support for confining these iNPs and thus prevent their aggregation. To date, a great variety of functional composites (commonly named as MOF@iNPs) have been synthesized and used for a wide range of

reactions. For example, MIL-101-(Cr)@iNPs composites (iNPs = Pt, Au, Pd, Cu/Pd, Pt/Pd, Au/Pd and Ni/Au) have shown good performance (conversions up to 100 %) in several reactions, such as CO oxidation, hydrogenation, Suzuki-Miyaura coupling and Ullman coupling (Figure 1.19a).<sup>70</sup>

Catalytic species have also been introduced into COFs. For example, Pd ions were postsynthetically loaded into the 2D imine-based COF-LZU1 to generate Pd/COF-LZU1. X-ray photoelectron spectroscopy (XPS) measurements suggested that the Pd ions were fixed between the COFs layers and coordinated to the nitrogen atoms of the framework. This COF showed excellent catalytic activity for Suzuki-Miyaura coupling reaction with yields up to 98 %. In addition, the catalyst showed high stability and recyclability for many catalytic cycles (Figure 1.19b).<sup>71</sup>

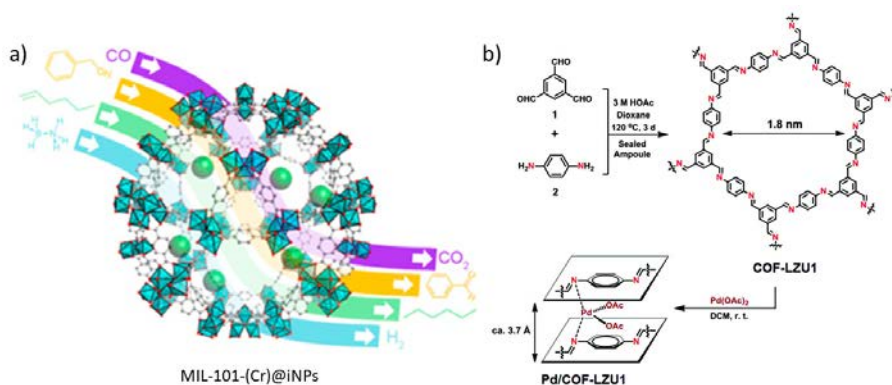


**Figure 1.19.** (a) Schematic illustration of some representative reactions catalyzed by MIL-101-(Cr)@iNPs.<sup>70</sup> (b) Representation of the synthesis of COF-LZU1 and Pd/COF-LZU1.<sup>71</sup>

### 1.4.3 Water adsorption applications

As seen above, great efforts have been devoted in the design, synthesis and modification of MOFs in order to increase their adsorption capabilities for gases such as CO<sub>2</sub>, CH<sub>4</sub> and H<sub>2</sub>. In this sense, water adsorption has received less attention mainly due to the low hydrolytic stability of the first generation of MOFs (e.g. MOF-5 and HKUST-1). However, the advent of MOFs with high water stability aroused the

scientific interest for using these materials for water adsorption applications since they can show high water uptake, tunability, and type V isotherms. Some of these applications include water harvesting, humidity control and adsorption heat pumps and chillers. In the following sections, these applications are discussed.

#### **1.4.3.1 Water harvesting applications**

Freshwater scarcity has increased during the last decades to the point that two-thirds of the global population live under conditions of severe shortfall of water.<sup>72</sup> One of the strategies to overcome this problem consists on capturing the atmospheric water since it corresponds to 10% of all available fresh water. Currently, water is captured from air by atmospheric water generators (AWGs), in which water vapour is condensed by chilling air below its dew point. However, large energy input is required to drive the AWG processes. In this sense, adsorption-based water harvesting system has been proposed as an environmentally friendly alternative to replace the traditional AWGs. These adsorption-water harvesting systems are based on an adsorption-desorption cycle, where water is adsorbed from air during the night (low temperature and high relative humidity (RH)) and released during the day (high temperature). The main advantage of these systems is that they can be powered by low grade, renewable and abundant energy sources, as for example, solar-thermal heating. In these sense, MOFs are promising materials for water harvesting applications due to their water and cycling stability, high working capacity (high water adsorption) and isotherms with a steep increase in water uptake within a narrow range of RH (type IV or V isotherm). In fact, a MOF with a steep uptake in a narrow pressure region between 10-30 % RH can be suitable for harvesting in North Africa (20 % RH) or a MOF with steep increase around 40 % can be suitable in India.<sup>73</sup>

Recently, Yaghi and co-workers developed an adsorption-based water harvesting device using MOF-801. This MOF is composed of 12-connected Zr-based clusters  $[\text{Zr}_6\text{O}_4(\text{OH})_4(-\text{COO})_{12}]$  linked by fumarate ligands into a 3D extended porous

framework. This MOF has a high water uptake of  $0.29 \text{ g g}^{-1}$  at RH of 20 % and a low regeneration temperature of  $40 \text{ }^\circ\text{C}$ . They demonstrated that, during the day ( $65 \text{ }^\circ\text{C}$ )-night ( $25 \text{ }^\circ\text{C}$ ) cycle, this device was capable of harvesting  $0.24 \text{ L}$  of water per kilogram of MOF without additional input of energy. This proof-of-concept showed the potential of MOF for harvesting applications using only renewable solar-thermal energy (Figure 1.20).<sup>74</sup>

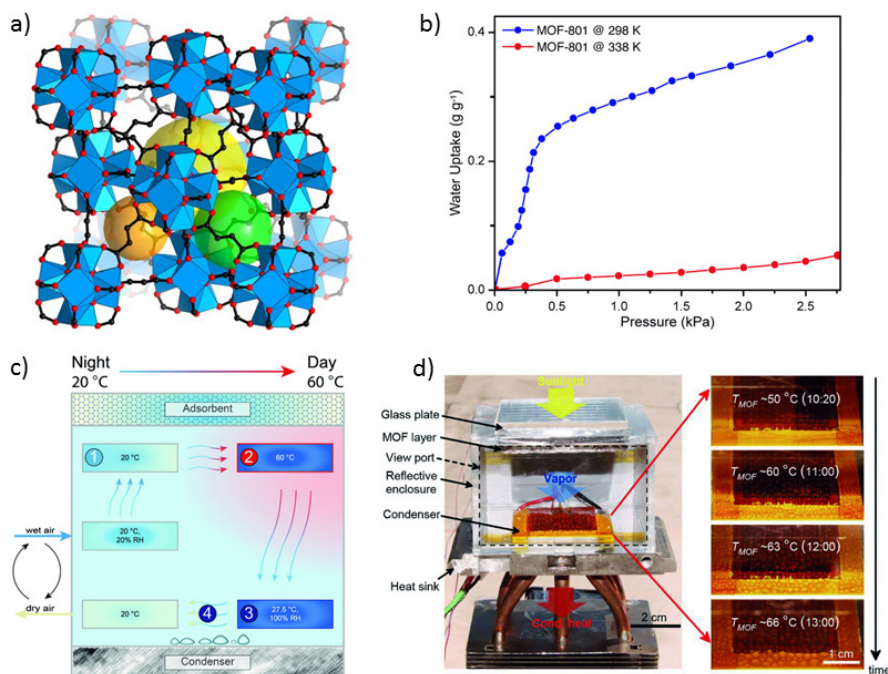


**Figure 1.20.** (a) Crystal structure of MOF-801 illustrating the tetrahedral and octahedral cages. (b) Water adsorption isotherms of MOF-801 at 298 and 338 K. (c) Schematic representation of the water harvesting device. (d) Photograph of the water harvesting device, the insert shows the formation of water droplets the upon increasing the temperature of the MOF.<sup>73</sup>

In another example, Dinca *et al.* reported the water harvesting capacity of the mesoporous MOF  $\text{Co}_2\text{Cl}_2(\text{BTDD})$  (BTDD = bis(1H-1,2,3-triazolo[4,5-b],[4',5'-i])dibenzo[1,4]dioxin). This MOF is composed of 1D chains of five-coordinated Co(II) ions linked by triazolate ligands. The 3D structure displays a honeycomb network with

channels of 22 Å of diameter along the *c*-axis. The water adsorption isotherm (type IV) of  $\text{Co}_2\text{Cl}_2(\text{BTDD})$  showed a steep uptake at  $\text{RH} = 28\%$  (water uptake of  $0.82 \text{ g}_{\text{H}_2\text{O}} \text{ g}_{\text{MOF}}^{-1}$ ), which is attributed to the pore filling. Before this step, the water is adsorbed due to cluster adsorption around the unsaturated metal sites. The potential of  $\text{Co}_2\text{Cl}_2(\text{BTDD})$  to generate potable water in desert regions was evaluated by simulating realistic day/night temperature and RH conditions (daytime =  $45^\circ\text{C}$  and  $5\%$  RH; night time =  $25^\circ\text{C}$  and  $35\%$  RH). Under these conditions, they found that this MOF could generate  $0.82 \text{ g}_{\text{H}_2\text{O}} \text{ g}_{\text{MOF}}^{-1}$  of potable water; nearly double the quantity of fresh water compared to the best material previously reported (Figure 1.21).<sup>75</sup>

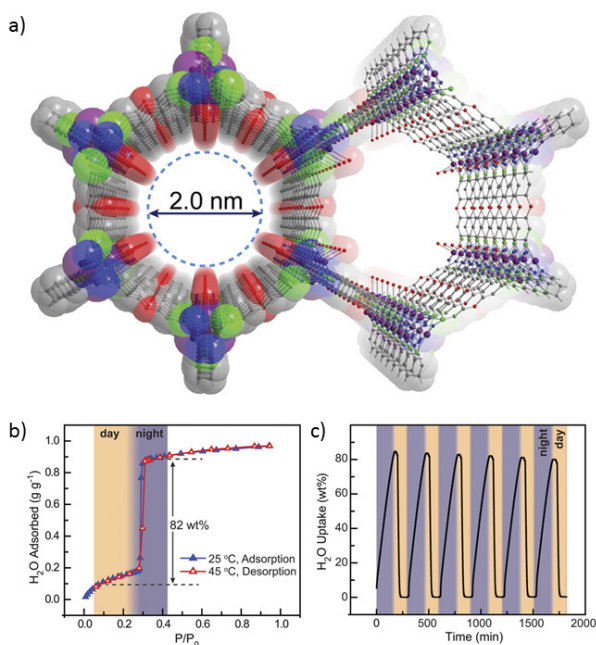


**Figure 1.21.** (a) Structure of  $\text{Co}_2\text{Cl}_2(\text{BTDD})$  projected along the *c*-axis. (b) Water adsorption isotherms of  $\text{Co}_2\text{Cl}_2(\text{BTDD})$  at  $25^\circ\text{C}$  and  $45^\circ\text{C}$ . (c) Water adsorption cycles between  $45^\circ\text{C}$  and  $5\%$  RH (day), and  $25^\circ\text{C}$  and  $35\%$  RH (night).<sup>75</sup>

### 1.4.3.2 Humidity control

Humidity control is fundamental to the proper functioning of any space since it can protect occupants from adverse health effects, including upper respiratory symptoms, cough, wheeze, etc. Additionally, damp indoor environments promote the growth of mold, mildew, and other fungi. Thereby, healthy and comfortable environments should have optimal indoor humidity levels of approximately between 40 % and 60 % RH. This means that an ideal adsorbent material should swiftly adsorb water when the humidity levels exceed 60 % RH and desorb water when the humidity levels drop below 40 % RH. Nevertheless, very few examples are known of materials capable of this dual functionality since most of the traditional porous materials adsorb and desorb water vapour at the same relative humidity.

In this sense, MOFs with high hysteresis between the adsorption and desorption curves (“S”-shaped isotherm) are ideal for humidity control since it can adsorb water vapor when the humidity is too high and release water vapor when room humidity falls too low (dual functionality).<sup>76</sup> Eddaoudi *et al.* explored for the first time the possibility of using MOFs as humidity control systems. They synthesized a hybrid microporous highly connected rare-earth-based **Y-shp-MOF-5**  $[Y_9(\mu_3-O)_2(\mu_3-OH)_{12}(OH)_2(H_2O)_7(BTEB)_3(DMA)_3]$ , where BTEB = 1,2,4,5-tetrakis(4-carboxyphenyl)benzene]. The water adsorption isotherm (“S” shape) of **Y-shp-MOF-5** showed a steep uptake between 55-75 % RH, reaching maximum water uptake of 0.5 g g<sup>-1</sup>. Interestingly, a hysteresis loop at pressures between 30-50 % RH was observed in the desorption branch. In fact, this hysteresis loop was beneficial for autonomous dehumidification/humidification since **Y-shp-MOF-5** adsorbs water at 50 % RH and release water at 45 % RH. In addition, **Y-shp-MOF-5** exhibited high stability and humidity control performance over more than 200 moisture adsorption-desorption cycles (Figure 1.22).<sup>77</sup>

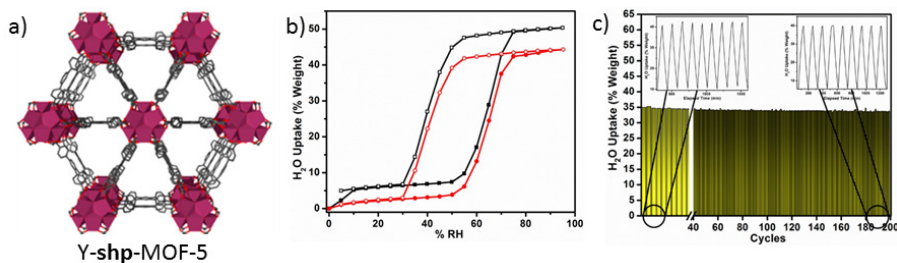


**Figure 1.22.** (a) Crystal structure of *Y-shp*-MOF-5. (b) Water adsorption isotherms of *Y-shp*-MOF-5 at 25 °C (black) and water adsorption isotherm after re-activation at 125 °C (red). (c) Water adsorption cycles between 25 and 85 % RH.<sup>77</sup>

### 1.4.3.3 Adsorption Heat Transformation Applications

Finally, MOFs are promising adsorbents for adsorption heat transformation systems (AHT) (adsorption heat pumps and chillers) due to their water and cycling stability, high working capacity within the working range of RH (type V isotherms) and low regeneration temperatures. Recently, AHT systems have been proposed as a more environmental friendly alternative to replace the conventional compression systems, as they avoid the use of hydrofluorocarbons as refrigerants that mainly contribute to the emissions of the greenhouse gases. The main advantages of AHTs are: (i) the use of low temperature as primary energy source (*e.g.* waste heat or solar collectors); and (ii) the use of water as a working fluid.<sup>78</sup>

The AHT systems are based in adsorption/desorption cycles that consist of four steps: isosteric heating (I-II), isobaric desorption (II-III), isosteric cooling (III-IV), and isobaric adsorption (IV-I). These steps are represented in the isosteric cycle diagram shown in Figure 1.23.

*Isosteric heating (I-II):* The adsorbent vessel is disconnected from the condenser and the evaporator. The adsorbent is heated from  $T_1$  to  $T_2$  without desorption and the pressure is increased to  $P_{ev}$  to  $P_{con}$ . At this point, the adsorbent is fully saturated with water ( $W_{max}$ ).

*Isobaric desorption (II-III):* The adsorption vessel is connected to the condenser and the water is desorbed when the system reaches the desorption temperature ( $T_{des}$ ). At this point, heat is released to the environment ( $Q_{con}$ ) when the water is condensed in the condenser at an intermediate temperature.

*Isotheric cooling (III-IV):* The adsorbent vessel is disconnected from the condenser and the pressure is reduced to  $P_{ev}$  by cooling the vessel from  $T_{des}$  to  $T_3$ . At this point, the adsorbent is completely desorbed and can be used again for the adsorption process.

*Isobaric adsorption (IV-I):* The adsorbent vessel is connected to the evaporator and the water evaporation is started. During the water evaporation, **useful cold** is produced. In addition, water is adsorbed until reaches the maximum loading capacity of the adsorbent ( $W_{max}$ ). During this step, **useful heat** is released.<sup>79</sup>

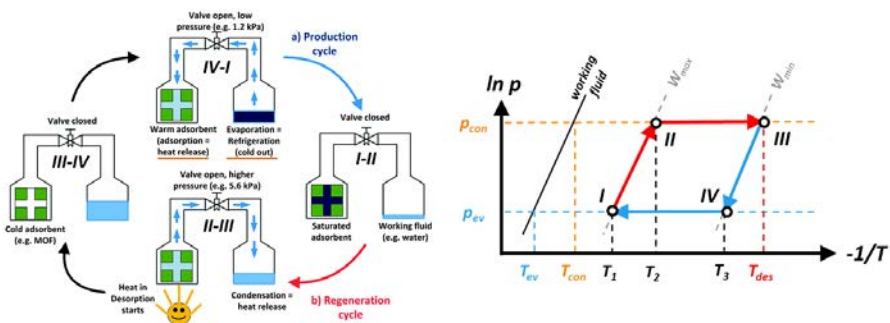
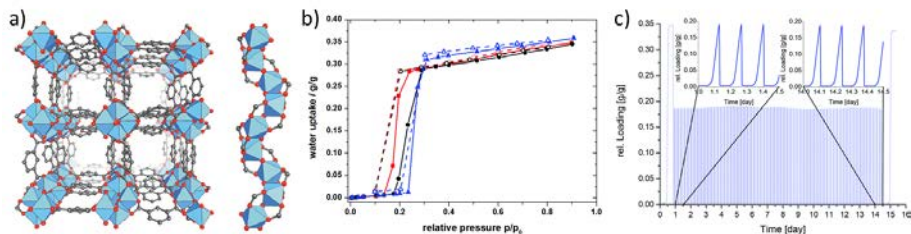


Figure 1.23. Schematic representation of the principle of heat transformation cycle (left)<sup>78</sup> and isotheric diagram of an adsorption heat pump cycle (right).<sup>80</sup>

For a good performance of the AHT systems, water sorption properties of MOFs/COFs must be accomplish some features, that including: the water adsorption should occur in a working pressure range between 5 % RH and 35 % RH; the adsorption capacity should be higher than  $0.2 \text{ g g}^{-1}$ ; there must be a steep increase in water uptake with small hysteresis (type V isotherm); the regeneration temperature must be lower than  $120 \text{ }^\circ\text{C}$  and cycle stability during the adsorption and desorption cycles. A good example was reported by Janiak *et al.*, who studied the water sorption behavior

of the microporous CAU-10-H ( $[Al(OH)(benzene-1,3dicarboxylate)] \cdot nH_2O$ ). The water adsorption isotherm (type V) of CAU-10-H showed a steep uptake at 20 % RH and a water uptake of  $0.34 \text{ g}_{H_2O} \text{ g}_{MOF}^{-1}$ . Remarkable, this material showed high stability after 700 water adsorption-desorption cycles, which makes it suitable for AHT applications (Figure 1.24).<sup>81</sup>



**Figure 1.24.** (a) Crystal structure of CAU-10-H. (b) Water sorption isotherms of CAU-10-H at 25 °C (red) 40 °C (black) and 60 °C (blue). (c) Water sorption cycles.<sup>81</sup>

In another example, Aristov and co-workers studied the water adsorption performance of the MOF termed  $NH_2\text{-MIL-125}$  ( $Ti_8O_8(OH)_4\text{-}(NH_2\text{-BDC})_6$ ) and its potential for adsorption air-conditioning applications. They demonstrated that this MOF can adsorb large quantities of water (up to  $0.42 \text{ g g}^{-1}$ ) and can be regenerated at very low temperature (348 K) under operational conditions for adsorption chillers (Temperature of evaporation = 283 K and adsorption and condensation temperature = 303 K). In addition, they found that this MOF exhibited a coefficient of performance (COP, which is the commonly parameter to describe the energetic efficiency) of 0.80, which means that 1 J of wasted heat can be used to generate 0.80 J of cold at 283 K. Remarkably,  $NH_2\text{-MIL-125}$  is one of the most energy efficient materials reported for air conditioning applications.<sup>82</sup>

## 1.5 Synthesis of MOFs and COFs towards their industrial exploitation

As seen in the previous sections, the development in the field of MOFs and COFs has growth exponentially over the past 20 years due to their unique properties that are not observed in other porous materials. The first age of this field was based in the study of the assembly of their molecular building blocks and their structural determination. The second age was based in the exploration of their properties for many of the aforementioned research areas. The third age of this field is in its early stages, and it is based in their industrial exploitation and commercialization.<sup>83</sup> Here, the challenges for using these porous materials in real-world applications lie not only in their inherent properties but also in the ability to produce them at the required scale. Usually, the laboratory-scale synthesis (milligram scale) of MOFs/COFs is carried out using costly and toxic solvents in sealed reactor vessels (solvothermal method) under harsh conditions, including high temperatures, high pressures and long reaction times. Therefore, up-scaling this solvothermal synthesis remains challenging due to their inherent costs related to the requirement of pressure-sealed vessels and heating machinery for working at high and controlled temperatures and for several days. In addition, another limitation in the scale-up of these materials concerns the fact that these solids nucleated at a reactor vessel surface and therefore, the size of the vessel becomes a significant parameter since reactions that proceed satisfactorily in small vessels may not always scale well to larger vessels at identical reaction conditions.<sup>84</sup> In these sense, it is important to establish facile (avoiding harsh conditions), inexpensive and rapid (continuous process) methods for the industrially viable production of MOFs and COFs. To address these challenges, researchers have developed novel energy efficient and cost-effective synthetic methodologies in the last few years. Some of these methods include electrochemical, mechanochemical, continuous flow and spray-drying synthesis.<sup>85</sup> In the following sections, the recent advances in the alternative synthesis of MOFs and COFs are discussed.

### 1.5.1 Electrochemical synthesis

Two main approaches have been used for the electrochemical synthesis of MOFs: (i) anodic dissolution; and (ii) cathodic deposition. The anodic dissolution is based on applying an appropriate voltage (or current) to induce the release of metal ions from the metallic electrode. Then, these metal ions immediately react with the organic ligands present in the solution leading to the MOF formation. The anodic dissolution is typically carried out in a two-electrode set-up without a reference electrode, in which protic solvents are added to ensure the evolution of hydrogen and avoid the reduction of the metal ions at the counter electrode. In addition, it is recommended to use a counter electrode with a suitable overpotential for hydrogen evolution or to add a sacrificial compound (*e.g.* acrylonitrile, acrylic or maleic esters) that are preferentially reduced instead of the metal ions (Figure 1.25a).<sup>86</sup> This approach was first patented by BASF in 2005. They synthesized HKUST-1 by immersing two copper plates (anode and cathode) in a methanolic solution of BTC. After 150 min at 12–19 V (current of 1.3 A), octahedral crystals of HKUST-1 were obtained. The BET surface area of the electro-synthesized HKUST-1 was 1820 m<sup>2</sup> g<sup>-1</sup>, which is higher than that reported for the solvothermally synthesized MOF (1550 m<sup>2</sup> g<sup>-1</sup>). BASF Company have been used this method for the synthesis of Basolite Z1200 (ZIF-8) and Basolite C300 (HKUST-1) at the kilogram scale in a continuous-flow pilot plant.<sup>87</sup>

Since this pioneer report, electrochemical synthesis has been widely used for MOF synthesis. Recently, Fransaer and co-workers proposed the mechanism for the anodic dissolution of HKUST-1, which consist of four phases: (i) Initial nucleation, in which the Cu (II) ions are released to the BTC solution and, when a critical ion concentration is reached, the nucleation of HKUST-1 starts on the surface of the anode; (ii) Growth of HKUST-1 islands, in which after the first nuclei are formed, new crystals tend to nucleated next to them, forming islands; (iii) Intergrowth, in which the nucleation is progressive and the crystals already nucleated grow to dimensions of several microns (depending on the synthesis time); and (iv) Crystal detachment, in

which the copper substrate below the MOF layer is constantly dissolving due to the formation of Cu (II) ions, creating voids below the MOF layer. Thus, the fragile layers of HKUST-1 crystals are easily detached (Figure 1.25c).<sup>88</sup> Alternatively, Denayer and co-workers studied the effect of different water/organic solvent mixtures (*e.g.* methanol, ethanol and N,N-dimethylformamide (DMF)) in the electrochemical synthesis of HKUST-1. They found that the crystal size increases when increasing the water content in methanol or ethanol mixtures. While octahedral crystals were formed in H<sub>2</sub>O/DMF mixtures.<sup>89</sup> In another example, thin films of Zn<sub>3</sub>(BTC)<sub>2</sub> were prepared by immersion of two zinc plates into a solution of BTC and ammonium fluoride (supporting electrolyte) and applying a voltage of 2 V at 65 °C.<sup>90</sup> Gascon *et al.* reported the electrochemical synthesis via anodic dissolution of several archetypical MOFs, including HKUST-1, ZIF-8, MIL-100(Al), MIL-53(Al), and NH<sub>2</sub>-MIL-53(Al) in shorter times and milder conditions than the traditional solvothermal method.<sup>91</sup> Despite these advantages, the anodic dissolution approach has some limitations: (i) the anode is used to produce the metal cations and thus, it is erode in a continuous manner throughout the synthesis; and (ii) the selection of the anode metal is limited since the anode is also used as the metal resource.

By other hand, the cathodic deposition approach is based on applying a voltage (or current) to induce the reduction of a so-called probase in order to generate basic species (*e.g.* nitrite ions coming from the reduction of nitrates). These basic species deprotonate the organic ligands, which then react with metal cations, resulting in the formation of crystalline MOF on the cathode surface. The advantages of this approach are the possibility to perform the reactions in a single step at room temperature and using a wide variety of conductive surfaces and deposit MOFs composed of almost any metal ions since the metal salt is dissolved in the electrolyte solution together with the ligand and the probase (Figure 1.25c). In 2011, Dinca *et al.* first investigated the synthesis of MOFs by cathodic deposition. They demonstrated the formation of MOF-5 from a electrolyte solution of BDC and zinc nitrate in DMF:water at room temperature in only 15 min under cathodic potential. They found that the nitrate counteranions

play an important role during the synthesis since they can act as a probase for the deprotonation of the BDC linkers.<sup>92</sup> More recently, Ameloot and co-workers combined both the anodic and cathodic electrochemical deposition to perform the synthesis of UiO-66. The film deposition of UiO-66 was performed at 383 K by applying a voltage of 6-9 V (current of 80 mA) to the zirconium electrodes (electrolyte solution consisted of a mixture of BDC, DMF, nitric acid (electrolyte), water and acetic acid). Interestingly, they found that when the acetic acid concentration increased, the complexation of released Zr(IV) ions also increased leading to a decrease of the anodic deposition. On the contrary, when the concentration of acetic acid decreased, the concentration of released Zr(IV) ions increased, thereby increasing the deposition on the cathode.<sup>93</sup>

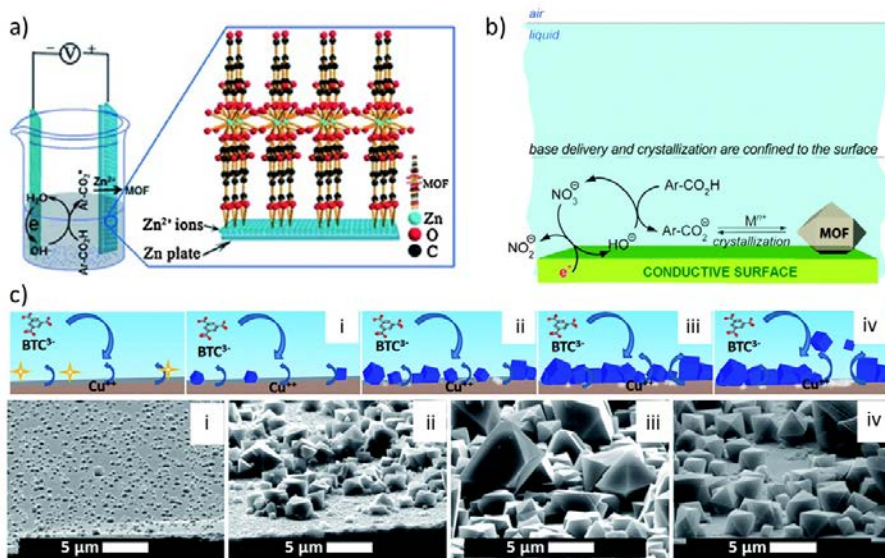


Figure 1.25. Electrochemical synthesis of MOFs by (a) anodic dissolution and (b) cathodic deposition.<sup>86,92</sup> (c) Proposed mechanism of HKUST-1 formation by anodic dissolution.<sup>88</sup>

## 1.5.2 Mechanochemical synthesis

Mechanochemical synthesis is based in chemical reactions that are induced and/or sustained by the application of mechanical force (mechanical energy), such as by grinding or milling. The main advantages of mechanosynthesis are that it can promote reactions between solids with stoichiometric control (quantitative yields) at room temperature in short periods of time and without any or with minimal amounts of solvents. In fact, MOF precursors with low solubility, such as metal oxides, carbonates and hydroxides, can be used as starting materials.<sup>94</sup> Mechanochemical reactions can be performed manually using a mortar and pestle or electronically using mechanical ball mills. In general, reactions under well-controlled and reproducible conditions are performed using the mechanical ball mill. To date, there are three different approaches for the mechanochemical production of MOFs: Solvent-Free Grinding (SFG), Liquid-Assisted Grinding (LAG), and Ion-and Liquid Assisted Grinding (ILAG).<sup>95</sup>

### 1.5.2.1 Solvent-Free Grinding Approach

Solvent-Free Grinding (SFG) is the simplest method and involves grinding a physical mixture of two or more reactants without solvent. James *et al.* first showed the possibility of using this synthetic method for MOFs by showing the solvent-free mechanochemical synthesis of Cu(INA)<sub>2</sub> (where INA = isonicotinic acid). This synthesis was performed by grinding together copper acetate and isonicotinic acid for 10 min in a steel ball bearing at an oscillation rate of 25 Hz.<sup>96</sup> Two years later, the same group reported a screening study, in which sixty different combinations of twelve divalent metal salts and five bridging organic ligands were grinded. Interestingly, several crystalline structures were obtained, including the microporous HKUST-1 and Cu(INA)<sub>2</sub>.<sup>97</sup> The zeolitic imidazolate framework, ZIF-8 (Zn(mim)<sub>2</sub>), was also synthesized by grinding together ZnO and 2-methylimidazole (Hmim). After milling for 96 h, porous ZIF-8 could be obtained with a BET surface area 1480 m<sup>2</sup> g<sup>-1</sup>. The advantage of using

metal oxides as the metal source for the synthesis of MOFs is that only water is formed as a by-product, thus allowing the complete elimination of the purification step.<sup>98</sup> Recently, MIL-101(Cr) was also rapidly synthesized without the addition of HF by grinding together  $\text{Cr}(\text{NO}_3)_3$  and BDC at room temperature for 30 min. The resulting solid mixture was then heated at 220 °C for 4 h, yielding a crystalline MIL-101(Cr) with a BET surface area of 3517  $\text{m}^2 \text{g}^{-1}$ .<sup>99</sup>

In 2015, James and co-workers showed the synthesis of HKUST-1, ZIF-8 and aluminium fumarate MOF with a twin-screw extrusion (TSE) at the kilogram scale. The twin-screw extrusion is based in two co- or counter-rotating screws transport material along a barrel and subject it to shearing and compression forces due to the presence of mixing/kneading elements incorporated into the screw design. ZIF-8 was synthesized by extruding zinc carbonate and Hmim at 200 °C. The extrudate was collected and activated to give a solid with a BET surface area of 1603  $\text{m}^2 \text{g}^{-1}$ . Similarly, aluminium fumarate was obtained by introducing a mixture of aluminium sulphate, sodium hydroxide and fumaric acid into the twin extruder at 150 °C. The activated MOF exhibited a BET surface area of 1010  $\text{m}^2 \text{g}^{-1}$  (Figure 1.26a).<sup>100</sup>

Similarly, the SFG approach can be used for the production of COFs. Here, Banerjee *et al.* reported for the first time the SFG synthesis of three thermally and chemically stable COFs (denoted TpPa-1, TpPa-2 and TpBD; where Tp = 1,3,5-triformylphloroglucinol, Pa-1 = *p*-phenylenediamine, Pa-2 = 2,5-dimethyl-*p*-phenylenediamine and BD = benzidine). The syntheses were performed by grinding together the starting materials for 40 min in a mortar at room temperature. Although the crystallinity and porosity of these mechanochemically synthesized COFs were moderate, this strategy provided valuable insight towards the synthetic development for large-scale, green, and time-saving COF production.<sup>101</sup> The same group also demonstrated the use of mechanical grinding to perform the delamination of COFs, transforming them into covalent organic nanosheets (CONs). The resulting exfoliated CONs showed a graphene-like layered morphology.<sup>101</sup>

### 1.5.2.2 Liquid-Assisted Grinding (LAG) Approach

The Liquid-Assisted Grinding (LAG) method serves to improve the crystallization of MOFs/COFs and accelerate their synthesis. This approach consists on adding small quantities of liquid phase (catalytic amounts) to increase the mobility of the reagents during the mechanochemical reaction. For example, HKUST-1 and MOF-14 ( $\text{Cu}_3(\text{BTB})_2$ , BTB = 4,4',4''-benzenetribenzoate) were synthesized by ball milling. The MOFs were obtained by grinding together copper acetate monohydrate with the corresponding linkers in presence of 1 mL of ethanol for 25 min at 40 Hz. Acetic acid was formed as a by-product, which was further removed by stirring HKUST-1 in methanol for 30 min, reaching a BET surface area of  $1713 \text{ m}^2 \text{ g}^{-1}$ .<sup>102</sup> More recently, Frisčić *et al.* demonstrated the synthesis at the gram scale of Zn-MOF-74 by milling ZnO and 2,5-dihydroxyterephthalic acid and using 250  $\mu\text{L}$  of water or DMF as the grinding liquid. *In situ* synchrotron X-ray diffraction monitoring of the reaction course revealed an unusual stepwise process in which a close-packed intermediate reacts to form the open framework (Figure 1.26b).<sup>103</sup> Similarly, the synthesis of UiO-66 and UiO-66-NH<sub>2</sub> at the gram scale were performed by mixing pre-assembled Zr-oxo clusters ( $\text{Zr}_6\text{O}_4(\text{OH})_4(\text{methacrylate})_{12}$ ) with terephthalic acid in the presence of microliters of MeOH or DMF and grinding for 75 min and 90 min, respectively. Interestingly, the use of corrosive  $\text{ZrCl}_4$ , HCl and  $\text{ZrOCl}_2$  were avoided using this approach.<sup>104</sup>

The use of LAG approach for the synthesis of COFs has been explored by Banerjee and co-workers. The COFs termed TpTh, DhaTph and LZU-1 (TFBPa-1) (Th = Terephthalic dihydrazide; Dha = 2,5-dihydroxyterephthalaldehyde; Tph = tetra(pamino-phenyl)porphyrin; TFB = 1,3,5-triformylbenzene) were synthesized by milling the organic linkers in presence of catalytic amounts of a mixture of acetic acid : dioxane : mesitylene at room temperature for 90 min. The products were obtained in high purity and yields.<sup>105</sup> Very recently, the use of *p*-toluenesulfonic acid (PTSA) as a molecular organizer has shown to be important during the mechanochemical synthesis of COFs since it can induces reversibility, resulting in a more ordered networks. In fact, twelve

COFs with high surface areas and crystallinity were synthesized in a two-step process. In the first step, a mixture of the organic linkers, PTSA and water (100  $\mu\text{L}$ ) were ground for 20 min at room temperature. Then, in a second step, the solid mixtures were heated at 170  $^{\circ}\text{C}$  for 60 seconds. Interestingly, they also explored the large-scale ( $\sim 10 \text{ g h}^{-1}$ ) synthesis of COFs using a twin-screw extruder (TSE) (Figure 1.26c). XRPD and BET surface area measurements of the powders confirmed the good formation of highly crystalline COFs in all cases.<sup>106</sup>

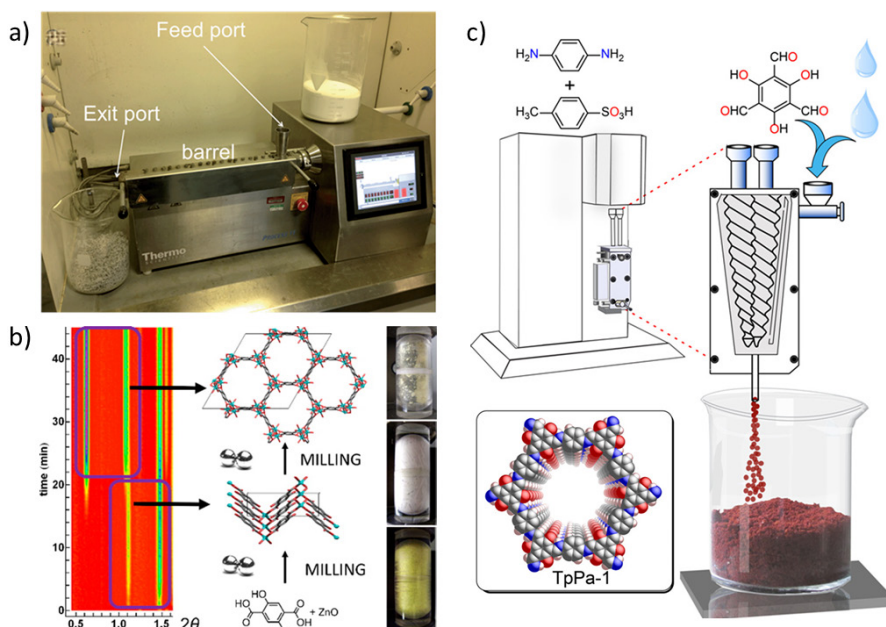


**Figure 1.26.** (a) Twin screw extruder with the key parts highlighted<sup>100</sup>. (b) Time-resolved in situ X-ray for LAG of ZnO and H<sub>4</sub>dhta (left) and schematic representation of the formation of Zn-MOF-74 by LGA.<sup>103</sup> (c) Synthesis of TpPa-1 by extrusion.<sup>106</sup>

### 1.5.2.3 Ion-and Liquid Assisted Grinding (ILAG)

In the third mechanochemical approach, ion-and Liquid Assisted Grinding (ILAG), catalytic amounts of ionic salts are used to induce, enhance, and direct the MOF formation. The first report of the ILAG approach addressed the formation of a zinc-pillared MOF based on terephthalic acid and 1,4-diazabicyclo[2.2.2]octane

(dabco). This MOF was synthesized after 45 min of reaction by adding catalytic amounts of sulphates or nitrates salts into the mixture. Using the same starting materials, but replacing the nitrate salt with sulphate, yielded the same pillared-layered structure but with kagome-based topology, demonstrating the active role of the salt additive in controlling the topology of the MOF.<sup>107</sup> In a very recent report, ZIF-8 was synthesized by milling ZnO and Hmim in presence of zinc acetate dihydrate. They demonstrated that, by adding zinc acetate dihydrate as both a Zn source and a catalyst, its formation could be accelerated due to the formation of acetic acid (*in situ*) that promotes the acid dissolution of ZnO. XRPD and N<sub>2</sub> adsorption measurements revealed the formation of a highly porous (BET surface area = 1720 m<sup>2</sup> g<sup>-1</sup>) and crystalline ZIF-8.<sup>108</sup>

### 1.5.3 Flow Synthesis

As mentioned above, an important limitation in the production of MOFs and COFs is the difficulty to transfer the lab-scale synthesis to large scale since it demands the optimization of many parameters. To overcome this limitation, the continuous flow methodology has been proposed as an alternative to batch synthesis. In flow synthesis, the chemical reactions occur in a continuously flowing stream in a tube or pipe rather than in a reaction vessel. The main advantages of this method are: (i) the heat and mass transfer is increased because the surface area-to-volume ratio in a flow reactor is much higher than in a batch reactor; (ii) a precise control over the reaction parameters, which facilitates the synthesis optimization; (iii) the reduction of the amount of solvent during the synthesis; and (iv) it is a scalable method. During the last years, numerous works have been reported using microfluidics, plug flow and stirred tank reactors. In this section, we will focus in synthetic methods using plug flow reactors (PFR). In this approach, the reagents are pumped through a tube or pipe and consumed as they flow down the length of the reactor.<sup>109</sup>

Gimeno-Fabre *et al.* reported for the first time the synthesis of HKUST-1 and Ni-CPO-27 using the PFR approach. MOFs were obtained by inducing their crystallisation from a stream of dissolved reagents by rapid mixing with a pre-heated water flow (up to 300 °C). The high temperatures were used in order to increase the rate of crystal growth.<sup>110</sup> Wang and co-workers used the continuous-flow microreactor-assisted solvothermal system for the synthesis of HKUST-1. Remarkably, the reaction was performed in 5 min (residence time) with a 97 % of production yield. They also demonstrated that the particle size of HKUST-1 could be adjusted from 150 nm to 4 µm by changing the temperature and the relative ratios of the solvents.<sup>111</sup> The versatility of continuous flow reactors to produce MOFs was further demonstrated by Rubio-Martinez *et al.* They synthesized HKUST-1, UiO-66 and NOTT-400 using a PFA reactor in 5, 10, and 15 min, respectively. Surprisingly, they increased the production rates from 2 to 60 g h<sup>-1</sup> using a macro-scale reactor, while maintained the quality of the MOFs in terms of crystallinity and porosity (Figure 1.27).<sup>112</sup> In a subsequent report, the same group reported the synthesis of aluminum fumarate using 4 different stainless-steel tubular flow reactors (reactor volumes of 10, 107, 374 and 1394 L). Interestingly, very high production rates were obtained when the 1394 L pilot scale reactor was used.<sup>113</sup> In addition, the reactor design used in this work demonstrated the possibility to translate reaction parameters from the laboratory scale to pilot scale without any re-optimization of the synthesis. Similarly, a water-based continuous flow synthesis of UiO-66-NH<sub>2</sub> and Zr-fumarate was reported by Stock and co-workers, in which a slurry of the starting materials was pumped in a flow reactor at 80 °C.<sup>114</sup>

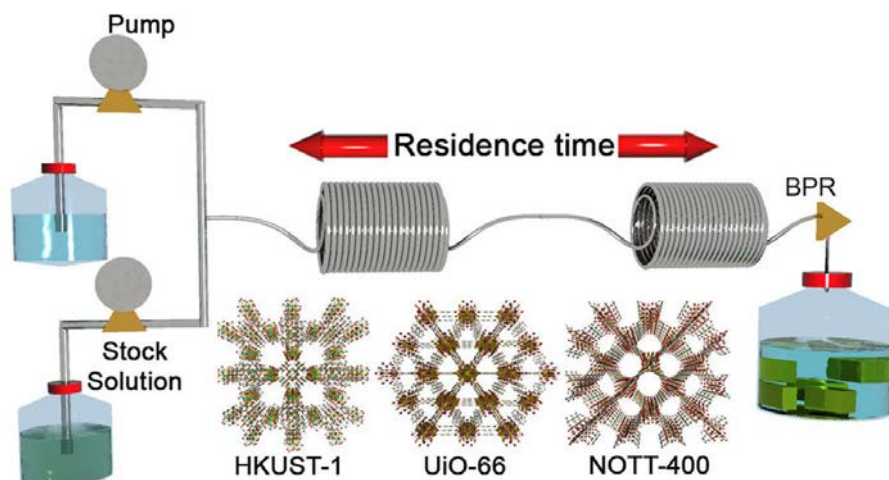


**Figure 1.27.** Schematic representation showing the continuous flow synthesis of MOFs.<sup>112</sup>

Peng *et al.* reported the first example of continuous flow synthesis of COFs. They produced COF-LZU-1 in 11 seconds at room temperature using a PTFE reactor yielding a space-time yield (STY) of  $703 \text{ kg m}^{-3} \text{ day}^{-1}$ . The resultant COF exhibited a surface area of  $453 \text{ m}^2 \text{ g}^{-1}$ , which was consistent with those reported for solvothermal synthesis.<sup>115</sup>

### 1.5.4 Spray-Drying Technique

Spray-drying is a common technique used in the industrial sector to produce a dry powder from a liquid feed (solutions, slurries or emulsions) in one simple and continuous process. Spray-drying has its origin in United States and was first patented in 1872 by Samuel Percy.<sup>116</sup> However, this technology gained importance during the World War II due to the continuous production of milk powder and the need to reduce the transport weight and volume of food and other species. Since post-war period, the process has been widely used in chemical, food and pharmaceutical industries.

Spray-drying is defined as the transformation of a fluid from a liquid state into a dried particulate form by spraying the fluid into a hot drying medium. The main principle of this method is based on the fast evaporation of the solvent by application

of heat to the feed product (droplets), inducing the precipitation in the aerosol droplet. The mechanism of the spray-drying process consists in: (i) Rapid evaporation of the solvent when the droplet is exposed to hot gas. At this stage, the droplet is heated from its initial temperature to the wet bulb temperature (heat transfer from the gas phase to the liquid phase). During this period, the removal of solvent is constant and the droplet surface remains saturated with solvent (mass transport from the liquid vapour of the droplet to the gas phase) and its temperature is constant. (ii) A thin shell of solid particles is formed at the droplet surface "*crust formation*" when the solute reaches a concentration beyond its saturation concentration. (iii) After the crust formation, the evaporation rate is controlled by the rate of vapor diffusion through the dried surface shell. At this stage ("*falling rate period*"), the temperature of the particles increases. (iv) Finally, as the moisture content decreases, the crust formation increases, and the droplet temperature ultimately rises towards the dry-bulb temperature of the air.<sup>117</sup>

The spray-drying process starts with the atomization of the solution into a large number of droplets. For example, a cubic meter of liquid forms approximately  $2 \times 10^{12}$  uniform 100 micron-sized droplets (total surface area of  $\approx 60,000 \text{ m}^2$ ). This is beneficial since a fast drying rate is achieved due to the high surface-to-volume ratio. This step can be accomplished by using an atomizer (rotary, ultrasonic or two-fluid nozzle atomizers). For instance, the feed can be atomized when the liquid impacts with high-velocity  $\text{N}_2$  or air using the two-fluid nozzle. The shear field created by the compressed air atomizes the liquid and produces the droplets. Then, the aerosol droplets are contacted and suspended in a hot gas stream causing the rapid evaporation of solvent from the surface of the droplets. Finally, the solid particles are separated by centrifugal force using a cyclone and accumulated in a collector (Figure 1.28).



the process was based on the atomization of a solution of MOF precursors into a spray of microdroplets by an atomizing device (e.g. two or three fluid nozzle). Then, the droplets were mixed with a stream of hot gas at a certain temperature in the drying chamber, inducing the solvent evaporation. At this point, there is a diffusion of the reactants to the droplet surface and the reaction starts when a certain concentration is reached. Finally, the MOF crystallization occurs on the surface of the droplet and the resulting MOF nanoparticles accumulate and merge to form hollow spherical MOF superstructures. Thus, the spray-drying methodology enables the production —even up to the kilogram-scale— of archetypical MOFs such as HKUST-1 and related paddle-wheel Cu(II)-based MOFs (Figure 1.29 and Table 1.1) in high yields and without any loss of sorption capabilities. They also found that this method could be extended to other MOF families such as IRMOF, CPOs, and ZIFs.

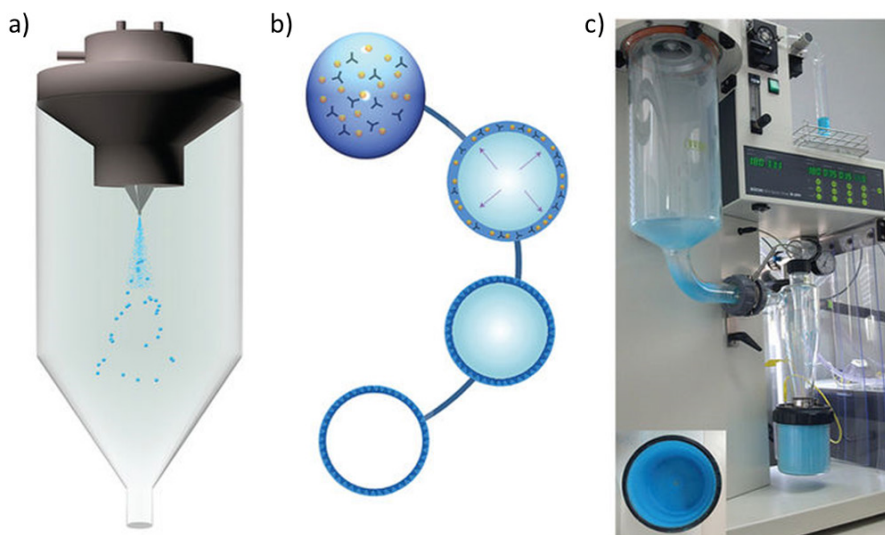


**Figure 1.29.** (a) Schematic representation of the spray-drying process used to synthesise HKUST-1. (b) Proposed spherical superstructure formation process. (c) Photograph of the spray-dryer after it use in synthesising large amounts of HKUST-1.<sup>118</sup>

**Table 1.1.** MOFs synthesized by spray-drying technique.<sup>118</sup>

MOF	Metal Ion	Ligand	Yield (%)	S <sub>BET</sub> (m <sup>2</sup> g <sup>-1</sup> )
HKUST-1	Cu(II)	BTC	70	1260
Cu-BDC	Cu(II)	BDC	70	543
NOTT-100	Cu(II)	BPTC	54	1140
MOF-14	Cu(II)	BTB	30	-
MOF-5	Zn(II)	BDC	60	1215
IRMOF-3	Zn(II)	NH <sub>2</sub> -BDC	70	-
ZIF-8	Zn(II)	MiM	10	941
MIL-88B	Fe(III)	NH <sub>2</sub> -BDC	27	-

The same year, Garcia-Marquez and co-workers demonstrated the feasibility of the spray-drying technique for the synthesis of HKUST-1, ZIF-8 and template-assisted Fe(BTC)<sub>2</sub>. They showed that, by adding a template to the precursor solution, the formation of mesophases was avoided. However, the porosity of the templated-Fe<sub>3</sub>(BTC)<sub>2</sub> was significantly lower than that reported for Basolite F300.<sup>119</sup> One advantage of spray-drying as a synthetic method is the possibility to synthesize multi-metallic MOFs, without any technological changes. With this approach, Wang *et al.* reported the synthesis of lanthanide-based MOF in which the ratio of Tb (III)/Eu(III) was controlled. They showed that the resulting MOF nanoparticles could be used as nanothermometers with high sensitivity, reproducibility, and low-temperature uncertainty.<sup>120</sup> More recently, microfluidic jet spray-drying technology has been used for the synthesis of MIL-101. The particle size (up to 80 μm) and morphology of the MOF was controlled by adjusting the solid concentration of the suspension and the drying temperature.<sup>121</sup> Kubo *et al.* studied the effects of various copper sources and pH on the spray-drying synthesis of HKUST-1. The optimum spray-drying conditions (Cu(HCOO)<sub>2</sub> and pH = 4.38) lead to spherical HKUST-1 superstructures with BET surface area of 1300 m<sup>2</sup> g<sup>-1</sup>.<sup>122</sup>

The spray-drying technique has been used to combine different materials to create capsules and composites. In these sense, Maspoch and co-workers demonstrated the potential of spray-drying to produce MOF-based composites. They synthesized different composites by spraying a mixture of different substances such as magnetic inorganic nanoparticles, NaCl, and fluorescent molecules with the MOFs precursors.<sup>118</sup> The same authors showed the synthesis of MOF@polymer composites by spray-drying. In this specific case, pre-synthesized HKUST-1 nanocrystals were encapsulated into polystyrene spheres to enhance the hydrolytic stability of HKUST-1.<sup>123</sup> Alternatively, Gholampour *et al.* encapsulated palladium nanoparticles into ZIF-8 by spray-drying technique. The Pd@ZIF-8 composites were catalytically active for alkenes hydrogenation reactions.<sup>124</sup>

## 1.6 References

- (1) Davis, M. E. *Nature* **2002**, *417*, 813.
- (2) Batten Stuart, R.; Champness Neil, R.; Chen, X.-M.; Garcia-Martinez, J.; Kitagawa, S.; Öhrström, L.; O’Keeffe, M.; Paik Suh, M.; Reedijk, J. In *Pure Appl. Chem.* 2013; Vol. 85, p 1715.
- (3) Kitagawa, S. *Faraday Discuss.* **2017**, *201*, 395.
- (4) Hoskins, B. F.; Robson, R. *J. Am. Chem. Soc.* **1989**, *111*, 5962.
- (5) Hoskins, B. F.; Robson, R. *J. Am. Chem. Soc.* **1990**, *112*, 1546.
- (6) Abrahams, B. F.; Hoskins, B. F.; Michail, D. M.; Robson, R. *Nature* **1994**, *369*, 727.
- (7) Fujita, M.; Kwon, Y. J.; Washizu, S.; Ogura, K. *J. Am. Chem. Soc.* **1994**, *116*, 1151.
- (8) Yaghi, O. M.; Li, H. *J. Am. Chem. Soc.* **1995**, *117*, 10401.
- (9) Subramanian, S.; Zaworotko, M. J. *Angew. Chem., Int. Ed. Engl.* **1995**, *34*, 2127.
- (10) Kondo, M.; Yoshitomi, T.; Matsuzaka, H.; Kitagawa, S.; Seki, K. *Angew. Chem., Int. Ed. Engl.* **1997**, *36*, 1725.
- (11) Rowsell, J. L. C.; Yaghi, O. M. *Microporous Mesoporous Mater.* **2004**, *73*, 3.
- (12) Li, H.; Eddaoudi, M.; Groy, T. L.; Yaghi, O. M. *J. Am. Chem. Soc.* **1998**, *120*, 8571.
- (13) Kitagawa, S.; Kitaura, R.; Noro, S.-i. *Angew. Chem. Int. Ed.* **2004**, *43*, 2334.
- (14) Kim, H. K.; Yun, W. S.; Kim, M.-B.; Kim, J. Y.; Bae, Y.-S.; Lee, J.; Jeong, N. C. *J. Am. Chem. Soc.* **2015**, *137*, 10009.
- (15) Chui, S. S.-Y.; Lo, S. M.-F.; Charmant, J. P. H.; Orpen, A. G.; Williams, I. D. *Science* **1999**, *283*, 1148.
- (16) Li, H.; Eddaoudi, M.; O’Keeffe, M.; Yaghi, O. M. *Nature* **1999**, *402*, 276.
- (17) Eddaoudi, M.; Moler, D. B.; Li, H.; Chen, B.; Reineke, T. M.; O’Keeffe, M.; Yaghi, O. M. *Acc. Chem. Res.* **2001**, *34*, 319.
- (18) Yaghi, O. M.; O’Keeffe, M.; Ockwig, N. W.; Chae, H. K.; Eddaoudi, M.; Kim, J. *Nature* **2003**, *423*, 705.
- (19) Kim, J.; Chen, B.; Reineke, T. M.; Li, H.; Eddaoudi, M.; Moler, D. B.; O’Keeffe, M.; Yaghi, O. M. *J. Am. Chem. Soc.* **2001**, *123*, 8239.
- (20) Rungtaweeworanit, B.; Diercks, C. S.; Kalmutzki, M. J.; Yaghi, O. *Faraday Discuss.* **2017**, *201*, 9.
- (21) Yaghi, O. M. *J. Am. Chem. Soc.* **2016**, *138*, 15507.
- (22) Eddaoudi, M.; Kim, J.; Rosi, N.; Vodak, D.; Wachter, J.; O’Keeffe, M.; Yaghi, O. M. *Science* **2002**, *295*, 469.
- (23) Diercks, C. S.; Yaghi, O. M. *Science* **2017**, *355*.
- (24) Côté, A. P.; Benin, A. I.; Ockwig, N. W.; O’Keeffe, M.; Matzger, A. J.; Yaghi, O. M. *Science* **2005**, *310*, 1166.
- (25) Waller, P. J.; Gándara, F.; Yaghi, O. M. *Acc. Chem. Res.* **2015**, *48*, 3053.

- (26) Li, H.; Pan, Q. Y.; Ma, Y. C.; Guan, X. Y.; Xue, M.; Fang, Q. R.; Yan, Y. S.; Valtchev, V.; Qiu, S. L. *J. Am. Chem. Soc.* **2016**, *138*, 14783.
- (27) Jiang, J.; Zhao, Y.; Yaghi, O. M. *J. Am. Chem. Soc.* **2016**, *138*, 3255.
- (28) Feng, X.; Ding, X.; Jiang, D. *Chem. Soc. Rev.* **2012**, *41*, 6010.
- (29) El-Kaderi, H. M.; Hunt, J. R.; Mendoza-Cortés, J. L.; Côté, A. P.; Taylor, R. E.; O'Keeffe, M.; Yaghi, O. M. *Science* **2007**, *316*, 268.
- (30) Uribe-Romo, F. J.; Hunt, J. R.; Furukawa, H.; Klöck, C.; O'Keeffe, M.; Yaghi, O. M. *J. Am. Chem. Soc.* **2009**, *131*, 4570.
- (31) Xu, H.; Gao, J.; Jiang, D. *Nat. Chem.* **2015**, *7*, 905.
- (32) Stegbauer, L.; Schwinghammer, K.; Lotsch, B. V. *Chem. Sci.* **2014**, *5*, 2789.
- (33) Kuhn, P.; Antonietti, M.; Thomas, A. *Angew. Chem. Int. Ed.* **2008**, *47*, 3450.
- (34) Jin, E.; Asada, M.; Xu, Q.; Dalapati, S.; Addicoat, M. A.; Brady, M. A.; Xu, H.; Nakamura, T.; Heine, T.; Chen, Q.; Jiang, D. *Science* **2017**, *357*, 673.
- (35) Millward, A. R.; Yaghi, O. M. *J. Am. Chem. Soc.* **2005**, *127*, 17998.
- (36) Furukawa, H.; Ko, N.; Go, Y. B.; Aratani, N.; Choi, S. B.; Choi, E.; Yazaydin, A. Ö.; Snurr, R. Q.; O'Keeffe, M.; Kim, J.; Yaghi, O. M. *Science* **2010**, *329*, 424.
- (37) Rabbani, M. G.; Sekizkardes, A. K.; Kahveci, Z.; Reich, T. E.; Ding, R.; El-Kaderi, H. M. *Chem. Eur. J.* **2013**, *19*, 3324.
- (38) Trickett, C. A.; Helal, A.; Al-Maythaly, B. A.; Yamani, Z. H.; Cordova, K. E.; Yaghi, O. M. *Nature Reviews Materials* **2017**, *2*, 17045.
- (39) Dietzel, P. D. C.; Johnsen, R. E.; Fjellvag, H.; Bordiga, S.; Groppo, E.; Chavan, S.; Blom, R. *Chem. Commun.* **2008**, 5125.
- (40) Dietzel, P. D. C.; Besikiotis, V.; Blom, R. *J. Mater. Chem.* **2009**, *19*, 7362.
- (41) Sumida, K.; Rogow, D. L.; Mason, J. A.; McDonald, T. M.; Bloch, E. D.; Herm, Z. R.; Bae, T.-H.; Long, J. R. *Chem. Rev.* **2012**, *112*, 724.
- (42) McDonald, T. M.; Lee, W. R.; Mason, J. A.; Wiers, B. M.; Hong, C. S.; Long, J. R. *J. Am. Chem. Soc.* **2012**, *134*, 7056.
- (43) Fracaroli, A. M.; Furukawa, H.; Suzuki, M.; Dodd, M.; Okajima, S.; Gándara, F.; Reimer, J. A.; Yaghi, O. M. *J. Am. Chem. Soc.* **2014**, *136*, 8863.
- (44) Huang, N.; Krishna, R.; Jiang, D. *J. Am. Chem. Soc.* **2015**, *137*, 7079.
- (45) Nugent, P.; Rhodus, V.; Pham, T.; Tudor, B.; Forrest, K.; Wojtas, L.; Space, B.; Zaworotko, M. *Chem. Commun.* **2013**, *49*, 1606.
- (46) Skarmoutsos, I.; Belmabkhout, Y.; Adil, K.; Eddaoudi, M.; Maurin, G. *J. Phys. Chem. C* **2017**, *121*, 27462.
- (47) Nugent, P.; Belmabkhout, Y.; Burd, S. D.; Cairns, A. J.; Luebke, R.; Forrest, K.; Pham, T.; Ma, S.; Space, B.; Wojtas, L.; Eddaoudi, M.; Zaworotko, M. *J. Nature* **2013**, *495*, 80.
- (48) Bhatt, P. M.; Belmabkhout, Y.; Cadiau, A.; Adil, K.; Shekhah, O.; Shkurenko, A.; Barbour, L. J.; Eddaoudi, M. *J. Am. Chem. Soc.* **2016**, *138*, 9301.
- (49) Adil, K.; Bhatt, P. M.; Belmabkhout, Y.; Abtab, S. M. T.; Jiang, H.; Assen, A. H.; Mallick, A.; Cadiau, A.; Aqil, J.; Eddaoudi, M. *Adv. Mater.* **2017**, *29*, 1702953.
- (50) Ning, H.; Ping, W.; A., A. M.; Thomas, H.; Donglin, J. *Angew. Chem. Int. Ed.* **2017**, *56*, 4982.
- (51) He, Y.; Zhou, W.; Qian, G.; Chen, B. *Chem. Soc. Rev.* **2014**, *43*, 5657.

- (52) Gallagher, J. *Nature Energy* **2018**, *3*, 86.
- (53) Peng, Y.; Krungleviciute, V.; Eryazici, I.; Hupp, J. T.; Farha, O. K.; Yildirim, T. *J. Am. Chem. Soc.* **2013**, *135*, 11887.
- (54) Tian, T.; Zeng, Z.; Vulpe, D.; Casco, M. E.; Divitini, G.; Midgley, P. A.; Silvestre-Albero, J.; Tan, J.-C.; Moghadam, P. Z.; Fairen-Jimenez, D. *Nat. Mater.* **2017**, *17*, 174.
- (55) Wu, H.; Simmons, J. M.; Liu, Y.; Brown, C. M.; Wang, X. S.; Ma, S.; Peterson, V. K.; Southon, P. D.; Kepert, C. J.; Zhou, H. C.; Yildirim, T.; Zhou, W. *Chem. Eur. J.* **2010**, *16*, 5205.
- (56) Jiang, J.; Furukawa, H.; Zhang, Y.-B.; Yaghi, O. M. *J. Am. Chem. Soc.* **2016**, *138*, 10244.
- (57) Furukawa, H.; Yaghi, O. M. *J. Am. Chem. Soc.* **2009**, *131*, 8875.
- (58) Suh, M. P.; Park, H. J.; Prasad, T. K.; Lim, D.-W. *Chem. Rev.* **2012**, *112*, 782.
- (59) Farha, O. K.; Özgür Yazaydın, A.; Eryazici, I.; Malliakas, C. D.; Hauser, B. G.; Kanatzidis, M. G.; Nguyen, S. T.; Snurr, R. Q.; Hupp, J. T. *Nat. Chem.* **2010**, *2*, 944.
- (60) Ma, S.; Eckert, J.; Forster, P. M.; Yoon, J. W.; Hwang, Y. K.; Chang, J.-S.; Collier, C. D.; Parise, J. B.; Zhou, H.-C. *J. Am. Chem. Soc.* **2008**, *130*, 15896.
- (61) Liu, J.; Chen, L.; Cui, H.; Zhang, J.; Zhang, L.; Su, C.-Y. *Chem. Soc. Rev.* **2014**, *43*, 6011.
- (62) Horike, S.; Dincă, M.; Tamaki, K.; Long, J. R. *J. Am. Chem. Soc.* **2008**, *130*, 5854.
- (63) Mondloch, J. E.; Bury, W.; Fairen-Jimenez, D.; Kwon, S.; DeMarco, E. J.; Weston, M. H.; Sarjeant, A. A.; Nguyen, S. T.; Stair, P. C.; Snurr, R. Q.; Farha, O. K.; Hupp, J. T. *J. Am. Chem. Soc.* **2013**, *135*, 10294.
- (64) Shultz, A. M.; Farha, O. K.; Hupp, J. T.; Nguyen, S. T. *J. Am. Chem. Soc.* **2009**, *131*, 4204.
- (65) Lin, S.; Diercks, C. S.; Zhang, Y.-B.; Kornienko, N.; Nichols, E. M.; Zhao, Y.; Paris, A. R.; Kim, D.; Yang, P.; Yaghi, O. M.; Chang, C. J. *Science* **2015**, *349*, 1208.
- (66) V., B. A.; G., G. M.; F., K.; M., M.; J., G. *ChemSusChem* **2015**, *8*, 809.
- (67) Diercks, C. S.; Liu, Y.; Cordova, K. E.; Yaghi, O. M. *Nat. Mater.* **2018**, *17*, 301.
- (68) Badawy, A. M. E.; Luxton, T. P.; Silva, R. G.; Scheckel, K. G.; Suidan, M. T.; Tolaymat, T. M. *Environ. Sci. Technol.* **2010**, *44*, 1260.
- (69) Kocjan, A.; Logar, M.; Shen, Z. *Sci. Rep.* **2017**, *7*, 2541.
- (70) Falcaro, P.; Ricco, R.; Yazdi, A.; Imaz, I.; Furukawa, S.; Maspooh, D.; Ameloot, R.; Evans, J. D.; Doonan, C. J. *Coord. Chem. Rev.* **2016**, *307*, Part 2, 237.
- (71) Ding, S.-Y.; Gao, J.; Wang, Q.; Zhang, Y.; Song, W.-G.; Su, C.-Y.; Wang, W. *J. Am. Chem. Soc.* **2011**, *133*, 19816.
- (72) Mekonnen, M. M.; Hoekstra, A. Y. *Science Advances* **2016**, *2*.
- (73) Kalmutzki, M. J.; Diercks, C. S.; Yaghi, O. M. *Adv. Mater.*, *0*, 1704304.
- (74) Kim, H.; Yang, S.; Rao, S. R.; Narayanan, S.; Kapustin, E. A.; Furukawa, H.; Umans, A. S.; Yaghi, O. M.; Wang, E. N. *Science* **2017**, *356*, 430.
- (75) Rieth, A. J.; Yang, S.; Wang, E. N.; Dincă, M. *ACS Central Science* **2017**, *3*, 668.
- (76) Rieth, A. J.; Dincă, M. *Joule* **2018**, *2*, 18.
- (77) AbdulHalim, R. G.; Bhatt, P. M.; Belmabkhout, Y.; Shkurenko, A.; Adil, K.; Barbour, L. J.; Eddaoudi, M. *J. Am. Chem. Soc.* **2017**, *139*, 10715.

- (78) Canivet, J.; Fateeva, A.; Guo, Y.; Coasne, B.; Farrusseng, D. *Chem. Soc. Rev.* **2014**, *43*, 5594.
- (79) Demir, H.; Mobedi, M.; Ülkü, S. *Renewable Sustainable Energy Rev.* **2008**, *12*, 2381.
- (80) de Lange, M. F.; Verouden, K. J. F. M.; Vlugt, T. J. H.; Gascon, J.; Kapteijn, F. *Chem. Rev.* **2015**, *115*, 12205.
- (81) Frohlich, D.; Henninger, S. K.; Janiak, C. *Dalton Transactions* **2014**, *43*, 15300.
- (82) Gordeeva, L. G.; Solovyeva, M. V.; Aristov, Y. I. *Energy* **2016**, *100*, 18.
- (83) Maurin, G.; Serre, C.; Cooper, A.; Ferey, G. *Chem. Soc. Rev.* **2017**, *46*, 3104.
- (84) Silva, P.; Vilela, S. M. F.; Tome, J. P. C.; Almeida Paz, F. A. *Chem. Soc. Rev.* **2015**, *44*, 6774.
- (85) Stock, N.; Biswas, S. *Chem. Rev.* **2011**, *112*, 933.
- (86) Al-Kutubi, H.; Gascon, J.; Sudhölter, E. J. R.; Rassaei, L. *ChemElectroChem* **2015**, *2*, 462.
- (87) Mueller, U.; Schubert, M.; Teich, F.; Puetter, H.; Schierle-Arndt, K.; Pastre, J. J. *Mater. Chem.* **2006**, *16*, 626.
- (88) Campagnol, N.; Van Assche, T. R. C.; Li, M.; Stappers, L.; Dinca, M.; Denayer, J. F. M.; Binnemans, K.; De Vos, D. E.; Fransaeer, J. *J. Mater. Chem. A* **2016**, *4*, 3914.
- (89) Van Assche, T. R. C.; Campagnol, N.; Muselle, T.; Terryn, H.; Fransaeer, J.; Denayer, J. F. M. *Microporous Mesoporous Mater.* **2016**, *224*, 302.
- (90) Li, W.-J.; Lu, J.; Gao, S.-Y.; Li, Q.-H.; Cao, R. *J. Mater. Chem. A* **2014**, *2*, 19473.
- (91) Martinez Joaristi, A.; Juan-Alcañiz, J.; Serra-Crespo, P.; Kapteijn, F.; Gascon, J. *Cryst. Growth Des.* **2012**, *12*, 3489.
- (92) Li, M.; Dincă, M. *J. Am. Chem. Soc.* **2011**, *133*, 12926.
- (93) Stassen, I.; Styles, M.; Van Assche, T.; Campagnol, N.; Fransaeer, J.; Denayer, J.; Tan, J.-C.; Falcaro, P.; De Vos, D.; Ameloot, R. *Chem. Mater.* **2015**, *27*, 1801.
- (94) James, S. L.; Adams, C. J.; Bolm, C.; Braga, D.; Collier, P.; Friscic, T.; Grepioni, F.; Harris, K. D. M.; Hyett, G.; Jones, W.; Krebs, A.; Mack, J.; Maini, L.; Orpen, A. G.; Parkin, I. P.; Shearouse, W. C.; Steed, J. W.; Waddell, D. C. *Chem. Soc. Rev.* **2012**, *41*, 413.
- (95) Friscic, T. *J. Mater. Chem.* **2010**, *20*, 7599.
- (96) Hessel, C. M.; Pattani, V. P.; Rasch, M.; Panthani, M. G.; Koo, B.; Tunnell, J. W.; Korgel, B. A. *Nano Lett.* **2011**, *11*, 2560.
- (97) Pichon, A.; James, S. L. *CrystEngComm* **2008**, *10*, 1839.
- (98) Tanaka, S.; Kida, K.; Nagaoka, T.; Ota, T.; Miyake, Y. *Chem. Commun.* **2013**, *49*, 7884.
- (99) Leng, K.; Sun, Y.; Li, X.; Sun, S.; Xu, W. *Cryst. Growth Des.* **2016**, *16*, 1168.
- (100) Crawford, D.; Casaban, J.; Haydon, R.; Giri, N.; McNally, T.; James, S. L. *Chem. Sci.* **2015**, *6*, 1645.
- (101) Biswal, B. P.; Chandra, S.; Kandambeth, S.; Lukose, B.; Heine, T.; Banerjee, R. *J. Am. Chem. Soc.* **2013**, *135*, 5328.
- (102) Klimakow, M.; Klobes, P.; Thünemann, A. F.; Rademann, K.; Emmerling, F. *Chem. Mater.* **2010**, *22*, 5216.

- (103) Julien, P. A.; Užarević, K.; Katsenis, A. D.; Kimber, S. A. J.; Wang, T.; Farha, O. K.; Zhang, Y.; Casaban, J.; Germann, L. S.; Etter, M.; Dinnebier, R. E.; James, S. L.; Halasz, I.; Friščić, T. *J. Am. Chem. Soc.* **2016**, *138*, 2929.
- (104) Uzarevic, K.; Wang, T. C.; Moon, S.-Y.; Fidelli, A. M.; Hupp, J. T.; Farha, O. K.; Friscic, T. *Chem. Commun.* **2016**, *52*, 2133.
- (105) Das, G.; Balaji Shinde, D.; Kandambeth, S.; Biswal, B. P.; Banerjee, R. *Chem. Commun.* **2014**, *50*, 12615.
- (106) Karak, S.; Kandambeth, S.; Biswal, B. P.; Sasmal, H. S.; Kumar, S.; Pachfule, P.; Banerjee, R. *J. Am. Chem. Soc.* **2017**, *139*, 1856.
- (107) Friščić, T.; Reid, D. G.; Halasz, I.; Stein, R. S.; Dinnebier, R. E.; Duer, M. J. *Angew. Chem. Int. Ed.* **2010**, *49*, 712.
- (108) Tanaka, S.; Nagaoka, T.; Yasuyoshi, A.; Hasegawa, Y.; Denayer, J. F. M. *Cryst. Growth Des.* **2018**, *18*, 274.
- (109) Rubio-Martinez, M.; Avci-Camur, C.; Thornton, A. W.; Imaz, I.; MasPOCH, D.; Hill, M. R. *Chem. Soc. Rev.* **2017**, *46*, 3453.
- (110) Gimeno-Fabra, M.; Munn, A. S.; Stevens, L. A.; Drage, T. C.; Grant, D. M.; Kashtiban, R. J.; Sloan, J.; Lester, E.; Walton, R. I. *Chem. Commun.* **2012**, *48*, 10642.
- (111) Kim, K.-J.; Li, Y. J.; Kreider, P. B.; Chang, C.-H.; Wannemacher, N.; Thallapally, P. K.; Ahn, H.-G. *Chem. Commun.* **2013**, *49*, 11518.
- (112) Rubio-Martinez, M.; Batten, M. P.; Polyzos, A.; Carey, K.-C.; Mardel, J. I.; Lim, K.-S.; Hill, M. R. *Sci. Rep.* **2014**, *4*, 5443.
- (113) Rubio-Martinez, M.; Hadley, T. D.; Batten, M. P.; Constanti-Carey, K.; Barton, T.; Marley, D.; Mönch, A.; Lim, K.-S.; Hill, M. R. *ChemSusChem* **2016**, *9*, 938.
- (114) Reinsch, H.; Waitschat, S.; Chavan, S. M.; Lillerud, K. P.; Stock, N. *Eur. J. Inorg. Chem.* **2016**, 4490.
- (115) Peng, Y.; Wong, W. K.; Hu, Z.; Cheng, Y.; Yuan, D.; Khan, S. A.; Zhao, D. *Chem. Mater.* **2016**, *28*, 5095.
- (116) Percy, S.; US Patent: 1872.
- (117) Anandharamakrishnan, C.; S, P. I. *Spray Drying Techniques for Food Ingredient Encapsulation*; Wiley, 2015.
- (118) Carné-Sánchez, A.; Imaz, I.; Cano-Sarabia, M.; MasPOCH, D. *Nat Chem* **2013**, *5*, 203.
- (119) Garcia Marquez, A.; Horcajada, P.; Grosso, D.; Ferey, G.; Serre, C.; Sanchez, C.; Boissiere, C. *Chem. Commun.* **2013**, *49*, 3848.
- (120) Zhuopeng, W.; Duarte, A.; Arnau, C. S.; S., B. C. D.; Inhar, I.; Daniel, M.; João, R.; D., C. L. *Adv. Funct. Mater.* **2015**, *25*, 2824.
- (121) Zhang, A.; Li, X.-Y.; Zhang, S.; Yu, Z.; Gao, X.; Wei, X.; Wu, Z.; Wu, W. D.; Chen, X. D. *J. Colloid Interface Sci.* **2017**, *506*, 1.
- (122) Kubo, M.; Saito, T.; Shimada, M. *Microporous Mesoporous Mater.* **2017**, *245*, 126.
- (123) Arnau, C. S.; C., S. K.; Carlos, C.; Majid, N.; Inhar, I.; Daniel, M. *Adv. Mater.* **2015**, *27*, 869.
- (124) Gholampour, N.; Chaemchuen, S.; Hu, Z.-Y.; Mousavi, B.; Van Tendeloo, G.; Verpoort, F. *Chem. Eng. J.* **2017**, *322*, 702.



# Chapter 2

---

## Objectives



As illustrated in **Chapter 1**, a new age in materials chemistry started with the discovery of MOFs and COFs. In particular, the introduction of reticular chemistry represented a revolutionary strategy that gave chemists infinite opportunities toward the design and construction of novel functional materials with tunable porosity and high surface areas. Indeed, as shown in **Chapter 1**, these properties render MOFs and COFs as promising materials for multiple applications of commercial interest, including gas storage, water harvesting, adsorptive heat transformation systems and catalysis. These possibilities have promoted a rapid and explosive pace of expansion in this field and as a result, academia and industry have begun to propose several initiatives towards the commercialization of these porous materials. However, despite these efforts, the scientific community has also recognized that the use of these materials could be limited by the challenges pertaining to their production methods at large scale since harsh conditions are usually needed to synthesize them. In this sense, as also illustrated in **Chapter 1**, novel approaches for their synthesis have been developed recently. In particular, the spray-drying method has emerged as a promising technology for the synthesis of MOFs at large scale. However, spray-drying is still in its embryonic stage and therefore, there are many challenges that need to be overcome.

In this context, the motivation of this Thesis emerged to face the main drawbacks that limit the applicability of spray-drying as a general method for synthesis of these porous solids. Thus, the main objective of this Thesis consists on developing new strategies to synthesize MOFs, COFs and composites using the spray-drying technique. To achieve this objective, different specific objectives have been proposed:

- ❖ Develop a new approach to synthesize high-nuclearity MOFs (*e.g.* UiO-66), taking advantage of the versatility of the spray-drying technique that enables different ways to process the precursor solution.
- ❖ Demonstrate that the spray-drying method can be used to synthesize pillared MOFs based in anionic pillars. We aim to study the formation of the outstanding isorecticular M-XF<sub>6</sub> materials (X = Si, Ti) and their adsorption properties. In

addition, we aim to extend the spray-drying method to synthesize hydrogen-bonded pillared porous networks beyond the materials based on coordination bonds.

- ❖ Demonstrate the potential of the spray-drying technique to perform covalent chemistry. We aim to study Schiff-base condensation reactions between discrete organic molecules, either on the pore surface of MOFs (post-synthetic modification) or for the synthesis of COFs.
- ❖ Use the capabilities of the spray-drying method to encapsulate and prepare MOF/COF-based composite materials. Here, we aim to combine MOFs and COFs with other functional materials or MOFs into COFs to achieve composites with synergistic or collective properties.

# Chapter 3

---

## Synthesis of Microspherical High-Nuclearity MOFs by Spray-Drying Continuous-Flow Method

This Chapter is based on the following publication:

---

Garzón-Tovar, L.; Cano-Sarabia, M.; Carne-Sanchez, A.; Carbonell, C.; Imaz, I.; MasPOCH, D. *React. Chem. Eng.* **2016**, *1*, 533.

---



### 3.1 Introduction

Over the past decade, industrial exploitation of metal–organic frameworks (MOFs) has garnered significant interest due to their exceptional porosity that could be harnessed for countless practical applications. However, despite these possibilities, the industrial applicability and economic feasibility of MOFs are currently limited, owing to a dearth of practical and cost-effective methods for pilot-scale synthesis. In this context, one approach that has traditionally been proposed for MOFs is solvothermal synthesis, which is usually conducted in closed reactors and its scalability remains challenging due to long reaction times and high production costs. However, as mentioned in **Chapter 1** other processes have recently begun to be developed in the hopes of achieving continuous, solvent-free and/or green synthesis of MOFs. These methods basically include mechanochemistry,<sup>1,2</sup> electrochemistry,<sup>3</sup> and continuous-flow techniques,<sup>4,5</sup> some of which obviate the toxic solvents or cumbersome filtration of earlier methods.<sup>6</sup>

As discussed in **Chapter 1**, the well-known industrial technique of spray-drying can also be considered a general, low-cost and scalable method for the continuous synthesis of MOFs in the form of spherical structures, nanoparticles and composites.<sup>7</sup> This methodology enabled the production —even up to the kilogram-scale— of archetypical MOFs such as HKUST-1 and related paddle-wheel Cu(II)-based MOFs (*e.g.* Cu-BDC, NOTT-100) in high yields and without any loss of sorption capabilities. However, despite this progress in the continuous and large scale production of these materials, MOFs assembled from high-nuclearity secondary-building units (SBUs) are a more challenging target. Indeed, the spray-drying synthesis of these materials results in low yields and/or poor sorption capabilities. This problem could be attributed to the inherently rapid drying kinetics in spray-drying, which complicate the formation of high nuclearity SBUs. In fact, several studies have suggested that the formation of SBUs is cardinal in MOF assembly, as they are most likely required for the nucleation and subsequent crystal growth of MOFs.<sup>8-10</sup>

Metal-organic frameworks assembled from high-nuclearity SBUs have special interest due to their high chemical and thermal stability, which confer them potential for practical applications. Compared with paddle wheel Cu(II)/Zn(II)-based MOFs, in which two metal ions (binuclear cluster) are bridged by four carboxylic groups in syn-syn mode and solvent or water ligand in the axial position,<sup>11</sup> high nuclearity MOFs are less labile to ligand substitution (*e.g.* water) due to their high connectivity between their clusters. In fact, steric factors can reduce the hydrolysis of the MOFs because the the highly connected SBUs can create a crowding effect that prevents the formation of water clusters near the metal ions.<sup>12</sup>

In this chapter, we describe an updated version of our spray-drying method, which enhances production of high-nuclearity MOFs. Specifically, by introducing a continuous-flow reactor at the entrance of the spray-dryer (Figure 3.1a-b), we have devised a continuous two-step method that marries the benefits of both systems. It works as follows: firstly, the precursor solution containing the metal salt and the organic linker is injected into a continuous coil flow reactor encased in a thermostatic oil tank, where it is heated at a certain temperature ( $T_1$ ) to promote SBU formation and nucleation. Here, the residence time ( $t$ ) of the precursor solution in the coil flow reactor is controlled by the rate of the pump (the *feed rate*). Since the outlet flow of the reactor is connected directly to the nozzle of the spray-dryer, the pre-heated solution is automatically injected into the spray-drier at the same feed rate. The solution is then atomized using a two-fluid nozzle, and is dried at a certain temperature ( $T_2$ ) and flow rate, such that the MOF growth is confined to individual micro-reactors (*i.e.* the atomized droplets).<sup>7</sup> The whole continuous process enables the collection of dried MOFs shaped in the form of microspherical superstructures (beads). Furthermore, the solvent used can simply be recovered, making the process both cost- and waste-efficient.

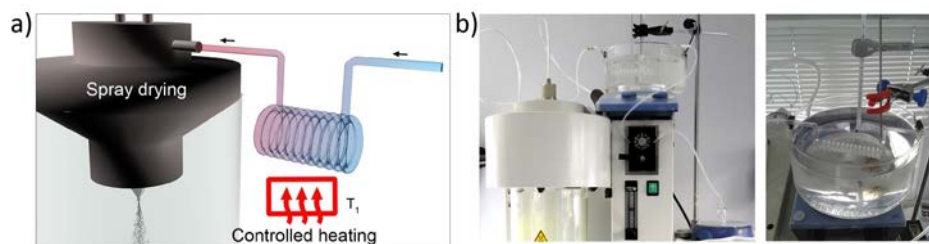


**Figure 3.1.** (a) Schematic illustration and (b) photograph showing the set-up for spray-drying continuous flow-assisted synthesis of high-nuclearity MOFs.

We first demonstrated the performance of our new method by assembling several members of the UiO-66 series, including the iconic UiO-66<sup>13</sup> and the related MOFs UiO-66-NH<sub>2</sub>,<sup>14</sup> UiO-66-NO<sub>2</sub>,<sup>14</sup> UiO-66-Acetamido,<sup>15</sup> UiO-66-Br,<sup>14</sup> UiO-66-(OH)<sub>2</sub>,<sup>16</sup> UiO-66-1,4-NDC (where 1,4-NDC is 1,4-naphthalenedicarboxylate)<sup>15</sup> and UiO-66-2,6-NDC (where 2,6-NDC is 2,6-naphthalenedicarboxylate).<sup>17,18</sup> We then extended the synthesis to other high-nuclearity MOFs such as Fe-BTC/MIL-100<sup>19</sup> and [Ni<sub>8</sub>(OH)<sub>4</sub>(H<sub>2</sub>O)<sub>2</sub>(L)<sub>6</sub>]<sub>n</sub> (where L = 1*H*-pyrazole-4-carboxylic acid).<sup>20</sup> These examples cover some of the best-known MOFs built from high-nuclearity metal clusters. We envision that by introducing different organic linkers into the MOF precursor solution before synthesis begins, we should be able to use our spray-drying continuous-flow method to prepare microspherical multivariate (MTV)-MOFs.<sup>21,22</sup>

## 3.2 Results and Discussion

### 3.2.1 Synthesis of UiO-66

We began with the synthesis of UiO-66, a robust, closely-packed, three-dimensional cubic MOF assembled by connecting hexanuclear [Zr<sub>6</sub>O<sub>4</sub>(OH)<sub>4</sub>] oxoclusters through 1,4-terephthalate (BDC) linkers (Figure 3.2).<sup>23</sup> UiO-66, which typically exhibits surface areas ( $S_{\text{BET}}$ ) ranging from 1100-1250 m<sup>2</sup>·g<sup>-1</sup>,<sup>13</sup> has already been synthesized by various methods, including solvothermal (typical yields = 90-97 %; reaction time = 24 h),<sup>24,25</sup> hydrothermal (yield = 63 %; reaction time = 24 h),<sup>26</sup> and continuous flow (yield = 63%) syntheses.<sup>5</sup>

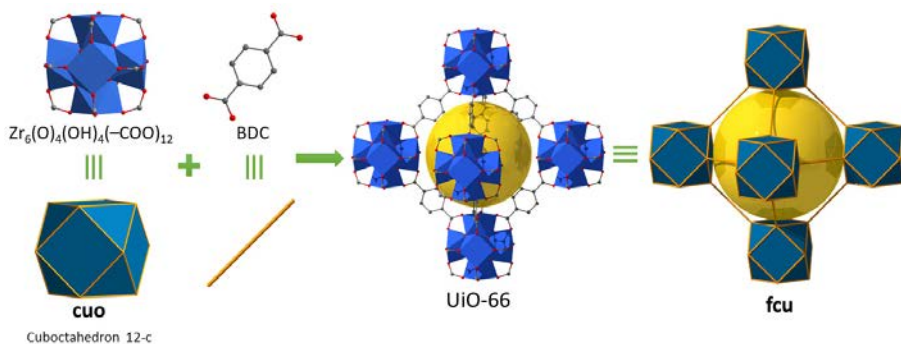


**Figure 3.2.** Schematic representation of the **UiO-66** with **fcu** topology.

In our optimized spray-drying continuous flow-assisted synthesis (SDCF) of **UiO-66**, a precursor solution containing  $ZrCl_4$ , BDC,  $H_2O$  and DMF in a molar ratio of 1:1:40:135 (concentration of  $ZrCl_4 = 0.1$  M) was injected into the coil flow reactor at a feed rate of  $2.4 \text{ mL min}^{-1}$  and at a  $T_1$  of  $115 \text{ }^\circ\text{C}$ . The residence time inside the coil flow reactor was 63 s. The resulting pre-heated solution was then spray dried at a  $T_2$  of  $180 \text{ }^\circ\text{C}$  and a flow rate of  $336 \text{ mL min}^{-1}$ , using a B-290 Mini Spray Dryer (BUCHI Labortechnik), immediately affording a white powder. This powder was washed with DMF and ethanol, and finally dried at  $80 \text{ }^\circ\text{C}$  (yield = 70 %). Note here that, under these optimized conditions, the space-time yield (STY) is  $19.6 \text{ Kg m}^{-3} \text{ day}^{-1}$  (Equation 3.1). This STY is much higher than that previously reported using the conventional spray-drying method ( $4.0 \text{ Kg m}^{-3} \text{ day}^{-1}$ ), in which the reactant solution was also preheated for two hours before spraying.<sup>7</sup>

$$STY = \frac{\text{Production rate} \left( \frac{\text{Kg}}{\text{day}} \right)}{\text{Feed rate} \left( \frac{\text{m}^3}{\text{h}} \right) \times 24\text{h}} \quad (3.1)$$

Field-emission scanning electron microscopy (FESEM) images, Elemental mapping with energy dispersive X-ray spectrometry (EDX) and X-ray powder diffraction (XRPD) patterns of the resulting solid revealed the homogeneous formation of **UiO-66** in the form of spherical beads (Figure 3.3). These microscale beads comprise multiple **UiO-66** nanoparticles, contain a dense core, and have an average diameter of  $4.3 \pm 2.6 \text{ }\mu\text{m}$ . The microporosity of the synthesized **UiO-66** was confirmed by nitrogen-

adsorption measurements, which gave an  $S_{\text{BET}}$  value of  $1106 \text{ m}^2 \text{ g}^{-1}$  (Figure 3.3f). This value is consistent with previously reported values,<sup>13</sup> thus confirming the quality of our synthesized **UiO-66**.

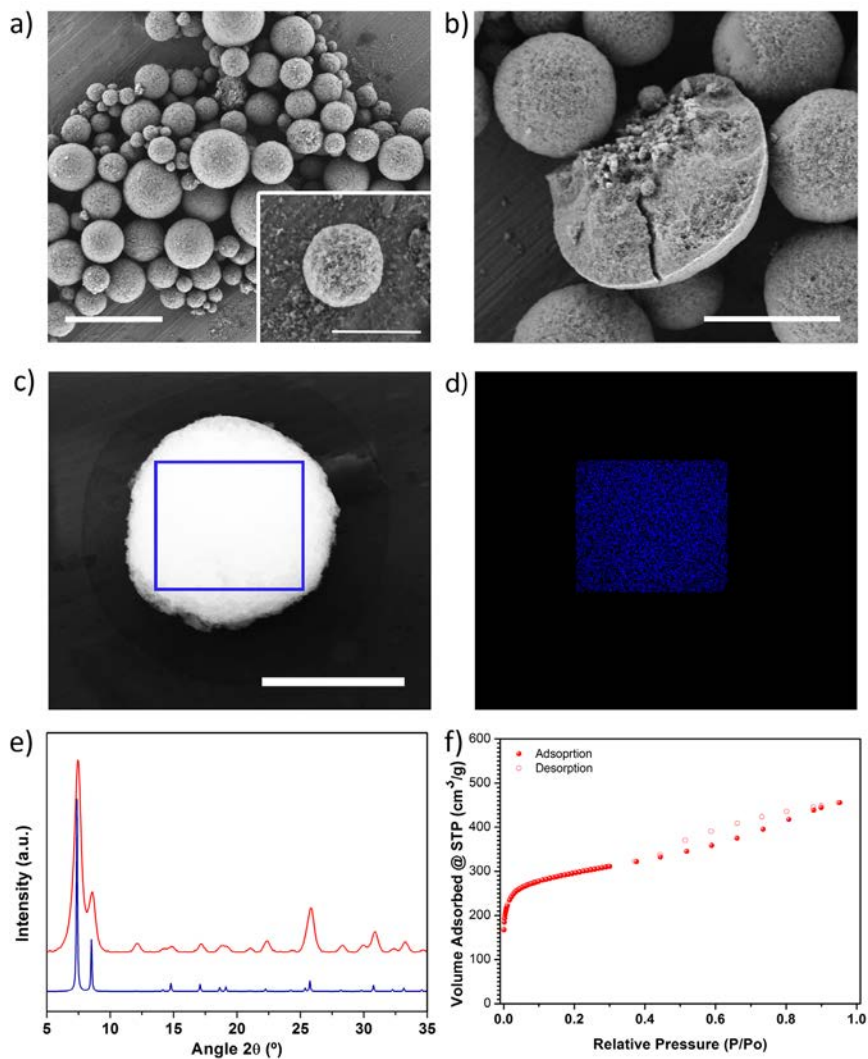


**Figure 3.3.** (a) FESEM images of the microspherical beads of **UiO-66**. (b) Broken bead showing that these spheres are compact. (c,d) Elemental mapping with EDX performed on a single spherical bead of **UiO-66**, showing the homogeneous distribution of Zr (blue). (e) XRPD pattern of **UiO-66** powder (red), as compared to the corresponding simulated powder pattern (dark blue). (f)  $\text{N}_2$  adsorption isotherm of the synthesized **UiO-66**. Scale bars: (a, c)  $5 \mu\text{m}$ , (b)  $3 \mu\text{m}$ , and (inset)  $1 \mu\text{m}$ .

We would like to point out that the spherical MOF superstructures (beads) that we prepared with our spray-drying continuous flow-assisted process are highly compact, unlike the hollow superstructures that we had previously obtained by spray-drying.<sup>7</sup> We attribute this difference to the formation, inside the reactor, of a suspension containing a primary nucleus. In a general spray-drying process, the atomized droplets are exposed to hot air, the solvent evaporates and consequently, the droplet surface shrinks.<sup>27</sup> During this process, hollow superstructures are formed when there is a non-linear change in precursor concentration at the droplet: specifically, it causes the formation of an impermeable shell and the generation of gas at the core.<sup>28,29</sup> However, in our case, uniform precursor concentration and droplet temperature are reached, owing to the presence of the uniformly-distributed nuclei in the droplet. The rate at which the nucleus can be brought to the surface by diffusion is lower than the rate at which the nucleus can grow during the drying-evaporation process. This difference favors a linear change in precursor concentration and temperature at the droplet, and consequently, drives the formation of dense superstructures.

To prove that the effective synthesis of **UiO-66** results from using both techniques in tandem, rather than simply from one of them, we separately performed the spray-drying step and the continuous-flow step using the aforementioned conditions. Spray-drying alone afforded a non-porous amorphous solid (Figure 3.4), whereas continuous-flow synthesis alone provided **UiO-66** (Figure 3.5), albeit in a much lower yield (12 %) and quality ( $S_{\text{BET}} = 708 \text{ m}^2 \text{ g}^{-1}$ ) than that obtained when the two methods were combined.

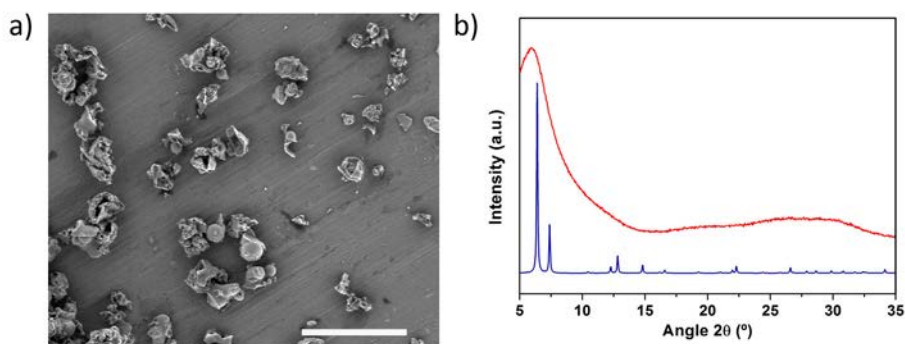


**Figure 3.4.** Synthesis of **UiO-66** using only the spray-drying technique. (a) FESEM image showing the amorphous material, and (b) XRPD pattern of the non-porous amorphous solid compared with the simulated powder pattern for **UiO-66** (black). Scale bar: 10  $\mu\text{m}$ .

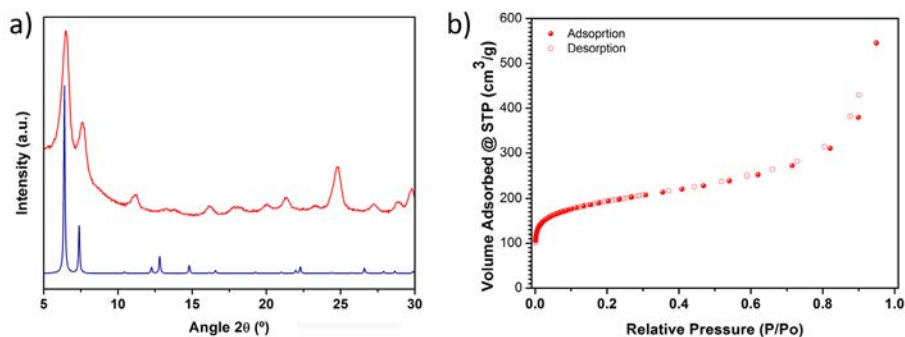


**Figure 3.5.** Synthesis of **UiO-66** using only the continuous flow synthesis. (a) XRPD pattern of this powder compared to the simulated powder pattern for **UiO-66** (dark blue), and (b)  $\text{N}_2$  adsorption isotherm of the collected powder.

To optimize the synthesis of a given MOF using our spray-drying continuous flow-assisted method, one can adjust the standard reaction parameters: the reagents and solvents used, the stoichiometry of the precursor solution, and the concentration of the precursors. Moreover, one can tune method-specific parameters such as the residence time ( $t$ ), the two temperatures ( $T_1$  and  $T_2$ ), and the flow rate. Accordingly, we began our optimization of the synthesis of **UiO-66** by selecting  $\text{ZrCl}_4$  and BDC as reagents; DMF and  $\text{H}_2\text{O}$  as solvents; an initial concentration of 0.1 M for both reagents; a final molar ratio ( $\text{Zr}/\text{BDC}/\text{H}_2\text{O}/\text{DMF}$ ) of 1:1:30:135; a  $T_1$  of 115  $^\circ\text{C}$ ; a  $T_2$  of 180  $^\circ\text{C}$ ; and a flow rate of 336  $\text{mL min}^{-1}$ . It is important to highlight here that we introduced water

into the precursor solution because it is known to favor the formation of **UiO-66**.<sup>16,25</sup> Also, we selected a concentration of 0.1 M because it is the maximum concentration that has already been demonstrated for the continuous flow synthesis of **UiO-66**.<sup>5,30</sup> We chose a  $T_2$  of 180 °C because it is the minimum temperature needed to fully evaporate DMF inside the spray-drier, and we chose a flow rate of 336 mL min<sup>-1</sup> because we had previously found it to be optimal for the spray-drying synthesis of MOFs.<sup>7</sup>

Using the pre-defined conditions described above, we sought to optimize the residence time ( $t$ ) of the precursor solution in the coil flow reactor. To this end, we systematically varied  $t$  (35, 41, 48, 63, 94 or 130 s, which correspond to feed rates of 4.5, 3.6, 3.0, 2.4, 1.8 or 1.2 mL·min<sup>-1</sup>, respectively) to evaluate its effect on the purity, yield and  $S_{\text{BET}}$  of the synthesized **UiO-66** (Table 3.1; Figure 3.6). We found that the optimal  $t$  value was 63 s.

**Table 3.1.** Summary of the  $S_{\text{BET}}$  values, yield and purity obtained for different samples in the optimisation of the feed rate in the synthesis of **UiO-66**.

Equivalents of water (x)	Feed rate (mL min <sup>-1</sup> )	Residence time (s)	$T_1$ (°C)	Yield (%)	Purity (%)	$S_{\text{BET}}$ (m <sup>2</sup> g <sup>-1</sup> )	Pore Volume (cm <sup>3</sup> g <sup>-1</sup> ) <sup>a</sup>
30	4.5	35	115	32	25	555	0.255
30	3.6	41	115	28	22	875	0.406
30	3.0	48	115	55	38	893	0.405
30	2.4	63	115	52	36	1044	0.485
30	1.8	94	115	77	48	667	0.273
30	1.2	130	115	90	57	687	0.278

<sup>a</sup> The micropore volume was determined by application of the Dubinin–Radushkevich equation to the  $N_2$  adsorption isotherm in an adequate range of linearity.

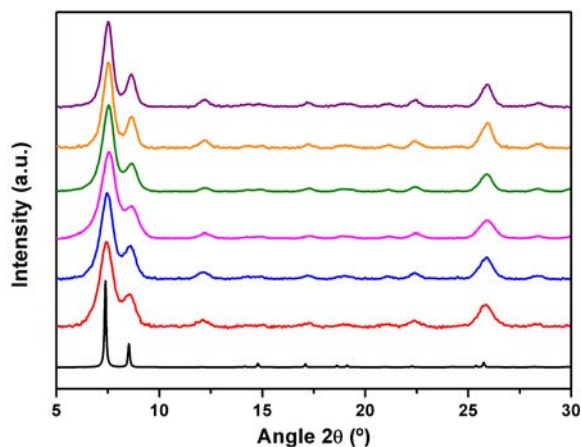


**Figure 3.6.** XRPD patterns of the **UiO-66** powders collected after their synthesis at different reaction times (Red:  $t = 35$  s; feed rate =  $4.5 \text{ mL min}^{-1}$ , Blue:  $t = 41$  s; feed rate =  $3.6 \text{ mL min}^{-1}$ , Pink:  $t = 48$  s; feed rate =  $3.0 \text{ mL min}^{-1}$ , Green:  $t = 63$  s; feed rate =  $2.4 \text{ mL min}^{-1}$ , Orange:  $t = 94$  s; feed rate =  $1.8 \text{ mL min}^{-1}$ , Purple:  $t = 130$  s; feed rate =  $1.2 \text{ mL min}^{-1}$ ), as compared to the simulated powder pattern for **UiO-66** (black).

Interestingly, we observed clogging effects at  $t$  values of 94 s and 130 s, which we ascribed to the formation of large precipitates of **UiO-66** inside the coil flow reactor. Importantly, we observed that at 94 s and 130 s, the **UiO-66** (most of which had been synthesized in the coil flow reactor) exhibited much lower  $S_{\text{BET}}$  values ( $667$  and  $687 \text{ m}^2 \text{ g}^{-1}$ , respectively) than that produced at  $t = 63$  s ( $1044 \text{ m}^2 \text{ g}^{-1}$ ). This observation was crucial because it further confirmed the benefits of the spray-drying step on the crystal growth of **UiO-66**. Indeed, when we reproduced the reaction using only the continuous-flow process (without the spray drying step; residence time = 94 s), the **UiO-66** was obtained in relatively high yield (58 %, Figure 3.7) but with a low  $S_{\text{BET}}$  value ( $610 \text{ m}^2 \text{ g}^{-1}$ ), which was comparable to that obtained with the spray-drying continuous flow-assisted method using the same residence time. This result confirmed that as the residence time increases, the proportion of the **UiO-66** synthesized in the coil flow reactor increases and the quality of the product decreases.

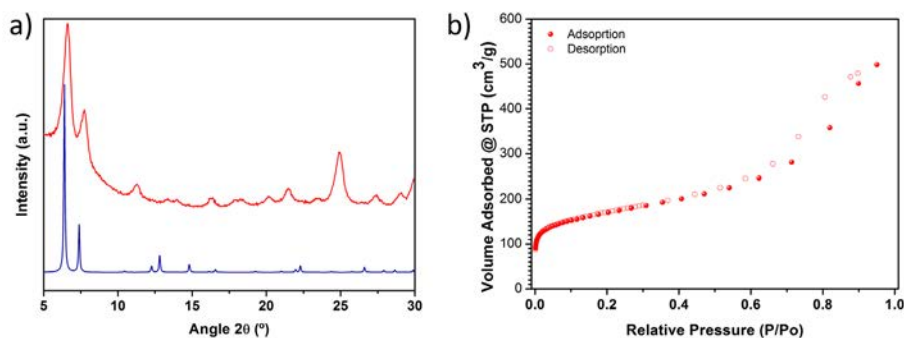


**Figure 3.7.** Synthesis of **UiO-66** using only the continuous flow synthesis; residence time = 94 s. (a) XRPD pattern of this powder compared to the simulated powder pattern for **UiO-66** (dark blue), and (b)  $N_2$  adsorption isotherm of the collected powder.

Having determined the optimum residence time for the spray-drying continuous flow-assisted synthesis of **UiO-66**, we then studied the effects of  $H_2O$  as co-solvent by varying the equivalents of it ( $x = 20, 30, 40, 45$  or  $50$ ; see Table 3.2 and Figure. 3.8) in the  $Zr/BDC/H_2O/DMF$  (molar ratio =  $1:1:x:135$ ) precursor solution. As expected,<sup>16,25</sup> we found that increasing the amount of  $H_2O$  led to better yields: thus at  $x = 40$ , the yield was 70 % ( $S_{BET} = 1106 \text{ m}^2 \text{ g}^{-1}$ ), and at  $x = 45$ , the yield was 84 % ( $S_{BET} = 963 \text{ m}^2 \text{ g}^{-1}$ ). However, we could not surpass a value of  $x = 50$ , the value at which the precursor solution begins to boil inside the coil flow reactor, consequently impeding its correct flow.

**Table 3.2.** Summary of the  $S_{BET}$  values, yield and purity obtained for different samples in the optimisation of the equivalents of water ( $x$ ) in the synthesis of **UiO-66**.

Equivalents of water ( $x$ )	Feed rate ( $\text{mL min}^{-1}$ )	Residence time (s)	$T_1$ ( $^{\circ}\text{C}$ )	Yield (%)	Purity (%)	$S_{BET}$ ( $\text{m}^2 \text{ g}^{-1}$ )	Pore Volume ( $\text{cm}^3 \text{ g}^{-1}$ ) <sup>a</sup>
20	2.4	63	115	9	6	X	X
30	2.4	63	115	52	36	1044	0.485
40	2.4	63	115	70	54	1106	0.495
45	2.4	63	115	84	59	963	0.399

<sup>a</sup> The micropore volume was determined by application of the Dubinin–Radushkevich equation to the  $N_2$  adsorption isotherm in an adequate range of linearity.

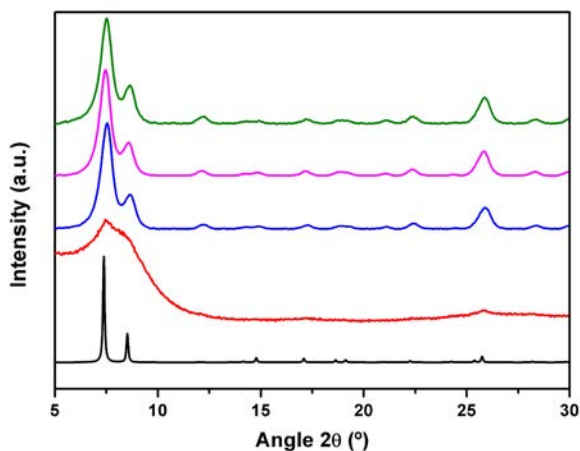


**Figure 3.8.** XRPD patterns of the UiO-66 powders collected after their synthesis at different equivalents of water (Red:  $x = 20$ ; Blue:  $x = 30$ ; Pink:  $x = 40$ ; Green:  $x = 45$ ), as compared to the simulated powder pattern for UiO-66 (black).

Finally, we also studied the effect of  $T_1$  in the coil flow reactor, by decreasing the value from 115 °C to 90 °C (Table 3.3 and Figure 3.9). We observed that this decrease causes a decrease in the yield and in the  $S_{\text{BET}}$ . This observation was very important because it corroborated that a minimum  $T_1$  is required in the coil flow reactor to generate sufficient energy to induce nucleation.

**Table 3.3.** Summary of the  $S_{\text{BET}}$  values, yield and purity obtained for different samples in the optimisation of the bath temperature ( $T_1$ ) in the synthesis of UiO-66.

Equivalents of Water ( $x$ )	Feed rate (mL min <sup>-1</sup> )	Residence Time (s)	$T_1$ (°C)	Yield (%)	Purity (%)	$S_{\text{BET}}$ (m <sup>2</sup> g <sup>-1</sup> )	Pore Volume (cm <sup>3</sup> g <sup>-1</sup> ) <sup>a</sup>
45	2.4	63	92	68	50	465	0.192
45	2.4	63	101	71	52	648	0.263
45	2.4	63	105	65	46	935	0.391
45	2.4	63	110	84	59	931	0.408
45	2.4	63	115	84	59	963	0.399

<sup>a</sup> The micropore volume was determined by application of the Dubinin–Radushkevich equation to the N<sub>2</sub> adsorption isotherm in an adequate range of linearity..

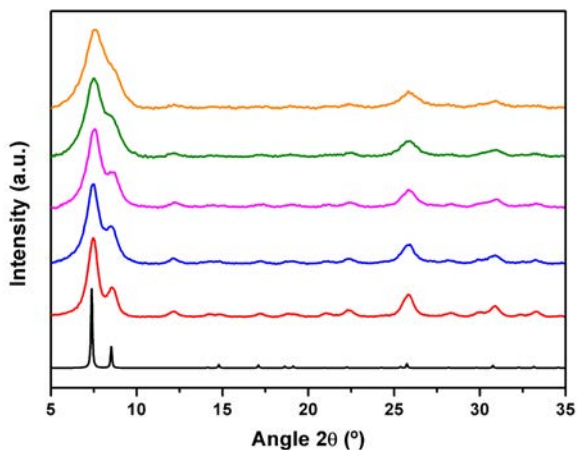


**Figure 3.9.** XRPD patterns of the **UiO-66** powders collected after their synthesis at different bath temperatures ( $T_1$ ) (Red: 115 °C, Blue: 110 °C, Pink: 105 °C, Green: 100 °C, Orange: 90 °C), as compared to the simulated powder pattern for **UiO-66** (black).

### 3.2.2 Isorecticular synthesis of UiO-66 series

To demonstrate the generality of our approach for high-nuclearity MOFs, we used it to synthesize several other members of the UiO-66 series, including **UiO-66-NH<sub>2</sub>**, **UiO-66-NO<sub>2</sub>**, **UiO-66-Acetamido**, **UiO-66-Br**, **UiO-66-(OH)<sub>2</sub>**, **UiO-66-1,4-NDC** and **UiO-66-2,6-NDC**. Figure 3.10i show typical FESEM images of the resulting microspherical beads (0.5 - 5.9  $\mu\text{m}$ ) created by the close packing of smaller crystals (Table 3.4). The different samples reveal a rather broad size distribution. This is mainly because the synthetic conditions used for each UiO-66 were optimized to synthesize them in a good quality and yield instead of optimizing the droplet size distribution, a parameter that usually depends on the liquid viscosity, surface tension, mass rate of atomization air and liquid feed rate. For all synthesized members of the UiO-66 series, XRPD studies confirmed their phase purity (Figure 3.10ii), whereas nitrogen physical adsorption confirmed their microporosity: all the calculated BET surface areas were similar to previously reported values (Figure 3.10iii and Table 3.4).

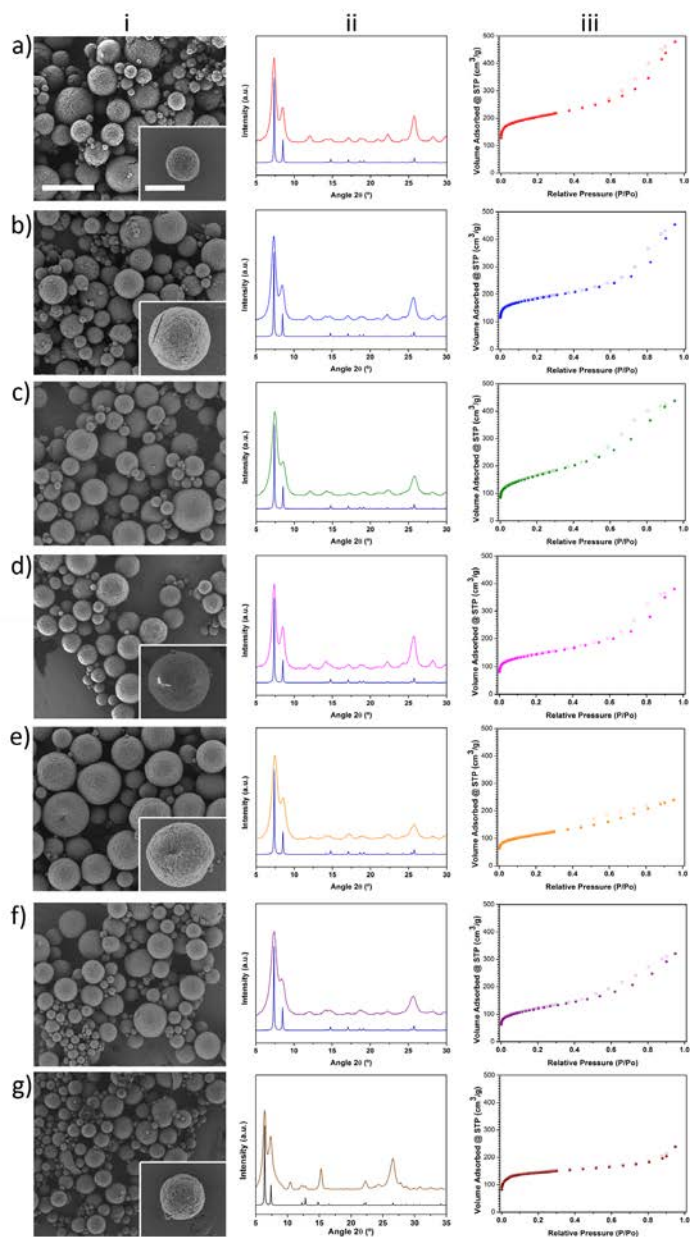


**Figure 3.10.** Isoreticular series of **UiO-66** synthesized by **CFSD**. The list of the MOFs comprises (a) **UiO-66-NH<sub>2</sub>**, (b) **UiO-66-NO<sub>2</sub>**, (c) **UiO-66-Acetamido**, (d) **UiO-66-Br**, (e) **UiO-66-(OH)<sub>2</sub>**, (g) **UiO-66-1,4-NDC** and (f) **UiO-66-2,6-NDC**. The FESEM images of the synthesized microspherical MOFs beads, the corresponding experimental and simulated (dark blue) XRPD patterns (for comparison) and their N<sub>2</sub> adsorption isotherms, are shown for each MOF. Scale bars: 10 μm (all images) and 5 μm (all insets).

**Table 3.4.** Summary of the average particle sizes,  $S_{\text{BET}}$  values, yield and purity of the different MOFs prepared by the spray-drying continuous-flow method.

MOF	Average diameter ( $\mu\text{m}$ ) <sup>a</sup>	Yield (%)	Purity (%)	$S_{\text{BET}}$ ( $\text{m}^2 \text{g}^{-1}$ )
UiO-66-NH <sub>2</sub>	4.8 ± 2.2	67	49	752
UiO-66-NO <sub>2</sub>	4.9 ± 2.0	62	49	679
UiO-66-Acetamido	3.6 ± 1.7	51	41	586
UiO-66-Br	3.1 ± 1.8	68	62	527
UiO-66-(OH) <sub>2</sub>	5.4 ± 2.2	81	67	401
UiO-66-1,4-NDC	7.3 ± 1.9	45	45	431
UiO-66-2,6-NDC	4.7 ± 2.6	49	37	557

<sup>a</sup> measured by laser diffraction measurements (LD).

### 3.2.3 Synthesis of Fe-BTC/MIL-100 and $[\text{Ni}_8(\text{OH})_4(\text{H}_2\text{O})_2(\text{L})_6]_n$

We then extended our synthesis of high-nuclearity MOFs to **Fe-BTC/MIL-100** and  $[\text{Ni}_8(\text{OH})_4(\text{H}_2\text{O})_2(\text{L})_6]_n$ , whose SBUs are a trinuclear iron cluster and an octanuclear nickel cluster, respectively. Microspherical beads of **Fe-BTC/MIL-100** were obtained in very high yield (78 %) and with a  $S_{\text{BET}}$  value of 1039  $\text{m}^2 \text{g}^{-1}$  (Figure 3.11b,d and f). We would like to point out to the reader that, whilst the XRPD pattern exhibited low crystallinity and the  $S_{\text{BET}}$  value is much lower than the value obtained for **Fe-BTC/MIL-100** synthesized under solvothermal conditions ( $S_{\text{BET}} = 2200 \text{ m}^2 \text{g}^{-1}$ ), it is nevertheless comparable to that of the commercially available material Basolite F300 (maximum  $S_{\text{BET}} = 1040 \text{ m}^2 \text{g}^{-1}$ )<sup>31,32</sup> and to that of material previously synthesized by spray-drying ( $S_{\text{BET}} = 600$  or  $1010 \text{ m}^2 \text{g}^{-1}$ ).<sup>33</sup> However, unlike the previously reported spray-drying synthesis, our spray-drying continuous flow-assisted method does not require the use of surfactants. Alternatively,  $[\text{Ni}_8(\text{OH})_4(\text{H}_2\text{O})_2(\text{L})_6]_n$  was obtained as a highly crystalline material (yield = 60 %; see Figure 3.11a,c and e), with a higher  $S_{\text{BET}}$  value (377  $\text{m}^2 \text{g}^{-1}$ ) than that previously reported (205  $\text{m}^2 \text{g}^{-1}$ ).<sup>20</sup>

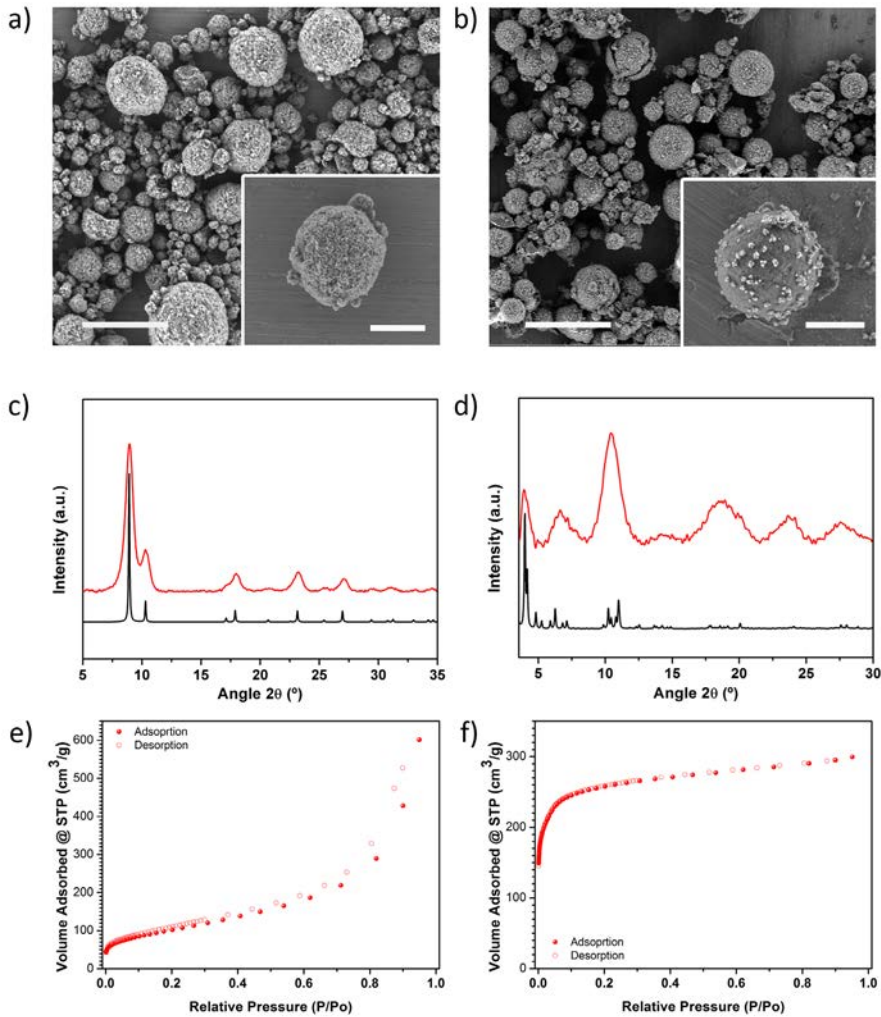


**Figure 3.11.** Representative FESEM images showing a general view of the microspherical beads of (a)  $[\text{Ni}_8(\text{OH})_4(\text{H}_2\text{O})_2(\text{L})_6]_n$  and (b) MIL-100. (c) XRPD pattern of the obtained powder compared with the simulated powder pattern of  $[\text{Ni}_8(\text{OH})_4(\text{H}_2\text{O})_2(\text{L})_6]_n$  (black). (d) XRPD pattern of the obtained powder compared with the simulated powder pattern of the MIL-100.  $\text{N}_2$  adsorption isotherms of (e)  $[\text{Ni}_8(\text{OH})_4(\text{H}_2\text{O})_2(\text{L})_6]_n$  and (f) MIL-100.

Scale bars: (a) 10  $\mu\text{m}$  and (b) 20  $\mu\text{m}$ . Insets: (a) 5  $\mu\text{m}$  and (b) 2  $\mu\text{m}$ .

### 3.2.4 Synthesis of MTV-MOFs

Having demonstrated that our spray-drying continuous flow-assisted method enables the formation of high-nuclearity microspherical MOFs, we pondered whether it could also serve for the synthesis of **MTV-MOFs** that would combine the characteristics of different organic linkers. To explore this possibility, we reproduced the spray-drying continuous flow-assisted synthesis of **UiO-66**, except that instead of pure BDC, we used a mixture of BDC and Br-BDC, testing different BDC/BDC-Br molar ratios (1:0.5, 1:1 or 1:2). In all cases, FESEM and XRPD of the resulting white solids confirmed the formation of the characteristic beads made of pure **UiO-66**-type phase (Figure 3.12a and Figure 3.13a-c).

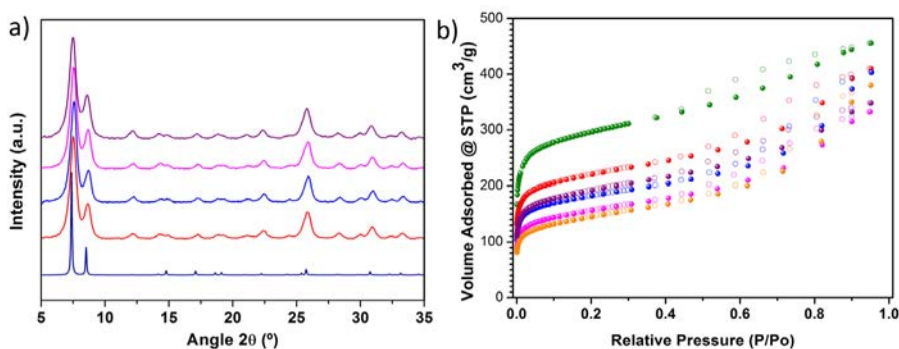


**Figure 3.12.** (a) XRPD patterns of the **MTV-UiO-66** collected after their synthesis at different BDC/BDC-Br molar ratios (Red: 1:0.6, Blue: 1:1.3, Pink: 1:2.3) and at BDC/BDC-Br/BDC-NH<sub>2</sub> molar ratio of 1:1.1:0.6 (purple), as compared to the simulated powder pattern for UiO-66 (dark blue). (b) N<sub>2</sub> adsorption isotherms of the synthesised **UiO-66** (Green), **UiO-66-Br** (Orange) and **MTV-UiO-66** at different BDC/BDC-Br molar ratios (Red: 1:0.6, Blue: 1:1.3, Pink: 1:2.3) and at BDC/BDC-Br/BDC-NH<sub>2</sub> molar ratio of 1:1.1:0.6 (purple).

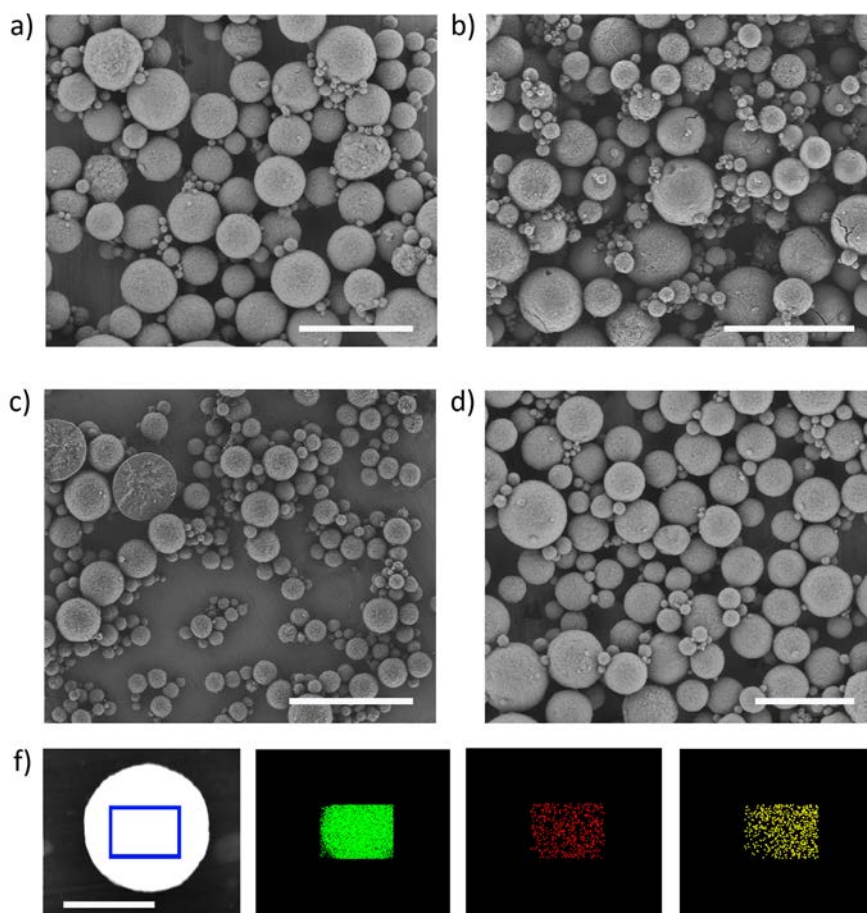


**Figure 3.13.** SEM images of **MTV-Uio-66** series. (a) **MTV-Uio-66** showing BDC:BDC-Br molar ratio of 1:0.6, (b) **MTV-Uio-66** showing BDC:BDC-Br molar ratio of 1:1.3, (c) **MTV-Uio-66** showing BDC:BDC-Br molar ratio of 1:2.3, and (d) **MTV-Uio-66** showing BDC:BDC-Br:BDC-NH<sub>2</sub> molar ratio of 1:1.1:0.6. (f) Elemental mapping with EDX performed on a single spherical bead of **MTV-Uio-66** (BDC, BDC-Br and BDC-NH<sub>2</sub>), showing the homogeneous distribution of Zr (green), Br (red) and N (yellow). Scale bars: (a,c,d) 10  $\mu$ m, (b) 20  $\mu$ m, (c) 5  $\mu$ m.

Quantitative analyses of the digested microspherical beads by <sup>1</sup>H-NMR spectroscopy (Figure 3.14a) confirmed that both linkers were present in the synthesized **MTV-Uio-66** samples, revealing BDC/BDC-Br molar ratios of 1:0.6, 1:1.3 or 1:2.3. Interestingly, these ratios were close to those expected from the corresponding input ratios used in the reaction mixtures. We further studied the porosity of all the synthesized **MTV-Uio-66** through nitrogen sorption measurements conducted at 77 K.

Remarkably, all the products were porous to  $N_2$ . As expected, the  $S_{BET}$  values decreased with increasing equivalents of BDC-Br:  $818 \text{ m}^2 \text{ g}^{-1}$  for 0.6;  $678 \text{ m}^2 \text{ g}^{-1}$  for 1.3; and  $570 \text{ m}^2 \text{ g}^{-1}$  for 2.3 (Figure 3.12b). We attributed this trend to an increase in steric hindrance resulting from the introduction of more (bulky) BDC-Br linkers into the **UiO-66** framework.

66

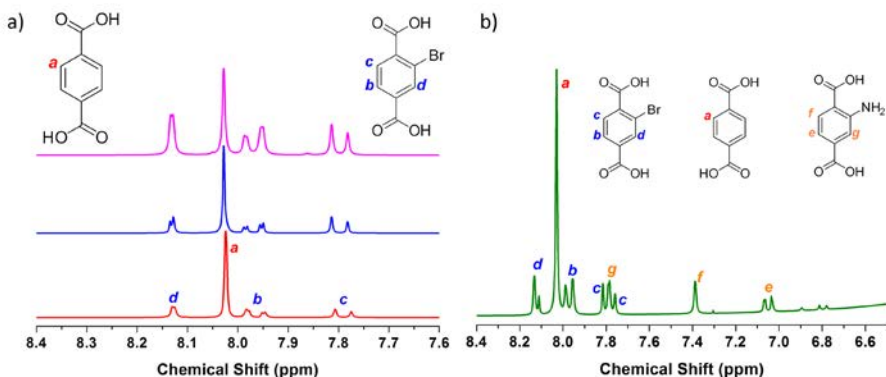


**Figure 3.14.** (a)  $^1\text{H-NMR}$  spectra of the digested samples of the **MTV-UiO-66** synthesised at different BDC/BDC-Br molar ratios (Red: 1:0.6, Blue: 1:1.3, Pink: 1:2.3). (b)  $^1\text{H-NMR}$  spectra of the digested sample of the **MTV-UiO-66** prepared by mixing BDC, BDC-Br and BDC-NH<sub>2</sub> ligands.

Finally, we sought to increase the complexity of the synthesized **MTV-UiO-66** by mixing the BDC, BDC-Br and BDC-NH<sub>2</sub> linkers at a molar ratio of 1:1:1. Again, FESEM and XRPD of the resulting product (a yellow solid) revealed the formation of microspherical beads made of pure **UiO-66**-type phase (Figure 3.12a and Figure 3.13d), whereas the  $^1\text{H-NMR}$  spectrum confirmed the presence of the three linkers at a molar ratio (BDC/BDC-Br/BDC-NH<sub>2</sub>) of 1:1.1:0.6 (Figure 3.14b). The presence of these linkers was further confirmed by elemental mapping with energy dispersive X-ray spectrometry (EDX) performed on a single bead, which revealed a highly uniform distribution of Zr, Br and N atoms (Figure 3.13f). Additionally, this MOF was found to be porous to  $N_2$ , exhibiting an  $S_{BET}$  of  $707 \text{ m}^2 \text{ g}^{-1}$  (Figure 3.12b).

### 3.3 Conclusions

In conclusion, we have reported an updated version of the spray-drying methodology for MOF fabrication, which enables simultaneous synthesis and shaping of microspherical high-nuclearity MOF beads. This new method is based on incorporating a continuous flow reactor at the entrance of the spray-drier. It thus combines the advantages of continuous flow to those of spray-drying, providing MOFs in good yields, with excellent porosity and highly dense cores. Furthermore, it is amenable to the fabrication of **MTV MOFs**, thereby opening up new avenues for fine-tuning the porosity of these materials. We hope that our new method, together with existing ones (*e.g.* mechanosynthesis, electrochemistry, and continuous-flow chemistry), will facilitate the industrial development and exploitation of MOFs.

### 3.4 Experimental Section

#### 3.4.1 Materials and methods

Zirconium chloride, nickel acetate tetrahydrate, iron(III) nitrate nonahydrate, terephthalic acid, 2-aminoterephthalic acid, 2-bromoterephthalic acid, 2-nitroterephthalic acid, 2,5-dihydroxyterephthalic acid, 1,4-naphthalenedicarboxylic acid, 2,6-naphthalenedicarboxylic acid, benzene-1,3,5-tricarboxylic acid and 1*H*-pyrazole-4-carboxylic acid were purchased from Sigma Aldrich. Dimethylformamide was obtained from Fisher Chemical. All the reagents were used without further purification. Deionized water, obtained with a Milli-Q<sup>®</sup> system (18.2 M $\Omega$ -cm), was used in all reactions. 2-acetamidoterephthalic acid was synthesised according to the reported procedure.<sup>34</sup>

X-ray powder diffraction (XRPD) patterns were collected on an X'Pert PRO MPDP analytical diffractometer (Panalytical) at 45 kV, 40 mA using CuK $\alpha$  radiation ( $\lambda = 1.5419 \text{ \AA}$ ). Nitrogen adsorption and desorption measurements were done at 77 K using an Autosorb-IQ-AG analyser (Quantachrome Instruments). Field-Emission Scanning

Electron Microscopy (FESEM) images were collected on a FEI Magellan 400L scanning electron microscope at an acceleration voltage of 2.0 KV and FEI Quanta 650F scanning electron microscope at an acceleration voltage of 20.0 KV, using aluminum as support.  $^1\text{H}$  NMR spectra were acquired on a Bruker Avance DRX-250 spectrometer, using a solution prepared by digesting 10 mg of sample in a mixture of 48% HF (20  $\mu\text{L}$ ) and DMSO- $d_6$  (600  $\mu\text{L}$ ). The size distributions were determined by laser diffraction (LD) on a Mastersizer2000 (Malvern Instruments).

### 3.4.2 Spray-drying continuous flow-assisted synthesis of UiO-66 series

In a typical synthesis, a solution 0.1 M of  $\text{ZrCl}_4$  and 0.1 M of organic ligand in 15 mL of a mixture of DMF and  $\text{H}_2\text{O}$  (5.48:1) was injected into the coil flow reactor (Pyrex tube, inner diameter: 3 mm) at a feed rate of 2.4  $\text{mL}\cdot\text{min}^{-1}$  and at a  $T_1$  of 115  $^\circ\text{C}$ . The resulting pre-heated solution was then spray-dried at a  $T_2$  of 180  $^\circ\text{C}$  and a flow rate of 336  $\text{mL}\cdot\text{min}^{-1}$  using a Dryer B-290 Mini Spray (BUCHI Labortechnik; spray cap: 0.5-mm-hole). Finally, the collected solid was dispersed in DMF at room temperature under stirring overnight and precipitated by centrifugation. This process was repeated twice with ethanol instead of DMF. The final product was dried for 12 h at 80  $^\circ\text{C}$ . **UiO-66:** Yield = 70 %; Purity = 54 %;  $S_{\text{BET}} = 1106 \text{ m}^2 \text{ g}^{-1}$ . **UiO-66-NH<sub>2</sub>:** Yield = 67 %; Purity = 49 %;  $S_{\text{BET}} = 752 \text{ m}^2 \text{ g}^{-1}$ . **UiO-66-NO<sub>2</sub>:** Yield = 62 %; Purity = 49 %;  $S_{\text{BET}} = 679 \text{ m}^2 \text{ g}^{-1}$ . **UiO-66-Acetamido:** Yield = 51 %; Purity = 41 %;  $S_{\text{BET}} = 586 \text{ m}^2 \text{ g}^{-1}$ . **UiO-66-Br:** Yield = 68 %; Purity = 62 %;  $S_{\text{BET}} = 527 \text{ m}^2 \text{ g}^{-1}$ . **UiO-66-(OH)<sub>2</sub>:** Yield = 81 %; Purity = 67 %;  $S_{\text{BET}} = 401 \text{ m}^2 \text{ g}^{-1}$ . **UiO-66-1,4-NDC:** Yield = 45 %; Purity = 45 %;  $S_{\text{BET}} = 431 \text{ m}^2 \text{ g}^{-1}$ . **UiO-66-2,6-NDC:** Yield = 49 %; Purity = 37 %;  $S_{\text{BET}} = 557 \text{ m}^2 \text{ g}^{-1}$ .

### 3.4.3 Spray-drying continuous flow-assisted synthesis of $[\text{Ni}_8(\text{OH})_4(\text{H}_2\text{O})_2(\text{L})_6]_n$ .

A solution 0.02 M of  $\text{Ni}(\text{CH}_3\text{COO})_2 \cdot 4\text{H}_2\text{O}$  and 0.015 M of 1*H*-pyrazole-4-carboxylic acid in 20 mL of a mixture of DMF and  $\text{H}_2\text{O}$  (4:1) was injected into the coil flow reactor (Pyrex tube, inner diameter: 3 mm) at a feed rate of  $2.4 \text{ mL min}^{-1}$  and at a  $T_1$  of  $100 \text{ }^\circ\text{C}$ . The resulting pre-heated solution was then spray-dried at a  $T_2$  of  $180 \text{ }^\circ\text{C}$  and a flow rate of  $336 \text{ mL min}^{-1}$  using a B-290 Mini Spray Dryer (BUCHI Labortechnik; spray cap: 0.5-mm-hole). Finally, the collected solid was dispersed in EtOH and precipitated by centrifugation. This two-step washing process was repeated with  $\text{Et}_2\text{O}$ . The final product was dried for 12 h at  $60 \text{ }^\circ\text{C}$ . Yield = 60 %; Purity = 81 %;  $S_{\text{BET}} = 377 \text{ m}^2 \text{ g}^{-1}$ .

### 3.4.4 Spray-drying continuous flow-assisted synthesis of Fe-BTC/MIL-100.

A solution 0.1 M of  $\text{Fe}(\text{NO}_3)_3 \cdot 9\text{H}_2\text{O}$  and 0.07 M of BTC in 15 mL of DMF was injected into the coil flow reactor (Pyrex tube, inner diameter: 3 mm) at a feed rate of  $2.4 \text{ mL min}^{-1}$  and at a  $T_1$  of  $135 \text{ }^\circ\text{C}$ . The resulting pre-heated solution was then spray-dried at a  $T_2$  of  $180 \text{ }^\circ\text{C}$  and a flow rate of  $336 \text{ mL min}^{-1}$  using a B-290 Mini Spray Dryer (BUCHI Labortechnik; spray cap: 0.5-mm-hole). Finally, the collected solid was dispersed in  $\text{H}_2\text{O}$  and precipitated by centrifugation. This two-step washing process was repeated with EtOH. The final product was dried for 12 h at  $70 \text{ }^\circ\text{C}$ . Yield = 78 %; Purity = 58 %;  $S_{\text{BET}} = 1039 \text{ m}^2 \text{ g}^{-1}$ .

### 3.4.5 Spray-drying continuous flow-assisted synthesis of the MTV-UiO-66 made of two linkers.

A solution 0.1 M of  $\text{ZrCl}_4$  and 0.1 M of the ligand mixture (BDC and Br-BDC) in 15 mL of a mixture of DMF and  $\text{H}_2\text{O}$  (12.9:1) was injected into the coil flow reactor (Pyrex

tube, inner diameter: 3 mm) at a feed rate of  $2.4 \text{ mL min}^{-1}$  and at a  $T_1$  of  $115 \text{ }^\circ\text{C}$ . The resulting pre-heated solution was then spray-dried at a  $T_2$  of  $180 \text{ }^\circ\text{C}$  and a flow rate of  $336 \text{ mL}\cdot\text{min}^{-1}$  using a B-290 Mini Spray Dryer (BUCHI Labortechnik; spray cap: 0.5-mm-hole). Finally, the collected solid was dispersed in DMF at room temperature under stirring overnight and precipitated by centrifugation. This process was repeated twice with ethanol instead of DMF. The final product was dried for 12 h at  $80 \text{ }^\circ\text{C}$ .

### **3.4.6 Spray-drying continuous flow-assisted synthesis of the MTV-UiO-66 made of three linkers.**

A solution  $0.1 \text{ M}$  of  $\text{ZrCl}_4$ ,  $0.015 \text{ M}$  of BDC,  $0.015 \text{ M}$  of  $\text{NH}_2\text{-BDC}$  and  $0.015 \text{ M}$  of Br-BDC in  $15 \text{ mL}$  of a mixture of DMF and  $\text{H}_2\text{O}$  (12.9:1) was injected into the coil flow reactor (Pyrex tube, inner diameter: 3 mm) at a feed rate of  $2.4 \text{ mL min}^{-1}$  and at a  $T_1$  of  $115 \text{ }^\circ\text{C}$ . The resulting pre-heated solution was then spray-dried at a  $T_2$  of  $180 \text{ }^\circ\text{C}$  and a flow rate of  $336 \text{ mL min}^{-1}$  using a B-290 Mini Spray Dryer (BUCHI Labortechnik; spray cap: 0.5-mm-hole). Finally, the collected solid was dispersed in DMF at room temperature under stirring overnight and precipitated by centrifugation. This process was repeated twice with ethanol instead of DMF. The final product was dried for 12 h at  $80 \text{ }^\circ\text{C}$ .

### 3.5 References

- (1) James, S. L.; Adams, C. J.; Bolm, C.; Braga, D.; Collier, P.; Friscic, T.; Grepioni, F.; Harris, K. D.; Hyett, G.; Jones, W.; Krebs, A.; Mack, J.; Maini, L.; Orpen, A. G.; Parkin, I. P.; Shearouse, W. C.; Steed, J. W.; Waddell, D. C. *Chem. Soc. Rev.* **2012**, *41*, 413.
- (2) Crawford, D.; Casaban, J.; Haydon, R.; Giri, N.; McNally, T.; James, S. L. *Chem. Sci.* **2015**, *6*, 1645.
- (3) Martinez Joaristi, A.; Juan-Alcañiz, J.; Serra-Crespo, P.; Kapteijn, F.; Gascon, J. *Crystal Growth & Design* **2012**, *12*, 3489.
- (4) Bayliss, P. A.; Ibarra, I. A.; Perez, E.; Yang, S.; Tang, C. C.; Poliakoff, M.; Schroder, M. *Green Chem.* **2014**, *16*, 3796.
- (5) Rubio-Martinez, M.; Batten, M. P.; Polyzos, A.; Carey, K.-C.; Mardel, J. I.; Lim, K.-S.; Hill, M. R. *Sci. Rep.* **2014**, *4*, 5443.
- (6) Garzon-Tovar, L.; Carne-Sanchez, A.; Carbonell, C.; Imaz, I.; Maspoch, D. *J. Mater. Chem. A* **2015**, *3*, 20819.
- (7) Carné-Sánchez, A.; Imaz, I.; Cano-Sarabia, M.; Maspoch, D. *Nat Chem* **2013**, *5*, 203.
- (8) Shekhah, O.; Wang, H.; Zacher, D.; Fischer, R. A.; Woll, C. *Angew. Chem. Int. Ed. Engl.* **2009**, *48*, 5038.
- (9) Cantu, D. C.; McGrail, B. P.; Glezakou, V.-A. *Chem. Mater.* **2014**, *26*, 6401.
- (10) Surble, S.; Millange, F.; Serre, C.; Ferey, G.; Walton, R. I. *Chem. Commun.* **2006**, 1518.
- (11) Vagin, S.; Ott, A. K.; Rieger, B. *Chem. Ing. Tech.* **2007**, *79*, 767.
- (12) Burtch, N. C.; Jasuja, H.; Walton, K. S. *Chem. Rev.* **2014**, *114*, 10575.
- (13) Cavka, J. H.; Jakobsen, S.; Olsbye, U.; Guillou, N.; Lamberti, C.; Bordiga, S.; Lillerud, K. P. *J. Am. Chem. Soc.* **2008**, *130*, 13850.
- (14) Kandiah, M.; Nilsen, M. H.; Usseglio, S.; Jakobsen, S.; Olsbye, U.; Tilset, M.; Larabi, C.; Quadrelli, E. A.; Bonino, F.; Lillerud, K. P. *Chem. Mater.* **2010**, *22*, 6632.
- (15) Garibay, S. J.; Cohen, S. M. *Chem. Commun.* **2010**, 46, 7700.
- (16) Katz, M. J.; Brown, Z. J.; Colón, Y. J.; Siu, P. W.; Scheidt, K. A.; Snurr, R. Q.; Hupp, J. T.; Farha, O. K. *Chemical communications (Cambridge, England)* **2013**, *49*, 9449.
- (17) Bon, V.; Senkovska, I.; Weiss, M. S.; Kaskel, S. *CrystEngComm* **2013**, *15*, 9572.
- (18) Guillerm, V.; Ragon, F.; Dan-Hardi, M.; Devic, T.; Vishnuvarthan, M.; Campo, B.; Vimont, A.; Clet, G.; Yang, Q.; Maurin, G.; Ferey, G.; Vittadini, A.; Gross, S.; Serre, C. *Angew. Chem. Int. Ed. Engl.* **2012**, *51*, 9267.
- (19) Horcajada, P.; Surble, S.; Serre, C.; Hong, D.-Y.; Seo, Y.-K.; Chang, J.-S.; Greneche, J.-M.; Margiolaki, I.; Ferey, G. *Chem. Commun.* **2007**, 2820.
- (20) Padial, N. M.; Quartapelle Procopio, E.; Montoro, C.; López, E.; Oltra, J. E.; Colombo, V.; Maspéro, A.; Masciocchi, N.; Galli, S.; Senkovska, I.; Kaskel, S.; Barea, E.; Navarro, J. A. R. *Angew. Chem. Int. Ed.* **2013**, *52*, 8290.
- (21) Deng, H.; Doonan, C. J.; Furukawa, H.; Ferreira, R. B.; Towne, J.; Knobler, C. B.; Wang, B.; Yaghi, O. M. *Science* **2010**, *327*, 846.

- (22) Zhang, Y. B.; Furukawa, H.; Ko, N.; Nie, W.; Park, H. J.; Okajima, S.; Cordova, K. E.; Deng, H.; Kim, J.; Yaghi, O. M. *J. Am. Chem. Soc.* **2015**, *137*, 2641.
- (23) Kim, M.; Cohen, S. M. *CrystEngComm* **2012**, *14*, 4096.
- (24) Kim, S.-N.; Lee, Y.-R.; Hong, S.-H.; Jang, M.-S.; Ahn, W.-S. *Catal. Today* **2015**, *245*, 54.
- (25) Ragon, F.; Horcajada, P.; Chevreau, H.; Hwang, Y. K.; Lee, U. H.; Miller, S. R.; Devic, T.; Chang, J.-S.; Serre, C. *Inorg. Chem.* **2014**, *53*, 2491.
- (26) Hu, Z.; Peng, Y.; Kang, Z.; Qian, Y.; Zhao, D. *Inorg. Chem.* **2015**, *54*, 4862.
- (27) Gauvin, W. H.; Katta, S. *AIChE J.* **1976**, *22*, 713.
- (28) Shabde, V. S.; Hoo, K. A. *Industrial & Engineering Chemistry Research* **2006**, *45*, 8329.
- (29) Okuyama, K.; Wuled Lenggoro, I. *Chem. Eng. Sci.* **2003**, *58*, 537.
- (30) Waitschat, S.; Wharmby, M. T.; Stock, N. *Dalton Trans* **2015**, *44*, 11235.
- (31) Henninger, S. K.; Schmidt, F. P.; Henning, H. M. *Appl. Therm. Eng.* **2010**, *30*, 1692.
- (32) Dhakshinamoorthy, A.; Alvaro, M.; Horcajada, P.; Gibson, E.; Vishnuvarthan, M.; Vimont, A.; Grenèche, J.-M.; Serre, C.; Daturi, M.; Garcia, H. *ACS Catalysis* **2012**, *2*, 2060.
- (33) Garcia Marquez, A.; Horcajada, P.; Grosso, D.; Ferey, G.; Serre, C.; Sanchez, C.; Boissiere, C. *Chem Commun (Camb)* **2013**, *49*, 3848.
- (34) Karmakar, A.; Guedes da Silva, M. F. C.; Pombeiro, A. J. L. *Dalton Transactions* **2014**, *43*, 7795.

# Chapter 4

---

## Continuous One-Step Synthesis of Porous M-XF<sub>6</sub>-based Metal-Organic and Hydrogen-Bonded Frameworks

This Chapter is based on the following publication:

---

Guillerm, V.; Garzón-Tovar, L.; Yazdi, A.; Imaz, I.; Juanhuix, J.; Maspoch, D.  
*Chem. Eur. J.* **2017**, *23*, 6829.

---



## 4.1 Introduction

The environmental impact associated to the energy demand is a major problem worldwide.<sup>1</sup> For example; CO<sub>2</sub> emission caused by humanity—CO<sub>2</sub> concentration at the South Pole recently passed the milestone of 400 ppm for the first time in the last 4 million years<sup>2</sup>—contributes highly to the climate change. In this sense, 2016 has also been the first year that the weekly average CO<sub>2</sub> concentration monitored in the Mona Loa observatory did not go below this key value, meaning that the average global temperature is likely to increase more than the 1.5 °C warming threshold.<sup>3</sup>

To address the current and future energy needs while mitigating the environmental impact, one of the strategies has been the development of efficient CO<sub>2</sub> capture, storage and separation materials for achieving cleaner combustible supplies.<sup>4,5</sup> These materials mainly include zeolites, activated carbons, metal-organic frameworks (MOFs) and covalent-organic frameworks (COFs).<sup>6-8</sup> Among these innovative materials, as showed in **Chapter 1**, an old-fashioned class of fluorinated materials<sup>9-15</sup> have recently been brought back to the spotlight by the Eddaoudi and Zaworotko groups thanks to their exceptional uptake and selectivity towards CO<sub>2</sub> and hydrocarbons.<sup>16-26</sup> These MOFs (Figure 4.1) are constructed from the assembly of pre-made M-XF<sub>6</sub> pillars (M = Co, Ni, Cu, Zn; X = Si, Ti, Sn, Zr, Ge, V, Ga) with N-donor type ligands (*e.g.* pyrazine (pyz), pyridil-based ligands etc.).

However, despite these great developments, the scientific community and industry still need to join their efforts in transferring these materials from the laboratory to industry. A very important step here is the optimization of their fabrication.<sup>27-38</sup> This fabrication must always aim for fast and scalable one-step processes that produce ready-to-use products without the need of additional purification and drying steps. In this Chapter, we demonstrated that the spray-drying method allows production of several isorecticular M-XF<sub>6</sub>-based CO<sub>2</sub> sorbents fulfilling all these requirements.

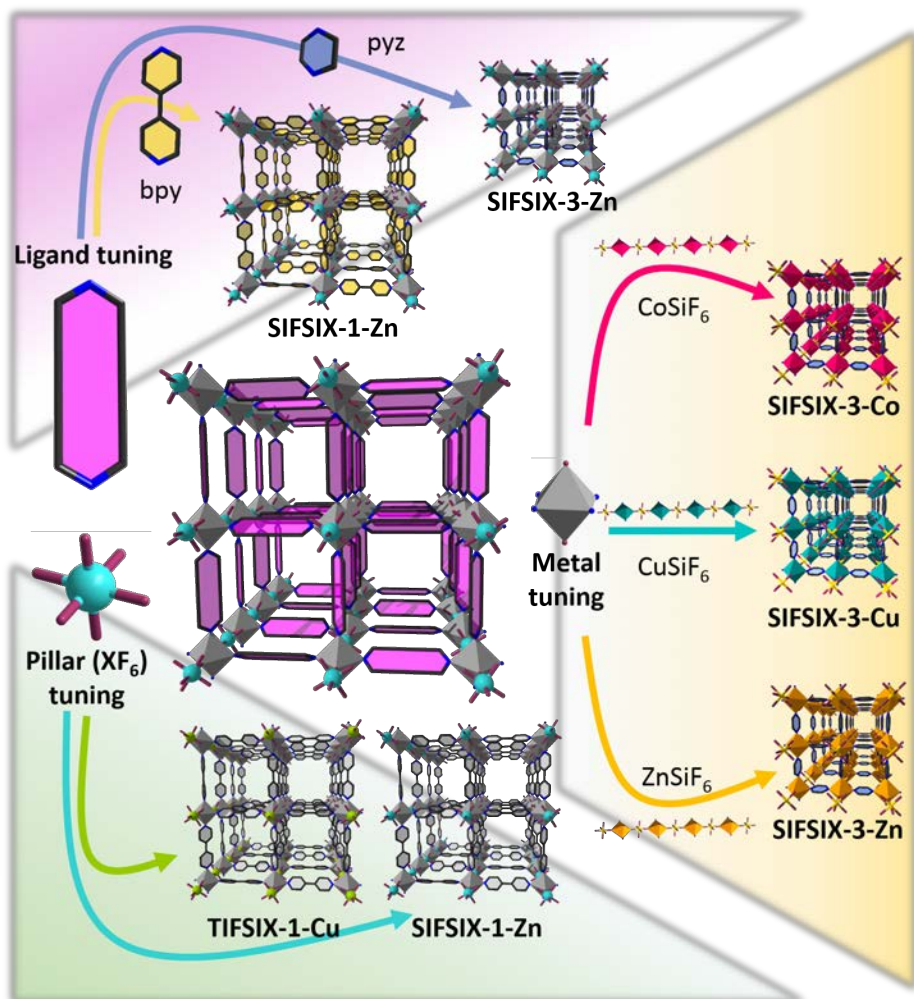


**Figure 4.1.** Schematic representation of the different isoreticular *pcu*  $M\text{-XF}_6$ -based MOFs synthesized via spray-drying. Note here that this technique allows synthesizing this class of MOFs varying the metal ion (Co, Cu, Zn), anionic pillar ( $[\text{SiF}_6]^{2-}$ ,  $[\text{TiF}_6]^{2-}$ ) and ligand (pyrazine, 4,4'-bipyridine).

As we illustrated in **Chapter 1** and **Chapter 3**,<sup>38-41</sup> the spray-drying technique is a scalable and fast method allowing continuous synthesis of MOFs in the form of spherical superstructures or beads based on the assembly of nanosized crystals.<sup>41</sup> The strong expertise acquired from these previous studies, among several reports suggesting the capital importance of the formation of the inorganic secondary building unit (SBU) for the nucleation and growth of MOFs,<sup>42-46</sup> convinced us that premed

pillars of the M-XF<sub>6</sub> MOF platform would be ideal candidates for spray-drying synthesis.

We therefore successfully embarked on the spray-drying-based synthesis of several M-XF<sub>6</sub> materials, showing that this method is also compatible for reticular synthesis and metal tuning, ligand elongation and pillar substitution. Importantly, their rapid synthesis (a few minutes versus a few hours up to a few days) does not negatively affect their sorption properties, demonstrating in most cases their ready-to-use character without the need of additional purification steps or time consuming repeated solvent exchange procedures. Moreover, we also demonstrate that spray-drying can be used not only to synthesize porous materials based on coordination bonds but also based on hydrogen bonds.

## 4.2 Results and Discussion

### 4.2.1 Synthesis and characterization of SIFSIX-3-M materials

The one-step spray-drying synthesis consisted on the combined atomization of two methanolic solutions containing 1) M-SiF<sub>6</sub> (M = Co, Cu, Zn) and 2) pyz at 85 °C, which produced fine powders that were collected with a minimum amount of methanol (MeOH). Collection of these powders in methanol was a crucial protection step as we found that they were air-sensitive (*vide infra*). To assess the quality of the as-made **SIFSIX-3-M** MOFs, their CO<sub>2</sub> sorption properties were compared with those of their bulk analogues. For this, the spray-drying-synthesized **SIFSIX-3-M** collected in methanol were directly transferred from the spray-drier collector to sorption cells, and dried and evacuated for 12 h at 65 °C. Then, their CO<sub>2</sub> uptake at 298 K was measured. Notably, we confirmed that spray-dried **SIFSIX-3-M** did not require additional solvent exchange or purification step to exhibit remarkable CO<sub>2</sub> capacities at low pressure and 298 K (Figure 4.2h, Table 4.1), with an uptake less than 10 % lower than the reported bulk materials.

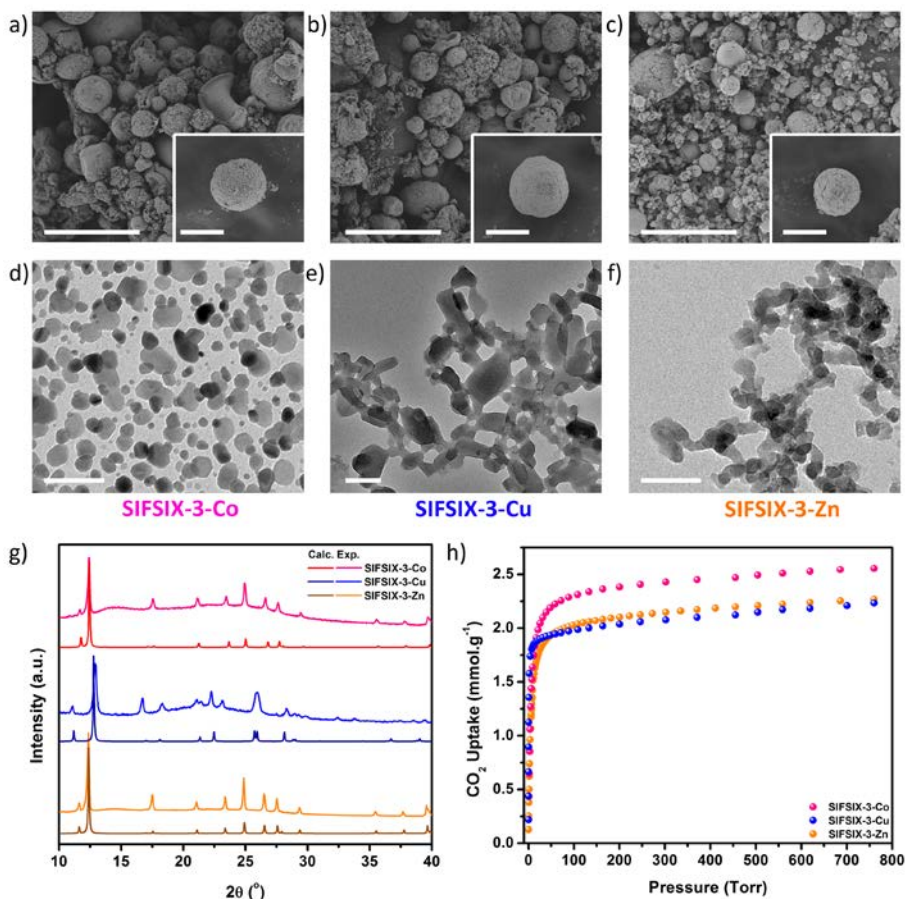


**Figure 4.2.** Representative FESEM images of (a) *SIFSIX-3-Co*, (b) *SIFSIX-3-Cu*, and (c) *SIFSIX-3-Zn*. TEM images of (d) *SIFSIX-3-Co*, (e) *SIFSIX-3-Cu*, and (f) *SIFSIX-3-Zn*. (g) XRPD patterns of the SD-synthesized *SIFSIX-3-M*. (h) CO<sub>2</sub> sorption isotherms at 298 K for *SIFSIX-3-M*. Scale bars for FESEM: 15  $\mu\text{m}$  and 5  $\mu\text{m}$  (insets). Scale bars for TEM: (d, f) 100 nm and (e) 200 nm.

Spray-drying-synthesized *SIFSIX-3-M* were further characterized by X-ray powder diffraction (XRPD), from which experimental patterns were in excellent agreement with the theoretical diagrams calculated from the corresponding structures (Figure 4.2g), demonstrating both the high crystallinity and purity of the MOFs.

The morphology of the materials was also investigated by field-emission scanning electron microscopy (FESEM), showing in all cases the occurrence of

nanosized **SIFSIX-3-M** crystals assembled into spherical superstructures or beads; a shape that is typical from MOFs assembled by the spray-drying method. The sizes of these superstructures were  $7.9 \pm 4.8 \mu\text{m}$  for **SIFSIX-3-Co**,  $6.9 \pm 3.4 \mu\text{m}$  for **SIFSIX-3-Cu**, and  $3.5 \pm 2.7 \mu\text{m}$  for **SIFSIX-3-Zn** (Figure 4.2 a-c).<sup>39-41,47,48</sup> Moreover, FESEM images confirmed the homogeneity of the materials, as already suggested by the absence of crystalline impurity peaks in the XRPD patterns.

To finally determine the size of crystals composing the superstructures, they were disassembled by sonication and immediately transferred to a transmission electron microscopy (TEM) grid. TEM images confirmed the formation of nanocrystals with a size of  $32 \pm 13 \text{ nm}$  for **SIFSIX-3-Co**,  $80 \pm 12 \text{ nm}$  for **SIFSIX-3-Cu**, and  $28 \pm 9 \text{ nm}$  for **SIFSIX-3-Zn** (Figure 4.2d-f).

**Table 4.1.** Comparison of the CO<sub>2</sub> uptakes (760 torr, 298 K) in spray-dried and bulk **SIFSIX-3-M** MOFs.

MOF	CO <sub>2</sub> uptake (mmol g <sup>-1</sup> )	
	Bulk	Sprayed (% of bulk)
SIFSIX-3-Co	$\approx 2.79^{26}$	2.56 (92 %)
SIFSIX-3-Cu	$\approx 2.40^{17}$	2.23 (93 %)
SIFSIX-3-Zn	$\approx 2.46^{16}$	2.27 (92 %)

#### 4.2.1.1 Stability of **SIFSIX-3-M** materials in different media.

The use of methanol to collect the fine powders produced with the SD method is essential to protect and use the as-made **SIFSIX-3-M** MOFs.<sup>49</sup> Without this precaution, all nanosized **SIFSIX-3-M** MOFs suffered a fast degradation and a loss of their CO<sub>2</sub> sorption properties when they were exposed to ambient conditions. In addition, following the optimized washing procedure reported by Nugent *et al.*,<sup>16</sup> we observed that the spray-drying-synthesized **SIFSIX-3-Zn** was instantaneously solubilized upon addition of *N,N*-dimethylformamide (DMF), leading to a clear solution. Attempts to re-spray this clear solution did not allow re-assembly of the **SIFSIX-3-Zn**

framework. Instead, colourless single crystals (*versus* the yellow colour of **SIFSIX-3-Zn** crystals) appeared in the DMF solution after a period of *ca.* a month. This unknown structure, which crystallizes in *P*-1 space group, was solved by single crystal X-ray diffraction and appeared to be a cationic 1D coordination polymer with formula  $\{[\text{Zn}(\text{pyz})_2(\text{DMF})_2(\text{H}_2\text{O})_2] \cdot [\text{SiF}_6]\}$  (**1**). This structure results from the replacement of all  $\text{SiF}_6$  pillars and half of the pyz ligand by DMF and water molecules (Figure 4.3). The positive charge of this coordination polymer  $[\text{Zn}(\text{pyz})_2(\text{DMF})_2(\text{H}_2\text{O})_2]^{2+}$  is balanced by  $[\text{SiF}_6]^{2-}$  anions.

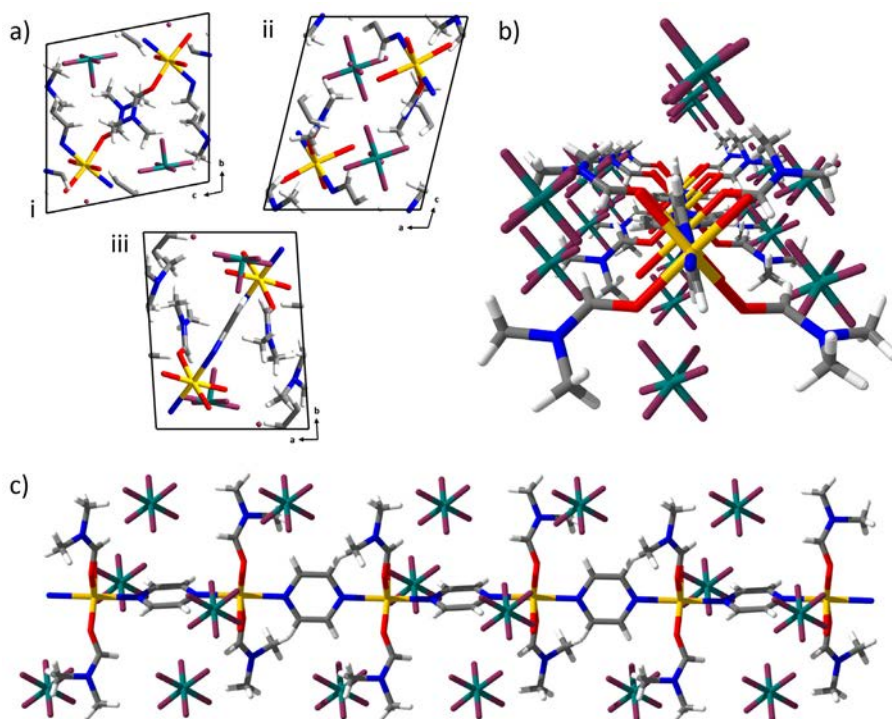


**Figure 4.3.** (a) View of one unit cell of **1** along the *a* axis (i), *b* axis (ii) and *c* axis (iii). (b) Structure of **1** along the 1D chain direction. (c) General view of the 1D chain in **1** along the 1D chain direction.

It is important to mention here that a similar behaviour was found when immersing **SIFSIX-3-Zn** in water, also leading to a complete solubilisation of the crystals. The incubation of nanosized **SIFSIX-3-Zn** in other organic solvents, including

acetonitrile, hexane, dichloromethane, chloroform, toluene, tetrahydrofuran and acetone, did not result in the solubilisation of the crystals but a fast phase transition into unidentified crystalline powders (Figure 4.4).

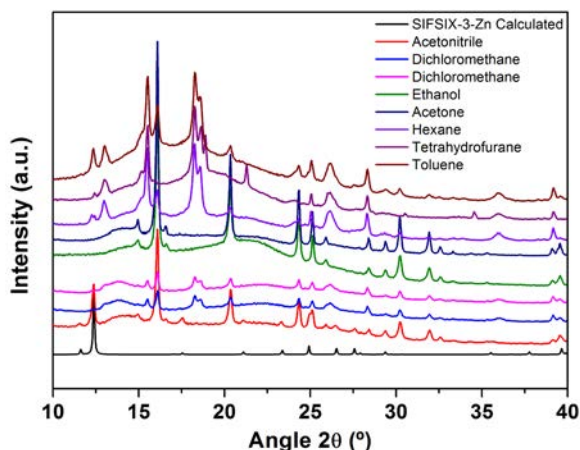


**Figure 4.4.** XRPD patterns of SD-synthesized **SIFSIX-3-Zn** superstructures after washing with various solvents.

The only tested solvent in which **SIFSIX-3-Zn** showed certain stability was MeOH. Initial incubation studies using microcrystals instead of nanocrystals—to easily follow the evolution by FESEM—showed that **SIFSIX-3-Zn** is also etched and finally solubilized in MeOH (Figure 4.5). However, we found that the minimum amount of MeOH needed for the complete solubilisation of the nanosized **SIFSIX-3-Zn** without stirring was around 0.14 mL<sub>MeOH</sub> per mg<sub>SIFSIX-3-Zn</sub>. In addition, below this amount of MeOH, **SIFSIX-3-Zn** remained stable and did not suffer any phase transition, as confirmed by XRPD. It is also worth mentioning that a similar behaviour occurred for the Cu and Co analogues. To this end, altogether these observations allowed us to define MeOH as the best solvent to collect these materials, which were in all cases collected using no more than 0.015 mL<sub>MeOH</sub> per mg of MOF.

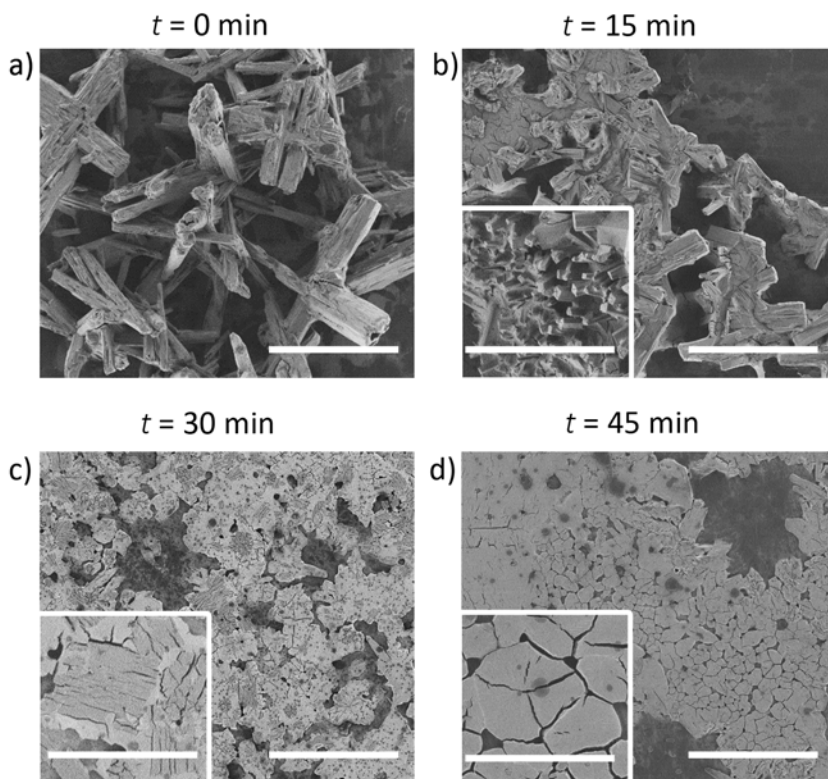


**Figure 4.5.** Crystal size evolution of *SIFSIX-3-Zn* upon etching in MeOH. Microcrystals ( $\approx 100 \mu\text{m}$  in length and  $\approx 20 \mu\text{m}$  in width) of *SIFSIX-3-Zn* were incubated in methanol, resulting on a rapid aggregation and visible etching of the bulk crystals after 15 min (b). In fact, most of the crystals were dissolved after 30 min, as evidenced by the almost clear solution (c). Crystals were totally dissolved after 45 min, leading to a clear, colourless solution (d). This etching process was accelerated when stirring the mixture of crystals with MeOH, obtaining a clear solution just after 5 min. Scale bars:  $50 \mu\text{m}$  and  $10 \mu\text{m}$  (insets)

## 4.2.2 Reticular chemistry: organic ligand and anionic pillar tuning

### 4.2.2.1 Synthesis and characterization of *SIFSIX-1-Zn*

In line with global efforts of the MOF community to use some network topologies as design platforms to rationally synthesize isorecticular MOFs,<sup>50-54</sup> we intended to take advantage of the already reported versatility of the  $\text{M-XF}_6$  platform<sup>11, 13, 16, 17, 20-26</sup> to demonstrate the suitability of the spray-drying method for reticular

chemistry. Following the successful synthesis of **SIFSIX-3-M** (M = Co, Cu and Zn), we successfully achieved the synthesis of an expanded analogue, **SIFSIX-1-Zn**,<sup>13</sup> by replacing the pyz ligand with the longer 4,4'-bipyridine (bpy). Here, a methanolic solution of  $\text{ZnSiF}_6$  was spray-dried along with a methanolic solution of bpy using a three-fluid nozzle at 85 °C. The resulting yellow spherical superstructures (size =  $7.9 \pm 3.6 \mu\text{m}$ ; Figure 4.6c) were collected and washed with MeOH. The material was obtained as a pure phase, as confirmed by XRPD (Figure 4.6c). It was found to be porous to  $\text{N}_2$  at 77 K, exhibiting an apparent BET area of  $1300 \text{ m}^2 \text{ g}^{-1}$  (Table 4.2, Figure 4.6d). Again, the nanosized nature of the **SIFSIX-1-Zn** crystals was confirmed by TEM; performed after disassembling the superstructures by sonication. The size of these nanocrystals was  $20 \pm 5 \text{ nm}$  (Figure 4.6b).

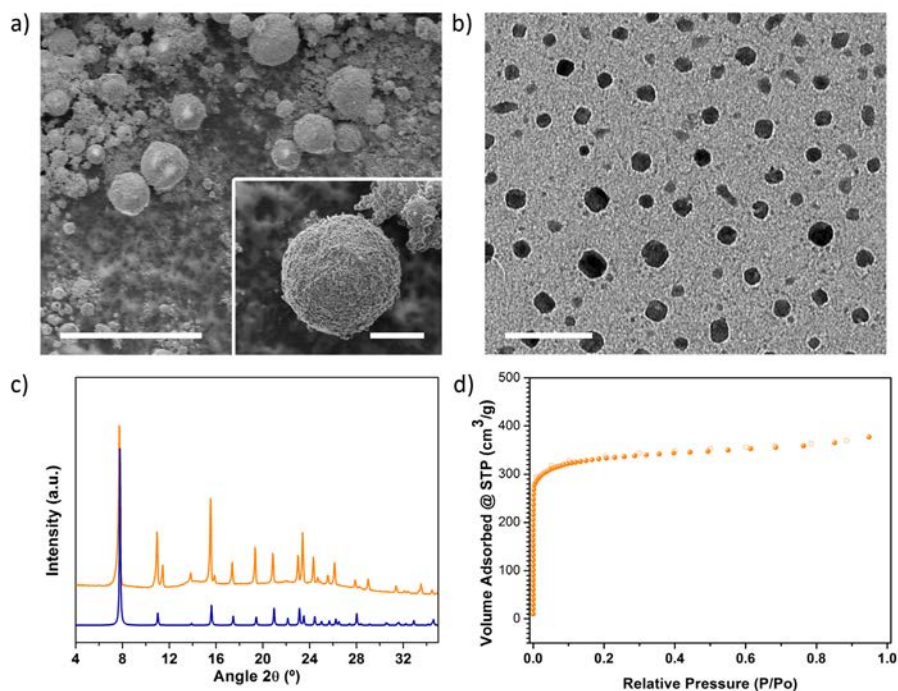


**Figure 4.6.** (a) Representative FESEM images of **SIFSIX-1-Zn** superstructures. (b) HRTEM image of **SIFSIX-1-Zn** nanocrystals. (c) XRPD pattern of **SIFSIX-1-Zn** (orange), compared with the simulated powder pattern (blue). (d)  $\text{N}_2$  adsorption isotherm of **SIFSIX-1-Zn**. Scale bars, FESEM:  $20 \mu\text{m}$  and  $5 \mu\text{m}$  (inset) and TEM:  $100 \text{ nm}$ .

#### 4.2.2.2 Synthesis and characterization of TIFSIX-1-Cu.

Recently, Nugent *et al.*<sup>21</sup> reported the possibility to not only vary the metal in this type of **pcu**-MOFs, but also the anion, by achieving the replacement of the pillaring  $[\text{SiF}_6]^{2-}$  anion by  $[\text{TiF}_6]^{2-}$ . Bulk **TIFSIX-1-Cu** is commonly synthesized using a layering of methanol and ethylene glycol at room temperature. However, this synthesis could not be reproduced in the spray-drier due to the high boiling point of ethylene glycol (197.3 °C). For this reason, we successfully replaced ethylene glycol by water, adjusting the spray-drying temperature to 150 °C. Thus, an aqueous solution of  $\text{Cu}(\text{NO}_3)_2 \cdot 2.5(\text{H}_2\text{O})$  and  $\text{TiF}_6(\text{NH}_4)_2$  was spray-dried along with a methanolic solution of bpy using a three-fluid nozzle at 150 °C.

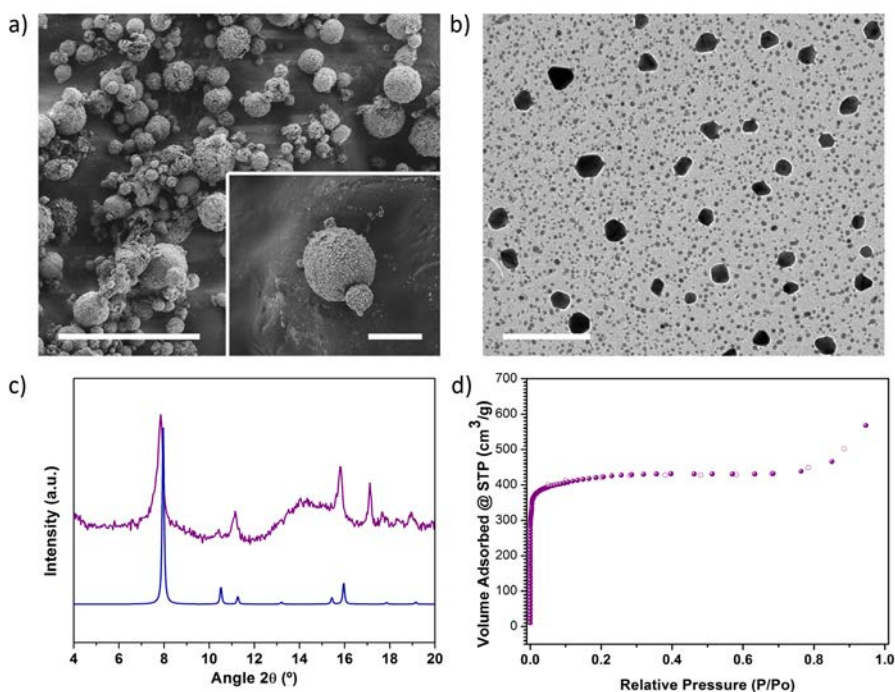


**Figure 4.7.** (a) Representative FESEM images of **TIFSIX-1-Cu** superstructures. (b) HRTEM image of **TIFSIX-1-Cu** nanocrystals. (c) XRPD pattern of **TIFSIX-1-Cu** (purple), compared with the simulated powder pattern (blue). (d)  $\text{N}_2$  adsorption isotherm of **TIFSIX-1-Cu**. Scale bars, FESEM: 20  $\mu\text{m}$  and 5  $\mu\text{m}$  (inset) and TEM: 200 nm.

The resulting grey/purple spherical superstructures (size =  $5.3 \pm 3.1 \mu\text{m}$ ; Figure 4.7a) were collected with MeOH. Their XRPD pattern was found to be in excellent agreement with the simulated pattern (Figure 4.7c).  $\text{N}_2$  sorption performed at 77 K revealed an apparent BET area of  $1650 \text{ m}^2 \text{ g}^{-1}$ . This value is very similar to that reported for the bulk material ( $1690 \text{ m}^2 \text{ g}^{-1}$ )<sup>21</sup> demonstrating the high quality of the spray-drying-synthesized **TIFSIX-1-Cu** MOF (Table 4.2, Figure 4.7d). The nanosized nature of the **TIFSIX-1-Cu** crystals (size =  $43 \pm 9 \text{ nm}$ , Figure 4.7b) was again confirmed by TEM performed after disassembling the superstructures by sonication.

### 4.2.3 Synthesis and characterization of supramolecular open material

Finally, due to the apparent ease of synthesis of these  $\text{M-XF}_6$  based MOFs by spray-drying technology, we selected another porous material, **MPM-1-TIFSIX**,<sup>19</sup> based on the supramolecular assembly of  $[\text{Cu}_2(\text{ade})_4(\text{TiF}_6)_2]$  (ade = adenine) paddlewheels (Figure 4.8). It is worth mentioning that, in the present case, the selected material to be synthesized by spray-drying was not a MOF but a supramolecular hydrogen-bonded network. To our knowledge, the aerosol synthesis of such kind of open materials based on weak bonding has not been reported yet.

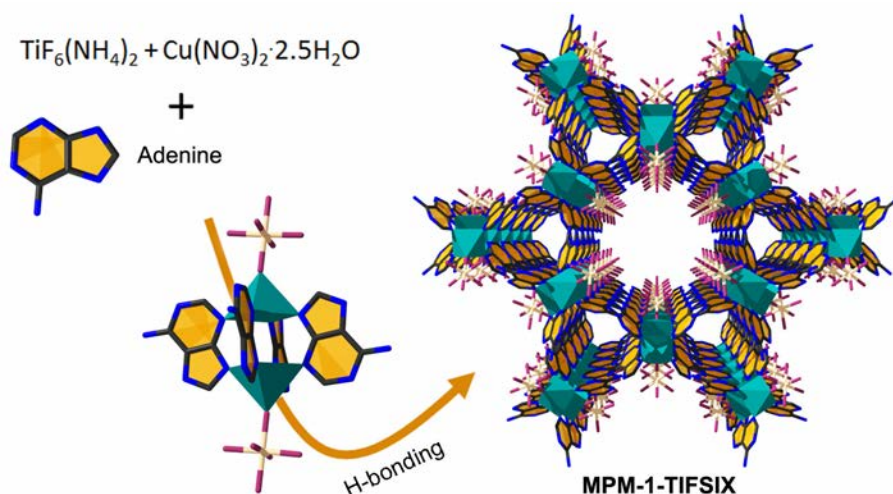


**Figure 4.8.** Schematic for the synthesis and structure of **MPM-1-TIFSIX-1**.

An aqueous solution of  $\text{Cu}(\text{NO}_3)_2 \cdot 2.5(\text{H}_2\text{O})$  and  $\text{TiF}_6(\text{NH}_4)_2$  was spray-dried along with a solution of adenine in water/acetonitrile mixture using a two-fluid nozzle at 150 °C. The resulting grey/purple spherical superstructures (size =  $6.1 \pm 3.1 \mu\text{m}$ ; Figure 4.9a) were collected with MeOH. Remarkably, the XRPD pattern was found to be in excellent agreement with the theoretical one (Figure 4.9c).  $\text{N}_2$  sorption performed at 77 K after a methanol solvent exchange procedure revealed an apparent BET area of  $805 \text{ m}^2 \text{ g}^{-1}$  ( $996 \text{ m}^2 \text{ g}^{-1}$  for bulk),<sup>19</sup> demonstrating the porosity of the SD-synthesized **MPM-1-TIFSIX** supramolecular material (Table 4.2, Figure 4.9d). In this case, TEM experiments performed after disassembling the superstructures by sonication showed **MPM-1-TIFSIX** crystals with a size of  $201 \pm 65 \text{ nm}$  (Figures 4.9b).

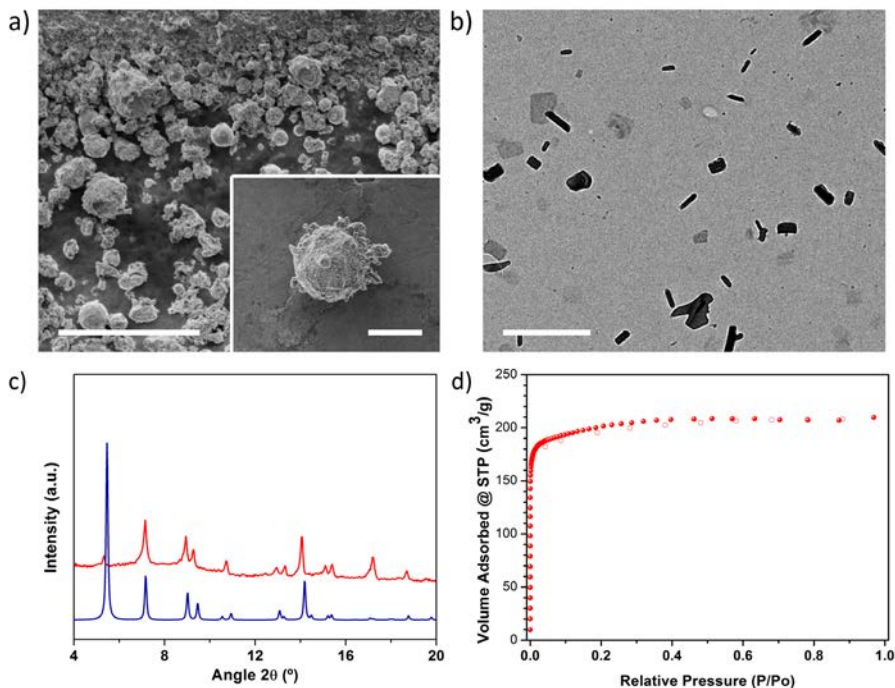


**Figure 4.9.** (a) Representative FESEM images of **MPM-1-TIFSIX** superstructures. (b) HRTEM image of **MPM-1-TIFSIX** nanocrystals. (c) XRPD pattern of **MPM-1-TIFSIX** (red), compared with the simulated powder pattern (blue). (d)  $\text{N}_2$  adsorption isotherm of **MPM-1-TIFSIX**. Scale bars, FESEM: 20  $\mu\text{m}$  and 5  $\mu\text{m}$  (inset) and TEM: 1  $\mu\text{m}$ .

**Table 4.2.** BET areas and pore volumes for **SIFSIX-1-Zn**, **TIFSIX-1-Cu** and **MPM-1-TIFSIX** ( $N_2$ , 77 K).

MOF	$S_{\text{BET}}$ ( $\text{m}^2 \cdot \text{g}^{-1}$ )	$V_{\text{micro}}$ ( $\text{cm}^3 \cdot \text{g}^{-1}$ ) at $P/P_0 = 0.3$	$V_t$ ( $\text{cm}^3 \cdot \text{g}^{-1}$ ) at $P/P_0 = 0.95$	Theo $V_t$ ( $\text{cm}^3 \cdot \text{g}^{-1}$ )
SIFSIX-1-Zn	1300	0.53	0.58	0.68
TIFSIX-1-Cu	1650	0.66	0.88	0.70
MPM-1-TIFSIX	805	0.32	0.32	0.39

### 4.3 Conclusions

We reported here the one-step and continuous synthesis of various  $\text{M-XF}_6$  based MOFs using the spray-drying technique. Using this method, these  $\text{M-XF}_6$  based MOFs could be synthesized at the nanoscale. There is no doubt that the possibility of obtaining and stabilizing nanosized  $\text{M-XF}_6$  based MOFs opens new avenues for the re-exploration of this old-fashioned sub-class of MOFs for emerging applications. In addition, we demonstrated the suitability of the SD method to perform fine structural tuning *via* ligand size variation (pyz *versus* bpy), anionic pillar substitution ( $[\text{SiF}_6]^{2-}$  *versus*  $[\text{TIF}_6]^{2-}$ ), and variation of metal ion (Co, Cu, and Zn). Importantly, this novel way to synthesize these materials does not jeopardize their sorption properties. This fact together with the short synthesis times and the absence of time consuming purification and solvent exchange procedures demonstrates the ability and competitiveness of spray-drying methods versus conventional ones for the fast production of ready-to-use sorbents. Finally, we anticipate the first aerosol synthesis of a supramolecular, hydrogen bonded porous network, **MPM-1-TIFSIX**, which opens new avenues for the synthesis of this class of porous materials using spray-drying.

## 4.4 Experimental Section

### 4.4.1 Materials and methods

All the materials were synthesized using a Mini Spray Dryer B-290 (BÜCHI Labortechnik). All solvents and reagents were purchased from Sigma-Aldrich, City Chemicals and Scharlab and used as received.

XRPD patterns were collected on a Panalytical X'pert diffractometer with monochromatic Cu-K $\alpha$  radiation ( $\lambda_{\text{Cu}} = 1.5406 \text{ \AA}$ ) under a Kapton film. Volumetric N<sub>2</sub> and CO<sub>2</sub> sorption isotherms were collected at 77 K (N<sub>2</sub>) and 298 K (CO<sub>2</sub>) using an ASAP 2020 HD (Micromeritics). Temperature was controlled by using a liquid nitrogen bath (77 K) or a Lauda Proline RP 890 chiller (298 K). For N<sub>2</sub> sorption at 77 K, micropore volumes ( $V_{\text{micro}}$ ) were calculated at  $P/P_0 = 0.3$ , whereas the total pore volumes ( $V_t$ ) were calculated at  $P/P_0 = 0.95$ . Field-emission scanning electron microscopy (FESEM) images were collected on scanning electron microscopes (FEI Magellan 400L XHR and Quanta 650 FEG) at acceleration voltage of 1.0 kV, and using dry powder on carbon as support. Transmission electron microscopy (TEM) images were obtained with a JEOL JEM 1400 at 100 kV. Prior to TEM, all superstructures immersed in MeOH were disassembled by sonication for 10 s in a Fisher Scientific FB15051 sonicator and then, directly transferred on the TEM grids. Average size range of superstructures and crystals has been calculated on 100 crystals/superstructures using the Image J software.

#### Crystallography

Crystallographic data for **1** were collected at 100 K at XALOC beamline at ALBA synchrotron<sup>55</sup> ( $\lambda = 0.79472 \text{ \AA}$ ). Data were indexed, integrated and scaled using the XDS program.<sup>56</sup> Absorption correction was not applied. The structure was solved by direct methods and subsequently refined by correction of  $F^2$  against all reflections, using SHELXS2013<sup>57</sup> and SHELXL2013<sup>58</sup> within the WinGX package.<sup>59</sup> All non-hydrogen atoms

were refined with anisotropic thermal parameters by full-matrix least-squares calculations on  $F^2$  using the program SHELXL2013. Hydrogen atoms were inserted at calculated positions and constrained with isotropic thermal parameters.

#### 4.4.2 Synthesis of SIFSIX-3-Co

A 6 mL methanolic solution of 300 mg (1.49 mmol) of  $\text{CoSiF}_6$  and a 6 mL methanolic solution of 325 mg (4.05 mmol) of pyz were simultaneously spray-dried using a 3-fluid nozzle, a feed rate of  $2.4 \text{ mL min}^{-1}$ , a flow rate of  $414 \text{ mL min}^{-1}$ , an inlet  $\text{N}_2$  temperature of  $85 \text{ }^\circ\text{C}$ , and a spray cap with a 0.5 mm hole. The light pink powder of **SIFSIX-3-Co** was recovered with a minimum amount of methanol (MeOH) (235 mg; 44 % yield based on Co).

#### 4.4.3 Synthesis of SIFSIX-3-Cu

A 6 mL methanolic solution of 300 mg (1.34 mmol) of  $\text{CuSiF}_6 \cdot \text{H}_2\text{O}$  and a 6 mL methanolic solution of 325 mg (4.05 mmol) of pyz were simultaneously spray-dried using a 3-fluid nozzle, a feed rate of  $2.4 \text{ mL min}^{-1}$ , a flow rate of  $414 \text{ mL min}^{-1}$ , an inlet  $\text{N}_2$  temperature of  $85 \text{ }^\circ\text{C}$ , and a spray cap with a 0.5 mm hole. The blue powder of **SIFSIX-3-Cu** was recovered with a minimum amount of MeOH (272 mg; 55 % yield based on Cu).

#### 4.4.4 Synthesis of SIFSIX-3-Zn

A 6 mL methanolic solution of 300 mg (1.45 mmol, anhydrous based) of  $\text{ZnSiF}_6 \cdot x\text{H}_2\text{O}$  and a 6 mL methanolic solution of 325 mg (4.05 mmol) of pyz were simultaneously spray-dried using a three-fluid nozzle, a feed rate of  $2.4 \text{ mL min}^{-1}$ , a flow rate of  $414 \text{ mL min}^{-1}$ , an inlet  $\text{N}_2$  temperature of  $85 \text{ }^\circ\text{C}$ , and a spray cap with a 0.5 mm hole. The yellow powder of **SIFSIX-3-Zn** was recovered with a minimum amount of MeOH (305 mg; 57 % yield based on Zn).

#### 4.4.5 Synthesis of SIFSIX-1-Zn

A 6 mL methanolic solution of 300 mg (1.45 mmol, anhydrous based) of  $\text{ZnSiF}_6 \cdot x\text{H}_2\text{O}$  and a 6 mL methanolic solution of 650 mg (4.16 mmol) of bpy were simultaneously spray-dried using a 3-fluid nozzle, a feed rate of  $2.4 \text{ mL min}^{-1}$ , a flow rate of  $414 \text{ mL min}^{-1}$ , an inlet  $\text{N}_2$  temperature of  $85 \text{ }^\circ\text{C}$ , and a spray cap with a 0.5 mm hole. The yellow powder of **SIFSIX-1-Zn** was recovered with a minimum amount of MeOH (302 mg; 40 % yield based on Zn). Sample was then washed with 5 mL of MeOH to remove potential contamination with the highly soluble, unreacted precursors.

#### 4.4.6 Synthesis of TIFSIX-1-Cu

A 6 mL aqueous solution of 30 mg (0.15 mmol) of  $\text{TiF}_6 \cdot (\text{NH}_4)_2$  and 35 mg (0.15 mmol) of  $\text{Cu}(\text{NO}_3)_2 \cdot 2.5(\text{H}_2\text{O})$  and a 6 mL methanolic solution of 46.8 mg (0.30 mmol) of bpy were simultaneously spray-dried using a 3-fluid nozzle, a feed rate of  $2.4 \text{ mL min}^{-1}$ , a flow rate of  $414 \text{ mL min}^{-1}$ , an inlet  $\text{N}_2$  temperature of  $130 \text{ }^\circ\text{C}$ , and a spray cap with a 0.5 mm hole. The blue powder of **TIFSIX-1-Cu** was recovered with a minimum amount of MeOH (64 mg; 79 % yield based on Cu).

#### 4.4.7 Synthesis of MPM-1-TIFSIX

A 12 mL aqueous solution of 30 mg (0.15 mmol) of  $\text{TiF}_6 \cdot (\text{NH}_4)_2$  and 35 mg (0.15 mmol) of  $\text{Cu}(\text{NO}_3)_2 \cdot 2.5(\text{H}_2\text{O})$  and a 12 mL  $\text{H}_2\text{O}:\text{CH}_3\text{CN}$  (1:1 vol.) solution of 82 mg (0.60 mmol) of adenine were simultaneously spray-dried using a 2-fluid nozzle and T-shaped system, a feed rate of  $2.4 \text{ mL min}^{-1}$ , a flow rate of  $414 \text{ mL min}^{-1}$ , an inlet  $\text{N}_2$  temperature of  $150 \text{ }^\circ\text{C}$ , and a spray cap with a 0.5 mm hole. The purple/grey powder of **MPM-1-TIFSIX** was recovered with a minimum amount of MeOH (110 mg; 74 % yield based on Zn). Prior to sorption measurements, this powder was immersed in MeOH for 3 days, refreshing the MeOH twice a day.

#### 4.4.8 Stability study of SIFSIX-3-Zn

A 6 mL methanolic solution of 300 mg (1.45 mmol, anhydrous based) of  $\text{ZnSiF}_6 \cdot x\text{H}_2\text{O}$  was injected to a 6 mL methanolic solution of 325 mg (4.05 mmol) of pyz at room temperature, without stirring. After 1 h, 1 mL of the solution containing the resulting microcrystals was pipetted from the middle of the vial and mixed with 2 mL of MeOH. Aliquots of the sample were transferred immediately to the microscope to avoid contact with air, and the morphology of the crystals was studied by FESEM after 15 min.

## 4.5 References

- (1) Monastersky, R. *Nature*. **2009**, *458*, 1091.
- (2) South Pole is the last place on Earth to pass a global warming milestone, <http://research.noaa.gov/News/NewsArchive/LatestNews/TabId/684/ArtMID/1768/ArticleID/11760/South-Pole-is-the-last-place-on-Earth-to-pass-a-global-warming-milestone.aspx>, (accessed June 28th, 2016).
- (3) Up-to-date weekly average CO<sub>2</sub> at Mauna Loa, <http://www.esrl.noaa.gov/gmd/ccgg/trends/weekly.html>, (accessed October 4th, 2016).
- (4) Sumida, K.; Rogow, D. L.; Mason, J. A.; McDonald, T. M.; Bloch, E. D.; Herm, Z. R.; Bae, T.-H.; Long, J. R. *Chem. Rev.* **2012**, *112*, 724.
- (5) Belmabkhout, Y.; Guillerm, V.; Eddaoudi, M. *Chem. Eng. J.* **2016**, *296*, 386.
- (6) Zhou, H. C.; Long, J. R.; Yaghi (Ed), O. M. In *Chem. Rev.* 2012; Vol. 673-1268, p 112.
- (7) Long, J. R.; Yaghi, O. M. In *Chem. Soc. Rev.* 2009; Vol. 1201-1508, p 38; c) Long, J. R.; Yaghi, O. M. In *Chem. Soc. Rev.* 2014; Vol. 5415-6172, p 43.
- (8) Dawson, R.; Cooper, A. I.; Adams, D. J. *Prog. Polym. Sci.* **2012**, *37*, 530.
- (9) Uemura, K.; Maeda, A.; Maji, T.-K.; Kanoo, P.; Kita, H. *Eur. J. Inorg. Chem.* **2009**, *2009*, 2329.
- (10) Dybtsev, D. N.; Chun, H.; Kim, K. *Angew. Chem. Int. Ed.* **2004**, *43*, 5033.
- (11) Noro, S.-I.; Kitagawa, S.; Kondo, M.; Seki, K. *Angew. Chem. Int. Ed.* **2000**, *39*, 2081.
- (12) Zaworotko, M. J. *Angew. Chem. Int. Ed.* **2000**, *39*, 3052.
- (13) Subramanian, S.; Zaworotko, M. J. *Angew. Chem. Int. Ed.* **1995**, *34*, 2127.
- (14) Noro, S.-I.; Kitaura, R.; Kondo, M.; Kitagawa, S.; Ishii, T.; Matsuzaka, H.; Yamashita, M. *J. Am. Chem. Soc.* **2002**, *124*, 2568.
- (15) Lin, M.-J.; Jouaiti, A.; Kyritsakas, N.; Hosseini, M. W. *CrystEngComm* **2009**, *11*, 189.
- (16) Nugent, P.; Belmabkhout, Y.; Burd, S. D.; Cairns, A. J.; Luebke, R.; Forrest, K.; Pham, T.; Ma, S.; Space, B.; Wojtas, L.; Eddaoudi, M.; Zaworotko, M. J. *Nature* **2013**, *495*, 80.
- (17) Shekhah, O.; Belmabkhout, Y.; Chen, Z.; Guillerm, V.; Cairns, A.; Adil, K.; Eddaoudi, M. *Nature Commun.* **2014**, *5*, 4228.
- (18) Kanoo, P.; Reddy, S. K.; Kumari, G.; Haldar, R.; Narayana, C.; Balasubramanian, S.; Maji, T. K. *Chem. Commun.* **2012**, *48*, 8487.
- (19) Nugent, P. S.; Rhodus, V. L.; Pham, T.; Forrest, K.; Wojtas, L.; Space, B.; Zaworotko, M. J. *J. Am. Chem. Soc.* **2013**, *135*, 10950;
- (20) Shekhah, O.; Belmabkhout, Y.; Adil, K.; Bhatt, P. M.; Cairns, A. J.; Eddaoudi, M. *Chem. Commun.* **2015**, *51*, 13595.
- (21) Nugent, P.; Rhodus, V.; Pham, T.; Tudor, B.; Forrest, K.; Wojtas, L.; Space, B.; Zaworotko, M. *Chem. Commun.* **2013**, *49*, 1606.

- (22) Burd, S. D.; Ma, S.; Perman, J. A.; Sikora, B. J.; Snurr, R. Q.; Thallapally, P. K.; Tian, J.; Wojtas, L.; Zaworotko, M. J. *J. Am. Chem. Soc.* **2012**, *134*, 3663.
- (23) Cui, X.; Chen, K.; Xing, H.; Yang, Q.; Krishna, R.; Bao, Z.; Wu, H.; Zhou, W.; Dong, X.; Han, Y.; Li, B.; Ren, Q.; Zaworotko, M. J.; Chen, B. *Science* **2016**, *353*, 141.
- (24) Cadiou, A.; Adil, K.; Bhatt, P. M.; Belmabkhout, Y.; Eddaoudi, M. *Science* **2016**, *353*, 137.
- (25) Manson, J. L.; Schlueter, J. A.; Garrett, K. E.; Goddard, P. A.; Lancaster, T.; Moeller, J.; Blundell, S. J.; Steele, A. J.; Franke-Chaudet, I.; Pratt, F. L.; Singleton, J.; Bendix, J.; Lapidus, S. H.; Uhlarz, M.; Ayala-Valenzuela, O.; McDonald, R.; Gurak, M.; Baines, C. *Chem. Commun.* **2016**.
- (26) Elsaidi, S. K.; Mohamed, M. H.; Schaef, H. T.; Kumar, A.; Lusi, M.; Pham, T.; Forrest, K. A.; Space, B.; Xu, W.; Halder, G. J.; Liu, J.; Zaworotko, M. J.; Thallapally, P. K. *Chem. Commun.* **2015**, *51*, 15530.
- (27) Silva, P.; Vilela, S. M. F.; Tome, J. P. C.; Almeida Paz, F. A. *Chem. Soc. Rev.* **2015**, *44*, 6774.
- (28) Czaja, A. U.; Trukhan, N.; Muller, U. *Chem. Soc. Rev.* **2009**, *38*, 1284.
- (29) Mueller, U.; Schubert, M.; Teich, F.; Puetter, H.; Schierle-Arndt, K.; Pastre, J. J. *Mater. Chem.* **2006**, *16*, 626.
- (30) Gaab, M.; Trukhan, N.; Maurer, S.; Gummaraju, R.; Müller, U. *Micropor. Mesopor. Mater.* **2012**, *157*, 131.
- (31) Crawford, D.; Casaban, J.; Haydon, R.; Giri, N.; McNally, T.; James, S. L. *Chem. Sci.* **2015**, *6*, 1645.
- (32) Rubio-Martinez, M.; Batten, M. P.; Polyzos, A.; Carey, K.-C.; Mardel, J. I.; Lim, K.-S.; Hill, M. R. *Sci. Rep.* **2014**, *4*, 5443.
- (33) Rubio-Martinez, M.; Hadley, T. D.; Batten, M. P.; Constanti-Carey, K.; Barton, T.; Marley, D.; Mönch, A.; Lim, K.-S.; Hill, M. R. *ChemSusChem* **2016**, *9*, 938.
- (34) Bayliss, P. A.; Ibarra, I. A.; Perez, E.; Yang, S.; Tang, C. C.; Poliakov, M.; Schroder, M. *Green Chem.* **2014**, *16*, 3796.
- (35) Faustini, M.; Kim, J.; Jeong, G.-Y.; Kim, J. Y.; Moon, H. R.; Ahn, W.-S.; Kim, D.-P. *J. Am. Chem. Soc.* **2013**, *135*, 14619.
- (36) Dunne, P. W.; Lester, E.; Walton, R. I. *React. Chem. Eng.* **2016**, *1*, 352.
- (37) Garzon-Tovar, L.; Carne-Sanchez, A.; Carbonell, C.; Imaz, I.; Maspoch, D. *J. Mater. Chem. A* **2015**, *3*, 20819.
- (38) Garzón-Tovar, L.; Cano-Sarabia, M.; Carné-Sánchez, A.; Carbonell, C.; Imaz, I.; Maspoch, D. *React. Chem. Eng.* **2016**, *1*, 533.
- (39) Wang, Z.; Ananias, D.; Carné-Sánchez, A.; Brites, C. D. S.; Imaz, I.; Maspoch, D.; Rocha, J.; Carlos, L. D. *Adv. Funct. Mater.* **2015**, *25*, 2824.
- (40) Carné-Sánchez, A.; Stylianou, K. C.; Carbonell, C.; Naderi, M.; Imaz, I.; Maspoch, D. *Adv. Mater.* **2015**, *27*, 869.
- (41) Carné-Sánchez, A.; Imaz, I.; Cano-Sarabia, M.; Maspoch, D. *Nat Chem* **2013**, *5*, 203.
- (42) Cantu, D. C.; McGrail, B. P.; Glezakou, V.-A. *Chem. Mater.* **2014**, *26*, 6401.
- (43) Shekhah, O.; Wang, H.; Zacher, D.; Fischer, R. A.; Woll, C. *Angew. Chem. Int. Ed. Engl.* **2009**, *48*, 5038.

- (44) Surble, S.; Millange, F.; Serre, C.; Ferey, G.; Walton, R. I. *Chem. Commun.* **2006**, 1518.
- (45) Guillerm, V.; Gross, S.; Serre, C.; Devic, T.; Bauer, M.; Ferey, G. *Chem. Commun.* **2010**, 46, 767.
- (46) Alezi, D.; Belmabkhout, Y.; Suyetin, M.; Bhatt, P. M.; Weseliński, Ł. J.; Solovyeva, V.; Adil, K.; Spanopoulos, I.; Trikalitis, P. N.; Emwas, A.-H.; Eddaoudi, M. *J. Am. Chem. Soc.* **2015**, 137, 13308.
- (47) Garcia Marquez, A.; Horcajada, P.; Grosso, D.; Ferey, G.; Serre, C.; Sanchez, C.; Boissiere, C. *Chem. Commun.* **2013**, 49, 3848.
- (48) Carné-Sánchez, A.; Imaz, I.; Stylianou, K. C.; MasPOCH, D. *Chem. Eur. J.* **2014**, 20, 5192.
- (49) Mason, J. A.; McDonald, T. M.; Bae, T.-H.; Bachman, J. E.; Sumida, K.; Dutton, J. J.; Kaye, S. S.; Long, J. R. *J. Am. Chem. Soc.* **2015**, 137, 4787.
- (50) Guillerm, V.; Kim, D.; Eubank, J. F.; Luebke, R.; Liu, X.; Adil, K.; Lah, M. S.; Eddaoudi, M. *Chem. Soc. Rev.* 2014, 43, 6141.
- (51) Eddaoudi, M.; Kim, J.; Rosi, N.; Vodak, D.; Wachter, J.; O'Keeffe, M.; Yaghi, O. M. *Science* **2002**, 295, 469.
- (52) Yaghi, O. M.; O'Keeffe, M.; Ockwig, N. W.; Chae, H. K.; Eddaoudi, M.; Kim, J. *Nature* **2003**, 423, 705.
- (53) Furukawa, H.; Cordova, K. E.; O'Keeffe, M.; Yaghi, O. M. *Science* **2013**, 341.
- (54) Guillerm, V.; Weseliński, Ł., J.; Belmabkhout, Y.; Cairns, A. J.; D'Elia, V.; Wojtas, Ł.; Adil, K.; Eddaoudi, M. *Nature Chem.* **2014**, 6, 673.
- (55) Juanhuix, J.; Gil-Ortiz, F.; Cuni, G.; Colldelram, C.; Nicolas, J.; Lidon, J.; Boter, E.; Ruget, C.; Ferrer, S.; Benach, J. *J. Synchr. Rad.* **2014**, 21, 679.
- (56) Kabsch, W. *Acta. Crystallogr. Sect. D* **2010**, 66, 125.
- (57) Sheldrick, G. M.; Dauter, Z.; Wilson, K. S.; Hope, H.; Sieker, L. C. *Acta. Crystallogr. Sect. D* **1993**, 49, 18.
- (58) Sheldrick, G. M. *Acta. Crystallogr. Sect. C* **2015**, 71, 3.
- (59) Farrugia, L. J. *Appl. Crystallogr.* **2012**, 45, 849.

# Chapter 5

---

## Composite Salt in Porous Metal-Organic Frameworks for Adsorption Heat Transformation

This Chapter is based on the following publication:

---

Garzón-Tovar, L.; Pérez-Carvajal, J.; Imaz, I.; Maspoch, D. *Adv. Funct. Mater.* **2017**, *27*, 1606424.

---



## 5.1 Introduction

The anthropogenic greenhouse gas emissions related to the demand of electrical energy by traditional space heating and air conditioning processes have increased over the past decade.<sup>1</sup> To solve this problem, several initiatives have been proposed to replace the traditional vapor compression devices by more environmentally friendly adsorptive heat transformation (AHT) systems, such as adsorption chillers, heat pumps and thermal batteries.<sup>2-4</sup> As illustrated in **Chapter 1**, these AHT systems are based on an adsorption-desorption cycle of a working fluid, where useful heat is released during the adsorption step and cold is produced during the evaporation of the working fluid. The main advantages of these systems are (i) the possibility to use low thermal energy sources (*e.g.* solar and waste heat) for regeneration and driving energy; and (ii) that water can be used as the working fluid.<sup>5</sup>

Despite these advantages, the AHT technologies are not yet competitive with conventional vapour compression systems due to the low performance of the working pair (adsorbent-adsorbate); sometimes associated to the low adsorption capacity of the adsorbent.<sup>6-7</sup> In this sense, inorganic adsorbents such as LiCl and CaCl<sub>2</sub> salts have been widely explored.<sup>8</sup> These compounds can adsorb a large amount of water because of their hygroscopic capacity. However, the presence of deliquescence phenomena, which can cause corrosion problems and limit their water uptake, depresses their performance in real applications.<sup>9</sup> A solution that has been traditionally proposed is the use of porous materials for confining these inorganic compounds. In the resulting Composite Salt in Porous Matrix (CSPM), the porous matrix mainly acts as a media to disperse the salt particles and can provide good heat and mass transport to these salt particles.<sup>8</sup> These CSPMs are usually produced by impregnation and saturation methods,<sup>6</sup> in which the inorganic solution is diffused into the porous matrix.<sup>10</sup> To date, different porous matrices have been explored for making CSPMs, including silica, filosilicates, activated carbon and microporous zeolites.<sup>11-13</sup> In an ideal material, however, the porous matrix also should adsorb water and provide efficient heat and

mass transfer. In this context, silica-based and activated carbons generally display very low adsorption uptake in the range of  $P/P_0 = 0.3-0.5$  due to its high hydrophobicity,<sup>14, 15</sup> and zeolites achieve their maximum capacity at low relative pressures, but it is difficult to regenerate them due to the high desorption temperatures required (*e.g.* Zeolite-13X: 150 °C; Zeolite-NaX: 360 °C).<sup>13, 16, 17</sup>

Currently, metal-organic frameworks (MOFs) has received great interest on water-sorption applications due to their high porosity, structural stability and tuneable composition (*e.g.* hydrophilic and hydrophobic moieties can co-exist in the same structure).<sup>18, 19</sup> As showed in **Chapter 1**, these potential applications include heat transformation processes;<sup>20-23</sup> proton conductivity;<sup>24-26</sup> air dehumidification;<sup>27</sup> and water delivery in remote areas.<sup>28</sup> It is noticed that some MOFs have a high water adsorbent capacity (*e.g.* MIL-101(Cr)-NH<sub>2</sub>: 1.05 g<sub>water</sub> g<sup>-1</sup><sub>MOF</sub>; MIL-100(Fe): 0.87 g<sub>water</sub> g<sup>-1</sup><sub>MOF</sub>; PIZOF-2 = 0.68 g<sub>water</sub> g<sup>-1</sup><sub>MOF</sub>),<sup>2, 20</sup> and that new strategies have started to be developed for improving these water adsorption capabilities. For example, Yan *et al.* have recently reported a new composite based on MIL-101 containing graphite oxide and exhibiting high water vapour capacity (maximum uptake up to 1.6 g<sub>water</sub> g<sup>-1</sup><sub>sorbent</sub>).<sup>29</sup> To the best of our knowledge, however, other MOF-based composites that enhance the water uptake and/or the use of MOFs as porous matrices to produce CSPMs have not been reported in the literature so far.

In this sense, we demonstrated in **Chapter 3** that the spray-drying method can be used to synthesize MOFs in the form of spherical compact beads built up from the assembly of nanosized crystals.<sup>30, 31</sup> An interesting feature of these superstructures is that their nitrogen adsorption isotherms at 77 K normally show a continuous increase of the N<sub>2</sub> uptake at partial pressures over 0.4, suggesting the presence of interparticular voids in the mesoporous range resulting from the assembly of MOF nanocrystals. Here, we take advantage of these voids and the inherent microporosity of MOFs to use these superstructures as porous matrices to confine inorganic salts. We show that this strategy is suitable to develop effective CSPMs based on MOFs for

adsorption heat transformation. For synthesizing these CSPMs, we chose UiO-66 and UiO-66-NH<sub>2</sub> as the porous MOF matrices, and CaCl<sub>2</sub> and LiCl as the inorganic salts. We chose UiO-66 and UiO-66-NH<sub>2</sub> because of their high thermal and water stability and its water sorption capabilities.<sup>32</sup> And we chose CaCl<sub>2</sub> and LiCl because their excellent water uptake capabilities.

## 5.2 Results and Discussion

### 5.2.1 Continuous-flow spray-drying synthesis

The composites were prepared by the spray-drying continuous-flow method, which enabled simultaneous synthesis and shaping of microspherical CSPMs made of CaCl<sub>2</sub> and UiO-66. In a typical experiment, a precursor solution containing ZrCl<sub>4</sub>, BDC, CaCl<sub>2</sub>·2H<sub>2</sub>O, H<sub>2</sub>O and DMF in a molar ratio of 1:1:1.6:40:135 (concentration of ZrCl<sub>4</sub> = 0.1 M) was injected into the coil flow reactor at a feed rate of 2.4 mL·min<sup>-1</sup> and at a  $T_1$  of 115 °C. The residence time inside the coil flow reactor was 63 s. The resulting pre-heated solution was then spray dried at a  $T_2$  of 180 °C and a flow rate of 336 mL min<sup>-1</sup>, using a B-290 Mini Spray Dryer (BUCHI Labortechnik). Once the solution had atomized, a white powder was collected from the spray dryer collector. This powder was analyzed through Field-Emission Scanning Electron Microscopy (FESEM), which revealed the homogeneous formation of the characteristic spherical superstructures with an average size of  $4.0 \pm 1.9 \mu\text{m}$  (Figure 5.1a-b). X-ray powder diffraction (XRPD) confirmed the presence of both UiO-66 and CaCl<sub>2</sub> hydrates forming the superstructures (Figure 5.1c). The content of Ca in the composites was estimated by digesting this powder (previously outgassed at 200 °C under vacuum) in H<sub>2</sub>SO<sub>4</sub> at 50 °C and analysed by ICP-OES, from which a CaCl<sub>2</sub> content of 38 % (hereafter,  $w_{\text{CaCl}_2}/w_{\text{CSPM}}$ ) in the composite (hereafter, **CaCl<sub>2</sub>@UiO-66\_38**) was determined. This percentage corresponds to the molar ratio of 1:1.5 (Zr<sup>4+</sup>:CaCl<sub>2</sub>), which is similar to the initial value (1:1.6), confirming that spray-drying is very efficient for incorporating CaCl<sub>2</sub> into the superstructures. Elemental mapping with energy dispersive X-ray spectrometry (EDX)

was also performed on a single superstructure, which revealed a highly uniform distribution of Zr, Ca and Cl atoms (Figure 5.1e).

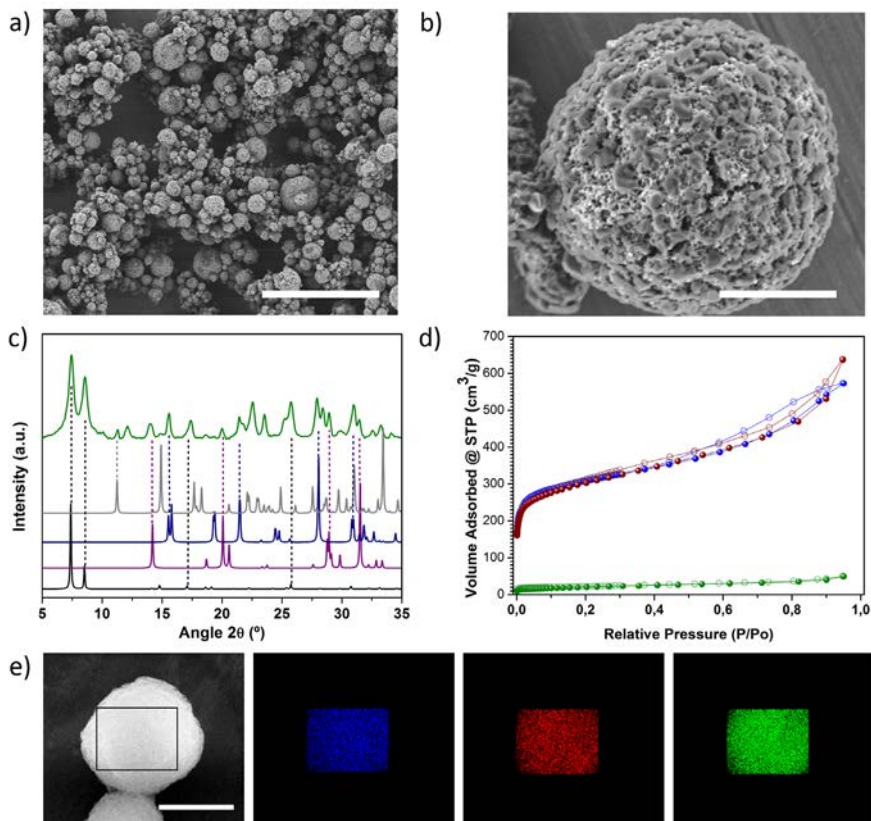


**Figure 5.1.** (a-b) Representative FESEM images of microspherical  $\text{CaCl}_2@\text{UiO-66}_{38}$  CPSMs. (c) XRPD pattern of  $\text{CaCl}_2@\text{UiO-66}_{38}$  powder (green), as compared to the corresponding simulated powder pattern of UiO-66 (black),  $\text{CaCl}_2 \cdot 2\text{H}_2\text{O}$  (purple),  $\text{CaCl}_2 \cdot 4\text{H}_2\text{O}\beta$  (grey) and  $\text{CaCl}_2 \cdot 4\text{H}_2\text{O}\gamma$  (dark blue). (d)  $\text{N}_2$  sorption isotherms of  $\text{CaCl}_2@\text{UiO-66}_{38}$  (green), pristine UiO-66 (blue) and  $\text{CaCl}_2@\text{UiO-66}_{38}$  after incubation in ethanol (red). (e) Elemental mapping with EDX performed on a single spherical superstructure of  $\text{CaCl}_2@\text{UiO-66}_{38}$ , showing the homogeneous distribution of Zr (blue), Ca (red) and Cl (green). Scale bars: 20  $\mu\text{m}$  (a) and 3  $\mu\text{m}$  (b-e).

Nitrogen physical adsorption measurements on  $\text{CaCl}_2@\text{UiO-66}_{38}$  (previously outgassed at 200 °C) showed a measured Brunauer-Emmett-Teller (BET) surface area of  $\approx 70 \text{ m}^2 \text{ g}^{-1}$ , which was very low compared to that of pristine UiO-66 superstructures that were also obtained by the spray-drying continuous-flow method ( $1106 \text{ m}^2 \text{ g}^{-1}$ )

(Figure 5.1d). We attribute this low microporosity to  $\text{CaCl}_2$  particles, which are somehow blocking the access of  $\text{N}_2$  molecules into the MOF micropores. This assumption was corroborated by removing the  $\text{CaCl}_2$  from the  **$\text{CaCl}_2@ \text{UiO-66}_{38}$**  composites by incubating them in ethanol for 12 h at room temperature. Under these conditions,  $\text{CaCl}_2$  was completely removed from the composites, as confirmed by the disappearance of the characteristic XRPD peaks of the  $\text{CaCl}_2$  hydrates (Figure 5.2a).

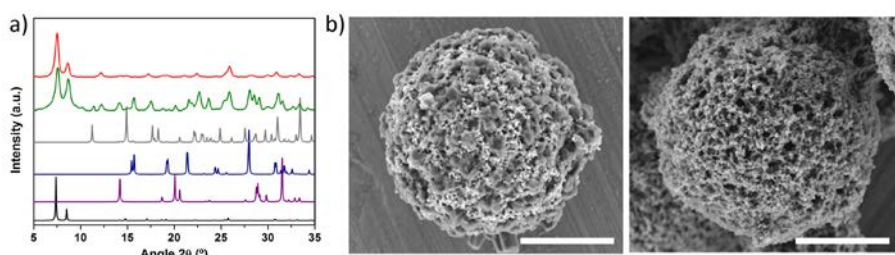


**Figure 5.2.** (a) XRPD patterns of the  **$\text{CaCl}_2@ \text{UiO-66}_{38}$**  (green) and after  $\text{CaCl}_2$  removal (red), compared to the simulated powder pattern for UiO-66 (black),  $\text{CaCl}_2 \cdot 2\text{H}_2\text{O}$  (purple),  $\text{CaCl}_2 \cdot 4\text{H}_2\text{O}\gamma$  (dark blue) and  $\text{CaCl}_2 \cdot 4\text{H}_2\text{O}\beta$  (grey). (b) FESEM images of microspherical  **$\text{CaCl}_2@ \text{UiO-66}_{38}$**  superstructures before (left) and after (right) incubation in ethanol. Scale bars:  $3 \mu\text{m}$ .

Remarkably, the resulting UiO-66 superstructures showed a  $S_{\text{BET}}$  value that increased up to  $1100 \text{ m}^2 \text{ g}^{-1}$  (Figure 5.1d). In addition, FESEM images of these UiO-66 superstructures revealed the formation of voids resulting from the dissolution of the  $\text{CaCl}_2$  crystals (Figure 5.2b). The presence of these voids was in concordance with the higher increase in the  $\text{N}_2$  adsorption in the range of pressures related to meso and macroporosity as well as with the pore size distribution curve, in which the presence of mesopores with 14 nm in diameter was evidenced after removing  $\text{CaCl}_2$  (Figure 5.3). In addition, the content of UiO-66 in the composite was estimated by weighting these superstructures, from which a UiO-66 content of 58 % w/w ( $w_{\text{UiO-66-1}}/w_{\text{CSPM}}$ ) was determined. This percentage is similar to the expected 62 % if the  **$\text{CaCl}_2@ \text{UiO-66}_{38}$**  is composed of  $\text{CaCl}_2$  and UiO-66. Altogether, these observations are important because they demonstrate that  $\text{CaCl}_2$  particles are confined in the micropores of UiO-66 and/or in the interparticular voids resulting from the assembly of UiO-66 nanocrystals in this class of superstructures.

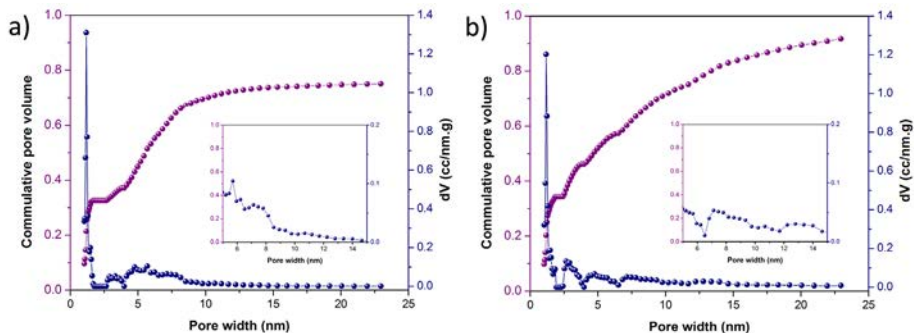


**Figure 5.3.** (a) Pore size distribution of UiO-66 superstructures. (b) Pore size distribution of **CaCl<sub>2</sub>@UiO-66\_38** after CaCl<sub>2</sub> removal. The pore size distribution was calculated using NDFT slit pore equilibrium model for carbon at 77 K.

### 5.2.2 Water sorption properties

Having determined the presence of both UiO-66 and CaCl<sub>2</sub> in **CaCl<sub>2</sub>@UiO-66\_38**, we then evaluated its water sorption properties. Water sorption isotherm of **CaCl<sub>2</sub>@UiO-66\_38** (previously outgassed at 200 °C) at 298 K showed two segments with steep increase in the water uptake (Figure 5.4). These two steps were attributed to the formation of CaCl<sub>2</sub>·0.33H<sub>2</sub>O at a relative humidity (RH) of 3 % (water uptake of 0.15 g<sub>water</sub> g<sup>-1</sup><sub>CSPM</sub>) and to the further transformation of this hydrate to CaCl<sub>2</sub>·2H<sub>2</sub>O at RHs from 10 % to 16 % (water uptake of 0.33 g<sub>water</sub> g<sup>-1</sup><sub>CSPM</sub>).<sup>10, 33</sup> Then, the sorption curve ascended monotonically, indicating the formation of an aqueous solution of the salt and reaching a maximum water uptake of 1.93 g<sub>water</sub> g<sup>-1</sup><sub>CSPM</sub> at a RH of 90%.<sup>10, 33</sup> Interestingly, an hysteresis loop at low pressures ( $P/P_0 = 0.10-0.16$ ) was observed in the desorption branch due to the structural changes in the transition from CaCl<sub>2</sub>·2H<sub>2</sub>O hydrate to CaCl<sub>2</sub>·0.33H<sub>2</sub>O hydrate, which is in agreement with other CSPMs based on mesoporous materials and salts crystals.<sup>10, 34</sup> Thus, we hypothesize that the water sorption takes place in the following steps: the anhydrous CaCl<sub>2</sub> particles confined in the micropores of UiO-66 and/or in the interparticular voids of superstructures adsorbs water and transforms to crystalline CaCl<sub>2</sub>·0.33H<sub>2</sub>O; then, this hydrate adsorbs more water and is transformed to crystalline CaCl<sub>2</sub>·2H<sub>2</sub>O; and finally, the salt is

completely dissolved filling the pores and/or voids. Here, we also performed eight water sorption-desorption cycles by alternatively exposing **CaCl<sub>2</sub>@UiO-66\_38** to humid (90 % RH) and dry (0 % RH) environments. Remarkably, the maximum uptake at 90 % RH (1.93 g<sub>water</sub> g<sup>-1</sup><sub>CSPM</sub>) remained constant with the number of cycles, confirming the stability of this CSPM to water sorption/desorption processes (Figure 5.4c).

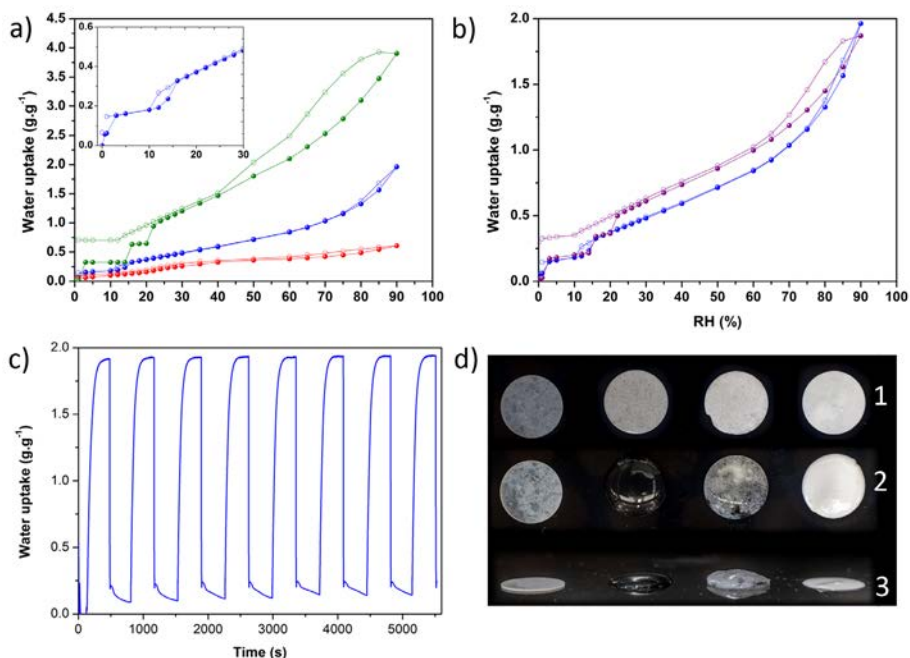


**Figure 5.4.** (a) Water sorption isotherms of UiO-66 (red), **CaCl<sub>2</sub>@UiO-66\_38** (blue) and CaCl<sub>2</sub> (green). Insert shows water adsorption isotherm of **CaCl<sub>2</sub>@UiO-66\_38** at low RHs. (b) Water adsorption isotherms of **CaCl<sub>2</sub>@UiO-66\_38** (blue) and the physical mixture (purple) (Adsorption: solid symbols; Desorption: open symbols). (c) Adsorption and desorption cycles for **CaCl<sub>2</sub>@UiO-66\_38**. (d) Photograph of the pellets of (from left to right) UiO-66, CaCl<sub>2</sub>·2H<sub>2</sub>O, physical mixture and **CaCl<sub>2</sub>@UiO-66\_38** before (1) and after (2 and 3) exposing them to a RH of 80 % at room temperature (2: top view, 3: lateral view).

Water isotherm of **CaCl<sub>2</sub>@UiO-66\_38** was compared with those of their individual components; that is, pristine UiO-66 superstructures and CaCl<sub>2</sub> (Figure 5.4a). As expected, **CaCl<sub>2</sub>@UiO-66\_38** showed an intermediate adsorption capacity. Indeed, the adsorption was higher than UiO-66 superstructures (maximum water uptake = 0.61

$\text{g}_{\text{water}} \text{g}^{-1}_{\text{UiO-66}}$ ), demonstrating that  $\text{CaCl}_2$  is very effective in increasing water uptake over the whole range of  $P/P_0$ , but lower than pristine  $\text{CaCl}_2$  (maximum water uptake =  $3.91 \text{ g}_{\text{water}} \text{g}^{-1}_{\text{CaCl}_2}$ ). However, the main differences appeared when compared the aspect of the three samples exposed to a RH of 80 % at room temperature. Under these conditions,  **$\text{CaCl}_2@ \text{UiO-66}_{38}$**  and UiO-66 remained as solid adsorbents while  $\text{CaCl}_2$  was dissolved with the water adsorbed due to the deliquescence effect (Figure 5.4d). Another difference was also found when desorption branches were compared.  $\text{CaCl}_2$  retained around  $0.70 \text{ g}_{\text{water}} \text{g}^{-1}_{\text{CaCl}_2}$  (17.9 % of the total uptake) at a RH of  $\approx 0$  %, whereas  **$\text{CaCl}_2@ \text{UiO-66}_{38}$**  retained only  $0.06 \text{ g}_{\text{water}} \text{g}^{-1}_{\text{CSPM}}$  (3.1 % of the total uptake).

To prove that the properties of  **$\text{CaCl}_2@ \text{UiO-66}_{38}$**  composite results from using the *in situ* spray-drying synthesis and shaping methodology rather than simply mixing UiO-66 and  $\text{CaCl}_2$ , we also performed the water sorption measurement of a physical mixture of  $\text{CaCl}_2$  and UiO-66 superstructures (38 % and 62 % (w/w), respectively). The total water uptake of this mixture ( $1.86 \text{ g}_{\text{water}} \text{g}^{-1}_{\text{mixture}}$ ) was slightly lower than the composite uptake (Figure 5.4b), but properly matched with the percentage of contribution of the individual components. Again, the differences were the liquefaction of the  $\text{CaCl}_2$  of this mixture when exposed to a RH of 80 % at room temperature (Figure 5.4d), and a water retention of  $0.30 \text{ g}_{\text{water}} \text{g}^{-1}_{\text{mixture}}$  (16.1 % of the total uptake) at a RH of  $\approx 0$  % (Figure 5.4b). This behavior is very similar to that found for the pristine  $\text{CaCl}_2$ , thereby confirming that a simple mixture is not enough for producing a composite that behaves as a solid adsorbent when adsorb water, as it does the spray-drying synthesized spherical superstructures.

### 5.2.3 Tuning the composition of $\text{CaCl}_2$

We then sought to assess the water sorption properties of  **$\text{CaCl}_2@ \text{UiO-66}$**  composites with diverse compositions, seeking to find an optimal  $\text{CaCl}_2/\text{UiO-66}$  ratio in terms of maximum capacity of UiO-66 superstructures to host  $\text{CaCl}_2$  while preventing its dissolution. Thus, we systematically synthesized a series of composites in which we

increased the initial molar ratios of  $\text{CaCl}_2$  from 1:2.6, 1:3.2, 1:4.8 to 1:6.4 ( $\text{Zr}^{4+}:\text{CaCl}_2$ ). Again, the content of Ca in the composites was estimated by digesting the as-made samples (previously outgassed at 200 °C under vacuum) in  $\text{H}_2\text{SO}_4$  at 50 °C and analyzed by ICP-OES (Table 5.1).

**Table 5.1.** Content of Ca in the composites estimated by digesting the as-made samples (previously outgassed at 200 °C under vacuum) in  $\text{H}_2\text{SO}_4$  at 50 °C and analysed by ICP-OES.

Composite	Initial molar ratio	Determined molar	% $\text{CaCl}_2$
	Zr:Ca	ratio Zr:Ca	(w/w)
$\text{CaCl}_2@ \text{UiO-66}$	1:1.6	1:1.5	38
	1:2.6	1:2.5	50
	1:3.2	1:2.8	53
	1:4.8	1:4.4	64
$\text{CaCl}_2@ \text{UiO-66-NH}_2$	1:1.6	1:1.5	38
Composite	Initial molar ratio	Determined molar	% LiCl
	Zr:Li	ratio Zr:Li	(w/w)
$\text{LiCl}@ \text{UiO-66}$	1:1.6	1:1.6	19

FESEM images revealed the formation of  $\text{CaCl}_2@ \text{UiO-66}_x$  for the first three samples (where  $x = 50, 53$  and  $64$  %  $w_{\text{CaCl}_2}/w_{\text{CSPM}}$ ) in the form of spherical superstructures (Figure 5.5). However,  $\text{CaCl}_2@ \text{UiO-66}_{64}$  sample was discarded because it showed the presence of non-encapsulated  $\text{CaCl}_2$  crystals together with the superstructures. In the case of a molar ratio of 1:6.4, crystalline spherical superstructures were not formed (Figure 5.5d). For the first two compositions, XRPD patterns confirmed the formation of UiO-66 and the presence of  $\text{CaCl}_2$  hydrates (Figure 5.6a).

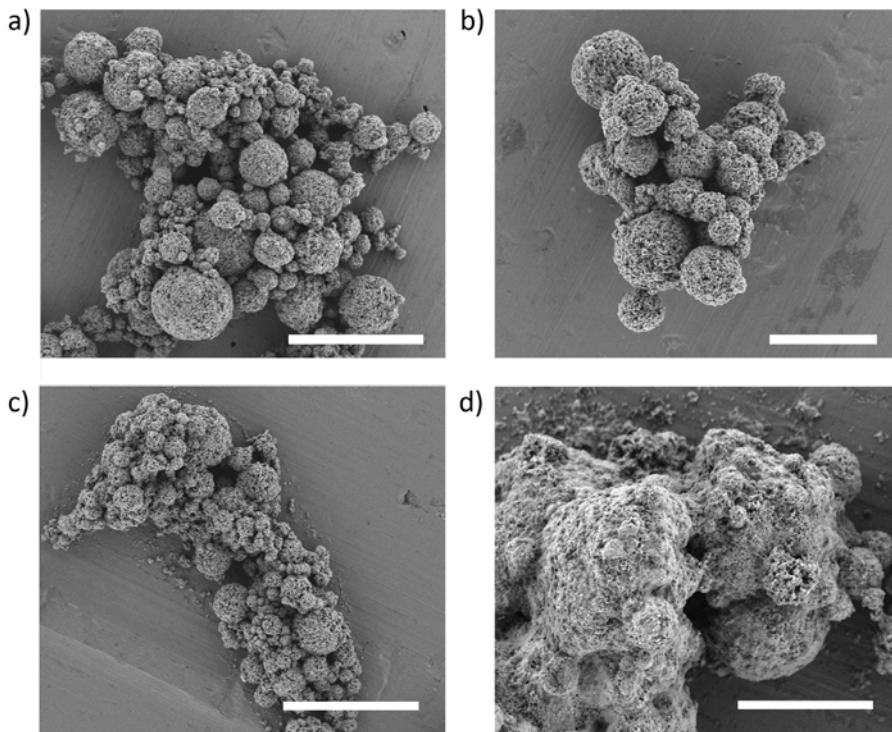


**Figure 5.5.** Representative FESEM images of (a)  $\text{CaCl}_2@UiO-66_{50}$ , (b)  $\text{CaCl}_2@UiO-66_{53}$ , (c)  $\text{CaCl}_2@UiO-66_{64}$ , and (d) composite prepared with a molar ratio of 1:6.4 ( $Zr^{4+} : CaCl_2$ ). Scale bars: 20  $\mu\text{m}$  (a, c) and 5  $\mu\text{m}$  (d).

To examine the water adsorption properties of the  $\text{CaCl}_2@UiO-66_{50}$  and  $\text{CaCl}_2@UiO-66_{53}$  CSPMs, water adsorption isotherms were measured at 298 K (Figure 5.6b). All resulting isotherms displayed the characteristic steps related to the formation of  $\text{CaCl}_2 \cdot 0.33\text{H}_2\text{O}$  and  $\text{CaCl}_2 \cdot 2\text{H}_2\text{O}$  hydrates, and the hysteresis loop in the desorption branch. The maximum uptake of the composites was 2.24  $\text{g}_{\text{water}} \text{g}^{-1}_{\text{CSPM}}$  ( $\text{CaCl}_2@UiO-66_{50}$ ) and 2.59  $\text{g}_{\text{water}} \text{g}^{-1}_{\text{CSPM}}$  ( $\text{CaCl}_2@UiO-66_{53}$ ) at RH of 90%. As expected, a greater amount of  $\text{CaCl}_2$  led to achieve a higher water uptake. As well, a higher amount of  $\text{CaCl}_2$  resulted in higher water retention values at a RH of  $\approx 0\%$ , as evidenced by the water retentions of 0.17  $\text{g}_{\text{water}} \text{g}^{-1}_{\text{mixture}}$  (7.6 % of the total uptake) for  $\text{CaCl}_2@UiO-66_{50}$  and of 0.20  $\text{g}_{\text{water}} \text{g}^{-1}_{\text{mixture}}$  (7.7 % of the total uptake) for  $\text{CaCl}_2@UiO-$

66\_53; in comparison to that observed in **CaCl<sub>2</sub>@UiO-66\_38** (3.1 % of the total uptake).

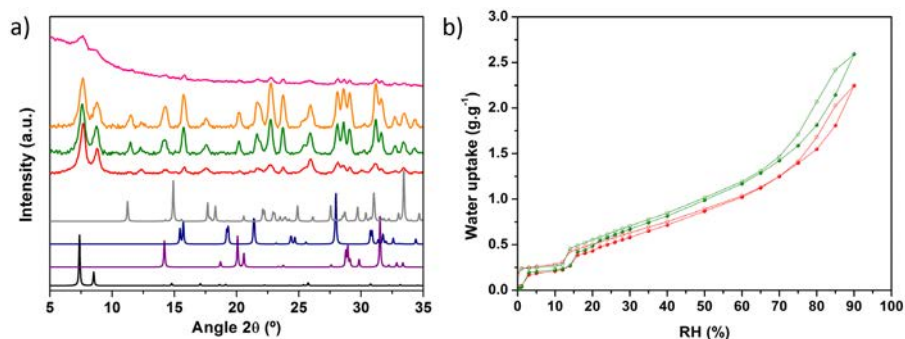


**Figure 5.6.** (a) XRPD patterns of **CaCl<sub>2</sub>@UiO-66\_50** (red), **CaCl<sub>2</sub>@UiO-66\_53** (green), **CaCl<sub>2</sub>@UiO-66\_64** (orange) and the composite prepared with a molar ratio of 1:6.4 ( $Zr^{4+} : CaCl_2$ ) (pink), as compared to the simulated powder pattern for UiO-66 (black),  $CaCl_2 \cdot 2H_2O$  (purple),  $CaCl_2 \cdot 4H_2O_\gamma$  (dark blue) and  $CaCl_2 \cdot 4H_2O_\beta$  (grey). (b) Water adsorption isotherms of **CaCl<sub>2</sub>@UiO-66\_50** (red) and **CaCl<sub>2</sub>@UiO-66\_53** (green) at 25 °C.

## 5.2.4 Synthesis of LiCl@UiO-66 and CaCl<sub>2</sub>@UiO-66-NH<sub>2</sub> composites

To demonstrate the generality of our approach, we used the spray-drying technique to synthesize other Salt@MOF CSPMs substituting the inorganic salt and the MOF. Thus, we prepared **LiCl@UiO-66** and **CaCl<sub>2</sub>@UiO-66-NH<sub>2</sub>** using the same conditions as for **CaCl<sub>2</sub>@UiO-66\_38**, except that instead of CaCl<sub>2</sub> in the first case and UiO-66 in the second case, we used LiCl and UiO-66-NH<sub>2</sub>, respectively. In both cases, pure microspherical superstructures were obtained, as confirmed by FESEM and XRPD (Figure 5.7a-d). The content of Li and Ca was also estimated by ICP-OES, from which a LiCl content of 19 % w/w in **LiCl@UiO-66\_19** and a CaCl<sub>2</sub> content of 38 % w/w in **CaCl<sub>2</sub>@UiO-66-NH<sub>2</sub>\_38** were determined. Here, water sorption measurements at 298 K showed that **LiCl@UiO-66\_19** exhibits a high water uptake of 1.53 g<sub>water</sub> g<sup>-1</sup><sub>CSPM</sub> at a RH of 90 % and a water retention of 0.07 g<sub>water</sub> g<sup>-1</sup><sub>CSPM</sub> (4.6 % of the total uptake) during desorption (Figure 5.7e-f). On the other hand, **CaCl<sub>2</sub>@UiO-66-NH<sub>2</sub>\_38** showed a maximum uptake of 1.76 g<sub>water</sub> g<sup>-1</sup><sub>CSPM</sub>, which is lower compared with its analogue

based on UiO-66, and it retained  $0.12 \text{ g}_{\text{water}} \text{ g}^{-1}_{\text{CSPM}}$  (6.8 % of the total uptake) of water at a RH of 0 %, which doubles that of its UiO-66 analogue.

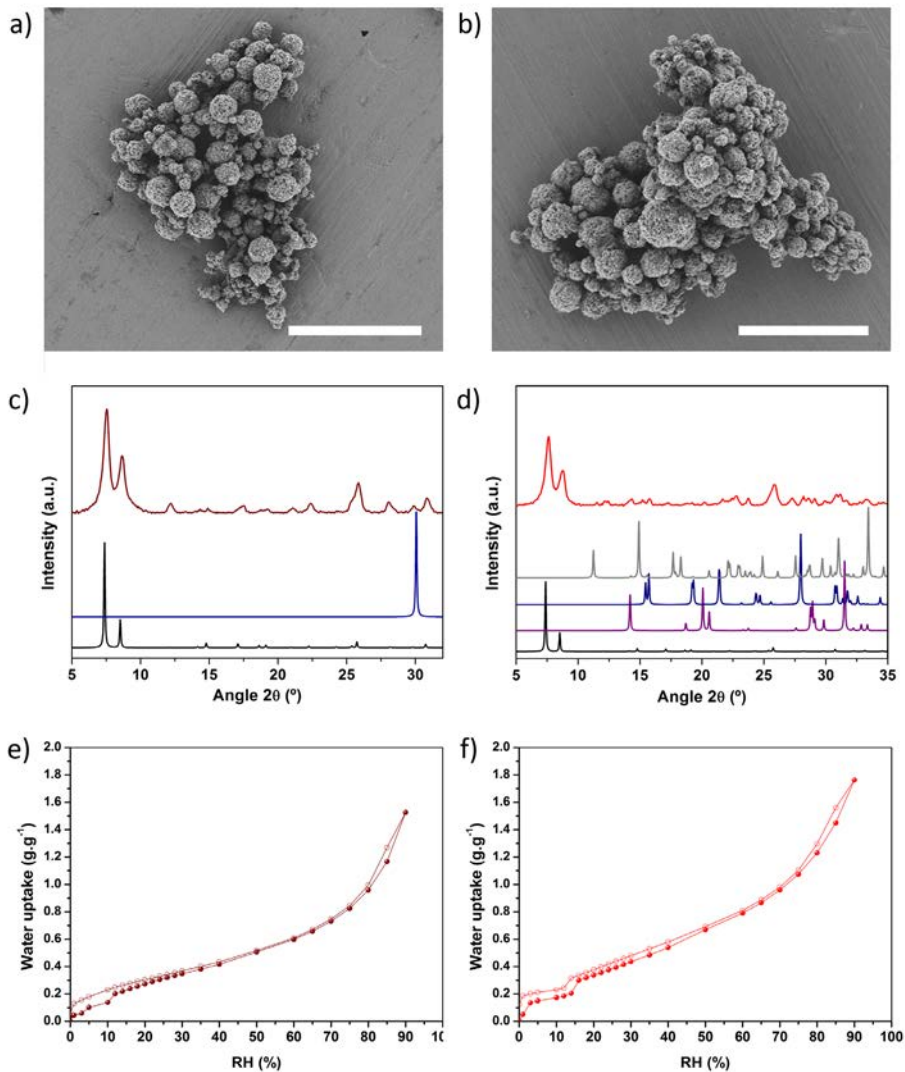


**Figure 5.7.** Representative FESEM images of (a)  $\text{LiCl}@UiO-66-19$  and (b)  $\text{CaCl}_2@UiO-66-NH_2-38$ . (c) XRPD diffractograms of  $\text{LiCl}@UiO-66-19$ , as compared to the simulated powder pattern for UiO-66 (black) and LiCl (dark blue). (d) XRPD patterns of  $\text{CaCl}_2@UiO-66-NH_2-38$  (red) compared to the simulated powder pattern for UiO-66 (black),  $\text{CaCl}_2 \cdot 2H_2O$  (purple),  $\text{CaCl}_2 \cdot 4H_2O$  (dark blue) and  $\text{CaCl}_2 \cdot 4H_2O\beta$  (grey). Water sorption isotherms of (e)  $\text{LiCl}@UiO-66-19$  (dark red) and (f)  $\text{CaCl}_2@UiO-66-NH_2-38$  (red). Scale bars:  $20 \mu\text{m}$ .

## 5.2.5 Thermal batteries application

Figure 5.8 summarizes the working capacity for all prepared materials and the most promising UiO-66-based CSPMs were tested as potential adsorbents in thermal batteries and adsorption heat pumps applications according to their working capacity ( $\Delta W$ ). Among them, thermal batteries have been recently explored as an alternative to the traditional air conditioning systems in electric vehicles. Traditionally, the climate control system is based in a vapour compression system where the compressor is driven by an electric battery with high power consumption, producing a decrease in the efficiency of the electric vehicle. Thermal batteries are based in a sorption and desorption cycles where large amounts of energy can be reversibly stored for provide heating and cooling efficiently. As consequence, the consumption of electric power decreases and the driving range of the electric vehicle increases.<sup>4, 35</sup>

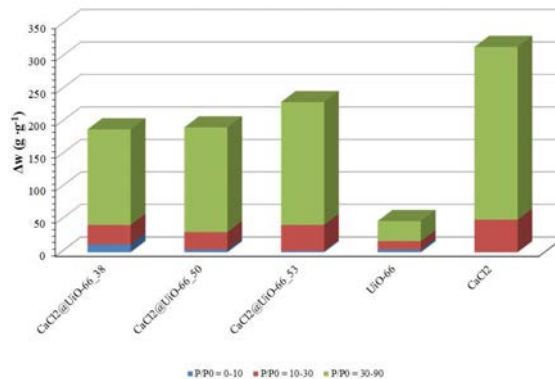


**Figure 5.8.** Working capacity calculated from the water isotherms for the composites, pristine UiO-66 and  $\text{CaCl}_2$ .

To evaluate our CSPMs as adsorbents for thermal batteries, we selected **CaCl<sub>2</sub>@UiO-66\_38** because it has the higher working capacity ( $\Delta w = 0.12 \text{ g}_{\text{water}} \text{ g}^{-1}_{\text{CSPM}}$ ) at  $P/P_0 = 0.1$  (Figure 5.4a). It is important to highlight here that water adsorption is desirable at a relative pressure of 0.1 to reduce the need of using compressors in the system.<sup>28</sup>

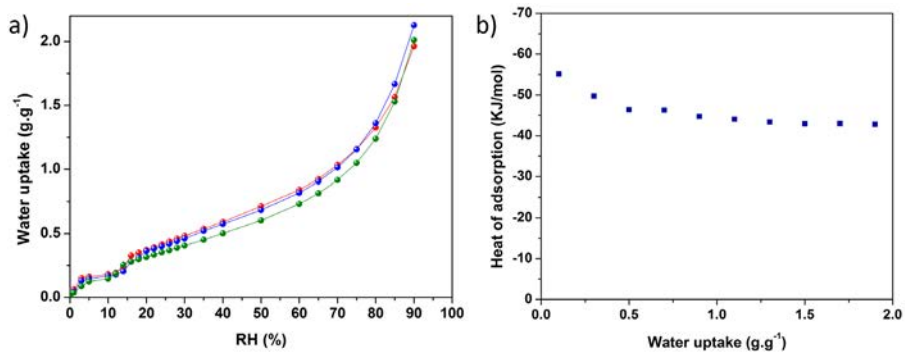


Figure 5.9. (a) Water sorption isotherms of  $\text{CaCl}_2@\text{UiO-66}_{38}$  at 30 °C (red), 40 °C (blue) and 50 °C (green).  
 (b) Heat of adsorption of  $\text{CaCl}_2@\text{UiO-66}_{38}$ .

Once  $\text{CaCl}_2@\text{UiO-66}_{38}$  was selected, the heat storage capacity ( $C_{HS}$ ) was estimated according to the Equation (5.1)<sup>2b</sup>

$$C_{HS} = \frac{\Delta H_{ads} \cdot \Delta w}{M_w} \quad (5.1)$$

where  $M_w$  is the water molar weight and  $\Delta H_{ads}$  is the heat of adsorption.  $\Delta H_{ads}$  of  $\text{CaCl}_2@\text{UiO-66}_{38}$  was calculated using water isotherms collected at different temperatures (25, 40 and 50 °C; Figure 5.9a), and then adjust to the Clausius-Clapeyron Equation (5.2)<sup>36</sup>

$$\Delta H_{ads} = -R \ln \left( \frac{P_2}{P_1} \right) \frac{T_1 \cdot T_2}{T_2 - T_1} \quad (5.2)$$

It was found that  $\Delta H_{ads}$  values decrease as water uptakes increase (from  $\approx 55$  kJ mol<sup>-1</sup> to  $\approx 43$  kJ mol<sup>-1</sup>; Figure 5.9b), and that  $\Delta H_{ads}$  was 55 kJ mol<sup>-1</sup> for a working capacity of 0.12 g<sub>water</sub> g<sup>-1</sup><sub>CSPM</sub>. These values are in agreement with the initial formation of the  $\text{CaCl}_2$  hydrate, where the water molecules are stronger bounded and then, a decrease to 43 kJ mol<sup>-1</sup> is due to the formation of an aqueous solution of  $\text{CaCl}_2$ .<sup>37</sup>

Finally, a  $C_{HS}$  value of 367 kJ kg<sup>-1</sup> was determined using Equation (5.1). According to primary technical targets for thermal batteries,<sup>38</sup> the minimum heat storage capacity should be 2.5 kWh. This means that 24.5 Kg of  $\text{CaCl}_2@\text{UiO-66}_{38}$  will be

required to achieve this capacity, which is less than the total weight of the system (35 Kg) suggested by U.S. Department of Energy (DOE).<sup>38</sup>

### 5.2.6 Adsorption chillers application

To evaluate our CSPMs as adsorbents for adsorption chillers, we selected **CaCl<sub>2</sub>@UiO-66\_53** because it had the higher working capacity at  $P/P_0 = 0.3$ , which is a typical value for practical applications.<sup>2</sup> In order to describe the performance and the efficiency of this system, the specific cooling power (SCP), an isosteric cycle diagram and the coefficient of performance (COP) were determined.

The average specific cooling power (SCP) describes the effectiveness of the system during the cooling process and is defined as the ratio of cooling power per mass of adsorbent per cycle time according to Equation (5.3)<sup>3</sup>

$$SCP = \frac{\Delta H_{vap} \cdot \Delta w \cdot 0.8}{M_w (\tau_{0.8ads} + \tau_{0.8des})} \quad (5.3)$$

where  $\Delta H_{vap}$  is the water enthalpy of evaporation,  $\Delta w$  is the working capacity of the **CaCl<sub>2</sub>@UiO-66\_53**/H<sub>2</sub>O pair,  $M_w$  is the water molar weight, and  $\tau_{0.8ads}$  and  $\tau_{0.8des}$  are the adsorption and desorption times when the conversion  $q = 0.8$  (Figure 5.10d).

An isosteric cycle diagram of an adsorption air conditioning cycle was analyzed to determine  $\Delta w$  and the desorption temperature ( $T_{des}$ ) (Figure 5.10b). This diagram was calculated using the water adsorption isobars at vapor pressures of 0.7, 1.2, 2.4, 3.7, 4.2 and 5.6 kPa (Figure 5.10a), and fixing the operational temperatures of the cycle to a temperature of evaporation ( $T_{ev}$ ) of 283 K and to a temperature of adsorption and condensation ( $T_{ad} = T_{con}$ ) of 303 K. In the isobaric adsorption (step IV-I), the water was adsorbed in the composite reaching a maximum uptake of 0.60 g<sub>water</sub> g<sup>-1</sup><sub>CSPM</sub>. Then, during the isosteric heating (I-II), the **CaCl<sub>2</sub>@UiO-66\_53** was fully saturated and the pressure increased from 1.2 kPa to 4.2 kPa by increasing the temperature from 303 K to 317 K without desorption. In the isobaric desorption (II-III), the heating was

continued and desorption process was started until reached a  $T_{\text{des}}$  of 370 K, in which the water uptake was minimal. Finally, in the isosteric cooling, decreasing the temperature reduced the pressure, and the composite was regenerated. In this cycle,  $\Delta w$  depends on the  $T_{\text{des}}$  (Figure 5.10c), where  $\Delta w$  increases from 0.3  $\text{g}_{\text{water}} \text{g}^{-1}_{\text{CSPM}}$  at  $T_{\text{des}} = 330 \text{ K}$  to 0.56  $\text{g}_{\text{water}} \text{g}^{-1}_{\text{CSPM}}$  at  $T_{\text{des}} = 370 \text{ K}$ . These values are higher compared to traditional adsorbents like zeolites, silica gel and other CSPMs (Table 5.2), and are in the range of some reported MOFs (*e.g.*  $\text{NH}_2\text{-MIL-125}$ : 0.39  $\text{g}_{\text{water}} \text{g}_{\text{MOF}}^{-1}$ ; CPO-27(Ni): 0.41  $\text{g}_{\text{water}} \text{g}_{\text{MOF}}^{-1}$ ; MOF-841: 0.44  $\text{g}_{\text{water}} \text{g}_{\text{MOF}}^{-1}$ ).<sup>3, 28, 39</sup>

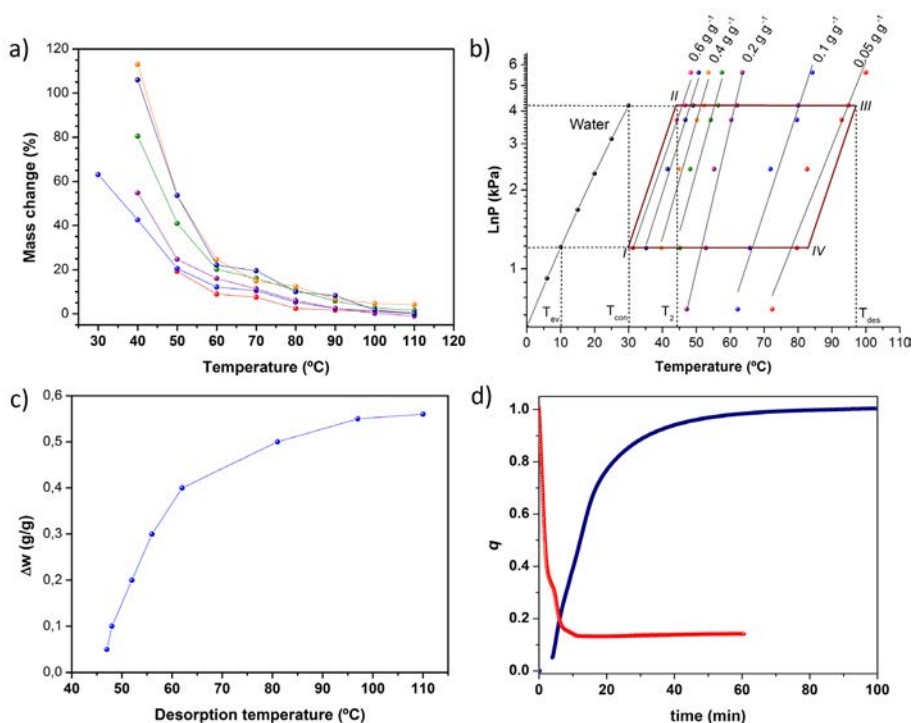


**Figure 5.10.** (a) Water sorption isobars of  $\text{CaCl}_2@UiO-66_{53}$  at vapor pressures of 0.7 (red), 1.2 (blue), 2.4 (purple), 3.7 (green), 4.2 (dark blue) and 5.6 kPa (orange). (b) Isosteric cycle diagram for  $\text{CaCl}_2@UiO-66_{53}$ /water working pair calculated for an air cooling cycle. (c) Working capacity as a function of the desorption temperature for the  $\text{CaCl}_2@UiO-66_{53}$ /water pair. (d) Kinetics of water sorption of  $\text{CaCl}_2@UiO-66_{53}$  at  $T = 303 \text{ K}$  and  $P = 1.24 \text{ kPa}$  (blue) and desorption at  $T = 370 \text{ K}$  and  $P = 5.4 \text{ kPa}$  (red).

The adsorption and desorption times were calculated from the kinetic curves of water adsorption and desorption (Figure 5.10d), which were performed under the standard  $T_{ad} = 303$  K,  $P_{ad} = 1.24$  kPa and  $P_{des} = 5.4$  kPa conditions and the determined  $T_{des} = 370$  K. From these curves, we found that  $\tau_{0.8ads}$  and  $\tau_{0.8des}$  were 1320 s and 380 s, respectively. Finally, a SCP value of  $631 \text{ W kg}^{-1}$  was calculated according to Equation 5.3.<sup>3</sup>

In an adsorption air conditioning system, COP is a factor that helps describing the energetic efficiency. COP is defined as the useful output energy divided by the energy required as input.<sup>40</sup> Thus, COP is the ratio of the vaporization heat ( $Q_{ev}$ ) and regeneration heat ( $Q_{reg}$ ) according to Equation (5.4)<sup>22</sup>

$$COP = \frac{Q_{ev}}{Q_{reg}} \quad (5.4)$$

Here, the vaporization ( $Q_{ev}$ ) and regeneration ( $Q_{reg}$ ) heats were calculated from Equations 5.5-5.8:

$$Q_{ev} = \frac{\Delta H_{vap}(T_{ev}) \cdot \rho \cdot m \cdot \Delta w}{M_w} \quad (5.5)$$

where  $\rho$  is the water density and  $m$  is the amount of **CaCl<sub>2</sub>@UiO-66\_53** used in the cycle.

$$Q_{reg} = Q_{I-II} + Q_{II-III} \quad (5.6)$$

$$Q_{I-II} = \int_{T_{con}}^{T_2} C_p^{cspm}(T) dT + \int_{T_{con}}^{T_2} \rho \cdot W_{max} C_p^{water}(T) dT \quad (5.7)$$

$$Q_{II-III} = \int_{T_2}^{T_{des}} C_p^{cspm}(T) dT + \int_{T_{con}}^{T_2} \rho \cdot \frac{W_{max} + W_{min}}{2} \cdot C_p^{water}(T) dT - \frac{1}{M_w} \int_{W_{min}}^{W_{max}} \rho \cdot \Delta H_{ads}(W) dW \quad (5.8)$$

where  $C_p^{cspm}$  is the heat capacity of **CaCl<sub>2</sub>@UiO-66\_53** and  $C_p^{water}$  is the heat capacity of water, and  $W_{max}$  and  $W_{min}$  are the water loading at points II and III, respectively, of the isosteric cycle diagram (Figure 5.10b).

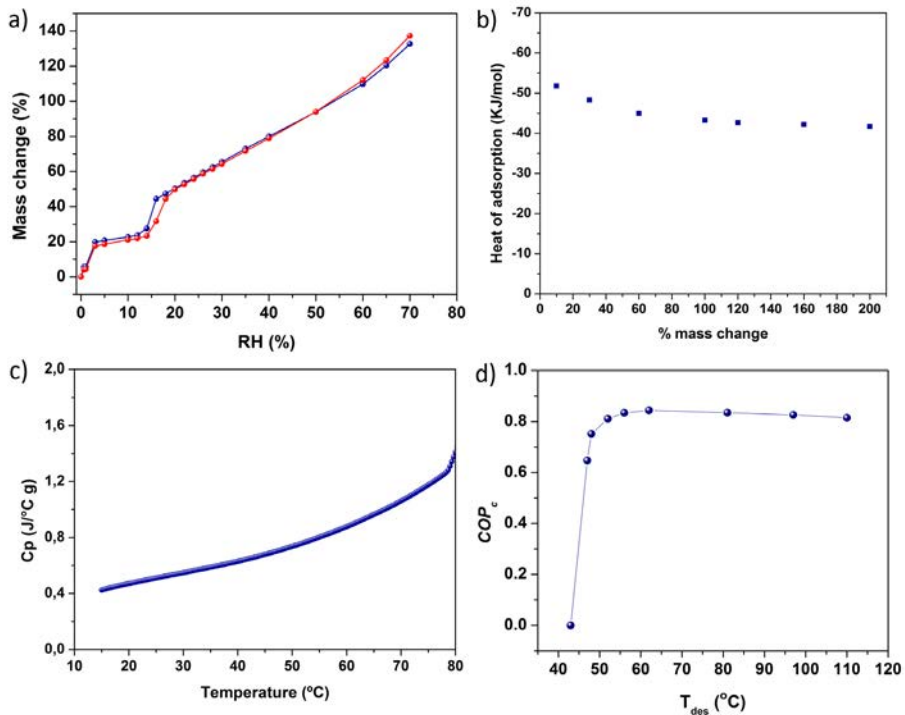


**Figure 5.11.** (a) Water adsorption isotherms of **CaCl<sub>2</sub>@UiO-66\_53** at 25 °C (blue), 40 °C (red). (b) Heat of adsorption of **CaCl<sub>2</sub>@UiO-66\_53**. (c) Heat capacity as a function of the desorption temperature for **CaCl<sub>2</sub>@UiO-66\_53**. (d) Coefficient of performance (COP) as a function of desorption temperature for the **CaCl<sub>2</sub>@UiO-66\_53**/Water working pair.

Thus, the sorption heat ( $\Delta H_{ads}$ ) of the working pair **CaCl<sub>2</sub>@UiO-66\_53**/water and the heat capacity ( $C_p$ ) of **CaCl<sub>2</sub>@UiO-66\_53** were initially determined. The  $\Delta H_{ads}$  was calculated using the Clausius-Clapeyron equation and water isotherms at two different temperatures (25 and 40 °C) (Figure 5.11a). As seen in the previous section, the  $\Delta H_{ads}$  decreased as water uptake increased (from  $\approx 52$  kJ mol<sup>-1</sup> to  $\approx 41$  kJ mol<sup>-1</sup>; Figure 5.11b). Afterwards, the  $C_p$  of **CaCl<sub>2</sub>@UiO-66\_53** was determined from Differential Scanning

Calorimetry (DSC) analysis, from which an average  $C_p$  of  $0.76 \text{ J g}^{-1} \text{ K}^{-1}$  was calculated over the temperature range of 303-353 K (Figure 5.11c).

Once we determined these parameters, COP was calculated as a function of  $T_{\text{des}}$  (Figure 5.11d). For a  $T_{\text{des}}$  from 330 to 383 K, a COP value of 0.83 remained almost constant, meaning that 0.83 J of cold can be generated from 1 J of waste heat (Table 5.2).

**Table 5.2.** Water loading, regeneration temperature, COPc, and SCP for selected materials compared with  $\text{CaCl}_2@UiO-66\_53$  composite.

Adsorbent	Water loading [g g <sup>-1</sup> ]	Regeneration temperature [°C]	COP <sub>c</sub>	SCP [W kg <sup>-1</sup> ]	Reference
$\text{CaCl}_2@UiO-66\_53$	0.60	57-110	0.83	631	This work
Silica gel	-	85	0.37	63.4	41
Activated carbon	0.19	115	0.37	65	42
Zeolite 13-X	0.25	310	0.38	25.7	43
AQSOA-FAM-Z02 (ALPO-34)	0.28	90	0.25-0.3	260	44
SWS-8L (Ca(NO <sub>3</sub> ) <sub>2</sub> @mesoporous silica)	-	90-95	0.18-0.31	190-389	45
SWS-9V (LiNO <sub>3</sub> @vermiculite)	0.4	70	0.59	96	46
$\text{CaCl}_2@Silica\text{-Carbon}$	0.43	115	0.7	378	42
NH <sub>2</sub> -MIL-125	0.42	90	0.8	3200	3
CPO-27(Ni)	0.41	130	0.45	440	39

Finally, we also studied the multiple adsorption-desorption cycles under operational conditions for air conditioning systems ( $P = 2.36 \text{ kPa}$ , and  $T_{\text{ads}} = 303 \text{ K}$  and  $T_{\text{des}} = 383 \text{ K}$ ). Figure 5.12 shows six consecutive cycles in which, after the first three cycles, a very small decrease in the water uptake (from  $0.63$  to  $0.61 \text{ g g}^{-1}$ ) was

observed. Then, water uptake becomes stable, without a significant loss of adsorption and desorption capacities during the remaining cycles.

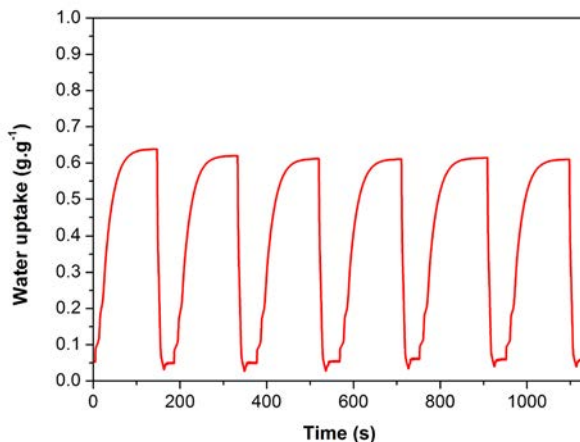


**Figure 5.12.** Adsorption-desorption cycles under operational conditions for air conditioning systems ( $P = 2.36$  kPa, and  $T_{ads} = 303$  K and  $T_{des} = 383$  K) for **CaCl<sub>2</sub>@UiO-66\_53**.

### 5.3 Conclusions

In conclusion, we have reported a continuous and fast methodology for the fabrication of MOF-based CSPM materials using the spray drying continuous flow method, which enables the simultaneous synthesis and shaping of microspherical MOF superstructures while confining the salts. This method also enables tuning the composition of the resulting CSPMs. We have demonstrated the applicability of these MOF-based CSPMs for potential applications in thermal batteries and refrigerator systems. For the first application, we have shown that **CaCl<sub>2</sub>@UiO-66\_38** exhibits a  $C_{HS}$  of  $367 \text{ kJ kg}^{-1}$ ; which fulfills the conditions suggested by the U.S. Department of Energy to use it in thermal batteries. For the latter application, the working pair **CaCl<sub>2</sub>@UiO-66\_53/water** displays a high capacity and energetic efficiency, exhibiting a COP of 0.83. This value is higher than traditional working pairs based on silica and zeolites and others CSPMs, which exhibit COP values from 0.3 to 0.6, (e.g. silica gel: 0.3; zeolite-NaX: 0.38; natural zeolite: 0.34; and LiCl@Silica: 0.41)<sup>6, 7</sup> and it is comparable with the

most energy efficient MOFs (NH<sub>2</sub>-MIL-125: 0.8; CAU-3: 0.7; MOF-841: 0.8) reported so far.<sup>3, 22, 40</sup> We believe that this methodology will facilitate the synthesis of other CSPMs, in which the nature of the MOF and the salt can be changed, as well as of new composites resulting from the combination of MOFs with other nanomaterials such as inorganic nanoparticles or graphene.

## 5.4 Experimental Section

### 5.4.1 Materials and methods

Zirconium chloride, calcium chloride, lithium chloride, terephthalic acid and 2-aminoterephthalic acid were purchased from Sigma Aldrich. Dimethylformamide was obtained from Fisher Chemical. All the reagents were used without further purification. Deionised water, obtained with a Milli-Q<sup>®</sup> system (18.2 MΩ cm), was used in all reactions.

X-ray powder diffraction (XRPD) patterns were collected on an X'Pert PRO MPDP analytical diffractometer (Panalytical) at 45 kV, 40 mA using CuK $\alpha$  radiation ( $\lambda = 1.5419 \text{ \AA}$ ). Field-Emission Scanning Electron Microscopy (FESEM) images were collected on a FEI Magellan 400L scanning electron microscope at an acceleration voltage of 2.0 KV and FEI Quanta 650F scanning electron microscope with Energy-dispersive X-ray spectroscopy (EDX) Inca 250 SSD XMax20 at an acceleration voltage of 20.0 KV, using aluminium as support. ICP-OES measurements were performed using a Perkin Elmer Optima 4300DV after HF digestion. Prior to the ICP analysis, samples were degassed under vacuum at 200 °C. Volumetric N<sub>2</sub> sorption isotherms were collected at 77 K using an AutosorbIQ-AG analyser (Quantachrome Instruments). Gravimetric water vapor sorption isotherms were measured using a DVS vacuum instrument (Surface Measurement Systems Ltd). The weight of the dried powder (~ 20 mg) was constantly monitored with a high resolution microbalance ( $\pm 0.1 \text{ }\mu\text{g}$ ) and recorded at 25 °C, 35 °C and 45 °C ( $\pm 0.2 \text{ }^\circ\text{C}$ ) under pure water vapor pressures. The

kinetics curves of water vapor adsorption were obtained measuring real time mass change. The isobars were recorded at different temperatures from 110 °C to 30 °C at a fixed pressure of 0.7, 1.2, 2.4, 3.7, 4.2 and 5.6 kPa. Prior to the sorption experiments, samples were degassed inside the chamber under vacuum at 200 °C for 6 h. The heat capacity measurements were performed on a Differential Scanning Calorimeter (Mettler Toledo). The heating rate used was 10 °C min<sup>-1</sup> from 10 °C to 90 °C and sapphire was used as a reference material.

#### **5.4.2 Spray-drying continuous flow-assisted synthesis of UiO-66 and UiO-66-NH<sub>2</sub> superstructures.**

In a typical synthesis, a solution 0.1 M of ZrCl<sub>4</sub> and 0.1 M of the organic ligand in 15 mL of a mixture of DMF and H<sub>2</sub>O (5.48:1) was injected into the coil flow reactor (Pyrex tube, inner diameter: 3 mm) at a feed rate of 2.4 mL min<sup>-1</sup> and at a  $T_1$  of 115 °C. The resulting pre-heated solution was then spray-dried at a  $T_2$  of 180 °C and a flow rate of 336 mL min<sup>-1</sup> using a Dryer B-290 Mini Spray (BUCHI Labortechnik; spray cap: 0.5-mm-hole). Finally, the collected solid was dispersed in DMF at room temperature, stirred overnight and precipitated by centrifugation. This process was repeated twice with ethanol instead of DMF. The final product was dried for 12 h at 80 °C.

#### **5.4.3 Spray-drying continuous flow-assisted synthesis of UiO-66-based CSPMs.**

A 15 mL solution containing 0.1 M of ZrCl<sub>4</sub>, 0.1 M of terephthalic acid and a solution of CaCl<sub>2</sub>·H<sub>2</sub>O (at the concentration of 0.16, 0.26, 0.32, 0.48 and 0.64 M) or LiCl (at the concentration of 0.16) in a mixture of DMF and H<sub>2</sub>O (5.48:1) was injected into the coil flow reactor (Pyrex tube, inner diameter: 3 mm) at a feed rate of 2.4 mL min<sup>-1</sup> and at a  $T_1$  of 115 °C. The resulting pre-heated solution was then spray-dried at a  $T_2$  of 180 °C and a flow rate of 336 mL min<sup>-1</sup> using a Dryer B-290 Mini Spray (BUCHI Labortechnik; spray cap: 0.5-mm-hole), collecting a white solid.

#### 5.4.4 Spray-drying continuous flow-assisted synthesis of $\text{CaCl}_2@$ UiO-66- $\text{NH}_2$ .

A 15 ml solution containing 0.1 M of  $\text{ZrCl}_4$ , 0.1 M of 2-amino-terephthalic acid and 0.16 M of  $\text{CaCl}_2 \cdot \text{H}_2\text{O}$  in a mixture of DMF and  $\text{H}_2\text{O}$  (5.48:1) was injected into the coil flow reactor (Pyrex tube, inner diameter: 3 mm) at a feed rate of  $2.4 \text{ mL min}^{-1}$  and at a  $T_1$  of  $115 \text{ }^\circ\text{C}$ . The resulting pre-heated solution was then spray-dried at a  $T_2$  of  $180 \text{ }^\circ\text{C}$  and a flow rate of  $336 \text{ mL min}^{-1}$  using a Dryer B-290 Mini Spray (BUCHI Labortechnik; spray cap: 0.5-mm-hole), collecting a yellow solid.

## 5.5 References

- (1) Tatsidjodoung, P.; Le Pierrès, N.; Luo, L. *Renewable Sustainable Energy Rev.* **2013**, *18*, 327.
- (2) Canivet, J.; Fateeva, A.; Guo, Y.; Coasne, B.; Farrusseng, D. *Chem. Soc. Rev.* **2014**, *43*, 5594.
- (3) Gordeeva, L. G.; Solovyeva, M. V.; Aristov, Y. I. *Energy* **2016**, *100*, 18.
- (4) Narayanan, S.; Li, X.; Yang, S.; Kim, H.; Umans, A.; McKay, I. S.; Wang, E. N. *Appl. Energy* **2015**, *149*, 104.
- (5) Henninger, S. K.; Schmidt, F. P.; Henning, H. M. *Appl. Therm. Eng.* **2010**, *30*, 1692.
- (6) Gordeeva, L. G.; Aristov, Y. I. *Int. J. Low-Carbon Tech.* **2012**, *7*, 288;
- (7) Demir, H.; Mobedi, M.; Ülkü, S. *Renewable Sustainable Energy Rev.* **2008**, *12*, 2381.
- (8) Aristov, Y. I. *Appl. Therm. Eng.* **2013**, *50*, 1610.
- (9) Zhang, X. J.; Qiu, L. M. *Energy Convers. Manage.* **2007**, *48*, 320.
- (10) Yuan, Y.; Zhang, H.; Yang, F.; Zhang, N.; Cao, X. *Renewable Sustainable Energy Rev.* **2016**, *54*, 761.
- (11) Tashiro, Y.; Kubo, M.; Katsumi, Y.; Meguro, T.; Komeya, K. *J. Mater. Sci.* **2004**, *39*, 1315.
- (12) Meunier, F. *Appl. Therm. Eng.* **2013**, *61*, 830.
- (13) Bonaccorsi, L.; Calabrese, L.; Freni, A.; Proverbio, E.; Restuccia, G. *Appl. Therm. Eng.* **2013**, *50*, 1590.
- (14) Wang, W.; Wu, L.; Li, Z.; Fang, Y.; Ding, J.; Xiao, J. *Drying Technol.* **2013**, *31*, 1334.
- (15) Wei, X.; Wang, W.; Xiao, J.; Zhang, L.; Chen, H.; Ding, J. *Chem. Eng. J.* **2013**, *228*, 1133.
- (16) Wang, L.; Zhu, D.; Tan, Y. *Adsorption* **1999**, *5*, 279.
- (17) Szarzynski, S.; Feng, Y.; Pons, M. *Int. J. Refrig.* **1997**, *20*, 390.
- (18) Furukawa, H.; Ko, N.; Go, Y. B.; Aratani, N.; Choi, S. B.; Choi, E.; Yazaydin, A. Ö.; Snurr, R. Q.; O’Keeffe, M.; Kim, J.; Yaghi, O. M. *Science* **2010**, *329*, 424.
- (19) Seo, Y.-K.; Yoon, J. W.; Lee, J. S.; Lee, U. H.; Hwang, Y. K.; Jun, C.-H.; Horcajada, P.; Serre, C.; Chang, J.-S. *Microporous Mesoporous Mater.* **2012**, *157*, 137.
- (20) Ehrenmann, J.; Henninger, S. K.; Janiak, C. *Eur. J. Inorg. Chem.* **2011**, *2011*, 471.
- (21) Khutia, A.; Rammelberg, H. U.; Schmidt, T.; Henninger, S.; Janiak, C. *Chem. Mater.* **2013**, *25*, 790.
- (22) de Lange, M. F.; Verouden, K. J. F. M.; Vlugt, T. J. H.; Gascon, J.; Kapteijn, F. *Chem. Rev.* **2015**, *115*, 12205.
- (23) Cadiou, A.; Lee, J. S.; Damasceno Borges, D.; Fabry, P.; Devic, T.; Wharmby, M. T.; Martineau, C.; Foucher, D.; Taulelle, F.; Jun, C.-H.; Hwang, Y. K.; Stock, N.; De Lange, M. F.; Kapteijn, F.; Gascon, J.; Maurin, G.; Chang, J.-S.; Serre, C. *Adv. Mater.* **2015**, *27*, 4775.

- (24) Mallick, A.; Kundu, T.; Banerjee, R. *Chem. Commun.* **2012**, *48*, 8829.
- (25) Sahoo, S. C.; Kundu, T.; Banerjee, R. *J. Am. Chem. Soc.* **2011**, *133*, 17950.
- (26) Colodrero, R. M. P.; Olivera-Pastor, P.; Losilla, E. R.; Hernández-Alonso, D.; Aranda, M. A. G.; Leon-Reina, L.; Rius, J.; Demadis, K. D.; Moreau, B.; Villemin, D.; Palomino, M.; Rey, F.; Cabeza, A. *Inorg. Chem.* **2012**, *51*, 7689.
- (27) Guo, P.; Wong-Foy, A. G.; Matzger, A. J. *Langmuir* **2014**, *30*, 1921.
- (28) Furukawa, H.; Gandara, F.; Zhang, Y. B.; Jiang, J.; Queen, W. L.; Hudson, M. R.; Yaghi, O. M. *J. Am. Chem. Soc.* **2014**, *136*, 4369.
- (29) Yan, J.; Yu, Y.; Ma, C.; Xiao, J.; Xia, Q.; Li, Y.; Li, Z. *Appl. Therm. Eng.* **2015**, *84*, 118.
- (30) Carné-Sánchez, A.; Imaz, I.; Cano-Sarabia, M.; Maspoch, D. *Nat Chem* **2013**, *5*, 203.
- (31) Garzon-Tovar, L.; Cano-Sarabia, M.; Carne-Sanchez, A.; Carbonell, C.; Imaz, I.; Maspoch, D. *React. Chem. Eng.* **2016**, *1*, 533.
- (32) Kim, M.; Cohen, S. M. *CrystEngComm* **2012**, *14*, 4096.
- (33) Glaznev, I.; Ponomarenko, I.; Kirik, S.; Aristov, Y. *Int. J. Refrig.* 2011, *34*, 1244.
- (34) Aristov, Y. I.; Restuccia, G.; Cacciola, G.; Parmon, V. N. *Appl. Therm. Eng.* **2002**, *22*, 191.
- (35) Nam, Y. S.; Enright, R.; Maroo, S.; Wang, E. N.; Narayanan, S.; McKay, I. S. US, **2013**; Vol. 20130192281 A1.
- (36) Rouquerol, J.; Rouquerol, F.; Llewellyn, P.; Maurin, G.; Sing, K. S. W. *Adsorption by Powders and Porous Solids: Principles, Methodology and Applications*; Elsevier Science, **2013**.
- (37) Aristov, Y. I.; Tokarev, M. M.; Cacciola, G.; Restuccia, G. *React. Kinet. Catal. Lett.* **1996**, *59*, 325.
- (38) Advanced Research Projects Agency-DOE, HEATS Program Overview, [https://arpa-e.energy.gov/sites/default/files/documents/files/HEATS\\_ProgramOverview.pdf](https://arpa-e.energy.gov/sites/default/files/documents/files/HEATS_ProgramOverview.pdf), October 27, 2016.
- (39) Shi, B.; Al-Dadah, R.; Mahmoud, S.; Elsayed, A.; Elsayed, E. *Appl. Therm. Eng.* **2016**, *106*, 325.
- (40) de Lange, M. F.; van Velzen, B. L.; Ottevanger, C. P.; Verouden, K. J. F. M.; Lin, L.-C.; Vlugt, T. J. H.; Gascon, J.; Kapteijn, F. *Langmuir* **2015**, *31*, 12783.
- (41) Wang, D. C.; Xia, Z. Z.; Wu, J. Y.; Wang, R. Z.; Zhai, H.; Dou, W. D. *Int. J. Refrig.* **2005**, *28*, 1073.
- (42) Tso, C. Y.; Chao, C. Y. H. *Int. J. Refrig.* **2012**, *35*, 1626.
- (43) Zhang, L. Z. *Appl. Therm. Eng.* **2000**, *20*, 103.
- (44) Vasta, S.; Freni, A.; Sapienza, A.; Costa, F.; Restuccia, G. *Int. J. Refrig.* **2012**, *35*, 701.
- (45) Freni, A.; Sapienza, A.; Glaznev, I. S.; Aristov, Y. I.; Restuccia, G. *Int. J. Refrig.* **2012**, *35*, 518.
- (46) Sapienza, A.; Glaznev, I. S.; Santamaria, S.; Freni, A.; Aristov, Y. I. *Appl. Therm. Eng.* **2012**, *32*, 141.



# Chapter 6

---

## Spray-Drying for making Covalent Chemistry: Post-Synthetic Modification of Metal-Organic Frameworks

This Chapter is based on the following publication:

---

Garzón-Tovar, L.; Rodríguez-Hermida, S.; Imaz, I.; Maspoch, D. *J. Am. Chem. Soc.* **2017**, *139*, 897.

---



## 6.1 Introduction

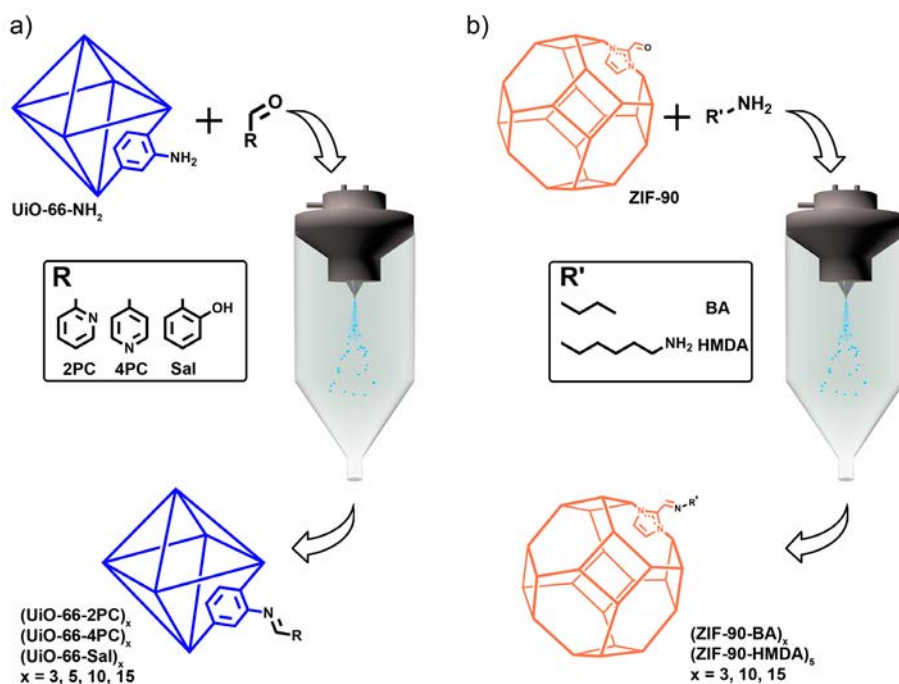
Metal-organic frameworks (MOFs), also known as porous coordination polymers (PCPs), have attracted much attention over the past decades due to their potential applications, such as in gas sorption and storage, catalysis, drug delivery and gas separation.<sup>1-3</sup> One of the main characteristics of MOFs is the ability to tailor their chemical functionality and/or pore surface chemistry, either by pre- or post-synthetic modification of the organic linker. Covalent post-synthetic modification (PSM) involves an organic reaction carried out on the organic linker while maintaining the MOF integrity.<sup>4,5</sup>

To date, there are many studies based on the PSM of MOFs involving linkers with different functional groups.<sup>6-9</sup> Among them, the most common reaction involves a Schiff-base condensation between an amine and an aldehyde to form an imine *via* water elimination. Using this chemistry, PSM of the 2-aminoterephthalate (NH<sub>2</sub>-bdc) linker of UiO-66-NH<sub>2</sub> has been widely studied.<sup>10-16</sup> For example, Lu *et al.* showed the successful PSM of UiO-66-NH<sub>2</sub> with salicylaldehyde (Sal) by heating a mixture of both species in acetonitrile at 40 °C for three days. Once functionalized, they further immobilized Cu(II) salts on the incorporated imine moiety, and used the resulting framework as an efficient catalyst for the aerobic oxidation of alcohols.<sup>10</sup> A similar strategy was also followed to synthesize efficient catalysts for the epoxidation of olefins, the hydrogenation of aromatics, and the reductive amination of aldehydes.<sup>11,12,13</sup> In these cases, UiO-66-NH<sub>2</sub> was post-synthetically modified with Sal, 2-pyridinecarboxylaldehyde, 4-pyridinecarboxylaldehyde, and 6-((diisopropylamino)methyl)picolinaldehyde followed by the immobilization of Mo(VI) and Ir(I). Also, other amino-terminated MOFs such as IRMOF-3 and Cr-MIL-101-NH<sub>2</sub> have been used for the development of efficient catalysts. Here, both MOFs were first reacted with pyridine-based aldehydes and then with Cu(I) and Co(II) salts to create heterogeneous catalysts for the synthesis of different 2-aminobenzothiazoles and the aerobic epoxidation of olefins, respectively.<sup>14,15</sup>

Yaghi *et al.* also reported the use of the Schiff-base condensation reaction to post-synthetically functionalize aldehyde-terminated MOFs. They reacted ZIF-90 with ethanolamine yielding the imine-derivative non-porous ZIF-92.<sup>17</sup> Following the same type of chemistry, ZIF-90 was recently labelled with an Alexa Fluor dye,<sup>18</sup> whereas a mixed ZIF-8-90 sample was post-functionalized with ethylenediamine. This latter PSM allowed the introduction of an aliphatic amine-terminated group to ZIF-8-90, enhancing its CO<sub>2</sub> sorption capacity.<sup>19</sup> In a more recent study, a superhydrophobic ZIF-90 exhibiting a water contact angle value of around 152° was prepared by reacting it with a polyfluorinated amine.<sup>20</sup>

In general, the synthetic conditions for the PSM of MOFs require long reaction times (from 1 to 3 days) and high temperatures. To overcome these limitations, some advances have been done on developing alternative methods for the PSM of MOFs. One of them is based on the PSM of IRMOF-3 and UiO-66-NH<sub>2</sub> by vapour diffusion.<sup>21</sup> This method allowed the PSM of both MOFs with high conversion rates after heating the solvent-free MOFs with the corresponding aldehyde at 100-120 °C using a vacuum system for 16 h.

As illustrated in **Chapter 3**, it has been demonstrated that the spray drying (SD) technique is a useful, continuous and scalable method to assemble metal ions and organic ligands to synthesize MOFs.<sup>22,23</sup> This method allowed the reaction times to be drastically reduced down to the second regime, without affecting the properties of the SD-synthesized MOFs. It also enables obtaining them in the form of dried powders and to recycle the solvent used during the fabrication. Here, we extended the use of SD to covalent organic reactions based on the Schiff-base condensation reaction aiming to be able to post-synthetically modify MOF crystals. UiO-66-NH<sub>2</sub> and ZIF-90 were selected as the target MOFs due to the uncoordinated and available amine and aldehyde groups within their structures, respectively (Scheme 6.1).

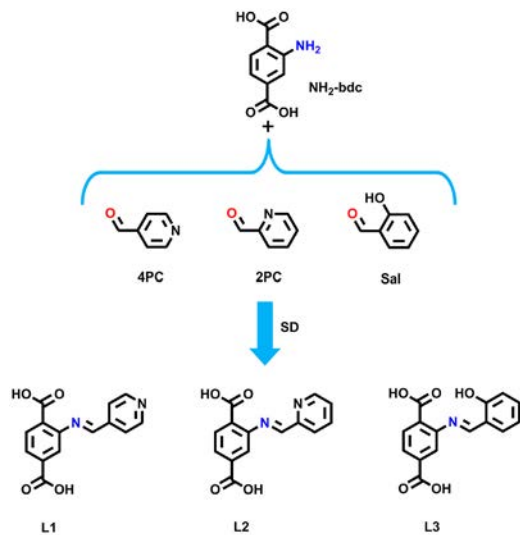


*Scheme 6.1.* Illustration of the covalent PSM performed in (a) UiO-66-NH<sub>2</sub> and (b) ZIF-90 under spray-drying conditions.

## 6.2 Results and Discussion

### 6.2.1 Organic Schiff-base condensation reactions conducted via spray-drying

To demonstrate that organic reactions and, in particular, Schiff-base condensation reactions between aldehydes and amines could be performed using the SD technique, we initially tested the formation of **2-((pyridin-4-ylmethylene)amino)terephthalic acid** using NH<sub>2</sub>-bdc and 4-pyridinecarboxylaldehyde (4PC) as reactants (Scheme 6.2).



*Scheme 6.2. Imine molecules synthesized via SD.*

This synthesis started with the mixture of  $\text{NH}_2\text{-bdc}$  and 4PC in ethanol (15 mL) at room temperature. The  $\text{NH}_2\text{-bdc}$ :4PC molar ratio was systematically changed from 1:1, 1:2 and 1:3. Each suspension was then spray-dried at a feed rate of  $3.0 \text{ mL min}^{-1}$  and an inlet temperature of  $130 \text{ }^\circ\text{C}$ , using a Mini Spray Dryer B-290. This inlet temperature was selected to ensure the evaporation of ethanol as well as to force the evaporation of the water formed during the Schiff-base condensation reaction. For each reaction, a yellow powder was collected after 5 min.  $^1\text{H-NMR}$  spectra of all collected powders confirmed the imine formation by the appearance of a peak at 8.17 ppm corresponding to the imine proton (Figure 6.1a). The synthesis of **2-((pyridin-4-ylmethylene)amino)terephthalic acid** was further corroborated by  $^{13}\text{C-NMR}$  (peak corresponding to the carbon atom of the  $\text{CH=N}$  imine group at 163 ppm; Figure 6.1b) and ESI-MS (calculated for  $[\text{M}-\text{H}]^-$   $[\text{C}_{14}\text{H}_9\text{N}_2\text{O}_4]^-$ :  $m/z = 269.0568$ ; found  $m/z = 269.0566$ ; Figure 6.1c). We finally determined the conversion rate of each reaction by comparing the integration of the peaks at 8.17 ppm (imine proton) and at 7.02 ppm (aromatic proton of the unreacted  $\text{NH}_2\text{-bdc}$ ). The conversion rates were 37 %, 84 % and 92 % for the  $\text{NH}_2\text{-bdc}$ :4PC molar ratios of 1:1, 1:2 and 1:3, respectively.

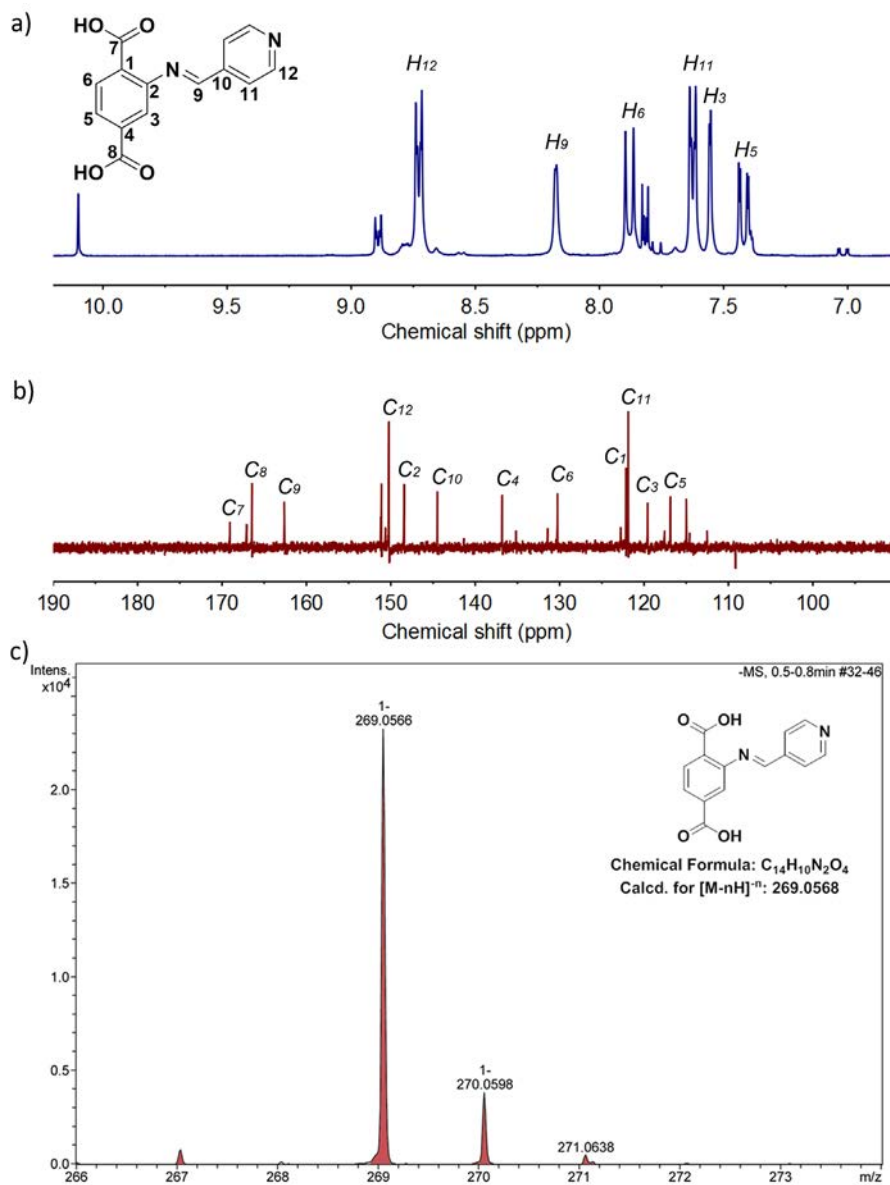


**Figure 6.1.** (a)  $^1\text{H-NMR}$  and (b)  $^{13}\text{C-NMR}$  spectra, collected in  $\text{DMSO-d}_6$ , of **2-((pyridin-4-ylmethylene)amino)terephthalic acid** synthesized using a  $\text{NH}_2\text{-bdc}:\text{4PC}$  molar ratio of 1:3. Only the peaks corresponding to the imine molecule are shown. (c) ESI-MS spectrum of **2-((pyridin-4-ylmethylene)amino)terephthalic acid**.

We then extended the spray-drying synthesis to two other imine compounds (Scheme 6.2). The syntheses were done using the same conditions as those for **2-((pyridin-4-ylmethylene)-amino)terephthalic acid**, except that, instead of 4PC, we used 2-pyridinecarboxylaldehyde (2PC; conversion rate: 87 %) and Sal (conversion rate: 75 %) in a NH<sub>2</sub>-bdc:2PC/Sal molar ratio of 1:3. In both cases, the expected imine compounds were successfully synthesized, as confirmed by <sup>1</sup>H- and <sup>13</sup>C-NMR and ESI-MS (Annex 2). The high conversion rates obtained in these Schiff-base condensation reactions are remarkable if we consider that, to the best of our knowledge, this is the first time that discrete organic molecules have been synthesized *via* spray-drying. It is well known that, in these condensation reactions, water is produced so that its removal favours the formation of imines following the Le Chatelier's principle. Since spray-drying is based on the fast evaporation of the liquid, we reason that water can be rapidly removed from the atomized droplets during the Schiff-base reaction, thereby favouring the formation of the imine bond.

### 6.2.2 PSM of UiO-66-NH<sub>2</sub>

Once we proved the spray-drying synthesis of imine compounds *via* Schiff-base condensation, we then transferred the same type of chemistry to MOF crystals. For this, we selected UiO-66-NH<sub>2</sub> as the first test case scenario because the amino groups of the NH<sub>2</sub>-bdc linkers are pointing into the pores, and of its high chemical and thermal stability.

A series of ethanolic colloidal suspensions (15 mL) containing UiO-66-NH<sub>2</sub> [synthesized under solvothermal conditions; particle size = 245 ± 65 nm; obtained as pure phase as confirmed by X-ray powder diffraction (XRPD), scanning electron microscopy (SEM), N<sub>2</sub> sorption isotherm ( $S_{\text{BET}} = 914 \text{ m}^2 \text{ g}^{-1}$ ) and <sup>13</sup>C MAS-NMR; see Figure 6.2] and the aldehydes 4PC, 2PC and Sal were initially prepared at molar ratios of NH<sub>2</sub>-bdc:aldehyde corresponding to 1:3, 1:5, 1:10 and 1:15.

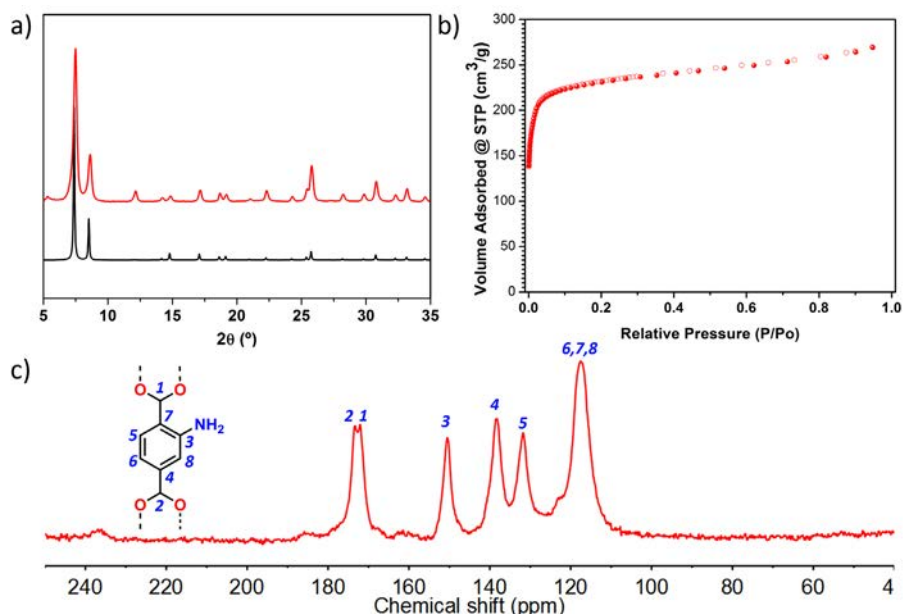


**Figure 6.2.** (a) Simulated (black) and synthesized (red) XRPD patterns of UiO-66-NH<sub>2</sub>. (b) N<sub>2</sub> adsorption isotherm of synthesized UiO-66-NH<sub>2</sub>. (c) <sup>13</sup>C MAS-NMR spectrum of UiO-66-NH<sub>2</sub>.

Each suspension was then spray-dried under the same conditions as those for the pure condensation spray-drying reactions. Once the suspensions had atomized, the different yellow powders were collected from the spray dryer collector, cleaned with ethanol four times and once with acetone, and finally dried at 85 °C for 12 h. The different samples were named as **(UiO-66-4PC)<sub>x</sub>**, **(UiO-66-2PC)<sub>x</sub>** and **(UiO-66-Sal)<sub>x</sub>** (where *x* is 3, 5, 10 and 15, depending on the equivalents of aldehyde used). Field-emission scanning electron microscopy (FESEM) of all dried powders revealed that initial size and morphology of the parent UiO-66-NH<sub>2</sub> crystals did not change during the SD process (Figure 6.3a-c). XRPD indicated that all crystalline powders retain the crystallinity of the parent UiO-66-NH<sub>2</sub> MOF (Figures 6.3d-f).

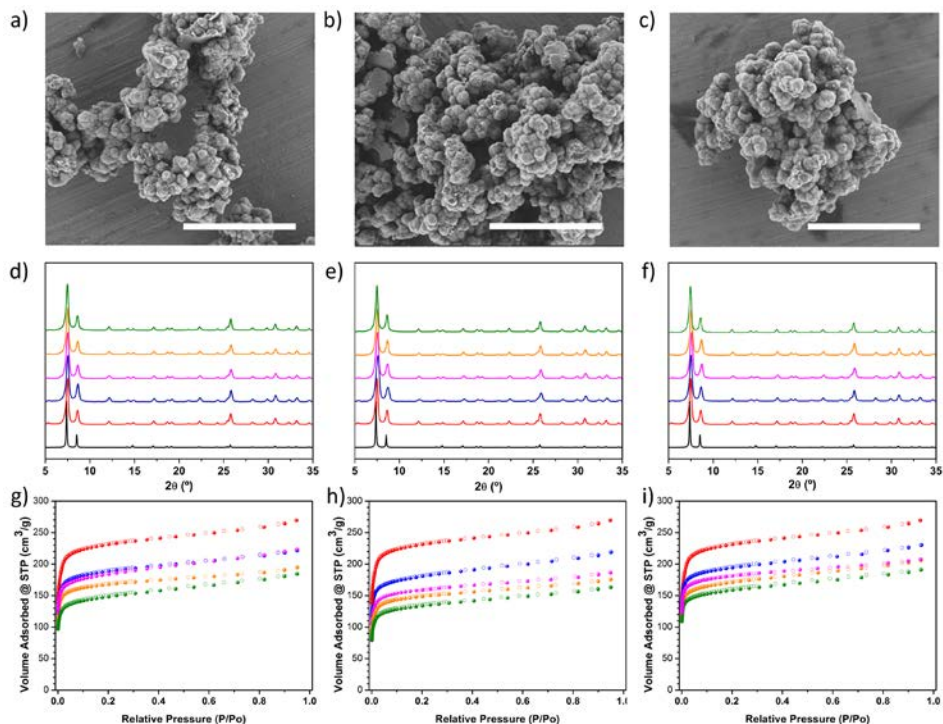


**Figure 6.3.** FESEM images of (a)  $(\text{UiO-66-4PC})_{15}$ , (b)  $(\text{UiO-66-2PC})_{15}$  and (c)  $(\text{UiO-66-Sal})_{15}$ . Scale bars: 5  $\mu\text{m}$ . XRPD patterns of (d)  $(\text{UiO-66-4PC})_x$ , (e)  $(\text{UiO-66-2PC})_x$ , and (f)  $(\text{UiO-66-Sal})_x$  in comparison to the activated  $\text{UiO-66-NH}_2$  (red) and the simulated powder pattern of  $\text{UiO-66}$  (black).  $\text{N}_2$  sorption isotherms of (g)  $(\text{UiO-66-2PC})_x$ , (h)  $(\text{UiO-66-4PC})_x$ , and (i)  $(\text{UiO-66-Sal})_x$  synthesized with different equivalents of aldehyde. For comparison,  $\text{N}_2$  sorption isotherms of activated  $\text{UiO-66-NH}_2$  (red) are also included. Colour code: Blue:  $x = 3$ ; Pink:  $x = 5$ ; Orange:  $x = 10$ ; Green:  $x = 15$ ,

To confirm the PSM of  $\text{UiO-66-NH}_2$  with the different aldehydes, we first performed  $^{13}\text{C}$  MAS-NMR on  $(\text{UiO-66-2PC})_{15}$ ,  $(\text{UiO-66-4PC})_{15}$  and  $(\text{UiO-66-Sal})_{15}$  (Figure 6.4). All spectra showed the appearance of a new signal centred at 160-161 ppm, which was attributed to the carbon atom of the  $\text{CH=N}$  imine group. This peak is consistent with the one observed at 160-162 ppm in the  $^{13}\text{C}$ -NMR spectra of the imine compounds previously synthesized *via* spray-drying. It is also in agreement with the  $^{13}\text{C}$  MAS-NMR signal associated to the imine carbon in other reported post-functionalized  $\text{UiO-66s}$ .<sup>11,12</sup>

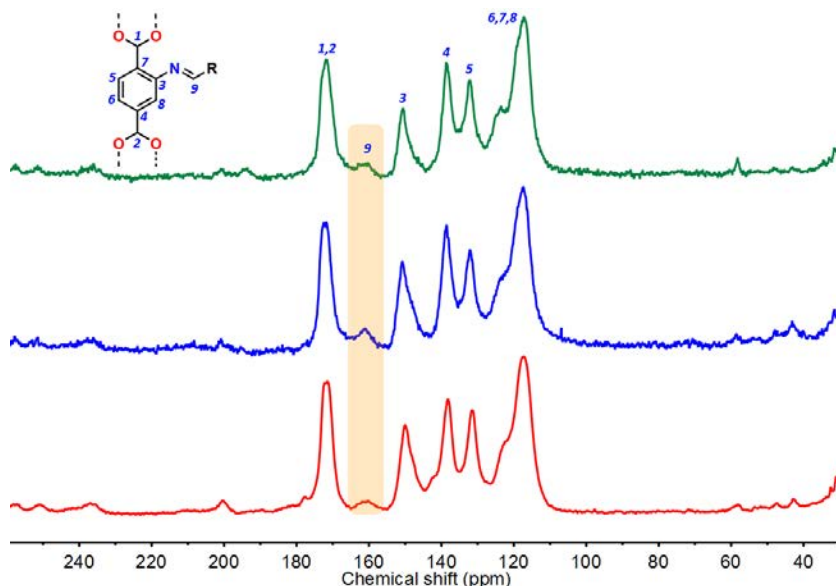


**Figure 6.4.**  $^{13}\text{C}$  MAS-NMR spectra of  $(\text{UiO-66-4PC})_{15}$  (red),  $(\text{UiO-66-2PC})_{15}$  (blue) and  $(\text{UiO-66-Sal})_{15}$  (green). The signal of CH=N imine group is highlighted.

The degree of post-synthetic conversion was analysed by first digesting the samples and then analysing the resulting solutions by  $^1\text{H-NMR}$ . From the digestion under acidic conditions, the MOF framework is destroyed and the released imine molecules are hydrolysed forming the  $\text{NH}_2\text{-bdc}$  and the corresponding aldehyde. We then calculated the conversion rate by comparison of the integration of one peak at 7.36 ppm corresponding to  $\text{NH}_2\text{-bdc}$  and those peaks at 7.98, 8.52 and 7.52 ppm corresponding to 4PC, 2PC and Sal, respectively (Figures 6.5, also see Annex 2). Also note here that all samples were previously washed three times with ethanol and acetone, and then dried at 85 °C overnight before their digestion. This activation process ensures the removal of all nonreacted aldehyde molecules adsorbed in the pores of the MOFs during the spray-drying process, as confirmed by FT-IR (Figures 6.5). Table 6.1 lists the degrees of conversion calculated for all synthesized samples. From this data, it was clear that the degree of conversion increases while increasing the equivalents of aldehyde used in the reaction.

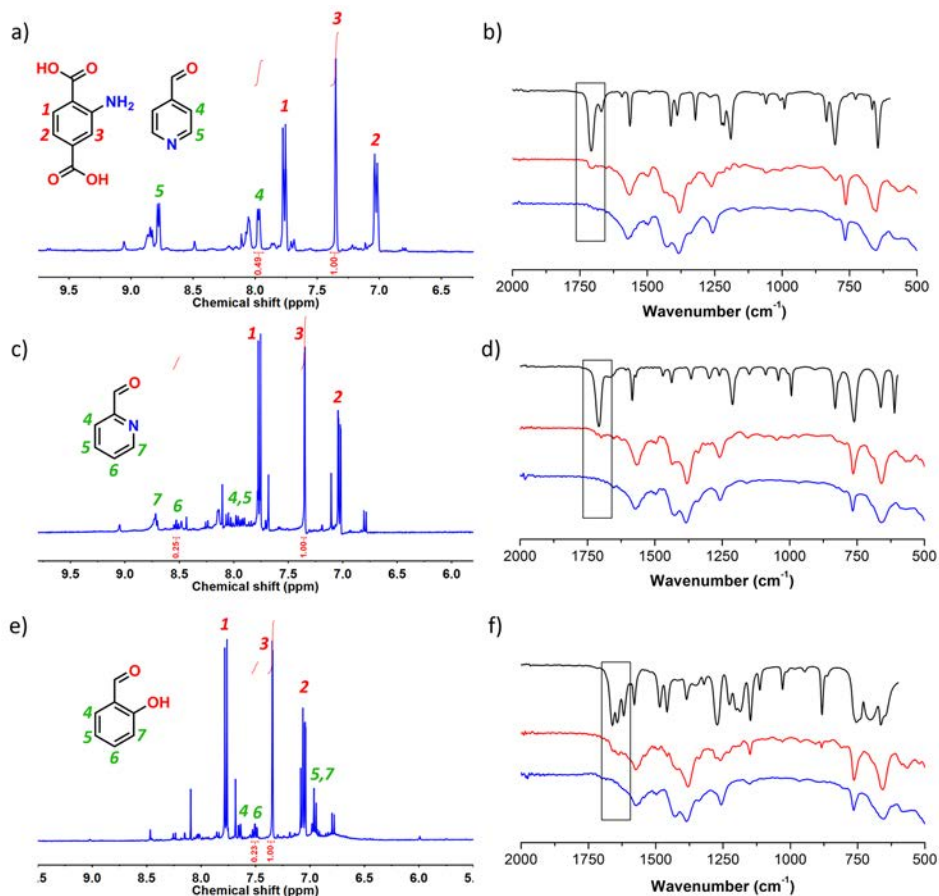


**Figure 6.5.**  $^1\text{H}$  NMR spectra of the digested (a)  $(\text{UiO-66-4PC})_{15}$ , (c)  $(\text{UiO-66-2PC})_{15}$  and (e)  $(\text{UiO-66-Sal})_{15}$  in  $\text{HF}/\text{DMSO-}d_6$ . FT-IR spectra of (b)  $(\text{UiO-66-4PC})_{15}$ , (d)  $(\text{UiO-66-2PC})_{15}$  and (f)  $(\text{UiO-66-Sal})_{15}$  before (red) and after (blue) activation, in comparison to the spectrum of 4PC, 2PC and Sal (black), respectively. The region of the band corresponding to the  $\text{C}=\text{O}$  stretch of the aldehyde is highlighted.

For example, the degree of conversion increased from 13 % to 20 % between  $(\text{UiO-66-2PC})_3$  and  $(\text{UiO-66-2PC})_{15}$ . It is important to highlight here that the degree of conversion achieved by SD are higher than the ones reported for the PSM of  $\text{UiO-66-NH}_2$  with the same aromatic aldehydes.<sup>10,13</sup> The only exception was the conversion rate of 29 % reported by Bokhoven and co-workers for the formation of  $(\text{UiO-66-Sal})$  via the vapour-phase method.<sup>21</sup> However, this latter method is a non-continuous method, which requires vacuum and 16 h to achieve this conversion rate.

N<sub>2</sub> adsorption isotherms were finally measured at 77 K on all activated samples that were further degassed at 200 °C for 12 h under vacuum. We found that the surface area and pore volumes decreased for the samples showing a higher degree of conversion (Table 6.1, Figures 6.3g-i). We attributed this trend to the fact that the new imine moieties grafted on the pores are bulkier than the amino group.

**Table 6.1.** BET areas, pore volumes and % of conversion of UiO-66-NH<sub>2</sub>, (UiO-66-2PC)<sub>x</sub>, (UiO-66-4PC)<sub>x</sub> and (UiO-66-Sal)<sub>x</sub>.

MOF	<i>x</i>	S <sub>BET</sub> (m <sup>2</sup> g <sup>-1</sup> )	Pore vol. (cm <sup>3</sup> g <sup>-1</sup> ) <sup>a</sup>	Conversion (%) <sup>b</sup>
UiO-66-NH <sub>2</sub>	--	914	0.3729	--
(UiO-66-2PC) <sub>x</sub>	3	699	0.2954	13
	5	625	0.2576	16
	10	586	0.2412	17
	15	516	0.2190	20
(UiO-66-4PC) <sub>x</sub>	3	736	0.3056	9
	5	712	0.3015	16
	10	621	0.2652	18
	15	573	0.2441	20
(UiO-66-Sal) <sub>x</sub>	3	761	0.3151	11
	5	709	0.2923	14
	10	665	0.2789	16
	15	616	0.2587	19

<sup>a</sup> Calculated at P/P0 ≈ 0.4. <sup>b</sup> Calculated from <sup>1</sup>H-NMR spectra of the digested samples.

### 6.2.3 PSM of ZIF-90.

To explore the versatility of the PSM *via* spray-drying, we then switched to a terminal aldehyde-containing MOF to postfunctionalize it with amine molecules. To this end, we selected ZIF-90 that is built up from imidazole-2-carboxaldehyde (ICA) and Zn(II) ions, giving rise to a **sod**-3D porous network showing a pore size around 11 Å and a pore size window around 3.5 Å. Following a similar synthetic procedure as for the

PSM of UiO-66-NH<sub>2</sub>, three ethanolic suspensions of ZIF-90 [synthesized at room temperature; particle size = 41 ± 9 nm; obtained as pure phase as confirmed by XRPD, SEM, N<sub>2</sub> sorption isotherm (*S*<sub>BET</sub> = 1070 m<sup>2</sup> g<sup>-1</sup>) and <sup>13</sup>C MAS-NMR; see Figure 6.6] and butylamine (BA) were initially prepared at molar ratios of ICA:BA corresponding to 1:3, 1:10 and 1:15.

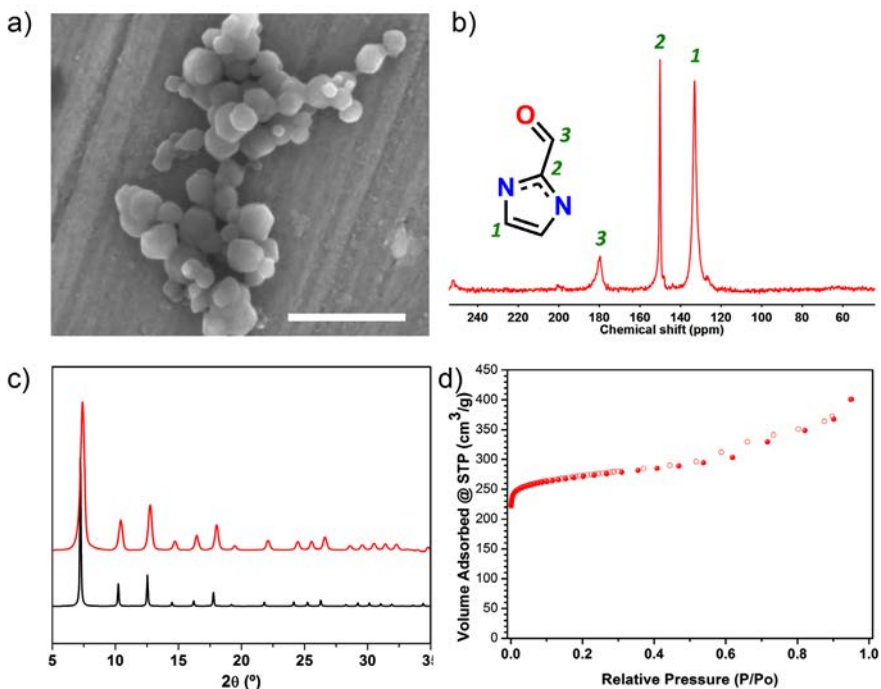


**Figure 6.6.** (a) FESEM image of ZIF-90. (b) <sup>13</sup>C MAS-NMR spectrum of ZIF-90. (c) XRPD pattern of simulated (black) and synthesized (red) ZIF-90. (d) N<sub>2</sub> adsorption isotherm of ZIF-90. Scale bars: (a) 2 μm and (b) 200 nm.

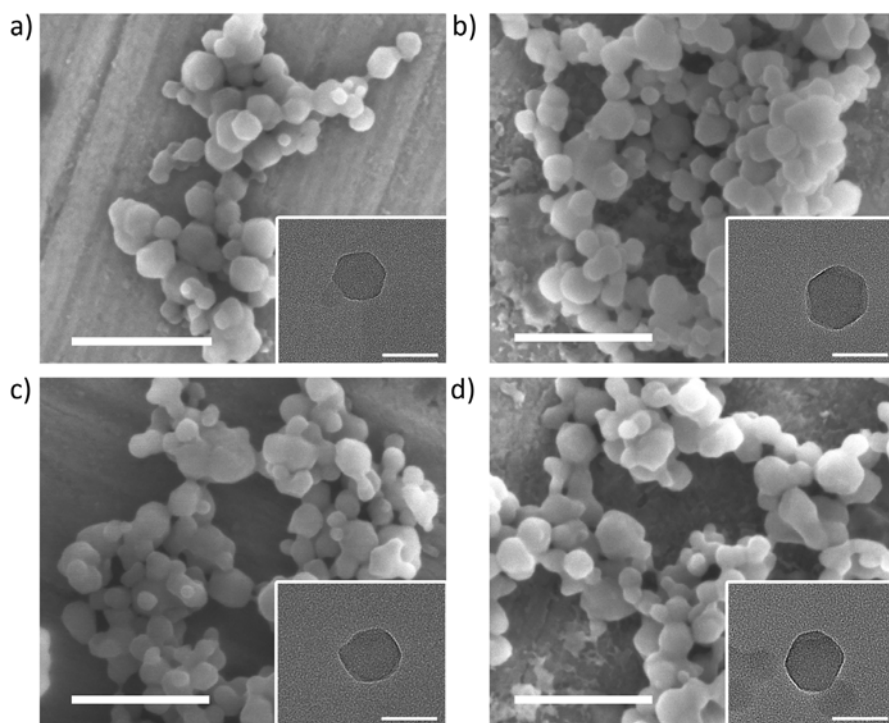


**Figure 6.7.** FESEM and TEM images of (a) ZIF-90, (b)  $(\text{ZIF-90-BA})_3$ , (c)  $(\text{ZIF-90-BA})_{10}$ , (d)  $(\text{ZIF-90-BA})_{15}$ . Scale bars: 200 nm (FESEM images) and to 50 nm (TEM images, insets).

Each suspension was then spray-dried under the same above-mentioned conditions. Once the suspensions had atomized, the different pale yellow powders were collected from the spray dryer collector, cleaned with ethanol five times and once with acetone, and finally dried at 85 °C for 12 h. Again, the resulting powders were named as  $(\text{ZIF-90-BA})_x$ , where  $x$  is the number of equivalents of BA. Similarly, FESEM and TEM revealed that initial size and morphology of the parent ZIF-90 crystals did not change during the spray-drying process (Figure 6.7), whereas XRPD indicated that all crystalline powders retain the parent **sod** structure (Figures 6.8b).

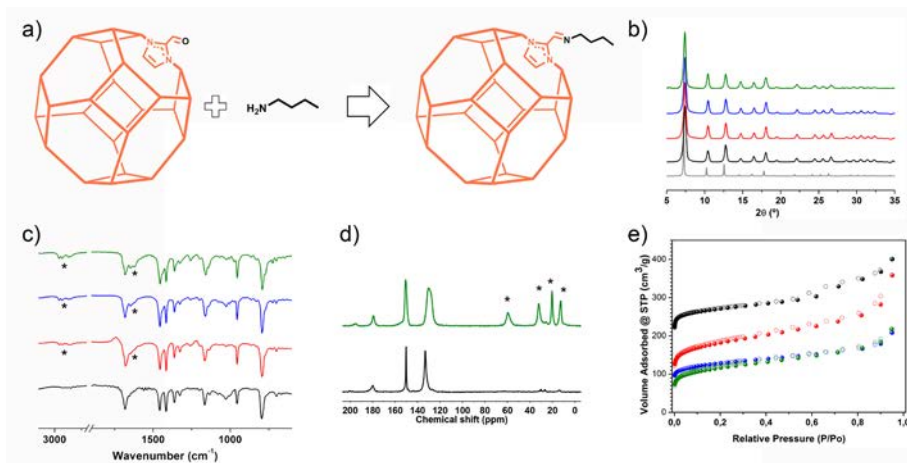


**Figure 6.8.** (a) Schematic representation of the PSM of ZIF-90 with butylamine via SD. (b) XRPD patterns of ZIF-90 and  $(\text{ZIF-90-BA})_x$ , as compared to the simulated powder pattern for the crystal structure of ZIF-90 (grey). (c) IR spectra of ZIF-90 and  $(\text{ZIF-90-BA})_x$ , highlighting the aliphatic C-H and imine C=N vibrational bands with an asterisk (\*). (d)  $^{13}\text{C}$  MAS-NMR spectra of ZIF-90 and  $(\text{ZIF-90-BA})_{15}$ , where the peaks corresponding to the butyl chains are highlighted with an asterisk (\*). (e)  $\text{N}_2$  sorption isotherms at 77 K of ZIF-90 and  $(\text{ZIF-90-BA})_x$ . In b-e), ZIF-90 (black),  $(\text{ZIF-90-BA})_3$  (red),  $(\text{ZIF-90-BA})_{10}$  (blue), and  $(\text{ZIF-90-BA})_{15}$  (green).

In this case, the formation of imidazol-2-butylmethanimine (IBI) was initially confirmed by FT-IR spectroscopy. Two sets of new bands appeared in the IR spectra of the post-synthetic functionalized ZIF-90 (Figure 6.8c): 1) the band corresponding to the C=N group, centered at  $\approx 1644\text{ cm}^{-1}$ , whose intensity increased as the equivalents of BA were increased; and 2) the aliphatic C-H stretching of the butyl moiety within the  $3000\text{-}2700\text{ cm}^{-1}$  range. Moreover, no band corresponding to  $-\text{NH}_2$  was observed, indicating that there was not unreacted BA inside the pores of ZIF-90. The formation of IBI was further corroborated by the peaks observed in the  $^{13}\text{C}$  MAS-NMR spectra at 59, 32, 20 and 13 ppm, which were all attributed to the butyl chain (Figure 6.8d). The peak at 59 ppm was assigned to the methylene group bonded to imine nitrogen. Moreover, the signal of the aldehyde group was observed at 195 ppm, indicating that not all carbonyl groups were reacted. Finally, the formation of IBI was undoubtedly confirmed by identifying it in the solution resulting from dissolving all  $(\text{ZIF-90-BA})$  samples using acetic acid.

Indeed,  $^1\text{H-NMR}$  spectra showed peaks at 8.55 and 3.82 ppm that were attributed to the  $\text{CH}=\text{N}$  imine proton and the  $\text{N}-\text{CH}_2$  methylene protons of IBI, respectively. On the other hand, the peak at  $m/z = 152.1180$  in the ESI-MS spectra, matches with the molecular formula of the protonated IBI  $[\text{C}_8\text{H}_{13}\text{N}_3]^+$  ( $m/z = 152.1182$ ). Note here that, under these conditions, IBI was also partially hydrolyzed (Figure 6.9a, also see Annex 2).

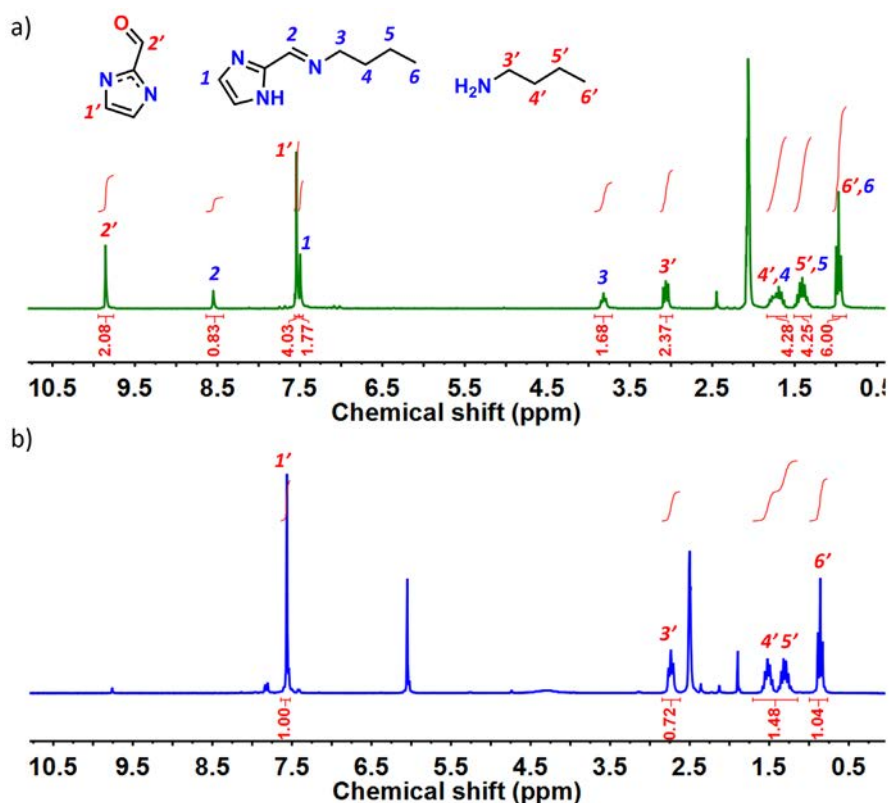


**Figure 6.9.** (a)  $^1\text{H-NMR}$  spectrum of the digested  $(\text{ZIF-90-BA})_{15}$  in  $\text{CD}_3\text{CO}_2\text{D}$ . (b)  $^1\text{H-NMR}$  spectrum of the digested sample  $(\text{ZIF-90-BA})_{15}$  in  $\text{DCl}/\text{DMSO-}d_6$ .

In order to quantify the conversion rate,  $^1\text{H-NMR}$  spectra of the digested samples in  $\text{DCl}$ ,  $\text{DMSO-}d_6$  were collected (Figure 6.9b, see also Annex 2). Under these stronger acidic conditions, ZIF-90 is dissolved and the released IBI is completely hydrolyzed forming ICA and BA. Thus, the degree of conversion was measured by

comparison of the integration of the peaks at 7.57 and 0.86 ppm corresponding to ICA and BA, respectively. We found that the conversion rates were 25 % for **(ZIF-90-BA)<sub>3</sub>**, 32 % for **(ZIF-90-BA)<sub>10</sub>** and 42 % for and **(ZIF-90-BA)<sub>15</sub>**.

These results were consistent with the gradual decrease of the  $S_{\text{BET}}$  values (determined by the  $\text{N}_2$ -sorption isotherms at 77 K) as the conversion rate (introduction of more bulky butyl chains) was also increased (Figures 6.8e). The calculated  $S_{\text{BET}}$  were 670, 483 and 424  $\text{m}^2 \text{g}^{-1}$  for **(ZIF-90-BA)<sub>3</sub>**, **(ZIF-90-BA)<sub>10</sub>**, and **(ZIF-90-BA)<sub>15</sub>**, respectively. These values corresponded to a loss of 39 %, 45 % and 63 % of the  $S_{\text{BET}}$  of the parent ZIF-90.

Previous studies have shown that the introduction of alkyl chains in the pore surfaces of a MOF increases its hydrophobicity.<sup>24,25</sup> We therefore studied the surface wettability of all post-functionalized ZIF-90 samples by measuring the contact angle ( $\Theta_c$ ) on pressed pellet disks of ZIF-90, **(ZIF-90-BA)<sub>3</sub>**, **(ZIF-90-BA)<sub>10</sub>**, and **(ZIF-90-BA)<sub>15</sub>**. The  $\Theta_c$  in each case was 90.4°, 93.3°, 96.1° and 99.3°, respectively-confirming an increase in the hydrophobicity when the conversion rate increases (Figure 6.10).

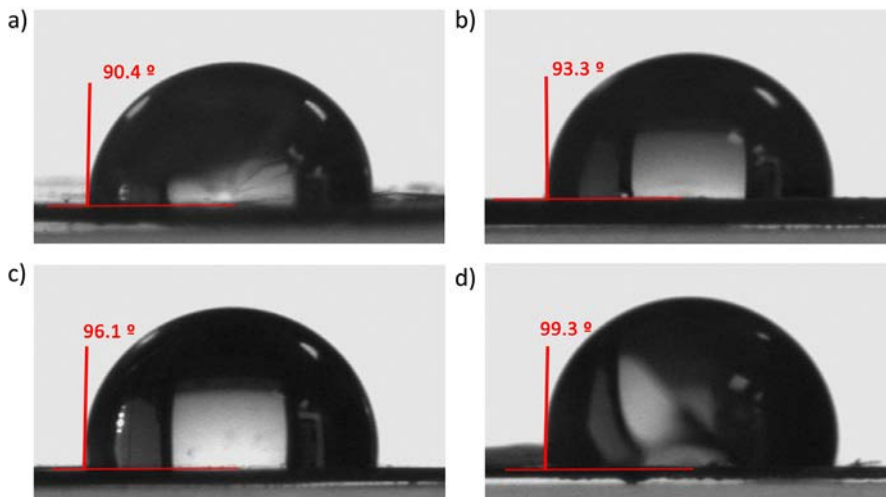


**Figure 6.10.** Contact angle measurements on pressed pellet disks of: (a) ZIF-90, (b) **(ZIF-90-BA)<sub>3</sub>**, (c) **(ZIF-90-BA)<sub>10</sub>** and (d) **(ZIF-90-BA)<sub>15</sub>**.

Finally, the effect of the particle size on this spray-drying solid/liquid reaction was studied. To this end, a suspension containing larger ZIF-90 crystals (particle size:  $18 \pm 9 \mu\text{m}$ , Figure 6.11) and ICA (using ICA:BA 1:15 molar ratio) were spray-dried under the same experimental conditions as described above, *vide supra*. Here, a conversion rate of 22 % was determined by analyzing the  $^1\text{H}$ -NMR spectra of the digested sample (Figure 6.11c). This value is lower than the one obtained when ZIF-90 nanoparticles were used (42 %), and it is comparable to other conversion rates found in aldehyde-terminated ZIF particles of similar size.<sup>25,26</sup>

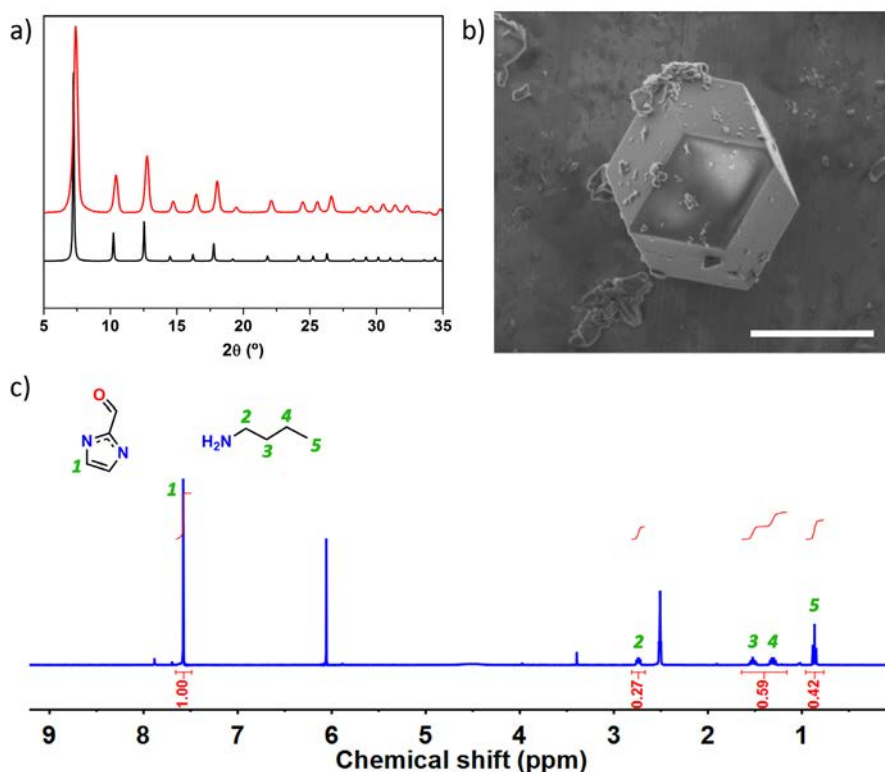


**Figure 6.11.** (a) XRPD pattern of simulated (black) and synthesized (red) ZIF-90 crystals. (b) FESEM image of ZIF-90 crystals. Scale bars:  $5 \mu\text{m}$ . (c)  $^1\text{H}$  NMR spectrum of the digested sample  $(\text{ZIF-90-BA})_{15}$  in DCI/ $\text{DMSO-}d_6$ .

## 6.2.4 PSM of ZIF-90 with a diamine molecule.

We further evaluated the PSM *via* spray-drying by using hexamethylenediamine (HMDA) to crosslink nearby aldehyde groups located on the pores of ZIF-90 (Figure 6.13a). It is important to mention here that PSM of ZIFs with terminal and aliphatic diamine molecules, such as ethylenediamine, have already been reported. For example, Balkus and co-workers cross-linked neighbouring SIM-1 crystals with ethylenediamine to form a highly compact selective water/methanol membrane.<sup>27</sup>

Following the procedure applied in the previous PSMs *via* spray-drying, an ethanolic suspension of ZIF-90 and HMDA (molar ratio aldehyde:amine = 1:5) was spray-dried under the same above-mentioned conditions. The collected powder called **(ZIF-90-HMDA)<sub>5</sub>**, was also cleaned with ethanol five times and once with acetone, and dried at 85 °C for 12 h. Again, we did not observe any significant change in the crystal size and morphology during the spray-drying process (Figure 6.12a), and the XRPD indicated that the collected crystals retain the parent ZIF-90 structure (Figure 6.12b).

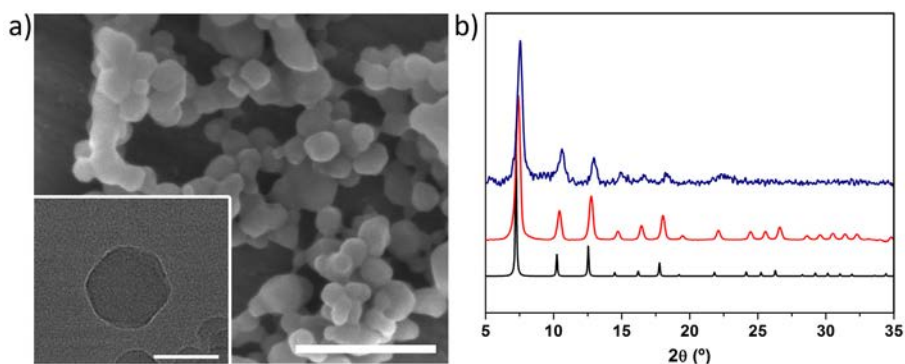


**Figure 6.12.** (a) FESEM and TEM images of **(ZIF-90-HMDA)<sub>5</sub>**. (b) XRPD patterns of the simulated ZIF-90 (black), as-synthesized ZIF-90 (red) and **(ZIF-90-HMDA)<sub>5</sub>** (blue). Scale bars: 200 nm (FESEM) and 50 nm (TEM).

The FT-IR spectrum of **(ZIF-90-HMDA)<sub>5</sub>** showed the presence of the characteristic C-H stretching bands of the hexamethyl chains at 2930 and 2850  $\text{cm}^{-1}$  as well as a new band centred at 1630  $\text{cm}^{-1}$  corresponding to the C=N group (Figure

6.13b). Moreover, the absence of the characteristic vibrational bands of the  $\text{NH}_2$  groups suggested that both amino groups of the HMDA were reacted. Altogether these observations agree well with an effective crosslinking of the aldehyde groups located on the pores of ZIF-90 using HMDA.

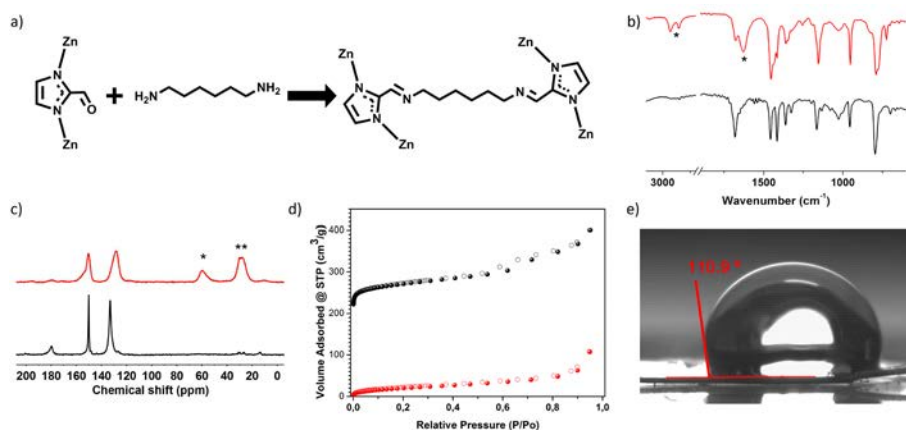


**Figure 6.13.** (a) Schematic representation of the PSM of ZIF-90 with hexamethylenediamine. (b) IR spectra of ZIF-90 (black) and  $(\text{ZIF-90-HMDA})_5$  (red), highlighting the aliphatic C-H and imine C=N vibrational bands with an asterisk (\*). (c)  $^{13}\text{C}$  MAS-NMR spectra of ZIF-90 (black) and  $(\text{ZIF-90-HMDA})_5$  (red), where the peaks at the alkyl region are highlighted with an asterisk (\*). (d)  $\text{N}_2$  sorption isotherms of ZIF-90 (black) and  $(\text{ZIF-90-HMDA})_5$  (red). (e) Contact angle image of pressed pellet diskhand-packed crystals of  $(\text{ZIF-90-HMDA})_5$ .

We further studied this crosslinking by  $^{13}\text{C}$  MAS-NMR. The spectrum of  $(\text{ZIF-90-HMDA})_5$  showed a low intensity of the peak at 179 ppm corresponding to the aldehyde group, suggesting a low concentration of this group within the framework (Figure 6.13c). This result agrees well with the FT-IR spectrum, in which a low intensity of the band at  $1675\text{ cm}^{-1}$  corresponding to the aldehyde group was also observed (Figure 6.13b). On the other hand, three signals in the alkyl-region (60, 30 and 27 ppm) were observed, indicating high symmetry in  $(\text{ZIF-90-HMDA})_5$ . The downfield signal was attributed to the  $-\text{N}=\text{CH}_2-$  methylene groups, and the other two signals to the four  $-\text{CH}_2-$  methylene groups of the diimine bridge. In fact, we did not detect the characteristic peak of the  $-\text{CH}_2-\text{NH}_2$  methylene centered at  $\approx 40\text{ ppm}$ ,<sup>19</sup> which would indicate that HMDA was only attached by one of its amine groups.

The presence of the diimine cross-linking molecule *N,N'*-(hexane-1,6-diyl)bis(1-imidazol-2-yl)methanimine) (Figure 6.13a) was finally confirmed by analyzing the solution resulting from the digestion of (ZIF-90-HMDA)<sub>5</sub> in acetic acid by <sup>1</sup>H-NMR and ESI-MS (Figure 6.14a, see also Annex 2). The peaks at 8.58 ppm and 3.83 ppm in the <sup>1</sup>H-NMR spectrum were attributed to the CH=N imine proton and the N-CH<sub>2</sub> methylene protons of the diamine molecule, respectively. On the other hand, in the ESI-MS spectrum, the peak at *m/z* = 273.1836 matches with the molecular formula of the protonated *N,N'*-(hexane-1,6-diyl)bis(1-imidazol-2-yl)methanimine) [C<sub>14</sub>H<sub>20</sub>N<sub>6</sub>]<sup>+</sup> (*m/z* = 273.1822).

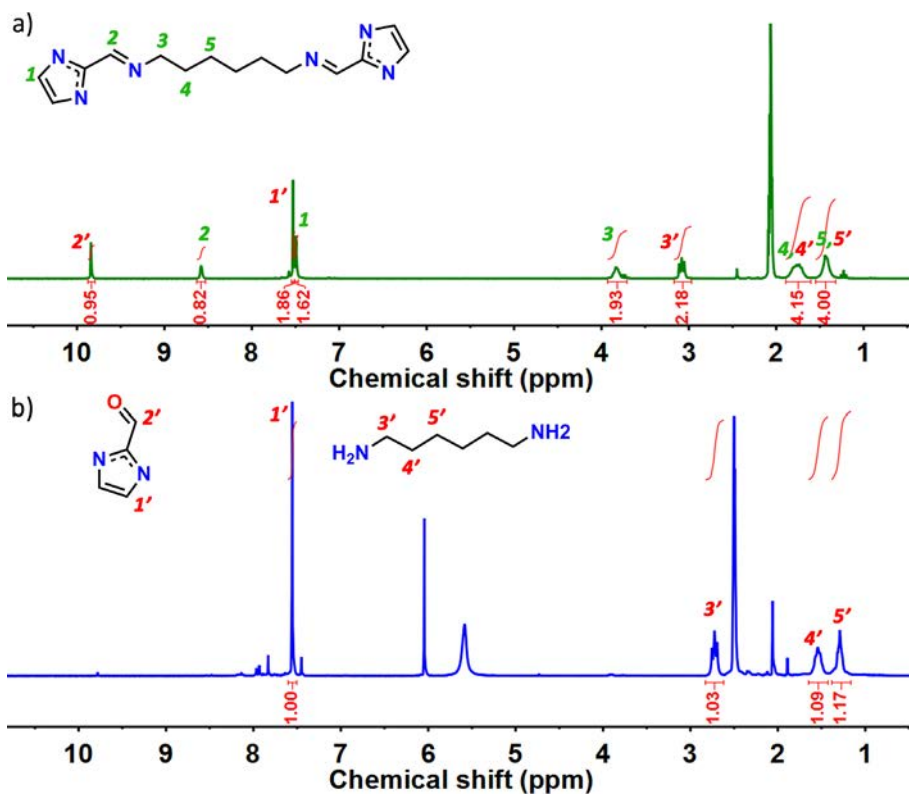


Figure 6.14. (a) <sup>1</sup>H NMR spectrum of the digested (ZIF-90-HMDA)<sub>5</sub> in CD<sub>3</sub>CO<sub>2</sub>D. (b) <sup>1</sup>H NMR spectrum of the digested (ZIF-90-HMDA)<sub>5</sub> in DCl/DMSO-d<sub>6</sub>.

The  $^1\text{H-NMR}$  spectrum of the digested **(ZIF-90-HMDA)<sub>5</sub>** in strong acidic conditions (DCI,  $\text{DMSO-}d_6$ ) was collected to quantify its yield of conversion (Figure 6.14b). Comparison of the integration of the signals corresponding to ICA (7.56 ppm) and HMDA (1.30 ppm) revealed that there are 35 % of HMDA, meaning that 70 % of the ICA linkers were functionalized.

This high conversion of cross-linked ICA linkers in **(ZIF-90-HMDA)<sub>5</sub>** should therefore involve a remarkable closure of its pores and reduction of its surface area in comparison to its parent ZIF-90. This assumption was confirmed by measuring the  $S_{\text{BET}}$  from the  $\text{N}_2$ -sorption isotherm at 77 K. We found a  $S_{\text{BET}}$  of  $69 \text{ m}^2 \text{ g}^{-1}$  that corresponds to a reduction of 93 % of the original  $S_{\text{BET}}$  of ZIF-90 (Table 6.2, Figures 6.13d). The contact angle ( $\Theta_c$ ) was also measured on pressed pellet disk of **(ZIF-90-HMDA)<sub>5</sub>**, giving a value of  $110.9^\circ$ , that correspond to a higher hydrophobic surface in comparison to the different **(ZIF-90-BA)<sub>x</sub>** samples (Figures 6.13e).

**Table 6.2.** BET areas, pore volumes and % of conversion of ZIF-90, **(ZIF-90-BA)<sub>x</sub>** and **(ZIF-90-HMDA)<sub>5</sub>**.

MOF	$x$	$S_{\text{BET}}$ ( $\text{m}^2 \text{ g}^{-1}$ )	Pore vol. ( $\text{cm}^3 \text{ g}^{-1}$ ) <sup>a</sup>	Conver. (%) <sup>b</sup>
ZIF-90		1070	0.4412	---
<b>(ZIF-90-BA)<sub>x</sub></b>	3	670	0.3150	25
	10	483	0.2166	32
	15	424	0.2042	42
<b>(ZIF-90-HMDA)<sub>5</sub></b>	5	69	0.0377	70

<sup>a</sup> Calculated at  $P/P_0 \approx 0.4$ . <sup>b</sup> Calculated from  $^1\text{H-NMR}$  spectra of the digested samples.

### 6.3 Conclusions

We have reported a highly versatile and effective methodology to post-synthetically modify MOFs via Schiff-base condensation reactions. This strategy can be applied to MOFs with either terminal aldehyde or amine groups, reduces their PSM time, and enables their continuous PSM with good rates of conversion. Therefore, it should facilitate the PSM of MOFs for numerous applications, including catalysis,

sensor technology, pollutant removal, and separation. This method also allowed the efficient crosslinking of the terminal aldehydes groups of ZIF-90 using a diamine molecule, thereby blocking their porosity and opening up new avenues for future triggered delivery systems. Finally, it also enables performing Schiff-base condensation reactions between discrete amine and aldehyde molecules, opening new perspectives in organic chemistry synthesis.

## **6.4 Experimental Section**

### **6.4.1 Materials and methods**

Zirconium chloride, zinc acetate hexahydrate, 2-aminoterephthalic acid, 4-pyridinecarboxaldehyde, 2-pyridinecarboxaldehyde, salicylaldehyde, trimethylamine, butylamine and hexamethylenediamine were purchased from Sigma Aldrich. 2-imidazolecarboxaldehyde was obtained from TCI. Dimethylformamide was obtained from Fisher Chemical. Ethanol absolute was purchased from Scharlab S.L. All the reagents were used without further purification. Deionised water was obtained with a Milli-Q® system (18.2 MΩ·cm).

ESI-MS spectra were recorded on a microTOF-Q Bruker Daltonics spectrometer. X-ray powder diffraction (XRPD) patterns were collected on an X'Pert PRO MPDP analytical diffractometer (Panalytical) at 45 kV, 40 mA using CuKα radiation ( $\lambda = 1.5419$  Å). Nitrogen adsorption and desorption measurements were done at 77 K using an Autosorb-IQ-AG analyzer (Quantachrome Instruments). Field-Emission Scanning Electron Microscopy (FESEM) images were collected on a FEI Magellan 400L scanning electron microscope at an acceleration voltage of 2.0 KV, using aluminium as support. TEM images were collected on a Transmission Electron Microscopy (TEM; FEI Tecnai G2 F20) at 200 KV. Fourier transform infra-red (FT-IR) spectra were recorded on a Bruker Tensor 27FTIR spectrometer equipped with a Golden Gate diamond attenuated total reflection (ATR) cell, in transmittance mode at room temperature. Static contact

angle measurements were performed on hand-packed powders using a Krüss DSA 100 drop shape analyzer. A 4- $\mu\text{L}$  droplet of deionized water was placed onto the sample surface in sessile mode at a speed of 135.2  $\mu\text{L min}^{-1}$ .  $^{13}\text{C}\{^1\text{H}\}$  cross-polarization (CP-MAS) experiments were performed at room temperature on a Bruker Avance III 9.4T spectrometer equipped with a double channel 4.0 mm MAS probe. Sample spinning was set to 12 kHz in all experiments.  $^1\text{H}$  NMR experiments of the imine molecules and of the digested ZIFs samples were carried out on a Bruker Avance DRX-250 spectrometer.  $^1\text{H}$ -NMR spectra of the digested UiO-66s were collected on a 400MHz Bruker AVANCE III spectrometer.

## 6.4.2 Synthesis of Imines

### 6.4.2.1 Synthesis of 2-((pyridin-4-ylmethylene)amino)terephthalic acid



2-aminoterephthalic acid (0.150 g, 0.828 mmol) was dispersed in 15 mL of ethanol by sonication for 10 min. Then, 80  $\mu\text{L}$ , 160  $\mu\text{L}$  or 240  $\mu\text{L}$  of 4-pyridinecarboxaldehyde (0.85, 1.70 or 2.55 mmol, respectively) was added to the dispersion at room temperature and stirring for 5 min. The resulting reaction mixture was then spray-dried at an inlet temperature of 130  $^{\circ}\text{C}$ , a feed rate of 3.0  $\text{mL min}^{-1}$  and a flow rate of 336  $\text{mL min}^{-1}$  using a Mini Spray Dryer B-290 (BUCHI Labortechnik; spray cap: 0.5-mm-hole). A yellow powder was collected after 5 min (Conversion for 1:3 eq bdc-NH<sub>2</sub>:4PC: 92 %).  $^1\text{H}$  NMR (250 MHz, DMSO-*d*<sub>6</sub>):  $\delta$  (ppm) = 8.76 – 8.69 (m, 2H), 8.18 (d,  $J$  = 2.1 Hz, 1H), 7.88 (d,  $J$  = 8.0 Hz, 1H), 7.65 – 7.60 (m, 2H), 7.55 (d,  $J$  = 1.5 Hz, 1H), 7.42 (dd,  $J$  = 8.2, 1.6 Hz, 1H).  $^{13}\text{C}$  NMR (63 MHz, DMSO-*d*<sub>6</sub>):  $\delta$  (ppm) = 169.05, 166.45,

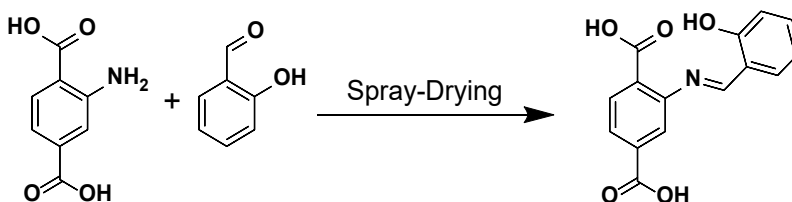
162.62, 150.23, 148.41, 144.49, 136.80, 130.26, 122.15, 121.88, 119.58, 116.86.  $m/z$  calculated for  $[C_{14}H_{10}N_2O_4\cdot H]^-$ : 269.0568; found 269.0566  $[M-H]^-$ .

#### 6.4.2.2 Synthesis of 2-((pyridin-2-ylmethylene)amino)terephthalic acid



2-aminoterephthalic acid (0.150 g, 0.828 mmol) was dispersed in 15 mL of ethanol by sonication for 10 min. Then, 2-Pyridinecarboxaldehyde (0.24 mL, 2.52 mmol) was added to the dispersion at room temperature and stirring for 5 min. The resulting reaction mixture was then spray-dried at an inlet temperature of 130 °C, a feed rate of 3.0 mL min<sup>-1</sup> and a flow rate of 336 mL min<sup>-1</sup> using a Mini Spray Dryer B-290 (BUCHI Labortechnik; spray cap: 0.5-mm-hole). A yellow powder was collected after 5 min (Conversion: 87 %). <sup>1</sup>H NMR (250 MHz, DMSO-*d*<sub>6</sub>)  $\delta$  (ppm) = 8.67 (d,  $J$  = 4.8 Hz, 1H), 8.20 (s, 1H), 7.96 (dd,  $J$  = 7.8, 1.7 Hz, 1H), 7.87 (d,  $J$  = 8.3 Hz, 1H), 7.72 (dd,  $J$  = 7.5, 1.4 Hz, 1H), 7.60 (d,  $J$  = 1.7 Hz, 1H), 7.52 (ddd,  $J$  = 7.7, 4.8, 1.4 Hz, 1H), 7.39 (dd,  $J$  = 6.9, 1.5 Hz, 1H). <sup>13</sup>C NMR (63 MHz, DMSO-*d*<sub>6</sub>)  $\delta$  (ppm) = 169.05, 167.07, 162.85, 150.26, 149.12, 148.39, 137.69, 135.15, 131.41, 128.44, 124.86, 121.68, 119.17, 117.56.  $m/z$  calculated for  $[C_{14}H_{10}N_2O_4\cdot H]^-$ : 269.0568; found 269.0562  $[M-H]^-$ .

#### 6.4.2.3 Synthesis of 2-((2-hydroxybenzylidene)amino)terephthalic acid



2-aminoterephthalic acid (0.150 g, 0.828 mmol) was dispersed in 15 mL of ethanol by sonication for 10 min. Then, salicylaldehyde (0.265 mL, 2.49 mmol) was added to the dispersion at room temperature and stirring for 5 min. The resulting reaction mixture was then spray-dried at an inlet temperature of 130 °C, a feed rate of 3.0 mL min<sup>-1</sup> and a flow rate of 336 mL min<sup>-1</sup> using a Mini Spray Dryer B-290 (BUCHI Labortechnik; spray cap: 0.5-mm-hole). An orange powder was collected after 5 min (Conversion: 75 %). <sup>1</sup>H NMR (250 MHz, DMSO-*d*<sub>6</sub>) δ (ppm) = 8.95 (s, 1H), 7.94 (d, *J* = 7.2 Hz, 1H), 7.77 (d, *J* = 8.3 Hz, 1H), 7.66 (m, 1H), 7.38 (s, 1H), 7.07 – 6.91 (m, 3H). <sup>13</sup>C NMR (63 MHz, DMSO-*d*<sub>6</sub>) δ (ppm) = 169.05, 167.08, 166.42, 160.71, 151.19, 136.41, 135.15, 131.42, 129.18, 119.48, 119.10, 117.56, 117.22, 114.60, 112.53. *m/z* calculated for [C<sub>15</sub>H<sub>11</sub>NO<sub>5</sub>H]<sup>+</sup>: 284.0553; found 284.05620[M-H]<sup>+</sup>.

### 6.4.3 Synthesis of UiO-66-NH<sub>2</sub>

UiO-66-NH<sub>2</sub> was synthesized following a previously reported method.<sup>1</sup> In a typical synthesis, 11.652 g (0.05 mol) of ZrCl<sub>4</sub> was dissolved in 250 mL of DMF at room temperature under stirring for 15 min. In a separate flask, NH<sub>2</sub>-bdc (9.058 g, 0.05 mol) was dissolved in 250 mL of DMF at room temperature under stirring for 15 min. The yellow NH<sub>2</sub>-bdc solution obtained was added to the ZrCl<sub>4</sub> solution, followed by addition of 35 mL of HCl 37% under stirring. The resulting mixture was heated at 120 °C under stirring for 2 h. The obtained solid was collected by centrifugation at 9000 rpm for 5 min, washed two times with 100 mL of DMF for 12 h at 120 °C and three times with 100 mL of absolute ethanol for 12 h at 60 °C. Finally, the resulting powder was dried at 85 °C overnight. (Yield = 75 %).

### 6.4.4 Synthesis of (UiO-66-4PC)<sub>x</sub>

0.150 g (0.085 mmol) of UiO-66-NH<sub>2</sub> was dispersed in ethanol (15 mL) by sonication for 10 min. Then, 144 μL, 240 μL, 480 μL or 720 μL of 4-pyridinecarboxaldehyde was added to the dispersion at room temperature and stirring

for 5 min. The resulting reaction mixture was then spray-dried at an inlet temperature of 130 °C, a feed rate of 3.0 mL min<sup>-1</sup> and a flow rate of 336 mL min<sup>-1</sup> using a Mini Spray Dryer B-290 (BUCHI Labortechnik; spray cap: 0.5-mm-hole). A yellow powder was collected after 5 min. The resulting solid was then dispersed in 20 mL of ethanol and precipitated by centrifugation at 9000 rpm for 5 min. This process was repeated four times. The final product was washed one time with acetone and centrifuged again at 9000 rpm and dried for 12 h at 85 °C.

#### **6.4.5 Synthesis of (UiO-66-2PC)<sub>x</sub>**

0.150 g (0.085 mmol) of UiO-66-NH<sub>2</sub> was dispersed in ethanol (15 mL) by sonication for 10 min. Then, 144 μL, 240 μL, 480 μL or 720 μL of 2-pyridinecarboxaldehyde was added to the dispersion at room temperature and stirring for 5 min. The resulting reaction mixture was then spray-dried at an inlet temperature of 130 °C, a feed rate of 3.0 mL min<sup>-1</sup> and a flow rate of 336 mL min<sup>-1</sup> using a Mini Spray Dryer B-290 (BUCHI Labortechnik; spray cap: 0.5-mm-hole). A yellow powder was collected after 5 min. The resulting solid was then dispersed in 20 mL of ethanol and precipitated by centrifugation at 9000 rpm for 5 min. This process was repeated four times. The final product was washed one time with acetone and centrifuged again at 9000 rpm and dried for 12 h at 85 °C.

#### **6.4.6 Synthesis of (UiO-66-Sal)<sub>x</sub>**

0.150 g (0.085 mmol) of UiO-66-NH<sub>2</sub> was dispersed in ethanol (15 mL) by sonication for 10 min. Then, 160 μL, 240 μL, 540 μL or 810 μL of salicylaldehyde was added to the dispersion at room temperature and stirring for 5 min. The resulting reaction mixture was then spray-dried at an inlet temperature of 130 °C, a feed rate of 3.0 mL min<sup>-1</sup> and a flow rate of 336 mL min<sup>-1</sup> using a Mini Spray Dryer B-290 (BUCHI Labortechnik; spray cap: 0.5-mm-hole). A yellow powder was collected after 5 min. The resulting solid was then dispersed in 20 mL of ethanol and precipitated by

centrifugation at 9000 rpm for 5 min. This process was repeated four times. The final product was washed one time with acetone and centrifuged again at 9000 rpm and dried for 12 h at 85 °C.

#### **6.4.7 Synthesis of ZIF-90 (Nanoparticles)**

ZIF-90 was synthesized following a previously reported method.<sup>2</sup> In a typical synthesis, 0.200 g (2.10 mmol) of imidazolate-2-carboxyaldehyde was dissolved in 150 mL of DMF at 100 °C under stirring for 1 h and then cooled to room temperature. In a separate flask, 0.223 g (0.75 mmol) of  $\text{Zn}(\text{NO}_3)_2 \cdot 6\text{H}_2\text{O}$  was dissolved in 50 mL of DMF at room temperature. The resulting solution was added to the imidazolate-2-carboxyaldehyde solution under stirring, followed by addition of 0.27 mL of trimethylamine (1.96 mmol). The resulting mixture was stirred for 1 min at room temperature and then 100 mL of ethanol was added. The particles were collected by centrifugation at 9000 rpm for 8 min, washed five times with ethanol, and finally, dried at 70 °C overnight. (Yield = 70 %).

#### **6.4.8 Synthesis of (ZIF-90-BA)<sub>x</sub>**

ZIF-90 (0.100 g, 0.39 mmol) was dispersed in 15 mL of ethanol by sonication for 10 min. Then, 230  $\mu\text{L}$ , 770  $\mu\text{L}$  or 1200  $\mu\text{L}$  of butylamine was added to the dispersion of ZIF-90 at room temperature and stirring for 5 min. The resulting reaction mixture was then spray-dried at an inlet temperature of 130 °C, a feed rate of 3.0 mL min<sup>-1</sup> and a flow rate of 336 mL min<sup>-1</sup> using a Mini Spray Dryer B-290 (BUCHI Labortechnik; spray cap: 0.5-mm-hole). A yellow powder was collected after 5 min. The resulting solid was then dispersed in 20 mL of ethanol and precipitated by centrifugation at 9000 rpm for 8 min. This process was repeated five times. The final product was washed one time with acetone and centrifuged again at 9000 rpm and dried for 12 h at 85 °C.

### 6.4.9 Synthesis of ZIF-90-HMDA

ZIF-90 (0.100 g, 0.39 mmol) was dispersed in 15 mL of ethanol by sonication for 10 min. Then, hexamethylenediamine (0.45 g, 3.9 mmol) was added to a dispersion of ZIF-90 at room temperature and stirring for 5 min. The resulting reaction mixture was then spray-dried at an inlet temperature of 130 °C, a feed rate of 3.0 mL min<sup>-1</sup> and a flow rate of 336 mL min<sup>-1</sup> using a Mini Spray Dryer B-290 (BUCHI Labortechnik; spray cap: 0.5-mm-hole). A yellow powder was collected after 5 min. The resulting solid was then dispersed in 20 mL of ethanol and precipitated by centrifugation at 9000 rpm for 8 min. This process was repeated five times. The final product was washed one time with acetone and centrifuged again at 9000 rpm and dried for 12 h at 85 °C.

### 6.4.10 Synthesis of ZIF-90 (Crystals)

ZIF-90 was synthesized following a previously reported method.<sup>3</sup> In a typical synthesis, a solid mixture of 0.384 g (4.00 mmol) of imidazolate-2-carboxyaldehyde, 0.296 g (1.00 mmol) of Zn(NO<sub>3</sub>)<sub>2</sub>·6H<sub>2</sub>O and 0.068 g (1.00 mmol) of sodium formate was dissolved in 40 mL of methanol at room temperature by sonication. The resulting solution was placed in a Teflon-lined stainless steel autoclave and heated at 85 °C for 24 h. The crystals were isolated by centrifugation at 9000 rpm for 7 min, washed three times with methanol and finally, dried at room temperature for 24 h.

### 6.4.11 Synthesis of (ZIF-90-BA)<sub>15</sub>

ZIF-90 crystals (0.090 g, 0.35 mmol) were dispersed in 15 mL of ethanol by sonication for 20 min. Then, 1080 μL of butylamine was added to the dispersion of ZIF-90 at room temperature and stirring for 5 min. The resulting reaction mixture was then spray-dried at an inlet temperature of 130 °C, a feed rate of 3.0 mL min<sup>-1</sup> and a flow rate of 336 mL min<sup>-1</sup> using a Mini Spray Dryer B-290 (BUCHI Labortechnik; spray cap: 0.5-mm-hole). A yellow powder was collected after 5 min. The resulting solid was then dispersed in 20 mL of ethanol and precipitated by centrifugation at 9000 rpm for 8

min. This process was repeated five times. The final product was washed one time with acetone and centrifuged again at 9000 rpm and dried for 12 h at 85 °C.

#### **6.4.12 Activation protocol**

All washed samples (with ethanol and acetone and then dried at 85 °C overnight) were degassed at 200 °C for 12 h under vacuum. In the case of UiO-66-NH<sub>2</sub>-based samples, FT-IR spectra were collected after heating at 85 °C to confirm the removal of the unreacted aldehydes prior to the N<sub>2</sub> sorption measurement at 77 K.

## 6.5 References

- (1) Furukawa, H.; Ko, N.; Go, Y. B.; Aratani, N.; Choi, S. B.; Choi, E.; Yazaydin, A. Ö.; Snurr, R. Q.; O’Keeffe, M.; Kim, J.; Yaghi, O. M. *Science* **2010**, *329*, 424.
- (2) Horcajada, P.; Gref, R.; Baati, T.; Allan, P. K.; Maurin, G.; Couvreur, P.; Ferey, G.; Morris, R. E.; Serre, C. *Chem. Rev.* **2012**, *112*, 1232.
- (3) Carné, A.; Carbonell, C.; Imaz, I.; Maspoch, D. *Chem. Soc. Rev.* **2011**, *40*, 291.
- (4) Evans, J. D.; Sumbly, C. J.; Doonan, C. J. *Chem. Soc. Rev.* **2014**, *43*, 5933.
- (5) Doonan, C. J.; Morris, W.; Furukawa, H.; Yaghi, O. M. *J. Am. Chem. Soc.* **2009**, *131*, 9492.
- (6) Kim, M.; Cahill, J. F.; Prather, K. A.; Cohen, S. M. *Chem. Commun.* **2011**, *47*, 7629.
- (7) Garibay, S. J.; Cohen, S. M. *Chem. Commun.* **2010**, *46*, 7700.
- (8) Kim, M.; Cohen, S. M. *CrystEngComm* **2012**, *14*, 4096.
- (9) Kandiah, M.; Usseglio, S.; Svelle, S.; Olsbye, U.; Lillerud, K. P.; Tilset, M. *J. Mater. Chem.* **2010**, *20*, 9848.
- (10) Hou, J.; Luan, Y.; Tang, J.; Wensley, A. M.; Yang, M.; Lu, Y. *J. Mol. Catal. A: Chem.* **2015**, *407*, 53.
- (11) Pintado-Sierra, M.; Rasero-Almansa, A. M.; Corma, A.; Iglesias, M.; Sánchez, F. *J. Catal.* **2013**, *299*, 137.
- (12) Rasero-Almansa, A. M.; Corma, A.; Iglesias, M.; Sanchez, F. *Green Chem.* **2014**, *16*, 3522.
- (13) Tang, J.; Dong, W.; Wang, G.; Yao, Y.; Cai, L.; Liu, Y.; Zhao, X.; Xu, J.; Tan, L. *RSC Advances* **2014**, *4*, 42977.
- (14) Wang, J.; Yang, M.; Dong, W.; Jin, Z.; Tang, J.; Fan, S.; Lu, Y.; Wang, G. *Catal. Sci. Technol.* **2016**, *6*, 161.
- (15) Liu, J.; Zhang, X.; Yang, J.; Wang, L. *Appl. Organomet. Chem.* **2014**, *28*, 198.
- (16) Saleem, H.; Rafique, U.; Davies, R. P. *Microporous Mesoporous Mater.* **2016**, *221*, 238.
- (17) Morris, W.; Doonan, C. J.; Furukawa, H.; Banerjee, R.; Yaghi, O. M. *J. Am. Chem. Soc.* **2008**, *130*, 12626.
- (18) Jones, C. G.; Stavila, V.; Conroy, M. A.; Feng, P.; Slaughter, B.; Ashley, C. E.; Allendorf, M. D. *ACS Appl. Mater. Interfaces* **2016**, *8*, 7623.
- (19) Thompson, J. A.; Brunelli, N. A.; Lively, R. P.; Johnson, J. R.; Jones, C. W.; Nair, S. J. *Phys. Chem. C* **2013**, *117*, 8198.
- (20) Liu, C.; Liu, Q.; Huang, A. *Chem. Commun.* **2016**, *52*, 3400.
- (21) Servalli, M.; Ranocchiaro, M.; Van Bokhoven, J. A. *Chem. Commun.* **2012**, *48*, 1904.
- (22) Carné-Sánchez, A.; Imaz, I.; Cano-Sarabia, M.; Maspoch, D. *Nat Chem* **2013**, *5*, 203.
- (23) Garzon-Tovar, L.; Cano-Sarabia, M.; Carne-Sanchez, A.; Carbonell, C.; Imaz, I.; Maspoch, D. *React. Chem. Eng.* **2016**, *1*, 533.
- (24) Nguyen, J. G.; Cohen, S. M. *J. Am. Chem. Soc.* **2010**, *132*, 4560.

- (25) Canivet, J.; Aguado, S.; Daniel, C.; Farrusseng, D. *ChemCatChem* **2011**, *3*, 675.
- (26) Agudo, S.; Canivet, J.; Farrusseng, D. *Chem. Commun.* **2010**, *46*, 7999.
- (27) Marti, A. M.; Tran, D.; Balkus, K. J. *J. Porous Mater.* **2015**, *22*, 1275.
- (28) Ragon, F.; Horcajada, P.; Chevreau, H.; Hwang, Y. K.; Lee, U. H.; Miller, S. R.; Devic, T.; Chang, J.-S.; Serre, C. *Inorg. Chem.* **2014**, *53*, 2491



# Chapter 7

---

## Spray Drying for Making Covalent Chemistry II: Synthesis of Covalent–Organic Framework Superstructures and related Composites

This Chapter is based on the following publication:

---

Garzón-Tovar, L.; Avci-Camur, C.; Rodriguez-San-Miguel, D.; Imaz, I.; Zamora, F.; MasPOCH, D. *Chem. Commun.* **2017**, 53, 11372.

---



## 7.1 Introduction

Covalent Organic Frameworks (COFs) are an emerging class of crystalline porous materials, where two-dimensional (2D) or three-dimensional (3D) architectures are formed from organic building blocks linked by dynamic covalent bonds (*e.g.* imine, boroxine,  $\beta$ -keto-enamine and azine).<sup>1-3</sup> As illustrated in **Chapter 1**, these materials are characterized by their high porosity, high thermal stability and low mass density, which confer them potential for myriad applications, such as gas sorption and storage,<sup>4-7</sup> catalysis,<sup>8-10</sup> sensors<sup>11-13</sup> and optoelectronics.<sup>14,15</sup> Seeking to exploit these possibilities, researchers have developed several fabrication methods for COFs, including not only the traditional solvothermal synthesis but also microwave,<sup>16</sup> microfluidic,<sup>17</sup> mechanochemical,<sup>18</sup> ionothermal,<sup>19</sup> and continuous-flow synthesis.<sup>20,21</sup>

While many efforts have been devoted to the synthesis of new COFs and to their production methods, there is a growing interest in structuring these COFs at the micro/macroscale forming more complex, high-order super- or mesostructures from the assembly of COF nanoparticles. As their Metal-Organic Framework (MOF) counterparts,<sup>22,23</sup> these type of structures made from COF nanocrystals are especially attractive due to the possibility of (i) controlling the shaping and sizing of COFs at the micro/macroscale, two parameters that are very important to control for many applications; (ii) enhancing the initial performance *via* design of their morphology; and (iii) combining COFs with other materials to create functional composites, which can further expand the scope for applications.<sup>24-27</sup>

To date, there are a few studies based on the creation of COF superstructures. For example, Banerjee *et al.* synthesized a highly crystalline and porous COF in the form of hollow spheres that were used for immobilizing the enzyme trypsin.<sup>28</sup> In a more recent study, core-shell microspheres containing Fe<sub>3</sub>O<sub>4</sub> nanoclusters were synthesized using a template assisted route. The resulting hybrid microspheres showed photothermal conversion ability after exposing them to near infrared light.<sup>25</sup>

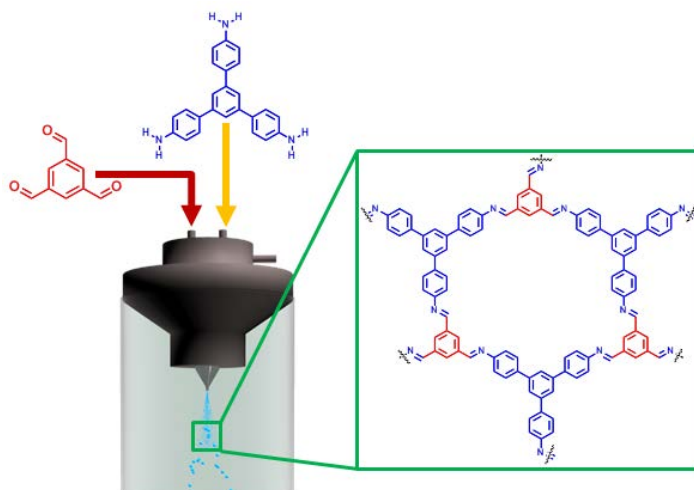
Despite these advances, synthesis of higher-order COF superstructures is still challenging mainly due to the harsh conditions usually needed to synthesize highly crystalline COF nanoparticles. In these sense, we demonstrated in **Chapter 3** that the spray drying method can be used to synthesize MOFs in the form of spherical hollow or compact superstructures made from the assembly of MOF nanoparticles.<sup>29-32</sup> Additionally, we also have demonstrated in **Chapter 6** that spray drying is also an effective methodology to perform Schiff-base condensation reactions, either between discrete organic molecules or on the pore surfaces of MOFs.<sup>33</sup> In this chapter, we combine both achievements and extend the applicability of spray drying to synthesize imine-based COF nanocrystals while structuring them into spherical hollow superstructures. This strategy consists in a two-step process. In a first step, the spray drying allows the formation and shaping of amorphous imine-based polymer spheres. Then, in a second step, these spheres are subjected to a dynamic covalent chemistry to crystallize them under similar conditions to those reported by Dichtel *et al.*<sup>34</sup> Remarkably, after the crystallization step, the resulting superstructures preserve the initial size and morphology of the amorphous spheres. Further, we show that this strategy enables integrating guest functional materials, either molecules or other nanomaterials, in these COF superstructures.

## 7.2 Results and Discussion

### 7.2.1 Synthesis of COF-TAPB-BTCA

Initially, we began with the synthesis of superstructures of **COF-TAPB-BTCA**, a two-dimensional COF assembled from two trigonal building blocks, 1,3,5-benzenetricalbaldehyde (BTCA) and 1,3,5-tris-(4-aminophenyl)benzene (TAPB).<sup>35</sup> In a typical first step, a 0.03 mol L<sup>-1</sup> solution of BTCA in a mixture of DMSO and acetic acid (9:1 v/v) and a 0.03 mol L<sup>-1</sup> solution of TAPB in DMSO were independently atomized using a three-fluid nozzle at a feed rate of 3.0 mL min<sup>-1</sup>, a flow rate of 336 mL min<sup>-1</sup> and an inlet temperature of 200 °C, using a B-290 Mini Spray Dryer (BÜCHI

Labortechnique). This atomization immediately afforded a yellow powder (Scheme 7.1). Note here that the use of three-fluid nozzle ensured that the two reactants only come in contact inside the drying chamber avoiding the clogging of the nozzle.



**Scheme 7.1.** Schematic representation of the spray drying synthesis of *COF-TAPB-BTCA*.

Field-emission scanning electron microscopy (FESEM) images and X-ray powder diffraction (XRPD) performed on the intermediate collected solid revealed the homogeneous formation of amorphous spheres with an average size of  $2.2 \pm 1.1 \mu\text{m}$  (Figure 7.1).

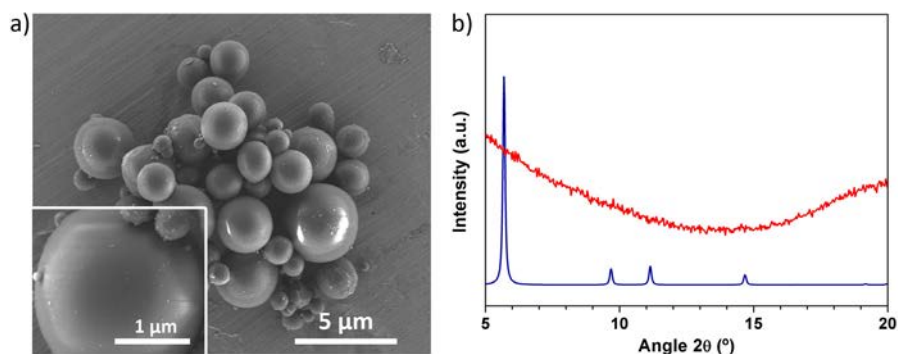


**Figure 7.1.** (a) Representative FESEM images of amorphous *COF-TAPB-BTCA* spheres. (b) XRPD patterns of the amorphous *COF-TAPB-BTCA* (red) compared to the simulated powder pattern for *COF-TAPB-BTCA* (blue).

Since the spray-drying is based on the fast evaporation of the solvent, we reasoned that the kinetic product was obtained instead of thermodynamic one. The formation of the imine-based polymer was confirmed by FT-IR spectroscopy and solid-state  $^{13}\text{C}$  magic angle spinning nuclear magnetic resonance (MAS NMR). The FT-IR spectrum showed the presence of the typical imine ( $\text{C}=\text{N}$ ) band at  $1633\text{ cm}^{-1}$  and the absence of the band corresponding to free  $\text{—NH}_2$  between  $3300\text{--}3500\text{ cm}^{-1}$ , indicating the absence of unreacted TAPB. The imine formation was further corroborated by the appearance of a signal at  $158\text{ ppm}$  in the  $^{13}\text{C}$  MAS NMR spectrum, which was attributed to the carbon atom of the  $\text{C}=\text{N}$  imine group (Figure 7.2).

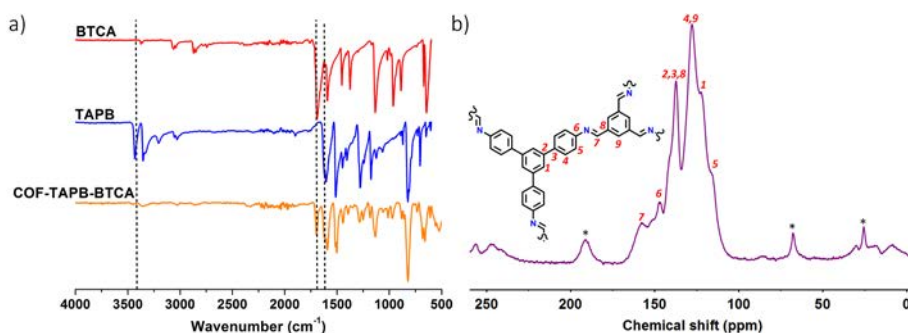


**Figure 7.2.** (a) FT-IR spectra of BTCA (red) and TAPB (blue) and amorphous COF-TAPB-BTCA (orange), highlighting the imine  $\text{C}=\text{N}$  vibrational bands and the disappearance of the  $\text{N-H}$  stretching bands. (b)  $^{13}\text{C}$  MAS-NMR spectrum of amorphous COF-TAPB-BTCA. The peaks corresponding to the  $\text{CH}_2$  groups of the residual THF and terminal aldehyde groups in the amorphous COF-TAPB-BTCA are highlighted with asterisks.

These results are in agreement with those previously reported for COF-TAPB-BTCA.<sup>35</sup> In a second step, this imine-based polymer was subjected to a dynamic covalent chemistry process. Thus, the amorphous spheres were dispersed in a mixture of 1,4-dioxane/mesitylene/water/acetic acid and heated at  $80\text{ }^\circ\text{C}$  for 192 h. The isolated material did not show significant spectroscopic changes in both FT-IR and  $^{13}\text{C}$  MAS NMR spectra (Figure 7.3).

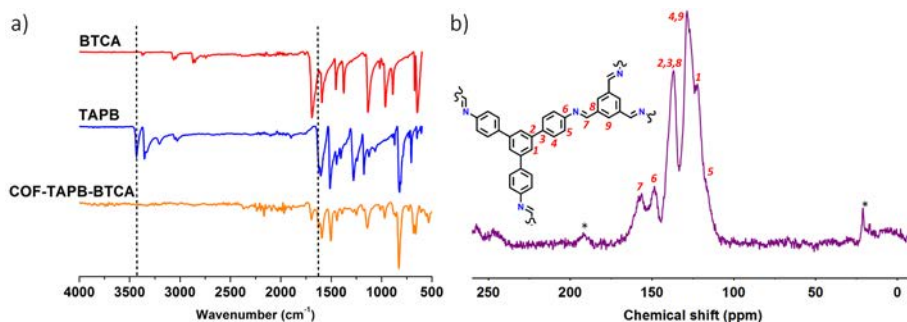


**Figure 7.3.** (a) FT-IR spectra of BTCA (red) and TAPB (blue) and crystalline **COF-TAPB-BTCA** (orange), highlighting the imine C=N vibrational bands and the disappearance of N-H stretching bands. (b)  $^{13}\text{C}$  MAS-NMR spectrum of crystalline **COF-TAPB-BTCA**. The peaks corresponding to the  $\text{CH}_3$  groups of the residual toluene and terminal aldehyde groups in the crystalline **COF-TAPB-BTCA** are highlighted with asterisks.

However, FESEM and High-resolution transmission electron microscopy (HR-TEM) images displayed the formation of hollow superstructures in which their walls are created by the close packing of COF nanoparticles (Figure 7.4a-c). Remarkably, these superstructures retained both shape and size of the amorphous spheres. The XRPD pattern of these superstructures showed the most intense peak at  $5.5^\circ$ , which properly match with the simulated **COF-TAPB-BTCA** structure (Figure 7.4d). The microporosity of the **COF-TAPB-BTCA** superstructures was confirmed by  $\text{N}_2$  adsorption measurements, which gave a BET surface area of  $911 \text{ m}^2 \text{ g}^{-1}$ . This value is consistent with that previously reported for **COF-TAPB-BTCA** (Figure 7.4e).<sup>30</sup> Finally, thermogravimetric analysis (TGA) revealed the high thermal stability of **COF-TAPB-BTCA** superstructures (up to  $500^\circ\text{C}$ ), following by a loss weight due to the decomposition of the framework (Figure 7.4f).

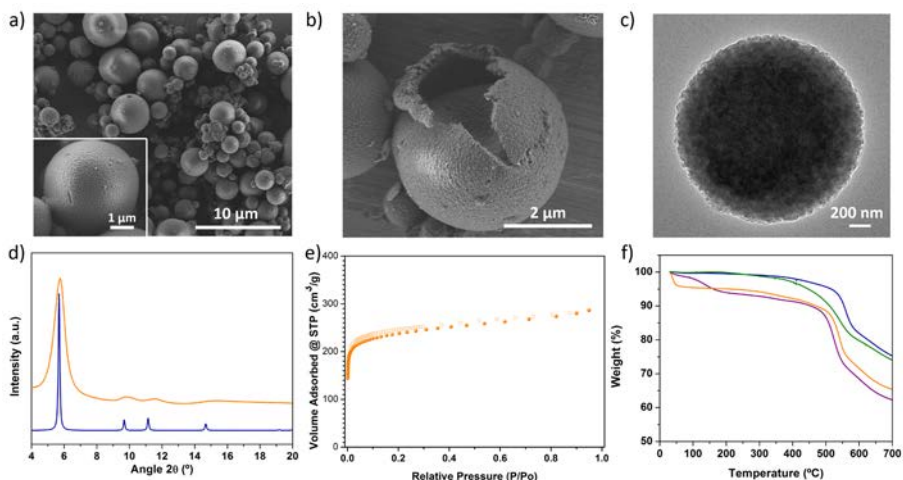


**Figure 7.4.** (a) Representative FESEM images of microspherical **COF-TAPB-BTCA** superstructures (b) FESEM image of mechanically broken superstructure, revealing the hollow cavity. (c) HR TEM images of crystalline **COF-TAPB-BTCA** superstructure, revealing the presence of COF nanocrystals. (d) XRPD pattern of **COF-TAPB-BTCA** (orange), compared with the simulated powder pattern (blue). (e)  $N_2$  adsorption isotherm of **COF-TAPB-BTCA**. (f) TGA of the as-synthesized amorphous (purple) and crystalline (orange) **COF-TAPB-BTCA** compared with the amorphous (green) and crystalline (blue) samples after they have been degassed at 150 °C for 12 h under vacuum.

## 7.2.2 Synthesis of COF-LZU1 and COF-TAPB-PDA

To demonstrate the generality of our approach, we used similar synthetic conditions to synthesize other imine-based COF superstructures. To this end, we selected the recently discovered **COF-LZU1**<sup>8</sup> and **COF-TAPB-PDA**.<sup>34</sup> **COF-LZU1** was synthesized by the condensation of BTCA and *p*-phenylenediamine (PPD), whereas **COF-TAPB-PDA** was synthesized from TAPB and terephthalaldehyde (PDA). In both cases, after the two-step process, FESEM and HRTEM images and XRPD of the resulting solids revealed the formation of crystalline microspherical superstructures of the desired COFs (Figure 7.5).

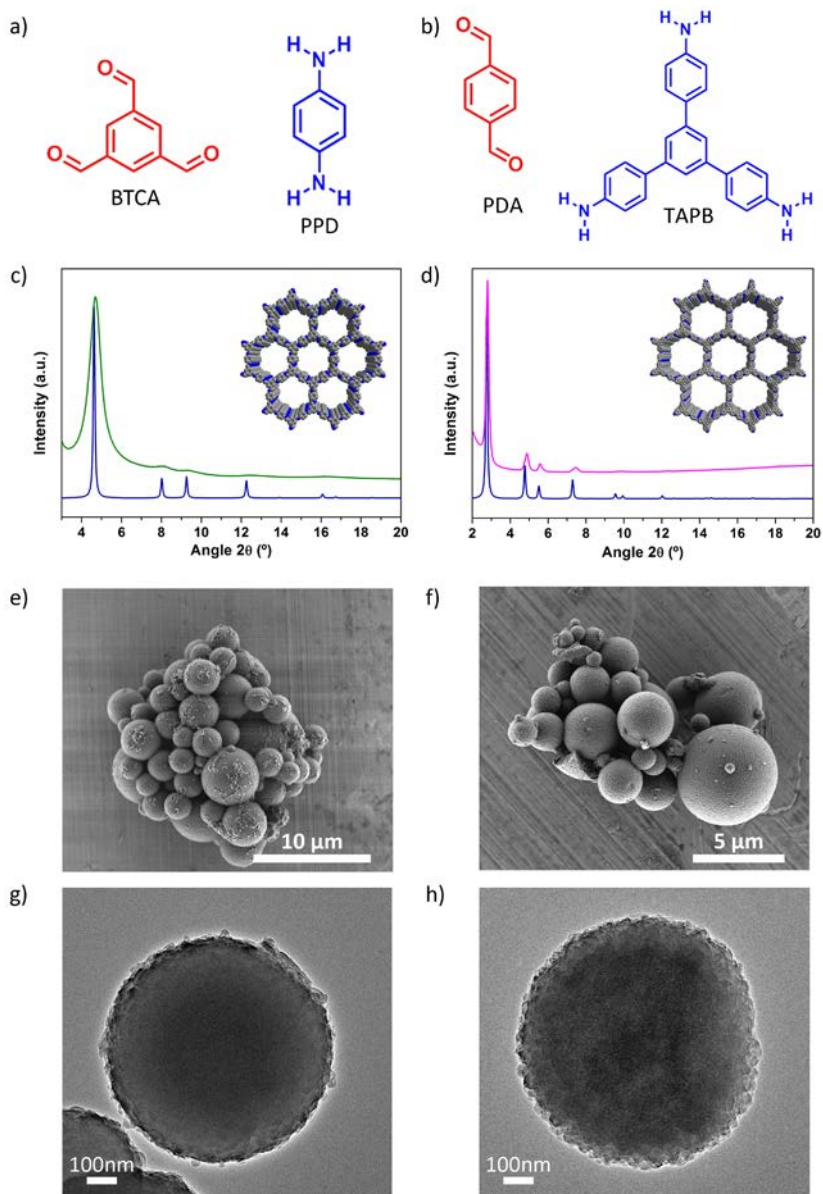


**Figure 7.5.** (a,b) Representation of the building blocks used to synthesize (a) COF-LZU1 and (b) COF-TAPB-PDA. (c) XRPD pattern of the obtained COF-LZU1 (green) compared with simulated powder pattern (blue). (d) XRPD pattern of the obtained COF-TAPB-PDA (pink) compared with simulated powder pattern (blue). (e,f) FESEM images showing the general view of the microspherical (e) COF-LZU1 and (f) COF-TAPB-PDA superstructures. (g,h). HRTEM images of the (g) crystalline COF-LZU1 and (h) COF-TAPB-PDA superstructures.

FT-IR spectra of **COF-LZU1** and **COF-TAPB-PDA** showed the presence of the characteristic C=N stretching band at 1618 and 1628  $\text{cm}^{-1}$ , respectively. Moreover, the formation of imine was further corroborated by the peaks observed in the  $^{13}\text{C}$  MAS NMR spectra at 157 ppm for **COF-LZU1** and 158 ppm for **COF-TAPB-PDA** (Figures 7.6).

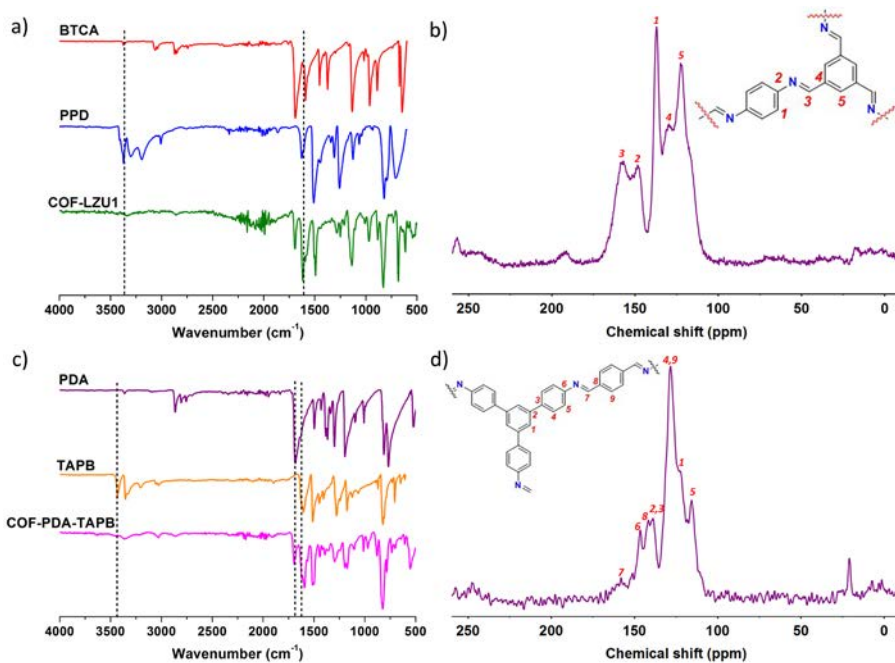


**Figure 7.6.** (a,c) FT-IR spectra of BTCA (red), PPD (blue), PDA (purple) and TAPB (orange) and crystalline **COF-LZU1** (green) and crystalline **COF-PDA-TAPB** (pink), highlighting the imine C=N vibrational bands and the disappearance of the N-H stretching bands. (b,d)  $^{13}\text{C}$  MAS-NMR spectra of the (b) crystalline **COF-LZU1** and (d) **COF-PDA-TAPB** superstructures.

Additionally, the microporosity of the COFs was confirmed by  $\text{N}_2$  adsorption analysis, from which BET surface areas of  $319 \text{ m}^2 \text{ g}^{-1}$  for **COF-LZU1** and  $1162 \text{ m}^2 \text{ g}^{-1}$  for **COF-TAPB-PDA** were calculated (Figure 7.7). These values are consistent with those previously reported.<sup>8,34</sup>

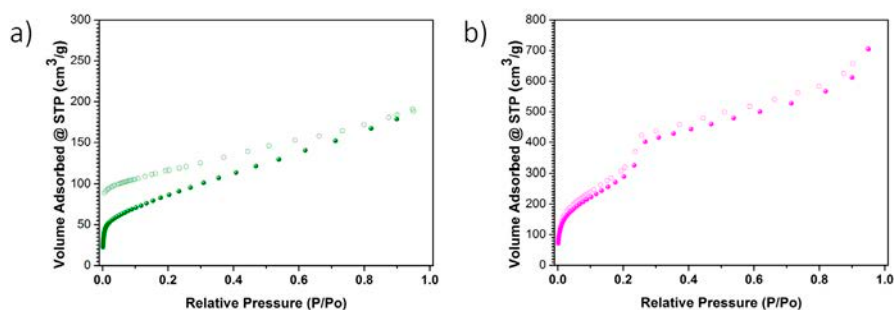
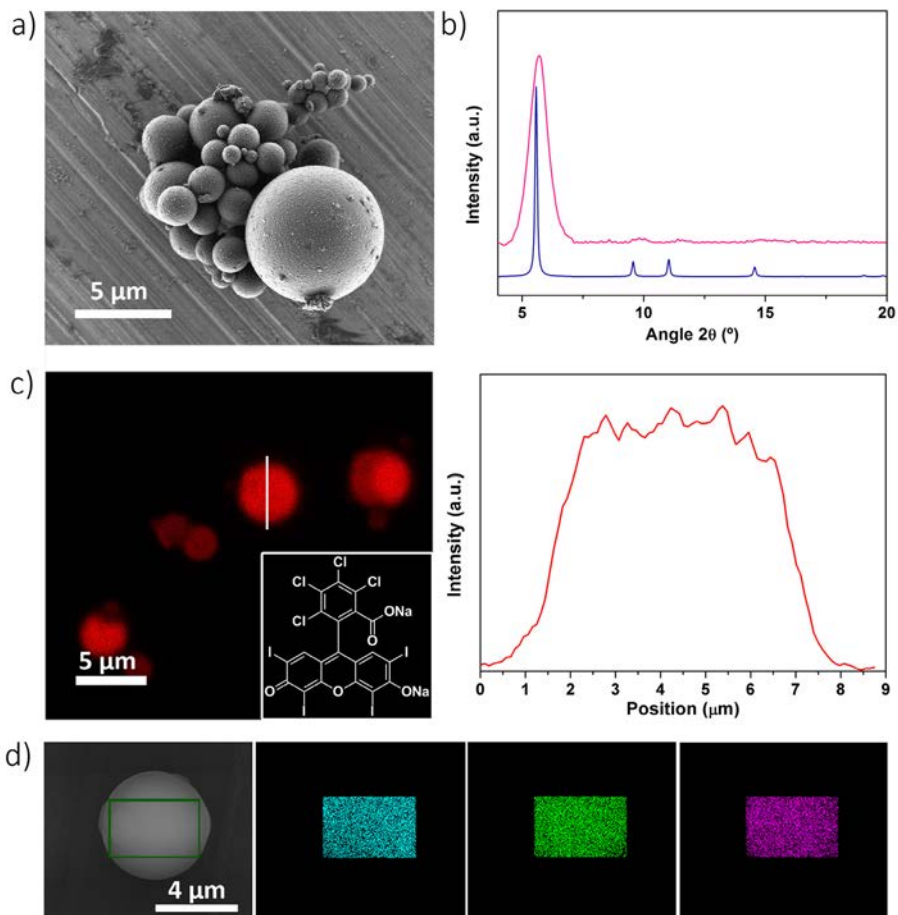


Figure 7.7.  $N_2$  adsorption isotherms of (a) COF-LZU1 and (b) COF-TAPB-PDA.

## 7.2.3 Synthesis of COF-based Composites

### 7.2.3.1 Synthesis of Rose-bengal@COF-TAPB-BTCA

Having demonstrated that our spray-drying methodology enables the formation of hollow COF superstructures, we envisioned to use it as a simple method for integrating other functional substances to these superstructures and thus, create COF-based composites.<sup>36-38</sup> To explore this possibility, we synthesized **Rose-bengal@COF-TAPB-BTCA** superstructures by reproducing the formation of **COF-TAPB-BTCA** superstructures but dissolving Rose bengal in the initial precursor solution. FESEM images and XRPD patterns revealed the formation of crystalline microspherical superstructures of **COF-TAPB-BTCA**, confirming that their synthesis was not affected by the presence of the dye (Figure 7.8a-b). The presence of Rose bengal was confirmed by elemental mapping with energy dispersive X-ray spectrometry (EDX) performed on a single superstructure, which revealed a highly uniform distribution of Cl, I, and Na atoms (Figure 7.8d). Additionally, the successful encapsulation of this dye was visualized by confocal images, where the intensity profile and the confocal image taken on a single sphere revealed the homogeneous distribution of Rose bengal (Figure 7.8c).



**Figure 7.8.** (a) FESEM image showing the microspherical **Rose-bengal@COF-TAPB-BTCA** superstructures. (b) XRPD pattern of the obtained composite (pink) compared with the simulated powder pattern of **COF-TAPB-BTCA** (blue). (c) Confocal fluorescence image of **Rose-bengal@COF-TAPB-BTCA** superstructures and their fluorescence intensity profile. Inset: chemical structure of rose Bengal. (d) Elemental mapping with EDX performed on a single spherical superstructure of **Rose-bengal@COF-TAPB-BTCA**, showing the homogeneous distribution Na (cyan), Cl (green) and I (pink).

Finally, to evaluate the possibility to release encapsulated molecules from these COF superstructures, **Rose-bengal@COF-TAPB-BTCA** composite was incubated in ethanol for different periods of time and the dye released was quantified by fluorescence spectroscopy (Figure 7.9). Notably, a dye release of 32 % was observed

for the first day, achieving a release of 56 % after 8 days. This slow release suggests that the dye is in fact located on the pores of the COF nanocrystals rather than on their crystal surface.

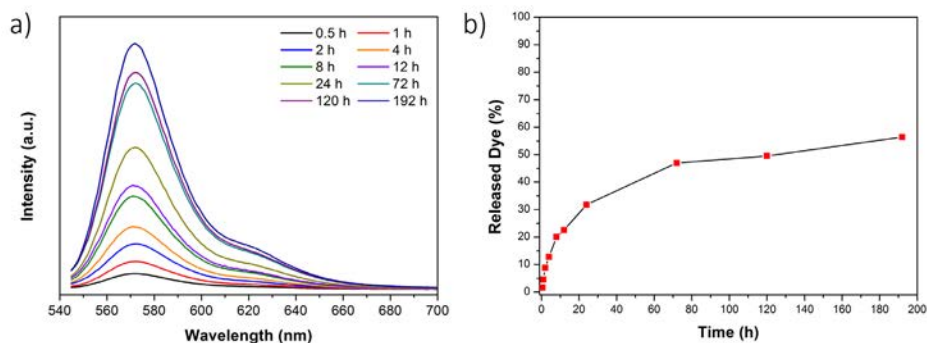


**Figure 7.9.** (a) Fluorescence emission spectra of *Rose-bengal@COF-TAPB-BTCA* (collected at  $\lambda_{exc} = 525$  nm) at different periods of incubation. (b) *Rose Bengal* release from the composite.

### 7.2.3.2 Synthesis of $\text{Fe}_3\text{O}_4@$ COF-TAPB-BTCA

To further explore the formation of COF-based composites using this strategy, we incorporated magnetic  $\text{Fe}_3\text{O}_4$  nanoparticles dispersed in the precursor solution. Under the same conditions,  $\text{Fe}_3\text{O}_4$  nanoparticles (8 nm diameter) were encapsulated into the **COF-TAPB-BTCA** superstructures, as confirmed by HAADF-STEM and HRTEM images and XRPD (Figure 7.10a-b). The content of Fe in the composite was estimated by Inductively Coupled Plasma-Mass spectrometry (ICP-MS), from which a  $\text{Fe}_3\text{O}_4$  content of 2.8 % w/w in the composite was determined. EDX mapping performed on a single superstructure showed the distribution of N, Fe and O atoms, confirming the presence of  $\text{Fe}_3\text{O}_4$  into the superstructures (Figure 7.10c). Also, as indication of the encapsulation, a colloidal suspension of the composite was exposed to a magnet and rapidly attracted to it (Figure 7.11a). Similarly, magnetic measurements performed on the composite confirmed the magnetic character, exhibiting a characteristic hysteresis loop with a coercive field of 240 Oe at 10 K (Figure 7.11b).

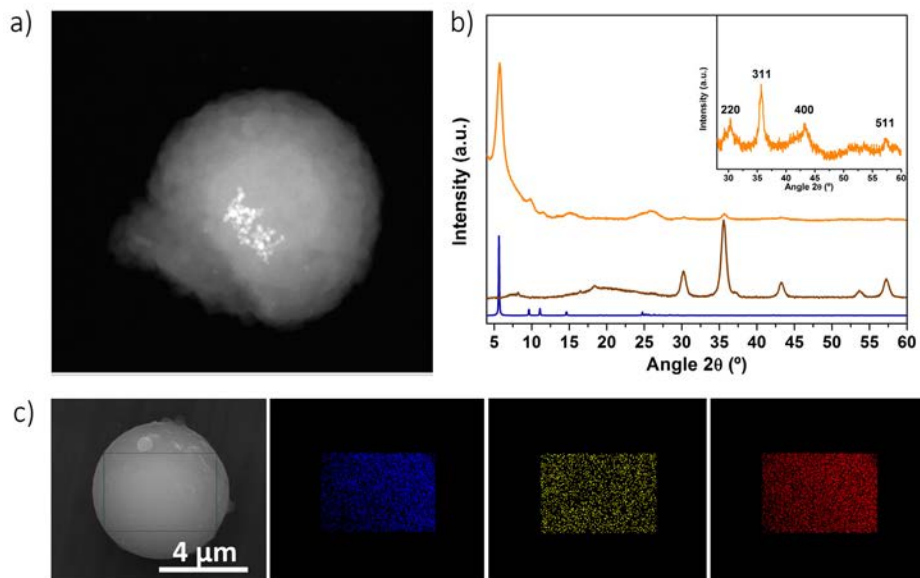


**Figure 7.10.** (a) HAADF-STEM image of single  $\text{Fe}_3\text{O}_4@\text{COF-TAPB-BTCA}$  superstructure. (b) XRPD pattern of  $\text{Fe}_3\text{O}_4@\text{COF-TAPB-BTCA}$  (orange) compared with the experimental powder pattern of  $\text{Fe}_3\text{O}_4$  nanoparticles (brown) and the simulated XRPD pattern of  $\text{COF-TAPB-BTCA}$  (blue). The inset shows the XRPD pattern of the composite in the range of  $2\theta$  from  $25^\circ$  to  $60^\circ$ , highlighting the peaks of the cubic structure of the  $\text{Fe}_3\text{O}_4$  NPs (JCPDS Card No. 19-629). (c) Elemental mapping with EDX performed on a single spherical superstructure of  $\text{Fe}_3\text{O}_4@\text{COF-TAPB-BTCA}$ , showing the homogeneous distribution of N (blue), Fe (yellow) and O (red).

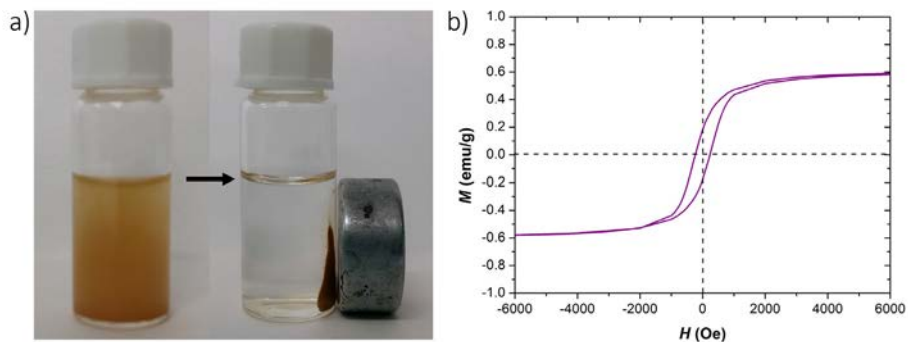


**Figure 7.11.** (a) Photographs of the dispersion of  $\text{Fe}_3\text{O}_4@\text{COF-TAPB-BTCA}$  superstructures before and after exposed to a magnet. (b) Magnetic hysteresis loop of  $\text{Fe}_3\text{O}_4@\text{COF-TAPB-BTCA}$  measured at 10 K ( $M_{\text{sat}} = 0.6 \text{ emu}\cdot\text{g}^{-1}$ ).

## 7.3 Conclusion

We have reported a highly versatile and effective methodology to simultaneously synthesize and shaping microspherical hollow imine-based COF superstructures. This method also enables making COF-based composites by simple adding the selected functional materials during the spray-drying synthesis.

## 7.4 Experimental Section

### 7.4.1 Materials and methods

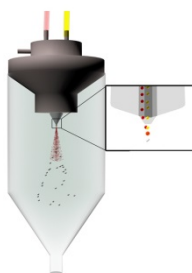
1,3,5-benzenetricalbaldehyde, *p*-phenylenediamine, terephthalaldehyde, 1,4-dioxane, acetic acid and mesitylene were purchased from Sigma Aldrich. 1,3,5-tris-(4-aminophenyl)benzene was obtained from TCI. THF, DMSO, acetone and toluene were obtained from Fisher Chemical. All the reagents were used without further purification. Deionised water was obtained with a Milli-Q<sup>®</sup> system (18.2 M $\Omega$ -cm).

XRPD patterns were collected on an X'Pert PRO MPDP analytical diffractometer (Panalytical) at 45 kV, 40 mA using CuK $\alpha$  radiation ( $\lambda = 1.5419 \text{ \AA}$ ). Nitrogen adsorption and desorption measurements were done at 77 K using an Autosorb-IQ-AG analyser (Quantachrome Instruments). FESEM images were collected on a FEI Magellan 400L scanning electron microscope at an acceleration voltage of 2.0 KV, using aluminium as support. HAADF-STEM and HR-TEM images were collected on a Transmission Electron Microscope (TEM; FEI Tecnai G2 F20) at 200 KV. Fourier transform infrared (FT-IR) spectra were recorded on a Bruker Tensor 27FTIR spectrometer equipped with a Golden Gate diamond attenuated total reflection (ATR) cell, in transmittance mode at room temperature. Fluorescence emission spectra were recorded on a Carey Eclipse Fluorescence Spectrophotometer at an excitation wavelength of 525 nm. ICP-MS measurements were performed using an Agilent 7500 after aqua regia digestion. <sup>13</sup>C {<sup>1</sup>H} cross-polarization (CP-MAS) experiments were performed at room temperature on a Bruker Avance III 9.4T spectrometer equipped with a double channel 4.0 mm MAS

probe. Sample spinning was set to 12 kHz in all experiments. Thermogravimetric analysis (TGA) was performed on a Pyris 8000 Thermo Gravimetric Analyzer at a heating rate of 10 °C min<sup>-1</sup> from 30 °C to 700 °C under nitrogen. Magnetic hysteresis loop at 10 K was measured with a Quantum Design MPMS XL SQUID Magnetometer.

## 7.4.2 General description of the multi-fluid nozzle used in the spray-drying process

### 7.4.2.1 Three-fluid nozzle

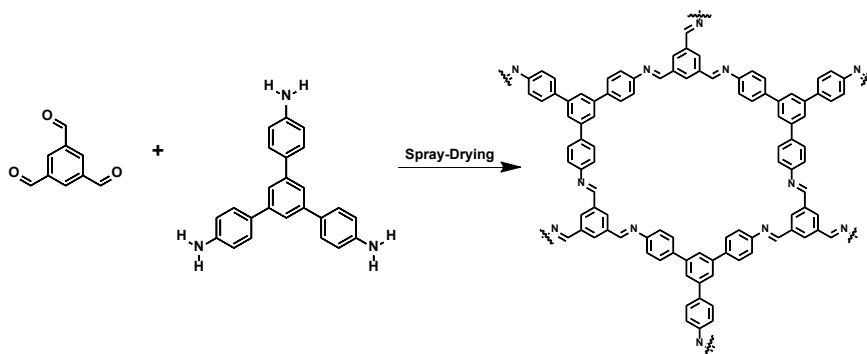


*Scheme 7.2. Schematic representation of the three-fluid nozzle.*

In the three-fluid mode, the solutions that contain the COF precursors are pumped individually through the two separate inner channels of the nozzle while the drying gas flows through the third channel. Thus, the two solutions only come in contact at the nozzle tip, where the three channels meet. This three-fluid mode allows spraying incompatible or reactive precursors avoiding the fast precipitation before the process.

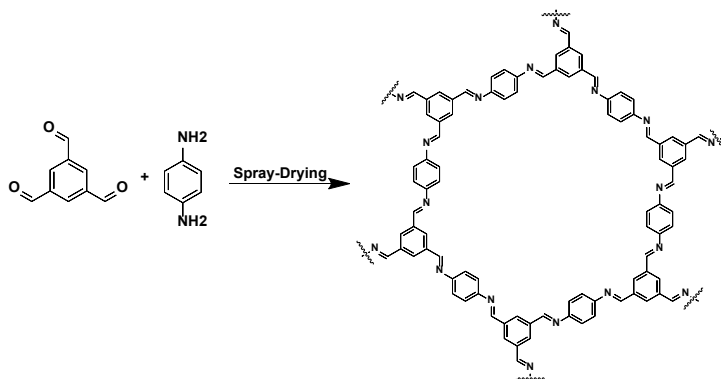
### 7.4.3 Synthetic procedures

#### 7.4.3.1 Spray-drying synthesis of COF-TAPB-BTCA



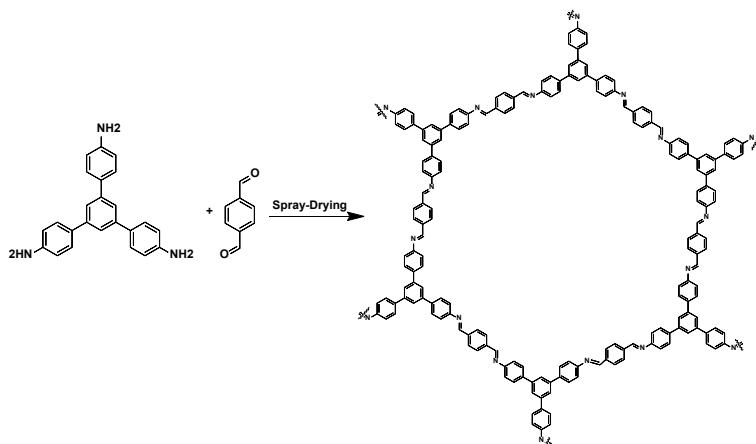
A solution of 136.5 mg of 1,3,5-benzenetricaldehyde (BTCA) in 30 mL of a mixture of DMSO and acetic acid (9:1 v/v) and a solution of 281.2 mg of 1,3,5-tris-(4-aminophenyl)benzene (TAPB) in 30 mL of DMSO were independently atomized using a three-fluid nozzle at a feed rate of  $3.0 \text{ mL min}^{-1}$ , a flow rate of  $336 \text{ mL min}^{-1}$  and an inlet temperature of  $200 \text{ }^\circ\text{C}$ , using a B-290 Mini Spray Dryer (BÜCHI Labortechnik). A yellow powder was collected after 10 min. The resulting solid was then dispersed in 20 mL of THF and precipitated by centrifugation at 9000 rpm for 4 min. This process was repeated three times. The final product was washed three times with acetone and centrifuged again at 9000 rpm and dried for 48 h at room temperature.

### 7.4.3.2 Spray-drying synthesis of COF-LZU1



A solution of 165 mg of BTCA in 6 mL of a mixture of 1,4-dioxane and acetic acid (2:1 v/v) and a solution of 162 mg of *p*-phenylenediamine in 6 mL of 1,4-dioxane were independently atomized using a two fluid nozzle in T-mode at a feed rate of 3.0 mL min<sup>-1</sup>, a flow rate of 336 mL min<sup>-1</sup> and an inlet temperature of 150 °C, using a B-290 Mini Spray Dryer (BÜCHI Labortechnik). A yellow powder was collected after 2 min. The resulting solid was then dispersed in 20 mL of THF and precipitated by centrifugation at 9000 rpm for 4 min. This process was repeated three times. The final product was washed three times with acetone and centrifuged again at 9000 rpm and dried for 48 h at room temperature.

### 7.4.3.3 Spray-drying synthesis of COF-PDA-TAPB



A solution of 92.3 mg of terephthalaldehyde in 21.5 mL of a mixture of 1,4-dioxane, mesitylene water and acetic acid (1.9:0.37:0.66:1 v/v) and a solution of 162.1 mg of 1,3,5-tris-(4-aminophenyl)benzene in 21.5 mL of a mixture of 1,4-dioxane and mesitylene (9.8:1 v/v) were independently atomized using a three-fluid nozzle at a feed rate of 3.0 mL min<sup>-1</sup>, a flow rate of 336 mL·min<sup>-1</sup> and an inlet temperature of 150 °C, using a B-290 Mini Spray Dryer (BÜCHI Labortechnik). A yellow powder was collected after 7 min. The resulting solid was then dispersed in 20 mL of toluene and precipitated by centrifugation at 9000 rpm for 4 min. This process was repeated three times. The final product was washed three times with acetone and centrifuged again at 9000 rpm and dried for 48 h at room temperature.

### 7.4.3.4 Spray-drying synthesis of Rose-bengal@COF-TAPB-BTCA

A solution of 67.3 mg of BTCA in 15 mL of a mixture of DMSO and acetic acid (9:1 v/v) and a solution of 143.4 mg of TAPB and 20 mg of rose bengal in 15 mL of DMSO were independently atomized using a three-fluid nozzle at a feed rate of 3.0 mL min<sup>-1</sup>, a flow rate of 336 mL·min<sup>-1</sup> and an inlet temperature of 200 °C, using a B-290 Mini Spray Dryer (BÜCHI Labortechnik). A pink powder was collected after 5 min. The resulting solid was then dispersed in 20 mL of THF and precipitated by

centrifugation at 9000 rpm for 4 min. This process was repeated six times. The final product was washed three times with acetone and centrifuged again at 9000 rpm and dried for 48 h at room temperature.

#### **7.4.3.5 Spray-drying synthesis of $\text{Fe}_3\text{O}_4@\text{COF-TAPB-BTCA}$**

0.6 mL of  $\text{Fe}_3\text{O}_4$  6.3 mmol  $\text{L}^{-1}$  in DMF was added to a solution of 286.3 mg of TAPB in 30 mL of DMSO. The resulting mixture and a solution of 136.9 mg of BTCA in 30 mL of a mixture of DMSO and acetic acid (9:1 v/v) were independently atomized using a three-fluid nozzle at a feed rate of 3.0 mL  $\text{min}^{-1}$ , a flow rate of 336 mL  $\text{min}^{-1}$  and an inlet temperature of 200 °C, using a B-290 Mini Spray Dryer (BÜCHI Labortechnik). A brown powder was collected after 10 min. The resulting solid was then dispersed in 20 mL of THF and precipitated by centrifugation at 9000 rpm for 4 min. This process was repeated three times. The final product was washed three times with acetone and centrifuged again at 9000 rpm and dried for 48 h at room temperature.

#### **7.4.4 Amorphous to crystalline transformation process**

The amorphous to crystalline transformation was performed following a previously reported method.<sup>34</sup> 80 mg of COF was dispersed in a mixture of 1,4-dioxane and mesitylene (9:1 v/v). Then, 1.75 mL of water and 2.6 mL of acetic acid were to the dispersion at room temperature and stirring for 5 min. The resulting mixture was heated at 80 °C under stirring for 8 days. The obtained solid was collected by centrifugation at 9000 rpm for 4 min, washed three times with 10 mL of toluene and dried at 60 °C overnight. All washed samples were degassed at 150 °C for 12 h under vacuum prior to the  $\text{N}_2$  sorption measurement at 77 K.

## 7.5 References

- (1) Waller, P. J.; Gándara, F.; Yaghi, O. M. *Acc. Chem. Res.* **2015**, *48*, 3053.
- (2) Ding, S.-Y.; Wang, W. *Chem. Soc. Rev.* **2013**, *42*, 548.
- (3) Thote, J.; Barike Aiyappa, H.; Rahul Kumar, R.; Kandambeth, S.; Biswal, B. P.; Balaji Shinde, D.; Chaki Roy, N.; Banerjee, R. *IUCrJ* **2016**, *3*, 402.
- (4) Furukawa, H.; Yaghi, O. M. *J. Am. Chem. Soc.* **2009**, *131*, 8875.
- (5) Doonan, C. J.; Tranchemontagne, D. J.; Glover, T. G.; Hunt, J. R.; Yaghi, O. M. *Nat Chem* **2010**, *2*, 235.
- (6) Rabbani, M. G.; Sekizkardes, A. K.; Kahveci, Z.; Reich, T. E.; Ding, R.; El-Kaderi, H. M. *Chem. Eur. J.* **2013**, *19*, 3324.
- (7) Han, S. S.; Furukawa, H.; Yaghi, O. M.; Goddard, W. A. *J. Am. Chem. Soc.* **2008**, *130*, 11580.
- (8) Ding, S.-Y.; Gao, J.; Wang, Q.; Zhang, Y.; Song, W.-G.; Su, C.-Y.; Wang, W. *J. Am. Chem. Soc.* **2011**, *133*, 19816.
- (9) Li, H.; Pan, Q. Y.; Ma, Y. C.; Guan, X. Y.; Xue, M.; Fang, Q. R.; Yan, Y. S.; Valtchev, V.; Qiu, S. L. *J. Am. Chem. Soc.* **2016**, *138*, 14783.
- (10) Fang, Q. R.; Gu, S.; Zheng, J.; Zhuang, Z. B.; Qiu, S. L.; Yan, Y. S. *Angew. Chem. Int. Ed.* **2014**, *53*, 2878.
- (11) Das, G.; Biswal, B. P.; Kandambeth, S.; Venkatesh, V.; Kaur, G.; Addicoat, M.; Heine, T.; Verma, S.; Banerjee, R. *Chem. Sci.* **2015**, *6*, 3931.
- (12) Yuan, Y.; Ren, H.; Sun, F. X.; Jing, X. F.; Cai, K.; Zhao, X. J.; Wang, Y.; Wei, Y.; Zhu, G. S. *J. Mater. Chem.* **2012**, *22*, 24558.
- (13) Ding, S.-Y.; Dong, M.; Wang, Y.-W.; Chen, Y.-T.; Wang, H.-Z.; Su, C.-Y.; Wang, W. *J. Am. Chem. Soc.* **2016**, *138*, 3031.
- (14) Wan, S.; Guo, J.; Kim, J.; Ihee, H.; Jiang, D. *Angew. Chem.* **2008**, *120*, 8958.
- (15) Mahmood, J.; Lee, E. K.; Jung, M.; Shin, D.; Jeon, I.-Y.; Jung, S.-M.; Choi, H.-J.; Seo, J.-M.; Bae, S.-Y.; Sohn, S.-D.; Park, N.; Oh, J. H.; Shin, H.-J.; Baek, J.-B. *Nat. Commun.* **2015**, *6*, 6486.
- (16) Wei, H.; Chai, S.; Hu, N.; Yang, Z.; Wei, L.; Wang, L. *Chem. Commun.* **2015**, *51*, 12178.
- (17) Rodriguez-San-Miguel, D.; Abrishamkar, A.; Navarro, J. A. R.; Rodriguez-Trujillo, R.; Amabilino, D. B.; Mas-Balleste, R.; Zamora, F.; Puigmarti-Luis, J. *Chem. Commun.* **2016**, *52*, 9212.
- (18) Biswal, B. P.; Chandra, S.; Kandambeth, S.; Lukose, B.; Heine, T.; Banerjee, R. *J. Am. Chem. Soc.* **2013**, *135*, 5328.
- (19) Kuhn, P.; Antonietti, M.; Thomas, A. *Angew. Chem. Int. Ed.* **2008**, *47*, 3450.
- (20) Karak, S.; Kandambeth, S.; Biswal, B. P.; Sasmal, H. S.; Kumar, S.; Pachfule, P.; Banerjee, R. *J. Am. Chem. Soc.* **2017**, *139*, 1856.
- (21) Peng, Y.; Wong, W. K.; Hu, Z.; Cheng, Y.; Yuan, D.; Khan, S. A.; Zhao, D. *Chem. Mater.* **2016**, *28*, 5095.
- (22) Furukawa, S.; Reboul, J.; Diring, S.; Sumida, K.; Kitagawa, S. *Chem. Soc. Rev.* **2014**, *43*, 5700.

- (23) Carné-Sánchez, A.; Imaz, I.; Stylianou, K. C.; Maspoch, D. *Chem. Eur. J.* **2014**, *20*, 5192.
- (24) Rodríguez-San-Miguel, D.; Corral-Perez, J. J.; Gil-Gonzalez, E.; Cuellas, D.; Arauzo, J.; Monsalvo, V. M.; Carcelen, V.; Zamora, F. *CrystEngComm* **2017**.
- (25) Tan, J.; Namuangruk, S.; Kong, W.; Kungwan, N.; Guo, J.; Wang, C. *Angew. Chem. Int. Ed.* **2016**, *55*, 13979.
- (26) Shi, X.; Yao, Y.; Xu, Y.; Liu, K.; Zhu, G.; Chi, L.; Lu, G. *ACS Appl. Mater. Interfaces* **2017**, *9*, 7481.
- (27) Halder, A.; Kandambeth, S.; Biswal, B. P.; Kaur, G.; Roy, N. C.; Addicoat, M.; Salunke, J. K.; Banerjee, S.; Vanka, K.; Heine, T.; Verma, S.; Banerjee, R. *Angew. Chem. Int. Ed.* **2016**, *55*, 7806.
- (28) Kandambeth, S.; Venkatesh, V.; Shinde, D. B.; Kumari, S.; Halder, A.; Verma, S.; Banerjee, R. *Nat. Commun.* **2015**, *6*, 6786.
- (29) Carné-Sánchez, A.; Imaz, I.; Cano-Sarabia, M.; Maspoch, D. *Nat Chem* **2013**, *5*, 203.
- (30) Garzon-Tovar, L.; Cano-Sarabia, M.; Carne-Sanchez, A.; Carbonell, C.; Imaz, I.; Maspoch, D. *React. Chem. Eng.* **2016**, *1*, 533.
- (31) Guillerm, V.; Garzon-Tovar, L.; Yazdi, A.; Imaz, I.; Juanhuix, J.; Maspoch, D. *Chem. Eur. J.* **2017**, *23*, 6829.
- (32) Garzón-Tovar, L.; Pérez-Carvajal, J.; Imaz, I.; Maspoch, D. *Adv. Funct. Mater.* **2017**, *27*, 1606424.
- (33) Garzón-Tovar, L.; Rodríguez-Hermida, S.; Imaz, I.; Maspoch, D. *J. Am. Chem. Soc.* **2017**, *139*, 897.
- (34) Smith, B. J.; Overholts, A. C.; Hwang, N.; Dichtel, W. R. *Chem. Commun.* **2016**, 52, 3690.
- (35) de la Pena Ruigomez, A.; Rodríguez-San-Miguel, D.; Stylianou, K. C.; Cavallini, M.; Gentili, D.; Liscio, F.; Milita, S.; Roscioni, O. M.; Ruiz-Gonzalez, M. L.; Carbonell, C.; Maspoch, D.; Mas-Balleste, R.; Segura, J. L.; Zamora, F. *Chem. Eur. J.* **2015**, *21*, 10666.
- (36) Mullangi, D.; Nandi, S.; Shalini, S.; Sreedhala, S.; Vinod, C. P.; Vaidhyanathan, R. *Sci. Rep.* **2015**, *5*, 10876.
- (37) Mullangi, D.; Shalini, S.; Nandi, S.; Choksi, B.; Vaidhyanathan, R. *J. Mater. Chem. A* **2017**, *5*, 8376.
- (38) Wang, P.; Wu, Q.; Han, L.; Wang, S.; Fang, S.; Zhang, Z.; Sun, S. *RSC Advances* **2015**, *5*, 27290.

# Conclusions

---



## General Conclusions

The efforts in this Thesis were addressed to positioning the spray-drying technique as a general and reliable methodology for the synthesis of MOFs, COFs and MOF/COF-based composites.

Firstly, we showed the potential of the spray-drying technique to synthesize a broad spectrum of MOFs in the form of spherical superstructures. In the first stage, we have developed a new set-up based on incorporating a continuous flow reactor at the entrance of the spray-drier. With this new set-up, we have demonstrated the versatility of this new approach synthesizing numerous members of diverse high-nuclearity MOF families such as, the isorecticular series of **UiO-66**, **Fe-BTC/MIL-100** and **[Ni<sub>8</sub>(OH)<sub>4</sub>(H<sub>2</sub>O)<sub>2</sub>(L)<sub>6</sub>]<sub>n</sub>** as compact microspherical superstructures (beads) in high yields and quality in terms of their BET surface areas. Among these MOFs, **UiO-66** synthesis was used as the model reaction to study the main experimental parameters affecting the spray-drying continuous flow synthesis in terms of yield and porosity. Moreover, we have also demonstrated that this methodology can be used for synthesizing multivariate (MTV) MOFs from complex mixtures of different ligands. In the second stage, we have also demonstrated that the spray-drying technique can be used to synthesize MOFs based on nitrogen-donor and anionic pillar ligands. As a test case scenario, we have performed the synthesis of the **SIFSIX-3-M** materials with high yields and good CO<sub>2</sub> sorption properties. In this study, we also confirmed the suitability of the spray-drying method for reticular chemistry by tuning the ligand size and the anionic pillar. Thus, the **SIFSIX-1-Zn** and **TIFSIX-1-Cu** materials were synthesized. In addition, we have shown for the first time that the spray-drying technique can be used to synthesize supramolecular, hydrogen bonded porous materials based on the assembly of this anionic pillars and adenine (**MPM-1-TIFSIX**). Overall, the work done in this part of the Thesis demonstrated that the spray-drying is a versatile and general methodology for the synthesis of MOFs.

Once the potential of spray-drying in the synthesis of MOFs was demonstrated, we exploited its capacities to synthesize MOF-based composites. In particular, hygroscopic salts, such as  $\text{CaCl}_2$  and  $\text{LiCl}$ , were encapsulated *in situ* during the synthesis of UiO-66 beads and their water sorption properties were evaluated. Interestingly, the water uptakes of the composites were higher than pristine MOF and the retention of water after the desorption process was significantly lower compare to the pristine salt. We also demonstrated the potential applicability of these composites for applications in adsorption heat transformation processes such as thermal batteries and chillers. Indeed, we showed that, for both applications, our materials presented good performance compared to the traditional working pairs based on silica or zeolites. For instance, the working pair **CaCl<sub>2</sub>@UiO-66\_53/water** showed a high capacity and energetic efficiency (COP = 0.83), which is significantly higher than other “composite salt in porous matrix” (CSPMs).

Then, we demonstrated the potential of the spray-drying technique to perform covalent chemistry. Firstly, we showed that Schiff based condensation reactions can be performed between discrete molecules and either in the pores of the MOFs in a very fast and continuous way. To this end, UiO-66-NH<sub>2</sub> and ZIF-90 were post-synthetically modified with three different aldehydes and two different primary alkyl amines, achieving conversion efficiencies up to 20 and 42 %, respectively. Moreover, we demonstrated that the aldehydes groups in ZIF-90 can be cross-linked by using a diamine molecule with a conversion efficiency of 70 %. This cross-linking has been completely characterized thanks to the combination of different techniques, such as FT-IR, <sup>1</sup>H-NMR, <sup>13</sup>C MAS NMR and ESI-MS.

These results open new opportunities for the exploration and expansion of the spray-drying technique to perform covalent reactions. Accordingly, we finally developed a strategy based on the use of the spray-drying combined with a dynamic covalent chemistry process. Here, we synthesized three different crystalline imine-based COFs superstructures with comparable sorption properties with the bulk

analogues. In addition, we demonstrated that this strategy enables the formation of COF-based composites by encapsulating two different species, Rose Bengal (dye) and magnetic nanoparticles ( $\text{Fe}_2\text{O}_3$ ), into the COF superstructures.



# Glossary

---



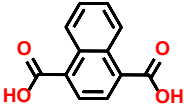
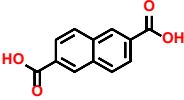
## Acronyms

Abbreviation	Definition
<b>AHT</b>	Adsorption Heat Transformation
<b>ANG</b>	Adsorbed Natural Gas
<b>AWG</b>	Atmospheric Water Generators
<b>BASF</b>	Badische Anilin- und Soda-Fabrik
<b>BET</b>	Brunauer-Emmett-Teller
<b>CAU</b>	Christian Albrechts University
<b>CNG</b>	Compressed Natural Gas
<b>COF</b>	Covalent-Organic Framework
<b>CON</b>	Covalent Organic Nanosheet
<b>COP</b>	Coefficient of Performance
<b>CSD</b>	Cambridge Structural Database
<b>CSPM</b>	Composite Salt in Porous Matrix
<b>CTF</b>	Covalent Triazine Framework
<b>DCC</b>	Dynamic Covalent Chemistry
<b>DMA</b>	<i>N,N</i> -Dimethylacetamide
<b>DMF</b>	<i>N,N</i> -Dimethylformamide
<b>DMSO</b>	Dimethyl Sulfoxide
<b>DOE</b>	US Department of Energy
<b>EDX</b>	Elemental Mapping with Energy Dispersive X-ray Spectrometry
<b>FESEM</b>	Field-Emission Scanning Electron Microscopy
<b>FT-IR</b>	Fourier-Transform Infrared Spectroscopy
<b>HAADF-STEM</b>	High-Angle Annular Dark-Field Scanning Transmission Electron Microscopy
<b>HKUST</b>	Hong Kong University of Science and Technology
<b>HR-TEM</b>	High-Resolution Transmission Electron Microscopy
<b>ICP-OES</b>	Inductively Coupled Plasma – Optical Emission Spectroscopy
<b>ILAG</b>	Ion-and Liquid Assisted Grinding
<b>INPs</b>	Inorganic Nanoparticles
<b>IRMOF</b>	Isorecticular MOF
<b>IUPAC</b>	International Union of Pure and Applied Chemistry
<b>LAG</b>	Liquid-Assisted Grinding
<b>LZU</b>	Lanzhou University
<b>MAS NMR</b>	Magic Angle Spinning Nuclear Magnetic Resonance
<b>MIL</b>	Material Institut Lavoisier

<b>MOF</b>	Metal-Organic Framework
<b>MTV</b>	Multivariate
<b>NG</b>	Natural Gas
<b>NOTT</b>	Nottingham University
<b>NU</b>	Northwestern University
<b>PCN</b>	Porous Coordination Network
<b>PCP</b>	Porous Coordination Polymer
<b>PFA</b>	Perfluoroalkoxy alkane
<b>PTFE</b>	Polytetrafluoroethylene
<b>RH</b>	Relative Humidity
<b>RON</b>	Research Octane Number
<b>SBU</b>	Secondary Building Unit
<b>SD</b>	Spray-Drying
<b>SDCF</b>	Spray-Drying Continuous Flow
<b>SFG</b>	Solvent-Free Grinding
<b>STP</b>	Standard Temperature & Pressure
<b>TGA</b>	Thermogravimetric Analysis
<b>TOF</b>	Turnover Frequency
<b>TON</b>	Turnover Number
<b>TSE</b>	Twin-Screw Extrusion
<b>UiO</b>	University of Oslo
<b>UTSA</b>	University of Texas at San Antonio
<b>XRPD</b>	X-ray Powder Diffraction
<b>ZIF</b>	Zeolitic Imidazolate Framework

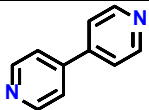
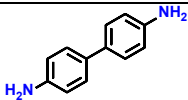
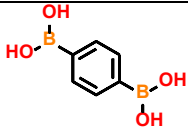
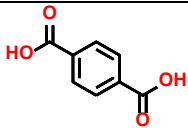
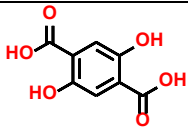
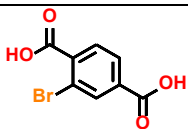
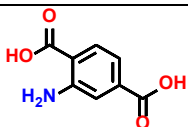
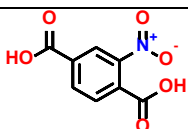
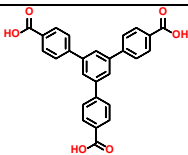
---

### Organic Ligands

Abbreviation	Definition	Structure
<b>1,4-NDC</b>	1,4-naphthalenedicarboxylic acid	
<b>2,6-NDC</b>	2,6-naphthalenedicarboxylic acid	

---

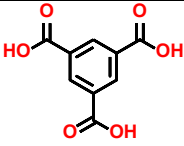
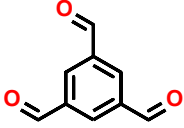
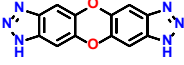
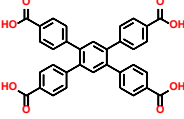
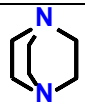
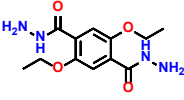
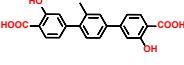
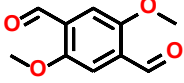
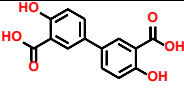
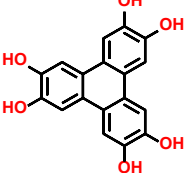
---

<b>4,4'-bpy</b>	4,4'-bipyridine	
<b>BD</b>	benzidine	
<b>BDBA</b>	benzene-1,4-diboronic acid	
<b>BDC</b>	1,4-benzenedicarboxylic acid	
<b>BDC-(OH)2/DHTP</b>	2,5-dihydroxyterephthalic acid	
<b>BDC-Br</b>	2-bromoterephthalic acid	
<b>BDC-NH2</b>	2-aminoterephthalic acid	
<b>BDC-NO2</b>	2-nitroterephthalic acid	
<b>BFBIm</b>	5,6-bis(4-formylbenzyl)-1,3-dimethyl-benzimidazolium bromide	
<b>BTB</b>	4,4',4''-benzenetribenzoate	

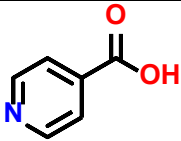
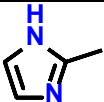
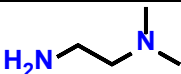
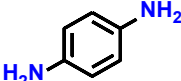
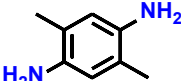
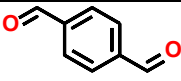
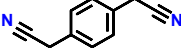
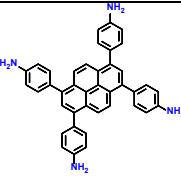
---

## Acronyms

---

<b>BTC</b>	benzene-1,3,5-tricarboxylic acid	
<b>BTCA</b>	1,3,5-benzenetricaldehyde	
<b>BTDD</b>	bis(1H-1,2,3-triazolo[4,5-b],[4',5'-i])dibenzo[1,4]dioxin	
<b>BTEB/TCPB</b>	1,2,4,5-tetrakis(4-carboxyphenyl)benzene	
<b>BTT</b>	1,3,5-tris(2H-tetrazol-5-yl)benzene	
<b>DABCO</b>	1,4-diazabicyclo[2.2.2]octane	
<b>DETH</b>	2,5-diethoxy-terephthalohydrazide	
<b>DH<sub>3</sub>PhDC</b>	2',5'-dimethyl-3,3''-dihydroxy-[1,1':4',1''-terphenyl]-4,4''-dicarboxylic acid	
<b>DMTP</b>	dimethoxyterephthaldehyde	
<b>dobpdc</b>	4,4'-Dihydroxybiphenyl-3,3'-dicarboxylic acid	
<b>HHTP</b>	2,3,6,7,10,11-Hexahydroxytriphenylene	

---

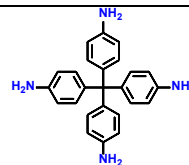
<b>INA</b>	isonicotinic acid	
<b>mim</b>	2-methylimidazole	
<b>MMEM</b>	N,N-dimethylethylenediamine	
<b>PPD/Pa-1</b>	<i>p</i> -phenylenediamine	
<b>Pa-2</b>	2,5-dimethyl- <i>p</i> -phenylenediamine	
<b>PDA</b>	terephthalaldehyde	
<b>PDAN</b>	1,4-phenylenediacetonitrile	
<b>PO</b>	5,15-dipyridyl-10,20-bis(pentafluorophenyl) porphyrin	
<b>PyTTA</b>	4,4',4'',4'''-(pyrene-1,3,6,8-tetrayl) tetraaniline	
<b>PYZ</b>	pyrazine	

---

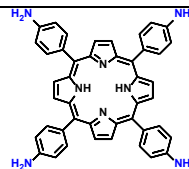
## Acronyms

---

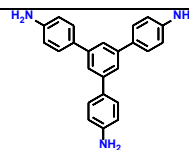
**TAM** tetra(4-aminophenyl)methane



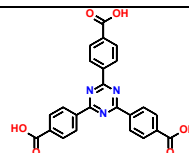
**TAP** 5,10,15,20-tetrakis(4-aminophenyl)-21H,23H-porphine cobalt(II)



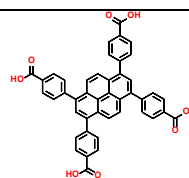
**TAPB** 1,3,5-tris-(4-aminophenyl)benzene



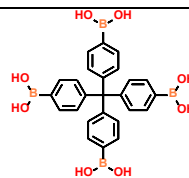
**TATB** 4,4',4''-s-triazine-2,4,6-triyltribenzoate)



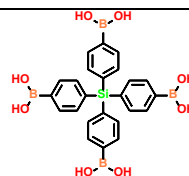
**TBAPy** 1,3,6,8-tetra(4'-carboxyphenyl)pyrene



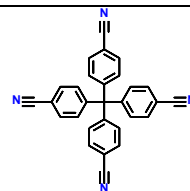
**TBPM** tetra(4-dihydroxyborylphenyl)methane



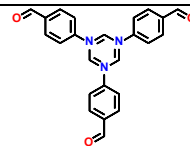
**TBPS** tetra(4-dihydroxyborylphenyl) silane



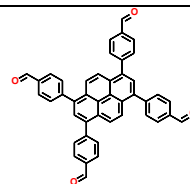
**TCTPM** 4,4',4'',4'''-tetracyanotetraphenylmethane



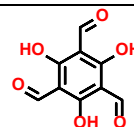
**TFPT** 1,3,5-tris-(4-formyl-phenyl)triazine



**TFPPy** 1,3,6,8-tetrakis(4-formylphenyl)pyrene



**Tp** 1,3,5-triformylphloroglucinol





# Annex 1

---



## List of Publications

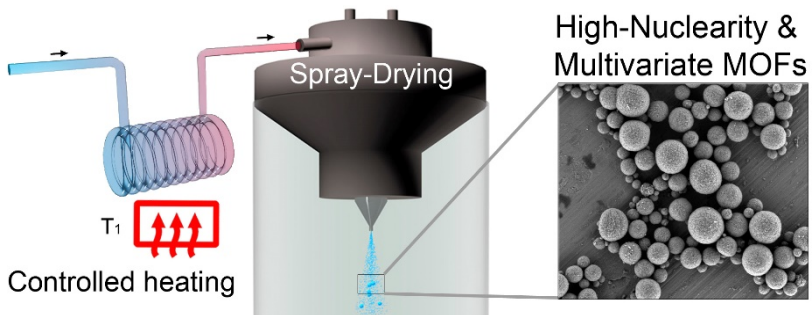
The publications related to the main objectives of this PhD Thesis are listed below:

1. **Garzón-Tovar, L.**, Cano-Sarabia, M., Carne-Sánchez, A., Carbonell, C., Imaz, I. and Maspoch, D. "A spray-drying continuous-flow method for simultaneous synthesis and shaping of microspherical high nuclearity MOF beads". *Reaction Chemistry & Engineering*, **2016**, 1, 533-539.
2. Guillerm, V., **Garzón-Tovar, L.**, Yazdi, A., Imaz, I., Juanhuix, J. and Maspoch, D. "Continuous One-Step Synthesis of Porous M-XF<sub>6</sub>-Based Metal-Organic and Hydrogen-Bonded Frameworks". *Chemistry—A European Journal*, **2017**, 23, 6829-6835.
3. **Garzón-Tovar, L.**, Pérez-Carvajal, J., Imaz, I. and Maspoch, D. "Composite Salt in Porous Metal-Organic Frameworks for Adsorption Heat Transformation". *Advanced Functional Materials*, **2017**, 27, 1606424.
4. **Garzón-Tovar, L.**, Rodríguez-Hermida, S., Imaz, I. and Maspoch, D. "Spray Drying for Making Covalent Chemistry: Postsynthetic Modification of Metal–Organic Frameworks". *Journal of the American Chemical Society*, **2017**, 139, 897-903.
5. **Garzón-Tovar, L.**, Avci-Camur, C., Rodríguez-San-Miguel, D., Imaz, I., Zamora, F. and Maspoch, D. "Spray drying for making covalent chemistry II: synthesis of covalent-organic framework superstructures and related composites". *Chemical Communications*, **2017**, 53, 11372-11375.

The author of this Thesis also contributed his work in the following publications (not included in the present manuscript) and the files are included:

6. **Garzón-Tovar, L.**, Carne-Sánchez, A., Carbonell, C., Imaz, I. and Maspoch, D. “Optimised room temperature, water-based synthesis of CPO-27-M metal-organic frameworks with high space-time yields”. *Journal of Materials Chemistry A*, **2015**, 3, 20819-20826.
7. Yazdi, A., Abo Markeb, A., **Garzón-Tovar, L.**, Patarroyo, J., Moral-Vico, J., Alonso, A., Sánchez, A., Bastus, N., Imaz, I., Font, X., Puntès, V. and Maspoch, D. “Core-shell Au/CeO<sub>2</sub> nanoparticles supported in UiO-66 beads exhibiting full CO conversion at 100 °C”. *Journal of Materials Chemistry A*, **2017**, 5, 13966-13970.
8. Espín, J., **Garzón-Tovar, L.**, Carne-Sánchez, A., Imaz, I. and Maspoch, D. “Photothermal activation of Metal-Organic Frameworks using a UV-Vis light source”. *ACS Applied Materials & Interfaces*, **2018**, 10, 9555-9562
9. **Garzón-Tovar, L.**, Espín, J., Boix, G., Imaz, I. and Maspoch, D. “The photothermal effect in MOFs: covalent post-synthetic modification of MOFs mediated by UV-Vis light under solvent-free conditions”. *Chemical Communications*, **2018**, 54, 4184.

# A spray-drying continuous-flow method for simultaneous synthesis and shaping of microspherical high nuclearity MOF beads







Cite this: *React. Chem. Eng.*, 2016, 1, 533

## A spray-drying continuous-flow method for simultaneous synthesis and shaping of microspherical high nuclearity MOF beads†

L. Garzón-Tovar,<sup>a</sup> M. Cano-Sarabia,<sup>a</sup> A. Carné-Sánchez,<sup>a</sup> C. Carbonell,<sup>a</sup> I. Imaz<sup>a\*</sup> and D. Maspoch<sup>a,b</sup>

Metal-organic frameworks (MOFs) are among the most attractive porous materials currently available. However, one of the challenges precluding their industrial exploitation is the lack of methods for their continuous production. In this context, great advances have been enabled by recently discovered, novel continuous-fabrication methods such as mechanosynthesis, electrochemistry, continuous-flow synthesis and spray-drying. Herein we report the benefits of coupling two of these processes—spray-drying and continuous flow—for continuous synthesis of MOFs assembled from high-nuclearity secondary building units (SBUs). Using the resulting spray-drying continuous flow-assisted synthesis, we have prepared numerous members of diverse MOF families, including the UiO-66, Fe-BTC/MIL-100 and  $[\text{Ni}_6(\text{OH})_4(\text{H}_2\text{O})_2(\text{L})_6]$ , (where L = 1*H*-pyrazole-4-carboxylic acid) series. Interestingly, all of these MOFs were automatically obtained as compact microspherical superstructures (beads). We anticipate that our strategy could be easily employed for synthesizing and shaping multivariate (MTV) MOFs.

Received 24th March 2016,  
Accepted 6th July 2016

DOI: 10.1039/c6re00065g

rsc.li/reaction-engineering

### Introduction

Metal-organic frameworks (MOFs) are an emerging class of crystalline porous materials that have garnered major interest due to their varied chemical composition, diverse pore sizes and shapes, large surface areas, tailored internal surfaces, and flexible structures. These properties make MOFs potentially useful for myriad applications, including gas storage, separation, catalysis, molecular sensing, heat-pump processes, contaminant removal, and drug delivery.<sup>1–6</sup> However, despite these possibilities, the industrial applicability and economic feasibility of MOFs are currently limited, owing to a dearth of practical and cost-effective methods for pilot-scale synthesis. In this context, one approach that has traditionally been proposed for MOFs is solvothermal synthesis, which is usually conducted in closed reactors. However, other processes have recently begun to be developed in the hopes of achieving continuous, solvent-free and/or green synthesis of MOFs. These methods basically include mechanosynthesis,<sup>7,8</sup>

electrochemistry,<sup>9</sup> continuous-flow techniques<sup>10,11</sup> and spray-drying,<sup>12,13</sup> some of which obviate the toxic solvents or cumbersome filtration of earlier methods.

We recently reported that the well-known industrial technique of spray-drying can also be considered as a general, low-cost and scalable method for the continuous synthesis of MOFs in the form of spherical structures, nanoparticles and composites.<sup>12</sup> Initially, we found that this methodology enables the production—even up to the kilogram scale—of archetypical MOFs such as HKUST-1 and related paddle-wheel Cu(II)-based MOFs (e.g. Cu-BDC, NOTT-100) in high yields and without any loss of sorption capabilities. We also found that this method could be extended to other MOF families such as MILs, UiOs, and ZIFs. However, whilst most MOFs could be synthesised *via* spray-drying, MOFs assembled from high-nuclearity second-building units (SBUs) are a more challenging target. Indeed, most of our attempts at spray-drying synthesis of these materials result in low yields and/or poor sorption capabilities. We attributed this problem chiefly to the inherently rapid drying kinetics in spray-drying, which complicate the formation of high nuclearity SBUs. In fact, several studies have suggested that the formation of SBUs is cardinal in MOF assembly, as they are most likely required for the nucleation and subsequent crystal growth of MOFs.<sup>14–16</sup>

Herein we describe an updated version of our spray-drying method, which enhances the production of high-nuclearity MOFs. Specifically, by introducing a continuous-flow reactor

<sup>a</sup> Catalan Institute of Nanoscience and Nanotechnology (ICN2), CSIC and The Barcelona Institute of Science and Technology, Campus UAB, Bellaterra, 08193 Barcelona, Spain. E-mail: inhar.imaz@icn.cat, daniel.maspoch@icn.cat

<sup>b</sup> ICREA, Pg. Lluís Companys 23, 08010 Barcelona, Spain

† Electronic supplementary information (ESI) available: Synthetic procedure, tables listing the yield,  $S_{\text{BET}}$  values and synthesis conditions of UiO-66, obtained by systematically varying the feed rate, equivalents of water, and bath temperature. XRD patterns,  $N_2$  isotherms and SEM images of the materials synthesised. See DOI: 10.1039/c6re00065g

at the entrance of the spray dryer (Fig. 1a and b), we have devised a continuous two-step method that combines the benefits of both systems. It works as follows: firstly, the precursor solution containing the metal salt and the organic linker is injected into a continuous coil flow reactor encased in a thermostatic oil tank, where it is heated at a certain temperature ( $T_1$ ) to promote SBU formation and nucleation. Here, the residence time ( $t$ ) of the precursor solution in the coil flow reactor is controlled by the rate of the pump (the *feed rate*). Since the outlet flow of the reactor is directly connected to the nozzle of the spray-dryer, the pre-heated solution is automatically injected into the spray-drier at the same feed rate. The solution is then atomised using a two-fluid nozzle and dried at a certain temperature ( $T_2$ ) and flow rate, such that the MOF growth is confined to individual micro-reactors (*i.e.* the atomised droplets).<sup>12</sup> The whole continuous process enables the collection of dried MOFs shaped in the form of microspherical superstructures (beads). Furthermore, the solvent used can simply be recovered, making the process both cost- and waste-efficient.

We first demonstrated the performance of our new method by assembling several members of the UiO-66 series, including the ionic UiO-66<sup>17</sup> and related MOFs UiO-66-NH<sub>2</sub>,<sup>18</sup> UiO-66-NO<sub>2</sub>,<sup>18</sup> UiO-66-acetamido,<sup>19</sup> UiO-66-Br,<sup>18</sup> UiO-66-(OH)<sub>2</sub>,<sup>20</sup> UiO-66-1,4-NDC (where 1,4-NDC is 1,4-naphthalenedicarboxylate)<sup>19</sup> and UiO-66-2,6-NDC (where 2,6-NDC is 2,6-naphthalenedicarboxylate).<sup>21,22</sup> We then extended the synthesis to other high-nuclearity MOFs such as Fe-BTC/MIL-100<sup>23</sup> and [Ni<sub>6</sub>(OH)<sub>4</sub>(H<sub>2</sub>O)<sub>2</sub>(L)<sub>6</sub>]<sub>n</sub> (where L = 1*H*-pyrazole-4-carboxylic acid).<sup>24</sup> These examples cover some of the best-known MOFs built from high-nuclearity metal

clusters. We envision that by introducing different organic linkers into the MOF precursor solution before the synthesis begins, we should be able to use our spray-drying continuous-flow method to prepare microspherical multivariate (MTV) MOFs.<sup>25,26</sup>

## Results and discussion

We began with the synthesis of UiO-66, a robust, closely-packed, three-dimensional cubic MOF assembled by connecting hexanuclear [Zr<sub>6</sub>O<sub>4</sub>(OH)<sub>4</sub>] oxoclusters through 1,4-terephthalate (BDC) linkers.<sup>27</sup> UiO-66, which typically exhibits surface areas ( $S_{\text{BET}}$ ) ranging from 1100–1250 m<sup>2</sup> g<sup>-1</sup>,<sup>17</sup> has already been synthesised by various methods, including solvothermal (typical yields = 90–97%; reaction time = 24 h),<sup>28,29</sup> hydrothermal (yield = 63%; reaction time = 24 h),<sup>30</sup> and continuous flow (yield = 63%) syntheses.<sup>11</sup> In our optimised spray-drying continuous flow-assisted synthesis of UiO-66, a precursor solution containing ZrCl<sub>4</sub>, BDC, H<sub>2</sub>O and DMF in a molar ratio of 1 : 1 : 40 : 135 (concentration of ZrCl<sub>4</sub> = 0.1 M) was injected into the coil flow reactor at a feed rate of 2.4 mL min<sup>-1</sup> and at a  $T_1$  of 115 °C. The residence time inside the coil flow reactor was 63 s. The resulting pre-heated solution was then spray dried at a  $T_2$  of 180 °C and a flow rate of 336 mL min<sup>-1</sup>, using a B-290 Mini Spray Dryer (BUCHI Labortechnik), immediately affording a white powder. This powder was washed with DMF and ethanol, and finally dried at 80 °C (yield = 70%). Note here that, under these optimized conditions, the space-time yield (STY) is 19.6 kg m<sup>-3</sup> d<sup>-1</sup>. This STY is much higher than that previously reported using the conventional spray drying method (4.0 kg m<sup>-3</sup> d<sup>-1</sup>), in which the reactant solution was also preheated for two hours before spraying.<sup>12</sup>

Field-emission scanning electron microscopy (FESEM) images and X-ray powder diffraction (XRPD) patterns of the resulting solid revealed the homogeneous formation of UiO-66 in the form of spherical beads (Fig. 1c–e and S1†). These microscale beads comprise multiple UiO-66 nanoparticles, contain a dense core, and have an average diameter of 4.3 ± 2.6 μm (Fig. S1†). The microporosity of the synthesised UiO-66 was confirmed by nitrogen-adsorption measurements, which gave an  $S_{\text{BET}}$  value of 1106 m<sup>2</sup> g<sup>-1</sup> (Fig. S2†). This value is consistent with previously reported values,<sup>17</sup> thus confirming the quality of our synthesised UiO-66.

We would like to point out that the spherical MOF superstructures (beads) that we prepared using our spray-drying continuous flow-assisted process are highly compact, unlike the hollow superstructures that we had previously obtained by spray-drying.<sup>12</sup> We attribute this difference to the formation, inside the reactor, of a suspension containing a primary nucleus. In a general spray-drying process, the atomised droplets are exposed to hot air, the solvent evaporates and consequently, the droplet surface shrinks.<sup>31</sup> During this process, hollow superstructures are formed when there is a non-linear change in precursor concentration at the droplet: specifically, it causes the formation of an impermeable shell and

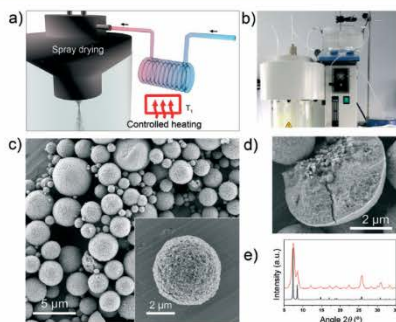


Fig. 1 (a, b) Schematic illustration (a) and photograph (b) showing the set-up for spray-drying continuous flow-assisted synthesis of high-nuclearity MOFs. (c) Representative FESEM images of microspherical UiO-66 beads prepared by this process. (d) FESEM image of a mechanically broken bead, revealing the dense core. (e) XRPD diffractogram of UiO-66 powder (red), as compared to the corresponding simulated powder pattern (black). Scale bars: 5 μm (c) and 2 μm (d, and c, inset).

the generation of gas at the core.<sup>32,33</sup> However, in our case, uniform precursor concentration and droplet temperature are reached, owing to the presence of the uniformly-distributed nuclei in the droplet. The rate at which the nucleus can be brought to the surface by diffusion is lower than the rate at which the nucleus can grow during the drying- evaporation process. This difference favours a linear change in precursor concentration and temperature at the droplet, and consequently, drives the formation of dense superstructures.

To prove that the effective synthesis of UiO-66 results from using both techniques in tandem, rather than simply from one of them, we separately performed the spray-drying step and the continuous-flow step using the aforementioned conditions. Spray-drying alone afforded a non-porous amorphous solid (Fig. S3†), whereas continuous-flow synthesis alone provided UiO-66 (Fig. S4†), albeit in a much lower yield (12%) and quality ( $S_{\text{BET}} = 708 \text{ m}^2 \text{ g}^{-1}$ ) than that obtained when the two methods were combined.

To optimise the synthesis of a given MOF using our spray-drying continuous flow-assisted method, one can adjust the standard reaction parameters: the reagents and solvents used, the stoichiometry of the precursor solution, and the concentration of the precursors. Moreover, one can tune method-specific parameters such as the residence time ( $t$ ), the two temperatures ( $T_1$  and  $T_2$ ), and the flow rate. Accordingly, we began our optimisation of the synthesis of UiO-66 by selecting  $\text{ZrCl}_4$  and BDC as reagents, DMF and  $\text{H}_2\text{O}$  as solvents, an initial concentration of 0.1 M for both reagents, a final molar ratio ( $\text{Zr/BDC}/\text{H}_2\text{O}/\text{DMF}$ ) of 1:1:30:135, a  $T_1$  of 115 °C, a  $T_2$  of 180 °C, and a flow rate of 336  $\text{ml min}^{-1}$ . It is important to highlight here that we introduced water into the precursor solution because it is known to favour the formation of UiO-66.<sup>20,29</sup> Also, we selected a concentration of 0.1 M because it is the maximum concentration that has already been demonstrated for the continuous flow synthesis of UiO-66.<sup>11,34</sup> We chose a  $T_2$  of 180 °C because it is the minimum temperature needed to fully evaporate DMF inside the spray-drier, and we chose a flow rate of 336  $\text{ml min}^{-1}$  because we had previously found it to be optimal for the spray-drying synthesis of MOFs.<sup>12</sup>

Using the pre-defined conditions described above, we sought to optimise the residence time ( $t$ ) of the precursor solution in the coil flow reactor. To this end, we systematically varied  $t$  (35, 41, 48, 63, 94 or 130 s, which correspond to feed rates of 4.5, 3.6, 3.0, 2.4, 1.8 or 1.2  $\text{ml min}^{-1}$ , respectively) to evaluate its effect on the purity, yield and  $S_{\text{BET}}$  of the synthesised UiO-66 (Table S1; Fig. S5†). We found that the optimal  $t$  value was 63 s. Interestingly, we observed clogging effects at  $t$  values of 94 s and 130 s, which we ascribed to the formation of large precipitates of UiO-66 inside the coil flow reactor. Importantly, we observed that at 94 s and 130 s, the UiO-66 (most of which had been synthesised in the coil flow reactor) exhibited much lower  $S_{\text{BET}}$  values (667 and 687  $\text{m}^2 \text{ g}^{-1}$ , respectively) than that produced at  $t = 63$  s (1044  $\text{m}^2 \text{ g}^{-1}$ ). This observation was crucial because it further con-

firmed the benefits of the spray-drying step in the crystal growth of UiO-66. Indeed, when we reproduced the reaction using only the continuous-flow process (without the spray drying step; residence time = 94 s), UiO-66 was obtained in relatively high yield (58%, Fig. S6†) but with a low  $S_{\text{BET}}$  value (610  $\text{m}^2 \text{ g}^{-1}$ ), which was comparable to that obtained with the spray-drying continuous flow-assisted method using the same residence time. This result confirmed that as the residence time increases, the proportion of UiO-66 synthesised in the coil flow reactor increases and the quality of the product decreases.

Having determined the optimum residence time for the spray-drying continuous flow-assisted synthesis of UiO-66, we then studied the effects of  $\text{H}_2\text{O}$  as a co-solvent by varying the equivalents of it ( $x = 20, 30, 40, 45$  or 50; see Table S2 and Fig. S7†) in the  $\text{Zr/BDC}/\text{H}_2\text{O}/\text{DMF}$  (molar ratio = 1:1: $x$ :135) precursor solution. As expected,<sup>20,29</sup> we found that increasing the amount of  $\text{H}_2\text{O}$  led to better yields: thus at  $x = 40$ , the yield was 70% ( $S_{\text{BET}} = 1106 \text{ m}^2 \text{ g}^{-1}$ ), and at  $x = 45$ , the yield was 84% ( $S_{\text{BET}} = 963 \text{ m}^2 \text{ g}^{-1}$ ). However, we could not surpass a value of  $x = 50$ , the value at which the precursor solution begins to boil inside the coil flow reactor, consequently impeding its correct flow.

Finally, we also studied the effect of  $T_1$  in the coil flow reactor, by decreasing the value from 115 °C to 90 °C (Table S3 and Fig. S8†). We observed that this decrease causes a decrease in the yield and in the  $S_{\text{BET}}$ . This observation was very important because it corroborated that a minimum  $T_1$  is required in the coil flow reactor to generate sufficient energy to induce nucleation.

To demonstrate the generality of our approach for high-nuclearity MOFs, we used it to synthesise several other members of the UiO-66 series, including UiO-66- $\text{NH}_2$ , UiO-66- $\text{NO}_2$ , UiO-66-acetamido, UiO-66-Br, UiO-66-(OH)<sub>2</sub>, UiO-66-1,4-NDC and UiO-66-2,6-NDC. Fig. 2a-d and f show typical FESEM images of the resulting microspherical beads (0.5–5.9  $\mu\text{m}$ ) created by the close packing of smaller crystals (Fig. S9 and Table S4†). The different samples reveal a rather broad size distribution. This is mainly because the synthetic conditions used for each UiO-66 were optimized to synthesise them in a good quality and yield instead of optimizing the droplet size distribution, a parameter that usually depends on the liquid viscosity, surface tension, mass rate of atomization air and liquid feed rate. For all synthesised members of the UiO-66 series, XRPD studies confirmed their phase purity (Fig. 2e and g), whereas nitrogen physical adsorption confirmed their microporosity: all the calculated BET surface areas were similar to previously reported values (Fig. 2h and S10–S16†).

We then extended our synthesis of high-nuclearity MOFs to Fe-BTC/MIL-100 and  $[\text{Ni}_6(\text{OH})_4(\text{H}_2\text{O})_2(\text{L})_6]_n$ , whose SBUs are a trinuclear iron cluster and an octanuclear nickel cluster, respectively. Microspherical beads of Fe-BTC/MIL-100 were obtained in very high yield (78%) and with a  $S_{\text{BET}}$  value of 1039  $\text{m}^2 \text{ g}^{-1}$  (Fig. 3b and d and S17†). We would like to point out to the reader that, whilst the XRD pattern exhibited low

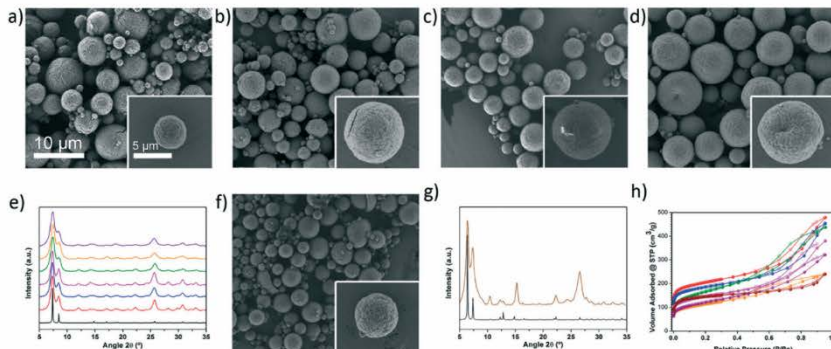


Fig. 2 Representative FESEM images showing the microspherical beads of a) UiO-66-NH<sub>2</sub>, b) UiO-66-NO<sub>2</sub>, c) UiO-66-Br, d) UiO-66-(OH)<sub>2</sub>, and f) UiO-66-2,6-NDC. e) XRPD diffractograms of the UiO-66 series (red: UiO-66-NH<sub>2</sub>, blue: UiO-66-NO<sub>2</sub>, pink: UiO-66-Br, green: UiO-66-acetamido, orange: UiO-66-(OH)<sub>2</sub>, purple: UiO-66-1,4-NDC), as compared to the simulated powder pattern for UiO-66 (black). g) XRPD diffractogram of UiO-66-2,6-NDC (coffee), as compared with the simulated pattern (black). h) N<sub>2</sub> adsorption isotherms of the synthesised UiO-66 series (red: UiO-66-NH<sub>2</sub>, blue: UiO-66-NO<sub>2</sub>, pink: UiO-66-Br, green: UiO-66-acetamido, orange: UiO-66-(OH)<sub>2</sub>, purple: UiO-66-1,4-NDC, coffee: UiO-66-2,6-NDC). Scale bars: 10 μm (all images) and 5 μm (all insets).

crystallinity and the  $S_{\text{BET}}$  value is much lower than the value obtained for Fe-BTC/MIL-100 synthesised under solvothermal conditions ( $S_{\text{BET}} = 2200 \text{ m}^2 \text{ g}^{-1}$ ), it is nevertheless comparable to that of the commercially available material Basolite F300 (maximum  $S_{\text{BET}} = 1040 \text{ m}^2 \text{ g}^{-1}$ )<sup>35,36</sup> and to that of the material previously synthesised by spray-drying ( $S_{\text{BET}} = 600$  or  $1010 \text{ m}^2 \text{ g}^{-1}$ ).<sup>13</sup> However, unlike the previously reported spray-drying synthesis, our spray-drying continuous flow-assisted method does not require the use of surfactants.

Alternatively,  $[\text{Ni}_6(\text{OH})_4(\text{H}_2\text{O})_2(\text{L})_6]_n$  was obtained as a highly crystalline material (yield = 60%; see Fig. 3a and c and S18†), with a higher  $S_{\text{BET}}$  value ( $377 \text{ m}^2 \text{ g}^{-1}$ ) than that previously reported ( $205 \text{ m}^2 \text{ g}^{-1}$ ).<sup>24</sup>

Having demonstrated that our spray-drying continuous flow-assisted method enables the formation of high-nuclearity microspherical MOFs, we pondered whether it could also be used for the synthesis of MTV MOFs that would combine the characteristics of different organic linkers. To explore this possibility, we reproduced the spray-drying continuous flow-assisted synthesis of UiO-66, except that instead of pure BDC, we used a mixture of BDC and Br-BDC, testing different BDC/BDC-Br molar ratios (1:0.5, 1:1 or 1:2). In all cases, FESEM and XRPD of the resulting white solids confirmed the formation of the characteristic beads made of pure UiO-66-type phase (Fig. 4a, b and S19†). Quantitative analyses of the digested microspherical beads by <sup>1</sup>H-NMR spectroscopy (Fig. 4c and S20†) confirmed that both linkers were present in the synthesised MTV-UiO-66 samples, revealing BDC/BDC-Br molar ratios of 1:0.6, 1:1.3 or 1:2.3. Interestingly, these ratios were close to those expected from the corresponding input ratios used in the reaction mixtures. We further studied the porosity of all the synthesised MTV-UiO-66 through nitrogen sorption measurements conducted at 77 K. Remarkably, all the products were porous to N<sub>2</sub>. As expected, the  $S_{\text{BET}}$  values decreased with increasing equivalents of BDC-Br: 818  $\text{m}^2 \text{ g}^{-1}$  for 0.6; 678  $\text{m}^2 \text{ g}^{-1}$  for 1.3; and 570  $\text{m}^2 \text{ g}^{-1}$  for 2.3 (Fig. 4d and S21–S23†). We attributed this trend to an increase in steric hindrance resulting from the introduction of more (bulky) BDC-Br linkers into the UiO-66 framework.

Finally, we sought to increase the complexity of the synthesised MTV-UiO-66 by mixing the BDC, BDC-Br and

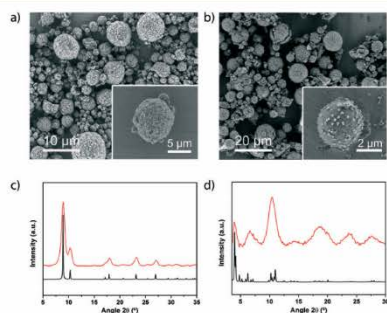


Fig. 3 (a) Representative FESEM images showing a general view of the microspherical beads of a)  $[\text{Ni}_6(\text{OH})_4(\text{H}_2\text{O})_2(\text{L})_6]_n$ , and b) MIL-100. c) XRPD diffractogram of the obtained powder compared with the simulated powder pattern of  $[\text{Ni}_6(\text{OH})_4(\text{H}_2\text{O})_2(\text{L})_6]_n$  (black). d) XRPD diffractogram of the obtained powder compared with the simulated powder pattern of MIL-100. Scale bars: 10 μm (a) and 20 μm (b). Insets: 5 μm (a) and 2 μm (b).

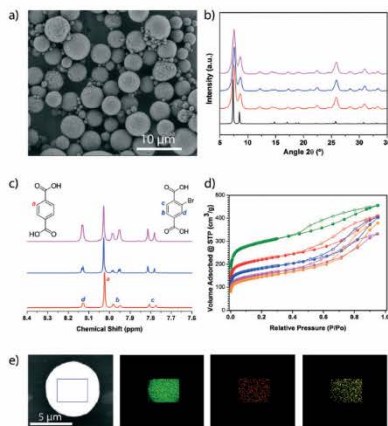


Fig. 4 (a) Representative FESEM image showing a general view of the microspherical beads of the MTV-UiO-66 with a BDC/BDC-Br molar ratio of 1:0.6. (b) XRPD diffractograms of the MTV-UiO-66 collected after their synthesis at different BDC/BDC-Br molar ratios (red: 1:0.6, blue: 1:1.3, pink: 1:2.3), as compared to the simulated powder pattern for UiO-66 (black). (c)  $^1\text{H}$ -NMR spectra of the digested samples of the MTV-UiO-66 synthesised at different BDC/BDC-Br molar ratios (red: 1:0.6, blue: 1:1.3, pink: 1:2.3). (d)  $\text{N}_2$  adsorption isotherms of the synthesised UiO-66 (green), UiO-66-Br (orange) and MTV-UiO-66 at different BDC/BDC-Br molar ratios (red: 1:0.6, blue: 1:1.3, pink: 1:2.3). (e) Elemental mapping with EDX performed on a single spherical bead of MTV-UiO-66 (BDC, BDC-Br and BDC- $\text{NH}_2$ ), showing the homogeneous distribution of Zr (green), Br (red) and N (yellow). Scale bar: 10  $\mu\text{m}$  (a) and 5  $\mu\text{m}$  (e).

BDC- $\text{NH}_2$  linkers at a molar ratio of 1:1:1. Again, FESEM and XRPD of the resulting product (a yellow solid) revealed the formation of microspherical beads made of pure UiO-66-type phase, whereas the  $^1\text{H}$  NMR spectrum confirmed the presence of the three linkers at a molar ratio (BDC/BDC-Br/BDC- $\text{NH}_2$ ) of 1:1.1:0.6 (Fig. S19, S24, and S25 $^\dagger$ ). The presence of these linkers was further confirmed by elemental mapping with energy dispersive X-ray spectrometry (EDX) performed on a single bead, which revealed a highly uniform distribution of Zr, Br and N atoms (Fig. 4e). Additionally, this MOF was found to be porous to  $\text{N}_2$ , exhibiting an  $S_{\text{BET}}$  of 707  $\text{m}^2 \text{g}^{-1}$  (Fig. S26 $^\dagger$ ).

## Conclusions

In conclusion, we have reported an updated version of our spray-drying methodology for MOF fabrication, which enables simultaneous synthesis and shaping of microspherical high-nuclearity MOF beads. This new method is based on incorporating a continuous flow reactor at the entrance of the spray-drier. It thus combines the advantages of continuous

flow to those of spray-drying, providing MOFs in good yields, with excellent porosity and highly dense cores. Furthermore, it is amenable to the fabrication of MTV MOFs, thereby opening up new avenues for fine-tuning the porosity of these materials. We hope that our new method, together with existing ones (e.g. mechanochemistry, electrochemistry, and continuous-flow chemistry), will facilitate the industrial development and exploitation of MOFs.

## Experimental section

### Materials and methods

Zirconium chloride, nickel acetate tetrahydrate, iron(III) nitrate nonahydrate, terephthalic acid, 2-aminoterephthalic acid, 2-bromoterephthalic acid, 2-nitroterephthalic acid, 2,5-dihydroxyterephthalic acid, 1,4-naphthalenedicarboxylic acid, 2,6-naphthalenedicarboxylic acid, benzene-1,3,5-tricarboxylic acid and 1*H*-pyrazole-4-carboxylic acid were purchased from Sigma Aldrich. Dimethylformamide was obtained from Fisher Chemical. All the reagents were used without further purification. Deionised water, obtained with a Milli-Q $^\circledR$  system (18.2  $\text{M}\Omega \text{ cm}$ ), was used in all reactions. 2-Acetamidoterephthalic acid was synthesised according to a reported procedure. $^{37}$

X-ray powder diffraction (XRPD) patterns were collected on an X'Pert PRO MPDP analytical diffractometer (Panalytical) at 45 kV and 40 mA using  $\text{CuK}\alpha$  radiation ( $\lambda = 1.5419 \text{ \AA}$ ). Nitrogen adsorption and desorption measurements were performed at 77 K using an Autosorb-IQ-AG analyser (Quantachrome Instruments). Field-emission scanning electron microscopy (FESEM) images were collected on a FEI Magellan 400 L scanning electron microscope at an acceleration voltage of 2.0 kV and a FEI Quanta 650F scanning electron microscope at an acceleration voltage of 20.0 kV, using aluminium as a support.  $^1\text{H}$  NMR spectra were acquired on a Bruker Avance DRX-250 spectrometer, using a solution prepared by digesting 10 mg of sample in a mixture of 48% HF (20  $\mu\text{L}$ ) and  $\text{DMSO-}d_6$  (600  $\mu\text{L}$ ). The size distributions were determined by laser diffraction (LD) on a Mastersizer2000 (Malvern Instruments).

### Spray-drying continuous flow-assisted synthesis of UiO-66 series

In a typical synthesis, a solution of 0.1 M  $\text{ZrCl}_4$  and 0.1 M organic ligand in 15 ml of a mixture of DMF and  $\text{H}_2\text{O}$  (5.48:1) was injected into the coil flow reactor (Pyrex tube, inner diameter: 3 mm) at a feed rate of 2.4  $\text{ml min}^{-1}$  and at a  $T_1$  of 115  $^\circ\text{C}$ . The resulting pre-heated solution was then spray-dried at a  $T_2$  of 180  $^\circ\text{C}$  and a flow rate of 336  $\text{ml min}^{-1}$  using a Dryer B-290 Mini Spray (BUCHI Labortechnik; spray cap: 0.5 mm-hole). Finally, the collected solid was dispersed in DMF at room temperature under stirring overnight and precipitated by centrifugation. This process was repeated twice with ethanol instead of DMF. The final product was dried for 12 h at 80  $^\circ\text{C}$ . **UiO-66**: yield = 70%; purity = 54%;  $S_{\text{BET}} = 1106 \text{ m}^2 \text{g}^{-1}$ . **UiO-66- $\text{NH}_2$** : yield = 67%; purity = 49%;  $S_{\text{BET}} = 752 \text{ m}^2 \text{g}^{-1}$ . **UiO-66- $\text{NO}_2$** : yield = 62%; purity = 49%;  $S_{\text{BET}} = 679$

$\text{m}^2 \text{g}^{-1}$ . **UiO-66-acetamido**: yield = 51%; purity = 41%;  $S_{\text{BET}} = 586 \text{ m}^2 \text{g}^{-1}$ . **UiO-66-Br**: yield = 68%; purity = 62%;  $S_{\text{BET}} = 527 \text{ m}^2 \text{g}^{-1}$ . **UiO-66-(OH)<sub>2</sub>**: yield = 81%; purity = 67%;  $S_{\text{BET}} = 401 \text{ m}^2 \text{g}^{-1}$ . **UiO-66-1,4-NDC**: yield = 45%; purity = 45%;  $S_{\text{BET}} = 431 \text{ m}^2 \text{g}^{-1}$ . **UiO-66-2,6-NDC**: yield = 49%; purity = 37%;  $S_{\text{BET}} = 557 \text{ m}^2 \text{g}^{-1}$ .

#### Spray-drying continuous flow-assisted synthesis of $[\text{Ni}_6(\text{OH})_4(\text{H}_2\text{O})_2(\text{L})_6]_n$

A solution of 0.02 M  $\text{Ni}(\text{CH}_3\text{COO})_2 \cdot 4\text{H}_2\text{O}$  and 0.015 M 1*H*-pyrazole-4-carboxylic acid in 20 ml of a mixture of DMF and  $\text{H}_2\text{O}$  (4:1) was injected into the coil flow reactor (Pyrex tube, inner diameter: 3 mm) at a feed rate of  $2.4 \text{ ml min}^{-1}$  and at a  $T_1$  of 100 °C. The resulting pre-heated solution was then spray-dried at a  $T_2$  of 180 °C and a flow rate of  $336 \text{ ml min}^{-1}$  using a B-290 Mini Spray Dryer (BUCHI Labortechnik; spray cap: 0.5 mm-hole). Finally, the collected solid was dispersed in EtOH and precipitated by centrifugation. This two-step washing process was repeated with  $\text{Et}_2\text{O}$ . The final product was dried for 12 h at 60 °C. Yield = 60%; purity = 81%;  $S_{\text{BET}} = 377 \text{ m}^2 \text{g}^{-1}$ .

#### Spray-drying continuous flow-assisted synthesis of Fe-BTC/MIL-100

A solution of 0.1 M  $\text{Fe}(\text{NO}_3)_3 \cdot 9\text{H}_2\text{O}$  and 0.07 M BTC in 15 ml of DMF was injected into the coil flow reactor (Pyrex tube, inner diameter: 3 mm) at a feed rate of  $2.4 \text{ ml min}^{-1}$  and at a  $T_1$  of 135 °C. The resulting pre-heated solution was then spray-dried at a  $T_2$  of 180 °C and a flow rate of  $336 \text{ ml min}^{-1}$  using a B-290 Mini Spray Dryer (BUCHI Labortechnik; spray cap: 0.5 mm-hole). Finally, the collected solid was dispersed in  $\text{H}_2\text{O}$  and precipitated by centrifugation. This two-step washing process was repeated with EtOH. The final product was dried for 12 h at 70 °C. Yield = 78%; purity = 58%;  $S_{\text{BET}} = 1039 \text{ m}^2 \text{g}^{-1}$ .

#### Spray-drying continuous flow-assisted synthesis of the MTV-UiO-66 made of two linkers

A solution of 0.1 M  $\text{ZrCl}_4$  and 0.1 M ligand mixture (BDC and Br-BDC) in 15 ml of a mixture of DMF and  $\text{H}_2\text{O}$  (12.9:1) was injected into the coil flow reactor (Pyrex tube, inner diameter: 3 mm) at a feed rate of  $2.4 \text{ ml min}^{-1}$  and at a  $T_1$  of 115 °C. The resulting pre-heated solution was then spray-dried at a  $T_2$  of 180 °C and a flow rate of  $336 \text{ ml min}^{-1}$  using a B-290 Mini Spray Dryer (BUCHI Labortechnik; spray cap: 0.5 mm-hole). Finally, the collected solid was dispersed in DMF at room temperature under stirring overnight and precipitated by centrifugation. This process was repeated twice with ethanol instead of DMF. The final product was dried for 12 h at 80 °C.

#### Spray-drying continuous flow-assisted synthesis of the MTV-UiO-66 made of three linkers

A solution of 0.1 M  $\text{ZrCl}_4$ , 0.015 M BDC, 0.015 M  $\text{NH}_2\text{-BDC}$  and 0.015 M Br-BDC in 15 ml of a mixture of DMF and  $\text{H}_2\text{O}$

(12.9:1) was injected into the coil flow reactor (Pyrex tube, inner diameter: 3 mm) at a feed rate of  $2.4 \text{ ml min}^{-1}$  and at a  $T_1$  of 115 °C. The resulting pre-heated solution was then spray-dried at a  $T_2$  of 180 °C and a flow rate of  $336 \text{ ml min}^{-1}$  using a B-290 Mini Spray Dryer (BUCHI Labortechnik; spray cap: 0.5 mm-hole). Finally, the collected solid was dispersed in DMF at room temperature under stirring overnight and precipitated by centrifugation. This process was repeated twice with ethanol instead of DMF. The final product was dried for 12 h at 80 °C.

## Acknowledgements

This work was supported by the MINECO-Spain under the Project MAT2015-65354-C2-1-R and the EU FP7 project ERC-Co 615954. I. I. thanks the MINECO for a Ramón y Cajal Fellowship (RYC-2010-06530). ICN2 acknowledges support of the Spanish MINECO through the Severo Ochoa Centers of Excellence Programme (Grant SEV-2013-0295).

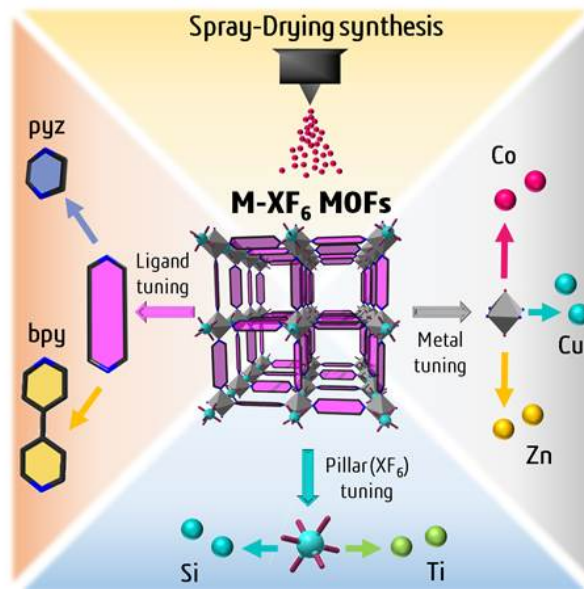
## Notes and references

- H. C. Zhou and S. Kitagawa, Special issue on metal-organic framework materials, *Chem. Soc. Rev.*, 2009, 1201.
- J. R. Long and O. M. Yaghi, Special issue on metal-organic framework materials, *Chem. Soc. Rev.*, 2014, 43, 5403.
- H. Furukawa, N. Ko, Y. B. Go, N. Aratani, S. B. Choi, E. Choi, A. Ö. Yazaydin, R. Q. Snurr, M. O'Keeffe, J. Kim and O. M. Yaghi, *Science*, 2010, 329, 424-428.
- P. Horcajada, R. Gref, T. Baati, P. K. Allan, G. Maurin, P. Couvreur, G. Férey, R. E. Morris and C. Serre, *Chem. Rev.*, 2012, 112, 1232-1268.
- M. D. Allendorf and V. Stavila, *CrystEngComm*, 2015, 17, 229-246.
- A. Carné, C. Carbonell, I. Imaz and D. Maspoch, *Chem. Soc. Rev.*, 2011, 40, 291-305.
- S. L. James, C. J. Adams, C. Bolm, D. Braga, P. Collier, T. Friscic, F. Grepioni, K. D. Harris, G. Hyett, W. Jones, A. Krebs, J. Mack, L. Maini, A. G. Orpen, I. P. Parkin, W. C. Shearouse, J. W. Steed and D. C. Waddell, *Chem. Soc. Rev.*, 2012, 41, 413-447.
- D. Crawford, J. Casaban, R. Haydon, N. Giri, T. McNally and S. L. James, *Chem. Sci.*, 2015, 6, 1645-1649.
- A. Martínez Joaristi, J. Juan-Alcañiz, P. Serra-Crespo, F. Kapteijn and J. Gascon, *Cryst. Growth Des.*, 2012, 12, 3489-3498.
- P. A. Bayliss, I. A. Ibarra, E. Perez, S. Yang, C. C. Tang, M. Poliakoff and M. Schroder, *Green Chem.*, 2014, 16, 3796-3802.
- M. Rubio-Martínez, M. P. Batten, A. Polyzos, K.-C. Carey, J. I. Mardel, K.-S. Lim and M. R. Hill, *Sci. Rep.*, 2014, 4, 5443.
- A. Carné-Sánchez, I. Imaz, M. Cano-Sarabia and D. Maspoch, *Nat. Chem.*, 2013, 5, 203-211.
- A. García Marquez, P. Horcajada, D. Grosso, G. Férey, C. Serre, C. Sanchez and C. Boissiere, *Chem. Commun.*, 2013, 49, 3848-3850.

- 14 O. Shekhhah, H. Wang, D. Zacher, R. A. Fischer and C. Woll, *Angew. Chem., Int. Ed.*, 2009, 48, 5038–5041.
- 15 D. C. Cantu, B. P. McGrail and V.-A. Glezakou, *Chem. Mater.*, 2014, 26, 6401–6409.
- 16 S. Surble, F. Millange, C. Serre, G. Ferey and R. I. Walton, *Chem. Commun.*, 2006, 1518–1520, DOI: 10.1039/B600709K.
- 17 J. H. Cavka, S. Jakobsen, U. Olsbye, N. Guillou, C. Lamberti, S. Bordiga and K. P. Lillerud, *J. Am. Chem. Soc.*, 2008, 130, 13850–13851.
- 18 M. Kandiah, M. H. Nilsen, S. Usseglio, S. Jakobsen, U. Olsbye, M. Tilset, C. Larabi, E. A. Quadrelli, F. Bonino and K. P. Lillerud, *Chem. Mater.*, 2010, 22, 6632–6640.
- 19 S. J. Garibay and S. M. Cohen, *Chem. Commun.*, 2010, 46, 7700–7702.
- 20 M. J. Katz, Z. J. Brown, Y. J. Colón, P. W. Siu, K. A. Scheidt, R. Q. Snurr, J. T. Hupp and O. K. Farha, *Chem. Commun.*, 2013, 49, 9449–9451.
- 21 V. Bon, I. Senkovska, M. S. Weiss and S. Kaskel, *CrystEngComm*, 2013, 15, 9572–9577.
- 22 V. Guillermin, F. Ragon, M. Dan-Hardi, T. Devic, M. Vishnuvarthan, B. Campo, A. Vimont, G. Clet, Q. Yang, G. Maurin, G. Ferey, A. Vittadini, S. Gross and C. Serre, *Angew. Chem., Int. Ed.*, 2012, 51, 9267–9271.
- 23 P. Horcajada, S. Surble, C. Serre, D.-Y. Hong, Y.-K. Seo, J.-S. Chang, J.-M. Grenèche, I. Margiolaki and G. Ferey, *Chem. Commun.*, 2007, 2820–2822, DOI: 10.1039/B704325B.
- 24 N. M. Padiál, E. Quartapelle Procopio, C. Montoro, E. López, J. E. Oltra, V. Colombo, A. Maspero, N. Masciocchi, S. Galli, I. Senkovska, S. Kaskel, E. Barea and J. A. R. Navarro, *Angew. Chem., Int. Ed.*, 2013, 52, 8290–8294.
- 25 H. Deng, C. J. Doonan, H. Furukawa, R. B. Ferreira, J. Towne, C. B. Knobler, B. Wang and O. M. Yaghi, *Science*, 2010, 327, 846–850.
- 26 Y. B. Zhang, H. Furukawa, N. Ko, W. Nie, H. J. Park, S. Okajima, K. E. Cordova, H. Deng, J. Kim and O. M. Yaghi, *J. Am. Chem. Soc.*, 2015, 137, 2641–2650.
- 27 M. Kim and S. M. Cohen, *CrystEngComm*, 2012, 14, 4096–4104.
- 28 S.-N. Kim, Y.-R. Lee, S.-H. Hong, M.-S. Jang and W.-S. Ahn, *Catal. Today*, 2015, 245, 54–60.
- 29 F. Ragon, P. Horcajada, H. Chevreau, Y. K. Hwang, U. H. Lee, S. R. Miller, T. Devic, J.-S. Chang and C. Serre, *Inorg. Chem.*, 2014, 53, 2491–2500.
- 30 Z. Hu, Y. Peng, Z. Kang, Y. Qian and D. Zhao, *Inorg. Chem.*, 2015, 54, 4862–4868.
- 31 W. H. Gauvin and S. Katta, *AIChE J.*, 1976, 22, 713–724.
- 32 V. S. Shabde and K. A. Hoo, *Ind. Eng. Chem. Res.*, 2006, 45, 8329–8337.
- 33 K. Okuyama and I. Wuled Lenggoro, *Chem. Eng. Sci.*, 2003, 58, 537–547.
- 34 S. Waitschat, M. T. Wharmby and N. Stock, *Dalton Trans.*, 2015, 44, 11235–11240.
- 35 <http://www.sigmaaldrich.com/technical-documents/articles/materials-science/metal-organic-frameworks/basolite-f300-commercial.html>, (accessed 03/12/2015, 2015).
- 36 A. Dhakshinamoorthy, M. Alvaro, P. Horcajada, E. Gibson, M. Vishnuvarthan, A. Vimont, J.-M. Grenèche, C. Serre, M. Daturi and H. Garcia, *ACS Catal.*, 2012, 2, 2060–2065.
- 37 A. Karmakar, M. F. C. Guedes da Silva and A. J. L. Pombeiro, *Dalton Trans.*, 2014, 43, 7795–7810.



# Continuous One-Step Synthesis of Porous M-XF<sub>6</sub>-Based Metal-Organic and Hydrogen-Bonded Frameworks





**Metal-organic Frameworks** | Hot Paper |

**Continuous One-Step Synthesis of Porous M-XF<sub>6</sub>-Based Metal-Organic and Hydrogen-Bonded Frameworks**

 Vincent Guillerm,<sup>[a]</sup> Luis Garzón-Tovar,<sup>[a]</sup> Amirali Yazdi,<sup>[a]</sup> Inhar Imaz,<sup>[a]</sup> Jordi Juanhuix,<sup>[b]</sup> and Daniel Maspoch<sup>\*,[a, c]</sup>

**Abstract:** Metal-organic frameworks (MOFs) built up from connecting M-XF<sub>6</sub> pillars through N-donor ligands are among the most attractive adsorbents and separating agents for CO<sub>2</sub> and hydrocarbons today. The continuous, one-step spray-drying synthesis of several members of this isorecticular MOF family varying the anionic pillar (XF<sub>6</sub> = [SiF<sub>6</sub>]<sup>2-</sup> and [TiF<sub>6</sub>]<sup>2-</sup>), the N-donor organic ligand (pyrazine and 4,4'-bipyridine) and the metal ion (M = Co, Cu and Zn) is demonstrated here. This synthetic method allows them to be obtained in the form of spherical superstructures assembled from nanosized crystals. As confirmed by CO<sub>2</sub> and N<sub>2</sub> sorption studies, most of the M-XF<sub>6</sub>-based MOFs synthesised

through spray-drying can be considered "ready-to-use" sorbents as they do not need additional purification and time consuming solvent exchange steps to show comparable porosity and sorption properties with the bulk/single-crystal analogues. Stability tests of nanosized M-SiF<sub>6</sub>-based MOFs confirm their low stability in most solvents, including water and DMF, highlighting the importance of protecting them once synthesised. Finally, for the first time it was shown that the spray-drying method can also be used to assemble hydrogen-bonded open networks, as evidenced by the synthesis of **MPM-1-TIFSiX**.

**Introduction**

The environmental impact associated with energy demand is a major problem worldwide.<sup>[1]</sup> For example, CO<sub>2</sub> emission caused by humanity-CO<sub>2</sub> concentration at the South Pole recently passed the milestone of 400 ppm for the first time in the last 4 million years<sup>[2]</sup>, contributes highly to climate change. In this sense, 2016 has also been the first year that the weekly average CO<sub>2</sub> concentration monitored in the Mona Loa observatory did not go below this key value, meaning that the average global temperature is likely to increase more than the 1.5 °C warming threshold.<sup>[3]</sup>

To address the current and future energy needs while mitigating the environmental impact, one of the strategies has been the development of efficient CO<sub>2</sub> capture, storage, and separation materials for achieving cleaner combustible supplies.<sup>[4]</sup> These materials mainly include zeolites, activated car-

bons, metal-organic frameworks (MOFs) and covalent-organic frameworks (COFs).<sup>[5]</sup> Among these innovative materials, an old-fashioned class of fluorinated materials<sup>[6]</sup> have recently been brought back to the spotlight by the Eddaoudi and Zaworotko groups thanks to their exceptional uptake and selectivity towards CO<sub>2</sub> and hydrocarbons.<sup>[7]</sup> These MOFs (Figure 1) are constructed from the assembly of pre-made M-XF<sub>6</sub> pillars (M = Co, Ni, Cu, Zn; X = Si, Ti, Sn, Zr, Ge, V, Ga) with N-donor type ligands (e.g., pyrazine (pyz), pyridyl-based ligands etc.).

However, despite these great developments, the scientific community and industry still need to join their efforts in transferring these materials from the laboratory to industry. A very important step here is the optimisation of their fabrication.<sup>[8]</sup> This fabrication must always aim for fast and scalable one-step processes that produce ready-to-use products without the need of additional purification and drying steps. Here we report a synthetic method that allows production of several isorecticular M-XF<sub>6</sub>-based CO<sub>2</sub> sorbents fulfilling all these requirements.

Our team recently introduced a well-established industrial spray-drying (SD) technique as a new synthetic way to prepare various MOFs (Scheme S1 in Supporting Information).<sup>[9,10]</sup> The SD technique is a scalable and fast method allowing continuous synthesis of MOFs in the form of spherical superstructures or beads based on the assembly of nanosized crystals.<sup>[9,11]</sup> The strong expertise acquired from these previous studies, among several reports suggesting the capital importance of the formation of the inorganic secondary building unit (SBU) for the nucleation and growth of MOFs,<sup>[10]</sup> convinced us that premade

[a] Dr. V. Guillerm, L. Garzón-Tovar, A. Yazdi, Dr. I. Imaz, Prof. Dr. D. Maspoch  
Catalan Institute of Nanoscience and Nanotechnology (ICN2)  
CSIC and The Barcelona Institute of Science and Technology  
Campus UAB, Bellaterra, 08193 Barcelona (Spain)  
E-mail: daniel.maspoch@icn2.cat

[b] Dr. J. Juanhuix  
ALBA Synchrotron  
Cerdanyola del Vallès, 08290 Barcelona (Spain)

[c] Prof. Dr. D. Maspoch  
ICREA  
Pg. Lluís Companys 23, 08010 Barcelona (Spain)

Supporting Information and the ORCID identification numbers for the authors of this article can be found under <https://doi.org/10.1002/chem.201605507>.

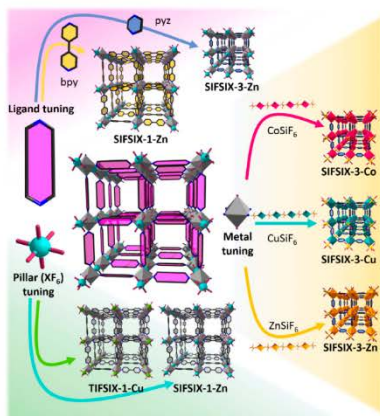


**Figure 1.** Schematic representation of the different isorecticular pcu M-XF<sub>6</sub>-based MOFs synthesised through spray-drying. Note here that this technique allows synthesising this class of MOFs whilst varying the metal ion (Co, Cu, Zn), anionic pillar ([SIF<sub>6</sub>]<sup>3-</sup>, [TIF<sub>6</sub>]<sup>2-</sup>) and ligand (pyrazine, 4,4'-bipyridine).

pillars of the M-XF<sub>6</sub> MOF platform would be ideal candidates for SD synthesis.

We therefore successfully embarked on the SD-based synthesis of several M-XF<sub>6</sub> materials, showing that this method is also compatible for reticular synthesis and metal tuning, ligand elongation and pillar substitution. Importantly, their rapid synthesis (a few minutes versus a few hours up to a few days) does not negatively affect their sorption properties, demonstrating in most cases their ready-to-use character without the need of additional purification steps or time consuming repeated solvent exchange procedures. Moreover, we also demonstrate that SD can be used not only to synthesise porous materials based on coordination bonds but also based on hydrogen bonds.

## Results and Discussion

### SIFSIX-3-M materials

#### Synthesis and characterisation

The one-step SD synthesis consisted of the combined atomisation of two methanolic solutions containing 1) M-SIF<sub>6</sub> (M=Co, Cu, Zn) and 2) pyz at 85 °C, which produced fine powders that were collected with a minimum amount of methanol (MeOH). Collection of these powders in methanol was a crucial protection step as we found that they were air-sensitive (see below). To assess the quality of the as-made SIFSIX-3-M MOFs, their CO<sub>2</sub> sorption properties were compared with those of their

bulk analogues. For this, the SD-synthesised SIFSIX-3-M collected in methanol were directly transferred from the spray drier collector to sorption cells, and dried and evacuated for 12 h at 65 °C. Then, their CO<sub>2</sub> uptake at 298 K was measured. Notably, we confirmed that spray-dried SIFSIX-3-M did not require additional solvent exchange or purification steps to exhibit remarkable CO<sub>2</sub> capacities at low pressure and 298 K (Figure 2h, Table 1), with an uptake less than 10% lower than the reported bulk materials.

SD-synthesised SIFSIX-3-M were further characterised by powder X-ray diffraction (PXRD), from which experimental patterns were in excellent agreement with the theoretical diagrams calculated from the corresponding structures (Figure 2g), demonstrating both the high crystallinity and purity of the MOFs.

The morphology of the materials was also investigated by field-emission scanning electron microscopy (FESEM), showing in all cases the occurrence of nanosized SIFSIX-3-M crystals assembled into spherical superstructures or beads; a shape that is typical for MOFs assembled by the SD method. The sizes of these superstructures were 7.9 ± 4.8 μm for SIFSIX-3-Co, 6.9 ± 3.4 μm for SIFSIX-3-Cu and 3.5 ± 2.7 μm for SIFSIX-3-Zn (Figure 2 a–c and Figure S14a in Supporting Information).<sup>10,11</sup> Moreover, FESEM images confirmed the homogeneity of the materials, as already suggested by the absence of crystalline impurity peaks in the PXRD diagrams.

To finally determine the size of crystals composing the superstructures, they were disassembled by sonication and immediately transferred to a transmission electron microscopy (TEM) grid. TEM images confirmed the formation of nanocrystals with a size of 32 ± 13 nm for SIFSIX-3-Co, 80 ± 12 nm for SIFSIX-3-Cu and 28 ± 9 nm for SIFSIX-3-Zn (Figure 2 d–f and Figure S14b).

#### Stability in different media

The use of methanol to collect the fine powders produced with the SD method is essential to protect and use the as-made SIFSIX-3-M MOFs.<sup>12</sup> Without this precaution, all nanosized SIFSIX-3-M MOFs suffered a fast degradation and a loss of their CO<sub>2</sub> sorption properties when they were exposed to ambient conditions. In addition, following the optimised washing procedure reported by Nugent et al.,<sup>12a</sup> we observed that the SD-synthesised SIFSIX-3-Zn was instantaneously solubilised upon addition of *N,N*-dimethylformamide (DMF), leading to a clear solution. Attempts to re-spray this clear solution did not allow the re-assembly of the SIFSIX-3-Zn framework. Instead, colourless single crystals (versus the yellow colour of SIFSIX-3-Zn crystals) appeared in the DMF solution after a period of ca. one month. This unknown structure, which crystallises in the P1 space group, was solved by single-crystal X-ray diffraction and appeared to be a cationic 1D coordination polymer with formula  $[(Zn(py)_2(DMF)_2(H_2O)_2)_n(SIF_6)]^+$  (1). This structure results from the replacement of all SIF<sub>6</sub> pillars and half of the pyz ligand by DMF and water molecules (Table S1, Figures S15–19). The positive charge of this coordination polymer  $[Zn(py)_2(DMF)_2(H_2O)_2]^+$  is balanced by [SIF<sub>6</sub>]<sup>2-</sup> anions.

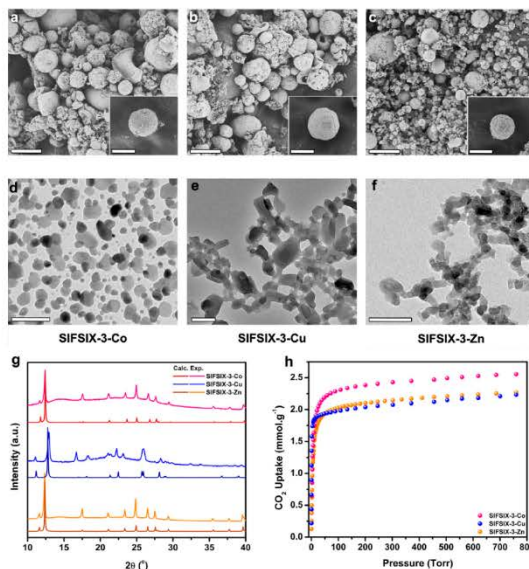


**Figure 2.** Representative FESEM images of (a) SIFSIX-3-Co, (b) SIFSIX-3-Cu and (c) SIFSIX-3-Zn. TEM images of (d) SIFSIX-3-Co, (e) SIFSIX-3-Cu and (f) SIFSIX-3-Zn. (g) PXRD patterns of the SD-synthesised SIFSIX-3-M. (h) CO<sub>2</sub> sorption isotherms at 298 K for SIFSIX-3-M. Scale bars for FESEM: 15 and 5 µm (insets). Scale bars for TEM: 100 nm (d, f) and 200 nm (e).

MOF	CO <sub>2</sub> uptake [mmol g <sup>-1</sup> ]	
	Bulk	Sprayed (% of bulk)
SIFSIX-3-Co	≈ 2.79 <sup>(7d)</sup>	2.56 (92%)
SIFSIX-3-Cu	≈ 2.40 <sup>(7e)</sup>	2.23 (93%)
SIFSIX-3-Zn	≈ 2.46 <sup>(7f)</sup>	2.27 (91%)

It is important to mention here that a similar behaviour was found when immersing SIFSIX-3-Zn in water, also leading to a complete solubilisation of the crystals. The incubation of nanosized SIFSIX-3-Zn in other organic solvents, including acetonitrile, hexane, dichloromethane, chloroform, toluene, tetrahydrofuran and acetone, did not result in the solubilisation of the crystals but instead a fast phase transition into unidentified crystalline powders (Figure S20).

The only tested solvent in which SIFSIX-3-Zn showed certain stability was MeOH. Initial incubation studies using microcrystals instead of nanocrystals, to easily follow the evolution by FESEM, showed that SIFSIX-3-Zn is also etched and finally solubilised in MeOH (Figure S13). However, we found that the

minimum amount of MeOH needed for the complete solubilisation of the nanosized SIFSIX-3-Zn without stirring was around 0.14 mL<sub>MeOH</sub> per mg<sub>SIFSIX-3-Zn</sub>. In addition, below this amount of MeOH, SIFSIX-3-Zn remained stable and did not suffer any phase transition, as confirmed by PXRD. It is also worth mentioning that a similar behaviour occurred for the Cu and Co analogues. To this end, altogether these observations allowed us to define MeOH as the best solvent to collect these materials, which were in all cases collected using no more than 0.015 mL<sub>MeOH</sub> per mg of MOF.

### Reticular chemistry: organic ligand and anionic pillar tuning

#### Synthesis and characterisation of SIFSIX-1-Zn

In line with global efforts of the MOF community to use some network topologies as design platforms to rationally synthesise isorecticular MOFs,<sup>133</sup> we intended to take advantage of the already reported versatility of the M-XF<sub>6</sub> platform<sup>[6(c),7(a),8-9(k)]</sup> to demonstrate the suitability of the SD method for reticular chemistry. Following the successful synthesis of SIFSIX-3-M (M = Co, Cu and Zn), we achieved the synthesis of an expanded analogue, SIFSIX-1-Zn,<sup>[6(e)]</sup> by replacing the pyz ligand with

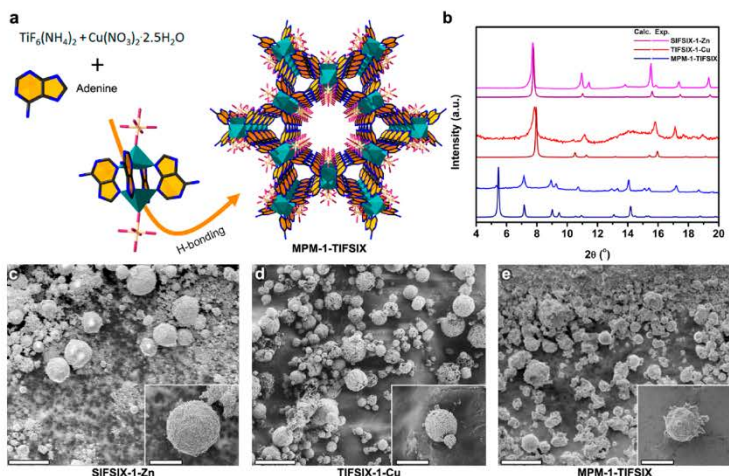


**Figure 3.** (a) Schematic for the synthesis and structure of **MPM-1-TIFSIX-1**; (b) comparison of theoretical and experimental PXRD diagrams of **MPM-1-TIFSIX**, **TIFSIX-1-Cu** and **SIFSIX-1-Zn**; FESEM images of (c) **SIFSIX-1-Zn**, (d) **TIFSIX-1-Cu** and (e) **MPM-1-TIFSIX**. Scale bars for FESEM: 20 and 5 μm (insets).

the longer 4,4'-bipyridine (bpy). Here, a methanolic solution of  $\text{ZnSiF}_6$  was spray-dried along with a methanolic solution of bpy using a 3-fluid nozzle at 85 °C. The resulting yellow spherical superstructures (size =  $7.9 \pm 3.6$  μm; Figure 3c and Figure S14a in Supporting Information) were collected and washed with MeOH. The material was obtained as a pure phase, as confirmed by PXRD (Figure 3b). It was found to be porous to  $\text{N}_2$  at 77 K, exhibiting an apparent BET surface area of  $1300 \text{ m}^2 \text{ g}^{-1}$  (Table 2, Figure S21). Again, the nanosized nature of the **SIFSIX-1-Zn** crystals was confirmed by TEM; performed after disassembling the superstructures by sonication. The size of these nanocrystals was  $20 \pm 5$  nm (Figures S14b, S24).

MOF	$A_{\text{BET}}$ [ $\text{m}^2 \text{ g}^{-1}$ ]	$V_{\text{micro}}$ [ $\text{cm}^3 \text{ g}^{-1}$ ] $P/P_0 = 0.3$	$V_t$ [ $\text{cm}^3 \text{ g}^{-1}$ ] $P/P_0 = 0.95$	Theo. $V_t$ [ $\text{cm}^3 \text{ g}^{-1}$ ]
SIFSIX-1-Zn	1300	0.53	0.58	0.68
TIFSIX-1-Cu	1650	0.66	0.88	0.70
MPM-1-TIFSIX	805	0.32	0.32	0.39

#### Synthesis and characterisation of TIFSIX-1-Cu

Recently, Nugent et al.<sup>[71]</sup> reported the possibility to not only vary the metal in this type of pcu-MOF, but also the anion, by achieving the replacement of the pillaring  $[\text{SiF}_6]^{2-}$  anion by

$[\text{TlF}_6]^{2-}$ . Bulk **TIFSIX-1-Cu** is commonly synthesised using a layering of methanol and ethylene glycol at room temperature. However, this synthesis could not be reproduced in the spray-drier due to the high boiling point of ethylene glycol (197.3 °C). For this reason, we successfully replaced ethylene glycol by water, adjusting the SD temperature to 150 °C. Thus, an aqueous solution of  $\text{Cu}(\text{NO}_3)_2 \cdot 2.5\text{H}_2\text{O}$  and  $\text{TlF}_6(\text{NH}_4)_2$  was spray-dried along with a methanolic solution of bpy using a 3-fluid nozzle at 150 °C. The resulting grey/purple spherical superstructures (size =  $5.3 \pm 3.1$  μm; Figure 3d and Figure S14a) were collected with MeOH. Their PXRD pattern was found to be in excellent agreement with the theoretical diagram (Figure 3b).  $\text{N}_2$  sorption performed at 77 K revealed an apparent BET surface area of  $1650 \text{ m}^2 \text{ g}^{-1}$ . This value is very similar to that reported for the bulk material ( $1690 \text{ m}^2 \text{ g}^{-1}$ )<sup>[71]</sup> demonstrating the high quality of the SD-synthesised **TIFSIX-1-Cu** MOF (Table 2, Figure S22). The nanosized nature of the **TIFSIX-1-Cu** crystals (size =  $43 \pm 9$  nm, Figures S14b, S25) was again confirmed by TEM performed after disassembling the superstructures by sonication.

#### Synthesis and characterisation of supramolecular open material

Finally, due to the apparent ease of synthesis of these M-XF<sub>6</sub> based MOFs by SD technology, we selected another porous material, **MPM-1-TIFSIX**,<sup>[72]</sup> based on the supramolecular assembly of  $[\text{Cu}_4(\text{ade})_4(\text{TlF}_6)_4]$  (ade = adenine) paddlewheels (Fig-

ure 3a). It is worth mentioning that, in the present case, the selected material to be synthesised by SD was not a MOF but a supramolecular hydrogen-bonded network. To our knowledge, the aerosol synthesis of such kind of open materials based on weak bonding has not been reported yet.

An aqueous solution of  $\text{Cu}(\text{NO}_3)_2 \cdot 2.5\text{H}_2\text{O}$  and  $\text{TlF}_6(\text{NH}_4)_2$  was spray-dried along with a solution of adenine in water/acetone/nitrile mixture using a 2-fluid nozzle (Scheme S3 in Supporting Information) at 150 °C. The resulting grey/purple spherical superstructures (size =  $6.1 \pm 3.1 \mu\text{m}$ ; Figure 3e and Figure S14a) were collected with MeOH. Remarkably, the PXRD diagram was found to be in excellent agreement with the theoretical one (Figure 3b).  $\text{N}_2$  sorption performed at 77 K after a methanol solvent exchange procedure revealed an apparent BET surface area of  $805 \text{ m}^2 \text{ g}^{-1}$  ( $996 \text{ m}^2 \text{ g}^{-1}$  for bulk),<sup>[7d]</sup> demonstrating the porosity of the SD-synthesised **MPM-1-TIFSIX** supramolecular material (Table 2, Figure S3). In this case, TEM experiments performed after disassembling the superstructures by sonication showed **MPM-1-TIFSIX** crystals with a size of  $201 \pm 65 \text{ nm}$  (Figures S14b, S26).

## Conclusion

We reported here the one-step and continuous synthesis of various M-XF<sub>6</sub> based MOFs using the SD technique. Using this method, these M-XF<sub>6</sub> based MOFs could be synthesised at the nanoscale. There is no doubt that the possibility of obtaining and stabilizing nanosized M-XF<sub>6</sub> based MOFs opens new avenues for the re-exploration of this old-fashioned sub-class of MOFs for emerging applications. In addition, we demonstrated the suitability of the SD method to perform fine structural tuning through ligand size variation (pyz versus bpy), anionic pillar substitution ([SIF<sub>6</sub>]<sup>2-</sup> versus [TlF<sub>6</sub>]<sup>2-</sup>) and variation of metal ion (Co, Cu and Zn). Importantly, this novel way to synthesise these materials does not jeopardise their sorption properties. This fact together with the short synthesis times and the absence of time consuming purification and solvent exchange procedures demonstrates the ability and competitiveness of SD methods versus conventional ones for the fast production of ready-to-use sorbents. Finally, we demonstrated the first aerosol synthesis of a supramolecular, hydrogen-bonded porous network, **MPM-1-TIFSIX**, which opens new avenues for the synthesis of this class of porous materials using SD.

## Experimental Section

### Materials

All the materials were synthesised using a Mini Spray Dryer B-290 (BÜCHI Labortechnik). All solvents and reagents were purchased from Sigma-Aldrich, City Chemicals or Scharlab and used as received.

### Synthesis of SIFSIX-3-Co

6 mL of a methanolic solution of  $\text{CoSiF}_6$  (300 mg, 1.49 mmol) and 6 mL of a methanolic solution of pyz (325 mg, 4.05 mmol) were si-

multaneously spray-dried using a 3-fluid nozzle (Scheme S2 in Supporting Information), a feed rate of  $2.4 \text{ mL min}^{-1}$ , a flow rate of  $414 \text{ mL min}^{-1}$ , an inlet  $\text{N}_2$  temperature of 85 °C and a spray cap with a 0.5 mm hole. The light pink powder of **SIFSIX-3-Co** was recovered with a minimum amount of MeOH (235 mg; 44% yield based on Co). IR:  $\tilde{\nu} = 690$  (s), 1062 (s), 1124 (w), 1153 (m), 1421 (s), 1628 (m), 1660 (m), 3196 (br), 3403 (br),  $3522 \text{ cm}^{-1}$  (w) (Figure S1).

### Synthesis of SIFSIX-3-Cu

6 mL of a methanolic solution of  $\text{CuSiF}_6 \cdot \text{H}_2\text{O}$  (300 mg, 1.34 mmol) and 6 mL of a methanolic solution of pyz (325 mg, 4.05 mmol) were simultaneously spray-dried using a 3-fluid nozzle, a feed rate of  $2.4 \text{ mL min}^{-1}$ , a flow rate of  $414 \text{ mL min}^{-1}$ , an inlet  $\text{N}_2$  temperature of 85 °C and a spray cap with a 0.5 mm hole. The blue powder of **SIFSIX-3-Cu** was recovered with a minimum amount of MeOH (272 mg; 55% yield based on Cu). IR:  $\tilde{\nu} = 686$  (s), 822 (s), 1078 (s), 1132 (s), 1161 (s), 1429 (s), 1652 (m), 1660 (m), 3147 (m),  $3325 \text{ cm}^{-1}$  (br) (Figure S2).

### Synthesis of SIFSIX-3-Zn

6 mL of a methanolic solution of  $\text{ZnSiF}_6 \cdot x\text{H}_2\text{O}$  (300 mg, 1.45 mmol, anhydrous based) and 6 mL of a methanolic solution of pyz (325 mg, 4.05 mmol) were simultaneously spray-dried using a 3-fluid nozzle, a feed rate of  $2.4 \text{ mL min}^{-1}$ , a flow rate of  $414 \text{ mL min}^{-1}$ , an inlet  $\text{N}_2$  temperature of 85 °C and a spray cap with a 0.5 mm hole. The yellow powder of **SIFSIX-3-Zn** was recovered with a minimum amount of MeOH (305 mg; 57% yield based on Zn). IR:  $\tilde{\nu} = 686$  (s), 822 (w), 1062 (s), 1099 (w), 1128 (w), 1161 (w), 1425 (s), 1635 (s), 1660 (m),  $3432 \text{ cm}^{-1}$  (br) (Figure S3).

### Synthesis of SIFSIX-1-Zn

6 mL of a methanolic solution of  $\text{ZnSiF}_6 \cdot x\text{H}_2\text{O}$  (300 mg, 1.45 mmol, anhydrous based) and 6 mL of a methanolic solution of bpy (650 mg, 4.16 mmol) were simultaneously spray-dried using a 3-fluid nozzle, a feed rate of  $2.4 \text{ mL min}^{-1}$ , a flow rate of  $414 \text{ mL min}^{-1}$ , an inlet  $\text{N}_2$  temperature of 85 °C and a spray cap with a 0.5 mm hole. The yellow powder of **SIFSIX-1-Zn** was recovered with a minimum amount of MeOH (302 mg; 40% yield based on Zn). The sample was then washed with 5 mL of MeOH to remove potential contamination with the highly soluble, unreacted precursors. IR:  $\tilde{\nu} = 632$  (m), 649 (s), 764 (m), 806 (s), 851 (s), 1008 (m), 1062 (s), 1223 (m), 1317 (w), 1413 (s), 1491 (m), 1536 (m), 1611 (s), 1644 (w), 3230 (w),  $3345 \text{ cm}^{-1}$  (br) (Figure S4).

### Synthesis of TIFSIX-1-Cu

6 mL of an aqueous solution of  $\text{TlF}_6(\text{NH}_4)_2$  (30 mg, 0.15 mmol) and  $\text{Cu}(\text{NO}_3)_2 \cdot 2.5\text{H}_2\text{O}$  (35 mg, 0.15 mmol) and 6 mL of a methanolic solution of bpy (46.8 mg, 0.30 mmol) were simultaneously spray-dried using a 3-fluid nozzle, a feed rate of  $2.4 \text{ mL min}^{-1}$ , a flow rate of  $414 \text{ mL min}^{-1}$ , an inlet  $\text{N}_2$  temperature of 130 °C and a spray cap with a 0.5 mm hole. The blue powder of **TIFSIX-1-Cu** was recovered with a minimum amount of MeOH (64 mg; 79% yield based on Cu). IR:  $\tilde{\nu} = 632$  (s), 678 (w), 728 (m), 810 (s), 851 (w), 921 (w), 1012 (s), 1066 (s), 1223 (m), 1280 (s), 1326 (w), 1409 (s), 1471 (m), 1491 (m), 1536 (m), 1607 (s), 1644 (w), 3101 (w), 3283 (w),  $3357 \text{ cm}^{-1}$  (w) (Figure S5).

### Synthesis of MPM-1-TIFSIX

12 mL of an aqueous solution of  $\text{TiF}_4(\text{NH}_4)_2$  (30 mg, 0.15 mmol) and  $\text{Cu}(\text{NO}_3)_2 \cdot 2.5\text{H}_2\text{O}$  (35 mg, 0.15 mmol) and 12 mL of a  $\text{H}_2\text{O}:\text{CH}_3\text{CN}$  (1:1 vol.) solution of adenine (82 mg, 0.60 mmol) were simultaneously spray-dried using a 2-fluid nozzle and T-shaped system (Scheme S3), a feed rate of  $2.4 \text{ mL min}^{-1}$ , a flow rate of  $414 \text{ mL min}^{-1}$ , an inlet  $\text{N}_2$  temperature of  $150^\circ\text{C}$  and a spray cap with a  $0.5 \text{ mm}$  hole. The purple/grey powder of **MPM-1-TIFSIX** was recovered with a minimum amount of MeOH (110 mg; 74% yield based on Zn). Prior to sorption measurements, this powder was immersed in MeOH for 3 days, refreshing the MeOH twice a day. IR:  $\tilde{\nu} = 715$  (m), 789 (m), 827 (w), 806 (s), 889 (m), 938 (m), 1037 (w), 1107 (w), 1149 (w), 1231 (s), 1314 (s), 1409 (s), 1607 (s), 1652 (s), 1702 (w), 3089 (w), 3200 (w),  $3419 \text{ cm}^{-1}(\text{w})$  (Figure S6).

### Characterisation

PXRD diagrams were collected on a Panalytical X'pert diffractometer with monochromatic  $\text{Cu}_{\text{K}\alpha}$  radiation ( $\lambda_{\text{Cu}} = 1.5406 \text{ \AA}$ ) under a Kapton film. Fourier transform infrared (FTIR) spectra were recorded on a Bruker Tensor 27 FTIR spectrometer equipped with a Golden Gate diamond attenuated total reflection (ATR) cell, in transmittance mode at room temperature. The main IR bands (Figures S1–6) are reported as follow: strong (s), medium (m), weak (w) and broad (br). TGA curves (Figures S7–12) were measured in a PerkinElmer Pyris 1 under  $\text{O}_2$  atmosphere and a heating rate of  $10^\circ\text{C min}^{-1}$ . Volumetric  $\text{N}_2$  and  $\text{CO}_2$  sorption isotherms were collected at  $77 \text{ K}$  ( $\text{N}_2$ ) and  $298 \text{ K}$  ( $\text{CO}_2$ ) using an ASAP 2020 HD (Micromeritics). Temperature was controlled by using a liquid nitrogen bath ( $77 \text{ K}$ ) or a Lauda Proline RP 890 chiller ( $298 \text{ K}$ ). For  $\text{N}_2$  sorption at  $77 \text{ K}$ , micropore volumes ( $V_{\text{micropore}}$ ) were calculated at  $P/P_0 = 0.3$ , whereas the total pore volumes ( $V_{\text{total}}$ ) were calculated at  $P/P_0 = 0.95$ . Field-emission scanning electron microscopy (FESEM) images were collected on scanning electron microscopes (FEI Magellan 400 L XHR and Quanta 650 FEG) at an acceleration voltage of  $1.0 \text{ kV}$ , and using dry powder on carbon as support. Transmission electron microscopy (TEM) images were obtained with a JEOL JEM 1400 at  $100 \text{ kV}$ . Prior to TEM, all superstructures immersed in MeOH were disassembled by sonication for  $10 \text{ s}$  in a Fisher Scientific FB15051 sonicator and then directly transferred onto the TEM grids. The average size range of superstructures and crystals has been calculated on 100 crystals/superstructures using the Image J software.

### Stability study of SIFSIX-3-Zn

$6 \text{ mL}$  of a methanolic solution of  $\text{ZnSiF}_6 \cdot x\text{H}_2\text{O}$  (300 mg,  $1.45 \text{ mmol}$ , anhydrous based) was injected into  $6 \text{ mL}$  of a methanolic solution of pyz ( $325 \text{ mg}$ ,  $4.05 \text{ mmol}$ ) at room temperature, without stirring. After  $1 \text{ h}$ ,  $1 \text{ mL}$  of the solution containing the resulting microcrystals was pipetted from the middle of the vial and mixed with  $2 \text{ mL}$  of MeOH. Aliquots of the sample were transferred immediately to the microscope to avoid contact with air, and the morphology of the crystals was studied by FESEM after  $15 \text{ min}$  (Figure S13).

### Crystallography

Crystallographic data for **1** were collected at  $100 \text{ K}$  at XALOC beamline at ALBA synchrotron<sup>[14]</sup> ( $\lambda = 0.79472 \text{ \AA}$ ). Data were indexed, integrated and scaled using the XDS program.<sup>[15]</sup> Absorption correction was not applied. The structure was solved by direct methods and subsequently refined by correction of  $F^2$  against all reflections, using SHELXS2013<sup>[16]</sup> and SHELXL2013<sup>[17]</sup> within the WinGX package.<sup>[18]</sup> All non-hydrogen atoms were refined with ani-

sotropic thermal parameters by full-matrix least-squares calculations on  $F^2$  using the program SHELXL2013. Hydrogen atoms were inserted at calculated positions and constrained with isotropic thermal parameters.

### Acknowledgements

This work was supported by the MINECO-Spain through projects PN MAT2012-30994, 2014-SGR-80, EU FP7 ERC-Co 615954, and European Union's Horizon 2020 research and innovation programme under grant agreement No 685727. V.G. is grateful to the Generalitat de Catalunya for a Beatriu de Pinós fellowship (2014 BP-B 00155) and I.I. thanks the MINECO for a Ramón y Cajal fellowship (RYC-2010-06530). A.Y. and ICN2 acknowledge the support of the Spanish MINECO through the Severo Ochoa Centers of Excellence Program, under Grant SEV-2013-0295.

### Conflict of interest

The authors declare no conflict of interest.

**Keywords:**  $\text{CO}_2$  sorption · fluorinated materials · metal-organic frameworks · spray-drying · stability

- [1] R. Monastersky, *Nature* **2009**, *458*, 1091–1094.
- [2] South Pole is the last place on Earth to pass a global warming milestone <http://research.noaa.gov/News/NewsArchive/LatestNews/TabId/684/ArtMid/1768/ArticleID/11760/South-Pole-is-the-last-place-on-Earth-to-pass-a-global-warming-milestone.aspx> (accessed June 28<sup>th</sup>, 2016).
- [3] Up-to-date weekly average  $\text{CO}_2$  at Mauna Loa. <http://www.esrl.noaa.gov/gmd/ccgg/trends/weekly.html> (accessed October 4<sup>th</sup>, 2016).
- [4] a) K. Sumida, D. L. Rogow, J. A. Mason, T. M. McDonald, E. D. Bloch, Z. R. Herm, T.-H. Bae, J. R. Long, *Chem. Rev.* **2012**, *112*, 724–781; b) Y. Belmabkhout, V. Guillerm, M. Eddaoudi, *Chem. Eng. J.* **2016**, *296*, 386–397.
- [5] a) H. C. Zhou, J. R. Long, O. M. Yaghi, *Chem. Rev.* **2012**, *112*, 673–1268; b) J. R. Long, O. M. Yaghi, *Chem. Soc. Rev.* **2009**, *38*, 1213; c) J. R. Long, O. M. Yaghi, *Chem. Soc. Rev.* **2014**, *43*, 6288; d) R. Dawson, A. I. Cooper, D. J. Adams, *Prog. Polym. Sci.* **2012**, *37*, 530–563.
- [6] a) K. Uemura, A. Maeda, T. K. Maji, P. Kanoo, H. Kita, *Eur. J. Inorg. Chem.* **2009**, *2009*, 2329–2337; b) D. N. Dybtsev, H. Chun, K. Kim, *Angew. Chem. Int. Ed.* **2004**, *43*, 5033–5036; *Angew. Chem.* **2004**, *116*, 5143–5146; c) S.-I. Noro, S. Kitagawa, M. Kondo, K. Seki, *Angew. Chem. Int. Ed.* **2000**, *39*, 2081–2084; *Angew. Chem.* **2000**, *112*, 2161–2164; d) M. J. Zaworotko, *Angew. Chem. Int. Ed.* **2000**, *39*, 3052–3054; *Angew. Chem.* **2000**, *112*, 3180–3182; e) S. Subramanian, M. J. Zaworotko, *Angew. Chem. Int. Ed. Engl.* **1995**, *34*, 2127–2129; *Angew. Chem.* **1995**, *107*, 2295–2297; f) S.-I. Noro, R. Kitaura, M. Kondo, S. Kitagawa, T. Ishii, H. Matsuzaka, M. Yamashita, *J. Am. Chem. Soc.* **2002**, *124*, 2568–2583; g) M.-J. Lin, A. Jouaiti, N. Kyritsakas, M. W. Hosseini, *CrystEngComm* **2009**, *11*, 189–191.
- [7] a) P. Nugent, Y. Belmabkhout, S. D. Burd, A. J. Cairns, R. Luebke, K. Forrest, T. Pham, S. Ma, B. Space, L. Wojtas, M. J. Zaworotko, *Nature* **2013**, *495*, 80–84; b) O. Shekhat, Y. Belmabkhout, Z. Chen, V. Guillerm, A. Cairns, K. Adil, M. Eddaoudi, *Nat. Commun.* **2014**, *5*, 4228; c) P. Kanoo, S. K. Reddy, G. Kumari, R. Haldar, C. Narayana, S. Balasubramanian, T. K. Maji, *Chem. Commun.* **2012**, *48*, 8487–8489; d) P. S. Nugent, V. L. Rhodus, T. Pham, K. Forrest, L. Wojtas, B. Space, M. J. Zaworotko, *J. Am. Chem. Soc.* **2013**, *135*, 10950–10953; e) O. Shekhat, Y. Belmabkhout, K. Adil, P. M. Bhatti, A. J. Cairns, M. Eddaoudi, *Chem. Commun.* **2015**, *51*, 13595–13598; f) P. Nugent, V. Rhodus, T. Pham, B. Tudor, K. Forrest, L. Wojtas, B. Space, M. J. Zaworotko, *Chem. Commun.* **2013**, *49*, 1606–1608; g) S. D. Burd, S. Ma, J. A. Perman, B. J. Sikora,

- R. Q. Snurr, P. K. Thallapally, J. Tian, Ł. Wojtas, M. J. Zaworotko, *J. Am. Chem. Soc.* **2012**, *134*, 3663–3666; h) X. Cui, K. Chen, H. Xing, Q. Yang, R. Krishna, Z. Bao, H. Wu, W. Zhou, X. Dong, Y. Han, B. Li, Q. Ren, M. J. Zaworotko, B. Chen, *Science* **2016**, *353*, 141–144; i) A. Cadiou, K. Adil, P. M. Bhatt, Y. Belmabkhout, M. Eddaoudi, *Science* **2016**, *353*, 137–140; j) J. L. Manson, J. A. Schluter, K. E. Garrett, P. A. Goddard, T. Lancaster, J. Möller, S. J. Blundell, A. J. Steele, I. Franke, F. L. Pratt, J. Singleton, J. Bendix, S. H. Lapidus, M. Uhlarz, O. Ayala-Valenzuela, R. McDonald, M. Gurak, C. Baines, *Chem. Commun.* **2016**, *52*, 12653–12656; k) S. K. Elsaidi, M. H. Mohamed, H. T. Schaefer, A. Kumar, M. Lusi, T. Pham, K. A. Forrest, B. Space, W. Xu, G. J. Halder, J. Liu, M. J. Zaworotko, P. K. Thallapally, *Chem. Commun.* **2015**, *51*, 15530–15533.
- [8] a) P. Silva, S. M. F. Vilela, J. P. C. Tome, F. A. Almeida Paz, *Chem. Soc. Rev.* **2015**, *44*, 6774–6803; b) A. U. Czaja, N. Trukhan, U. Müller, *Chem. Soc. Rev.* **2009**, *38*, 1284–1293; c) U. Mueller, M. Schubert, F. Teich, H. Puetter, K. Schierle-Arndt, J. Pastré, *J. Mater. Chem.* **2006**, *16*, 626–636; d) M. Gaab, N. Trukhan, S. Maurer, R. Gummaraju, U. Müller, *Microporous Mesoporous Mater.* **2012**, *157*, 131–136; e) D. Crawford, J. Casaban, R. Haydon, N. Giri, T. McNally, S. L. James, *Chem. Sci.* **2015**, *6*, 1645–1649; f) M. Rubio-Martinez, M. P. Batten, A. Polyzos, K. C. Carey, J. I. Mardel, K. S. Lim, M. R. Hill, *Sci. Rep.* **2014**, *4*, 5443; g) M. Rubio-Martinez, T. D. Hadley, M. P. Batten, C. Constanti-Carey, T. Barton, D. Marley, A. Mönch, K. S. Lim, M. R. Hill, *ChemSusChem* **2016**, *9*, 938–941; h) P. A. Bayliss, I. A. Ibarra, E. Perez, S. Yang, C. C. Tang, M. Poliakoff, M. Schroder, *Green Chem.* **2014**, *16*, 3796–3802; i) M. Faustini, J. Kim, G.-Y. Jeong, J. Y. Kim, H. R. Moon, W.-S. Ahn, D.-P. Kim, *J. Am. Chem. Soc.* **2013**, *135*, 14619–14626; j) P. W. Dunne, E. Lester, R. I. Walton, *React. Chem. Eng.* **2016**, *1*, 352–360; k) L. Garzón-Tovar, A. Carné-Sánchez, C. Carbonell, I. Imaz, D. Maspocho, *J. Mater. Chem. A* **2015**, *3*, 20819–20826; l) L. Garzón-Tovar, M. Cano-Sarabia, A. Carné-Sánchez, C. Carbonell, I. Imaz, D. Maspocho, *React. Chem. Eng.* **2016**, *1*, 533–539.
- [9] a) Z. Wang, D. Ananias, A. Carné-Sánchez, C. D. S. Brites, I. Imaz, D. Maspocho, J. Rocha, L. D. Carlos, *Adv. Funct. Mater.* **2015**, *25*, 2824–2830; b) A. Carné-Sánchez, K. C. Stylianou, C. Carbonell, M. Naderi, I. Imaz, D. Maspocho, *Adv. Mater.* **2015**, *27*, 869–873; c) A. Carné-Sánchez, I. Imaz, M. Cano-Sarabia, D. Maspocho, *Nat. Chem.* **2013**, *5*, 203–211.
- [10] a) D. C. Cantu, B. P. McGrail, V.-A. Glezakov, *Chem. Mater.* **2014**, *26*, 6401–6409; b) O. Shekhat, H. Wang, D. Zacher, R. A. Fischer, C. Woll, *Angew. Chem. Int. Ed.* **2009**, *48*, 5038–5041; *Angew. Chem.* **2009**, *121*, 5138–5142; c) S. Surblé, F. Millange, C. Serre, G. Férey, R. L. Walton, *Chem. Commun.* **2006**, 1518–1520; d) V. Guillemin, S. Gross, C. Serre, T. Devic, M. Bauer, G. Férey, *Chem. Commun.* **2010**, *46*, 767–769; e) D. Alezi, Y. Belmabkhout, M. Suyetin, P. M. Bhatt, Ł. J. Weseliński, V. Solovyeva, K. Adil, I. Spanopoulos, P. N. Trikalitis, A.-H. Emwas, M. Eddaoudi, *J. Am. Chem. Soc.* **2015**, *137*, 13308–13318.
- [11] a) A. Garcia Marquez, P. Horcajada, D. Grosso, G. Férey, C. Serre, C. Sanchez, C. Boissière, *Chem. Commun.* **2013**, *49*, 3848–3850; b) A. Carné-Sánchez, I. Imaz, K. C. Stylianou, D. Maspocho, *Chem. Eur. J.* **2014**, *20*, 5192–5201.
- [12] J. A. Mason, T. M. McDonald, T.-H. Bae, J. E. Bachman, K. Sumida, J. J. Dutton, S. S. Kaye, J. R. Long, *J. Am. Chem. Soc.* **2015**, *137*, 4787–4803.
- [13] a) V. Guillemin, D. Kim, J. F. Eubank, R. Luebke, X. Liu, K. Adil, M. S. Lah, M. Eddaoudi, *Chem. Soc. Rev.* **2014**, *43*, 6141–6172; b) M. Eddaoudi, J. Kim, N. Rosi, D. Vodak, J. Wachter, M. O’Keeffe, O. M. Yaghi, *Science* **2002**, *295*, 469–472; c) O. M. Yaghi, M. O’Keeffe, N. W. Ockwig, H. K. Chae, M. Eddaoudi, J. Kim, *Nature* **2003**, *423*, 705–714; d) H. Furukawa, K. E. Cordova, M. O’Keeffe, O. M. Yaghi, *Science* **2013**, *341*, 1230444; e) V. Guillemin, Ł. J. Weseliński, J. Y. Belmabkhout, A. J. Cairns, V. D’Elia, Ł. Wojtas, K. Adil, M. Eddaoudi, *Nat. Chem.* **2014**, *6*, 673–680.
- [14] J. Juanhuix, F. Gil-Ortiz, G. Cuni, C. Colldéram, J. Nicolas, J. Lidon, E. Boter, C. Ruget, S. Ferrer, J. Benach, *J. Synchrotron Radiat.* **2014**, *21*, 679–689.
- [15] W. Kabsch, *Acta Crystallogr. Sect. D* **2010**, *66*, 125–132.
- [16] G. M. Sheldrick, Z. Dauter, K. S. Wilson, H. Hope, L. C. Sieker, *Acta Crystallogr. Sect. D* **1993**, *49*, 18–23.
- [17] G. M. Sheldrick, *Acta Crystallogr. Sect. C* **2015**, *71*, 3–8.
- [18] L. Farrugia, *J. Appl. Crystallogr.* **2012**, *45*, 849–854.

Manuscript received: November 24, 2016

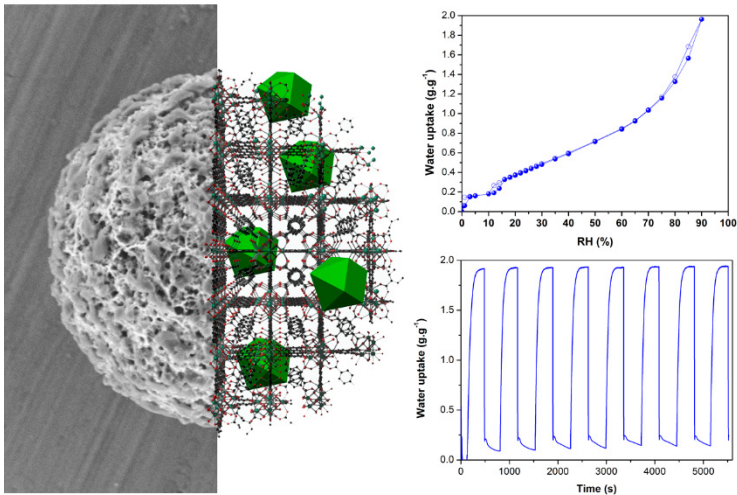
Accepted Article published: March 30, 2017

Final Article published: ■■■ 0000



# Composite Salt in Porous Metal-Organic Frameworks for Adsorption Heat Transformation

## Coupling $\text{CaCl}_2$ to MOFs



for adsorption heat transformation



# Composite Salt in Porous Metal-Organic Frameworks for Adsorption Heat Transformation

Luis Garzón-Tovar, Javier Pérez-Carvajal, Inhar Imaz,\* and Daniel Maspoch\*

Adsorptive heat transformation systems such as adsorption thermal batteries and chillers can provide space heating and cooling in a more environmental friendly way. However, their use is still hindered by their relatively poor performances and large sizes due to the limited properties of solid adsorbents. Here, the spray-drying continuous-flow synthesis of a new type of solid adsorbents that results from combining metal-organic frameworks (MOFs), such as UiO-66, and hygroscopic salts, such as  $\text{CaCl}_2$  has been reported. These adsorbents, commonly named as composite salt in porous matrix (CSPM) materials, allow improving the water uptake capabilities of MOFs while preventing their dissolution in the water adsorbed; a common characteristic of these salts due to the deliquescence effect. It is anticipated that MOF-based CSPMs, in which the percentage of salt can be tuned, are promising candidates for thermal batteries and chillers. In these applications, it is showed that a CSPM made of UiO-66 and  $\text{CaCl}_2$  (38% w/w) exhibits a heat storage capacity of  $367 \text{ kJ kg}^{-1}$ , whereas a second CSPM made of UiO-66 and  $\text{CaCl}_2$  (53% w/w) shows a specific cooling power of  $631 \text{ W kg}^{-1}$  and a coefficient of performance of 0.83, comparable to the best solid adsorbents reported so far.

## 1. Introduction

The anthropogenic greenhouse gas emissions related to the demand of electrical energy by traditional space heating and air conditioning processes have increased over the past decade.<sup>[1]</sup> To solve this problem, several initiatives have been proposed to replace the traditional vapor compression devices by more environmentally friendly adsorptive heat transformation (AHT) systems, such as adsorption chillers, heat pumps, and thermal batteries.<sup>[2]</sup> These AHT systems are based on an adsorption-desorption cycle of a working fluid, where useful heat is released during the adsorption step and cold is produced during the evaporation of the working fluid. The main advantages of these systems are (i) the possibility to use low thermal energy sources (e.g., solar and waste heat) for regeneration and driving energy and (ii) that water can be used as the working fluid.<sup>[3]</sup>

L. Garzón-Tovar, Dr. J. Pérez-Carvajal, Dr. I. Imaz, Prof. D. Maspoch  
 Catalan Institute of Nanoscience and Nanotechnology (ICN2)  
 CSIC and The Barcelona Institute of Science and Technology  
 Campus UAB, Bellaterra 08193, Barcelona, Spain  
 E-mail: inhar.imaz@icn2.cat; daniel.maspoch@icn2.cat  
 Prof. D. Maspoch  
 ICREA  
 Pg. Lluís Companys 23, 08010 Barcelona, Spain

DOI: 10.1002/adfm.201606424

Despite these advantages, the AHT technologies are not yet competitive with conventional vapor compression systems due to the low performance of the working pair (adsorbent-adsorbate); sometimes associated to the low adsorption capacity of the adsorbent.<sup>[4]</sup> In this sense, inorganic adsorbents such as  $\text{LiCl}$  and  $\text{CaCl}_2$  salts have been widely explored.<sup>[5]</sup> These compounds can adsorb a large amount of water because of their hygroscopic capacity. However, the presence of deliquescence phenomena, which can cause corrosion problems and limit their water uptake, depresses their performance in real applications.<sup>[6]</sup> A solution that has been traditionally proposed is the use of porous materials for confining these inorganic compounds. In the resulting composite salt in porous matrix (CSPM), the porous matrix mainly acts as a media to disperse the salt particles and can provide good heat and mass transport to these salt particles.<sup>[5]</sup> These CSPMs are usually produced by impregnation and saturation methods,<sup>[4a]</sup> in which the inorganic solution is diffused into the porous matrix.<sup>[7]</sup> To date, different porous matrices have been explored for making CSPMs, including silica, filosilicates, activated carbon, and microporous zeolites.<sup>[8]</sup> In an ideal material, however, the porous matrix also should adsorb water and provide efficient heat and mass transfer. In this context, silica-based and activated carbons generally display very low adsorption uptake in the range of  $P/P_0 = 0.3\text{--}0.5$  due to its high hydrophobicity,<sup>[9]</sup> and zeolites achieve their maximum capacity at low relative pressures, but it is difficult to regenerate them due to the high desorption temperatures required (e.g., Zeolite-13X:  $150 \text{ }^\circ\text{C}$ ; Zeolite-NaX:  $360 \text{ }^\circ\text{C}$ ).<sup>[8a,10]</sup>

Currently, the promising family of crystalline porous materials known as metal-organic frameworks (MOFs) has received great interest on water-sorption applications due to their high porosity, structural stability, and tuneable composition (e.g., hydrophilic and hydrophobic moieties can coexist in the same structure).<sup>[11]</sup> These potential applications include heat transformation processes,<sup>[12]</sup> proton conductivity,<sup>[13]</sup> air dehumidification,<sup>[14]</sup> and water delivery in remote areas.<sup>[15]</sup> It is noticed that some MOFs have a high water adsorbent capacity (e.g., MIL-101(Cr)- $\text{NH}_2$ :  $1.05 \text{ g}_{\text{water}} \text{ g}^{-1}_{\text{MOF}}$ ; MIL-100(Fe):  $0.87 \text{ g}_{\text{water}} \text{ g}^{-1}_{\text{MOF}}$ ; PIZOF-2 =  $0.68 \text{ g}_{\text{water}} \text{ g}^{-1}_{\text{MOF}}$ ).<sup>[2a,2a]</sup> and that new strategies have started to be developed for improving these water adsorption capabilities. For example, Yan et al. have recently reported a new composite based on MIL-101 containing graphite oxide

and exhibiting high water vapor capacity (maximum uptake up to  $1.6 \text{ g}_{\text{water}} \text{ g}^{-1} \text{ sorbent}$ ).<sup>[16]</sup> To the best of our knowledge, however, other MOF-based composites that enhance the water uptake and/or the use of MOFs as porous matrices to produce CSPMs have not been reported in the literature so far.

In this sense, we have recently reported that the spray-drying method can be used to synthesize MOFs in the form of spherical hollow or compact superstructure/beads built up from the assembly of nanosized crystals.<sup>[17]</sup> An interesting feature of these superstructures is that their nitrogen adsorption isotherms at 77 K normally show a continuous increase of the  $\text{N}_2$  uptake at partial pressures over 0.4, suggesting the presence of interparticular voids in the mesoporous range resulting from the assembly of MOF nanocrystals. Here, we take advantage of these voids and the inherent microporosity of MOFs to use these superstructures as porous matrices to confine inorganic salts. We show that this strategy is suitable to develop effective CSPMs based on MOFs for adsorption heat transformation. For synthesizing these CSPMs, we chose UiO-66 and UiO-66- $\text{NH}_2$  as the porous MOF matrices, and  $\text{CaCl}_2$  and  $\text{LiCl}$  as the inorganic salts. We chose UiO-66 and UiO-66- $\text{NH}_2$  because of their high thermal and water stability and its water sorption capabilities.<sup>[18]</sup> And we chose  $\text{CaCl}_2$  and  $\text{LiCl}$  because of their excellent water uptake capabilities.

## 2. Results and Discussion

### 2.1. Continuous-Flow Spray-Drying Synthesis

The composites were prepared by the spray-drying continuous-flow method, which enabled simultaneous synthesis and shaping of microspherical CSPMs made of  $\text{CaCl}_2$  and UiO-66. In a typical experiment, a precursor solution containing  $\text{ZrCl}_4$ , 1,4-benzene dicarboxylic acid,  $\text{CaCl}_2 \cdot 2\text{H}_2\text{O}$ ,  $\text{H}_2\text{O}$ , and dimethylformamide (DMF) in a molar ratio of 1:1:1.6:40:135 (concentration of  $\text{ZrCl}_4 = 0.1 \text{ M}$ ) was injected into the coil flow reactor at a feed rate of  $2.4 \text{ mL min}^{-1}$  and at a  $T_1$  of  $115 \text{ }^\circ\text{C}$ . The residence time inside the coil flow reactor was 63 s. The resulting preheated solution was then spray-dried at a  $T_2$  of  $180 \text{ }^\circ\text{C}$  and a flow rate of  $336 \text{ mL min}^{-1}$ , using a B-290 mini spray dryer (BUCHI Labortechnik). Once the solution had atomized, a white powder was collected from the spray dryer collector. This powder was analyzed through field-emission scanning electron microscopy (FESEM), which revealed the homogeneous formation of the characteristic spherical superstructures with an average size of  $4.0 \pm 1.9 \text{ }\mu\text{m}$  (Figure 1a). X-ray powder diffraction (XRPD) confirmed the presence of both UiO-66 and  $\text{CaCl}_2$  hydrates forming the superstructures (Figure 1b). The content of Ca in the composites was estimated by digesting this powder (previously outgassed at  $200 \text{ }^\circ\text{C}$  under vacuum) in  $\text{H}_2\text{SO}_4$  at  $50 \text{ }^\circ\text{C}$  and analyzed by Inductively Coupled Plasma - Optical Emission Spectroscopy (ICP-OES), from which a  $\text{CaCl}_2$  content of 38% (hereafter,  $w_{\text{CaCl}_2}/w_{\text{CSPM}}$ ) in the composite (hereafter,  $\text{CaCl}_2@$ UiO-66\_38) was determined. This percentage corresponds to the molar ratio of 1:1.5 ( $\text{Zr}^{4+}:\text{CaCl}_2$ ), which is similar to the initial value (1:1.6), confirming that spray-drying is very efficient for incorporating  $\text{CaCl}_2$  into the superstructures. Elemental mapping with energy dispersive X-ray spectrometry

(EDX) was also performed on a single superstructure, which revealed a highly uniform distribution of Zr, Ca, and Cl atoms (Figure 1c).

Nitrogen physical adsorption measurements on  $\text{CaCl}_2@$ UiO-66\_38 (previously outgassed at  $200 \text{ }^\circ\text{C}$ ) showed a measured Brunauer-Emmett-Teller (BET) surface area of  $\approx 70 \text{ m}^2 \text{ g}^{-1}$ , which was very low compared to that of pristine UiO-66 superstructures that were also obtained by the spray-drying continuous-flow method ( $1106 \text{ m}^2 \text{ g}^{-1}$ ) (Figure 1d). We attribute this low microporosity to  $\text{CaCl}_2$  particles, which are somehow blocking the access of  $\text{N}_2$  molecules into the MOF micropores. This assumption was corroborated by removing the  $\text{CaCl}_2$  from the  $\text{CaCl}_2@$ UiO-66\_38 composites by incubating them in ethanol for 12 h at room temperature. Under these conditions,  $\text{CaCl}_2$  was completely removed from the composites, as confirmed by the disappearance of the characteristic XRPD peaks of the  $\text{CaCl}_2$  hydrates (Figure S1, Supporting Information). Remarkably, the resulting UiO-66 superstructures showed a  $S_{\text{BET}}$  value that increased up to  $1100 \text{ m}^2 \text{ g}^{-1}$  (Figure 1d). In addition, FESEM images of these UiO-66 superstructures revealed the formation of voids resulting from the dissolution of the  $\text{CaCl}_2$  crystals (Figure 1e). The presence of these voids was in concordance with the higher increase in the  $\text{N}_2$  adsorption in the range of pressures related to meso and macroporosity as well as with the pore size distribution curve, in which the presence of mesopores with 14 nm in diameter was evidenced after removing  $\text{CaCl}_2$  (Figure S2, Supporting Information). In addition, the content of UiO-66 in the composite was estimated by weighting these superstructures, from which a UiO-66 content of 58% w/w ( $w_{\text{UiO-66-1}}/w_{\text{CSPM}}$ ) was determined. This percentage is similar to the expected 62% if the  $\text{CaCl}_2@$ UiO-66\_38 is composed of  $\text{CaCl}_2$  and UiO-66. Altogether, these observations are important because they demonstrate that  $\text{CaCl}_2$  particles are confined in the micropores of UiO-66 and/or in the interparticular voids resulting from the assembly of UiO-66 nanocrystals in this class of superstructures.

### 2.2. Water Sorption Properties

Having determined the presence of both UiO-66 and  $\text{CaCl}_2$  in  $\text{CaCl}_2@$ UiO-66\_38, we then evaluated its water sorption properties. Water sorption isotherm of  $\text{CaCl}_2@$ UiO-66\_38 (previously outgassed at  $200 \text{ }^\circ\text{C}$ ) at 298 K showed two segments with steep increase in the water uptake (Figure 2a). These two steps were attributed to the formation of  $\text{CaCl}_2 \cdot 0.33\text{H}_2\text{O}$  at a relative humidity (RH) of 3% (water uptake of  $0.15 \text{ g}_{\text{water}} \text{ g}^{-1} \text{ CSPM}$ ) and to the further transformation of this hydrate to  $\text{CaCl}_2 \cdot 2\text{H}_2\text{O}$  at RHs from 10% to 16% (water uptake of  $0.33 \text{ g}_{\text{water}} \text{ g}^{-1} \text{ CSPM}$ ).<sup>[7,19]</sup> Then, the sorption curve ascended monotonically, indicating the formation of an aqueous solution of the salt and reaching a maximum water uptake of  $1.93 \text{ g}_{\text{water}} \text{ g}^{-1} \text{ CSPM}$  at a RH of 90%.<sup>[7,19]</sup> Interestingly, a hysteresis loop at low pressures ( $P/P_0 = 0.10\text{--}0.16$ ) was observed in the desorption branch due to the structural changes in the transition from  $\text{CaCl}_2 \cdot 2\text{H}_2\text{O}$  hydrate to  $\text{CaCl}_2 \cdot 0.33\text{H}_2\text{O}$  hydrate, which is in agreement with other CSPMs based on mesoporous materials and salts crystals.<sup>[7,20]</sup> Thus, we hypothesize that the water sorption takes place in the following steps: the anhydrous  $\text{CaCl}_2$  particles confined

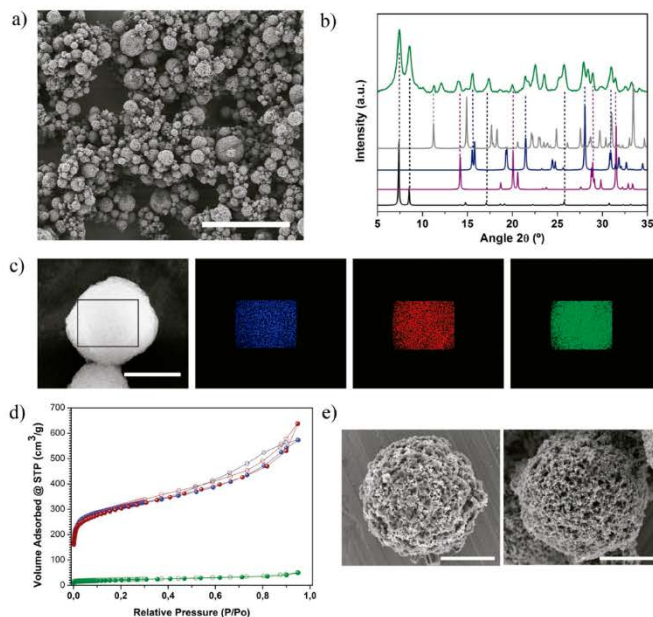


**Figure 1.** a) Representative FESEM image of microspherical  $\text{CaCl}_2@UiO-66_{38}$  CSPMs. b) XRPD pattern of  $\text{CaCl}_2@UiO-66_{38}$  powder (green), as compared to the corresponding simulated powder pattern of UiO-66 (black),  $\text{CaCl}_2\cdot 2\text{H}_2\text{O}$  (purple),  $\text{CaCl}_2\cdot 4\text{H}_2\text{O}\beta$  (gray) and  $\text{CaCl}_2\cdot 4\text{H}_2\text{O}\gamma$  (dark blue). c) Elemental mapping with EDX performed on a single spherical superstructure of  $\text{CaCl}_2@UiO-66_{38}$ , showing the homogeneous distribution of Zr (blue), Ca (red), and Cl (green). d)  $\text{N}_2$  sorption isotherms of  $\text{CaCl}_2@UiO-66_{38}$  (green), pristine UiO-66 (blue), and  $\text{CaCl}_2@UiO-66_{38}$  after incubation in ethanol (red). e) FESEM images of microspherical  $\text{CaCl}_2@UiO-66_{38}$  superstructures before (left) and after (right) incubation in ethanol. Scale bars: a) 20  $\mu\text{m}$ , c) 5  $\mu\text{m}$ , and e) 3  $\mu\text{m}$ .

in the micropores of UiO-66 and/or in the interparticular voids of superstructures adsorbs water and transforms to crystalline  $\text{CaCl}_2\cdot 0.33\text{H}_2\text{O}$ ; then, this hydrate adsorbs more water and is transformed to crystalline  $\text{CaCl}_2\cdot 2\text{H}_2\text{O}$ ; and finally, the salt is completely dissolved filling the pores and/or voids. Here, we also performed eight water sorption-desorption cycles by alternatively exposing  $\text{CaCl}_2@UiO-66_{38}$  to humid (90% RH) and dry (0% RH) environments. Remarkably, the maximum uptake at 90% RH ( $1.93 \text{ g}_{\text{water}} \text{ g}_{\text{CSPM}}^{-1}$ ) remained constant with the number of cycles, confirming the stability of this CSPM to water sorption/desorption processes (Figure 2c).

Water isotherm of  $\text{CaCl}_2@UiO-66_{38}$  was compared with those of their individual components; that is, pristine UiO-66 superstructures and  $\text{CaCl}_2$  (Figure 2a). As expected,  $\text{CaCl}_2@UiO-66_{38}$  showed an intermediate adsorption capacity. Indeed, the adsorption was higher than UiO-66 superstructures (maximum water uptake =  $0.61 \text{ g}_{\text{water}} \text{ g}_{\text{UiO-66}}^{-1}$ ), demonstrating that  $\text{CaCl}_2$  is very effective in increasing water uptake over the whole range of  $P/P_0$ , but lower than pristine  $\text{CaCl}_2$  (maximum water uptake =  $3.91 \text{ g}_{\text{water}} \text{ g}_{\text{CaCl}_2}^{-1}$ ). However, the main differences appeared when compared the aspect of the three samples

exposed to a RH of 80% at room temperature. Under these conditions,  $\text{CaCl}_2@UiO-66_{38}$  and UiO-66 remained as solid adsorbents while  $\text{CaCl}_2$  was dissolved with the water adsorbed due to the deliquescence effect (Figure 2d). Another difference was also found when desorption branches were compared.  $\text{CaCl}_2$  retained around  $0.70 \text{ g}_{\text{water}} \text{ g}_{\text{CaCl}_2}^{-1}$  (17.9% of the total uptake) at a RH of =0%, whereas  $\text{CaCl}_2@UiO-66_{38}$  retained only  $0.06 \text{ g}_{\text{water}} \text{ g}_{\text{CSPM}}^{-1}$  (3.1% of the total uptake).

To prove that the properties of  $\text{CaCl}_2@UiO-66_{38}$  composite result from using the in situ spray-drying synthesis and shaping methodology rather than simply mixing UiO-66 and  $\text{CaCl}_2$ , we also performed the water sorption measurement of a physical mixture of  $\text{CaCl}_2$  and UiO-66 superstructures (38% and 62% (w/w), respectively). The total water uptake of this mixture ( $1.86 \text{ g}_{\text{water}} \text{ g}_{\text{mixture}}^{-1}$ ) was slightly lower than the composite uptake (Figure 2b), but properly matched with the percentage of contribution of the individual components. Again, the differences were the liquefaction of the  $\text{CaCl}_2$  of this mixture when exposed to a RH of 80% at room temperature (Figure 2d), and a water retention of  $0.30 \text{ g}_{\text{water}} \text{ g}_{\text{mixture}}^{-1}$  (16.1% of the total uptake) at a RH of =0% (Figure 2b). This behavior is very similar to that

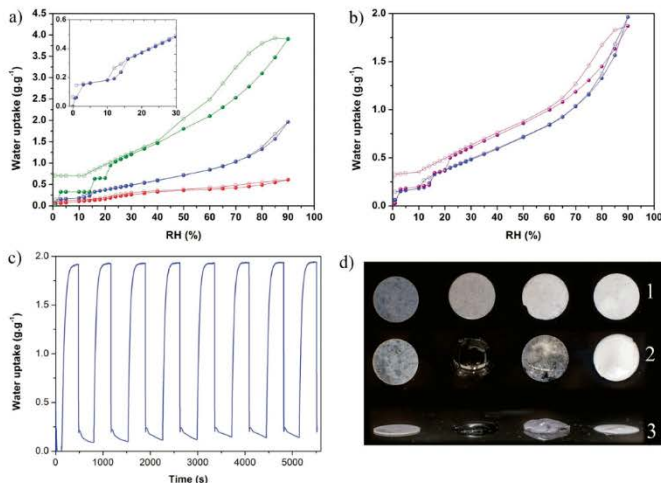


**Figure 2.** a) Water adsorption isotherms of UiO-66 (red),  $\text{CaCl}_2$ @UiO-66\_38 (blue), and  $\text{CaCl}_2$  (green). Insert shows water adsorption isotherm of  $\text{CaCl}_2$ @UiO-66\_38 at low RHs. b) Water adsorption isotherms of  $\text{CaCl}_2$ @UiO-66\_38 (blue) and the physical mixture (purple) (adsorption: solid symbols; desorption: open symbols). c) Adsorption and desorption cycles for  $\text{CaCl}_2$ @UiO-66\_38. d) Photograph of the pellets of (from left to right) UiO-66,  $\text{CaCl}_2 \cdot 2\text{H}_2\text{O}$ , physical mixture, and  $\text{CaCl}_2$ @UiO-66\_38 before (1) and after (2 and 3) exposing them to a RH of 80% at room temperature (2: top view, 3: lateral view).

found for the pristine  $\text{CaCl}_2$ , thereby confirming that a simple mixture is not enough for producing a composite that behaves as a solid adsorbent when adsorb water, as it does the spray-drying synthesized spherical superstructures.

### 2.3. Tuning the Composition of $\text{CaCl}_2$

We then sought to assess the water sorption properties of  $\text{CaCl}_2$ @UiO-66 composites with diverse compositions, seeking to find an optimal  $\text{CaCl}_2$ /UiO-66 ratio in terms of maximum capacity of UiO-66 superstructures to host  $\text{CaCl}_2$  while preventing its dissolution. Thus, we systematically synthesized a series of composites in which we increased the initial molar ratios of  $\text{CaCl}_2$  from 1:2.6, 1:3.2, 1:4.8 to 1:6.4 ( $\text{Zr}^{4+}$ : $\text{CaCl}_2$ ). Again, the content of Ca in the composites was estimated by digesting the as-made samples (previously outgassed at 200 °C under vacuum) in  $\text{H}_2\text{SO}_4$  at 50 °C and analyzed by ICP-OES (Table S1, Supporting Information). FESEM images revealed the formation of  $\text{CaCl}_2$ @UiO-66\_X for the first three samples (where X = 50%, 53%, and 64%  $w_{\text{CaCl}_2}/w_{\text{CSPM}}$ ) in the form of spherical superstructures (Figures 3a,b; Figure S3, Supporting Information). However,  $\text{CaCl}_2$ @UiO-66\_64 sample was discarded because it showed the presence of nonencapsulated  $\text{CaCl}_2$  crystals together with the superstructures. In the case of a molar ratio of 1:6.4, crystalline spherical superstructures were not formed (Figure S3, Supporting Information). For the first two compositions, XRPD patterns confirmed the formation of UiO-66 and the presence of  $\text{CaCl}_2$  hydrates (Figure 3c).

To examine the water adsorption properties of the  $\text{CaCl}_2$ @UiO-66\_50 and  $\text{CaCl}_2$ @UiO-66\_53 CSPMs, water adsorption isotherms were measured at 298 K (Figure 3d). All resulting isotherms displayed the characteristic steps related to the formation of  $\text{CaCl}_2 \cdot 0.33\text{H}_2\text{O}$  and  $\text{CaCl}_2 \cdot 2\text{H}_2\text{O}$  hydrates, and the hysteresis loop in the desorption branch. The maximum uptake of the composites was 2.24  $\text{g}_{\text{water}} \text{g}^{-1}_{\text{CSPM}}$  ( $\text{CaCl}_2$ @UiO-66\_50) and 2.59  $\text{g}_{\text{water}} \text{g}^{-1}_{\text{CSPM}}$  ( $\text{CaCl}_2$ @UiO-66\_53) at RH of 90%. As expected, a greater amount of  $\text{CaCl}_2$  led to achieve a higher water uptake. As well, a higher amount of  $\text{CaCl}_2$  resulted in higher water retention values at a RH of  $\approx 0\%$ , as evidenced by the water retentions of 0.17  $\text{g}_{\text{water}} \text{g}^{-1}_{\text{mixture}}$  (7.6% of the total uptake) for  $\text{CaCl}_2$ @UiO-66\_50 and of 0.20  $\text{g}_{\text{water}} \text{g}^{-1}_{\text{mixture}}$  (7.7% of the total uptake) for  $\text{CaCl}_2$ @UiO-66\_53; in comparison to that observed in  $\text{CaCl}_2$ @UiO-66\_38 (3.1% of the total uptake).

### 2.4. Synthesis of $\text{LiCl}$ @UiO-66 and $\text{CaCl}_2$ @UiO-66- $\text{NH}_2$ Composites

To demonstrate the generality of our approach, we used the spray-drying technique to synthesize other Salt@MOF CSPMs substituting the inorganic salt and the MOF. Thus, we prepared  $\text{LiCl}$ @UiO-66, and  $\text{CaCl}_2$ @UiO-66- $\text{NH}_2$  using the same conditions as for  $\text{CaCl}_2$ @UiO-66\_38, except that instead of  $\text{CaCl}_2$  in the first case and UiO-66 in the second case, we used  $\text{LiCl}$  and UiO-66- $\text{NH}_2$ , respectively. In both cases, pure microspherical superstructures were obtained, as confirmed by FESEM and XRPD (Figure 3e,g; Figure S4, Supporting Information). The

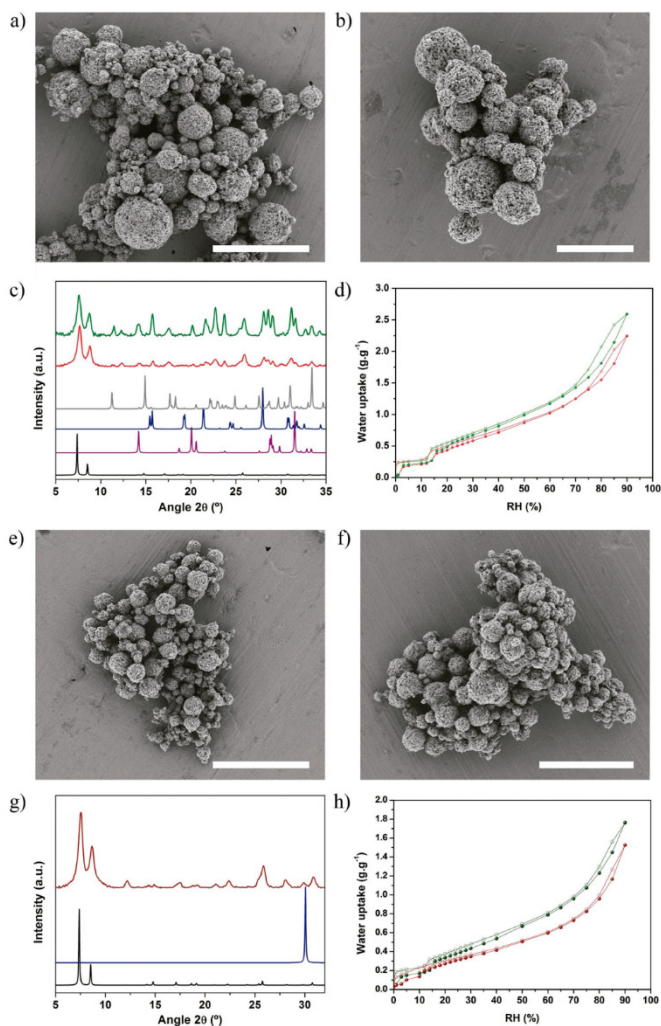


**Figure 3.** Representative FESEM images of a)  $\text{CaCl}_2@UiO-66-50$ , b)  $\text{CaCl}_2@UiO-66-53$ , e)  $\text{LiCl}@UiO-66-19$ , and f)  $\text{CaCl}_2@UiO-66-NH_2-38$ . c) XRPD diffractograms of  $\text{CaCl}_2@UiO-66-50$  (red) and  $\text{CaCl}_2@UiO-66-53$  (green), as compared to the simulated powder pattern for UiO-66 (black),  $\text{CaCl}_2\cdot 2H_2O$  (purple),  $\text{CaCl}_2\cdot 4H_2O\gamma$  (dark blue), and  $\text{CaCl}_2\cdot 4H_2O\beta$  (gray). d) Water adsorption isotherms of  $\text{CaCl}_2@UiO-66-50$  (red) and  $\text{CaCl}_2@UiO-66-53$  (green) at 25 °C. g) XRPD diffractograms of  $\text{LiCl}@UiO-66-19$ , as compared to the simulated powder pattern for UiO-66 (black) and  $\text{LiCl}$  (dark blue). h) Water adsorption isotherms of  $\text{LiCl}@UiO-66-19$  (dark red) and  $\text{CaCl}_2@UiO-66-NH_2-38$  (dark green). Scale bars: a,e) 20  $\mu\text{m}$  and b,f) 10  $\mu\text{m}$ .

content of Li and Ca was also estimated by ICP-OES, from which a LiCl content of 19% w/w in  $\text{LiCl}@UiO-66-19$  and a  $\text{CaCl}_2$  content of 38% w/w in  $\text{CaCl}_2@UiO-66-NH_2-38$  were determined.

Here, water sorption measurements at 298 K showed that  $\text{LiCl}@UiO-66-19$  exhibits a high water uptake of 1.53  $\text{g}_{\text{water}} \text{g}^{-1}_{\text{CSPM}}$  at a RH of 90% and a water retention of 0.07  $\text{g}_{\text{water}} \text{g}^{-1}_{\text{CSPM}}$  (4.6% of

the total uptake) during desorption (Figure 3h). On the other hand,  $\text{CaCl}_2@ \text{UiO}-66\text{-NH}_2\text{-38}$  showed a maximum uptake of  $1.76 \text{ g}_{\text{water}} \text{ g}^{-1}_{\text{CSPM}}$ , which is lower compared with its analogue based on UiO-66, and it retained  $0.12 \text{ g}_{\text{water}} \text{ g}^{-1}_{\text{CSPM}}$  (6.8% of the total uptake) of water at a RH of 0%, which doubles that of its UiO-66 analogue.

## 2.5. Thermal Batteries Application

Figure S5 (Supporting Information) summarizes the working capacity for all prepared materials and the most promising UiO-66-based CSPMs were tested as potential adsorbents in thermal batteries and adsorption heat pumps applications according to their working capacity ( $\Delta w$ ). Among them, thermal batteries have been recently explored as an alternative to the traditional air conditioning systems in electric vehicles. Traditionally, the climate control system is based on a vapor compression system where the compressor is driven by an electric battery with high power consumption, producing a decrease in the efficiency of the electric vehicle. Thermal batteries are based on a sorption and desorption cycles where large amounts of energy can be reversibly stored to provide heating and cooling efficiently. As a consequence, the consumption of electric power decreases and the driving range of the electric vehicle increases.<sup>[2c,21]</sup>

To evaluate our CSPMs as adsorbents for thermal batteries, we selected  $\text{CaCl}_2@ \text{UiO}-66\text{-38}$  because it has the higher working capacity ( $\Delta w = 0.12 \text{ g}_{\text{water}} \text{ g}^{-1}_{\text{CSPM}}$ ) at  $P/P_0 = 0.1$  (Figure 2a). It is important to highlight here that water adsorption is desirable at a relative pressure of 0.1 to reduce the need of using compressors in the system.<sup>[15]</sup>

Once  $\text{CaCl}_2@ \text{UiO}-66\text{-38}$  was selected, the heat storage capacity ( $C_{\text{HS}}$ ) was estimated according to the Equation (1)<sup>[2b]</sup>

$$C_{\text{HS}} = \frac{\Delta H_{\text{ads}} \cdot \Delta w}{M_w} \quad (1)$$

where  $M_w$  is the water molar weight and  $\Delta H_{\text{ads}}$  is the heat of adsorption.  $\Delta H_{\text{ads}}$  of  $\text{CaCl}_2@ \text{UiO}-66\text{-38}$  was calculated using water isotherms collected at different temperatures (25, 40, and 50 °C; Figure 4a), and then adjusted to the Clausius–Clapeyron Equation (2)<sup>[22]</sup>

$$\Delta H_{\text{ads}} = -R \ln \left( \frac{P_2}{P_1} \right) \frac{T_1 \cdot T_2}{T_2 - T_1} \quad (2)$$

It was found that  $\Delta H_{\text{ads}}$  values decrease as water uptakes increase (from  $\approx 55$  to  $\approx 43 \text{ kJ mol}^{-1}$ ; Figure 4b), and that  $\Delta H_{\text{ads}}$  was  $55 \text{ kJ mol}^{-1}$  for a working capacity of  $0.12 \text{ g}_{\text{water}} \text{ g}^{-1}_{\text{CSPM}}$ . These values are in agreement with the initial formation of the  $\text{CaCl}_2$  hydrate, where the water molecules are stronger bounded and then, a decrease to  $43 \text{ kJ mol}^{-1}$  is due to the formation of an aqueous solution of  $\text{CaCl}_2$ .<sup>[23]</sup>

Finally, a  $C_{\text{HS}}$  value of  $367 \text{ kJ kg}^{-1}$  was determined using Equation (1). According to primary technical targets for thermal batteries,<sup>[24]</sup> the minimum heat storage capacity should be 2.5 kWh. This means that 24.5 kg of  $\text{CaCl}_2@ \text{UiO}-66\text{-38}$  will be required to achieve this capacity, which is less than the total

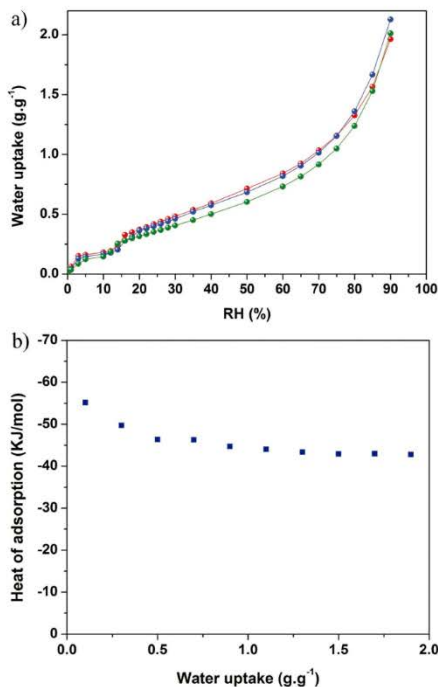


**Figure 4.** a) Water adsorption isotherms of  $\text{CaCl}_2@ \text{UiO}-66\text{-38}$  at 30 °C (red), 40 °C (blue), and 50 °C (green). b) Heat of adsorption of  $\text{CaCl}_2@ \text{UiO}-66\text{-38}$ .

weight of the system (35 kg) suggested by U.S. Department of Energy (DOE).<sup>[24]</sup>

## 2.6. Adsorption Chillers Application

To evaluate our CSPMs as adsorbents for adsorption chillers, we selected  $\text{CaCl}_2@ \text{UiO}-66\text{-53}$  because it had the higher working capacity at  $P/P_0 = 0.3$ , which is a typical value for practical applications.<sup>[2a]</sup> In order to describe the performance and the efficiency of this system, the specific cooling power (SCP), an isosteric cycle diagram and the coefficient of performance (COP) were determined.

The average SCP describes the effectiveness of the system during the cooling process and is defined as the ratio of cooling power per mass of adsorbent per cycle time according to Equation (3)<sup>[2b]</sup>

$$\text{SCP} = \frac{\Delta H_{\text{vap}} \cdot \Delta w \cdot 0.8}{M_w (\tau_{0.8\text{ads}} + \tau_{0.8\text{ads}})} \quad (3)$$

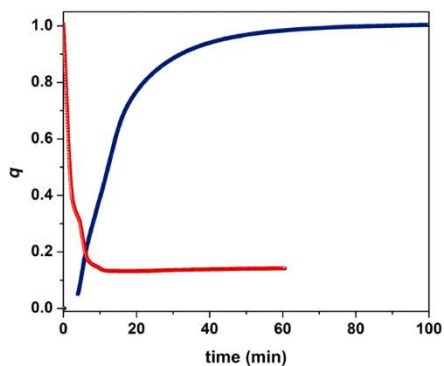


**Figure 5.** Kinetics of water adsorption of  $\text{CaCl}_2@ \text{UiO-66}_{53}$  at  $T = 303$  K and  $P = 1.24$  kPa (blue) and desorption at  $T = 370$  K and  $P = 5.4$  kPa (red).

where  $\Delta H_{\text{vap}}$  is the water enthalpy of evaporation,  $\Delta w$  is the working capacity of the  $\text{CaCl}_2@ \text{UiO-66}_{53}/\text{H}_2\text{O}$  pair,  $M_w$  is the water molar weight, and  $\tau_{0.8\text{ads}}$  and  $\tau_{0.8\text{des}}$  are the adsorption and desorption times when the conversion  $q = 0.8$  (Figure 5).

An isosteric cycle diagram of an adsorption air conditioning cycle was analyzed to determine  $\Delta w$  and the desorption temperature ( $T_{\text{des}}$ ) (Figure 6). This diagram was calculated using the water adsorption isobars at vapor pressures of 0.7, 1.2, 2.4, 3.7, 4.2, and 5.6 kPa (Figure S6, Supporting Information), and fixing the operational temperatures of the cycle to a temperature of evaporation ( $T_{\text{ev}}$ ) of 283 K and to a temperature of adsorption and condensation ( $T_{\text{ad}} = T_{\text{con}}$ ) of 303 K. In the isobaric adsorption (step IV–I), the water was adsorbed in the composite reaching a maximum uptake of  $0.60 \text{ g}_{\text{water}} \text{ g}^{-1} \text{CSPM}$ . Then,

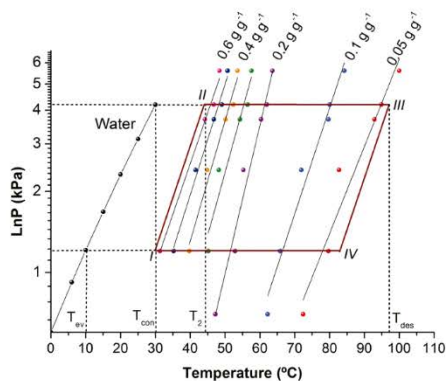


**Figure 6.** Isosteric cycle diagram for  $\text{CaCl}_2@ \text{UiO-66}_{53}/\text{water}$  working pair calculated for an air cooling cycle.

during the isosteric heating (I–II), the  $\text{CaCl}_2@ \text{UiO-66}_{53}$  was fully saturated and the pressure increased from 1.2 to 4.2 kPa by increasing the temperature from 303 to 317 K without desorption. In the isobaric desorption (II–III), the heating was continued and desorption process was started until reached a  $T_{\text{des}}$  of 370 K, in which the water uptake was minimal. Finally, in the isosteric cooling, decreasing the temperature reduced the pressure, and the composite was regenerated. In this cycle,  $\Delta w$  depends on the  $T_{\text{des}}$  (Figure S7, Supporting Information), where  $\Delta w$  increases from  $0.3 \text{ g}_{\text{water}} \text{ g}^{-1} \text{CSPM}$  at  $T_{\text{des}} = 330$  K to  $0.56 \text{ g}_{\text{water}} \text{ g}^{-1} \text{CSPM}$  at  $T_{\text{des}} = 370$  K. These values are higher compared to traditional adsorbents like zeolites, silica gel, and other CSPMs (Table 1), and are in the range of some reported MOFs (e.g.,  $\text{NH}_2\text{-MIL-12}$ :  $0.39 \text{ g}_{\text{water}} \text{ g}_{\text{MOF}}^{-1}$ ;  $\text{CPO-27(Ni)}$ :  $0.41 \text{ g}_{\text{water}} \text{ g}_{\text{MOF}}^{-1}$ ;  $\text{MOF-841}$ :  $0.44 \text{ g}_{\text{water}} \text{ g}_{\text{MOF}}^{-1}$ ).<sup>[2b,15,25]</sup>

The adsorption and desorption times were calculated from the kinetic curves of water adsorption and desorption (Figure 5), which were performed under the standard  $T_{\text{ad}} = 303$  K,  $P_{\text{ad}} = 1.24$  kPa, and  $P_{\text{des}} = 5.4$  kPa conditions and the determined  $T_{\text{des}} = 370$  K. From these curves, we found that  $\tau_{0.8\text{ads}}$  and  $\tau_{0.8\text{des}}$  were 1320 and 380 s, respectively. Finally, a SCP value of  $631 \text{ W kg}^{-1}$  was calculated according to Equation (3).<sup>[2b]</sup>

In an adsorption air conditioning system, COP is a factor that helps describing the energetic efficiency. COP is defined as the useful output energy divided by the energy required as input.<sup>[26]</sup> Thus, COP is the ratio of the vaporization heat ( $Q_{\text{ev}}$ ) and regeneration heat ( $Q_{\text{reg}}$ ) according to Equation (4)<sup>[12c]</sup>

$$\text{COP} = \frac{Q_{\text{ev}}}{Q_{\text{reg}}} \quad (4)$$

Here, the vaporization ( $Q_{\text{ev}}$ ) and regeneration ( $Q_{\text{reg}}$ ) heats were calculated from Equations (5)–(8)

$$Q_{\text{ev}} = \frac{\Delta H_{\text{vap}}(T_{\text{ev}}) \cdot \rho \cdot m \cdot \Delta w}{M_w} \quad (5)$$

where  $\rho$  is the water density and  $m$  is the amount of  $\text{CaCl}_2@ \text{UiO-66}_{53}$  used in the cycle.

$$Q_{\text{reg}} = Q_{\text{I-II}} + Q_{\text{II-III}} \quad (6)$$

$$Q_{\text{I-II}} = \int_{T_{\text{min}}}^{T_2} C_p^{\text{CSPM}}(T) dT + \int_{T_{\text{min}}}^{T_2} \rho \cdot W_{\text{max}} C_p^{\text{water}}(T) dT \quad (7)$$

$$Q_{\text{II-III}} = \int_{T_2}^{T_{\text{con}}} C_p^{\text{CSPM}}(T) dT + \int_{T_{\text{min}}}^{T_2} \rho \cdot \frac{W_{\text{max}} + W_{\text{min}}}{2} \cdot C_p^{\text{water}}(T) dT - \frac{1}{M_w} \int_{W_{\text{min}}}^{W_{\text{max}}} \rho \cdot \Delta H_{\text{ads}}(W) dW \quad (8)$$

where  $C_p^{\text{CSPM}}$  is the heat capacity of  $\text{CaCl}_2@ \text{UiO-66}_{53}$ ,  $C_p^{\text{water}}$  is the heat capacity of water, and  $W_{\text{max}}$  and  $W_{\text{min}}$  are the water loading at points II and III, respectively, of the isosteric cycle diagram (Figure 6).

**Table 1.** Water loading, regeneration temperature, COP<sub>c</sub>, and SCP for selected materials compared with CaCl<sub>2</sub>@UiO-66\_53 composite.

Adsorbent	Water loading [g g <sup>-1</sup> ]	Regeneration temperature [°C]	COP <sub>c</sub>	SCP [W kg <sup>-1</sup> ]	Reference
CaCl <sub>2</sub> @UiO-66_53	0.60	57–110	0.83	631	This work
Silica gel	–	85	0.37	63.4	[27]
Activated carbon	0.19	115	0.37	65	[28]
Zeolite 13-X	0.25	310	0.38	25.7	[29]
AQSOA-FAM-202 (ALPO-34)	0.28	90	0.25–0.3	260	[30]
SWS-8L (Ca(NO <sub>3</sub> ) <sub>2</sub> )@ mesoporous silica	–	90–95	0.18–0.31	190–389	[31]
SWS-9V (LiNO <sub>3</sub> )@ vermiculite)	0.4	70	0.59	96	[32]
CaCl <sub>2</sub> @silica-carbon	0.43	115	0.7	378	[28]
NH <sub>2</sub> -MIL-125	0.42	90	0.8	3200	[2b]
CPO-27(Ni)	0.41	130	0.45	440	[25]

Thus, the sorption heat ( $\Delta H_{\text{ads}}$ ) of the working pair CaCl<sub>2</sub>@UiO-66\_53/water and the heat capacity ( $C_p$ ) of CaCl<sub>2</sub>@UiO-66\_53 were initially determined. The  $\Delta H_{\text{ads}}$  was calculated using the Clausius–Clapeyron equation and water isotherms at two different temperatures (25 and 40 °C) (Figure S8, Supporting Information). As seen in the previous section, the  $\Delta H_{\text{ads}}$  decreased as water uptake increased (from  $\approx 52$  to  $\approx 41$  kJ mol<sup>-1</sup>; Figure S9, Supporting Information). Afterward, the  $C_p$  of CaCl<sub>2</sub>@UiO-66\_53 was determined from Differential Scanning Calorimetry (DSC) analysis, from which an average  $C_p$  of 0.76 J g<sup>-1</sup> K<sup>-1</sup> was calculated over the temperature range of 303–353 K (Figure S10, Supporting Information).

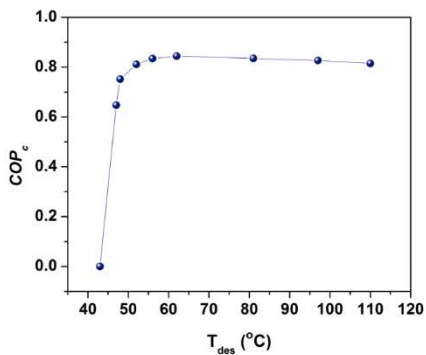
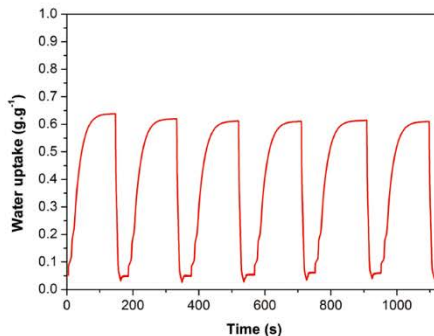
Once we determined these parameters, COP was calculated as a function of  $T_{\text{des}}$  (Figure 7). For a  $T_{\text{des}}$  from 330 to 383 K, a COP value of 0.83 remained almost constant, meaning that 0.83 J of cold can be generated from 1 J of waste heat.

Finally, we also studied the multiple adsorption–desorption cycles under operational conditions for air conditioning

systems ( $P = 2.36$  kPa, and  $T_{\text{ads}} = 303$  K, and  $T_{\text{des}} = 383$  K). Figure 8 shows six consecutive cycles in which, after the first three cycles, a very small decrease in the water uptake (from 0.63 to 0.61 g g<sup>-1</sup>) was observed. Then, water uptake became stable, without a significant loss of adsorption and desorption capacities during the remaining cycles.

### 3. Conclusion

In conclusion, we have reported a continuous and fast methodology for the fabrication of MOF-based CSPM materials using the spray-drying continuous flow method, which enables the simultaneous synthesis and shaping of microspherical MOF superstructures while confining the salts. This method also enables tuning the composition of the resulting CSPMs. We have demonstrated the applicability of these MOF-based CSPMs for potential applications in thermal batteries and refrigerator


**Figure 7.** Coefficient of performance (COP) as a function of desorption temperature for the CaCl<sub>2</sub>@UiO-66\_53/Water working pair.

**Figure 8.** Adsorption–desorption cycles under operational conditions for air conditioning systems ( $P = 2.36$  kPa, and  $T_{\text{ads}} = 303$  K and  $T_{\text{des}} = 383$  K) for CaCl<sub>2</sub>@UiO-66\_53.

systems. For the first application, we have shown that  $\text{CaCl}_2@$  UiO-66\_38 exhibits a  $C_{115}$  of  $367 \text{ kJ kg}^{-1}$ , which fulfills the conditions suggested by the U.S. Department of Energy to use it in thermal batteries. For the latter application, the working pair  $\text{CaCl}_2@$  UiO-66\_53/water displays a high capacity and energetic efficiency, exhibiting a COP of 0.83. This value is higher than traditional working pairs based on silica and zeolites and others CSPMs, which exhibit COP values from 0.3 to 0.6, (e.g., silica gel: 0.3; zeolite-NaX: 0.38; natural zeolite: 0.34; and  $\text{LiCl}@$  silica: 0.41)<sup>4</sup> and it is comparable with the most energy efficient MOFs ( $\text{NH}_2$ -ML-125: 0.8; CAU-3: 0.7; MOF-841: 0.8) reported so far.<sup>[2b,12c,26]</sup> We believe that this methodology will facilitate the synthesis of other CSPMs, in which the nature of the MOF and the salt can be changed, as well as of new composites resulting from the combination of MOFs with other nanomaterials such as inorganic nanoparticles or graphene.

#### 4. Experimental Section

**Materials and Methods:** Zirconium chloride, calcium chloride, lithium chloride, terephthalic acid, and 2-aminoterephthalic acid were purchased from Sigma-Aldrich. Dimethylformamide was obtained from Fisher Chemical. All the reagents were used without further purification. Deionized water, obtained with a Milli-Q system (18.2 M $\Omega$  cm), was used in all reactions.

RPD patterns were collected on an X'Pert PRO MPDP analytical diffractometer (Panalytical) at 45 kV, 40 mA using Cu K $\alpha$  radiation ( $\lambda = 1.5419 \text{ \AA}$ ). FESEM images were collected on a FEI Magellan 400L scanning electron microscope at an acceleration voltage of 2.0 kV and FEI Quanta 650F scanning electron microscope with EDX Inca 250 SSD XMax20 at an acceleration voltage of 20.0 kV, using aluminum as support. ICP-OES measurements were performed using a Perkin Elmer Optima 4300DV after sulphuric acid digestion. Prior to the ICP analysis, samples were degassed under vacuum at 200 °C. Volumetric  $\text{N}_2$  sorption isotherms were collected at 77 K using an AutosorbIQ-AG analyzer (Quantachrome Instruments). Gravimetric water vapor sorption isotherms were measured using a DVS vacuum instrument (Surface Measurement Systems Ltd). The weight of the dried powder (=20 mg) was constantly monitored with a high resolution microbalance ( $\pm 0.1 \mu\text{g}$ ) and recorded at 25, 35, and 45 °C ( $\pm 0.2$  °C) under pure water vapor pressures. The kinetics curves of water vapor adsorption were obtained measuring real time mass change. The isobars were recorded at different temperatures from 110 to 30 °C at fixed pressures of 0.7, 1.2, 2.4, 3.7, 4.2, and 5.6 kPa. Prior to the sorption experiments, samples were degassed inside the chamber under vacuum at 200 °C for 6 h. The heat capacity measurements were performed on a differential scanning calorimeter (Mettler Toledo). The heating rate used was 10 °C  $\text{min}^{-1}$  from 10 to 90 °C and sapphire was used as a reference material.

**Spray-Drying Continuous Flow-Assisted Synthesis of UiO-66 and UiO-66-NH<sub>2</sub> Superstructures:** UiO-66 and UiO-66-NH<sub>2</sub> superstructures were synthesized according to the method reported recently.<sup>[17b]</sup> In a typical synthesis, a solution 0.1 M of  $\text{ZrCl}_4$  and 0.1 M of the organic ligand in 15 mL of a mixture of DMF and  $\text{H}_2\text{O}$  (5.48:1) was injected into the coil flow reactor (Pyrex tube, inner diameter: 3 mm) at a feed rate of 2.4 mL  $\text{min}^{-1}$  and at a  $T_1$  of 115 °C. The resulting preheated solution was then spray-dried at a  $T_2$  of 180 °C and a flow rate of 336 mL  $\text{min}^{-1}$  using a Dryer B-290 Mini Spray (BUCHI Labortechnik; spray cap: 0.5 mm hole). Finally, the collected solid was dispersed in DMF at room temperature, stirred overnight, and precipitated by centrifugation. This process was repeated twice with ethanol instead of DMF. The final product was dried for 12 h at 80 °C.

**Spray-Drying Continuous Flow-Assisted Synthesis of UiO-66-Based CSPMs:** A 15 mL solution containing 0.1 M of  $\text{ZrCl}_4$ , 0.1 M of terephthalic acid, and a solution of  $\text{CaCl}_2\cdot\text{H}_2\text{O}$  (at the concentration of 0.16, 0.26,

0.32, 0.48, and 0.64 M) or LiCl (at the concentration of 0.16) in a mixture of DMF and  $\text{H}_2\text{O}$  (5.48:1) was injected into the coil flow reactor (Pyrex tube, inner diameter: 3 mm) at a feed rate of 2.4 mL  $\text{min}^{-1}$  and at a  $T_1$  of 115 °C. The resulting preheated solution was then spray-dried at a  $T_2$  of 180 °C and a flow rate of 336 mL  $\text{min}^{-1}$  using a Dryer B-290 Mini Spray (BUCHI Labortechnik; spray cap: 0.5 mm hole), collecting a white solid.

**Spray-Drying Continuous Flow-Assisted Synthesis of  $\text{CaCl}_2@$ UiO-66-NH<sub>2</sub>:** A 15 mL solution containing 0.1 M of  $\text{ZrCl}_4$ , 0.1 M of 2-aminoterephthalic acid and 0.16 M of  $\text{CaCl}_2\cdot\text{H}_2\text{O}$  in a mixture of DMF and  $\text{H}_2\text{O}$  (5.48:1) was injected into the coil flow reactor (Pyrex tube, inner diameter: 3 mm) at a feed rate of 2.4 mL  $\text{min}^{-1}$  and at a  $T_1$  of 115 °C. The resulting preheated solution was then spray-dried at a  $T_2$  of 180 °C and a flow rate of 336 mL  $\text{min}^{-1}$  using a Dryer B-290 Mini Spray (BUCHI Labortechnik; spray cap: 0.5 mm hole), collecting a yellow solid.

#### Supporting Information

Supporting Information is available from the Wiley Online Library or from the author.

#### Acknowledgements

This work was supported by the Spanish MINECO (Project PN MAT2015-65354-C2-1-R), the Catalan AGAUR (Project 2014 SGR 80), the ERC under the EU FP7 (ERC-Co 615954), and the European Union's Horizon 2020 research and innovation programme under Grant Agreement No. 685727. ICN2 acknowledges the support of the Spanish MINECO through the Severo Ochoa Centers of Excellence Programme (Grant No. SEV-2013-0295). The authors thank Dr. Vincent Guillem from the photographic work.

#### Keywords

batteries, composite materials, hybrid materials, metal-organic frameworks, porous materials

Received: December 6, 2016

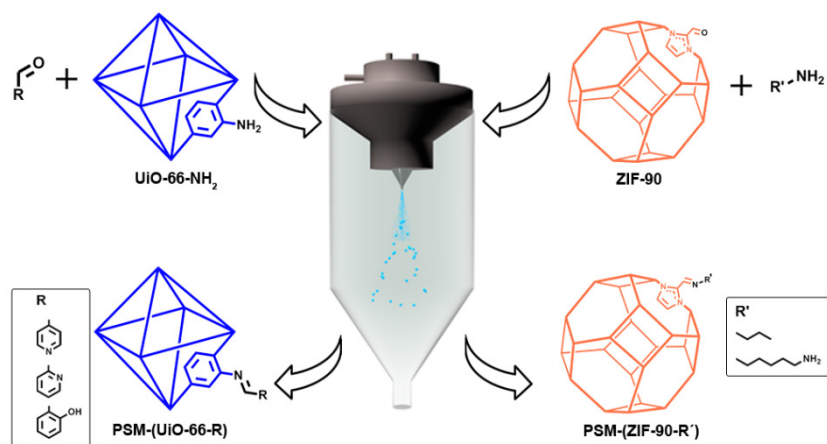
Revised: February 2, 2017

Published online: April 3, 2017

- [1] P. Tatsidjoudjoug, N. Le Pierrès, L. Luo, *Renewable Sustainable Energy Rev.* **2013**, *18*, 327.
- [2] a) J. Canivet, A. Fateeva, Y. Guo, B. Coasne, D. Farrusseng, *Chem. Soc. Rev.* **2014**, *43*, 5594; b) L. G. Gordeeva, M. V. Solov'yeva, Y. I. Aristov, *Energy* **2016**, *100*, 18; c) S. Narayanan, X. Li, S. Yang, H. Kim, A. Umans, I. S. McKay, E. N. Wang, *Appl. Energy* **2015**, *149*, 104.
- [3] S. K. Henninger, F. P. Schmidt, H. M. Henning, *Appl. Therm. Eng.* **2010**, *30*, 1692.
- [4] a) L. G. Gordeeva, Y. I. Aristov, *Int. J. Low-Carbon Technol.* **2012**, *7*, 288; b) H. Demir, M. Mobedi, S. Ülkü, *Renewable Sustainable Energy Rev.* **2008**, *12*, 2381.
- [5] Y. I. Aristov, *Appl. Therm. Eng.* **2013**, *50*, 1610.
- [6] X. J. Zhang, L. M. Qiu, *Energy Convers. Manage.* **2007**, *48*, 320.
- [7] Y. Yuan, H. Zhang, F. Yang, N. Zhang, X. Cao, *Renewable Sustainable Energy Rev.* **2016**, *54*, 761.
- [8] a) Y. Tashiro, M. Kubo, Y. Katsumi, T. Meguro, K. Komeya, *J. Mater. Sci.* **2004**, *39*, 1315; b) F. Meunier, *Appl. Therm. Eng.* **2013**, *61*, 830; c) L. Bonaccorsi, L. Calabrese, A. Freni, E. Proverbio, G. Restuccia, *Appl. Therm. Eng.* **2013**, *50*, 1590.

- [9] a) W. Wang, L. Wu, Z. Li, Y. Fang, J. Ding, J. Xiao, *Drying Technol.* **2013**, *31*, 1334; b) X. Wei, W. Wang, J. Xiao, L. Zhang, H. Chen, J. Ding, *Chem. Eng. J.* **2013**, *228*, 1133.
- [10] a) L. Wang, D. Zhu, Y. Tan, *Adsorption* **1999**, *5*, 279; b) S. Szarzynski, Y. Feng, M. Pons, *Int. J. Refrig.* **1997**, *20*, 390.
- [11] a) H. Furukawa, N. Ko, Y. B. Go, N. Aratani, S. B. Choi, E. Choi, A. Ö. Yazaydin, R. Q. Snurr, M. O'Keeffe, J. Kim, O. M. Yaghi, *Science* **2010**, *329*, 424; b) Y.-K. Seo, J. W. Yoon, J. S. Lee, U. H. Lee, Y. K. Hwang, C.-H. Jun, P. Horcajada, C. Serre, J.-S. Chang, *Micro-porous Mesoporous Mater.* **2012**, *157*, 137.
- [12] a) J. Ehrenmann, S. K. Henninger, C. Janiak, *Eur. J. Inorg. Chem.* **2011**, *2011*, 471; b) A. Khutia, H. U. Rammelberg, T. Schmidt, S. Henninger, C. Janiak, *Chem. Mater.* **2013**, *25*, 790; c) M. F. de Lange, K. J. F. M. Verouden, T. J. H. Vlugt, J. Gascon, F. Kapteijn, *Chem. Rev.* **2015**, *115*, 12205; d) A. Cadiau, J. S. Lee, D. Damasceno Borges, P. Fabry, T. Devic, M. T. Wharmby, C. Martineau, D. Foucher, F. Taulelle, C.-H. Jun, Y. K. Hwang, N. Stock, M. F. De Lange, F. Kapteijn, J. Gascon, G. Maurin, J.-S. Chang, C. Serre, *Adv. Mater.* **2015**, *27*, 4775.
- [13] a) A. Mallick, T. Kundu, R. Banerjee, *Chem. Commun.* **2012**, *48*, 8829; b) S. C. Sahoo, T. Kundu, R. Banerjee, *J. Am. Chem. Soc.* **2011**, *133*, 17950; c) R. M. P. Colodrero, P. Olivera-Pastor, E. R. Losilla, D. Hernández-Alonso, M. A. G. Aranda, L. Leon-Reina, J. Rius, K. D. Demadis, B. Moreau, D. Villemin, M. Palomino, F. Rey, A. Cabeza, *Inorg. Chem.* **2012**, *51*, 7689.
- [14] P. Guo, A. G. Wong-Foy, A. J. Matzger, *Langmuir* **2014**, *30*, 1921.
- [15] H. Furukawa, F. Gandara, Y. B. Zhang, J. Jiang, W. L. Queen, M. R. Hudson, O. M. Yaghi, *J. Am. Chem. Soc.* **2014**, *136*, 4369.
- [16] J. Yan, Y. Yu, C. Ma, J. Xiao, Q. Xia, Y. Li, Z. Li, *Appl. Therm. Eng.* **2015**, *84*, 118.
- [17] a) A. Carné-Sánchez, I. Imaz, M. Cano-Sarabia, D. Maspoch, *Nat. Chem.* **2013**, *5*, 203; b) L. Garzon-Tovar, M. Cano-Sarabia, A. Carne-Sanchez, C. Carbonell, I. Imaz, D. Maspoch, *React. Chem. Eng.* **2016**, *1*, 533.
- [18] M. Kim, S. M. Cohen, *CrystEngComm* **2012**, *14*, 4096.
- [19] I. Glaznev, I. Ponomarenko, S. Kirik, Y. Aristov, *Int. J. Refrig.* **2011**, *34*, 1244.
- [20] Y. I. Aristov, G. Restuccia, G. Cacciola, V. N. Parmon, *Appl. Therm. Eng.* **2002**, *22*, 191.
- [21] Y. S. Nam, R. Enright, S. Maroo, E. N. Wang, S. Narayanan, I. S. McKay, *US 20130192281 A1*, **2013**.
- [22] J. Rouquerol, F. Rouquerol, P. Llewellyn, G. Maurin, K. S. W. Sing, *Adsorption by Powders and Porous Solids: Principles, Methodology and Applications*, Academic Press, San Diego, CA, **2013**.
- [23] Y. I. Aristov, M. M. Tokarev, G. Cacciola, G. Restuccia, *React. Kinet. Catal. Lett.* **1996**, *59*, 325.
- [24] Advanced Research Projects Agency-DOE, HEATS Program Overview, [https://arpa-e.energy.gov/sites/default/files/documents/files/HEATS\\_ProgramOverview.pdf](https://arpa-e.energy.gov/sites/default/files/documents/files/HEATS_ProgramOverview.pdf) (accessed: October 2016).
- [25] B. Shi, R. Al-Dadah, S. Mahmoud, A. Elsayed, E. Elsayed, *Appl. Therm. Eng.* **2016**, *106*, 325.
- [26] M. F. de Lange, B. L. van Velzen, C. P. Ottevanger, K. J. F. M. Verouden, L.-C. Lin, T. J. H. Vlugt, J. Gascon, F. Kapteijn, *Langmuir* **2015**, *31*, 12783.
- [27] D. C. Wang, Z. Z. Xia, J. Y. Wu, R. Z. Wang, H. Zhai, W. D. Dou, *Int. J. Refrig.* **2005**, *28*, 1073.
- [28] C. Y. Tso, C. Y. H. Chao, *Int. J. Refrig.* **2012**, *35*, 1626.
- [29] L. Z. Zhang, *Appl. Therm. Eng.* **2000**, *20*, 103.
- [30] S. Vasta, A. Freni, A. Sapienza, F. Costa, G. Restuccia, *Int. J. Refrig.* **2012**, *35*, 701.
- [31] A. Freni, A. Sapienza, I. S. Glaznev, Y. I. Aristov, G. Restuccia, *Int. J. Refrig.* **2012**, *35*, 518.
- [32] A. Sapienza, I. S. Glaznev, S. Santamaria, A. Freni, Y. I. Aristov, *Appl. Therm. Eng.* **2012**, *32*, 141.

# Spray Drying for Making Covalent Chemistry: Postsynthetic Modification of Metal–Organic Frameworks





## Spray Drying for Making Covalent Chemistry: Postsynthetic Modification of Metal–Organic Frameworks

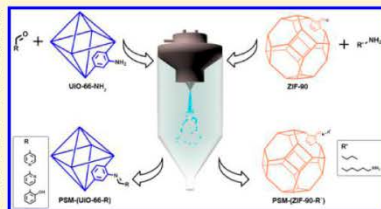
Luis Garzón-Tovar,<sup>†</sup> Sabina Rodríguez-Hermida,<sup>‡</sup> Inhar Imaz,<sup>‡</sup> and Daniel Maspocho<sup>\*†‡§</sup>

<sup>†</sup>Catalan Institute of Nanoscience and Nanotechnology (ICN2), CSIC and The Barcelona Institute of Science and Technology, Campus UAB, Bellaterra, 08193 Barcelona, Spain

<sup>‡</sup>ICREA, Pg. Lluís Companys 23, 08010 Barcelona, Spain

 Supporting Information

**ABSTRACT:** Covalent postsynthetic modification (PSM) of metal–organic frameworks (MOFs) has attracted much attention due to the possibility of tailoring the properties of these porous materials. Schiff-base condensation between an amine and an aldehyde is one of the most common reactions in the PSM of MOFs. Here, we report the use of the spray drying technique to perform this class of organic reactions, either between discrete organic molecules or on the pore surfaces of MOFs, in a very fast (1–2 s) and continuous way. Using spray drying, we show the PSM of two MOFs, the amine-terminated UiO-66-NH<sub>2</sub> and the aldehyde-terminated ZIF-90, achieving conversion efficiencies up to 20 and 42%, respectively. Moreover, we demonstrate that it can also be used to postsynthetically cross-link the aldehyde groups of ZIF-90 using a diamine molecule with a conversion efficiency of 70%.



### INTRODUCTION

Metal–organic frameworks (MOFs), also known as porous coordination polymers (PCPs), have attracted much attention over the past decades due to their potential applications, such as in gas sorption and storage, catalysis, drug delivery, and gas separation.<sup>1–3</sup> One of the main characteristics of MOFs is the ability to tailor their chemical functionality and/or pore surface chemistry, either by pre- or postsynthetic modification of the organic linker. Covalent postsynthetic modification (PSM) involves an organic reaction carried out on the organic linker while maintaining the MOF integrity.<sup>4,5</sup>

To date, there are many studies based on the PSM of MOFs involving linkers with different functional groups.<sup>6–9</sup> Among them, the most common reaction involves a Schiff-base condensation between an amine and an aldehyde to form an imine via water elimination. Using this chemistry, PSM of the 2-aminoterephthalate (NH<sub>2</sub>-bdc) linker of UiO-66-NH<sub>2</sub> has been widely studied.<sup>10–16</sup> For example, Lu et al. showed the successful PSM of UiO-66-NH<sub>2</sub> with salicylaldehyde (Sal) by heating a mixture of both species in acetonitrile at 40 °C for 3 days. Once functionalized, they further immobilized Cu(II) salts on the incorporated imine moiety, and used the resulting framework as an efficient catalyst for the aerobic oxidation of alcohols.<sup>10</sup> A similar strategy was also followed to synthesize efficient catalysts for the epoxidation of olefins, the hydrogenation of aromatics, and the reductive amination of aldehydes.<sup>11–13</sup> In these cases, UiO-66-NH<sub>2</sub> was postsynthetically modified with Sal, 2-pyridinecarboxaldehyde, 4-pyridinecarboxaldehyde, and 6-((diisopropylamino)methyl)-

picolinaldehyde followed by the immobilization of Mo(VI) and Ir(I). Also, other amino-terminated MOFs such as IRMOF-3 and Cr-MIL-101-NH<sub>2</sub> have been used for the development of efficient catalysts. Here, both MOFs were first reacted with pyridine-based aldehydes and then with Cu(I) and Co(II) salts to create heterogeneous catalysts for the synthesis of different 2-aminobenzothiazoles and the aerobic epoxidation of olefins, respectively.<sup>14,15</sup>

Yaghi et al. also reported the use of the Schiff-base condensation reaction to postsynthetically functionalize aldehyde-terminated MOFs. They reacted ZIF-90 with ethanolamine, yielding the imine-derivative nonporous ZIF-92.<sup>17</sup> Following the same type of chemistry, ZIF-90 was recently labeled with an Alexa Fluor dye,<sup>18</sup> whereas a mixed ZIF-8-90 sample was postfunctionalized with ethylenediamine. This latter PSM allowed the introduction of an aliphatic amine-terminated group to ZIF-8-90, enhancing its CO<sub>2</sub> sorption capacity.<sup>19</sup> In a more recent study, a superhydrophobic ZIF-90 exhibiting a water contact angle value of around 152° was prepared by reacting it with a polyfluorinated amine.<sup>20</sup>

In general, the synthetic conditions for the PSM of MOFs require long reactions times (from 1 to 3 days) and high temperatures. To overcome these limitations, some advances have been done on developing alternative methods for the PSM of MOFs. One of them is based on the PSM of IRMOF-3 and UiO-66-NH<sub>2</sub> by vapor diffusion.<sup>21</sup> This method allowed the

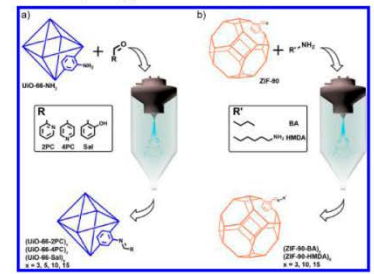
Received: October 28, 2016

Published: January 3, 2017

PSM of both MOFs with high conversion rates after heating the solvent-free MOFs with the corresponding aldehyde at 100–120 °C using a vacuum system for 16 h.

Recently, it has been demonstrated that the spray drying (SD) technique is a useful, continuous, and scalable method to assemble metal ions and organic ligands to synthesize MOFs.<sup>22,23</sup> This method allowed the reaction times to be drastically reduced down to the second regime, without affecting the properties of the SD-synthesized MOFs. It also enables obtaining them in the form of dried powders and recycling the solvent used during the fabrication. Here, we extended the use of SD to covalent organic reactions based on the Schiff-base condensation reaction aiming to be able to postsynthetically modify MOF crystals. UiO-66-NH<sub>2</sub> and ZIF-90 were selected as the target MOFs due to the uncoordinated and available amine and aldehyde groups within their structures, respectively (Scheme 1).

**Scheme 1.** Illustration of the Covalent PSM Performed in (a) UiO-66-NH<sub>2</sub> and (b) ZIF-90 under SD Conditions



## RESULTS AND DISCUSSION

**Organic Schiff-Base Condensation Reactions Conducted via Spray Drying.** To demonstrate that organic reactions and, in particular, Schiff-base condensation reactions between aldehydes and amines could be performed using the SD technique, we initially tested the formation of 2-((pyridin-4-ylmethylene)amino)terephthalic acid using NH<sub>2</sub>-bdc and 4-pyridinecarboxaldehyde (4PC) as reactants (Scheme 2). This synthesis started with the mixture of NH<sub>2</sub>-bdc and 4PC in ethanol (15 mL) at room temperature. The NH<sub>2</sub>-bdc:4PC molar ratio was systematically changed from 1:1, 1:2, and 1:3. Each suspension was then spray-dried at a feed rate of 3.0 mL min<sup>-1</sup> and an inlet temperature of 130 °C, using a Mini Spray Dryer B-290. This inlet temperature was selected to ensure the evaporation of ethanol as well as to force the evaporation of the water formed during the Schiff-base condensation reaction. For each reaction, a yellow powder was collected after 5 min. <sup>1</sup>H NMR spectra of all collected powders confirmed the imine formation by the appearance of a peak at 8.17 ppm corresponding to the imine proton (Figures 1a and S1). The synthesis of 2-((pyridin-4-ylmethylene)amino)terephthalic acid was further corroborated by <sup>13</sup>C NMR (peak corresponding to the carbon atom of the CH=N imine group at 163 ppm; Figures 1b and S2) and ESI-MS (calculated for [M-H]<sup>-</sup> [C<sub>14</sub>H<sub>8</sub>N<sub>2</sub>O<sub>4</sub>]<sup>-</sup>: *m/z* = 269.0568; found *m/z* = 269.0566;

**Scheme 2.** Imine Molecules Synthesized via SD

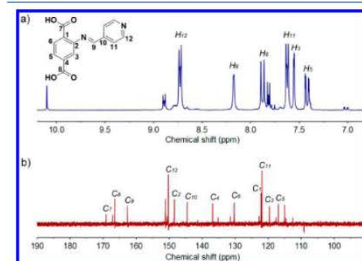
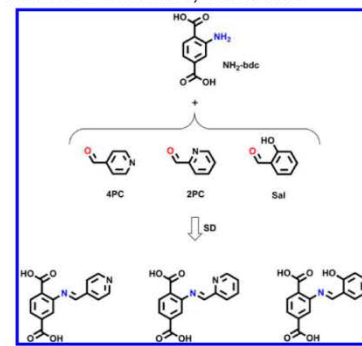


**Figure 1.** (a) <sup>1</sup>H NMR and (b) <sup>13</sup>C NMR spectra, collected in DMSO-*d*<sub>6</sub>, of 2-((pyridin-4-ylmethylene)amino)terephthalic acid synthesized using a NH<sub>2</sub>-bdc:4PC molar ratio of 1:3. Only the peaks corresponding to the imine molecule are shown.

Figure S3). We finally determined the conversion rate of each reaction by comparing the integration of the peaks at 8.17 ppm (imine proton) and at 7.02 ppm (aromatic proton of the unreacted NH<sub>2</sub>-bdc). The conversion rates were 37, 84, and 92% for the NH<sub>2</sub>-bdc:4PC molar ratios of 1:1, 1:2, and 1:3, respectively.

We then extended the SD synthesis to two other imine compounds (Scheme 2). The syntheses were done using the same conditions as those for 2-((pyridin-4-ylmethylene)amino)terephthalic acid, except that, instead of 4PC, we used 2-pyridinecarboxaldehyde (2PC; conversion rate: 87%) and Sal (conversion rate: 75%) in a NH<sub>2</sub>-bdc:2PC/Sal molar ratio of 1:3. In both cases, the expected imine compounds were successfully synthesized, as confirmed by <sup>1</sup>H and <sup>13</sup>C NMR and ESI-MS (Figures S4–S9).

The high conversion rates obtained in these Schiff-base condensation reactions are remarkable if we consider that, to the best of our knowledge, this is the first time that discrete organic molecules have been synthesized via SD. It is well known that, in these condensation reactions, water is produced so that its removal favors the formation of imines following the

Le Chatelier principle. Since SD is based on the fast evaporation of the liquid, we reason that water can be rapidly removed from the atomized droplets during the Schiff-base reaction, thereby favoring the formation of the imine bond.

**PSM of UiO-66-NH<sub>2</sub>.** Once we proved the SD synthesis of imine compounds via Schiff-base condensation, we then transferred the same type of chemistry to MOF crystals. For this, we selected UiO-66-NH<sub>2</sub> as the first test case scenario because the amino groups of the NH<sub>2</sub>-bdc linkers are pointing into the pores, and of its high chemical and thermal stability.

A series of ethanolic colloidal suspensions (15 mL) containing UiO-66-NH<sub>2</sub> [synthesized under solvothermal conditions; particle size = 245 ± 65 nm; obtained as pure phase as confirmed by X-ray powder diffraction (XRPD), scanning electron microscopy (SEM), N<sub>2</sub> sorption isotherm ( $S_{\text{BET}} = 914 \text{ m}^2 \text{ g}^{-1}$ ), and <sup>13</sup>C MAS NMR; see Figures S10–S12] and the aldehydes 4PC, 2PC, and Sal were initially prepared at molar ratios of NH<sub>2</sub>-bdc:aldehyde corresponding to 1:3, 1:5, 1:10, and 1:15. Each suspension was then spray-dried under the same conditions as those for the pure condensation SD reactions. Once the suspensions had atomized, the different yellow powders were collected from the spray dryer collector, cleaned with ethanol four times and once with acetone, and finally dried at 85 °C for 12 h. The different samples were named as (UiO-66-4PC)<sub>x</sub>, (UiO-66-2PC)<sub>x</sub>, and (UiO-66-Sal)<sub>x</sub> (where *x* is 3, 5, 10, and 15, depending on the equivalents of aldehyde used). Field-emission scanning electron microscopy (FESEM) of all dried powders revealed that the initial size and morphology of the parent UiO-66-NH<sub>2</sub> crystals did not change during the SD process (Figure S13). XRPD indicated that all crystalline powders retain the crystallinity of the parent UiO-66-NH<sub>2</sub> MOF (Figures 2b and S14–S16).

To confirm the PSM of UiO-66-NH<sub>2</sub> with the different aldehydes, we first performed <sup>13</sup>C MAS NMR on (UiO-66-2PC)<sub>3</sub>, (UiO-66-4PC)<sub>15</sub>, and (UiO-66-Sal)<sub>15</sub> (Figures 2a and S17–S19). All spectra showed the appearance of a new signal centered at 160–161 ppm, which was attributed to the carbon atom of the CH=N imine group. This peak is consistent with the one observed at 160–162 ppm in the <sup>13</sup>C NMR spectra of the imine compounds previously synthesized via SD (Figures S2, S5, and S8). It is also in agreement with the <sup>13</sup>C MAS NMR signal associated with the imine carbon in other reported postfunctionalized UiOs.<sup>11,12</sup>

The degree of postsynthetic conversion was analyzed by first digesting the samples and then analyzing the resulting solutions by <sup>1</sup>H NMR. From the digestion under acidic conditions, the MOF framework is destroyed and the released imine molecules are hydrolyzed forming the NH<sub>2</sub>-bdc and the corresponding aldehyde. We then calculated the conversion rate by comparison of the integration of one peak at 7.36 ppm corresponding to NH<sub>2</sub>-bdc and those peaks at 7.98, 8.52, and 7.52 ppm corresponding to 4PC, 2PC, and Sal, respectively (Figures S20–S32). Also note here that all samples were previously washed three times with ethanol and acetone, and then dried at 85 °C overnight before their digestion. This activation process ensures the removal of all nonreacted aldehyde molecules adsorbed in the pores of the MOFs during the SD process, as confirmed by FT-IR (Figures S33–S35). Table 1 lists the degrees of conversion calculated for all synthesized samples. From this data, it was clear that the degree of conversion increases while increasing the equivalents of aldehyde used in the reaction.

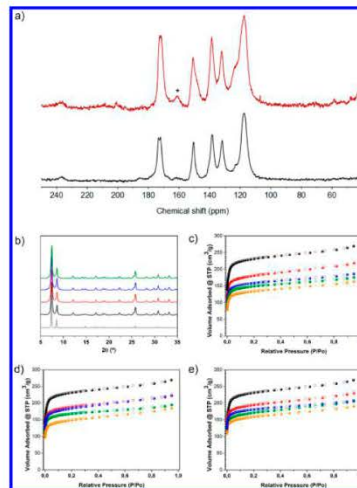


**Figure 2.** (a) <sup>13</sup>C MAS NMR spectra of (UiO-66-2PC)<sub>15</sub> (red) and UiO-66-NH<sub>2</sub> (black). The signal of the CH=N imine group is highlighted with an asterisk (\*). (b) XRPD patterns of simulated UiO-66-NH<sub>2</sub> (gray) and activated UiO-66-NH<sub>2</sub> (black), (UiO-66-2PC)<sub>15</sub> (red), (UiO-66-4PC)<sub>15</sub> (blue), and (UiO-66-Sal)<sub>15</sub> (green). (c–e) N<sub>2</sub> sorption isotherms of (c) (UiO-66-2PC)<sub>x</sub>, (d) (UiO-66-4PC)<sub>x</sub>, and (e) (UiO-66-Sal)<sub>x</sub> synthesized with different equivalents of aldehyde (*x*). In parts c–e, *x* = 3 (red), *x* = 5 (blue), *x* = 10 (green), and *x* = 15 (orange). For comparison, N<sub>2</sub> sorption isotherms of activated UiO-66-NH<sub>2</sub> (black) are also included.

**Table 1.** BET Areas, Pore Volumes, and % of Conversion of UiO-66-NH<sub>2</sub>, (UiO-66-2PC)<sub>x</sub>, (UiO-66-4PC)<sub>x</sub>, and (UiO-66-Sal)<sub>x</sub>

MOF	<i>x</i>	$S_{\text{BET}}$ ( $\text{m}^2 \text{ g}^{-1}$ )	pore vol. <sup>a</sup> ( $\text{cm}^3 \text{ g}^{-1}$ )	conversion <sup>b</sup> (%)
UiO-66-NH <sub>2</sub>		914	0.3729	
(UiO-66-2PC) <sub>x</sub>	3	699	0.2954	13
	5	625	0.2576	16
	10	586	0.2412	17
	15	516	0.2190	20
(UiO-66-4PC) <sub>x</sub>	3	736	0.3056	9
	5	712	0.3015	16
	10	621	0.2652	18
	15	573	0.2441	20
(UiO-66-Sal) <sub>x</sub>	3	761	0.3151	11
	5	709	0.2923	14
	10	665	0.2789	16
	15	616	0.2587	19

<sup>a</sup>Calculated at  $P/P_0 \approx 0.4$ . <sup>b</sup>Calculated from <sup>1</sup>H NMR spectra of the digested samples.

For example, the degree of conversion increased from 13 to 20% between (UiO-66-2PC)<sub>3</sub> and (UiO-66-2PC)<sub>15</sub>. It is

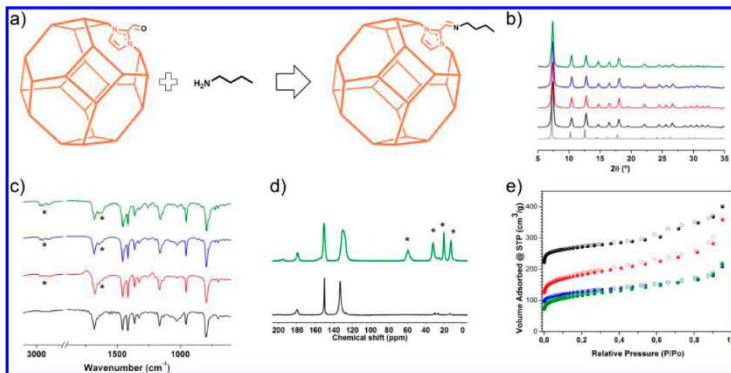


Figure 3. (a) Schematic representation of the PSM of ZIF-90 with butylamine via SD. (b) XRPD patterns of ZIF-90 and (ZIF-90-BA)<sub>x</sub> as compared to the simulated powder pattern for the crystal structure of ZIF-90 (gray). (c) IR spectra of ZIF-90 and (ZIF-90-BA)<sub>x</sub>, highlighting the aliphatic C—H and imine C=N vibrational bands with an asterisk (\*). (d) <sup>13</sup>C MAS NMR spectra of ZIF-90 and (ZIF-90-BA)<sub>x</sub>, where the peaks corresponding to the butyl chains are highlighted with an asterisk (\*). (e) N<sub>2</sub> sorption isotherms at 77 K of ZIF-90 and (ZIF-90-BA)<sub>x</sub>. In parts b–e, ZIF-90 (black), (ZIF-90-BA)<sub>3</sub> (red), (ZIF-90-BA)<sub>10</sub> (blue), and (ZIF-90-BA)<sub>15</sub> (green).

important to highlight here that the degree of conversion achieved by SD is higher than the ones reported for the PSM of UiO-66-NH<sub>2</sub> with the same aromatic aldehydes.<sup>10,13</sup> The only exception was the conversion rate of 29% reported by Bokhoven and co-workers for the formation of (UiO-66-Sal) via the vapor-phase method.<sup>21</sup> However, this latter method is a noncontinuous method, which requires a vacuum and 16 h to achieve this conversion rate.

N<sub>2</sub> sorption isotherms were finally measured at 77 K on all activated samples that were further degassed at 200 °C for 12 h under a vacuum. We found that the surface area and pore volumes decreased for the samples showing a higher degree of conversion (Table 1, Figures 2c–e and S36–S47). We attributed this trend to the fact that the new imine moieties grafted on the pores are bulkier than the amino group.

**PSM of ZIF-90.** To explore the versatility of the PSM via SD, we then switched to a terminal aldehyde-containing MOF to postfunctionalize it with amine molecules. To this end, we selected ZIF-90 that is built up from imidazole-2-carboxaldehyde (ICA) and Zn(II) ions, giving rise to a sod-3D porous network showing a pore size around 11 Å and a pore size window around 3.5 Å. Following a similar synthetic procedure as that for the PSM of UiO-66-NH<sub>2</sub>, three ethanolic suspensions of ZIF-90 [synthesized at room temperature; particle size = 41 ± 9 nm; obtained as pure phase as confirmed by XRPD, SEM, N<sub>2</sub> sorption isotherm ( $S_{\text{BET}} = 1070 \text{ m}^2 \text{ g}^{-1}$ ), and <sup>13</sup>C MAS NMR; see Figures S48–S50] and butylamine (BA) were initially prepared at molar ratios of ICA:BA corresponding to 1:3, 1:10, and 1:15. Each suspension was then spray-dried under the same above-mentioned conditions. Once the suspensions had atomized, the different pale yellow powders were collected from the spray dryer collector, cleaned with ethanol five times and once with acetone, and finally dried at 85 °C for 12 h. Again, the resulting powders were named as (ZIF-90-BA)<sub>x</sub>, where *x* is the number of equivalents of BA.

Similarly, FESEM and TEM revealed that the initial size and morphology of the parent ZIF-90 crystals did not change during the SD process (Figure S51), whereas XRPD indicated that all crystalline powders retain the parent sod structure (Figures 3b and S52). In this case, the formation of imidazol-2-butylmethanimine (IBI) was initially confirmed by FT-IR spectroscopy. Two sets of new bands appeared in the IR spectra of the postsynthetic functionalized ZIF-90 (Figure 3c): (1) the band corresponding to the C=N group, centered at  $\approx 1644 \text{ cm}^{-1}$ , whose intensity increased as the equivalents of BA were increased, and (2) the aliphatic C—H stretching of the butyl moiety within the 3000–2700  $\text{cm}^{-1}$  range. Moreover, no band corresponding to —NH<sub>2</sub> was observed, indicating that there was not unreacted BA inside the pores of ZIF-90. The formation of IBI was further corroborated by the peaks observed in the <sup>13</sup>C MAS NMR spectra at 59, 32, 20, and 13 ppm, which were all attributed to the butyl chain (Figure 3d). The peak at 59 ppm was assigned to the methylene group bonded to imine nitrogen. Moreover, the signal of the aldehyde group was observed at 195 ppm, indicating that not all carbonyl groups were reacted. Finally, the formation of IBI was undoubtedly confirmed by identifying it in the solution resulting from dissolving all (ZIF-90-BA)<sub>x</sub> samples using acetic acid (Figures S53–S55). Indeed, <sup>1</sup>H NMR spectra showed peaks at 8.55 and 3.82 ppm that were attributed to the CH=N imine proton and the N—CH<sub>2</sub> methylene protons of IBI, respectively. On the other hand, the peak at  $m/z = 152.1180$  in the ESI-MS spectra matches with the molecular formula of the protonated IBI [ $\text{C}_9\text{H}_{13}\text{N}_2$ ]<sup>+</sup> ( $m/z = 152.1182$ ). Note here that, under these conditions, IBI was also partially hydrolyzed.

In order to quantify the conversion rate, <sup>1</sup>H NMR spectra of the digested samples in DCl, DMSO-*d*<sub>6</sub> were collected (Figure S56–S59). Under these stronger acidic conditions, ZIF-90 is dissolved and the released IBI is completely hydrolyzed, forming ICA and BA. Thus, the degree of conversion was

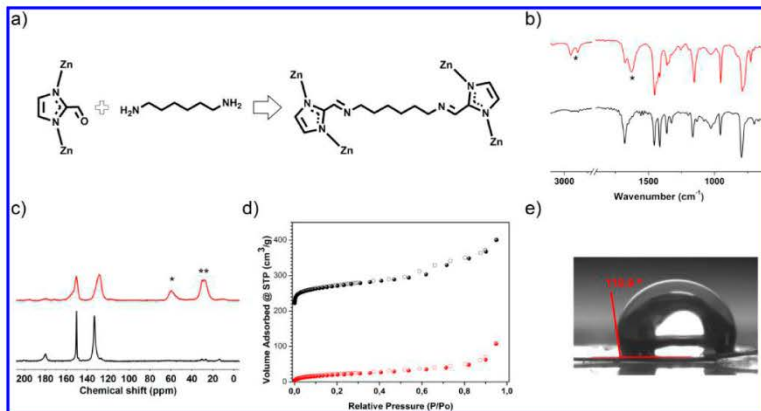


**Figure 4.** (a) Schematic representation of the PSM of ZIF-90 with hexamethylenediamine. (b) IR spectra of ZIF-90 (black) and (ZIF-90-HMDA)<sub>3</sub> (red), highlighting the aliphatic C—H and imine C=N vibrational bands with an asterisk (\*). (c) <sup>13</sup>C MAS NMR spectra of ZIF-90 (black) and (ZIF-90-HMDA)<sub>3</sub> (red), where the peaks at the alkyl region are highlighted with an asterisk (\*). (d) N<sub>2</sub> sorption isotherms of ZIF-90 (black) and (ZIF-90-HMDA)<sub>3</sub> (red). (e) Contact angle image of a pressed pellet disk of (ZIF-90-HMDA)<sub>3</sub>.

measured by comparison of the integration of the peaks at 7.57 and 0.86 ppm corresponding to ICA and BA, respectively. We found that the conversion rates were 25% for (ZIF-90-BA)<sub>3</sub>, 32% for (ZIF-90-BA)<sub>10</sub>, and 42% for (ZIF-90-BA)<sub>15</sub>.

These results were consistent with the gradual decrease of the  $S_{\text{BET}}$  values (determined by the N<sub>2</sub> sorption isotherms at 77 K) as the conversion rate (introduction of more bulky butyl chains) was also increased (Figures 3e and S60–S62). The calculated  $S_{\text{BET}}$  values were 670, 483, and 424 m<sup>2</sup> g<sup>-1</sup> for (ZIF-90-BA)<sub>3</sub>, (ZIF-90-BA)<sub>10</sub>, and (ZIF-90-BA)<sub>15</sub>, respectively. These values corresponded to a loss of 39, 45, and 63% of the  $S_{\text{BET}}$  of the parent ZIF-90.

Previous studies have shown that the introduction of alkyl chains in the pore surfaces of a MOF increases its hydrophobicity.<sup>24,25</sup> We therefore studied the surface wettability of all postfunctionalized ZIF-90 samples by measuring the contact angle ( $\Theta_c$ ) on pressed pellet disks of ZIF-90, (ZIF-90-BA)<sub>3</sub>, (ZIF-90-BA)<sub>10</sub>, and (ZIF-90-BA)<sub>15</sub>. The  $\Theta_c$  in each case was 90.4, 93.3, 96.1, and 99.3°, respectively—confirming an increase in the hydrophobicity when the conversion rate increases (Figure S63).

Finally, the effect of the particle size on this spray drying solid/liquid reaction was studied. To this end, suspensions containing larger ZIF-90 crystals (particle size:  $18 \pm 9$  μm, Figures S64–S65) and ICA (using ICA:BA 1:15 molar ratio) were spray-dried under the same experimental conditions as described above, *vide supra*. Here, a conversion rate of 22% was determined by analyzing the <sup>1</sup>H NMR spectra of the digested sample (Figure S66). This value is lower than the one obtained when ZIF-90 nanoparticles were used (42%), and it is comparable to other conversion rates found in aldehyde-terminated ZIF particles of similar size.<sup>25,26</sup>

**PSM of ZIF-90 with a Diamine Molecule.** We further evaluated the PSM via SD by using hexamethylenediamine

(HMDA) to cross-link nearby aldehyde groups located on the pores of ZIF-90 (Figure 4a). It is important to mention here that PSMs of ZIFs with terminal and aliphatic diamine molecules, such as ethylenediamine, have already been reported. For example, Balkus and co-workers cross-linked neighboring SIM-1 crystals with ethylenediamine to form a highly compact selective water/methanol membrane.<sup>27</sup>

Following the procedure applied in the previous PSMs via SD, an ethanolic suspension of ZIF-90 and HMDA (molar ratio aldehyde:amine = 1:5) was spray-dried under the same above-mentioned conditions. The collected powder called (ZIF-90-HMDA)<sub>3</sub> was also cleaned with ethanol five times and once with acetone, and dried at 85 °C for 12 h. Again, we did not observe any significant change in the crystal size and morphology during the SD process (Figure S67), and the XRPD indicated that the collected crystals retain the parent ZIF-90 structure (Figure S68).

The FT-IR spectrum of (ZIF-90-HMDA)<sub>3</sub> showed the presence of the characteristic C—H stretching bands of the hexamethyl chains at 2930 and 2850 cm<sup>-1</sup> as well as a new band centered at 1630 cm<sup>-1</sup> corresponding to the C=N group (Figure 4b). Moreover, the absence of the characteristic vibrational bands of the NH<sub>2</sub> groups suggested that both amino groups of the HMDA were reacted. Altogether these observations agree well with an effective cross-linking of the aldehyde groups located on the pores of ZIF-90 using HMDA.

We further studied this cross-linking by <sup>13</sup>C MAS NMR. The spectrum of (ZIF-90-HMDA)<sub>3</sub> showed a low intensity of the peak at 179 ppm corresponding to the aldehyde group, suggesting a low concentration of this group within the framework (Figure 4c). This result agrees well with the FT-IR spectrum, in which a low intensity of the band at 1675 cm<sup>-1</sup> corresponding to the aldehyde group was also observed (Figure 4b). On the other hand, three signals in the alkyl region (60, 30,

and 27 ppm) were observed, indicating high symmetry in (ZIF-90-HMDA)<sub>3</sub>. The downfield signal was attributed to the —N=CH<sub>2</sub>— methylene groups, and the other two signals to the four —CH<sub>2</sub>— methylene groups of the diimine bridge. In fact, we did not detect the characteristic peak of the —CH<sub>2</sub>—NH<sub>2</sub> methylene centered at ≈40 ppm,<sup>19</sup> which would indicate that HMDA was only attached by one of its amine groups. The presence of the diimine cross-linking molecule N,N'-(hexane-1,6-diyl)bis(1-imidazol-2-yl)methanimine (Figure 4a) was finally confirmed by analyzing the solution resulting from the digestion of (ZIF-90-HMDA)<sub>3</sub> in acetic acid by <sup>1</sup>H NMR and ESI-MS (Figure S69). The peaks at 8.58 and 3.83 ppm in the <sup>1</sup>H NMR spectrum were attributed to the CH=N imine proton and the N—CH<sub>2</sub> methylene protons of the diamine molecule, respectively. On the other hand, in the ESI-MS spectra, the peak at *m/z* = 273.1836 matches with the molecular formula of the protonated N,N'-(hexane-1,6-diyl)-bis(1-imidazol-2-yl)methanimine [C<sub>14</sub>H<sub>20</sub>N<sub>6</sub>]<sup>+</sup> (*m/z* = 273.1822).

The <sup>1</sup>H NMR spectrum of the digested (ZIF-90-HMDA)<sub>3</sub> in strong acidic conditions (DCl, DMSO-*d*<sub>6</sub>) was collected to quantify its yield of conversion (Figure S70). Comparison of the integration of the signals corresponding to ICA (7.56 ppm) and HMDA (1.30 ppm) revealed that there is 35% HMDA, meaning that 70% of the ICA linkers were functionalized.

This high conversion of cross-linked ICA linkers in (ZIF-90-HMDA)<sub>3</sub> should therefore involve a remarkable closure of its pores and reduction of its surface area in comparison to its parent ZIF-90. This assumption was confirmed by measuring the *S*<sub>BET</sub> from the N<sub>2</sub> sorption isotherm at 77 K. We found a *S*<sub>BET</sub> of 69 m<sup>2</sup> g<sup>-1</sup> that corresponds to a reduction of 93% of the original *S*<sub>BET</sub> of ZIF-90 (Table 2, Figures 4d and S71).

**Table 2. BET Areas, Pore Volumes, and % of Conversion of ZIF-90, (ZIF-90-BA)<sub>3</sub>, and (ZIF-90-HMDA)<sub>3</sub>**

MOF	<i>x</i>	<i>S</i> <sub>BET</sub> <sup>a</sup> (m <sup>2</sup> g <sup>-1</sup> )	pore vol. <sup>b</sup> (cm <sup>3</sup> g <sup>-1</sup> )	conver. <sup>b</sup> (%)
ZIF-90		1070	0.4412	
(ZIF-90-BA) <sub>3</sub>	3	670	0.3150	25
	10	483	0.2166	32
	15	424	0.2042	42
(ZIF-90-HMDA) <sub>3</sub>	5	69	0.0377	70

<sup>a</sup>Calculated at *P*/*P*<sub>0</sub> ≈ 0.4. <sup>b</sup>Calculated from <sup>1</sup>H NMR spectra of the digested samples.

The contact angle (Θ<sub>c</sub>) was also measured on a pressed pellet disk of (ZIF-90-HMDA)<sub>3</sub>, giving a value of 110.9° that corresponds to a higher hydrophobic surface in comparison to the different (ZIF-90-BA)<sub>3</sub> samples (Figure 4e).

## CONCLUSIONS

We have reported a highly versatile and effective methodology to postsynthetically modify MOFs via Schiff-base condensation reactions. This strategy can be applied to MOFs with either terminal aldehyde or amine groups, reduces their PSM time, and enables their continuous PSM with good rates of conversion. Therefore, it should facilitate the PSM of MOFs for numerous applications, including catalysis, sensor technology, pollutant removal, and separation. This method also allowed the efficient cross-linking of the terminal aldehydes groups of ZIF-90 using a diamine molecule, thereby blocking their porosity and opening up new avenues for future triggered

delivery systems. Finally, it also enables performing Schiff-base condensation reactions between discrete amine and aldehyde molecules, opening new perspectives in organic chemistry synthesis.

## MATERIALS AND METHODS

**General Procedure for Synthesis of Imine Ligands.** In a typical synthesis, a suspension of NH<sub>2</sub>-bdc and the corresponding aldehyde (4PC, 2PC, and 5a) in 15 mL of ethanol was spray-dried at an inlet temperature of 130 °C, a feed rate of 3.0 mL min<sup>-1</sup>, and a flow rate of 336 mL min<sup>-1</sup> using a Mini Spray Dryer B-290 (BÜCHI Labortechnik; spray cap: 0.5 mm hole). The collected solids were characterized by ESI-MS, and <sup>1</sup>H- and <sup>13</sup>C NMR spectroscopy. Full experimental details and characterization can be found in the Supporting Information.

**Synthesis of UiO-66-NH<sub>2</sub>.** UiO-66-NH<sub>2</sub> was synthesized through the previously reported method.<sup>20</sup> In a typical synthesis, 35 mL of HCl 37% was added to a solution 0.1 M ZrCl<sub>4</sub> and 0.1 M NH<sub>2</sub>-bdc in 500 mL of DMF. The resulting mixture was heated at 120 °C under stirring for 2 h. The obtained solid was collected by centrifugation and washed two times with 100 mL of DMF for 12 h at 120 °C and three times with 100 mL of absolute ethanol for 12 h at 60 °C. Finally, the resulting powder was dried at 85 °C overnight (yield = 75%). Characterization details can be found in the Supporting Information.

**Synthesis of ZIF-90.** ZIF-90 was synthesized through the previously reported method.<sup>18</sup> In a typical synthesis, 0.27 mL of trimethylamine (1.96 mmol) was added to a solution 0.01 M imidazole-2-carboxaldehyde and 3.75 mM Zn(NO<sub>3</sub>)<sub>2</sub>·6H<sub>2</sub>O in 200 mL of DMF. The resulting mixture was stirred for 1 min at room temperature, and then, 100 mL of ethanol was added. The particles were collected by centrifugation, washed five times with ethanol and one time with acetone, and finally dried at 85 °C overnight (yield = 70%). Characterization details can be found in the Supporting Information.

**General Synthesis of the PSM of UiO-66-NH<sub>2</sub>.** A 0.150 g portion of UiO-66-NH<sub>2</sub> (0.085 mmol) was suspended in ethanol (15 mL), and the corresponding aldehyde (4PC, 2PC, and 5a) was added to the dispersion. The resulting reaction mixture was then spray-dried at an inlet temperature of 130 °C, a feed rate of 3.0 mL min<sup>-1</sup>, and a flow rate of 336 mL min<sup>-1</sup> using a Mini Spray Dryer B-290 (BÜCHI Labortechnik; spray cap: 0.5 mm hole). A yellow powder was collected after 5 min. The resulting solid was then dispersed in 20 mL of ethanol and precipitated by centrifugation. This process was repeated four times. The final product was washed one time with acetone and dried for 12 h at 85 °C. In addition, as a control experiment, the above-mentioned method was reproduced, except that, instead of spray drying the reaction mixture, we heated it at 130 °C for 5 min. Under these conditions, a conversion rate of only 3% was found. Full experimental and characterization details can be found in the Supporting Information.

**General Synthesis of the PSM of ZIF-90.** A dispersion of ZIF-90 (0.100 g, 0.39 mmol) and the corresponding amine in 15 mL of ethanol was spray-dried at an inlet temperature of 130 °C, a feed rate of 3.0 mL min<sup>-1</sup>, and a flow rate of 336 mL min<sup>-1</sup> using a Mini Spray Dryer B-290 (BÜCHI Labortechnik; spray cap: 0.5 mm hole). A yellow powder was collected after 5 min. The resulting solid was then dispersed in 20 mL of ethanol and precipitated by centrifugation. This process was repeated five times. The final product was washed one time with acetone and dried for 12 h at 85 °C. In addition, as a control experiment, the above-mentioned method was reproduced, except that, instead of spray drying the reaction mixture, we heated it at 130 °C for 5 min. Under these conditions, the conversion rate was 0%. Full experimental and characterization details are reported in the Supporting Information.

**Quantification Protocol.** Samples were digested in strong acidic conditions, and their <sup>1</sup>H NMR spectra were collected to calculate the conversion of imine by the comparison of the integration of the characteristic signals of the corresponding reactants (amine and aldehyde). For the PSM of UiO-66-NH<sub>2</sub>, 10 mg of activated sample,

0.6 mL of DMSO-*d*<sub>6</sub> and 120  $\mu$ L of HF 5% were poured in a plastic NMR tube, and the mixture was sonicated for 1 h until a clear solution was obtained. For the PSM of ZIF-90, 10 mg of sample was digested with 20  $\mu$ L of DCl and 0.75 mL of DMSO-*d*<sub>6</sub>.

## ■ ASSOCIATED CONTENT

### Supporting Information

The Supporting Information is available free of charge on the ACS Publications website at DOI: 10.1021/jacs.6b11240.

Experimental procedures and characterization data (PDF)

## ■ AUTHOR INFORMATION

### Corresponding Author

\*daniel.maspoch@icn2.cat

### ORCID

Daniel Maspoch: 0000-0003-1325-9161

### Notes

The authors declare the following competing financial interest(s): The authors have a patent pending on the methods described in this manuscript.

## ■ ACKNOWLEDGMENTS

This work was supported by the EU FP7 ERC-Co 615954 and European Union's Horizon 2020 research and innovation program under grant agreement No. 685727. I.I. thanks the MINECO for the RyC fellowship RyC-2010-06530. ICN2 acknowledges the support of the Spanish MINECO through the Severo Ochoa Centers of Excellence Program, under Grant SEV-2013-0295.

## ■ REFERENCES

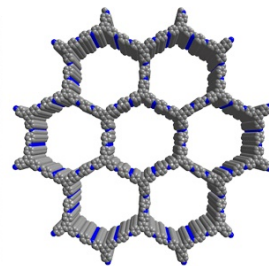
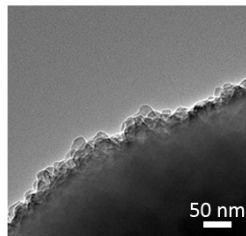
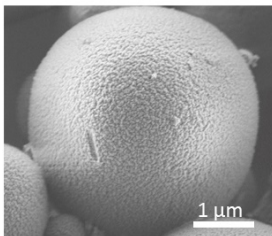
- (1) Furukawa, H.; Ko, N.; Go, Y. B.; Aratani, N.; Choi, S. B.; Choi, E.; Yazaydin, A. Ö.; Snurr, R. Q.; O'Keeffe, M.; Kim, J.; Yaghi, O. M. *J. Am. Chem. Soc.* **2010**, *132*, 424.
- (2) Horcajada, P.; Gref, R.; Baati, T.; Allan, P. K.; Maurin, G.; Couvreur, P.; Férey, G.; Morris, R. E.; Serre, C. *Chem. Rev.* **2012**, *112*, 1232.
- (3) Carné, A.; Carbonell, C.; Imaz, I.; Maspoch, D. *Chem. Soc. Rev.* **2011**, *40*, 291.
- (4) Evans, J. D.; Sumbly, C. J.; Doonan, C. J. *Chem. Soc. Rev.* **2014**, *43*, 5933.
- (5) Doonan, C. J.; Morris, W.; Furukawa, H.; Yaghi, O. M. *J. Am. Chem. Soc.* **2009**, *131*, 9492.
- (6) Kim, M.; Cahill, J. F.; Prather, K. A.; Cohen, S. M. *Chem. Commun.* **2011**, *47*, 7629.
- (7) Garibay, S. J.; Cohen, S. M. *Chem. Commun.* **2010**, *46*, 7700.
- (8) Kim, M.; Cohen, S. M. *CrystEngComm* **2012**, *14*, 4096.
- (9) Kandiah, M.; Usseglio, S.; Svelle, S.; Olsbye, U.; Lillerud, K. P.; Tilset, M. *J. Mater. Chem.* **2010**, *20*, 9848.
- (10) Hou, J.; Luan, Y.; Tang, J.; Wensley, A. M.; Yang, M.; Lu, Y. *J. Mol. Catal. A: Chem.* **2015**, *407*, 53.
- (11) Pintado-Sierra, M.; Rasero-Almansa, A. M.; Corma, A.; Iglesias, M.; Sánchez, F. *J. Catal.* **2013**, *299*, 137.
- (12) Rasero-Almansa, A. M.; Corma, A.; Iglesias, M.; Sanchez, F. *Green Chem.* **2014**, *16*, 3522.
- (13) Tang, J.; Dong, W.; Wang, G.; Yao, Y.; Cai, L.; Liu, Y.; Zhao, X.; Xu, J.; Tan, L. *RSC Adv.* **2014**, *4*, 42977.
- (14) Wang, J.; Yang, M.; Dong, W.; Jin, Z.; Tang, J.; Fan, S.; Lu, Y.; Wang, G. *Catal. Sci. Technol.* **2016**, *6*, 161.
- (15) Liu, J.; Zhang, X.; Yang, J.; Wang, L. *Appl. Organomet. Chem.* **2014**, *28*, 198.
- (16) Saleem, H.; Rañique, U.; Davies, R. P. *Micronorous Mesonorous Mater.* **2016**, *221*, 238.

- (17) Morris, W.; Doonan, C. J.; Furukawa, H.; Banerjee, R.; Yaghi, O. M. *J. Am. Chem. Soc.* **2008**, *130*, 12626.
- (18) Jones, C. G.; Stavila, V.; Conroy, M. A.; Feng, P.; Slaughter, B.; Ashley, C. E.; Aliendorf, M. D. *ACS Appl. Mater. Interfaces* **2016**, *8*, 7623.
- (19) Thompson, J. A.; Brunelli, N. A.; Lively, R. P.; Johnson, J. R.; Jones, C. W.; Nair, S. *J. Phys. Chem. C* **2013**, *117*, 8198.
- (20) Liu, C.; Liu, Q.; Huang, A. *Chem. Commun.* **2016**, *52*, 3400.
- (21) Servalli, M.; Ranocchiarri, M.; Van Bokhoven, J. A. *Chem. Commun.* **2012**, *48*, 1904.
- (22) Carné-Sánchez, A.; Imaz, I.; Cano-Sarabia, M.; Maspoch, D. *Nat. Chem.* **2013**, *5*, 203.
- (23) Garzón-Tovar, L.; Cano-Sarabia, M.; Carné-Sánchez, A.; Carbonell, C.; Imaz, I.; Maspoch, D. *React. Chem. Eng.* **2016**, *1*, 533.
- (24) Nguyen, J. G.; Cohen, S. M. *J. Am. Chem. Soc.* **2010**, *132*, 4560.
- (25) Canivet, J.; Aguado, S.; Daniel, C.; Farrusseng, D. *ChemCatChem* **2011**, *3*, 675.
- (26) Aguado, S.; Canivet, J.; Farrusseng, D. *Chem. Commun.* **2010**, *46*, 7999.
- (27) Marti, A. M.; Tran, D.; Balkus, K. J. *J. Porous Mater.* **2015**, *22*, 1275.
- (28) Ragon, F.; Horcajada, P.; Chevreau, H.; Hwang, Y. K.; Lee, U. H.; Miller, S. R.; Devic, T.; Chang, J.-S.; Serre, C. *Inorg. Chem.* **2014**, *53*, 2491.



## Spray drying for making covalent chemistry II: synthesis of covalent-organic framework superstructures and related composites

---







Cite this: *Chem. Commun.*, 2017, 53, 11372

Received 8th September 2017,  
Accepted 25th September 2017

DOI: 10.1039/c7cc07052g

rsc.li/chemcomm

## Spray drying for making covalent chemistry II: synthesis of covalent–organic framework superstructures and related composites†

Luis Garzón-Tovar,<sup>a</sup> Ceren Avci-Camur,<sup>a</sup> David Rodríguez-San-Miguel,<sup>b</sup> Inhar Imaz,<sup>a</sup> Félix Zamora<sup>b,c</sup> and Daniel Maspoch<sup>b,d</sup>

**Here we report a method that combines the spray-drying technique with a dynamic covalent chemistry process to synthesize zero-dimensional, spherical and microscale superstructures made from the assembly of imine-based COF nanocrystals. This methodology also enables the integration of other functional materials into these superstructures forming COF-based composites.**

Covalent organic frameworks (COFs) are an emerging class of crystalline porous materials, where two-dimensional (2D) or three-dimensional (3D) architectures are formed from organic building blocks linked by dynamic covalent bonds (e.g. imine, boroxine,  $\beta$ -keto-enamine and azine).<sup>1–3</sup> These materials are characterized by their high porosity, high thermal stability and low mass density, which confer them potential for myriad applications, such as gas sorption and storage,<sup>4–7</sup> catalysis,<sup>8–10</sup> sensors<sup>11–13</sup> and optoelectronics.<sup>14,15</sup> Seeking to exploit these possibilities, researchers have developed several fabrication methods for COFs, including not only the traditional solvothermal synthesis but also microwave,<sup>16</sup> microfluidic,<sup>17</sup> mechanochemical,<sup>18</sup> ionothermal,<sup>19</sup> and continuous-flow synthesis.<sup>20,21</sup>

While many efforts have been devoted to the synthesis of new COFs and to their production methods, there is a growing interest in structuring these COFs at the micro/macroscale forming more complex, high-order super- or mesostructures from the assembly of COF nanoparticles. As their metal–organic framework (MOF) counterparts,<sup>22,23</sup> these types of structures made

from COF nanocrystals are especially attractive due to the possibility of (i) controlling the shape and size of COFs at the micro/macroscale, two parameters that are very important to control for many applications; (ii) enhancing the initial performance *via* the design of their morphology; and (iii) combining COFs with other materials to create functional composites, which can further expand the scope for applications.<sup>24–27</sup>

To date, there have been a few studies based on the creation of COF superstructures. For example, Banerjee *et al.* synthesized a highly crystalline and porous COF in the form of hollow spheres that were used for immobilizing the enzyme trypsin.<sup>28</sup> In a more recent study, core–shell microspheres containing Fe<sub>3</sub>O<sub>4</sub> nanoclusters were synthesized using a template assisted route. The resulting hybrid microspheres showed a photothermal conversion ability after exposing them to near infrared light.<sup>25</sup>

Despite these advances, the synthesis of higher-order COF superstructures is still challenging mainly due to the harsh conditions usually needed to synthesize highly crystalline COF nanoparticles. In this sense, we have recently reported that the spray drying method can be used to synthesize MOFs in the form of spherical hollow or compact superstructures made from the assembly of MOF nanoparticles.<sup>29–32</sup> Additionally, we have recently reported that spray drying is also an effective methodology to perform Schiff-base condensation reactions, either between discrete organic molecules or on the pore surfaces of MOFs.<sup>33</sup> Herein, we combine both achievements and extend the applicability of spray drying to synthesize imine-based COF nanocrystals while structuring them into spherical hollow superstructures. This strategy consists of a two-step process. In the first step, the spray drying allows the formation and shaping of amorphous imine-based polymer spheres. Then, in a second step, these spheres are subjected to a dynamic covalent chemistry process to crystallize them under similar conditions to those reported by Dichtel *et al.*<sup>34</sup> Remarkably, after the crystallization step, the resulting superstructures preserve the initial size and morphology of the amorphous spheres. Further, we show that this strategy enables integrating

<sup>a</sup> Catalan Institute of Nanoscience and Nanotechnology (ICN2), CSIC and The Barcelona Institute of Science and Technology, Campus UAB, Bellaterra, 08193, Barcelona, Spain. E-mail: daniel.maspoch@icn2.cat

<sup>b</sup> Departamento de Química Inorgánica and Institute for Advanced Research in Chemical Sciences (IAChem), Universidad Autónoma de Madrid, Madrid, 28049, Spain. E-mail: felix.zamora@uam.es

<sup>c</sup> Instituto Madrileño de Estudios Avanzados en Nanociencia (IMDEA Nanociencia), Cantoblanco, 28049, Madrid, Spain

<sup>d</sup> ICREA, Pg. Lluís Companys 23, 08010, Barcelona, Spain

† Electronic supplementary information (ESI) available: Experimental procedures and additional characterization of the synthesized COFs. See DOI: 10.1039/c7cc07052g

guest functional materials, either molecules or other nano-materials, in these COF superstructures.

Initially, we began with the synthesis of superstructures of **COF-TAPB-BTCA**, a two-dimensional COF assembled from two trigonal building blocks, 1,3,5-benzenetricarbaldehyde (BTCA) and 1,3,5-tris-(4-aminophenyl)benzene (TAPB).<sup>35</sup> In a typical first step, a 0.03 mol L<sup>-1</sup> solution of BTCA in a mixture of DMSO and acetic acid (9:1 v/v) and a 0.03 mol L<sup>-1</sup> solution of TAPB in DMSO were independently atomized using a three-fluid nozzle at a feed rate of 3.0 mL min<sup>-1</sup>, a flow rate of 336 mL min<sup>-1</sup> and an inlet temperature of 200 °C, using a B-290 Mini Spray Dryer (BÜCHI Labortechnik). This atomization immediately afforded a yellow powder (Fig. 1a). Note here that the use of the three-fluid nozzle ensured that the two reactants only come in contact inside the drying chamber avoiding the clogging of the nozzle.

Field-emission scanning electron microscopy (FESEM) images and X-ray powder diffraction (XRPD) performed on the intermediate solid collected revealed the homogeneous formation of amorphous spheres with an average size of 2.2 ± 1.1 μm (Fig. 1b and Fig. S1, ESI†). Since the spray-drying method is based on the fast evaporation of the solvent, we reasoned that the kinetic product was obtained instead of the thermodynamic one. The formation of the imine-based polymer was confirmed by FT-IR spectroscopy and solid-state <sup>13</sup>C magic angle spinning nuclear magnetic resonance (MAS NMR) spectroscopy. The FT-IR spectrum showed the presence of the typical imine (C=N) band at 1633 cm<sup>-1</sup> and the absence of the band corresponding to free -NH<sub>2</sub> between 3300 and 3500 cm<sup>-1</sup>, indicating the absence of unreacted TAPB. The imine formation was further corroborated by the appearance of a signal at 158 ppm in the <sup>13</sup>C MAS NMR spectrum, which was attributed to the carbon atom of the C=N

imine group (Fig. S2, ESI†). These results are in agreement with those previously reported for **COF-TAPB-BTCA**.<sup>35</sup> In a second step, this imine-based polymer was subjected to a dynamic covalent chemistry process. Thus, the amorphous spheres were dispersed in a mixture of 1,4-dioxane/mesitylene/water/acetic acid and heated at 80 °C for 192 h. The isolated material did not show significant spectroscopic changes in both FT-IR and <sup>13</sup>C MAS NMR spectra (Fig. S3, ESI†). However, the FESEM and high-resolution transmission electron microscopy (HR-TEM) images displayed the formation of hollow superstructures in which their walls are created by the close packing of COF nanoparticles (Fig. 1c, d and Fig. S4, ESI†). Remarkably, these superstructures retained both the shape and size of the amorphous spheres (Fig. S5, ESI†). The XRPD pattern of these superstructures showed the most intense peak at 5.5°, which properly matches with the simulated **COF-TAPB-BTCA** structure (Fig. 1e and Fig. S6, ESI†). The microporosity of the **COF-TAPB-BTCA** superstructures was confirmed by N<sub>2</sub> adsorption measurements, which gave a BET surface area of 911 m<sup>2</sup> g<sup>-1</sup>. This value is consistent with that previously reported for **COF-TAPB-BTCA** (Fig. 1f).<sup>30</sup> Finally, thermogravimetric analysis (TGA) revealed the high thermal stability of the **COF-TAPB-BTCA** superstructures (up to 500 °C), following by a weight loss due to the decomposition of the framework (Fig. S7, ESI†).

To demonstrate the generality of our approach, we used similar synthetic conditions to synthesize other imine-based COF superstructures. To this end, we selected the recently discovered **COF-LZU1**<sup>8</sup> and **COF-TAPB-PDA**.<sup>34</sup> **COF-LZU1** was synthesized by the condensation of BTCA and *p*-phenylenediamine (PPD), whereas **COF-TAPB-PDA** was synthesized from TAPB and terephthalaldehyde (PDA). In both cases, after the two-step process,

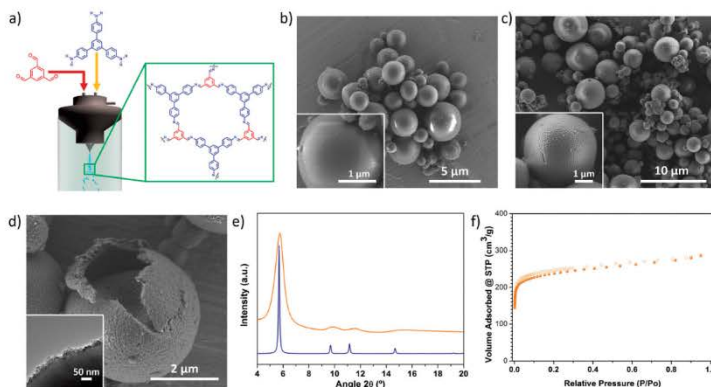
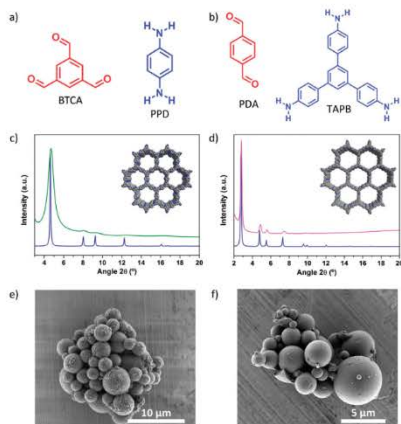


Fig. 1 (a) Schematic representation of the spray drying synthesis of **COF-TAPB-BTCA**. (b) Representative FESEM images of amorphous **COF-TAPB-BTCA** spheres. (c) Representative FESEM images of microspherical **COF-TAPB-BTCA** superstructures. (d) FESEM and HRTEM images of a mechanically broken superstructure, revealing the hollow cavity and that they are formed by COF nanocrystals. (e) XRPD diffractogram of **COF-TAPB-BTCA** (orange), compared with the simulated powder pattern (blue). (f) N<sub>2</sub> adsorption isotherm of **COF-TAPB-BTCA**.

ChemComm

View Article Online  
Communication

**Fig. 2** (a and b) Representation of the building blocks used to synthesize (a) **COF-LZU1** and (b) **COF-TAPB-PDA**. (c) XRPD diffractogram of the obtained **COF-LZU1** (green) compared with the simulated powder pattern (blue). (d) XRPD diffractogram of the obtained **COF-TAPB-PDA** (pink) compared with the simulated powder pattern (blue). (e and f) FESEM images showing the general view of the microspherical (e) **COF-LZU1** and (f) **COF-TAPB-PDA** superstructures.

FESEM and HR-TEM images and XRPD of the resulting solids revealed the formation of crystalline microspherical superstructures of the desired COFs (Fig. 2 and Fig. S8, S9, ESI<sup>†</sup>). FT-IR spectra of **COF-LZU1** and **COF-TAPB-PDA** showed the presence of the characteristic C=N stretching band at 1618 and 1628  $\text{cm}^{-1}$ , respectively. Moreover, the formation of imine was further corroborated by the peaks observed in the  $^{13}\text{C}$  MAS NMR spectra at 157 ppm for **COF-LZU1** and 158 ppm for **COF-TAPB-PDA** (Fig. S10 and S11, ESI<sup>†</sup>). Additionally, the microporosity of the COFs was confirmed by  $\text{N}_2$  adsorption analysis, from which the BET surface areas of 319  $\text{m}^2 \text{g}^{-1}$  for **COF-LZU1** and 1162  $\text{m}^2 \text{g}^{-1}$  for **COF-TAPB-PDA** were calculated (Fig. S12, ESI<sup>†</sup>). These values are consistent with those previously reported.<sup>8,34</sup>

Having demonstrated that our spray-drying methodology enables the formation of hollow COF superstructures, we envisioned to use it as a simple method for integrating other functional substances to these superstructures and thus, create COF-based composites.<sup>36–38</sup> To explore this possibility, we synthesized **Rose-bengal@COF-TAPB-BTCA** superstructures by reproducing the formation of **COF-TAPB-BTCA** superstructures but dissolving Rose bengal in the initial precursor solution. FESEM images and XRPD patterns revealed the formation of crystalline microspherical superstructures of **COF-TAPB-BTCA**, confirming that their synthesis was not affected by the presence of the dye (Fig. S13, ESI<sup>†</sup>). The presence of Rose bengal was confirmed by elemental mapping with energy dispersive X-ray spectrometry (EDX) performed on a single superstructure, which revealed a

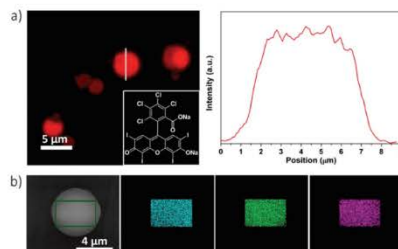


**Fig. 3** (a) Confocal fluorescence image of **Rose-bengal@COF-TAPB-BTCA** superstructures and their fluorescence intensity profile. Inset: Chemical structure of Rose bengal. (b) Elemental mapping with EDX performed on a single spherical superstructure of **Rose-bengal@COF-TAPB-BTCA**, showing the homogeneous distribution Na (cyan), Cl (green) and I (pink).

highly uniform distribution of Cl, I, and Na atoms (Fig. 3b). Additionally, the successful encapsulation of this dye was visualized by confocal images, where the intensity profile and the confocal image taken on a single sphere revealed the homogeneous distribution of Rose bengal (Fig. 3a). Finally, to evaluate the possibility to release the encapsulated molecules from these COF superstructures, the **Rose-bengal@COF-TAPB-BTCA** composite was incubated in ethanol for different periods of time, and the dye released was quantified by fluorescence spectroscopy (Fig. S14, ESI<sup>†</sup>). Notably, a dye release of 32% was observed for the first day, achieving a release of 56% after 8 days. This slow release suggests that the dye is in fact located on the pores of the COF nanocrystals rather than on their crystal surface.

To further explore the formation of COF-based composites using this strategy, we incorporated magnetic  $\text{Fe}_3\text{O}_4$  nanoparticles dispersed in the precursor solution. Under the same conditions,  $\text{Fe}_3\text{O}_4$  nanoparticles (8 nm diameter) were encapsulated

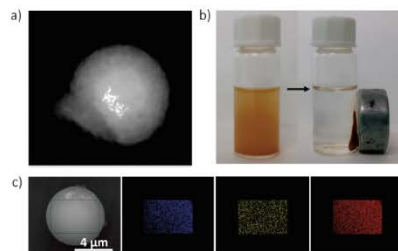


**Fig. 4** (a) HAADF-STEM image of a single  $\text{Fe}_3\text{O}_4@COF-TAPB-BTCA$  superstructure. (b) Photographs of the dispersion of  $\text{Fe}_3\text{O}_4@COF-TAPB-BTCA$  superstructures before and after exposure to a magnet. (c) Elemental mapping with EDX performed on a single spherical superstructure of  $\text{Fe}_3\text{O}_4@COF-TAPB-BTCA$ , showing the homogeneous distribution of N (blue), Fe (yellow) and O (red).

into the COF-TAPB-BTCA superstructures, as confirmed by HAADF-STEM and HR-TEM images and XRPD (Fig. 4a and Fig. S15, S16, ESI†). The content of Fe in the composite was estimated using inductively coupled plasma-mass spectrometry (ICP-MS), from which a Fe<sub>2</sub>O<sub>3</sub> content of 2.8% w/w in the composite was determined. EDX mapping performed on a single superstructure showed the distribution of N, Fe and O atoms, confirming the presence of Fe<sub>2</sub>O<sub>3</sub> into the superstructures (Fig. 4c). Also, as an indication of the encapsulation, a colloidal suspension of the composite was exposed to a magnet and rapidly attracted to it (Fig. 4b). Similarly, magnetic measurements performed on the composite confirmed its magnetic character, exhibiting a characteristic hysteresis loop with a coercive field of 240 Oe at 10 K (Fig. S17, ESI†).

In summary, we have reported a highly versatile and effective methodology to simultaneously synthesize and shape microspherical hollow imine-based COF superstructures. This method also enables making COF-based composites by simply adding the selected functional materials during the spray-drying synthesis.

This work was supported by the Spanish MINECO (project PN MAT2015-65354-C2-1-R), the Catalan AGAUR (project 2014 SGR 80), and the ERC under the EU FP7 (ERC-Co 615954). It was also funded by the CERCA Programme/Generalitat de Catalunya. ICN2 acknowledges the support of the Spanish MINECO through the Severo Ochoa Centers of Excellence Program under Grant SEV-2013-0295.

## Conflicts of interest

There are no conflicts to declare.

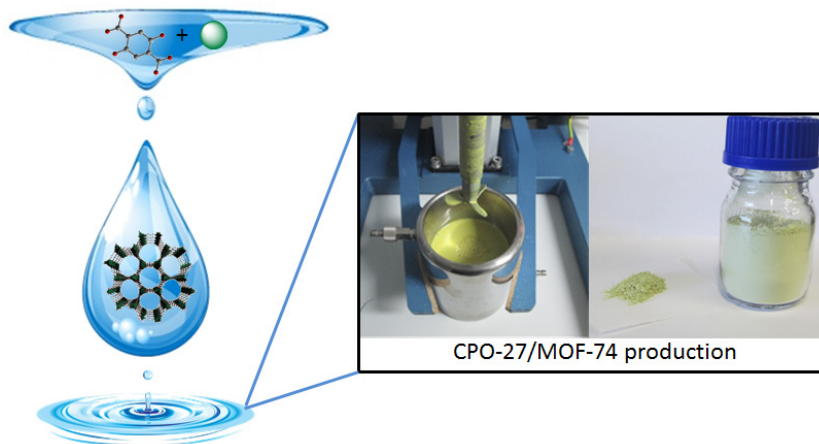
## Notes and references

- P. J. Waller, F. Gándara and O. M. Yaghi, *Acc. Chem. Res.*, 2015, **48**, 3053–3063.
- S.-Y. Ding and W. Wang, *Chem. Soc. Rev.*, 2013, **42**, 548–568.
- J. Thote, H. Barike Aiyappa, R. Rahul Kumar, S. Kandambeth, B. P. Biswal, D. Balaji Shinde, N. Chaki Roy and R. Banerjee, *IUCr*, 2016, **3**, 402–407.
- H. Furukawa and O. M. Yaghi, *J. Am. Chem. Soc.*, 2009, **131**, 8875–8883.
- C. J. Doonan, D. J. Tranchemontagne, T. G. Glover, J. R. Hunt and O. M. Yaghi, *Nat. Chem.*, 2010, **2**, 235–238.
- M. G. Rabbani, A. K. Sekizkardes, Z. Kahveci, T. E. Reich, R. Ding and H. M. El-Kaderi, *Chem. – Eur. J.*, 2013, **19**, 3324–3328.
- S. S. Han, H. Furukawa, O. M. Yaghi and W. A. Goddard, *J. Am. Chem. Soc.*, 2008, **130**, 11580–11581.
- S.-Y. Ding, J. Gao, Q. Wang, Y. Zhang, W.-G. Song, C.-Y. Su and W. Wang, *J. Am. Chem. Soc.*, 2011, **133**, 19816–19822.
- H. Li, Q. Y. Pan, Y. C. Ma, X. Y. Guan, M. Xue, Q. R. Fang, Y. S. Yan, V. Valchev and S. L. Qiu, *J. Am. Chem. Soc.*, 2016, **138**, 14783–14788.
- Q. R. Fang, S. Gu, J. Zheng, Z. B. Zhuang, S. L. Qiu and Y. S. Yan, *Angew. Chem., Int. Ed.*, 2014, **53**, 2878–2882.
- G. Das, B. P. Biswal, S. Kandambeth, V. Venkatesh, G. Kaur, M. Addicoat, T. Heine, S. Verma and R. Banerjee, *Chem. Sci.*, 2015, **6**, 3931–3939.
- Y. Yuan, H. Ren, F. X. Sun, X. F. Jing, K. Cai, X. J. Zhao, Y. Wang, Y. Wei and G. S. Zhu, *J. Mater. Chem.*, 2012, **22**, 24558–24562.
- S.-Y. Ding, M. Dong, Y.-W. Wang, Y.-T. Chen, H.-Z. Wang, C.-Y. Su and W. Wang, *J. Am. Chem. Soc.*, 2016, **138**, 3031–3037.
- S. Wan, J. Guo, J. Kim, H. Thee and D. Jiang, *Angew. Chem.*, 2008, **120**, 8958–8962.
- J. Mahmood, E. K. Lee, M. Jung, D. Shin, I.-Y. Jeon, S.-M. Jung, H.-J. Choi, J.-M. Seo, S.-Y. Bae, S.-D. Sohn, N. Park, J. H. Oh, H.-J. Shin and J.-B. Baek, *Nat. Commun.*, 2015, **6**, 6486.
- H. Wei, S. Chai, N. Hu, Z. Yang, L. Wei and L. Wang, *Chem. Commun.*, 2015, **51**, 12178–12181.
- D. Rodríguez-San-Miguel, A. Abrishamkar, J. A. R. Navarro, R. Rodríguez-Trujillo, D. B. Amabilino, R. Mas-Balleste, F. Zamora and J. Puigmarti-Luis, *Chem. Commun.*, 2016, **52**, 9212–9215.
- B. P. Biswal, S. Chandra, S. Kandambeth, B. Lukose, T. Heine and R. Banerjee, *J. Am. Chem. Soc.*, 2013, **135**, 5328–5331.
- P. Kuhn, M. Antonietti and A. Thomas, *Angew. Chem., Int. Ed.*, 2008, **47**, 3450–3453.
- S. Karak, S. Kandambeth, B. P. Biswal, H. S. Sasmal, S. Kumar, P. Pachfule and R. Banerjee, *J. Am. Chem. Soc.*, 2017, **139**, 1856–1862.
- Y. Peng, W. K. Wong, Z. Hu, Y. Cheng, D. Yuan, S. A. Khan and D. Zhao, *Chem. Mater.*, 2016, **28**, 5095–5101.
- S. Furukawa, J. Reboul, S. Diring, K. Sumida and S. Kitagawa, *Chem. Soc. Rev.*, 2014, **43**, 5700–5734.
- A. Carné-Sánchez, I. Imaz, K. C. Stylianou and D. Maspoch, *Chem. – Eur. J.*, 2014, **20**, 5192–5201.
- D. Rodríguez-San-Miguel, J. J. Corral-Perez, E. Gil-Gonzalez, D. Cuellas, J. Arauzo, V. M. Monsalvo, V. Carcelen and F. Zamora, *CrystEngComm*, 2017, **19**, 4872–4876.
- J. Tan, S. Namuangruk, W. Kong, N. Kungwan, J. Guo and C. Wang, *Angew. Chem., Int. Ed.*, 2016, **55**, 13979–13984.
- X. Shi, Y. Yao, Y. Xu, K. Liu, G. Zhu, L. Chi and G. Lu, *ACS Appl. Mater. Interfaces*, 2017, **9**, 7481–7488.
- A. Halder, S. Kandambeth, B. P. Biswal, G. Kaur, N. C. Roy, M. Addicoat, J. K. Salunke, S. Banerjee, K. Vanka, T. Heine, S. Verma and R. Banerjee, *Angew. Chem., Int. Ed.*, 2016, **55**, 7806–7810.
- S. Kandambeth, V. Venkatesh, D. B. Shinde, S. Kumari, A. Halder, S. Verma and R. Banerjee, *Nat. Commun.*, 2015, **6**, 6786.
- A. Carné-Sánchez, I. Imaz, M. Cano-Sarabia and D. Maspoch, *Nat. Chem.*, 2013, **5**, 203–211.
- L. Garzón-Tovar, M. Cano-Sarabia, A. Carne-Sanchez, C. Carbonell, I. Imaz and D. Maspoch, *React. Chem. Eng.*, 2016, **1**, 533–539.
- V. Guillermin, L. Garzón-Tovar, A. Yazdi, I. Imaz, J. Juanhuix and D. Maspoch, *Chem. – Eur. J.*, 2017, **23**, 6829–6835.
- L. Garzón-Tovar, J. Pérez-Carvajal, I. Imaz and D. Maspoch, *Adv. Funct. Mater.*, 2017, **27**, 1606424.
- L. Garzón-Tovar, S. Rodríguez-Hermida, I. Imaz and D. Maspoch, *J. Am. Chem. Soc.*, 2017, **139**, 897–903.
- B. J. Smith, A. C. Overholts, N. Hwang and W. R. Dichtel, *Chem. Commun.*, 2016, **52**, 3690–3693.
- A. de la Pena Ruizgomez, D. Rodríguez-San-Miguel, K. C. Stylianou, M. Cavallini, D. Gentili, F. Lisicci, S. Milita, O. M. Roscioni, M. L. Ruiz-Gonzalez, C. Carbonell, D. Maspoch, R. Mas-Balleste, J. L. Segura and F. Zamora, *Chem. – Eur. J.*, 2015, **21**, 10666–10670.
- D. Mullangi, S. Nandi, S. Shalini, S. Sreedhala, C. P. Vinod and R. Vaidhyanathan, *Sci. Rep.*, 2015, **5**, 10876.
- D. Mullangi, S. Shalini, S. Nandi, B. Choksi and R. Vaidhyanathan, *J. Mater. Chem. A*, 2017, **5**, 8376–8384.
- P. Wang, Q. Wu, L. Han, S. Wang, S. Fang, Z. Zhang and S. Sun, *RSC Adv.*, 2015, **5**, 27290–27294.

---

## Optimised room temperature, water-based synthesis of CPO-27-M metal-organic frameworks with high space-time yields

---







Cite this: *J. Mater. Chem. A*, 2015, 3, 20819

## Optimised room temperature, water-based synthesis of CPO-27-M metal–organic frameworks with high space-time yields†

L. Garzón-Tovar,<sup>a</sup> A. Carné-Sánchez,<sup>a</sup> C. Carbonell,<sup>a</sup> I. Imaz<sup>\*a</sup> and D. Maspoch<sup>\*ab</sup>

The exceptional porosity of Metal–Organic Frameworks (MOFs) could be harnessed for countless practical applications. However, one of the challenges currently precluding the industrial exploitation of these materials is a lack of green methods for their synthesis. Since green synthetic methods obviate the use of organic solvents, they are expected to reduce the production costs, safety hazards and environmental impact typically associated with MOF fabrication. Herein we describe the stepwise optimisation of reaction parameters (pH, reagent concentrations and reaction time) for the room temperature, water-based synthesis of several members of the CPO-27/MOF-74-M series of MOFs, including ones made from Mg(II), Ni(II), Co(II) and Zn(II) ions. Using this method, we built MOFs with excellent BET surface areas and unprecedented Space-Time Yields (STYs). Employing this approach, we have synthesised CPO-27-M MOFs with record BET surface areas, including 1279 m<sup>2</sup> g<sup>-1</sup> (CPO-27-Zn), 1351 m<sup>2</sup> g<sup>-1</sup> (CPO-27-Ni), 1572 m<sup>2</sup> g<sup>-1</sup> (CPO-27-Co), and 1603 m<sup>2</sup> g<sup>-1</sup> (CPO-27-Mg). We anticipate that our method could be applied to produce CPO-27-Ni, -Mg, -Co and -Zn with STYs of 44 kg m<sup>-3</sup> per day, 191 kg m<sup>-3</sup> per day, 1462 kg m<sup>-3</sup> per day and a record 18 720 kg m<sup>-3</sup> per day, respectively.

Received 2nd July 2015  
Accepted 8th September 2015  
DOI: 10.1039/c5ta04923g  
www.rsc.org/MaterialsA

### Introduction

Metal–Organic Frameworks (MOFs) are an emerging class of porous materials comprising metal components and organic ligands. They are characterised by extremely large surface areas ( $S_{\text{BET}}$ ) and high structural/compositional flexibility that confer them with potential for myriad applications, including gas sorption and separation, catalysis, sensing, and biomedicine, among many others.<sup>1–7</sup> Seeking to exploit this exceptional porosity, researchers have developed several methods for the industrial-scale fabrication of MOFs, including the classical solvothermal synthesis,<sup>8</sup> mechano-synthesis,<sup>9</sup> electrochemistry,<sup>10</sup> continuous flow techniques,<sup>11,12</sup> and spray-drying.<sup>13</sup> These methods are continuously being optimised in the hopes of finally enabling widespread use of MOFs in practical applications.

Optimisation of industrial MOF fabrication methods not only addresses the production rates, but also the related costs, safety hazards and environmental impact. One measure that

can simultaneously provide savings while improving safety and environmental friendliness is to use water as the only solvent. Along these lines, the company BASF has developed a water-based synthesis of aluminium fumarate (Basolite A520®) at the tonne scale, achieving the extremely high Space-Time Yield (STY) of 3600 kg m<sup>-3</sup> per day.<sup>14</sup> In fact, this breakthrough in the green synthesis of MOFs was awarded the Pierre Potier Prize.

Herein, we report another example of the green synthesis of MOFs: a room temperature, water-based synthesis of several members of the isostructural CPO-27-M (also known as MOF-74) family of the general structure  $M_2(\text{dhtp})$ , where dhtp = 2,5-dioxido-1,4-benzenedicarboxylate and M = Mg(II), Co(II), Ni(II) and Zn(II), with high production rates (STYs up to 18 500 kg m<sup>-3</sup> per day) while maintaining their excellent sorption capabilities.

Isostructural CPO-27-M MOFs are undoubtedly among the most widely studied MOFs, as they are highly porous ( $S_{\text{BET}}$  = 1039–1542 m<sup>2</sup> g<sup>-1</sup>) and stable and show hexagonal channels that can exhibit open metal sites and that can be easily functionalised with various groups.<sup>15,16</sup> Given these advantages, CPO-27-M MOFs are excellent candidates for catalysis,<sup>17</sup> storage and delivery of biologically relevant gases,<sup>18</sup> and separation and/or adsorption of gases (H<sub>2</sub>, CO, CH<sub>4</sub>, ammonia, etc.).<sup>19–27</sup> For instance, CPO-27-Mg has been widely reported to be among the best porous materials for CO<sub>2</sub> adsorption and separation due to its high selectivity, facile regeneration and high CO<sub>2</sub> dynamic-adsorption capacities.<sup>28–33</sup>

To date, the most common CPO-27-M syntheses involve solvothermal reactions of a solution containing the

<sup>a</sup>ICN2 (ICN-CSIC), Institut Català de Nanociència i Nanotecnologia, Esfera UAB 08193 Bellaterra, Spain. E-mail: inhar.imaz@icn.cat; daniel.maspoch@icn.cat

<sup>b</sup>Institució Catalana de Recerca i Estudis Avançats (ICREA), 08100 Barcelona, Spain

† Electronic supplementary information (ESI) available: XRD patterns of the CPO-27-M series obtained with different reaction times and concentration. Tables listing the yield,  $S_{\text{BET}}$  values and synthesis conditions of CPO-27-M. XRD pattern and N<sub>2</sub> isotherm for the synthesis of CPO-27-Zn at gram scale. SEM images of CPO-27-M series. See DOI: 10.1039/c5ta04923g

corresponding metal salt and dhpt in organic solvents (e.g. DMF) or mixtures of organic solvents and water.<sup>34–37</sup> However, very recent reports have shown that totally water-based routes for the synthesis of CPO-27-M are possible and that, despite the low aqueous solubility of dhpt, such methods can be efficient. Quadrelli *et al.* first reported the synthesis of CPO-27-Ni ( $S_{\text{BET}} = 1233 \text{ m}^2 \text{ g}^{-1}$ ) with an STY of  $680 \text{ kg m}^{-3}$  per day. They mixed an aqueous solution of Ni(n) acetate with an aqueous suspension of dhpt, and then heated the resulting mixture at reflux for 1 h.<sup>38</sup> Their success stems from the use of Ni(n) acetate because metal acetates in the MOF syntheses can be used as both the metal source and the base (acetate ion).<sup>39</sup> Thus, the basic character of the acetate ion promotes deprotonation of the dhpt and therefore, its dissolution in water and subsequent reaction with Ni(n) ions. More recently, Sánchez-Sánchez *et al.* adapted this method to synthesise CPO-27-Zn ( $S_{\text{BET}} = 1039 \text{ m}^2 \text{ g}^{-1}$ ; reaction time = 20 h) at room temperature, without the need for any heating, by introducing a minimum amount of NaOH.<sup>40</sup> However, to date, there have not been any reports demonstrating whether this route to CPO-27-Zn could afford similar or even higher STYs compared to that achieved in the hydrothermal synthesis of CPO-27-Ni, or whether it could be generalised to encompass CPO-27-M built up from metal ions other than Zn(n).

Seeking to further develop the aforementioned room-temperature, water-based chemistry, we have developed similar methods for several members of the CPO-27-M series, including ones made from Mg(n), Ni(n), Co(n), Cu(n) and Zn(n) ions. We optimised each method stepwise, by carefully studying the influence of reaction parameters on the purity and quality of the synthesised CPO-27-M and on the corresponding reaction yields. Specifically, we evaluated the pH, the reagent concentrations (of the metal acetate/nitrate [hereafter designed as *Met*] and of the dhpt), and the reaction time. We have proven that, except in the case of CPO-27-Cu, fine-tuning of these parameters for each CPO-27-M affords high-quality product (in terms of  $S_{\text{BET}}$ ) with high STYs.

## Experimental

### Reagents

Nickel acetate tetrahydrate, cobalt acetate tetrahydrate, magnesium nitrate hexahydrate, zinc acetate dehydrate, copper acetate hydrate, 2,5-dihydroxyterephthalic acid (dhpt) and sodium hydroxide were purchased from Sigma Aldrich. Methanol was obtained from Fisher Chemical. All the reagents were used without further purification. Deionised water, obtained with a Milli-Q® system (18.2 MΩ cm), was used in all reactions.

### General protocol for the synthesis and activation of CPO-27-M

Our protocol for the synthesis of CPO-27-M MOFs began with the addition of an aqueous solution of metal salt (*Met*) to an aqueous solution of dhpt and NaOH. The resulting reaction mixture, which contained the precursors *Met* (at the concentration  $C_1$ ) and dhpt (at the concentration  $C_2$ ), was stirred at room temperature for a certain period of time ( $t$ ). In all cases, the volume was 10 mL and the molar ratio (*Met*/dhpt) was 2.

After the time  $t$ , each resulting solid was collected by centrifugation, washed three times with water and methanol, dried at 70 °C overnight and weighed.

The prepared solids were characterised by XRPD, activated using a protocol recently described by Yaghi *et al.*,<sup>41</sup> and their respective  $S_{\text{BET}}$  values were measured. The activation protocol started with the immersion of the synthesised CPO-27-M in methanol for 6 days (12 days for CPO-27-Mg), during which the solvent was exchanged once daily. Then, each CPO-27-M was exposed to five consecutive heating ramps under vacuum [from room temperature to 80 °C; from 80 °C to 100 °C; from 100 °C to 150 °C; from 150 °C to 200 °C, and from 200 °C to 250 °C (265 °C for CPO-27-Zn) at a constant rate of 4 °C min<sup>-1</sup>, with the temperature held at 1 h at the end of each ramp; except for at 250 °C (265 °C for CPO-27-Zn), at which all samples were held for 12 h.

### Gram-scale synthesis of CPO-27-Zn

In a typical synthesis, an aqueous solution of  $\text{Zn}(\text{CH}_3\text{COO})_2 \cdot 2\text{H}_2\text{O}$  was rapidly added to an aqueous solution of dhpt and NaOH in a D15/CN10-F2 pilot-plant stirrer (DISPERMAT) equipped with a 1 L reactor. The volume of the reaction mixture was 500 mL; the molar ratio (*Met*/dhpt/NaOH/ $\text{H}_2\text{O}$ ), 2 : 1 : 4 : 304;  $C_1 = 0.365 \text{ mol L}^{-1}$ ; and  $C_2 = 0.183 \text{ mol L}^{-1}$ . This reaction mixture was stirred for 5 min at room temperature. The resulting solid was collected by centrifugation, washed three times with deionised water and methanol, and finally, dried at 70 °C overnight (weight: 32.5 g; yield: 97%).

### Characterisation

X-ray powder diffraction (XRPD) patterns were collected on an X'Pert PRO MPDP analytical diffractometer (Panalytical) at 45 kV, 40 mA using  $\text{CuK}\alpha$  radiation ( $\lambda = 1.5419 \text{ \AA}$ ). Nitrogen adsorption and desorption measurements were done at 77 K using an Autosorb-IQ-AG analyser (Quantachrome Instruments). Field-Emission Scanning Electron Microscopy (FE-SEM) images were collected on a FEI Magellan 400L scanning electron microscope at an acceleration voltage of 1.0–2.0 kV, using aluminium as support. Transmission electron microscopy (TEM) images were obtained with a FEI Tecnai G<sup>2</sup> F20.

## Results and discussion

### Space-time yield (STY)

Space-time yield is an industrial parameter that refers to the quantity of a product (kg) produced per unit volume ( $\text{m}^3$ ) per unit time (day). Widely used in the field of catalysis,<sup>42</sup> it has been employed by BASF to assess a given reaction/method for MOF production. Initial STY values reported by BASF include  $60 \text{ kg m}^{-3}$  per day for the solvothermal synthesis of Basolite A100 (or MIL-53-Al), and  $100 \text{ kg m}^{-3}$  per day and  $225 \text{ kg m}^{-3}$  per day for the electrochemical synthesis of Basolite Z1200 (or ZIF-8) and Basolite C300 (or HKUST-1),<sup>43</sup> respectively.

Since the initial work of BASF, increasingly higher STYs have been reported for MOF synthesis. Interestingly, very competitive STYs have begun to be reported for water-based green syntheses

of most iconic MOFs. Illustrative examples include a hydrothermal ( $T = 60\text{ }^{\circ}\text{C}$ ) synthesis of Basolite A520 (STY:  $3600\text{ kg m}^{-3}$  per day) and a microwave ( $T = 130\text{ }^{\circ}\text{C}$ ) synthesis of Al fumarate (STY:  $15\text{ }200\text{ kg m}^{-3}$  per day), reported by BASF and Maurin, Serre *et al.*, respectively.<sup>53,52</sup> Impressive STYs have also been reported for the synthesis of HKUST-1 at room temperature ( $2035\text{ kg m}^{-3}$  per day),<sup>54</sup> the hydrothermal ( $T = 160\text{ }^{\circ}\text{C}$ ) synthesis of MIL-100-Fe ( $1700\text{ kg m}^{-3}$  per day for),<sup>54</sup> the continuous flow hydrothermal ( $T = 250\text{ }^{\circ}\text{C}$ ) synthesis of MIL-53-Al ( $1300\text{ kg m}^{-3}$  per day for),<sup>52</sup> and the hydrothermal ( $T = 100\text{ }^{\circ}\text{C}$ ) synthesis of CPO-27-Ni ( $680\text{ kg m}^{-3}$  per day).<sup>38</sup>

#### Quality of a synthesised MOF

One parameter that is suitable for analysing the quality of a synthesised MOF is the surface area,<sup>55</sup> which is generally reported as either the BET surface area ( $S_{\text{BET}}$ ) or, less commonly, the Langmuir surface area. However, it is important to highlight here that  $S_{\text{BET}}$  is not a direct experimental value: it must be calculated from the  $N_2$  isotherm performed at  $77\text{ K}$  according to the BET model. This fact, when considered together with the (variable) quality of the synthesised MOF and the activation method used, mean that the  $S_{\text{BET}}$  values reported for a particular MOF can vary widely. A clear example of a MOF for which various  $S_{\text{BET}}$  values have been reported is our target, CPO-27-M (Table 1). Another reason for the differences among reported  $S_{\text{BET}}$  values for a particular MOF is the pressure range selected for calculating the value. In order to enable comparison of different  $S_{\text{BET}}$  values for a given MOF, even when the MOF has been synthesised by different methodologies, the use of two criteria has recently been suggested:<sup>55–57</sup> firstly, the straight line fitted to the BET plot must have a positive intercept; and secondly, the pressure range should be chosen such that  $v_{\text{ads}}(1 - P/P_0)$  always increases with  $P/P_0$ . Accordingly, in the study reported here, we chose the pressure range based on these criteria.

As stated above, a second parameter that must be taken into account when comparing  $S_{\text{BET}}$  values is the activation process, which can also vary for a particular MOF. For instance, CPO-27-M has been activated by various methods (see Table 1). For consistency in the study reported here, we activated all the CPO-27-M samples using the general activation method described by Yaghi *et al.*<sup>58</sup>

#### Optimisation of the room temperature water-based synthesis of CPO-27-M: STY versus quality

To increase the STY in a given MOF reaction, two parameters must be optimised: the quantity of pure MOF produced per unit volume, which must be maximised (mainly by balancing the maximum reaction yield and reagent concentrations); and the reaction time, which must be minimised. To optimise both parameters in our targeted syntheses of CPO-27-M, we followed a rational protocol comprising four steps. Firstly, we defined the maximum concentrations of Met ( $C_1$ ) and dhtp ( $C_2$ ) that could be used. We found that the limiting concentration in the reaction mixture was  $C_2 = 0.183\text{ mol L}^{-1}$ , which corresponds to the maximum amount of dhtp that could be dissolved at room

Table 1 Summary of activation methods and  $S_{\text{BET}}$  values reported for CPO-27-M

CPO-27-M	Activation method	$S_{\text{BET}}$ ( $\text{m}^2\text{ g}^{-1}$ )	References
Zn	$\Delta$ at a constant rate of $5\text{ }^{\circ}\text{C min}^{-1}$ from $25\text{ }^{\circ}\text{C}$ to $270\text{ }^{\circ}\text{C}$ , and then held at $270\text{ }^{\circ}\text{C}$ for 16 h	816	31
	$\Delta$ at a constant rate of $2\text{ }^{\circ}\text{C min}^{-1}$ from $25\text{ }^{\circ}\text{C}$ to $225\text{ }^{\circ}\text{C}$ , and then held at $265\text{ }^{\circ}\text{C}$ for 16 h	973	44
	$\Delta$ 10 h at $150\text{ }^{\circ}\text{C}$ , and then $\Delta$ 10 h at $265\text{ }^{\circ}\text{C}$	496	22
	$\Delta$ 18 h at $350\text{ }^{\circ}\text{C}$	867	45
	$\Delta$ 16 h at $100\text{ }^{\circ}\text{C}$	948	46
	$\Delta$ 72 h at $100\text{ }^{\circ}\text{C}$	885	27
	Not reported	1039	40
	$\Delta$ at a constant rate of $5\text{ }^{\circ}\text{C min}^{-1}$ from $25\text{ }^{\circ}\text{C}$ to $250\text{ }^{\circ}\text{C}$ , and then held at $250\text{ }^{\circ}\text{C}$ for 5 h.	1070	31
	$\Delta$ at a constant rate of $2\text{ }^{\circ}\text{C min}^{-1}$ from $25\text{ }^{\circ}\text{C}$ to $225\text{ }^{\circ}\text{C}$ , and then held at $265\text{ }^{\circ}\text{C}$ for 16 h	1199	44
	Ni	$\Delta$ 5 h at $250\text{ }^{\circ}\text{C}$	599
$\Delta$ 18 h at $350\text{ }^{\circ}\text{C}$		402	45
$\Delta$ 16 h at $100\text{ }^{\circ}\text{C}$		514	46
$\Delta$ 19 h at $200\text{ }^{\circ}\text{C}$ , and then $\Delta$ 1 h at $110\text{ }^{\circ}\text{C}$		1218	35
$\Delta$ 20 h at $150\text{ }^{\circ}\text{C}$		1233	38
$\Delta$ 12 h at $250\text{ }^{\circ}\text{C}$		1252	47
$\Delta$ 6 h at $250\text{ }^{\circ}\text{C}$		1350	26
$\Delta$ 72 h at $100\text{ }^{\circ}\text{C}$		1027	27
Not reported		1018	24
Not reported		1318	48
Co	$\Delta$ at a constant rate of $5\text{ }^{\circ}\text{C min}^{-1}$ from $25\text{ }^{\circ}\text{C}$ to $250\text{ }^{\circ}\text{C}$ , and then held at $250\text{ }^{\circ}\text{C}$ for 5 h.	1080	31
	$\Delta$ at a constant rate of $2\text{ }^{\circ}\text{C min}^{-1}$ from $25\text{ }^{\circ}\text{C}$ to $225\text{ }^{\circ}\text{C}$ , and then held at $265\text{ }^{\circ}\text{C}$ for 16 h	1292	44
	$\Delta$ 24 h at $250\text{ }^{\circ}\text{C}$	835	22
	$\Delta$ 18 h at $350\text{ }^{\circ}\text{C}$	521	45
	$\Delta$ 16 h at $100\text{ }^{\circ}\text{C}$	693	46
	$\Delta$ 5 h at $250\text{ }^{\circ}\text{C}$	1327	49
	$\Delta$ 72 h at $100\text{ }^{\circ}\text{C}$	1056	27
	Not reported	1089	24
	$\Delta$ at a constant rate of $5\text{ }^{\circ}\text{C min}^{-1}$ from $25\text{ }^{\circ}\text{C}$ to $250\text{ }^{\circ}\text{C}$ , and then held at $250\text{ }^{\circ}\text{C}$ for 5 h.	1495	31
	$\Delta$ at a constant rate of $2\text{ }^{\circ}\text{C min}^{-1}$ from $25\text{ }^{\circ}\text{C}$ to $225\text{ }^{\circ}\text{C}$ , and then held at $265\text{ }^{\circ}\text{C}$ for 16 h	1530	44
Mg	$\Delta$ 6 h at $250\text{ }^{\circ}\text{C}$	1206	22
	$\Delta$ 18 h at $350\text{ }^{\circ}\text{C}$	1007	45
	$\Delta$ 48 h at $240\text{ }^{\circ}\text{C}$ , and then $\Delta$ 1 h at $110\text{ }^{\circ}\text{C}$	1542	35
	Not reported	1415	24
	$\Delta$ 72 h at $100\text{ }^{\circ}\text{C}$	1332	27
	$\Delta$ 12 h at $250\text{ }^{\circ}\text{C}$	1416	47
	$\Delta$ 24 h at $250\text{ }^{\circ}\text{C}$	1249	33
	$\Delta$ 16 h at $250\text{ }^{\circ}\text{C}$	877	50

temperature under normal stirring conditions in 1 L of water in the presence of NaOH. By fixing the stoichiometry of metal ion and dhtp in CPO-27-M (the total molar ratio of Met/dhtp; to 2 : 1),  $C_1$  and the total molar ratio Met/dhtp/ $H_2O$  were then automatically defined to be  $0.365 \text{ mol L}^{-1}$  and 2 : 1 : 304, respectively. Secondly, we optimised the molar ratio of NaOH (hereafter designated as  $x$ ) for the total molar ratio Met/dhtp/ $H_2O = 2 : 1 : 304$ . For this, we studied the effect of the pH on the purity of the resulting CPO-27-M and on the reaction yields for a randomly selected reaction time of 24 h. At this point, we analysed the quality of the different CPO-27-M products synthesised at the optimum  $x$  by measuring their  $S_{\text{BET}}$ . We considered CPO-27-M samples that showed  $S_{\text{BET}}$  values greater than 90% of the highest reported  $S_{\text{BET}}$  values (Table 1) to be of sufficiently high quality. Thirdly, those with lower  $S_{\text{BET}}$  values were optimised for quality, by decreasing  $C_1$  and  $C_2$ . Finally, once we had determined the ideal  $C_1$ ,  $C_2$  and total molar ratio Met/dhtp/NaOH (2 : 1 : 4) that afforded the maximum quantity of each CPO-27-M per volume unit with acceptable quality, we determined the lowest reaction time for each CPO-27-M, in order to achieve the highest STY.

### Influence of the pH

We systematically studied a series of reactions that varied by total molar ratio (2 : 1 :  $x$  : 304, where  $x = 2, 3, 4, 5$  and 6), in order to determine the optimum  $x$  in terms of purity and reaction yield. In the case of CPO-27-Zn, we found that an unidentified crystalline phase was formed at  $x = 6$  (pH = 9.10); that a mixture of this amorphous phase and CPO-27-Zn was obtained at  $x = 5$  (pH = 8.43); that pure CPO-27-Zn was

synthesised at  $x = 4$  (pH = 7.20), in a yield of 98%; and that a mixture of CPO-27-Zn and a second crystalline phase was obtained at  $x = 2$  (pH = 6.27) and at  $x = 3$  (pH = 6.86) (Fig. 1a). These results are in concordance with those observed by Sánchez-Sánchez *et al.*<sup>40</sup> At  $x = 2$  and  $x = 3$ , we identified the second crystalline phase as  $[\text{Zn}(\text{H}_2\text{O})_2(\text{dhtp})]_m$ ,<sup>39</sup> in which only the two carboxylate groups—and not the two hydroxyl groups—of dhtp are deprotonated and coordinate to Zn(II) ions (Fig. S1†). Interestingly, this coordination is quite different to that observed in CPO-27-Zn, in which the two hydroxyl groups of dhtp are also deprotonated and coordinate to Zn(II) ions. Therefore, we reasoned that a minimum amount of NaOH is required to synthesise pure CPO-27-Zn, and that the optimum amount should be  $x = 4$ , in order to fully deprotonate the carboxylate and hydroxyl groups of dhtp for their subsequent coordination to Zn(II) ions. To further prove this assumption, we also ran the reaction at  $x = 3.25$ ,  $x = 3.5$  and  $x = 3.75$ . Albeit pure CPO-27-Zn samples were produced, the reaction yields were lower (yields: 86%, 93% and 95%, respectively) compared to that obtained at  $x = 4$  (yield: 98%).

We then extended the aforementioned systematic study to the other metal ions. Importantly, we found that  $x = 4$  was also optimal for the water-based synthesis of CPO-27-Ni, CPO-27-Co and CPO-27-Mg at room temperature. However, the final products of the reactions in which  $x$  was altered, varied slightly depending on the metal ion. In the case of CPO-27-Ni, a second crystalline phase mixed with CPO-27-Ni was observed at  $x = 2$  (pH = 5.92) (Fig. 1b). From  $x = 3$  to  $x = 5$ , pure CPO-27-Ni samples were synthesised in yields of 62% ( $x = 3$ ; pH = 6.77), 93% ( $x = 4$ ; pH = 7.84) and 72% ( $x = 5$ ; pH = 8.99). However,

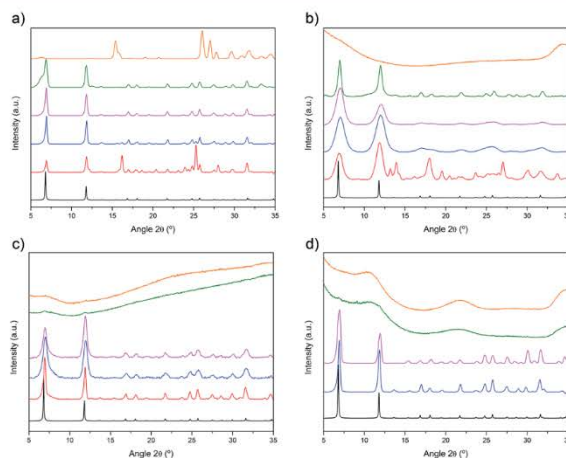


Fig. 1 XRPD diffractograms of the collected powder at different NaOH equivalents (red:  $x = 2$ , blue:  $x = 3$ , pink:  $x = 4$ , green:  $x = 5$ , orange:  $x = 6$ ) for: (a) CPO-27-Zn, (b) CPO-27-Ni, (c) CPO-27-Co and (d) CPO-27-Mg, as compared to the simulated powder pattern for CPO-27 (black).

unidentified amorphous solid was formed at  $x = 6$  (pH = 12.10). For CPO-27-Co, pure samples were synthesised in yields of 13% ( $x = 2$ ; pH = 5.64), 55% ( $x = 3$ ; pH = 5.96) and 98% ( $x = 4$ ; pH = 8.03) (Fig. 1c). At  $x = 5$  (pH = 10.04) and  $x = 6$  (pH = 11.05), the precipitation of amorphous solids was observed. Finally, in the case of CPO-27-Mg, no precipitation occurred at  $x = 2$  (pH = 4.61), whereas pure CPO-27-Mg samples were synthesised in yields of 48% ( $x = 3$ ; pH = 8.08) and 91% ( $x = 4$ ; pH = 9.18) (Fig. 1d). As with the cobalt MOF, amorphous solids were obtained at  $x = 5$  (pH = 10.36) and  $x = 6$  (pH = 11.95). Notice here that when the pH values are higher than 10, amorphous and unknown phases are formed in all cases. This observation is in concordance with the fact that these metal ions are not present as solvated ions above this pH, according to their Pourbaix diagrams.<sup>60</sup>

Interestingly, we observed completely different behaviour for the reaction of dhtp with Cu(II) ions at the different  $x$  than that which we had observed for the other metals. We did not observe formation of CPO-27-Cu in any of the reactions, but we did observe an unknown phase that did not correspond to any reported phase resulting from the association of dhtp and Cu(II) ions (Fig. S2†). A potential explanation for such differences could be the trend of Cu(II) ions to form Cu(OH)<sub>2</sub> phases, even at pH < 7. Indeed, by comparing the Pourbaix diagrams of the different metal ions at a concentration of ~0.3 mol L<sup>-1</sup>, one can observe that Ni(II), Zn(II), Mg(II) and Co(II) ions are stable as solvated ions until pH = 7, whereas Cu(II) ions show a higher tendency to form Cu(OH)<sub>2</sub> at this pH.<sup>60</sup>

We then determined the  $S_{\text{BET}}$  values of the different CPO-27-M synthesised at the optimum NaOH concentration ( $x = 4$ ), finding values of 900 m<sup>2</sup> g<sup>-1</sup> (CPO-27-Zn), 650 m<sup>2</sup> g<sup>-1</sup> (CPO-27-Ni), 1310 m<sup>2</sup> g<sup>-1</sup> (CPO-27-Co) and 1020 m<sup>2</sup> g<sup>-1</sup> (CPO-27-Mg). Based on these values, we determined that the CPO-27-Zn and CPO-27-Co were of sufficiently good quality and that their  $S_{\text{BET}}$  respective values fell above the 90% of the maximum reported  $S_{\text{BET}}$  (Table 1).

#### Effect of the concentrations of the reagents

Having determined that the CPO-27-Ni and CPO-27-Mg products did not pass our quality threshold, we sought to find the

maximum concentration of reagents that would provide good quality  $S_{\text{BET}}$  in their respective syntheses. To this end, we decreased  $C_1$  and  $C_2$ . Thus, we systematically varied  $C_1$  and  $C_2$  (maintaining the molar ratio Met/dhtp/NaOH = 2 : 1 : 4;  $C_1 = 0.273$  mol L<sup>-1</sup>, 0.182 mol L<sup>-1</sup>, 0.137 mol L<sup>-1</sup>, 0.091 mol L<sup>-1</sup> and 0.069 mol L<sup>-1</sup>) used in the synthesis of CPO-27-Ni and of CPO-27-Mg. Under the studied conditions, the highest  $C_1$  and  $C_2$  values that provided CPO-27-Ni (yield = 76%) with a good  $S_{\text{BET}}$  (1350 m<sup>2</sup> g<sup>-1</sup>) were  $C_1 = 0.069$  mol L<sup>-1</sup> and  $C_2 = 0.0345$  mol L<sup>-1</sup>. Note here that lower reagent concentrations led to a CPO-27-Ni that exhibited greater crystallinity and an enhanced  $S_{\text{BET}}$  (Table S1 and Fig. S3†). In the case of CPO-27-Mg, the optimal  $C_1$  and  $C_2$  were 0.273 mol L<sup>-1</sup> and 0.137 mol L<sup>-1</sup>, respectively. Under these conditions, CPO-27-Mg, obtained in good yield (96%), exhibited an  $S_{\text{BET}}$  of 1337 m<sup>2</sup> g<sup>-1</sup> (Table S1 and Fig. S4†). However, in this case the use of lower reagent concentrations produced CPO-27-Mg of lesser crystallinity. We compared these results to those for CPO-27-Ni, and tentatively attributed the difference to the need for a critical concentration of dhtp to break the highly stable [Mg(H<sub>2</sub>O)<sub>6</sub>] complexes in water and form the MOF.

#### Influence of the reaction time

Once we had determined the highest  $C_1$  and  $C_2$ , we finally evaluated the minimum reaction time that enables synthesis of each CPO-27-M (Table S2†). For this, we performed a series of reactions decreasing the reaction times from 24 h to 5 min. For each reaction, we determined the yield and we characterised the resulting solids by XRPD and BET analysis. For all samples that passed our quality  $S_{\text{BET}}$  control threshold, we calculated the STY, taking into account the precursor concentrations, the yield and the reaction time (Table 2).

The minimum reaction times for CPO-27-Ni and -Mg were found to be 6 h and 4 h, respectively (Fig. S5 and 6†). At these times, the synthesised CPO-27-Ni showed a  $S_{\text{BET}}$  of 1220 m<sup>2</sup> g<sup>-1</sup> (yield = 92%), whereas CPO-27-Mg showed a  $S_{\text{BET}}$  of 1376 m<sup>2</sup> g<sup>-1</sup> (yield = 81%) (Fig. S9†). Taking into account these values, the STYs of these processes were 44 kg m<sup>-3</sup> per day for CPO-27-Ni and 191 kg m<sup>-3</sup> per day for CPO-27-Mg. Fig. 2a and b shows representative Scanning Electron Microscopy (SEM) images for

Table 2 Comparison of the synthetic details, yield and  $S_{\text{BET}}$  values of CPO-27-M synthesised with the highest STY values and the highest  $S_{\text{BET}}$  values

CPO-27-M	$C_1$ (mol L <sup>-1</sup> )	$C_2$ (mol L <sup>-1</sup> )	Yield (%)	Time (h)	$S_{\text{BET}}$ (m <sup>2</sup> g <sup>-1</sup> )	$V_p^a$ (cm <sup>3</sup> g <sup>-1</sup> )	STY (kg m <sup>-3</sup> per day)
Zn (mg scale)	0.364	0.182	92	0.08	1154	0.44	17 986
Zn (g scale)	0.365	0.182	97	0.08	1076	0.40	18 720
Zn	0.364	0.182	98	0.17	1279	0.47	9501
Co	0.364	0.182	90	1	962	0.39	1462
Co	0.045	0.023	93	24	1572	0.57	16
Mg	0.273	0.137	81	4	1376	0.52	191
Mg	0.182	0.091	94	6	1603	0.60	98
Ni	0.069	0.035	92	6	1220	0.48	44
Ni	0.069	0.036	76	24	1351	0.53	9

<sup>a</sup> Pore volume was calculated at  $P/P_0 = 0.15$  ( $N_2$ , 77 K) using the Quantachrome ASIQWin software.

both materials, revealing the formation of CPO-27-Ni nanoparticles (mean size =  $44 \pm 7$  nm) and hexagonal rod-like crystals of CPO-27-Mg (length =  $1.1 \pm 0.2$   $\mu\text{m}$ ; width =  $0.7 \pm 0.1$   $\mu\text{m}$ ). In the case of CPO-27-Co (Fig. S7†), the minimum reaction time was 1 h, which provided nanoparticles (mean size =  $24 \pm 5$  nm) in 90% yield and with an  $S_{\text{BET}}$  of  $962 \text{ m}^2 \text{ g}^{-1}$  (Fig. 2c and S9†). The resulting STY of this reaction was  $1462 \text{ kg m}^{-3}$  per day. Notice here that in the case of CPO-27-Ni and -Co nanoparticles, the use of a centrifugation step instead of a conventional filtration step may be required for collecting them. This limiting step should also be considered in a realistic industrial production using this room temperature water-based synthesis.

However, the most surprising result that we found was for CPO-27-Zn (Fig. S8†), which we were able to synthesise in only 5 min, in an excellent yield of 92% and with an  $S_{\text{BET}}$  of  $1154 \text{ m}^2 \text{ g}^{-1}$  (Fig. S9†). Under these conditions, the STY of the process was as high as  $17\,986 \text{ kg m}^{-3}$  per day. Importantly, we also proved that this 5 min water-based synthesis of CPO-27-Zn is reproducible and can be synthesised at least to the gram scale (Fig. 2d and e). To scale up the reaction, we used the same conditions described above, except that we used larger quantities of each reagent (40.1 g Zn(Ac)<sub>2</sub>; 18.1 g dhtp; 14.6 g NaOH; and 0.5 L H<sub>2</sub>O) and a 1 L reactor. After only 5 min of reaction, 32.5 g (97% yield) of pure CPO-27-Zn ( $S_{\text{BET}} = 1076 \text{ m}^2 \text{ g}^{-1}$ ) was collected (Fig. S10†). Based on these experimental conditions, the STY of this gram-scale

process was  $18\,720 \text{ kg m}^{-3}$  per day. Fig. 2d and f shows SEM images for CPO-27-Zn synthesised at the milligram and gram scale, revealing the formation of hexagonal rod-like crystals in both cases. The length of CPO-27-Zn crystals synthesised at the gram scale (length =  $9.3 \pm 1.3$   $\mu\text{m}$ ; width =  $1.3 \pm 0.3$   $\mu\text{m}$ ) was slightly larger than those synthesised at the milligram scale (length =  $5.5 \pm 0.5$   $\mu\text{m}$ ; width =  $1.5 \pm 0.6$   $\mu\text{m}$ ). This difference is probably due to the sensitivity of the nucleation, and the crystal growth of CPO-27-Zn, to experimental factors such as the stirring homogeneity and rate.

Finally, the differences in the synthesis reaction rates of CPO-27-M materials [Zn(n) > Co(n) > Mg(n) > Ni(n)] may be explained as a result of the inertness or lability of the metal ions in the ligand exchange process. According with the water exchange rate constants of the complexes  $[\text{M}(\text{H}_2\text{O})_6]^{2+}$ , the lability of the metal ions follows the order of Zn(n) > Co(n) > Mg(n) > Ni(n).<sup>64</sup> As a consequence, the reaction rate between a highly labile  $[\text{Zn}(\text{H}_2\text{O})_6]^{2+}$  with a deprotonated ligand should be faster than the less labile  $[\text{Co}(\text{H}_2\text{O})_6]^{2+}$ . In fact, these results are consistent with previous studies reported for the synthesis of CPO-27 materials under different reaction conditions, also showing that ligand exchange kinetics depends of the lability of the metal ions, being the determining step in the reaction between the deprotonated dhtp and the metal ions.<sup>62,63</sup>

#### Optimisation of the room temperature water-based synthesis of CPO-27-M in terms of BET surface area

Given that the conditions that provide an optimal STY do not generally deliver the best quality MOF, we further evaluated the maximum achievable  $S_{\text{BET}}$  values for each CPO-27-M synthesised through the aforementioned reaction. By systematically modifying the same parameters (mainly, the precursor concentrations and the reaction time; Table 2), we ultimately observed that the  $S_{\text{BET}}$  values for CPO-27-Ni and CPO-27-Co increased with decreasing reagent concentrations and increasing reaction times. The best  $S_{\text{BET}}$  values were  $1351 \text{ m}^2 \text{ g}^{-1}$  for CPO-27-Ni (reaction time = 24 h;  $C_1 = 0.069 \text{ mol L}^{-1}$ ; yield = 76%; STY =  $9 \text{ kg m}^{-3}$  per day) and  $1572 \text{ m}^2 \text{ g}^{-1}$  for CPO-27-Co (reaction time = 24 h;  $C_1 = 0.045 \text{ mol L}^{-1}$ ; yield = 93%; STY =  $16 \text{ kg m}^{-3}$  per day). On the contrary, the  $S_{\text{BET}}$  values for CPO-27-Zn and CPO-27-Mg increased with increasing precursor concentrations and decreasing reaction times. The maximum  $S_{\text{BET}}$  values were found to be  $1279 \text{ m}^2 \text{ g}^{-1}$  for CPO-27-Zn (reaction time = 10 min;  $C_1 = 0.364 \text{ mol L}^{-1}$ ; yield = 98%; STY =  $9501 \text{ kg m}^{-3}$  per day) and  $1603 \text{ m}^2 \text{ g}^{-1}$  for CPO-27-Mg (reaction time = 6 h;  $C_1 = 0.182 \text{ mol L}^{-1}$ ; yield = 94%; STY =  $98 \text{ kg m}^{-3}$  per day) (Fig. S11†). Interestingly, all these synthesised CPO-27-M crystals showed similar morphologies and sizes in comparison to those obtained for the highest STYs (Fig. S12†).

## Conclusions

We have reported the stepwise optimisation of the room temperature, water-based synthesis of several members of the CPO-27/MOF-74-M series of MOFs, including ones made from Mg(n), Ni(n), Co(n) and Zn(n) ions. We evaluated the main

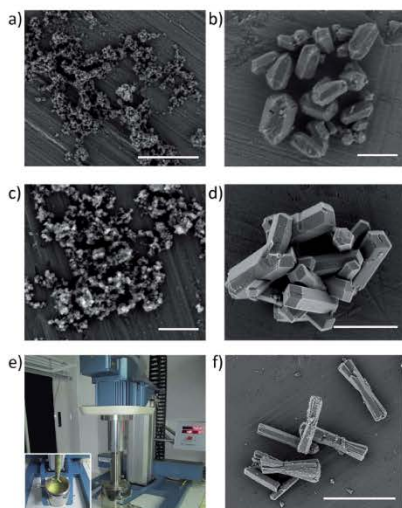


Fig. 2 Scanning electron microscope images of (a) CPO-27-Ni, (b) CPO-27-Mg, (c) CPO-27-Co, (d) CPO-27-Zn (mg-scale) and (f) CPO-27-Zn (gram-scale) synthesised with the highest STYs. (e) Pilot plant stirrer used in the scale-up synthesis of CPO-27-Zn. Scale bars: 1  $\mu\text{m}$  (a–c) and 5  $\mu\text{m}$  (d and f).

reaction parameters affecting this method and found that by fine-tuning the pH, reagent concentrations and reaction time for each case, we were able to fabricate CPO-27-M with excellent BET surface areas (up to 1603 m<sup>2</sup> g<sup>-1</sup>) and unprecedented STYS (as high as 18 720 kg m<sup>-3</sup> per day). The development of such green syntheses, which obviate the use of costly and harmful organic solvents yet enable the efficient fabrication of high quality MOFs, should ultimately facilitate the industrial exploitation of these materials.

## Acknowledgements

This work was supported by the Spanish MINECO (project PN MAT2012-30994) and the EC (project FP7 ERC-Co 61594). I. I. acknowledges the Spanish MINECO for a Ramón y Cajal grant. ICN2 acknowledges support of the Spanish MINECO through the Severo Ochoa Centres of Excellence Program (Grant SEV-2013-0295).

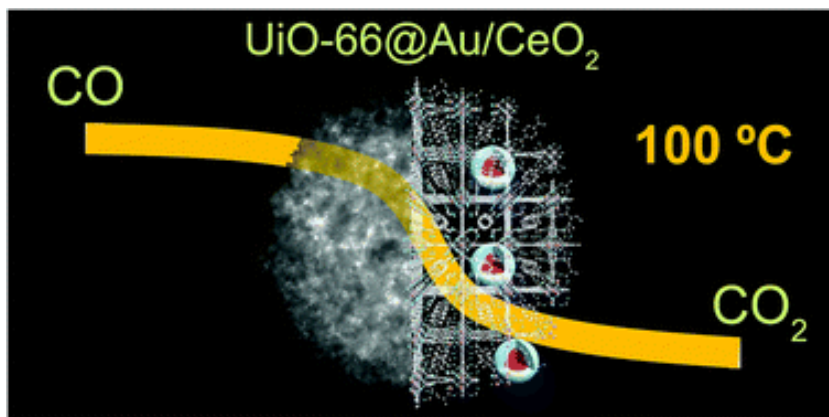
## Notes and references

- Special issue on metal-organic framework materials. *Chem. Soc. Rev.*, 2009, **38**, 1201.
- Special issue on metal-organic framework materials. *Chem. Soc. Rev.*, 2014, **43**, 5403.
- H. Furukawa, N. Ko, Y. B. Go, N. Aratani, S. B. Choi, E. Choi, A. Ö. Yazaydin, R. Q. Snurr, M. O'Keeffe, J. Kim and O. M. Yaghi, *Science*, 2010, **329**, 424–428.
- P. Horcajada, R. Gref, T. Baati, P. K. Allan, G. Maurin, P. Couvreur, G. Férey, R. E. Morris and C. Serre, *Chem. Rev.*, 2012, **112**, 1232–1268.
- M. D. Allendorf and V. Stavila, *CrystEngComm*, 2015, **17**, 229–246.
- A. Carné, C. Carbonell, I. Imaz and D. Maspoch, *Chem. Soc. Rev.*, 2011, **40**, 291–305.
- N. Stock and S. Biswas, *Chem. Rev.*, 2012, **112**, 933–969.
- U. Mueller, M. Schubert, F. Teich, H. Puetter, K. Schierle-Arndt and J. Pastre, *J. Mater. Chem.*, 2006, **16**, 626–636.
- S. L. James, C. J. Adams, C. Bolm, D. Braga, P. Collier, T. Friscic, F. Grepioni, K. D. Harris, G. Hyett, W. Jones, A. Krebs, J. Mack, L. Maini, A. G. Orpen, I. P. Parkin, W. C. Shearouse, J. W. Steed and D. C. Waddell, *Chem. Soc. Rev.*, 2012, **41**, 413–447.
- A. Martínez Joaristi, J. Juan-Alcañiz, P. Serra-Crespo, F. Kapteijn and J. Gascon, *Cryst. Growth Des.*, 2012, **12**, 3489–3498.
- M. Rubio-Martinez, M. P. Batten, A. Polyzos, K.-C. Carey, J. I. Mardel, K.-S. Lim and M. R. Hill, *Sci. Rep.*, 2014, **4**, 5443.
- P. A. Bayliss, I. A. Ibarra, E. Perez, S. Yang, C. C. Tang, M. Poliakoff and M. Schroder, *Green Chem.*, 2014, **16**, 3796–3802.
- A. Carné-Sánchez, I. Imaz, M. Cano-Sarabia and D. Maspoch, *Nat. Chem.*, 2013, **5**, 203–211.
- M. Gaab, N. Trukhan, S. Maurer, R. Gummaraju and U. Müller, *Microporous Mesoporous Mater.*, 2012, **157**, 131–136.
- N. L. Rosi, J. Kim, M. Eddaoudi, B. Chen, M. O'Keeffe and O. M. Yaghi, *J. Am. Chem. Soc.*, 2005, **127**, 1504–1518.
- P. D. C. Dietzel, Y. Morita, R. Blom and H. Fjellvåg, *Angew. Chem., Int. Ed.*, 2005, **44**, 6354–6358.
- P. Valvekens, M. Vandichel, M. Waroquier, V. van Speybroeck and D. de Vos, *J. Catal.*, 2014, **317**, 1–10.
- P. K. Allan, P. S. Wheatley, D. Aldous, M. I. Mohideen, C. Tang, J. A. Hriljac, I. L. Megson, K. W. Chapman, G. de Weireld, S. Vaesen and R. E. Morris, *Dalton Trans.*, 2012, **41**, 4060–4066.
- T. M. McDonald, J. A. Mason, X. Kong, E. D. Bloch, D. Gygi, A. Dani, V. Crocella, F. Giordano, S. O. Odoh, W. S. Drisdell, B. Vlaskovitch, A. L. Dzubak, R. Poloni, S. K. Schnell, N. Planas, K. Lee, T. Pascal, L. F. Wan, D. Prendergast, J. B. Neaton, B. Smit, J. B. Kortright, L. Gagliardi, S. Bordiga, J. A. Reimer and J. R. Long, *Nature*, 2015, **519**, 303–308.
- W. Zhou, H. Wu and T. Yildirim, *J. Am. Chem. Soc.*, 2008, **130**, 15268–15269.
- Z. Bao, S. Alnemrat, L. Yu, I. Vasiliev, Q. Ren, X. Lu and S. Deng, *Langmuir*, 2011, **27**, 13554–13562.
- T. Grant Glover, G. W. Peterson, B. J. Schindler, D. Britt and O. Yaghi, *Chem. Eng. Sci.*, 2011, **66**, 163–170.
- N. Wang, A. Mundstock, Y. Liu, A. Huang and J. Caro, *Chem. Eng. Sci.*, 2015, **124**, 27–36.
- L. Li, J. Yang, J. Li, Y. Chen and J. Li, *Microporous Mesoporous Mater.*, 2014, **198**, 236–246.
- M. H. Rosnes, M. Opitz, M. Frontzek, W. Lohstroh, J. P. Embs, P. A. Georgiev and P. D. C. Dietzel, *J. Mater. Chem. A*, 2015, **3**, 4827–4839.
- Y. Peng, V. Krungelvicute, I. Eryazici, J. T. Hupp, O. K. Farha and T. Yildirim, *J. Am. Chem. Soc.*, 2013, **135**, 11887–11894.
- H. Wu, W. Zhou and T. Yildirim, *J. Am. Chem. Soc.*, 2009, **131**, 4995–5000.
- K. Lee, J. D. Howe, L.-C. Lin, B. Smit and J. B. Neaton, *Chem. Mater.*, 2015, **27**, 668–678.
- X. Kong, E. Scott, W. Ding, J. A. Mason, J. R. Long and J. A. Reimer, *J. Am. Chem. Soc.*, 2012, **134**, 14341–14344.
- D. Britt, H. Furukawa, B. Wang, T. G. Glover and O. M. Yaghi, *Proc. Natl. Acad. Sci. U. S. A.*, 2009, **106**, 20637–20640.
- S. R. Caskey, A. G. Wong-Foy and A. J. Matzger, *J. Am. Chem. Soc.*, 2008, **130**, 10870–10871.
- J. A. Mason, T. M. McDonald, T. H. Bae, J. E. Bachman, K. Sumida, J. J. Dutton, S. S. Kaye and J. R. Long, *J. Am. Chem. Soc.*, 2015, **137**, 4787–4803.
- T. Remy, S. A. Peter, S. van der Perre, P. Valvekens, D. E. de Vos, G. V. Baron and J. F. M. Denayer, *J. Phys. Chem. C*, 2013, **117**, 9301–9310.
- J. Guasch, P. D. C. Dietzel, P. Collier and N. Acerbi, *Microporous Mesoporous Mater.*, 2015, **203**, 238–244.
- P. D. C. Dietzel, V. Besikiotis and R. Blom, *J. Mater. Chem.*, 2009, **19**, 7362.
- P. D. C. Dietzel, Y. Morita, R. Blom and H. Fjellvåg, *Angew. Chem., Int. Ed.*, 2005, **44**, 6354–6358.
- À. Ruyra, A. Yazdi, J. Espín, A. Carné-Sánchez, N. Roher, J. Lorenzo, I. Imaz and D. Maspoch, *Chem.–Eur. J.*, 2015, **21**, 2508–2518.

- 38 S. Cadot, L. Veyre, D. Luneau, D. Farrusseng and E. Alessandra Quadrelli, *J. Mater. Chem. A*, 2014, **2**, 17757–17763.
- 39 D. J. Tranchemontagne, J. R. Hunt and O. M. Yaghi, *Tetrahedron*, 2008, **64**, 8553–8557.
- 40 M. Sánchez-Sánchez, N. Getachew, K. Díaz, M. Díaz-García, Y. Chebude and I. Díaz, *Green Chem.*, 2015, **17**, 1500–1509.
- 41 L. J. Wang, H. Deng, H. Furukawa, F. Gándara, K. E. Cordova, D. Peri and O. M. Yaghi, *Inorg. Chem.*, 2014, **53**, 5881–5883.
- 42 K. Weissermel and H.-J. Arpe, in *Industrial Organic Chemistry*, Wiley-VCH Verlag GmbH, 2007, pp. 424–438.
- 43 A. U. Czaja, N. Trukhan and U. Muller, *Chem. Soc. Rev.*, 2009, **38**, 1284–1293.
- 44 J. J. Perry, S. L. Teich-McGoldrick, S. T. Meek, J. A. Greathouse, M. Haranczyk and M. D. Allendorf, *J. Phys. Chem. C*, 2014, **118**, 11685–11698.
- 45 M. Díaz-García, Á. Mayoral, I. Díaz and M. Sánchez-Sánchez, *Cryst. Growth Des.*, 2014, **14**, 2479–2487.
- 46 D. Ruano, M. Díaz-García, A. Alfayate and M. Sánchez-Sánchez, *ChemCatChem*, 2015, **7**, 674–681.
- 47 X. Wu, Z. Bao, B. Yuan, J. Wang, Y. Sun, H. Luo and S. Deng, *Microporous Mesoporous Mater.*, 2013, **180**, 114–122.
- 48 D.-J. Lee, Q. Li, H. Kim and K. Lee, *Microporous Mesoporous Mater.*, 2012, **163**, 169–177.
- 49 H.-Y. Cho, D.-A. Yang, J. Kim, S.-Y. Jeong and W.-S. Ahn, *Catal. Today*, 2012, **185**, 35–40.
- 50 P. D. C. Dietzel, R. Blom and H. Fjellvåg, *Eur. J. Inorg. Chem.*, 2008, **2008**, 3624–3632.
- 51 E. Leung, U. Müller, N. Trukhan, H. Mattenheimer, G. Cox and S. Blei, Patentanmeldung 10183283.0, 2010.
- 52 E. Alvarez, N. Guillou, C. Martineau, B. Bueken, B. van de Voorde, C. le Guillouzer, P. Fabry, F. Nouar, F. Taulelle, D. de Vos, J.-S. Chang, K. H. Cho, N. Ramsahye, T. Devic, M. Daturi, G. Maurin and C. Serre, *Angew. Chem., Int. Ed.*, 2015, **54**, 3664–3668.
- 53 J. Huo, M. Brightwell, S. El Hankari, A. Garai and D. Bradshaw, *J. Mater. Chem. A*, 2013, **1**, 15220–15223.
- 54 Y.-K. Seo, J. W. Yoon, J. S. Lee, U. H. Lee, Y. K. Hwang, C.-H. Jun, P. Horcajada, C. Serre and J.-S. Chang, *Microporous Mesoporous Mater.*, 2012, **157**, 137–145.
- 55 T. Düren, F. Millange, G. Férey, K. S. Walton and R. Q. Snurr, *J. Phys. Chem. C*, 2007, **111**, 15350–15356.
- 56 J. Rouquerol, F. Rouquerol, P. Llewellyn, G. Maurin and K. S. W. Sing, *Adsorption by Powders and Porous Solids: Principles, Methodology and Applications*, Elsevier Science, 2013.
- 57 P. Llewellyn, F. R. Reinoso, J. Rouquerol and N. Seaton, *Characterization of Porous Solids VII: Proceedings of the 7th International Symposium on the Characterization of Porous Solids (COPS-VII), 26–28 May 2005*, Elsevier Science, Aix-en-Provence, France, 2006.
- 58 L. J. Wang, H. Deng, H. Furukawa, F. Gándara, K. E. Cordova, D. Peri and O. M. Yaghi, *Inorg. Chem.*, 2014, **53**, 5881–5883.
- 59 N. E. Ghermani, G. Morgant, J. d'Angelo, D. Desmaële, B. Fraisse, F. Bonhomme, E. Dichi and M. Sgahier, *Polyhedron*, 2007, **26**, 2880–2884.
- 60 G. Wulfsberg, *Principles of Descriptive Inorganic Chemistry*, University Science Books, 1991.
- 61 C. E. Housecroft and A. G. Sharpe, *Inorganic Chemistry*, Pearson Prentice Hall, 2012.
- 62 R. El Osta, M. Feyand, N. Stock, F. Millange and R. I. Walton, *Powder Diffr.*, 2013, **28**, S256–S275.
- 63 E. Haque and S. H. Jung, *Chem. Eng. J.*, 2011, **173**, 866–872.

**Core-shell Au/CeO<sub>2</sub> nanoparticles  
supported in UiO-66 beads exhibiting full  
CO conversion at 100 °C**

---







Cite this: *J. Mater. Chem. A*, 2017, 5, 13966

Received 6th April 2017  
Accepted 12th June 2017

DOI: 10.1039/c7ta03006a

rsc.li/materials-a

## Core-shell Au/CeO<sub>2</sub> nanoparticles supported in UiO-66 beads exhibiting full CO conversion at 100 °C†

A. Yazdi,<sup>a</sup> A. Abo Markeb,<sup>b</sup> L. Garzón-Tovar,<sup>a</sup> J. Patarroyo,<sup>a</sup> J. Moral-Vico,<sup>b</sup> A. Alonso,<sup>\*b</sup> A. Sánchez,<sup>b</sup> N. Bastus,<sup>a</sup> I. Imaz,<sup>a</sup> X. Font,<sup>b</sup> V. Puntes<sup>†\*</sup> and D. Maspoch<sup>†\*</sup>

Hybrid core-shell Au/CeO<sub>2</sub> nanoparticles (NPs) dispersed in UiO-66 shaped into microspherical beads are created using the spray-drying continuous-flow method. The combined catalytic properties of nanocrystalline CeO<sub>2</sub> and Au in a single particle and the support and protective function of porous UiO-66 beads make the resulting composites show good performances as catalysts for CO oxidation ( $T_{50} = 72$  °C;  $T_{100} = 100$  °C) and recyclability.

Long-term exposure to carbon monoxide gas causes lethal damage to humans and animals.<sup>1</sup> In 2014 alone, 6381 kilotons of CO were released into the atmosphere, mainly from transportation, power plants and industrial activities.<sup>2</sup> To date, one of the most efficient solutions for mitigating CO emissions into the atmosphere is its catalytic oxidation to CO<sub>2</sub>.<sup>3,4</sup> Good-performance catalysts for CO oxidation are metal nanoparticles (NPs) such as Au, Pd, Pt and Ru NPs.<sup>5–8</sup> These NPs are usually supported on/in zeolites,<sup>9</sup> activated carbon,<sup>10</sup> and metal oxides, including alumina,<sup>11</sup> mesoporous silica,<sup>12</sup> ceria,<sup>13–17</sup> zirconia,<sup>18</sup> titania,<sup>19</sup> and iron oxides.<sup>4</sup> These supports avoid NP aggregation and, eventually, enhance the catalytic activity of NPs. A remarkable case is the use of nanocrystalline CeO<sub>2</sub> to support Au NPs.<sup>20,21</sup> In this particular composite, CeO<sub>2</sub> acts as an active support that enhances the catalytic performance of Au NPs for CO oxidation. Indeed, because CeO<sub>2</sub> has a high oxygen storage and release capacity<sup>22</sup> and facile oxygen vacancy formation, its surface can be easily enriched with oxygen vacancies so that Au NPs can strongly bind to these vacancies.<sup>23,24</sup> Also, the oxygen

vacancies in CeO<sub>2</sub> can create Ce<sup>3+</sup> ions, opening a new CO oxidation pathway by O<sub>2</sub> adsorbed on Au–Ce<sup>3+</sup> bridge sites.<sup>23</sup> Moreover, the interaction between the ceria and the metal NPs can prevent reorganization of the metallic atoms under operating conditions.<sup>22</sup>

Inspired by these latter results, herein we show a fast method that enables integrating pre-designed core-shell Au/CeO<sub>2</sub> NPs<sup>25–27</sup> into metal-organic frameworks (MOFs). Recently, MOFs have attracted much attention as new porous supports for catalytic NPs due to their exceptionally high surface areas, structural diversity and tailorable pore chemical functionalities.<sup>28</sup> For CO oxidation, Xu *et al.* have shown that ZIF-8 MOFs can support Au NPs to fully oxidize CO at a temperature of 225 °C.<sup>29</sup> Similarly, Pd and Pt NPs and hybrid Pd/Pt NPs supported on MIL-101, ZIF-8, UiO-67 and UiO-66 MOFs showed full CO conversion at temperatures ranging from 120 °C to 200 °C (Table 1).<sup>30–33</sup> In this work, we combine the catalytic properties for CO oxidation of both nanocrystalline CeO<sub>2</sub> and Au counterparts in a single particle entity, which is supported in UiO-66 beads using the spray-drying continuous-flow method. This method allows the simultaneous synthesis and shaping of MOF beads while encapsulating the pre-synthesized NPs in a fast, continuous one-step process.<sup>34–36</sup>

Table 1 Inorganic nanoparticles supported on MOFs for CO oxidation

Catalyst	NPs wt%	$T_{50}$ (°C)	$T_{100}$ (°C)	Ref.
UiO-66@Au/CeO <sub>2</sub>	7	72	100	This work
UiO-66@Au/CeO <sub>2</sub>	5.5	82	110	This work
UiO-67@Pt	5	100	120	33
MIL-101@Pt/Pd		160	175	30
MIL-101@Pt		160	175	30
UiO-66@Au/CeO <sub>2</sub>	2.8	98	180	This work
UiO-66@Pt	2	160	180	32
MIL-101@Pd		185	200	30
ZIF-8@Pt	2	170	200	31
ZIF-8@Au	5	170	225	29
UiO-66		369	440	This work

<sup>a</sup>Catalan Institute of Nanoscience and Nanotechnology (ICN2), CSIC, The Barcelona Institute of Science and Technology, Campus UAB, Bellaterra, 08193 Barcelona, Spain. E-mail: victor.puntes@icn2.cat; daniel.maspoch@icn2.cat

<sup>b</sup>Department of Chemical, Biological and Environmental Engineering, Escola d'Enginyeria, Universitat Autònoma de Barcelona, 08193 Bellaterra, Spain. E-mail: Amanda.Alonso@uab.cat

<sup>†</sup>Vall d'Hebron Institut de Recerca (VHIR), 08035, Barcelona, Spain

<sup>†</sup>ICREA, Pg. Lluís Companys 23, 08010 Barcelona, Spain

† Electronic supplementary information (ESI) available. See DOI: 10.1039/c7ta03006a

Our method started with the synthesis of core-shell Au/CeO<sub>2</sub> (Ce : Au = 1 : 1) NPs in water following the simultaneous reduction/oxidation of Au and Ce precursors (ESI†). Synthesized NPs had an average particle size of  $9.6 \pm 2.0$  nm and an Au core size of  $4.2 \pm 1.2$  nm (Fig. S1, ESI†). Then, they were functionalized with PVP, allowing them to be transferred from water to dimethylformamide (DMF). This step enables the dispersion of Au/CeO<sub>2</sub> NPs in the solvent needed for synthesizing the UiO-66 beads. Afterwards, 100 mg of terephthalic acid, 3 mL of acetic acid, 4 mL of Au/CeO<sub>2</sub> NPs (concentration =  $1 \text{ mg mL}^{-1}$ ) and 280  $\mu\text{L}$  of Zr(OPr)<sub>4</sub> were sequentially mixed in 40 mL of DMF. Note here that ZrCl<sub>4</sub>, which is the common salt used to synthesize UiO-66, was replaced by Zr(OPr)<sub>4</sub> because of the dissolution of CeO<sub>2</sub> in the acidic precursor solution when ZrCl<sub>4</sub> is utilized (Fig. S2, ESI†).<sup>37</sup> This mixture was injected into a coil flow reactor at a feed rate of  $2.4 \text{ mL min}^{-1}$  at  $115^\circ\text{C}$ . The resulting pre-heated solution was then spray dried at  $180^\circ\text{C}$  and a flow rate of  $336 \text{ mL min}^{-1}$  using a spray cap with a 0.5 mm diameter hole. The collected solid was dispersed in DMF and washed twice with DMF and ethanol.<sup>34</sup>

A final step involved its calcination at  $250^\circ\text{C}$  overnight in the presence of air. This calcination process facilitates the removal of PVP from the surface of Au/CeO<sub>2</sub> NPs. It also enhances the interfacial interaction of Au and CeO<sub>2</sub> and increases the crystallinity of CeO<sub>2</sub>, which leads to an enhancement of the oxygen generation/storage capacity of ceria.<sup>38–40</sup>

Field-emission scanning electron microscopy (FE-SEM) of the calcinated powder revealed the formation of spherical beads (average size =  $3.4 \pm 1.8 \mu\text{m}$ ) formed by the assembly of nanocrystals of UiO-66 (Fig. 1a). X-ray powder diffraction (XRPD) indicated that the beads were pure crystalline UiO-66 (Fig. 1j). Fig. 1b and c show high angle annular dark field scanning transmission electron microscopy (HAADF-STEM) results of these beads, confirming the encapsulation of well-dispersed Au/CeO<sub>2</sub> NPs inside them. In addition, energy dispersive X-ray spectroscopy (EDX) mapping of the beads showed the homogeneous distribution of Au and Ce inside the beads (Fig. 1k). The content of Au/CeO<sub>2</sub> in this composite was estimated by digesting the powder in a mixture of concentrated HCl and HNO<sub>3</sub> and analysed by inductively coupled plasma optical emission spectrometry (ICP-OES), from which a Au/CeO<sub>2</sub> content of 2.8% (Ce: 1.28%, Au: 1.31%) in the composite (hereafter, UiO-66@Au/CeO<sub>2</sub>-2.8) was determined. The comparison of this value to the initial percentage of Au/CeO<sub>2</sub> NPs added into the UiO-66 precursor solution leads to an encapsulation yield of 92%, confirming the efficiency of the spray drying method for incorporating Au/CeO<sub>2</sub> NPs into the UiO-66 beads. Finally, the adsorption capacity of UiO-66@Au/CeO<sub>2</sub>-2.8 was determined. N<sub>2</sub> physical adsorption measurements showed a measured Brunauer Emmet Teller (BET) surface area ( $A_{\text{BET}}$ ) of  $1095 \text{ m}^2 \text{ g}^{-1}$  (Fig. S3a, ESI†), very close to that of pristine UiO-66 superstructures.<sup>37</sup>

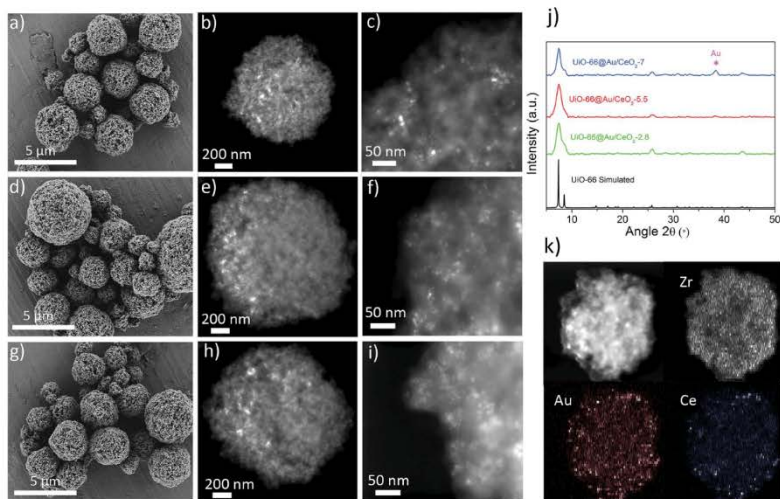


Fig. 1 (a–i) Representative FE-SEM and HAADF-STEM images of UiO-66@Au/CeO<sub>2</sub>-2.8 (a–c), UiO-66@Au/CeO<sub>2</sub>-5.5 (d–f) and UiO-66@Au/CeO<sub>2</sub>-7 (g–i). (j) XRPD patterns of UiO-66@Au/CeO<sub>2</sub>-2.8 (green), UiO-66@Au/CeO<sub>2</sub>-5.5 (red) and UiO-66@Au/CeO<sub>2</sub>-7 (blue) in comparison to the simulated pattern of UiO-66 (black). (k) Elemental mapping (Zr, Ce and Au) of the composite UiO-66@Au/CeO<sub>2</sub>-2.8.

The catalytic activity of the UiO-66@Au/CeO<sub>2</sub>-2.8 in CO oxidation was evaluated by the temperature-programmed oxidation method. The catalytic oxidation of CO was carried out in a fixed bed column reactor with dimensions of 9.0 cm in length and 0.5 cm in inner diameter set in a controlled temperature oven. 50 mg of the catalyst was packed into the column, and a mixture of gases consisting of 1% CO, 21% O<sub>2</sub> and 78% N<sub>2</sub> was allowed to pass through the column reactor at a constant flow rate of 100 mL min<sup>-1</sup>. After that, the catalyst was heated up to the desired temperature and maintained until a steady state was achieved. Within this interval of time, a set of samples of the outlet gas were withdrawn and analyzed to determine the CO conversion.

In an initial step, the catalytic activity of UiO-66 beads without Au/CeO<sub>2</sub> NPs was measured as a control reaction. As expected, UiO-66 beads showed no conversion of CO to CO<sub>2</sub> up to 200 °C, and full conversion took place at 440 °C (Fig. S4, ESI†). In contrast, the catalytic activity of UiO-66@Au/CeO<sub>2</sub>-2.8 was remarkably enhanced. As is shown in Fig. 2a, this composite showed a CO conversion starting at room temperature and exhibited a 50% (*T*<sub>50</sub>) and a 100% (*T*<sub>100</sub>) CO conversion at temperatures of 98 °C and 180 °C, respectively (Table 1).

It is known that, if no aggregation occurs, higher loading of NPs tends to increase the catalytic activity of this class of supported composites. To this end, we systematically synthesized a series of composites in which we increased the added amount of Au/CeO<sub>2</sub> NP dispersion (1 mg mL<sup>-1</sup>) in the precursor solution to 8.5 mL, 12 mL and 16 mL. Again, FE-SEM and HAADF-STEM images revealed the formation of beads containing Au/CeO<sub>2</sub> NPs for all samples (Fig. 1d–i). However, the latter sample was discarded because it showed the presence of a high amount of non-encapsulated Au/CeO<sub>2</sub> NPs together with the beads as well as lower crystallinity of UiO-66 (Fig. S5, ESI†). For the first two compositions, XRPD patterns confirmed the formation of UiO-66 (Fig. 1j), from which Au/CeO<sub>2</sub> contents of 5.5% (Ce: 2.48%, Au: 2.50%) and 7% (Ce: 3.22%, Au: 3.18%) in the composites (hereafter, UiO-66@Au/CeO<sub>2</sub>-5.5 and UiO-66@Au/CeO<sub>2</sub>-7) were determined. These amounts correspond to 91% and 74% of encapsulation efficiency for UiO-66@Au/CeO<sub>2</sub>-5.5 and UiO-66@Au/CeO<sub>2</sub>-7, respectively. Finally, N<sub>2</sub> physical adsorption measurements confirmed that both composites are porous, showing measured BET surface areas of 1070 and 870 m<sup>2</sup> g<sup>-1</sup> (Fig. S3b and c, ESI†).

Ensuing temperature-programmed oxidation measurements confirmed a clear improvement of CO conversion for both new composites, achieving lower *T*<sub>50</sub> and *T*<sub>100</sub> values by increasing the percentage of Au/CeO<sub>2</sub> NPs (Fig. 2a). In the case of UiO-66@Au/CeO<sub>2</sub>-5.5, *T*<sub>50</sub> and *T*<sub>100</sub> were found to be 82 °C and 110 °C, respectively. For UiO-66@Au/CeO<sub>2</sub>-7, these temperatures decreased down to 72 °C and 100 °C. Remarkably, in this latter case, a CO conversion of 3.8% was achieved at room temperature. Moreover, for this latter reaction, the activation energy was found to be 40.2 kJ mol<sup>-1</sup>, whereas the turnover frequency (TOF) values at temperatures of 30, 50, 75 and 100 °C were 10, 39, 106 and 204 h<sup>-1</sup>, respectively (for comparison purposes, the TOF values of other reported catalysts based on Au NPs are given in Table S1, ESI†).

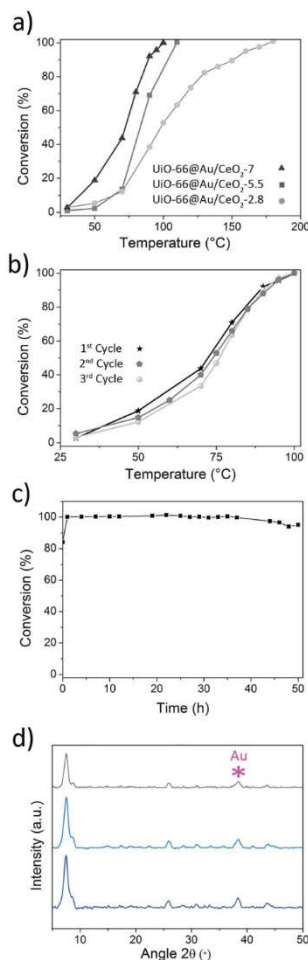


Fig. 2 (a) CO conversion rate as a function of reaction temperature for UiO-66@Au/CeO<sub>2</sub>-2.8, UiO-66@Au/CeO<sub>2</sub>-5.5 and UiO-66@Au/CeO<sub>2</sub>-7. (b) CO conversion rate as a function of reaction temperature for three consecutive cycles over the UiO-66@Au/CeO<sub>2</sub>-7 composite. (c) CO conversion rate at 100 °C for 12 hours over the UiO-66@Au/CeO<sub>2</sub>-7 composite. (d) XRPD patterns of the as-synthesized UiO-66@Au/CeO<sub>2</sub>-7 (blue) and after three temperature-programmed cycles (light blue) and 50 hours of continuous CO conversion (grey).

Finally, the recyclability of these composites was evaluated using the composite UiO-66@Au/CeO<sub>2</sub>-7 that shows a lower  $T_{100}$ . Initially, we performed three cycles of catalysis without detecting any loss of activity (Fig. 2b). After these cycles, the stability of UiO-66@Au/CeO<sub>2</sub>-7 was analyzed by XRPD that showed a complete retention of the crystallinity of UiO-66 (Fig. 2d), as also confirmed by its unaffected surface area ( $A_{\text{BET}} = 850 \text{ m}^2 \text{ g}^{-1}$ ). Similarly, no sign of NP sintering or aggregation and alteration of the morphology of the beads was observed by STEM and FE-SEM (Fig. S6, ESI<sup>†</sup>). Then, the catalytic activity of the UiO-66@Au/CeO<sub>2</sub>-7 sample was also studied for a longer period of time. For this, the conversion of CO was performed continuously at 100 °C for 50 hours, during which no loss of activity for the first 37 hours and a slight decrease of activity (5%) after 50 hours (Fig. 2c) were observed. We attributed this decrease in catalytic activity to a loss of crystallinity of UiO-66 (Fig. 2d) and its porosity capabilities ( $A_{\text{BET}} = 670 \text{ m}^2 \text{ g}^{-1}$ ).

In conclusion, we have described the formation of a new composite based on the entrapment and dispersion of core-shell Au/CeO<sub>2</sub> NPs into microsized spherical, porous UiO-66 beads using the spray-drying continuous-flow method. The combination of nanocrystalline CeO<sub>2</sub> and Au allows accessing to CO conversion  $T_{50}$  and  $T_{100}$  as low as 72 °C and 100 °C. These values are to our knowledge one of the lowest CO conversion temperatures achieved using catalysts based on NPs supported on MOFs. In addition, UiO-66 provides enough protection to avoid NP sintering/aggregation. We consider this method as a general approach for making composites consisting of functional NPs dispersed in MOFs already shaped into spherical beads, as demonstrated by the fact that other composites made of Pd NPs dispersed into UiO-66 beads (Fig. S7, ESI<sup>†</sup>) were also fabricated and tested for CO oxidation.

## Acknowledgements

This work was supported by the Spanish MINECO (projects PN MAT2015-65354-C2-1-R and MAT2015-70725-R), the Catalan AGAUR (projects 2014-SGR-80 and 2014-SGR-612), and the ERC under the EU FP7 (ERC-Co 615954). N. G. B. thanks the MINECO for her RyC grant RYC-2012-10991 and the financial support by the European Commission Seventh Framework Program (FP7) through the Marie Curie Career Integration Grant (322153-MINE). ICN2 acknowledges the support of the Spanish MINECO through the Severo Ochoa Centres of Excellence Programme, under Grant SEV-2013-0295.

## Notes and references

- R. A. Jones, J. A. Strickland, J. A. Stunkard and J. Siegel, *Toxicol. Appl. Pharmacol.*, 1971, **19**, 46–53.
- Environment and Climate Change Canada, Canadian Environmental Sustainability Indicators: Air Pollutant Emissions, 2016, <http://www.ec.gc.ca/indicateurs-indicators/default.asp?lang=en&n=E79F4C12-1>.
- L. Liu, F. Zhou, L. Wang, X. Qi, F. Shi and Y. Deng, *J. Catal.*, 2010, **274**, 1–10.
- B. Qiao, A. Wang, X. Yang, L. F. Allard, Z. Jiang, Y. Cui, J. Liu, J. Li and T. Zhang, *Nat. Chem.*, 2011, **3**, 634–641.
- M. S. Chen, Y. Cai, Z. Yan, K. K. Gath, S. Axnanda and D. W. Goodman, *Surf. Sci.*, 2007, **601**, 5326–5331.
- J. Wang, Z. Wang and C.-J. Liu, *ACS Appl. Mater. Interfaces*, 2014, **6**, 12860–12867.
- P. J. Berlowitz, C. H. F. Peden and D. W. Goodman, *J. Phys. Chem.*, 1988, **92**, 5213–5221.
- E. M. C. Alayon, J. Singh, M. Nachtegaal, M. Harfouche and J. A. van Bokhoven, *J. Catal.*, 2009, **263**, 228–238.
- W. Han, P. Zhang, Z. Tang and G. Lu, *Process Saf. Environ. Prot.*, 2014, **92**, 822–827.
- L. Wang, Y. Zhang, Y. Lou, Y. Guo, G. Lu and Y. Guo, *Fuel Process. Technol.*, 2014, **122**, 23–29.
- A. S. Ivanova, E. M. Slavinskaya, R. V. Gulyaev, V. I. Zaikovskii, O. A. Stonkus, I. G. Danilova, L. M. Phyasova, I. A. Polukhina and A. I. Boronin, *Appl. Catal., B*, 2010, **97**, 57–71.
- H. Wang and C.-J. Liu, *Appl. Catal., B*, 2011, **106**, 672–680.
- A. E. R. S. Khder, H. M. A. Hassan, M. A. Betiha, K. S. Khairou and A. A. Ibrahim, *React. Kinet., Mech. Catal.*, 2014, **112**, 61–75.
- D. Zhang, X. Du, L. Shi and R. Gao, *Dalton Trans.*, 2012, **41**, 14455–14475.
- W. Liu, X. Liu, L. Feng, J. Guo, A. Xie, S. Wang, J. Zhang and Y. Yang, *Nanoscale*, 2014, **6**, 10693–10700.
- D. Zhang, Y. Qian, L. Shi, H. Mai, R. Gao, J. Zhang, W. Yu and W. Cao, *Catal. Commun.*, 2012, **26**, 164–168.
- W. Liu, T. Deng, L. Feng, A. Xie, J. Zhang, S. Wang, X. Liu, Y. Yang and J. Guo, *CrystEngComm*, 2015, **17**, 4850–4858.
- C. M. Olmos, L. E. Chinchilla, J. J. Delgado, A. B. Hungria, G. Blanco, J. J. Calvino and X. Chen, *Catal. Lett.*, 2015, **146**, 144–156.
- J. Wang, S. A. Kondrat, Y. Wang, G. L. Brett, C. Giles, J. K. Bartley, L. Lu, Q. Liu, C. J. Kiely and G. J. Hutchings, *ACS Catal.*, 2015, **5**, 3575–3587.
- S. Carrettin, P. Concepcion, A. Corma, J. M. Lopez Nieto and V. F. Puntes, *Angew. Chem., Int. Ed.*, 2004, **43**, 2538–2540.
- M. Centeno, T. Ramirez Reina, S. Ivanova, O. Laguna and J. Odriozola, *Catalysts*, 2016, **6**, 158.
- N. J. Divins, I. Angurell, C. Escudero, V. Perez-Dieste and J. Llorca, *Science*, 2014, **346**, 620–623.
- H. Y. Kim, H. M. Lee and G. Henkelman, *J. Am. Chem. Soc.*, 2012, **134**, 1560–1570.
- C. Zhang, A. Michaelides and S. J. Jenkins, *Phys. Chem. Chem. Phys.*, 2011, **13**, 22–33.
- T. Mitsudome, M. Yamamoto, Z. Maeno, T. Mizugaki, K. Jitsukawa and K. Kaneda, *J. Am. Chem. Soc.*, 2015, **137**, 13452–13455.
- F. Zhu, G. Chen, S. Sun and X. Sun, *J. Mater. Chem. A*, 2013, **1**, 288–294.
- Y. H. Qu, F. Liu, Y. Wei, C. L. Gu, L. H. Zhang and Y. Liu, *Appl. Surf. Sci.*, 2015, **343**, 207–211.
- P. Falcaro, R. Ricco, A. Yazdi, I. Imaz, S. Furukawa, D. Maspoeh, R. Ameloot, J. D. Evans and C. J. Doonan, *Coord. Chem. Rev.*, 2016, **307**, 237–254.

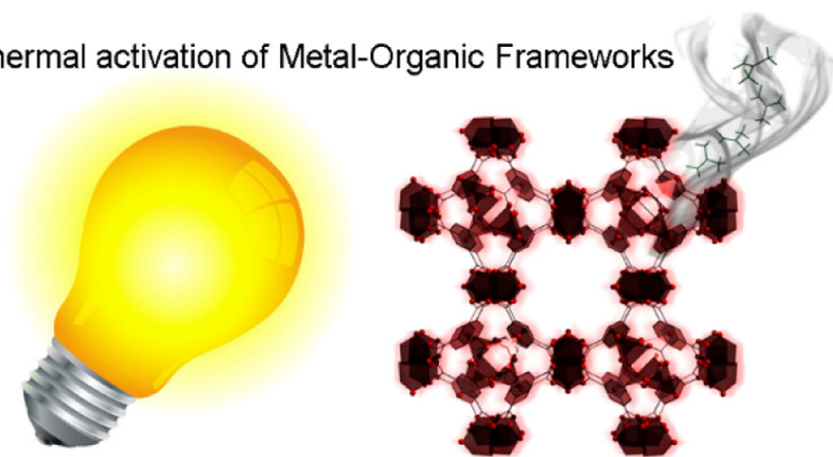
- 29 H.-L. Jiang, B. Liu, T. Akita, M. Haruta, H. Sakurai and Q. Xu, *J. Am. Chem. Soc.*, 2009, **131**, 11302–11303.
- 30 A. Aijaz, T. Akita, N. Tsumori and Q. Xu, *J. Am. Chem. Soc.*, 2013, **135**, 16356–16359.
- 31 G. Lu, S. Li, Z. Guo, O. K. Farha, B. G. Hauser, X. Qi, Y. Wang, X. Wang, S. Han, X. Liu, J. S. DuChene, H. Zhang, Q. Zhang, X. Chen, J. Ma, S. C. Loo, W. D. Wei, Y. Yang, J. T. Hupp and F. Huo, *Nat. Chem.*, 2012, **4**, 310–316.
- 32 W. Zhang, G. Lu, C. Cui, Y. Liu, S. Li, W. Yan, C. Xing, Y. R. Chi, Y. Yang and F. Huo, *Adv. Mater.*, 2014, **26**, 4056–4060.
- 33 G.-l. Zhuang, J.-q. Bai, X. Zhou, Y.-f. Gao, H.-l. Huang, H.-q. Cui, X. Zhong, C.-L. Zhong and J.-g. Wang, *Eur. J. Inorg. Chem.*, 2017, **2017**, 172–178.
- 34 L. Garzon-Tovar, M. Cano-Sarabia, A. Carne-Sanchez, C. Carbonell, I. Imaz and D. Maspoch, *React. Chem. Eng.*, 2016, **1**, 533–539.
- 35 A. Carné-Sánchez, I. Imaz, M. Cano-Sarabia and D. Maspoch, *Nat. Chem.*, 2013, **5**, 203–211.
- 36 J. P.-C. L. Garzon-Trovar, I. Imaz and D. Maspoch, *Adv. Funct. Mater.*, 2017, **27**, 1606424.
- 37 B. Rungtaweeworanit, J. Baek, J. R. Araujo, B. S. Archanjo, K. M. Choi, O. M. Yaghi and G. A. Somorjai, *Nano Lett.*, 2016, **16**, 7645–7649.
- 38 B. He, Q. Zhao, Z. Zeng, X. Wang and S. Han, *J. Mater. Sci.*, 2015, **50**, 6339–6348.
- 39 L. Zhou, X. Li, Z. Yao, Z. Chen, M. Hong, R. Zhu, Y. Liang and J. Zhao, *Sci. Rep.*, 2016, **6**, 23900.
- 40 Y. Liu, H.-S. Chen, J. Li and P. Yang, *RSC Adv.*, 2015, **5**, 37585–37591.



## Activation of Metal–Organic Frameworks Using a UV–Vis Light Source

---

Photothermal activation of Metal-Organic Frameworks





## Photothermal Activation of Metal–Organic Frameworks Using a UV–Vis Light Source

Jordi Espín,<sup>†</sup> Luis Garzón-Tovar,<sup>†</sup> Amau Carné-Sánchez,<sup>†</sup> Inhar Imaz,<sup>\*,†</sup> and Daniel MasPOCH<sup>\*,†,‡</sup>

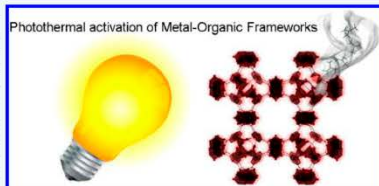
<sup>†</sup>Catalan Institute of Nanoscience and Nanotechnology (ICN2), CSIC and The Barcelona Institute of Science and Technology, Campus UAB, Bellaterra, 08193 Barcelona, Spain

<sup>‡</sup>ICREA, Pg. Lluís Companys 23, 08010 Barcelona, Spain

### Supporting Information

**ABSTRACT:** Metal–organic frameworks (MOFs) usually require meticulous removal of the solvent molecules to unlock their potential porosity. Herein, we report a novel one-step method for activating MOFs based on the photothermal effect induced by directly irradiating them with a UV–vis lamp. The localized light-to-heat conversion produced in the MOF crystals upon irradiation enables a very fast solvent removal, thereby significantly reducing the activation time to as low as 30 min and suppressing the need for time-consuming solvent-exchange procedures and vacuum conditions. This approach is successful for a broad range of MOFs, including HKUST-1, UiO-66–NH<sub>2</sub>, ZIF-67, CPO-27–M (M = Zn, Ni, and Mg), Fe–MIL-101–NH<sub>2</sub>, and IRMOF-3, all of which exhibit absorption bands in the light emission range. In addition, we anticipate that this photothermal activation can also be used to activate covalent organic frameworks (COFs).

**KEYWORDS:** metal–organic framework, photothermal effect, activation, UV–vis light, permanent porosity



### INTRODUCTION

Metal–organic frameworks (MOFs) are a class of porous crystalline materials built from the coordination of organic linkers and metal ions or clusters.<sup>1–3</sup> One of the main features of these materials is their high and tuneable porosity, which makes them good candidates for multiple applications, including gas storage and separation,<sup>4,5</sup> catalysis,<sup>6</sup> sensing,<sup>7</sup> and drug delivery,<sup>8</sup> among many others. However, a prerequisite before using MOFs in any of these applications is their activation or, in other words, the removal of all guest molecules located in their pores. These molecules can be either bound to the metal ions or residual from the synthesis solvent. The most common activation process currently entails a first step of solvent exchange, in which the solvents employed in the MOF synthesis and located in the pores are replaced by more volatile ones, followed by thermal evacuation of the solvent molecules by applying heat and/or vacuum. In other cases, in which this process damages the crystalline integrity of MOFs, milder alternative processes such as supercritical CO<sub>2</sub> drying, freeze-drying, and chemical treatment have proved useful.<sup>9</sup> However, most of these activation methods consist of multiple steps, require expensive equipment, and/or suffer from extensive use of solvents and time. Thus, although many efforts have been devoted to optimize MOF syntheses in terms of cost, safety, and environmental criteria, there is a lack of alternative one-step activation protocols that can be applied to as-synthesized MOFs.

Light-to-heat conversion (also known as the photothermal effect) has significant potential in evaporation processes because of the local nature of the heat generated, thereby minimizing heat diffusion and energy loss. This principle has already been employed in water evaporation devices by using inorganic nanoparticles,<sup>10–12</sup> polymers,<sup>13</sup> and carbon-based materials<sup>14</sup> as light-induced heaters. In MOFs, light has been exploited to trigger gas release<sup>15–18</sup> and in catalytic processes.<sup>19–21</sup> Herein, we report that this principle can be applied to activate as-synthesized MOFs in a single-step—suppressing any solvent-exchange procedure—by showing that, when irradiated with high-intensity UV–vis light, MOFs exhibiting absorption bands in the range 300–650 nm (light emission range) reach high temperatures (above 120 °C) within minutes and that this localized heat can efficiently remove the trapped and coordinated solvent molecules from the MOF structure, thereby generating activated MOFs in unprecedentedly short times at atmospheric pressure (Figure 1a). We have demonstrated this concept by activating several MOFs covering the most representative subfamilies, including HKUST-1, UiO-66, UiO-66–NH<sub>2</sub>, ZIF-8, ZIF-67, CPO-27–M (M = Zn, Ni, and Mg), Fe–MIL-101–NH<sub>2</sub>, and IRMOF-3. In all cases, the activated MOFs retain their crystallinity and show Brunauer–Emmett–Teller (BET) surface areas ( $S_{\text{BET}}$ ) com-

Received: January 11, 2018

Accepted: February 26, 2018

Published: February 26, 2018

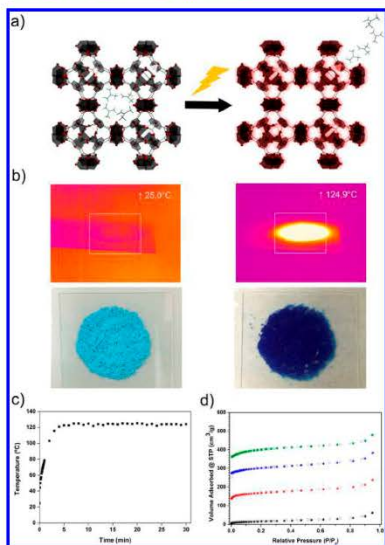


**Figure 1.** (a) Schematic representation of the photothermal activation of MOFs. (b) IR camera pictures (top) of HKUST-1 before (left) and during UV-vis irradiation (right). Photographs of HKUST-1 powder (bottom) before (left) and after (right) irradiation. (c) Temperature evolution as a function of time for HKUST-1 irradiated at a distance of 7 cm. (d)  $N_2$  adsorption isotherms for HKUST-1 after 30 min of heat treatment (red) and after photothermal activation for 5 min (blue) and 30 min (green), in comparison to the as-synthesized sample (black).

parable to the highest reported values. Moreover, a covalent organic framework (COF TAPP-BTCA) was activated using this method, suggesting that this concept could be extended to other COFs.

## EXPERIMENTAL SECTION

**Materials and Instrumentation.** Reagents and solvents were purchased from Sigma-Aldrich and Fisher Scientific, respectively, and used without further purification. Deionized (DI) water was obtained using a Milli-Q system (18.2 M $\Omega$  cm). X-ray powder diffraction (XRPD) patterns were collected using an X'Pert PRO MPDP analytical diffractometer (PANalytical) at 45 kV and 40 mA with a Cu K $\alpha$  radiation source ( $\lambda = 1.5419$  Å). Nitrogen adsorption measurements were carried out at 77 K using an Autosorb-iQ-AG analyzer (Quantachrome Instruments). Solid-state UV-vis spectra were recorded using a Cary 4000 spectrophotometer (Agilent Technologies) in the wavelength range 200–800 nm, previously preparing KBr pellets of the samples. The UV-vis high-intensity spot lamp without a filter (300–650 nm) was a bluepoint 4 ecocure (Hönle UV Technology), and the infrared camera was a PI 450 (Optris), working in a temperature range of 0–250 °C. Data were obtained using the PI Connect software.

**Synthetic Procedures. Synthesis of HKUST-1.** In a typical synthesis,<sup>22</sup> a solution of 2 g (8.5 mmol) of  $Cu(NO_3)_2 \cdot 2.5H_2O$  and 1.20 g (5.5 mmol) of 1,3,5-benzenetricarboxylic acid (BTC) in 50 mL of a mixture of dimethylformamide (DMF), ethanol, and water (1:1:1) was spray-dried in a B-290 mini-spray dryer (BÜCHI Labortechnik) at a feed rate of 4.5 mL·min<sup>-1</sup>, a flow rate of 336 mL·min<sup>-1</sup>, and an inlet temperature of 180 °C, using a spray cap with a 0.5 mm diameter hole. After 12 min, 2.13 g of blue powder was collected. This powder was washed several times with 40 mL of methanol and recovered by centrifugation. The final product was air-dried.

**Synthesis of UIO-66.** In a typical synthesis,<sup>23</sup> 0.68 g (2.9 mmol) of  $ZrCl_4$  in 15 mL of a mixture of DMF and water (5:48:1 v/v) was added to a solution of 0.48 g (2.9 mmol) of benzene-1,4-dicarboxylic acid (BDC) in 15 mL of DMF. The resulting mixture was heated at 120 °C under stirring for 2 h. The solid obtained was collected by centrifugation, washed twice with 20 mL of DMF and twice with 20 mL of absolute ethanol, and finally air-dried overnight.

**Synthesis of UIO-66-NH<sub>2</sub>.** In a typical synthesis,<sup>23</sup> 3.5 mL of 37% HCl was added to a solution of 1.17 g (5 mmol) of  $ZrCl_4$  and 0.91 g (5 mmol) of 2-aminoterephthalic acid (NH<sub>2</sub>-BDC) in 50 mL of DMF. The resulting mixture was heated at 120 °C under stirring for 2 h. The solid obtained was collected by centrifugation, washed twice with 20 mL of DMF and twice with 20 mL of absolute ethanol, and finally air-dried overnight.

**Synthesis of ZIF-8.** In a typical synthesis,<sup>24</sup> a solution of 0.30 g (1.4 mmol) of  $Zn(OAc)_2 \cdot 2H_2O$  in 5 mL of DI water was added to a solution of 1.12 g (13.6 mmol) of 2-methylimidazole (2-MIM) in 5 mL of DI water. The resulting mixture was homogenized by stirring for a few seconds, and then the mixture was left to stand at room temperature for 6 h. White crystals were recovered by centrifugation, washed three times with 20 mL of methanol, and finally air-dried.

**Synthesis of ZIF-67.** In a typical synthesis,<sup>24</sup> a solution of 0.60 g (2.4 mmol) of  $Co(OAc)_2 \cdot 4H_2O$  in 5 mL of DI water was added to a solution of 2.24 g (27.3 mmol) of 2-MIM in 5 mL of DI water. The resulting mixture was homogenized by stirring for a few seconds, and then the mixture was left to stand for 2 h at room temperature. Purple crystals were collected by centrifugation, washed three times with 20 mL of methanol, and finally air-dried.

**Synthesis of CPO-27-Zn.** In a typical synthesis,<sup>25</sup> a solution of 0.36 g (1.8 mmol) of 2,5-dihydroxyterephthalic acid (DHTA) and sodium hydroxide (0.29 g, 7.3 mmol) in 5.0 mL of DI water was added to a solution of 0.79 g (3.6 mmol) of  $Zn(OAc)_2 \cdot 2H_2O$  in 5.0 mL of DI water. The resulting yellow suspension was stirred for 60 min at room temperature. The product was collected by centrifugation, washed twice with DI water (30 mL) and twice with 30 mL of methanol, and finally air-dried overnight.

**Synthesis of CPO-27-Ni.** In a typical synthesis,<sup>25</sup> a solution of 0.09 g (0.5 mmol) of DHTA and sodium hydroxide (0.07 g, 1.8 mmol) in 10.0 mL of DI water was added to a solution of 0.22 g (0.88 mmol) of  $Ni(OAc)_2 \cdot 4H_2O$  in 10.0 mL of DI water. The resulting green solution was stirred at room temperature for 24 h. The product was collected by centrifugation, washed three times with 30 mL of DI water and three times with 30 mL of methanol, and finally air-dried overnight.

**Synthesis of CPO-27-Mg.** In a typical synthesis,<sup>25</sup> a solution of 0.18 g (0.9 mmol) of DHTA and sodium hydroxide (0.15 g, 3.8 mmol) in 5.0 mL of DI water was added to a solution of 0.48 g (2.2 mmol) of  $Mg(OAc)_2 \cdot 4H_2O$  in 5.0 mL of DI water. The resulting green suspension was stirred for 6 h at room temperature. The product was collected by centrifugation, washed three times with 30 mL of DI water and three times with 30 mL of methanol, and finally air-dried overnight.

**Synthesis of Fe-MIL-101-NH<sub>2</sub>.** The synthesis was adapted from reported procedures.<sup>26</sup> Thus, 0.68 g (2.5 mmol) of  $FeCl_3 \cdot 6H_2O$  in 7.5 mL of DMF was added to a solution of 0.225 g (1.2 mmol) of NH<sub>2</sub>-BDC in 7.5 mL of DMF, and the resulting mixture was heated at 120 °C for 24 h. The solid obtained was collected by centrifugation and then washed three times with 20 mL of DMF and twice with 20 mL of absolute ethanol. The resulting powder was air-dried overnight. To eliminate most of the free NH<sub>2</sub>-BDC, the product was dispersed in

DMF at 110 °C under stirring for 8 h and precipitated by centrifugation. This process was repeated three times.

**Synthesis of IRMOF-3.** The synthesis was adapted from reported procedures.<sup>27</sup> Thus, 1.20 g (4.0 mmol) of  $Zn(NO_3)_2 \cdot 6H_2O$  and 0.30 g (1.6 mmol) of  $NH_4-BDC$  were dissolved in 40 mL of DMF. The solution was divided into eight scintillation vials and heated at 100 °C for 24 h in an oven. Crystals were harvested from the bottom of these vials and then washed twice with 10 mL of DMF and 10 mL of chloroform. Dried crystals were kept under an argon atmosphere.

**Synthesis of COF TAPB-BTCA.** The COF TAPB-BTCA was synthesized following a previously reported method.<sup>28</sup> In a typical synthesis, 0.03 g (0.2 mmol) of 1,3,5-benzenetricarbaldehyde (BTCA) in 12.5 mL of acetone and 2.5 mL of acetic acid was added to a solution of 0.06 g (0.2 mmol) of 1,3,5-tris(4-aminophenyl)benzene (TAPB) in 12.5 mL of acetone. The resulting mixture was stirring for 1 h. The obtained yellow solid was collected by centrifugation and washed two times with 20 mL of acetone and two times with 20 mL of THF. After that, the solid was dispersed in a mixture of 1,4-dioxane and mesitylene (9:1 v/v), adding 1.75 mL of water and 2.6 mL of acetic acid under continuous stirring at room temperature. The resulting mixture was heated at 80 °C under stirring for 8 days. The obtained solid was collected by centrifugation at 9000 rpm for 4 min, washed three times with 10 mL of toluene, and finally air-dried.

**Light Guide-to-Sample Distance Effect.** It is known that the irradiance of a lamp changes depending on the proximity of the irradiated body. To assess the light intensity received per surface unit of MOF in our activation experiments, the detector of a power meter (Newport 1918-C) was systematically placed at different distances (3, 4, 5, 6, 7, 8, and 9 cm), the UV-vis lamp was turned on at 100% power, and the irradiance was measured for each distance. Figure S1 shows the irradiance ( $mW \cdot cm^{-2}$ ) as a function of inverse-squared distance ( $cm^{-2}$ ), which follows the inverse-square law ( $I \propto 1/r^2$ ).<sup>29,30</sup>

**Photothermal Effect Characterization.** One hundred milligrams of each MOF was spread on a quartz slide to form a thin round layer with the largest possible surface area (diameter of between 2 and 3.5 cm) at a distance of 7 cm from the light guide, which corresponds to an irradiance of 500  $mW \cdot cm^{-2}$ . The infrared camera was placed next to the irradiation setup focusing on the MOF sample, and video recording was started just before the UV-vis lamp was set to 100% intensity. The recorded video allowed the temperature change to be plotted against time. The blank experiment involved irradiating the quartz slide holder alone and proved that there was no change in temperature.

**UV-Vis Activation Procedure.** In a typical UV-vis activation experiment, 100 mg of each MOF was first placed in a three-neck round-bottom flask. The light guide was then introduced via the central neck and placed at a distance of 7 cm from the MOF sample. In some cases, the separation between the MOF and the light guide was reduced to 5 and 3 cm, corresponding to irradiances of 900 and 2650  $mW \cdot cm^{-2}$ , respectively. The neck was then wrapped with Parafilm. Both side necks were capped with a septum and a needle. One of these necks was used as the gas inlet attached to the argon tube, whereas the other served as the gas purge. Once the argon flow had been adjusted [8 normal liter per minute (NL $\cdot$ min $^{-1}$ )], the UV-vis lamp was turned on, irradiating the MOF sample for the desired time at 100% intensity (Figure S2). When the exposure time was finished, the light guide was removed from the flask, which was rapidly capped with a septum, kept under argon, and subsequently introduced into a glovebox, where the powder was weighed in the gas sorption cell under an argon atmosphere. The MOF sample was then transferred from the glovebox to the gas sorption equipment, where the  $N_2$  isotherm was measured for further BET surface area ( $S_{BET}$ ) calculation.

## RESULTS AND DISCUSSION

**Photothermal Activation of HKUST-1.** HKUST-1 was chosen to benchmark the UV-vis activation protocol because of its well-standardized activation process. Indeed, HKUST-1 is usually activated using several solvent-exchange steps (e.g., with dichloromethane or methanol), followed by a thermal treat-

ment (from 80 to 170 °C) under vacuum, thus resulting in  $S_{BET}$  values ranging from 1450 to 1800  $m^2 \cdot g^{-1}$  when fully activated.<sup>31,32</sup>

Our experiment started with an evaluation of the photothermal effect on a sample of as-synthesized HKUST-1 by monitoring the temperature change with irradiation time (Figure 1). It was found that HKUST-1 was immediately heated when exposed to UV-vis light, reaching a plateau at 120 °C after irradiation for 4–5 min (Figure 1b,c and Video S1). The strong photothermal effect could be rationalized by analyzing the solid-state UV-vis spectrum of HKUST-1, which showed a broad absorption band centered at 720 nm attributed to the d–d transitions of the Cu(II) in the paddle wheel,<sup>33</sup> which falls within the wavelength used in the irradiation experiments (Figures S3–S5). The contribution of this absorption band was further studied by irradiating HKUST-1 in wavelength ranges of 320–390 nm (UV) and of 390–500 nm (visible). As expected, in both cases, lower temperatures (40 and 60 °C, respectively) were reached, demonstrating that light of wavelengths close to the maximum absorption band in the visible range mainly contributes to the photothermal effect (Figure S6). It is noteworthy that the color of the HKUST-1 powder changed from sky blue to deep purple after the irradiation experiments (Figure 1b). This color change was a first clear evidence of the removal of the solvent molecules coordinated to the Cu(II) paddle wheel clusters.

To assess the efficiency of the photothermal activation, we then measured the XRPD and  $S_{BET}$  for HKUST-1 samples irradiated for 5 and 30 min without any further treatment (Figure 1d). XRPD indicated that both irradiated samples retain the crystallinity of the initial HKUST-1 MOF (Figure S7). Remarkably, HKUST-1 irradiated for only 5 min showed an  $S_{BET}$  of 1209  $m^2 \cdot g^{-1}$  (Figure S8), and increasing the irradiation time increased this value further. Indeed, after irradiation for 30 min, the  $S_{BET}$  value had increased to 1583  $m^2 \cdot g^{-1}$  (Figure S9). These results confirm that the photothermal effect in HKUST-1 is sufficiently intense to evacuate both trapped and coordinated solvent molecules from the framework. We hypothesize that the high efficiency of the photothermal activation method to evacuate solvent molecules is due to the localized heat generation, which minimizes heat loss. To further confirm this hypothesis, HKUST-1 was heated to 120 °C for 30 min but using an external heating source such as a heating mantle. In this case,  $S_{BET}$  of the thermally treated sample was significantly lower ( $S_{BET} = 655 m^2 \cdot g^{-1}$ , Figure S10), thus highlighting the benefits of UV-vis-induced localized heating on solvent removal from the HKUST-1 framework.

An important factor that can influence the photothermal activation of MOFs is the MOF-to-light guide distance. To evaluate this parameter, we studied the photothermal activation of HKUST-1 by reducing this distance to 5 and 3 cm, thus meaning that the irradiance increased to 900 and 2650  $mW \cdot cm^{-2}$ , respectively. As expected, shorter distances meant that HKUST-1 reached a higher temperature (Figure S11). When irradiated for 5 min, HKUST-1 reached a maximum of 187 °C (distance = 5 cm) and above 250 °C (distance = 3 cm). These different heating conditions were critical for HKUST-1 activation. Indeed, whereas HKUST-1 irradiated at 3 cm was found to be amorphous and nonporous, the sample irradiated at 5 cm retained its crystallinity and showed an  $S_{BET}$  of 1819  $m^2 \cdot g^{-1}$  (Figures S12 and S13). This result is remarkable because it demonstrates that HKUST-1 can be activated in only 5 min and that the MOF-to-light guide distance is a parameter

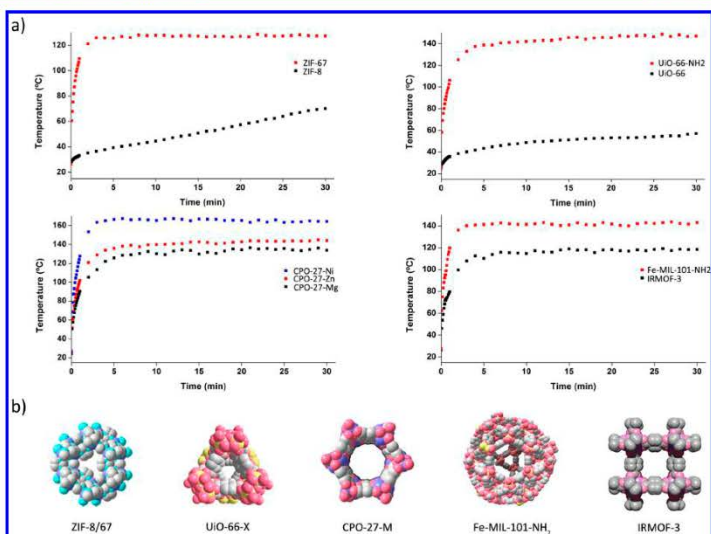


**Figure 2.** (a) Temperature evolution as a function of time for all studied MOFs when irradiated at a distance of 7 cm. (b) Representation of the crystalline structure of the studied MOFs.

that can be tuned to optimize the photothermal activation of MOFs (vide infra).

#### Versatility of the Photothermal Activation Method.

To demonstrate the scope of this activation method beyond HKUST-1, we used it to study the activation of a series of MOFs representing the major subfamilies of porous MOFs. The MOFs studied comprised UiO-66, UiO-66-NH<sub>2</sub>, ZIF-8, ZIF-67, CPO-27-M (where M is Zn(II), Ni(II), and Mg(II)), Fe-MIL-101-NH<sub>2</sub>, and IRMOF-3. Figure 2 shows the photothermal response of each of these MOFs as a function of time. Two different behaviors can be seen from this figure. Thus, MOFs that do not exhibit an absorption band in the range 300–650 nm (light emission range; Figures S17 and S27) showed a mild temperature increase after irradiation for 30 min. For example, UiO-66 and ZIF-8 were heated to 57 and 70 °C, respectively. In contrast, MOFs that show absorption bands in this range exhibited a much higher photothermal effect (Figures S18, S28, S36, S41, and S48). The temperatures reached for each of these MOFs irradiated for 30 min were as follows: IRMOF-3 (119 °C), ZIF-67 (127 °C), CPO-27-Mg (136 °C), Fe-MIL-101-NH<sub>2</sub> (143 °C), CPO-27-Zn (145 °C), UiO-66-NH<sub>2</sub> (149 °C), and CPO-27-Ni (167 °C). Moreover, as in HKUST-1, each of these latter MOFs reached their maximum temperature after irradiation for only 4–5 min.

Once the photothermal effect of the selected MOFs had been assessed, we studied their activation using the UV–vis light source. The photothermal activations of UiO-66 and UiO-66-NH<sub>2</sub> were initially compared because of the differences in their photothermal behaviors but similarities in their structures.

In addition, it is known that the activation of UiO-66 analogues is quite challenging because of the presence of DMF molecules in the pores, which cannot be completely removed unless a long solvent-exchange process is carried out. Accordingly, both MOFs were irradiated for 30 min, with no further treatment, and their XRPD patterns and  $S_{\text{BET}}$  were subsequently measured. Again, XRPD indicated that both irradiated samples retained the crystallinity of the initial UiO-66-type MOFs (Figures S19 and S20). However, the N<sub>2</sub> adsorption isotherms showed a clear difference in their activation (Figure 3a). Thus, whereas the irradiated UiO-66-NH<sub>2</sub> showed an  $S_{\text{BET}}$  of 1098 m<sup>2</sup>·g<sup>-1</sup> (close to the highest reported value,<sup>34,35</sup> Figure S22), the irradiated UiO-66 showed a much lower  $S_{\text{BET}}$  of 424 m<sup>2</sup>·g<sup>-1</sup>, in accordance with its weaker photothermal effect (Figures 2 and S21). This difference was further studied by first digesting the as-synthesized and irradiated UiO-66 and UiO-66-NH<sub>2</sub> samples and then analyzing the resulting solutions by <sup>1</sup>H NMR spectroscopy (Figures 3b,c, S23, and S24). We then calculated the percentage of DMF molecules removed from both frameworks during the activation process by comparison of the integration of one peak at 7.90 ppm corresponding to DMF and those at 8.02 and 7.78 ppm corresponding to BDC and NH<sub>2</sub>-BDC, respectively. From these data, it was clear that photothermal activation was more efficient at evacuating the DMF molecules from the UiO-66-NH<sub>2</sub> framework (94% of the initial DMF molecules were evacuated) than from the UiO-66 framework (only 55% were evacuated). This fact correlates well with the higher temperature and photothermal transduction efficiency ( $\eta$ ) reached by UiO-66-NH<sub>2</sub> (149 °C and

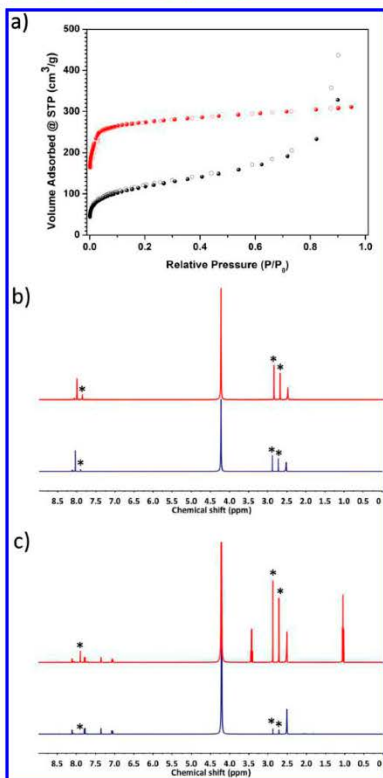


**Figure 3.** (a)  $N_2$  adsorption isotherms for UiO-66 (black) and UiO-66-NH<sub>2</sub> (red) after photothermal activation. (b)  $^1H$  NMR spectra of as-synthesized UiO-66 (red) and after photothermal activation (blue). (c)  $^1H$  NMR spectra of as-synthesized UiO-66-NH<sub>2</sub> (red) and after photothermal activation (blue). DMF peaks are highlighted with an asterisk (\*).

59.3%) in comparison to those reached by UiO-66 (57 °C and 5.0%) when irradiated for 30 min (Table 1 and section S10).

A similar but less pronounced trend was also found when both ZIF-8 and ZIF-67 were irradiated.  $S_{BET}$  for the irradiated ZIF-8 was 1130  $m^2 \cdot g^{-1}$  (calculated from the second step of the isotherm between 0.01 and 0.2  $P/P_0$ ; Figure S31), which is lower than typical reported values ( $S_{BET} \approx 1400$ – $1500 m^2 \cdot g^{-1}$ ).<sup>36,37</sup> In contrast, the photothermally activated ZIF-67 exhibited an  $S_{BET}$  of 1666  $m^2 \cdot g^{-1}$  (calculated from the second step of the isotherm between 0.01 and 0.2  $P/P_0$ ; Figure S32), which is comparable to the highest reported values.<sup>38</sup> In this

case, however, ZIF-8 showed a significant degree of activation despite its mild photothermal effect (Figure 2). We attribute this effect to the efficiency of the localized heat together with the lack of open metal sites in the structure and the nonhigh-boiling point solvents used in the synthesis (water) and washing (methanol) steps, which significantly reduces the energy required to remove occluded solvent molecules (Figures S33 and S34).

The efficient photothermal activation was further proven for Fe-MIL-101-NH<sub>2</sub> and IRMOF-3 (Figures S35–S44). In both cases, the irradiated MOFs exhibited good  $S_{BET}$  values of 1506 and 2556  $m^2 \cdot g^{-1}$ , respectively.<sup>39,40</sup> It is important to highlight here that IRMOF-3 has been reported to require supercritical CO<sub>2</sub> activation to achieve an optimum  $S_{BET}$  value (2850  $m^2 \cdot g^{-1}$ ).<sup>40</sup> Therefore, our activation method seems to respect less robust MOFs, most likely because of the localized and homogeneous heating produced and the lack of high vacuum conditions.

In accordance with this observation, we also tested our activation method with some CPO-27 analogues as activation of this MOF family is quite difficult because of the presence of open metal sites that strongly coordinate with water molecules.<sup>25</sup> Activation of these MOFs generally entails a long solvent-exchange process (from 6 to 12 days) with methanol followed by high-temperature thermal treatments (above 180 °C) under vacuum. Consequently, three members of this MOF family were activated by UV–vis light irradiation for 30 min. In all cases, irradiated CPO-27–Zn/CPO-27–Ni/CPO-27–Mg retained their initial crystallinity (Figures S49–S51) and showed a change in color, which was a first indication of the removal of solvent molecules coordinated to the respective metal centers (Figures S45–S47). In fact, the successful photothermal activation of CPO-27–Zn and CPO-27–Ni was accomplished with only 30 min of UV–vis irradiation, as demonstrated by the measured  $S_{BET}$  values of 932  $m^2 \cdot g^{-1}$  for CPO-27–Zn and 922  $m^2 \cdot g^{-1}$  for CPO-27–Ni (Figures 4a, S52, and S53).<sup>25</sup>

However, these activation conditions were not found to be optimum to efficiently activate CPO-27–Mg ( $S_{BET} = 416 m^2 \cdot g^{-1}$ , Figure S54). In this case, photothermal activation was optimized by reducing the MOF-to-light guide distance down to 5 cm (irradiance = 900  $mW \cdot cm^{-2}$ ) and 3 cm (irradiance = 2650  $mW \cdot cm^{-2}$ ; Figure S1). Under these new conditions, CPO-27–Mg reached temperatures of 184 and 250 °C, respectively, when irradiated for 30 min. In both cases, XRPD showed that the crystallinity was maintained (Figure S55). In addition, the measured  $S_{BET}$  values confirmed a better activation process, with values of 1062 and 1630  $m^2 \cdot g^{-1}$  (the latter being comparable to the highest reported values; Figure 4b)<sup>25</sup> when exposed to light powers of 900 and 2650  $mW \cdot cm^{-2}$ , respectively.

Finally, we opened up the possibility of using this photothermal activation method in covalent organic frameworks (COFs). To this end, a two-dimensional COF (COF TAPB–BTCA) assembled from two trigonal building blocks, BTCA and TAPB (Figure S61), was irradiated at a distance of 7 cm (irradiance = 500  $mW \cdot cm^{-2}$ ) for 30 min, obtaining an  $S_{BET}$  value of 1185  $m^2 \cdot g^{-1}$ , which is comparable to that reported in the literature (Figure S66).<sup>28</sup> Similar to the MOFs, this COF also reached a temperature of 136 °C after irradiation for 4–5 min.

Table 1. Summary of the Main Parameters of the Photothermally Activated Materials

material	photothermal temperature (°C)	$\eta$ (%) <sup>a</sup>	$S_{\text{BET}}$ ( $\text{m}^2\text{g}^{-1}$ )		residual solvent (%) <sup>b</sup>
			this work	reported	
HKUST-1	125	33.6	1583	1740 <sup>11</sup>	5.1 <sup>c</sup>
UiO-66	57	5.0	424	1580 <sup>15</sup>	11.2 <sup>b</sup>
UiO-66-NH <sub>2</sub>	149	59.3	1098	1200 <sup>15</sup>	3.4 <sup>b</sup>
ZIF-8	60	0.3	1130	1079 <sup>16</sup>	c
ZIF-67	127	50.0	1666	1319 <sup>18</sup>	c
CPO-27-Zn	145	23.8	932	1154 <sup>15</sup>	1.7 <sup>d</sup>
CPO-27-Ni	167	93.6	922	1351 <sup>15</sup>	0.4 <sup>d</sup>
CPO-27-Mg	136	21.6	1630	1603 <sup>15</sup>	2.0 <sup>d</sup>
Fe-MIL-101-NH <sub>2</sub>	143	86.6	1506	2436 <sup>19</sup>	1.8 <sup>d</sup>
IRMOF-3	119	25.8	2556	2850 <sup>10</sup>	3.0 <sup>d</sup>
COF-TAPB-BTCA	136	55.4	1185	1120 <sup>18</sup>	3.0 <sup>d</sup>

<sup>a</sup>Calculated as explained in the Supporting Information. <sup>b</sup>Calculated from the residual <sup>d</sup>DMF and EtOH, <sup>e</sup>DMF, <sup>f</sup>MeOH, and <sup>g</sup>acetone. <sup>c</sup>Note that H<sub>2</sub>O could not be determined by NMR.

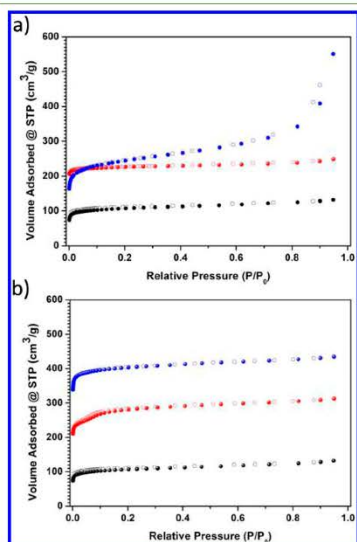


Figure 4. (a) N<sub>2</sub> adsorption isotherms of CPO-27-Mg (black), CPO-27-Zn (red), and CPO-27-Ni (blue) after irradiated at 500 mW·cm<sup>-2</sup>. (b) N<sub>2</sub> adsorption isotherms of CPO-27-Mg after irradiated at 500 (black), 900 (red), and 2650 mW·cm<sup>-2</sup> (blue).

## CONCLUSIONS

In summary, we have reported that a UV-vis lamp can be used to activate as-synthesized MOFs in a single step. MOFs with absorptions in the UV-vis wavelength range emitted by this lamp undergo a significant heating (120–220 °C) in 4–5 min. This localized light-to-heat conversion in the MOF crystals when irradiated enables a very fast solvent removal, thereby significantly reducing the activation time down to 30 min and

suppressing the need for time-consuming solvent-exchange procedures and vacuum conditions. We have found that the  $S_{\text{BET}}$  values obtained after photothermal activation for only 30 min are comparable to the highest reported values for conventionally activated HKUST-1, ZIF-67, UiO-66-NH<sub>2</sub>, Fe-MIL-101-NH<sub>2</sub>, IRMOF-3, and CPO-27-M (M = Ni, Zn, and Mg). Moreover, we have demonstrated that this activation method could be extended to COFs. Our findings should facilitate the integration of an activation step in processes in which MOFs/COFs are manufactured in a continuous way as well as the use of this photothermal effect in applications in which the triggered desorption of volatile species (e.g., water) is desired.

## ASSOCIATED CONTENT

### Supporting Information

The Supporting Information is available free of charge on the ACS Publications website at DOI: 10.1021/acsami.8b00557.

Lamp irradiance calibration, setup description, photographs and infrared camera pictures before and after irradiation, solid-state UV-vis spectra, XRPD patterns, N<sub>2</sub> adsorption isotherms, photothermal plots, NMR spectra, and photothermal transduction efficiency calculations (PDF)

Infrared camera video showing the temperature change against time (AVI)

## AUTHOR INFORMATION

### Corresponding Authors

<sup>✉</sup>E-mail: inhar.imaz@icn2.cat (I.I.).

<sup>✉</sup>E-mail: daniel.maspoeh@icn2.cat (D.M.).

### ORCID

Luis Garzón-Tovar: 0000-0003-0253-4041

Inhar Imaz: 0000-0002-0278-1141

Daniel Maspoeh: 0000-0003-1325-9161

### Author Contributions

The manuscript was written through contributions of all authors. All authors have given approval to the final version of the manuscript.

### Notes

The authors declare no competing financial interest.

### ■ ACKNOWLEDGMENTS

This work was supported by the Spanish MINECO (projects PN MAT2015-65354-C2-1-R), the Catalan AGAUR (project 2014 SGR 80), the ERC under the EU FP7 (ERC-Co 615954), and European Union's Horizon 2020 research and innovation programme under grant agreement no. 685727. It was also funded by the CERCA Programme/Generalitat de Catalunya. ICN2 acknowledges the support of the Spanish MINECO through the Severo Ochoa Centers of Excellence Program, under grant SEV-2013-0295. J.E. acknowledges the MINECO for the FPI fellowship.

### ■ ABBREVIATIONS

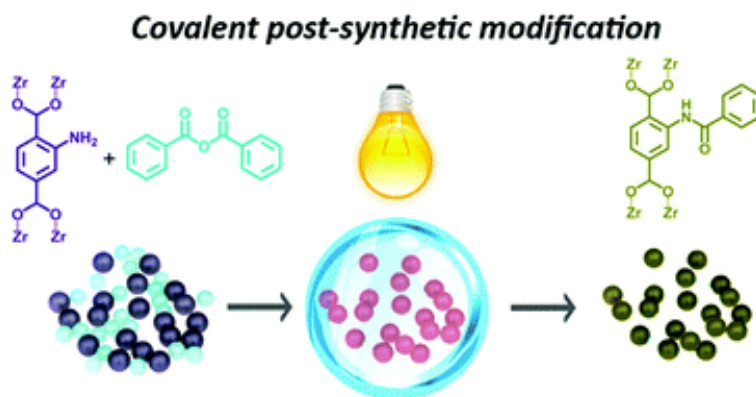
XRPD, X-ray powder diffraction; UV-vis, ultraviolet-visible; DI, deionized; MOF, metal-organic framework; COF, covalent organic framework; DMF, dimethylformamide; NMR, nuclear magnetic resonance; PTE, photothermal transduction efficiency

### ■ REFERENCES

- (1) Furukawa, H.; Ko, N.; Go, Y. B.; Aratani, N.; Choi, S. B.; Choi, E.; Yazaydin, A. Ö.; Snurr, R. Q.; O'Keeffe, M.; Kim, J.; Yaghi, O. M. Ultrahigh Porosity in Metal-Organic Frameworks. *Science* **2010**, *329*, 424–428.
- (2) Kitagawa, S.; Kitaura, R.; Noro, S.-I. Functional Porous Coordination Polymers. *Angew. Chem., Int. Ed.* **2004**, *43*, 2334–2375.
- (3) Zhou, H.-C.; Long, J. R.; Yaghi, O. M. Introduction to Metal-Organic Frameworks. *Chem. Rev.* **2012**, *112*, 673–674.
- (4) Murray, L. J.; Dinca, M.; Long, J. R. Hydrogen Storage in Metal-Organic Frameworks. *Chem. Soc. Rev.* **2009**, *38*, 1294–1314.
- (5) Makal, T. A.; Li, J.-R.; Lu, W.; Zhou, H.-C. Methane Storage in Advanced Porous Materials. *Chem. Soc. Rev.* **2012**, *41*, 7761–7779.
- (6) (a) Lee, J.; Farha, O. K.; Roberts, J.; Scheidt, K. A.; Nguyen, S. T.; Hupp, J. T. Metal-Organic Framework Materials as Catalysts. *Chem. Soc. Rev.* **2009**, *38*, 1450–1459. (b) Jiao, L.; Wang, Y.; Jiang, H.-L.; Xu, Q. Metal-Organic Frameworks as Platforms for Catalytic Applications. *Adv. Mater.* **2017**, *1703663*. (c) Yang, Q.; Xu, Q.; Jiang, H.-L. Metal-organic frameworks meet metal nanoparticles: synergistic effect for enhanced catalysis. *Chem. Soc. Rev.* **2017**, *46*, 4774–4808.
- (7) Kreno, L. E.; Leong, K.; Farha, O. K.; Allendorf, M.; Van Duyne, R. P.; Hupp, J. T. Metal-Organic Framework Materials as Chemical Sensors. *Chem. Rev.* **2012**, *112*, 1105–1125.
- (8) Horcajada, P.; Gref, R.; Baati, T.; Allan, P. K.; Maurin, G.; Couvreur, P.; Férey, G.; Morris, R. E.; Serre, C. Metal-Organic Frameworks in Biomedicine. *Chem. Rev.* **2012**, *112*, 1232–1268.
- (9) Mondloch, J. E.; Karagiaridi, O.; Farha, O. K.; Hupp, J. T. Activation of Metal-Organic Framework Materials. *CrystEngComm* **2013**, *15*, 9258–9264.
- (10) Neumann, O.; Urban, A. S.; Day, J.; Lal, S.; Nordlander, P.; Halas, N. J. Solar Vapor Generation Enabled by Nanoparticles. *ACS Nano* **2013**, *7*, 42–49.
- (11) Wang, Z.; Liu, Y.; Tao, P.; Shen, Q.; Yi, N.; Zhang, F.; Liu, Q.; Song, C.; Zhang, D.; Shang, W.; Deng, T. Bio-Inspired Evaporation Through Plasmonic Film of Nanoparticles at the Air–Water Interface. *Small* **2014**, *10*, 3234–3239.
- (12) Liu, Y.; Yu, S.; Feng, R.; Bernard, A.; Liu, Y.; Zhang, Y.; Duan, H.; Shang, W.; Tao, P.; Song, C.; Deng, T. A Bioinspired, Reusable, Paper-Based System for High-Performance Large-Scale Evaporation. *Adv. Mater.* **2015**, *27*, 2768–2774.
- (13) Zhang, L.; Tang, B.; Wu, J.; Li, R.; Wang, P. Hydrophobic Light-to-Heat Conversion Membranes with Self-Healing Ability for Interfacial Solar Heating. *Adv. Mater.* **2015**, *27*, 4889–4894.
- (14) Ghasemi, H.; Ni, G.; Marconnet, A. M.; Loomis, J.; Yerci, S.; Miljkovic, N.; Chen, G. Solar Steam Generation by Heat Localization. *Nat. Commun.* **2014**, *5*, 4449.
- (15) Li, H.; Hill, M. R.; Doblin, C.; Lim, S.; Hill, A. J.; Falcaro, P. Visible Light Triggered CO<sub>2</sub> Liberation from Silver Nanocrystals Incorporated Metal–Organic Frameworks. *Adv. Funct. Mater.* **2016**, *26*, 4815–4821.
- (16) Li, H.; Hill, M. R. Low-Energy CO<sub>2</sub> Release from Metal–Organic Frameworks Triggered by External Stimuli. *Acc. Chem. Res.* **2017**, *50*, 778–786.
- (17) Khaletskaia, K.; Reboul, J.; Methiklov, M.; Nakahama, M.; Diring, S.; Tsujimoto, M.; Isoda, S.; Kim, F.; Kamei, K.-I.; Fischer, R. A.; Kitagawa, S.; Furukawa, S. Integration of Porous Coordination Polymers and Gold Nanorods into Core–Shell Mesoscopic Composites toward Light-Induced Molecular Release. *J. Am. Chem. Soc.* **2013**, *135*, 10998–11005.
- (18) Diring, S.; Carné-Sánchez, A.; Zhang, J.; Ikemura, S.; Kim, C.; Inaba, H.; Kitagawa, S.; Furukawa, S. Light Responsive Metal-Organic Frameworks as Controllable CO-Releasing Cell Culture Substrates. *Chem. Sci.* **2017**, *8*, 2381–2386.
- (19) Yang, Q.; Xu, Q.; Yu, S.-H.; Jiang, H.-L. Pd Nanocubes@ZIF-8: Integration of Plasmon-Driven Photothermal Conversion with a Metal–Organic Framework for Efficient and Selective Catalysis. *Angew. Chem., Int. Ed.* **2016**, *55*, 3685–3689.
- (20) Wang, F.; Huang, Y.; Chai, Z.; Zeng, M.; Li, Q.; Wang, Y.; Xu, D. Photothermal-enhanced Catalysis in Core-shell Plasmonic Hierarchical Cu<sub>2</sub>S Microsphere@Zeolitic Imidazole Framework-8. *Chem. Sci.* **2016**, *7*, 6887–6893.
- (21) Chen, Y.-Z.; Wang, Z. U.; Wang, H.; Lu, J.; Yu, S.-H.; Jiang, H.-L. Singlet Oxygen-Engaged Selective Photo-Oxidation over Pt Nanocrystals/Porphyrinic MOF: The Roles of Photothermal Effect and Pt Electronic State. *J. Am. Chem. Soc.* **2017**, *139*, 2035–2044.
- (22) Carné-Sánchez, A.; Imaz, I.; Cano-Sarabia, M.; Maspocho, D. A Spray-Drying Strategy for Synthesis of Nanoscale Metal–Organic Frameworks and their Assembly into Hollow Superstructures. *Nat. Chem.* **2013**, *5*, 203–211.
- (23) Ragon, F.; Horcajada, P.; Chevreau, H.; Hwang, Y. K.; Lee, U.-H.; Müller, S. R.; Devic, T.; Chang, J.-S.; Serre, C. In Situ Energy-Dispersive X-ray Diffraction for the Synthesis Optimization and Scale-up of the Porous Zirconium Terephthalate UiO-66. *Inorg. Chem.* **2014**, *53*, 2491–2500.
- (24) Avci, C.; Ariñez-Soriano, J.; Carné-Sánchez, A.; Guillerm, V.; Carbonell, C.; Imaz, I.; Maspocho, D. Post-Synthetic Anisotropic Wet-Chemical Etching of Colloidal Sodalite ZIF Crystals. *Angew. Chem., Int. Ed.* **2015**, *54*, 14417–14421.
- (25) Garzón-Tovar, L.; Carné-Sánchez, A.; Carbonell, C.; Imaz, I.; Maspocho, D. Optimised Room Temperature, Water-Based Synthesis of CPO-27-M Metal-Organic Frameworks with High Space-Time Yields. *J. Mater. Chem. A* **2015**, *3*, 20819–20826.
- (26) Bauer, S.; Serre, C.; Devic, T.; Horcajada, P.; Marrot, J.; Férey, G.; Stock, N. High-Throughput Assisted Rationalization of the Formation of Metal Organic Frameworks in the Iron(III) Amino-terephthalate Solvothermal System. *Inorg. Chem.* **2008**, *47*, 7568–7576.
- (27) Tanabe, K. K.; Wang, Z.; Cohen, S. M. Systematic Functionalization of a Metal–Organic Framework via a Postsynthetic Modification Approach. *J. Am. Chem. Soc.* **2008**, *130*, 8508–8517.
- (28) Rodríguez-San-Miguel, D.; Yazdi, A.; Guillerm, V.; Pérez-Carvajal, J.; Puentes, V.; Maspocho, D.; Zamora, F. Confining Functional Nanoparticles into Colloidal Imine-Based COF Spheres by a Sequential Encapsulation–Crystallization Method. *Chem.—Eur. J.* **2017**, *23*, 8623–8627.
- (29) Born, M.; Wolf, E. *Principles of Optics: Electromagnetic Theory of Propagation, Interference and Diffraction of Light*; Cambridge University Press: Cambridge, 1999.
- (30) McCluney, W. R. *Introduction to Radiometry and Photometry*, 2nd ed.; Artech House Publishers: Boston/London, 2014.
- (31) Kim, H. K.; Yun, W. S.; Kim, M.-B.; Kim, J. Y.; Bae, Y.-S.; Lee, J.; Jeong, N. C. A Chemical Route to Activation of Open Metal Sites in the Copper-Based Metal–Organic Framework Materials HKUST-1 and Cu-MOF-2. *J. Am. Chem. Soc.* **2015**, *137*, 10009–10015.
- (32) Song, X.; Jeong, S.; Kim, D.; Lah, M. S. Transmetalations in Two Metal-Organic Frameworks with Different Framework Flex-

- ibilities: Kinetics and Core-Shell Heterostructure. *CrystallineComm* **2012**, *14*, 5753–5756.
- (33) Prestipino, C.; Regli, L.; Vitillo, J. G.; Bonino, F.; Damin, A.; Lamberti, C.; Zecchina, A.; Solari, P. L.; Kongshaug, K. O.; Bordiga, S. Local Structure of Framework Cu(II) in HKUST-1 Metallorganic Framework: Spectroscopic Characterization upon Activation and Interaction with Adsorbates. *Chem. Mater.* **2006**, *18*, 1337–1346.
- (34) Hu, Z.; Zhao, D. De facto Methodologies Toward the Synthesis and Scale-up Production of UiO-66-Type Metal-Organic Frameworks and Membrane Materials. *Dalton Trans.* **2015**, *44*, 19018–19040.
- (35) Katz, M. J.; Brown, Z. J.; Colón, Y. J.; Siu, P. W.; Scheidt, K. A.; Snurr, R. Q.; Hupp, J. T.; Farha, O. K. A Facile Synthesis of UiO-66, UiO-67 and their Derivatives. *Chem. Commun.* **2013**, *49*, 9449–9451.
- (36) Pan, Y.; Liu, Y.; Zeng, G.; Zhao, L.; Lai, Z. Rapid Synthesis of Zeolitic Imidazolate Framework-8 (ZIF-8) Nanocrystals in an Aqueous System. *Chem. Commun.* **2011**, *47*, 2071–2073.
- (37) Lee, Y.-R.; Jang, M.-S.; Cho, H.-Y.; Kwon, H.-J.; Kim, S.; Ahn, W.-S. ZIF-8: A Comparison of Synthesis Methods. *Chem. Eng. J.* **2015**, *271*, 276–280.
- (38) Shi, Q.; Chen, Z.; Song, Z.; Li, J.; Dong, J. Synthesis of ZIF-8 and ZIF-67 by Steam-Assisted Conversion and an Investigation of Their Tribological Behaviors. *Angew. Chem., Int. Ed.* **2011**, *50*, 672–675.
- (39) Savonnet, M.; Kockrick, E.; Camarata, A.; Bazer-Bachi, D.; Bats, N.; Lecocq, V.; Pintel, C.; Furrusseng, D. Combinatorial Synthesis of Metal-Organic Frameworks Libraries by Click-Chemistry. *New J. Chem.* **2011**, *35*, 1892–1897.
- (40) Nelson, A. P.; Farha, O. K.; Mulfort, K. L.; Hupp, J. T. Supercritical Processing as a Route to High Internal Surface Areas and Permanent Microporosity in Metal–Organic Framework Materials. *J. Am. Chem. Soc.* **2009**, *131*, 458–460.

## The photothermal effect in MOFs: covalent post-synthetic modification of MOFs mediated by UV-Vis light under solvent-free conditions





Cite this: *Chem. Commun.*, 2018, 54, 4184Received 26th February 2018,  
Accepted 29th March 2018

DOI: 10.1039/c8cc01593g

rsc.li/chemcomm

## The photothermal effect in MOFs: covalent post-synthetic modification of MOFs mediated by UV-Vis light under solvent-free conditions†

Jordi Espín,<sup>a,‡</sup> Lluís Garzón-Tovar,<sup>b,‡</sup> Gerard Boix,<sup>b,‡</sup> Inhar Imaz<sup>b,\*</sup> and Daniel Maspocho<sup>b,\*</sup>

**Here, we report the covalent post-synthetic modification (CPSM) of MOFs using the photothermal effect. Specifically, we subjected mixtures of a photothermally active MOF and another reagent to irradiation with a UV-Vis lamp. This caused the MOF to heat up, which in turn caused the other reagent to melt and subsequently react with the functional groups on the walls of the MOF pores. We have exploited this dual function of MOFs as both heater and host for CPSMs to achieve rapid formation of amides from the reaction of representative MOFs (UiO-66-NH<sub>2</sub> or MIL-101-NH<sub>2</sub>-Al) with anhydrides under solvent-free conditions. In addition, this approach enables more complex CPSMs in MOFs such as the formation of amides in UiO-66-NH<sub>2</sub> by using an aldehyde through a cascade reaction.**

Photo-irradiation of certain materials causes them to heat up. This is known as the photothermal effect. Ideally, one could exploit this conversion of light into heat to selectively increase the local temperature of a given material and its surroundings, while minimizing heat diffusion and energy loss. Photothermal materials have been harnessed for myriad applications such as cancer theranostics<sup>1–7</sup> and in water evaporation,<sup>8–10</sup> sterilisation<sup>11</sup> or desalination<sup>12,13</sup> devices. Such materials include organometallic complexes,<sup>14</sup> polymers,<sup>1,2,15</sup> carbon-based materials,<sup>6,12,16</sup> noble-metal and hybrid nanoparticles,<sup>9–11,13,17</sup> and semiconductors.<sup>5–7,18</sup>

Recently, we found that some porous metal–organic frameworks (MOFs) can exhibit a pronounced photothermal effect. After UV-Vis irradiation (300–650 nm), MOFs exhibiting absorption bands in this range can reach temperatures exceeding 120 °C within minutes. For example, 100 mg and 25 mg of the archetypical MOF UiO-66-NH<sub>2</sub> reaches a temperature of 140 °C and 78 °C, respectively, after only 5 minutes of irradiation (500 mW cm<sup>−2</sup>) at a light guide-to-sample distance of 7 cm (Fig. S1, ESI†).

We demonstrated that this localised heat can be used to efficiently remove trapped and coordinated solvent molecules from within the MOF structure to generate activated MOFs at atmospheric pressure in unprecedented short times.<sup>19</sup>

Covalent post-synthetic modifications (CPSMs) are employed to derivatise MOFs with diverse functional groups, which enables tailoring of physicochemical properties (e.g. wettability<sup>20,21</sup>) and of functions (e.g. catalysis<sup>22,23</sup> and gas sorption).<sup>24</sup> These modifications are generally done by reacting MOF crystals with other reagents in solution for long periods of time (from hours to days).<sup>25</sup> However, alternative methods have recently been proposed to reduce the solvent volume and/or the reaction time. For example, our group has shown that Schiff-base condensation reactions between aldehydes and amines inside MOFs can be performed in mere seconds, by using spray-drying.<sup>26</sup> The first reported solvent-free method for the post-synthetic modification of MOFs was vapour diffusion. Thus, Ranocchiari, Bokhoven *et al.* described the CPSM of solid amino-tagged MOFs by exposing them to vapours produced by heating liquid aldehydes or anhydrides at 120 °C under vacuum for 16 h.<sup>27</sup> More recently, Wuttke *et al.* reported a second solvent-free CPSM strategy based on the direct heating of a solid mixture of an amino-terminated MOF and a carboxylic acid derivative [acid anhydride, acid chloride or carboxylic acid] at ca. 100 °C for minutes.<sup>28</sup> Similarly, Richardson *et al.* demonstrated that a Newman–Kwart rearrangement on a dimethylthiocarbamate-functionalized IRMOF-9 occurs by direct heating it at 285 °C.<sup>29</sup>

In the study reported here, we extended our previous work on localised photothermal activation of MOFs to perform CPSMs of MOFs under solvent-free conditions. We show that MOFs, once mixed with another reagent and irradiated by a UV-Vis lamp, can simultaneously act as both heater and host for CPSMs. The MOF crystals reach high temperatures, thereby heating their surroundings and melting the other reagent, which then reacts with the functional groups of the MOF. As a final step of this process, the mixture is washed with a solvent to remove the unreacted chemical reagent, and the post-modified MOF is collected by centrifugation and dried. Three conditions must

<sup>a</sup> Catalan Institute of Nanoscience and Nanotechnology (IC2N), CSIC and The Barcelona Institute of Science and Technology, Campus UAB, Bellaterra, 08193 Barcelona, Spain. E-mail: daniel.maspocho@icn2.cat

<sup>b</sup> ICREA, Pg. Lluís Companys 23, 08010 Barcelona, Spain

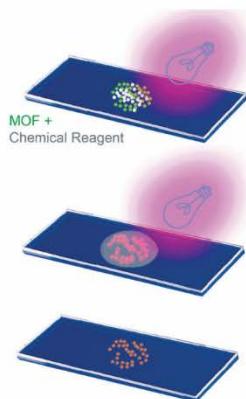
† Electronic supplementary information (ESI) available. See DOI: 10.1039/c8cc01593g

‡ Both authors contributed equally.

be met in this CPSM approach. Firstly, the MOF must have functional groups available for reaction. Secondly, the MOF must be photothermally active. And finally, the chemical reagent must melt at a temperature below that of the previously heated MOF.

To demonstrate the feasibility of this solvent-free, photo-induced CPSM method, we chose UiO-66-NH<sub>2</sub> as a representative MOF, as it is strongly photothermal (*vide supra*) and contains free amino groups available for derivatization. As a model reaction, we reacted this MOF with anhydrides to form amides. Thus, UiO-66-NH<sub>2</sub> was synthesised and activated under previously reported conditions, and obtained as a pure phase as confirmed by X-ray powder diffraction (XRPD) and N<sub>2</sub> adsorption measurements ( $S_{\text{BET}}$  value: 936 m<sup>2</sup> g<sup>-1</sup>; Fig. S2 and S3, ESI†).<sup>30</sup> Once synthesised, the activated UiO-66-NH<sub>2</sub> (25 mg) was mixed with maleic anhydride (MA) (melting point: 51–56 °C) at molar ratios (2-aminoterephthalate/MA) of 1:1, 1:3 and 1:6. Each solid mixture was placed between two quartz slides (Scheme 1). A light guide was fixed at a distance of 7 cm from the sample. Each pair of slides was then irradiated (irradiance: 500 mW cm<sup>-2</sup>) for 30 min, causing the MOF to reach a temperature of 78–82 °C (Fig. S4 and S5, ESI†). To ensure homogeneous light exposure, each slide pair was turned around after 15 minutes. Note that, as a control experiment, a solid sample of MA alone was irradiated for 30 minutes; it did not exhibit any temperature increase. Finally, the resulting irradiated mixtures were washed with DMF and acetone and dried at room temperature. The different samples were named as (UiO-66-MA)<sub>x</sub>, where x corresponds to the number of equivalents of anhydride.

Using XRPD, we confirmed that all three samples retained the crystallinity of the starting UiO-66-NH<sub>2</sub> (Fig. 1b and Fig. S6, ESI†).



**Scheme 1** Illustration of the photo-mediated CPSM of MOFs. Once irradiated with a UV-Vis lamp (top), a photothermally active MOF, previously mixed with another reagent, will heat up, causing the other reagent to melt (middle). This in turn drives the reaction of the reagent with the functional groups on the pore walls of the MOF (below).

To determine the degree of post-synthetic conversion, the digested powders (5% HF/DMSO-*d*<sub>6</sub>) were analysed by <sup>1</sup>H-NMR spectroscopy. The conversion rates were then calculated by comparing the integration of the peak corresponding to unmodified 2-aminoterephthalic acid (7.34 ppm) to that of the peak corresponding to the alkenyl hydrogens of the newly formed amide moiety (6.58 ppm). The conversion rates were 69.9% ± 0.4% for (UiO-66-MA)<sub>1</sub>, 85.1% ± 1.0% for (UiO-66-MA)<sub>3</sub> and 83.4% ± 0.3% for (UiO-66-MA)<sub>6</sub> (Fig. 1a and Fig. S7, ESI†). These values indicated that increasing the number of equivalents of MA from three to six did not provide a significant increase in product.

Having determined the optimal molar ratio of NH<sub>2</sub>-bdc/MA to be 1:3, we then decided to study the effects of using a stronger irradiation intensity or a longer reaction time on a mixture of photo-activated UiO-66-NH<sub>2</sub> and MA. To assess the intensity, we used 900 mW cm<sup>-2</sup> (instead of 500 mW cm<sup>-2</sup>, as above), which we attained by setting the distance between the light-guide and the sample to 5 cm (instead of 7 cm, as above). To study the reaction time, we irradiated the mixture for 60 min (instead of 30 min, as above). As confirmed by XRPD, neither of these more aggressive conditions altered the structure of the parent UiO-66-NH<sub>2</sub> (Fig. S8 and S9, ESI†). In these reactions, the post-synthetic conversions were 78.5% ± 1.5% for the reaction done at a distance of 5 cm and 83.2% ± 4.9% for the reaction irradiation at 60 min (Fig. S10, ESI†). These values were similar (or even lower) to those obtained under the original (milder) conditions. Thus, for optimal reaction conditions, we chose a NH<sub>2</sub>-bdc/MA molar ratio of 1:3; a light guide-to-sample distance of 7 cm (500 mW cm<sup>-2</sup>); and an irradiation time of 30 min.

We found further evidence of amide formation by electrospray-ionisation mass spectrometry (ESI-MS) of the digested (UiO-66-MA)<sub>3</sub>, which showed a peak at *m/z* = 278.0 that matched the molecular

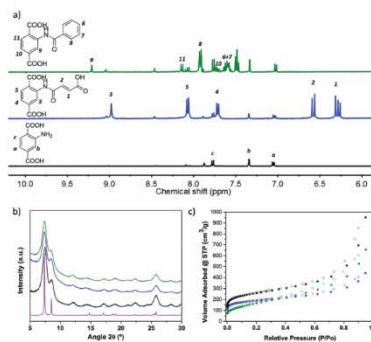


**Fig. 1** (a) <sup>1</sup>H NMR spectra of the digested (UiO-66-MA)<sub>3</sub> (blue), (UiO-66-BA)<sub>3</sub> (green) and UiO-66-NH<sub>2</sub> (black) in HF/DMSO-*d*<sub>6</sub>. (b) XRPD patterns for simulated UiO-66-NH<sub>2</sub> (purple), activated UiO-66-NH<sub>2</sub> (black), (UiO-66-MA)<sub>3</sub> (blue) and (UiO-66-BA)<sub>3</sub> (green). (c) N<sub>2</sub> sorption isotherms for UiO-66-NH<sub>2</sub> (black), (UiO-66-MA)<sub>3</sub> (blue) and (UiO-66-BA)<sub>3</sub> (green).

formula of the desired amide product  $[C_{12}H_9NO_7]^-$  ( $m/z = 278.0$ ) (Fig. S11, ESI†). Finally, the  $N_2$  sorption isotherm of (UiO-66-MA)<sub>3</sub> measured at 77 K showed an  $S_{BET}$  value of  $699 \text{ m}^2 \text{ g}^{-1}$ , confirming that the product MOF had a smaller surface area than the starting MOF, as expected for formation of amide groups, which are sterically bulkier than amino groups (Fig. 1c).<sup>31</sup>

We then applied our optimised conditions to the reaction of UiO-66-NH<sub>2</sub> with benzoic anhydride (BA) (melting point: 38–42 °C). Thus, a solid mixture of UiO-66-NH<sub>2</sub> (25 mg) and BA (NH<sub>2</sub>-bdc:BA molar ratio of 1:3) was irradiated at 500 mW cm<sup>-2</sup> for 30 min, reaching a temperature of 78–82 °C (Fig. S12 and S13, ESI†). The resulting (UiO-66-BA)<sub>3</sub> was first analysed by XRPD, which confirmed that it had retained the crystallinity of the parent MOF (Fig. 1b). As above, the formation of the expected amide group was corroborated by ESI-MS, in which the peak at  $m/z = 284.1$  matched the molecular formula of the product  $[C_{15}H_{10}NO_5]^-$  ( $m/z = 284.1$ ) (Fig. S14, ESI†). Also, as above, the formation of these amide groups led to a smaller surface area in the final MOF ( $S_{BET} = 621 \text{ m}^2 \text{ g}^{-1}$ ) (Fig. 1c).<sup>28</sup> In this case, comparing the integration of the <sup>1</sup>H-NMR peaks corresponding to unmodified 2-aminoterephthalic acid (7.34 ppm) and each amide moiety (8.14 ppm) revealed a conversion rate of  $48.6\% \pm 1.0\%$  (Fig. 1a). We attributed this lower conversion (relative to that for the reaction with MA) to the bulky phenyl substituents of BA, which may have slowed down diffusion of the reagent into the MOF pore channels.

To demonstrate the versatility of our CPSM method, we chose to study a second amino-tagged MOF: MIL-101-NH<sub>2</sub>(Al). This MOF is also photothermally active: when irradiated for 30 min at 265 mW cm<sup>-2</sup> (light guide-to-sample distance of 9 cm), it reaches a temperature of 61 °C; and when irradiated at 500 mW cm<sup>-2</sup>, reaches 72 °C (Fig. S15, ESI†). Thus, MIL-101-NH<sub>2</sub>(Al) was first synthesised under solvothermal conditions, which afforded it as a pure phase, as confirmed by XRPD and  $N_2$  sorption measurements ( $S_{BET} = 2702 \text{ m}^2 \text{ g}^{-1}$ ) (Fig. S16 and S17, ESI†).<sup>28</sup> Then, this MOF (25 mg) was reacted with either MA, under the optimised conditions for UiO-66-NH<sub>2</sub> (Fig. S18 and 19, ESI†), or BA, using the lower irradiance intensity of 265 mW cm<sup>-2</sup> (Fig. S22 and S23, ESI†). A lower intensity was used for the BA reaction because in initial tests, the value of 500 mW cm<sup>-2</sup> led to a decrease in the crystallinity of MIL-101-NH<sub>2</sub>(Al) due to a post-synthetic ligand exchange ( $62.9 \pm 1.8\%$ ) between the NH<sub>2</sub>-bdc ligands and benzoic acid molecules formed during the amide formation (Fig. S24 and S25, ESI†). The resulting (MIL-101-Al)-MA)<sub>3</sub> and (MIL-101-Al)-BA)<sub>3</sub> were analysed by XRPD and ESI-MS, which also confirmed that they each retained the crystallinity of the parent MOF (Fig. 2b) and exhibited the expected amide formation (Fig. S21 and S27, ESI†). The conversion rates were  $79.1\% \pm 1.4\%$  for (MIL-101-Al)-MA)<sub>3</sub> and  $44\% \pm 2.5\%$  for (MIL-101-Al)-BA)<sub>3</sub> (Fig. S20 and S26, ESI†). These results were consistent with the gradual decrease in surface area in each case, as indicated by the corresponding  $S_{BET}$  values (determined by the  $N_2$ -sorption isotherms at 77 K):  $549 \text{ m}^2 \text{ g}^{-1}$  for (MIL-101-Al)-MA)<sub>3</sub> and  $774 \text{ m}^2 \text{ g}^{-1}$  for (MIL-101-Al)-BA)<sub>3</sub> (Fig. 2b, Table 1).

The possibility to perform CPSMs under UV-Vis light allows one to incorporate photochemical reactions in these processes and therefore, provide researchers with novel reactions from

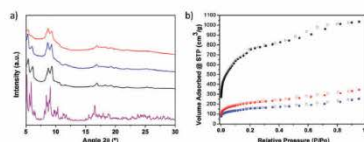


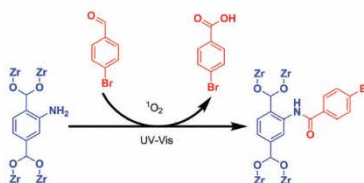
Fig. 2 (a) XRPD patterns for simulated MIL-101-NH<sub>2</sub>(Al) (purple), activated MIL-101-NH<sub>2</sub>(Al) (black), (MIL-101-(Al)-MA)<sub>3</sub> (blue) and (MIL-101-(Al)-BA)<sub>3</sub> (red). (b)  $N_2$  sorption isotherms of MIL-101-NH<sub>2</sub>(Al) (black), (MIL-101-(Al)-MA)<sub>3</sub> (blue) and (MIL-101-(Al)-BA)<sub>3</sub> (red).

Table 1 BET areas, pore volumes and conversion rates (%) for the synthesised and modified MOFs

MOF	$S_{BET}$ ( $\text{m}^2 \text{ g}^{-1}$ )	Pore vol. <sup>a</sup> ( $\text{cm}^3 \text{ g}^{-1}$ )	Conversion <sup>b</sup> (%)
UiO-66-NH <sub>2</sub>	936	0.4726	—
(UiO-66-MA) <sub>3</sub>	699	0.3375	85.1
(UiO-66-BA) <sub>3</sub>	621	0.3452	48.6
MIL-101-NH <sub>2</sub> (Al)	2702	1.277	—
(MIL-101-(Al)-MA) <sub>3</sub>	549	0.2662	79.1
(MIL-101-(Al)-BA) <sub>3</sub>	774	0.3742	44.0

<sup>a</sup> Calculated at  $P/P_0 \approx 0.4$ . <sup>b</sup> Calculated from <sup>1</sup>H-NMR spectra of the digested samples.

which to introduce functionalities to MOFs. For example, our CPSM approach provides a simple route towards creating an amide (rather than the expected imine) starting from an aldehyde (in this case, 4-bromobenzaldehyde (BrBA)) through a cascade reaction (Scheme 2). This reaction first involves the generation of a singlet oxygen by UV-Vis light that reacts with BrBA to produce 4-bromobenzoic acid (Fig. S28 and S29, ESI†).<sup>32</sup> Then, this carboxylic acid reacts with the amino groups of the MOF to produce the amide. CPSM through this cascade reaction was done by irradiating a solid mixture of UiO-66-NH<sub>2</sub> (25 mg) and BrBA (NH<sub>2</sub>-bdc:BrBA molar ratio of 1:6) at 500 mW cm<sup>-2</sup> for 30 min. The resulting (UiO-66-BrBA)<sub>6</sub> was first analysed by XRPD, which confirmed that it had retained the crystallinity of the parent MOF (Fig. S30, ESI†). Formation of the amide group was evidenced by ESI-MS, from which the peak at  $m/z = 362.0$  matched with the molecular formula of the amide product  $[C_{15}H_{10}BrNO_5]^-$  ( $m/z = 362.0$ ) (Fig. S31, ESI†). The conversion rate of this photo-induced cascade reaction was  $54.7\% \pm 3.4\%$  (Fig. S32, ESI†).



Scheme 2 Schematic representation of the CPSM reaction of UiO-66-NH<sub>2</sub> and BrBA forming an amide through a photoinduced cascade reaction.

In summary, we have shown that the photothermal effect in MOFs can be exploited for their CPSM in the solid state. Use of MOFs as photo-activated heaters should be amenable to performing other functions, such as triggering the release of species adsorbed in MOFs; confining reactions to the inside of MOF pores or to the crystal surfaces of MOFs; and increasing the efficiency of MOF catalysts.

This work was supported by the EU FP7 ERC-Co 615954, the Spanish MINECO (project PN MAT2015-65354-C2-1-R), and the Catalan AGAUR (project 2014 SGR 80). It was also funded by the CERCA Programme/Generalitat de Catalunya. ICN2 acknowledges the support of the Spanish MINECO through the Severo Ochoa Centers of Excellence Programme under Grant SEV-2013-0295. J. E. acknowledges the MINECO for the FPI fellowship.

## Conflicts of interest

There are no conflicts to declare.

## Notes and references

- 1 K. Yang, H. Xu, L. Cheng, C. Sun, J. Wang and Z. Liu, *Adv. Mater.*, 2012, **24**, 5586–5592.
- 2 L. Xu, L. Cheng, C. Wang, R. Peng and Z. Liu, *Polym. Chem.*, 2014, **5**, 1573–1580.
- 3 S. Li, X. Wang, R. Hu, H. Chen, M. Li, J. Wang, Y. Wang, L. Liu, F. Lv, X.-J. Liang and S. Wang, *Chem. Mater.*, 2016, **28**, 8669–8675.
- 4 C. Loo, A. Lowery, N. Halas, J. West and R. Drezek, *Nano Lett.*, 2005, **5**, 709–711.
- 5 X. Huang, W. Zhang, G. Guan, G. Song, R. Zou and J. Hu, *Acc. Chem. Res.*, 2017, **50**, 2529–2538.
- 6 C. M. Hessel, V. P. Pattani, M. Rasch, M. G. Panthani, B. Koo, J. W. Tunnell and B. A. Korgel, *Nano Lett.*, 2011, **11**, 2560–2566.
- 7 Q. Tian, F. Jiang, R. Zou, Q. Liu, Z. Chen, M. Zhu, S. Yang, J. Wang, J. Wang and J. Hu, *ACS Nano*, 2011, **5**, 9761–9771.
- 8 H. Ghasemi, G. Ni, A. M. Marconnet, J. Loomis, S. Yerci, N. Miljkovic and G. Chen, *Nat. Commun.*, 2014, **5**, 4449.
- 9 O. Neumann, A. S. Urban, J. Day, S. Lal, P. Nordlander and N. J. Halas, *ACS Nano*, 2013, **7**, 42–49.
- 10 Y. Liu, S. Yu, R. Feng, A. Bernard, Y. Liu, Y. Zhang, H. Duan, W. Shang, P. Tao, C. Song and T. Deng, *Adv. Mater.*, 2015, **27**, 2768–2774.
- 11 O. Neumann, C. Feronti, A. D. Neumann, A. Dong, K. Schell, B. Lu, E. Kim, M. Quinn, S. Thompson, N. Grady, P. Nordlander, M. Oden and N. J. Halas, *PNAS*, 2013, **110**, 11677–11681.
- 12 X. Li, W. Xu, M. Tang, L. Zhou, B. Zhu, S. Zhu and J. Zhu, *PNAS*, 2016, **113**, 13953–13958.
- 13 L. Zhou, Y. Tan, J. Wang, W. Xu, Y. Yuan, W. Cai, S. Zhu and J. Zhu, *Nat. Photonics*, 2016, **10**, 393.
- 14 X. He, X. He, S. Li, K. Zhuo, W. Qin, S. Dong, J. Chen, L. Ren, G. Liu and H. Xia, *Polym. Chem.*, 2017, **8**, 3674–3678.
- 15 I. H. El-Sayed, X. Huang and M. A. El-Sayed, *Cancer Lett.*, 2006, **239**, 129–135.
- 16 Y. Zeng, J. Yao, B. A. Horri, K. Wang, Y. Wu, D. Li and H. Wang, *Energy Environ. Sci.*, 2011, **4**, 4074–4078.
- 17 Z. Wang, Y. Liu, P. Tao, Q. Shen, N. Yi, F. Zhang, Q. Liu, C. Song, D. Zhang, W. Shang and T. Deng, *Small*, 2014, **10**, 3234–3239.
- 18 X. Bu, D. Zhou, J. Li, X. Zhang, K. Zhang, H. Zhang and B. Yang, *Langmuir*, 2014, **30**, 1416–1423.
- 19 J. Espin, L. Garzón-Tovar, A. Carné-Sánchez, I. Imaz and D. Maspoch, *ACS Appl. Mater. Interfaces*, 2018, **10**, 9555–9562.
- 20 H. N. Rubin and M. M. Reynolds, *Inorg. Chem.*, 2017, **56**, 5266–5274.
- 21 C. Liu, Q. Liu and A. Huang, *Chem. Commun.*, 2016, **52**, 3400–3402.
- 22 J. Wang, M. Yang, W. Dong, Z. Jin, J. Tang, S. Fan, Y. Lu and G. Wang, *Catal. Sci. Technol.*, 2016, **6**, 161–168.
- 23 C. J. Doonan, W. Morris, H. Furukawa and O. M. Yaghi, *J. Am. Chem. Soc.*, 2009, **131**, 9492–9493.
- 24 J. A. Thompson, N. A. Brunelli, R. P. Lively, J. R. Johnson, C. W. Jones and S. Nair, *J. Phys. Chem. C*, 2013, **117**, 8198–8207.
- 25 S. M. Cohen, *Chem. Rev.*, 2012, **112**, 970–1000.
- 26 L. Garzón-Tovar, S. Rodríguez-Hermida, I. Imaz and D. Maspoch, *J. Am. Chem. Soc.*, 2017, **139**, 897–903.
- 27 M. Servalli, M. Ranocchiarri and J. A. Van Bokhoven, *Chem. Commun.*, 2012, **48**, 1904–1906.
- 28 H. Hintz and S. Wuttke, *Chem. Mater.*, 2014, **26**, 6722–6728.
- 29 T. A. Ablott, M. Turzer, S. G. Telfer and C. Richardson, *Cryst. Growth Des.*, 2016, **16**, 7067–7073.
- 30 F. Ragon, P. Horcajada, H. Chevreau, Y. K. Hwang, U. H. Lee, S. R. Miller, T. Devic, J.-S. Chang and C. Serre, *Inorg. Chem.*, 2014, **53**, 2491–2500.
- 31 S. J. Garibay and S. M. Cohen, *Chem. Commun.*, 2010, **46**, 7700–7702.
- 32 N. Iqbal, S. Choi, Y. You and E. J. Cho, *Tetrahedron Lett.*, 2013, **54**, 6222–6225.

## List of Patents

The patent applications related to this PhD Thesis are listed below:

1. MasPOCH, D., Imaz, I. and Garzón-Tovar, L. "Method for the preparation of metal organic frameworks". Application Form No: EP16382120.0. Priority Date: 18-03-2016. **This patent was licensed to a private company (MOFapps) in 2016.**
2. MasPOCH, D., Imaz, I., Garzón-Tovar, L. and Rodríguez-Hermida, S. "A process for the post-synthetic modification of metal organic frameworks". Application Form No: EP16382601.9. Priority Date: 15-12-2016



# Annex 2

---



## Spectroscopic characterization of the materials synthesized in chapter 6

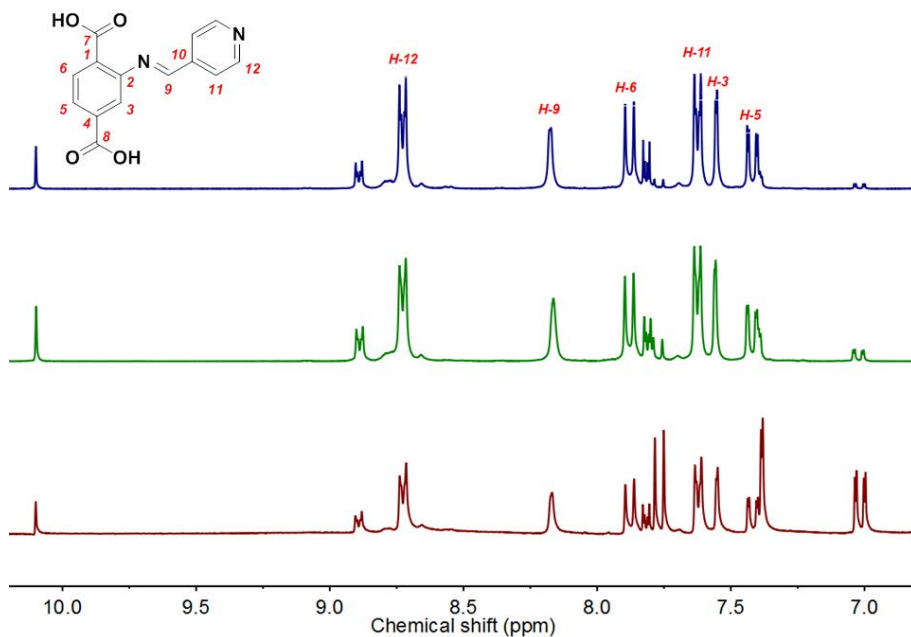


**Figure 1.**  $^1\text{H}$  NMR spectrum of 2-((pyridin-4-ylmethylene)amino)terephthalic acid synthesized using  $\text{NH}_2\text{-bdc}$ :4PC molar ratios of 1:1 (red), 1:2 (green) and 1:3 (blue) in  $\text{DMSO-d}_6$ .

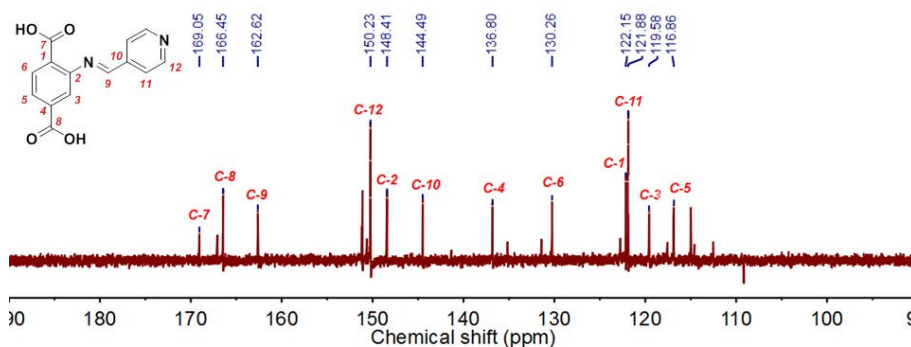


**Figure 2.**  $^{13}\text{C}$  NMR spectrum of 2-((pyridin-4-ylmethylene)amino)terephthalic acid in  $\text{DMSO-d}_6$ .

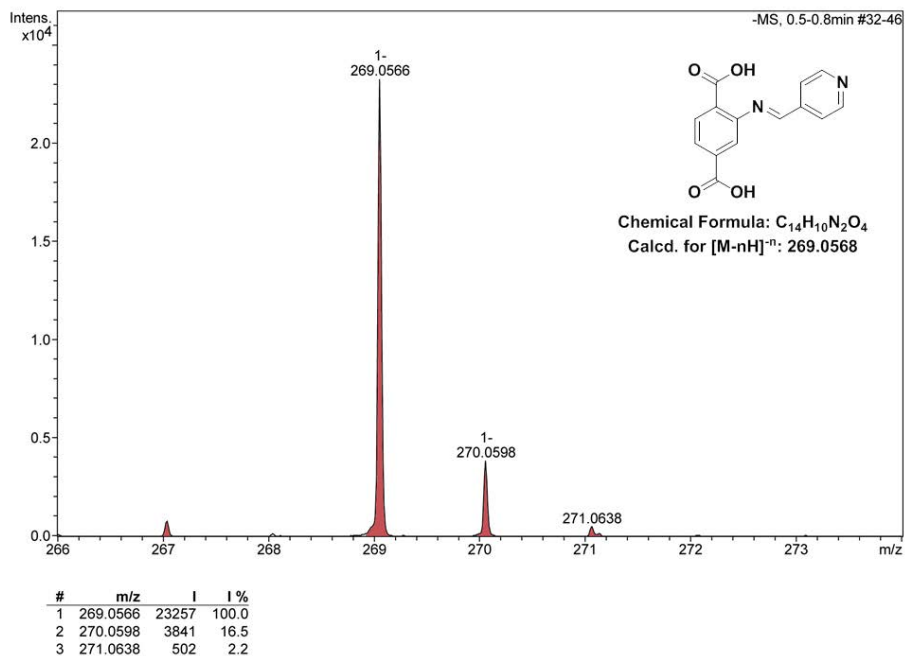


Figure 3. ESI-MS spectrum of 2-((pyridin-4-ylmethylene)amino)terephthalic acid.

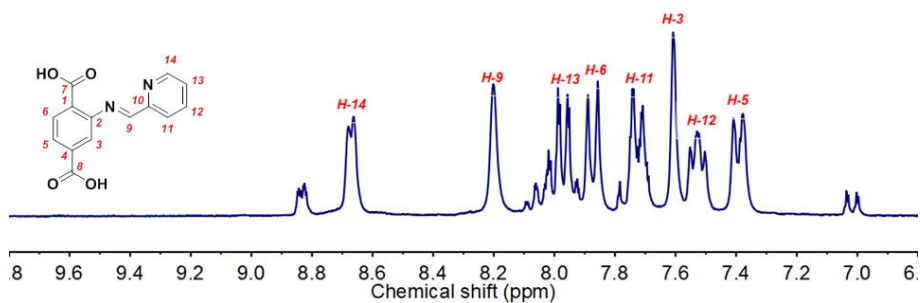


Figure 4. <sup>1</sup>H NMR spectrum of 2-((pyridin-2-ylmethylene)amino)terephthalic acid synthesized using NH<sub>2</sub>-*bdc*:2PC molar ratio of 1:3 in DMSO-*d*<sub>6</sub>.

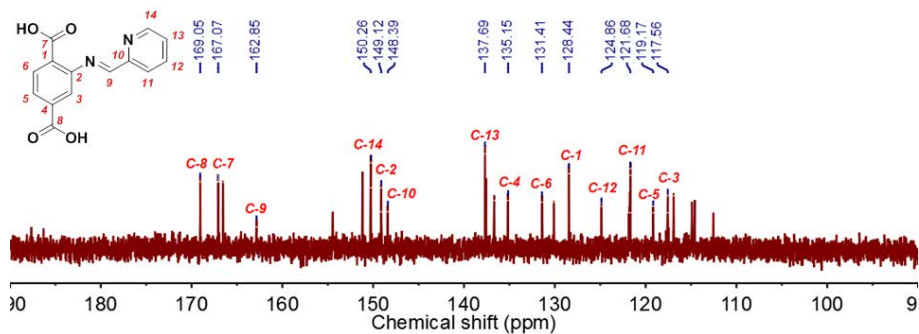


Figure 5.  $^{13}\text{C}$  NMR spectrum of 2-((pyridin-2-ylmethylene)amino)terephthalic acid in  $\text{DMSO-}d_6$ .

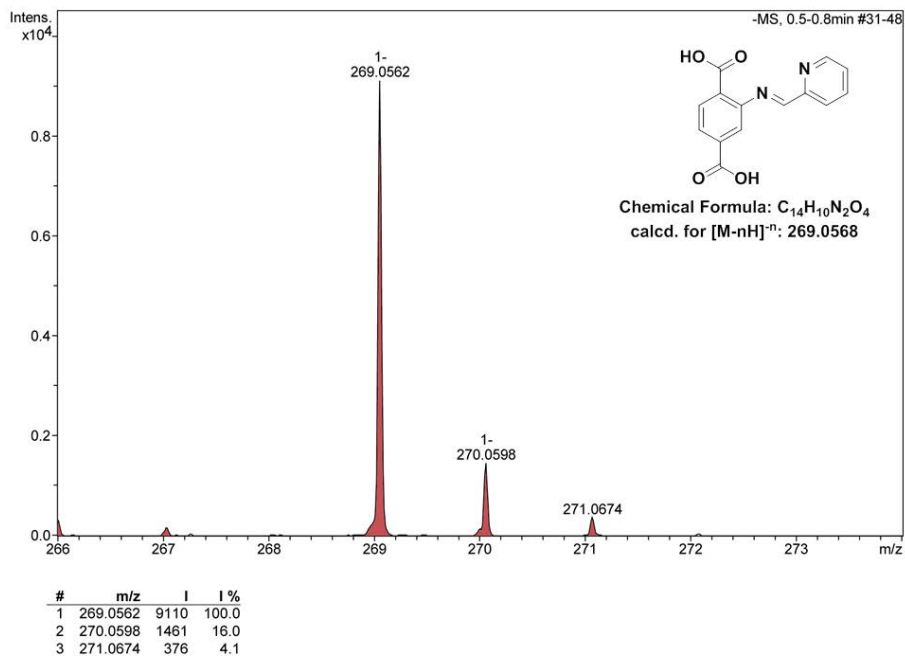
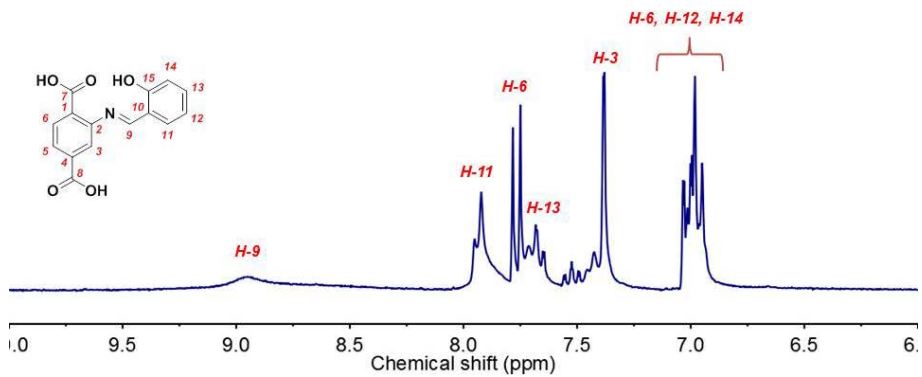
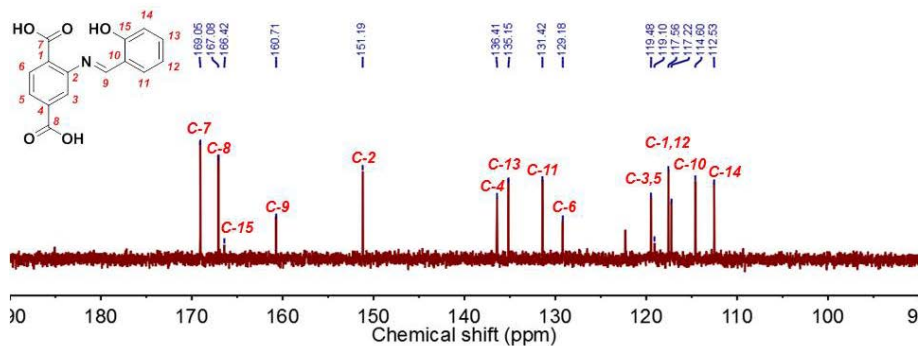


Figure 6. ESI-MS spectrum of 2-((pyridin-2-ylmethylene)amino)terephthalic acid.



**Figure 7.**  $^1\text{H}$  NMR spectrum of 2-((2-hydroxybenzylidene)amino)terephthalic acid synthesized using  $\text{NH}_2\text{-}bdc$ :Sal molar ratio of 1:3 in  $\text{DMSO-}d_6$ .



**Figure 8.**  $^{13}\text{C}$  NMR spectrum of 2-((2-hydroxybenzylidene)amino)terephthalic acid in  $\text{DMSO-}d_6$ .

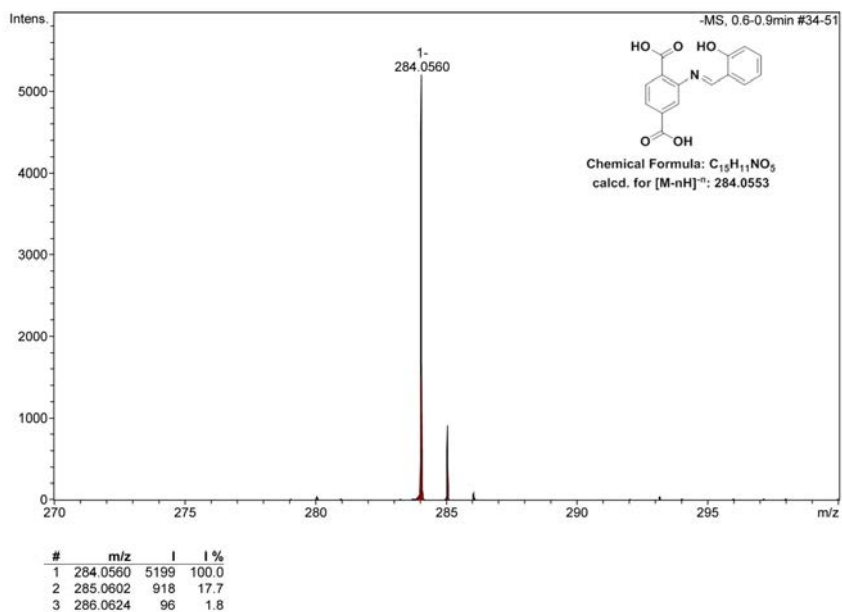


Figure 9. ESI-MS spectrum of 2-((2-hydroxybenzylidene)amino)terephthalic acid.

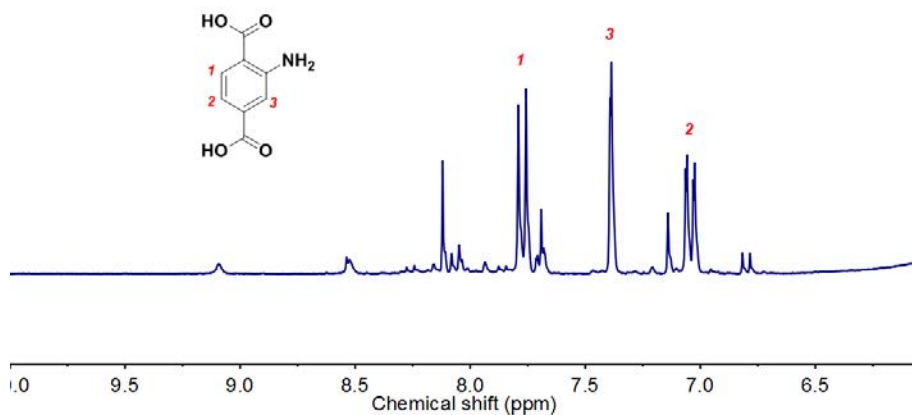


Figure 10.  $^1H$  NMR spectrum of the digested UiO-66-NH<sub>2</sub> in HF/DMSO-*d*<sub>6</sub>.

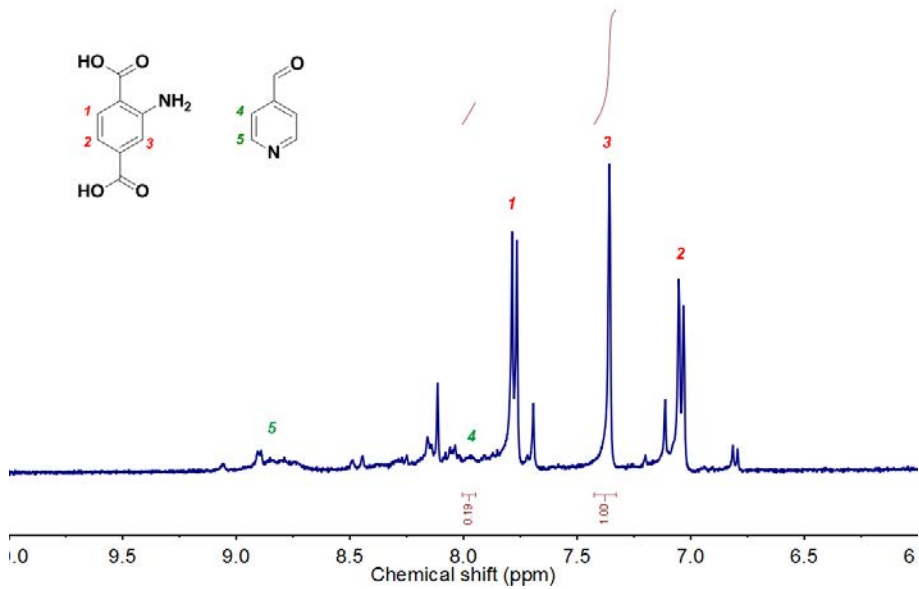


Figure 11.  $^1\text{H}$  NMR spectrum of the digested (UiO-66-4PC)<sub>3</sub> in HF/DMSO- $d_6$ .

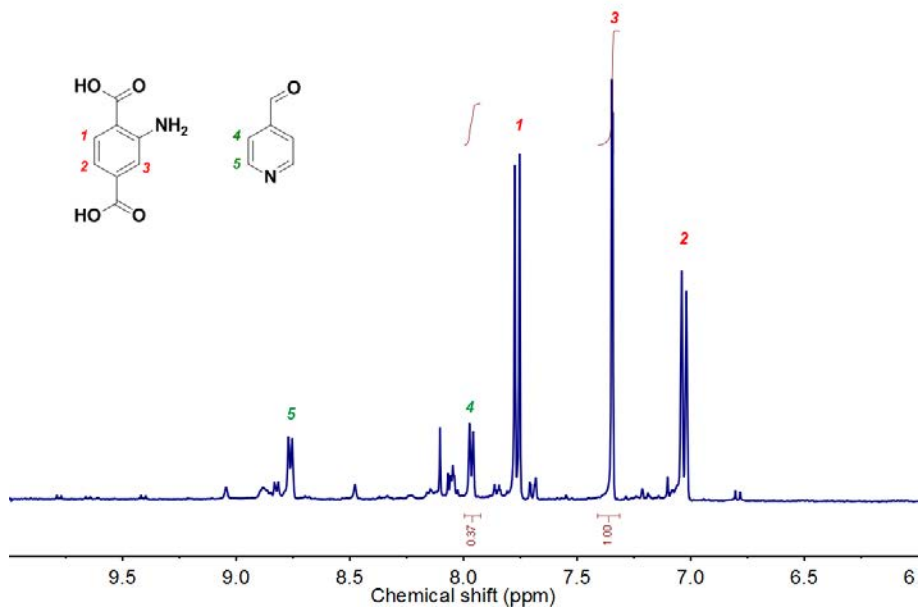


Figure 12.  $^1\text{H}$  NMR spectrum of the digested (UiO-66-4PC)<sub>5</sub> in HF/DMSO- $d_6$ .

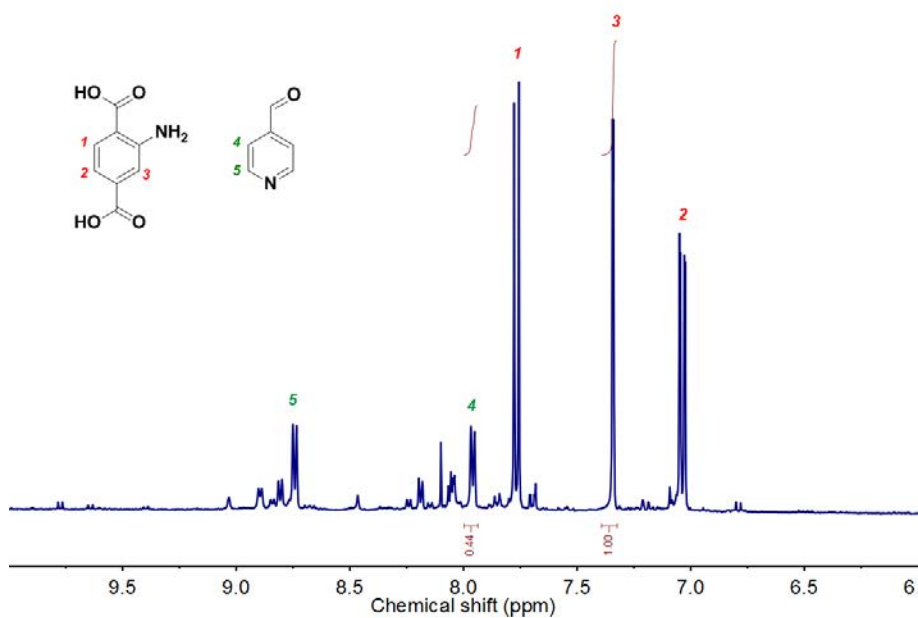


Figure 13.  $^1\text{H}$  NMR spectrum of the digested (UiO-66-4PC)<sub>10</sub> in HF/DMSO-*d*<sub>6</sub>.

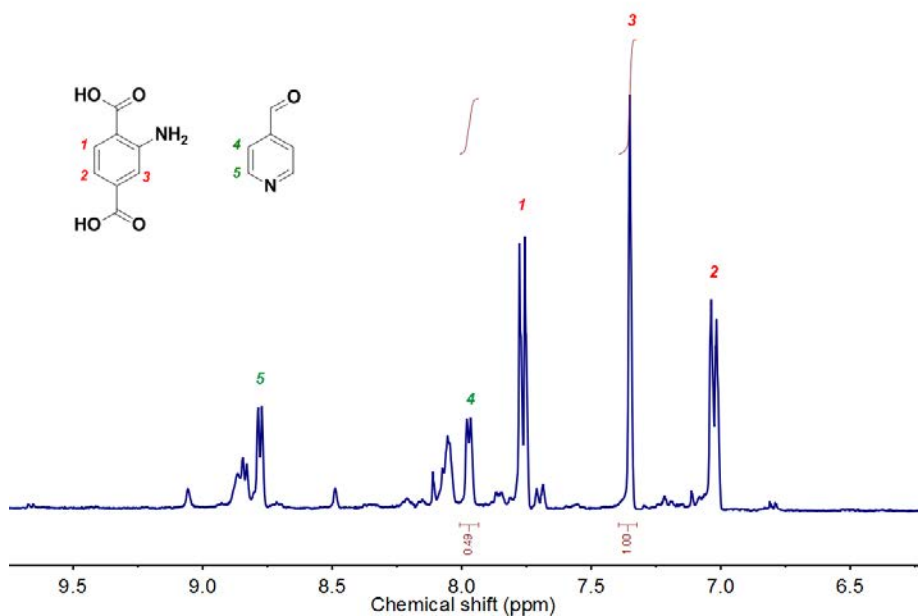


Figure 14.  $^1\text{H}$  NMR spectrum of the digested (UiO-66-4PC)<sub>15</sub> in HF/DMSO-*d*<sub>6</sub>.

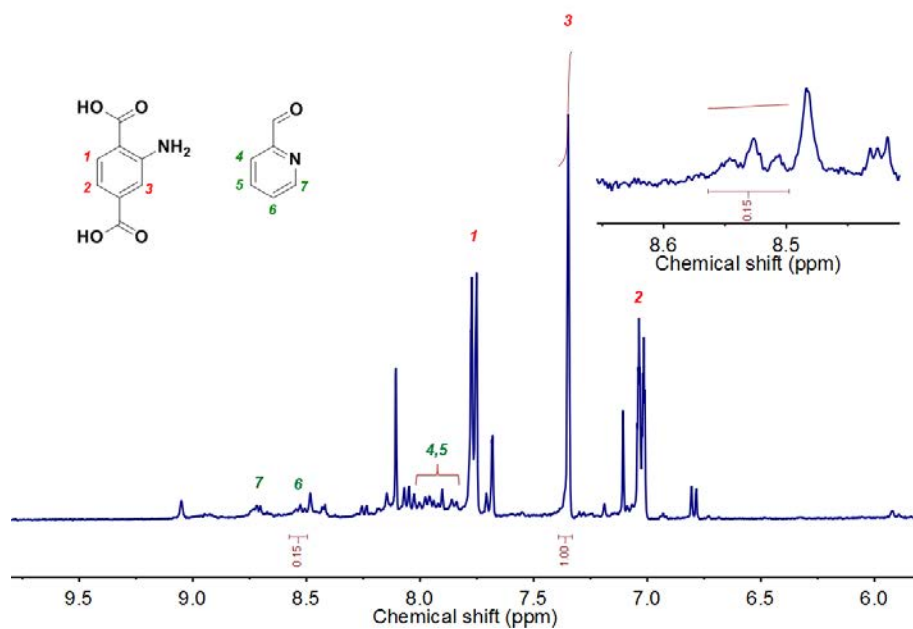


Figure 15.  $^1\text{H}$  NMR spectrum of the digested  $(\text{UiO-66-2PC})_3$  in  $\text{HF/DMSO-}d_6$ .

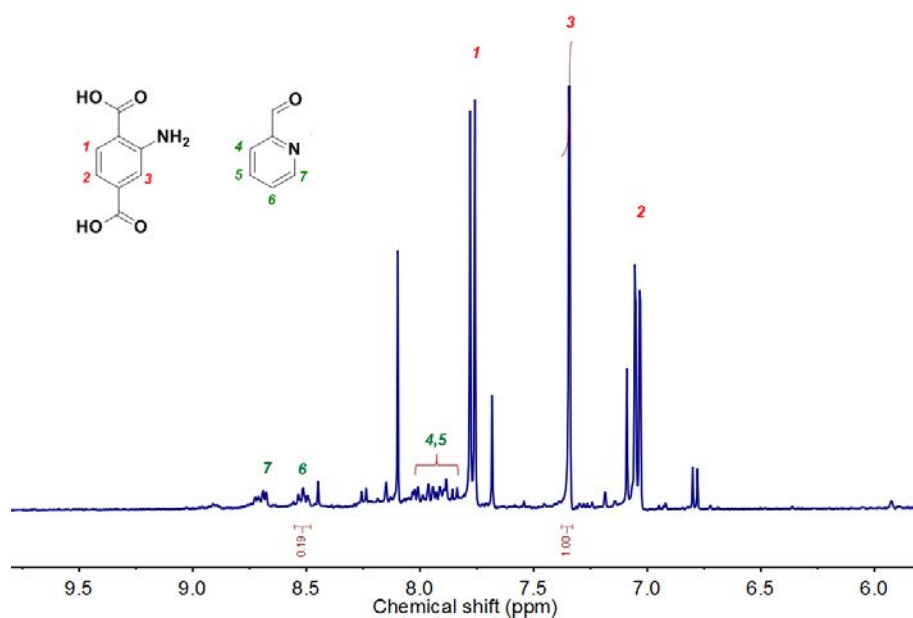


Figure 16.  $^1\text{H}$  NMR spectrum of the digested  $(\text{UiO-66-2PC})_5$  in  $\text{HF/DMSO-}d_6$ .

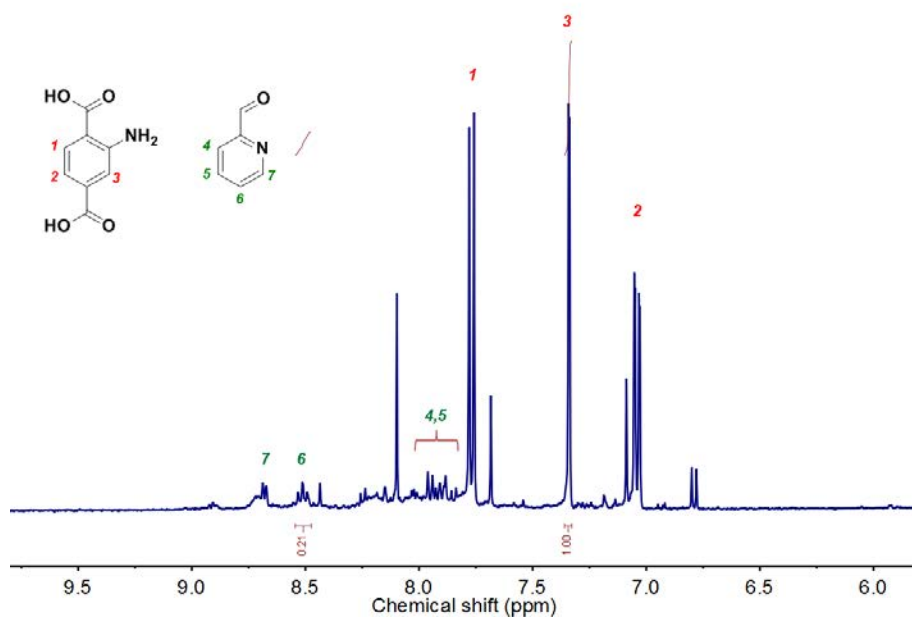


Figure 17.  $^1\text{H}$  NMR spectrum of the digested (UiO-66-2PC)<sub>10</sub> in HF/DMSO-*d*<sub>6</sub>.

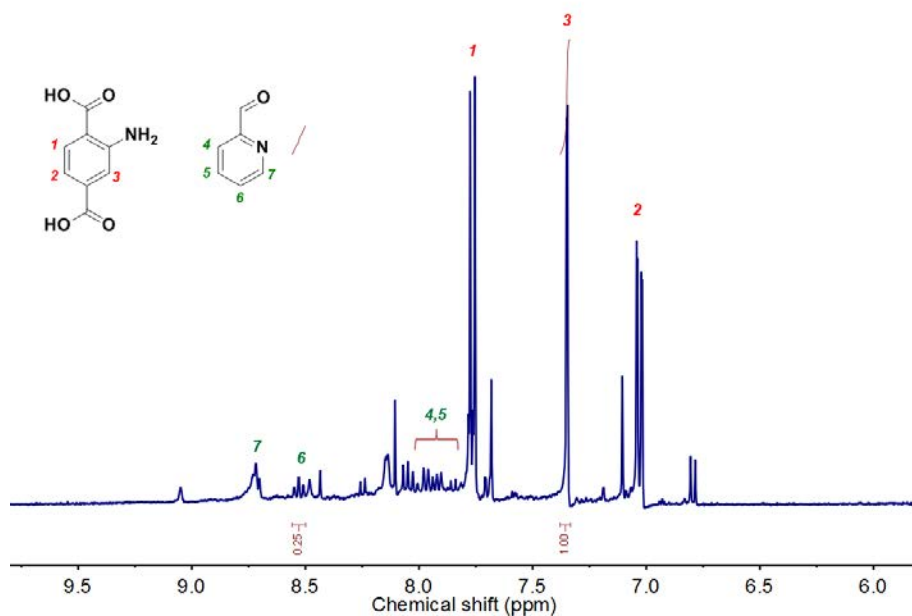


Figure 18.  $^1\text{H}$  NMR spectrum of the digested (UiO-66-2PC)<sub>15</sub> in HF/DMSO-*d*<sub>6</sub>.

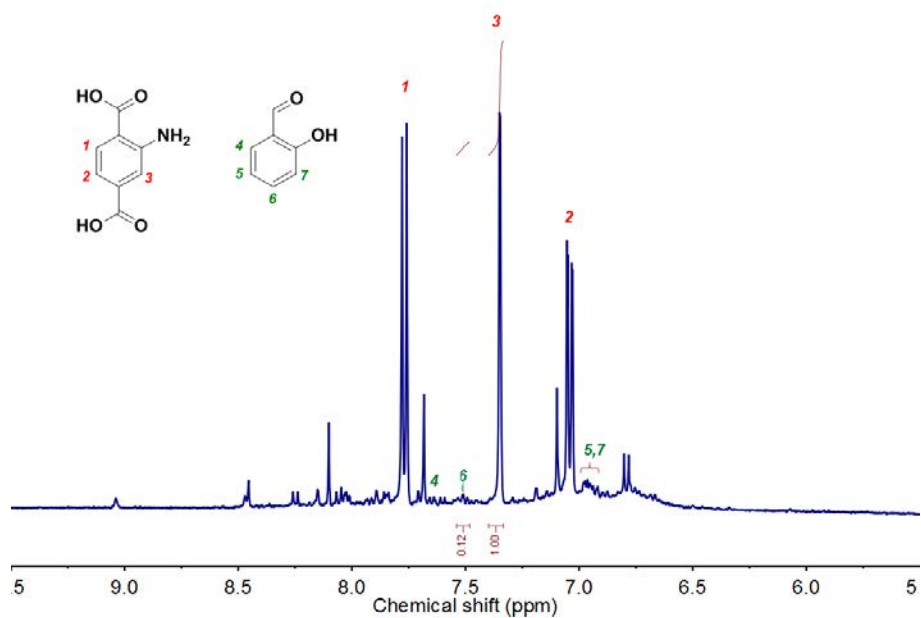


Figure 19. <sup>1</sup>H NMR spectrum of the digested (UiO-66-Sal)<sub>3</sub> in HF/DMSO-d<sub>6</sub>.

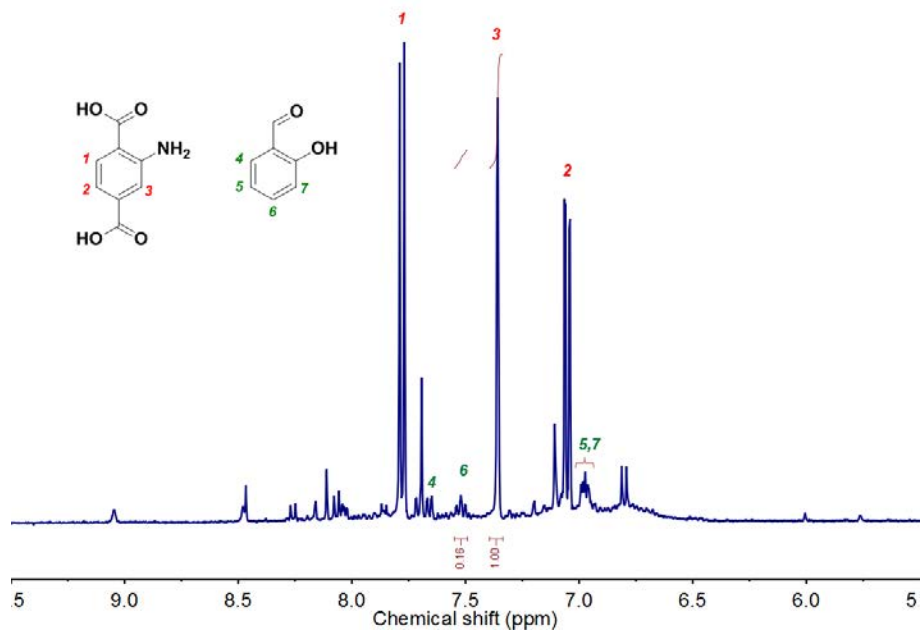


Figure 20. <sup>1</sup>H NMR spectrum of the digested (UiO-66-Sal)<sub>5</sub> in HF/DMSO-d<sub>6</sub>.

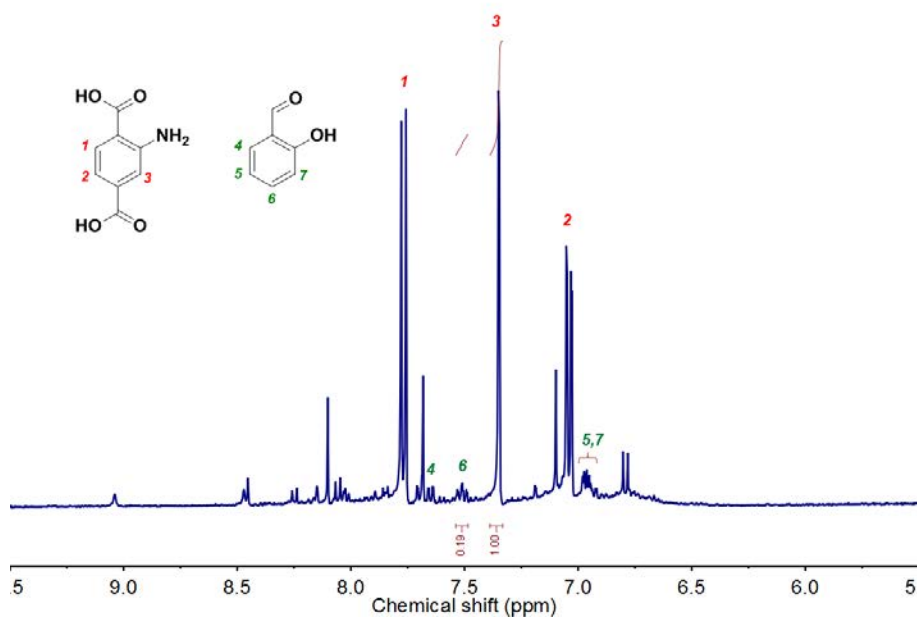


Figure 21. <sup>1</sup>H NMR spectrum of the digested (UiO-66-Sal)<sub>10</sub> in HF/DMSO-d<sub>6</sub>.

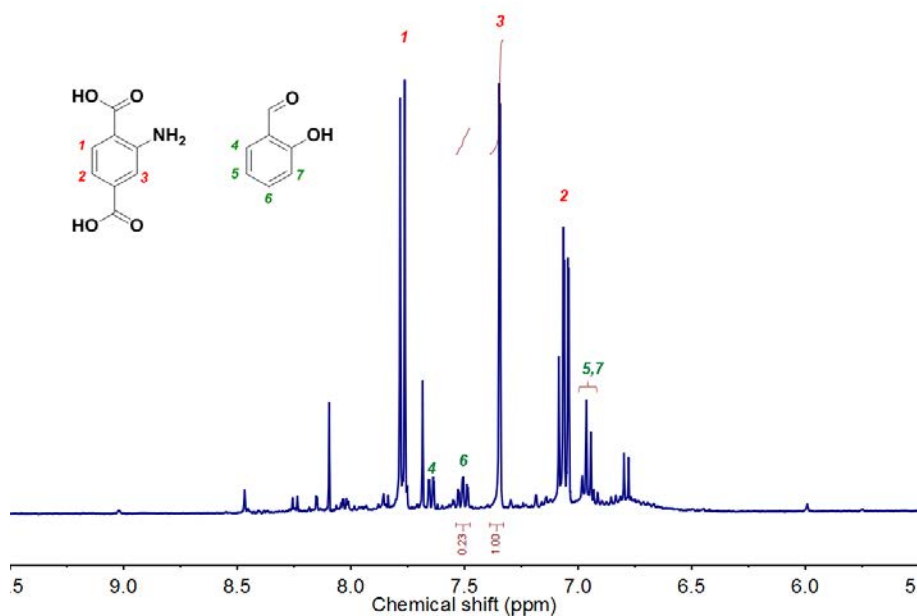
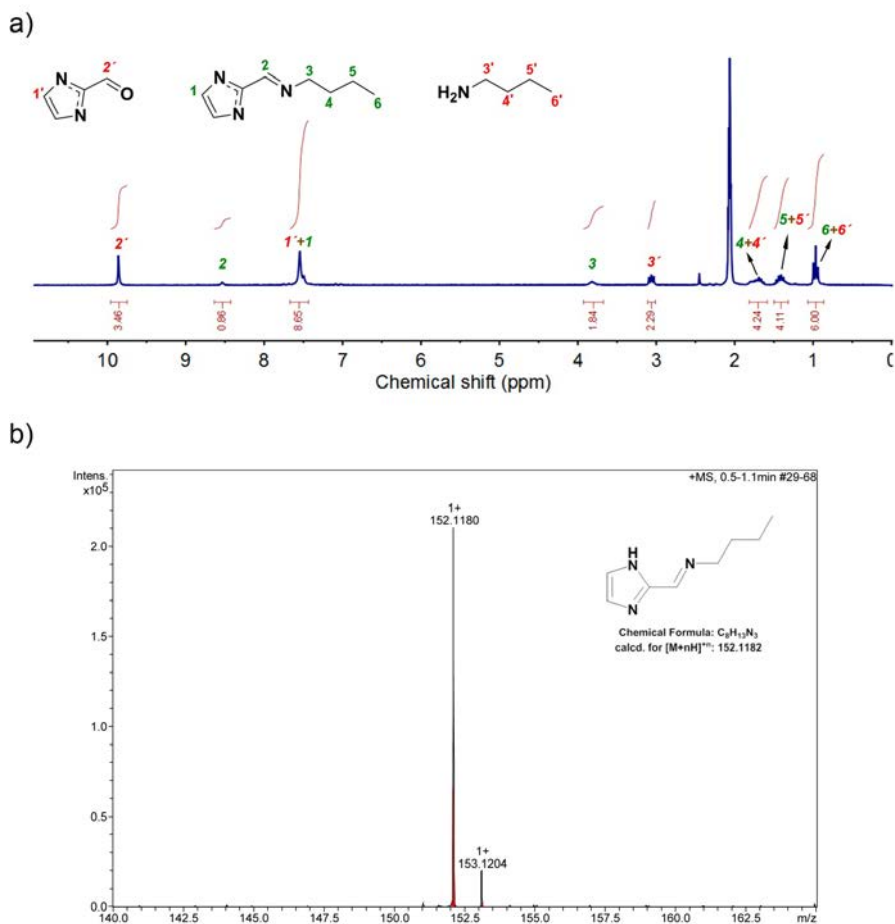
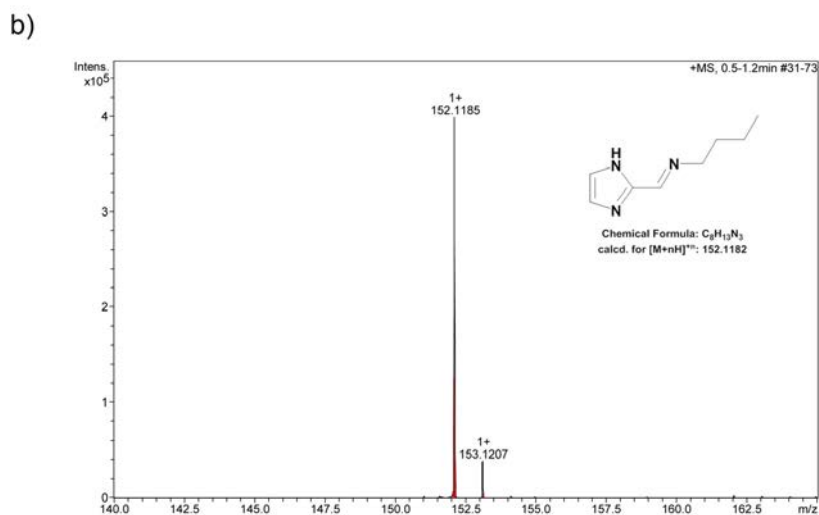
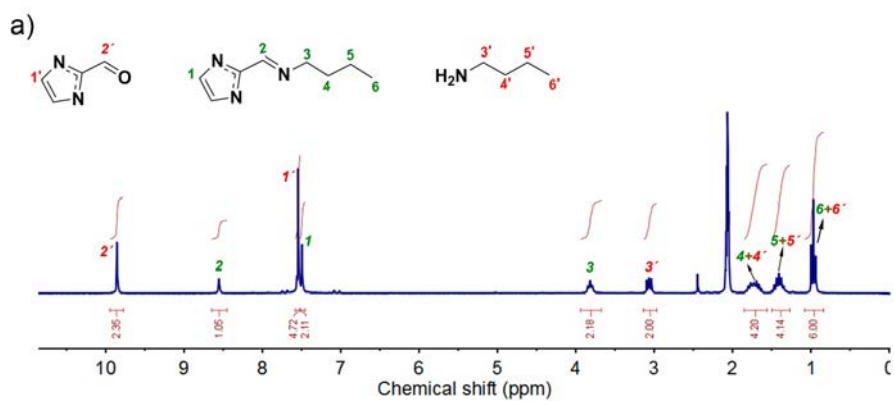


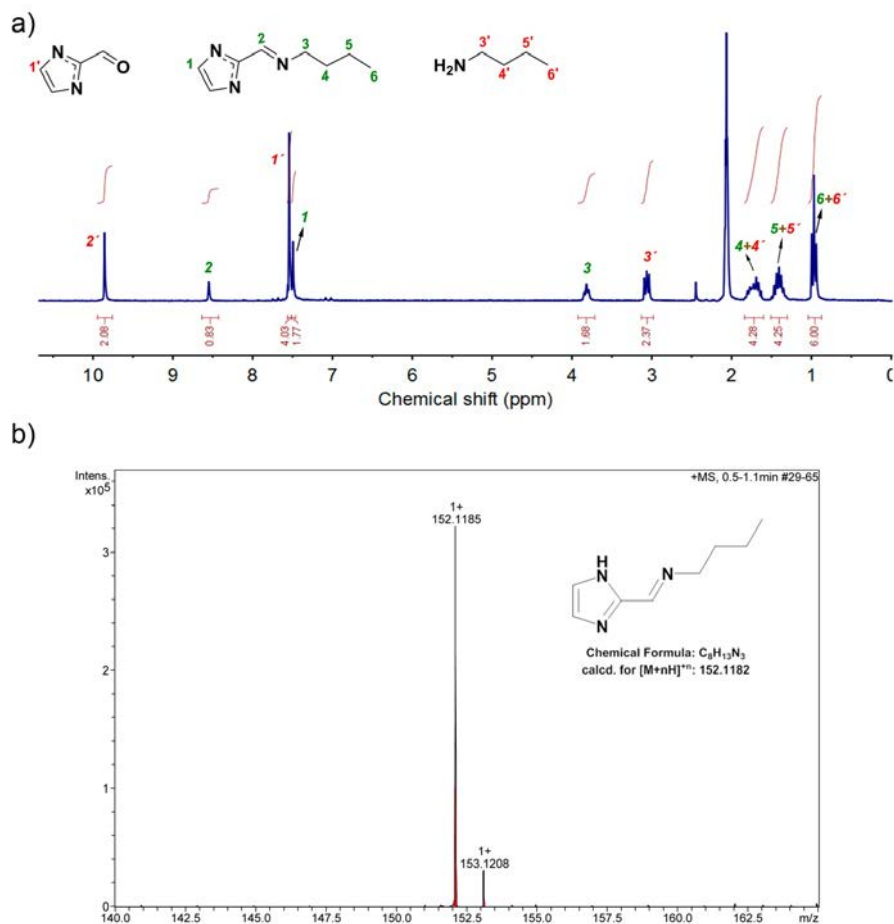
Figure 22. <sup>1</sup>H NMR spectrum of the digested (UiO-66-Sal)<sub>15</sub> in HF/DMSO-d<sub>6</sub>.



**Figure 23.** a)  $^1H$ -NMR spectrum of the digested  $(ZIF-90-BA)_3$  in  $CD_3CO_2D$ . b) ESI-MS spectrum of the digested  $(ZIF-90-BA)_3$  in  $CH_3CO_2H$ .



**Figure 24.** a)  $^1H$ -NMR spectrum of the digested (ZIF-90-BA) $_{10}$  in  $CD_3CO_2D$ . b) ESI-MS spectrum of the digested (ZIF-90-BA) $_{10}$  in  $CH_3CO_2H$ .



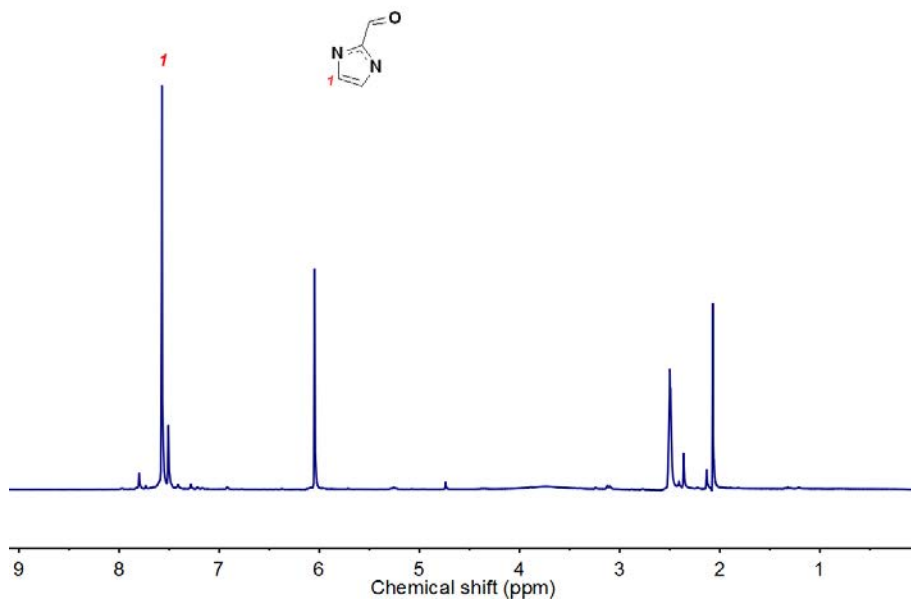


Figure 26.  $^1\text{H}$  NMR spectrum of the digested ZIF-90 in  $\text{DCl}/\text{DMSO}-d_6$ .

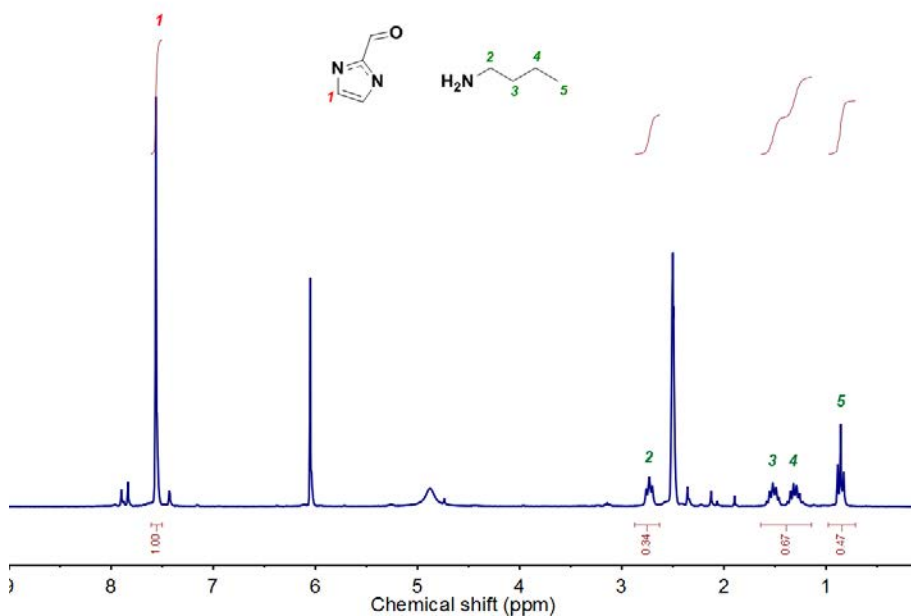


Figure 27.  $^1\text{H}$  NMR spectrum of the digested  $(\text{ZIF-90-BA})_3$  in  $\text{DCl}/\text{DMSO}-d_6$ .

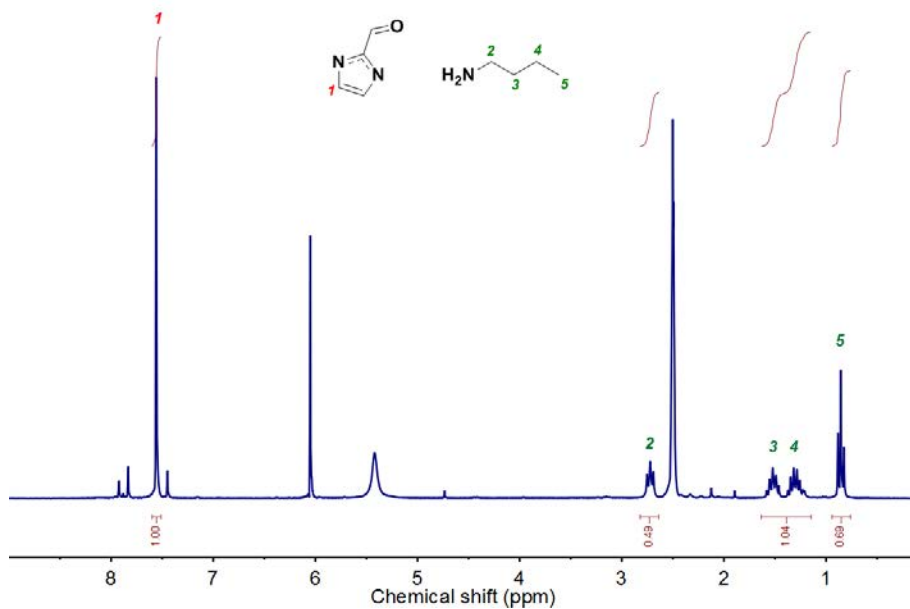


Figure 28.  $^1\text{H}$  NMR spectrum of the digested sample  $(\text{ZIF-90-BA})_{10}$  in  $\text{DCI}/\text{DMSO-}d_6$ .

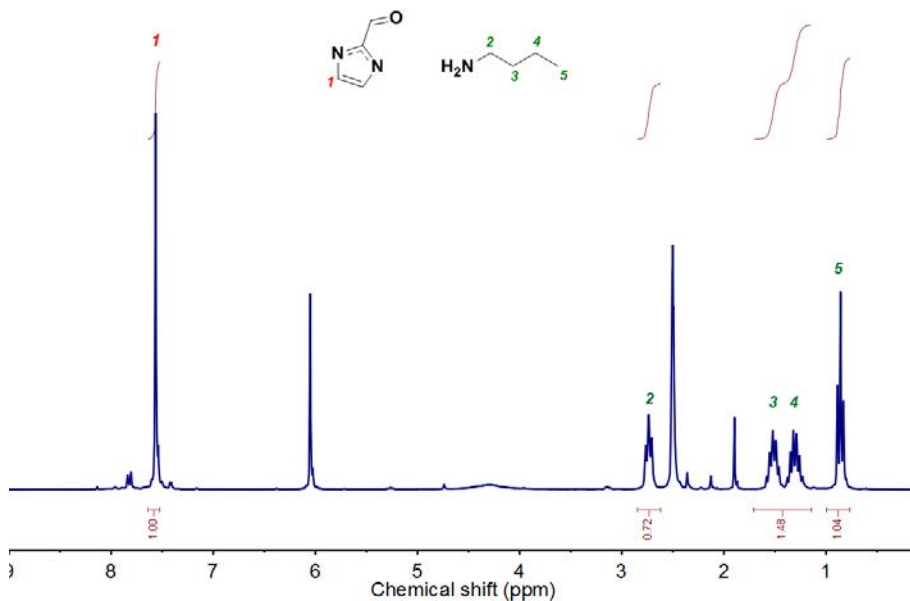
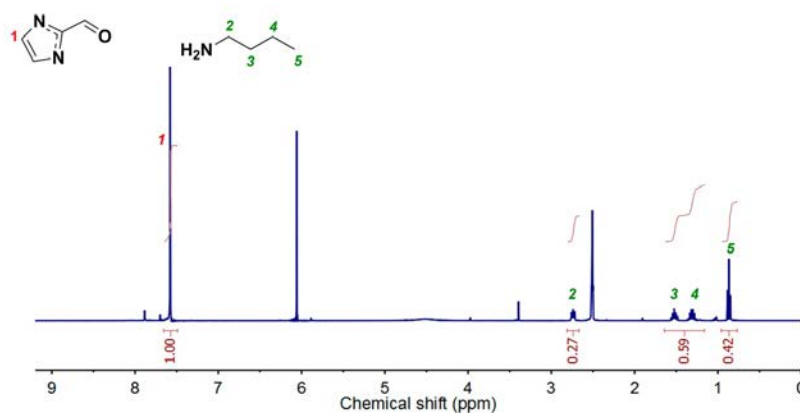
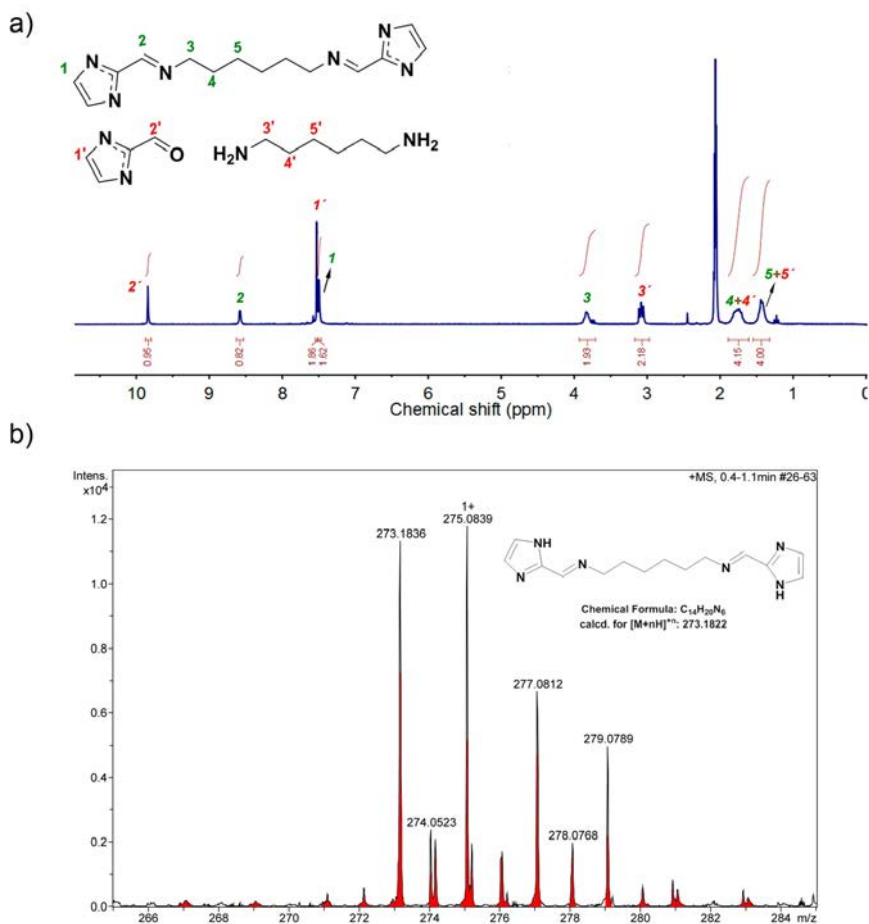


Figure 29.  $^1\text{H}$  NMR spectrum of the digested sample  $(\text{ZIF-90-BA})_{15}$  in  $\text{DCI}/\text{DMSO-}d_6$ .



**Figure 30.**  $^1\text{H}$  NMR spectrum of the digested sample  $(\text{ZIF-90-BA})_{15}$  in  $\text{DCI}/\text{DMSO-d}_6$ .



**Figure 31.** a)  $^1\text{H}$  NMR spectrum of the digested (ZIF-90-HMDA) $_5$  in  $\text{CD}_3\text{CO}_2\text{D}$ . b) ESI-MS spectrum of the digested (ZIF-90-HMDA) $_5$  in  $\text{CH}_3\text{CO}_2\text{H}$ .

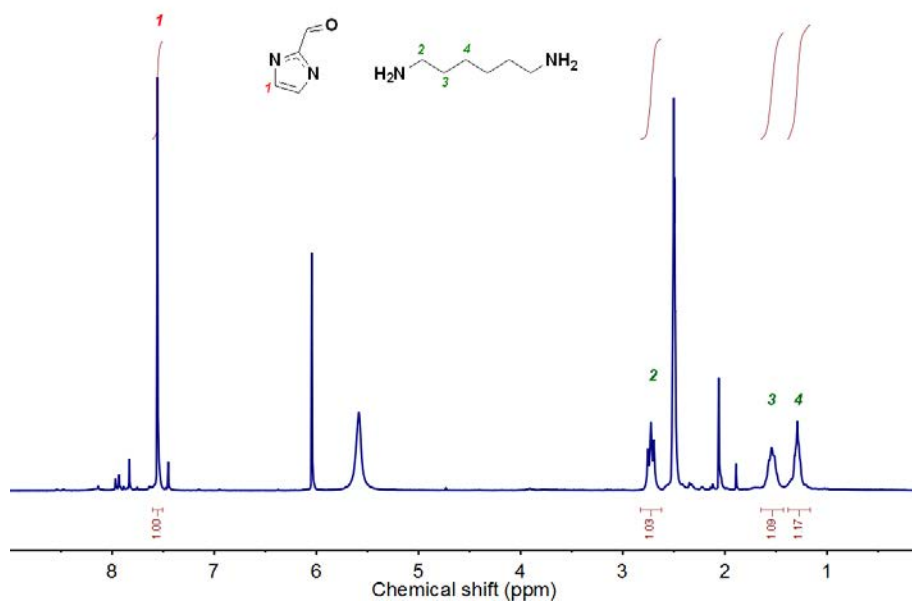


**Figure 32.**  $^1\text{H}$  NMR spectrum of the digested  $(\text{ZIF-90-HMDA})_5$  in  $\text{DCl/DMSO-}d_6$ .